Microstructure and Crystallographic Texture Evolution in TIMETAL® 6-2-4-6 Billet

Nima Nasseri

Department of Engineering Materials

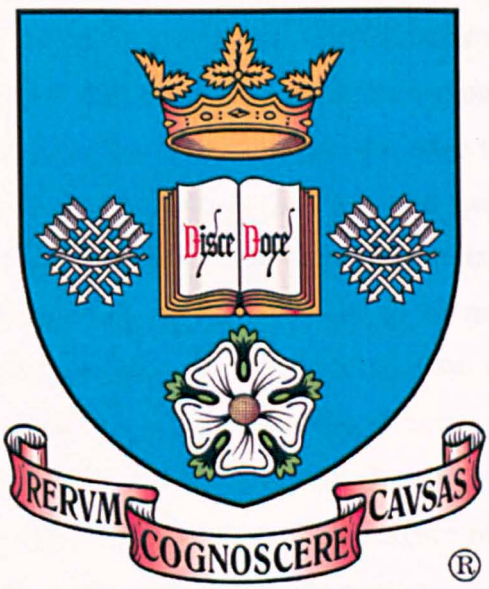

The University of Sheffield

Thesis submitted for the degree of Doctor of Philosophy

May 2009

SUMMARY

The effects of thermomechanical processing via open die forging on the microstructure and crystallographic texture of three different diameter billets of the $\alpha+\beta$ titanium TIMETAL® 6Al-2Sn-4Zr-6Mo were analysed. This work included a quantitative study of primary alpha (α_p) within the microstructure of the three billets with an objective of determining if any variation within the cross-section of the billet could be related back to the macroscopic deformation history during breakdown from the Vacuum Arc Remelting (VAR) ingot.

The metallographic observation within two of the $\alpha+\beta$ TIMETAL® 6Al-2Sn-4Zr-6Mo billets (313 mm and 213 mm diameter), that were manufactured using standard forging routes, revealed a bimodal microstructure consisting of relatively equiaxed α_p within an acicular transformed β matrix throughout the whole cross-section. The results showed, with the exception of the extreme edge to a depth of 10 mm, that the microstructure, at least at the scale at which it was quantified, is homogeneous regardless of its location with respect to the deformation axes. However, despite the microstructure being homogeneous radially, analysis of the microstructure at the centre of the larger billet revealed continuous α grains in addition to a slight increase in the total percentage of α_p volume. Another difference between these two billets was variation in the percentage of α_p volume. Although the total percentage of α_p volume in the larger billet was generally uniform, there was a higher percentage of α_p volume in the smaller sized billet when compared to the larger billet.

A third alternatively forged billet was also analysed. This billet underwent a major difference in its forging route when compared to the standard route in that it was $\alpha+\beta$ forged following the ingot breakdown above β transus temperature therefore resulting in termination of the prestrain and β recrystallisation stages of the standard route. Results showed a significant difference in the α_p size distribution meaning a higher percentage of α_p having a smaller grain size. In fact, the actual scale of the alternatively forged billet microstructure was smaller; however, there were some larger grains demonstrating an inhomogeneous microstructure. In addition, the grains were longer and thinner in shape.

This analysis was then further extended so as to determine whether the same could be said for crystallographic texture using the Electron Back Scatter Diffraction

(EBSD) technique. It was shown that the textures of both large and small diameter billets were strongly dependent on the strain imposed by the deformation process. Macrozones (regions of closely aligned grains) were also observed throughout all three billets stretching along each billet's longitudinal axis. At the edge of the larger billet, however, the widths of the macrozones were wider in comparison to those of the smaller billet. In general, the billets' textures were quite weak, however, there were some noticeable differences in the textures from the edge towards the centre of each billet. At the edge of the billet the crystallographic texture was aligned with the compression direction and, unlike the centre of the billet, had a strong influence of the variant selection mechanism was observed. Deformation symmetry was also particularly noticeable at the centre of the billets. Within the alternatively forged billet, however, it was observed that the strong texture seen at the centre of both previous billets had been replaced by a less intense fibre like texture along the longitudinal direction.

In order to analyse the global texture of the billet using EBSD, it was necessary to examine a number of samples from a variety of locations within the billet. There were, however, disadvantages to this procedure as there was a size limitation per sample and, although many samples were analysed, the results were not complete. For these reasons, heat tinting was used as an alternative method. During this research, results obtained from the heat tinting experiments were subject to adjustment in Corel PHOTO-PAINT and then compared directly to the actual texture measurements obtained by EBSD. The obvious disadvantage of heat tinting in comparison to EBSD was that it could not identify texture at a very specific location or give a very detailed analysis. However, when comparing heat tinting and EBSD images, it was determined that the colours generated by heat tinting gave some degree of texture information as the basal (0001) and pyramidal {10-11} planes could be detected based on the colour of their oxide. Additional advantages of heat tinting were that there was no size limit to the sample (providing that it was possible to grind and polish the sample and a laboratory furnace was available) and the procedure was less time consuming. Heat tinting was also used to confirm the presence of two separate deformation regimes located at the centre and edge of the billets.

TABLE OF CONTENTS

NOMENCLATURE

a	Lattice parameter (Å)
A	Constant (s^{-1})
Al	Aluminium
b	Burgers vector
bcc	Body centred cubic structure
c	Lattice parameter (Å)
c	Material constants (MPa)
Cd	Cadmium
Cl	Chlorine
Cr	Chromium
CR	Cooling rate (K/min)
d	Interplanar spacing between adjacent slip planes (μm)
d	Grain diameter (μm)
EBSD	Electron backscatter diffraction
ED	Extrusion direction
Fe	Iron
hcp	Hexagonal close packed crystal structure
hkl	Miller indices of crystal plane
IMI	Acronym for Imperial Metal Industries
IPF	Inverse pole figure
k	Material constants
k	Rate coefficient (MPa/s)
k_y	Strengthening coefficient ($MPa/\mu m^2$)
LCF	Low cycle fatigue
LS1, LS2, LS3, LS4	Samples taken from the large billet (plane parallel to the billet axis)
M_f	Martensitic finish temperature (°C)
Mg	Magnesium
MMC	Metal matrix composite
Mo	Molybdenum
M_S	Martensitic start temperature (°C)

Na	Sodium
Nb	Niobium
ND	Normal direction
NS1, NS2, NS3, NS4	Samples taken from the alternative forged billet (plane perpendicular to the billet axis)
NS1'	Samples taken from the alternative forged billet (plane parallel to the billet axis)
ODF	Orientation distribution function
OIM	Orientation Imaging Microscopy
PMC	Polymer matrix composites
Q	Activation energy (kJ mol^{-1})
R	Universal gas constant (kJ $mol^{-1}K^{-1}$)
R1, R2	Orthogonal marks placed on the billet at an intimidate stage of the processing
RD	Rolling direction
r	Crystallographic direction
S1, S2, S3, S4	Samples taken from the small billet (plane parallel to the billet axis)
S1', S2', S3'	Samples taken from the small billet (plane perpendicular to the billet axis)
SE	Secondary-electron
SEM	Scanning Electron Microscopy
Si	Silicon
Sn	Tin
T	Temperature (K)
Ta	Tantalum
TD	Transverse direction
TEM	Transmission Electron Microscopy
Ti	Titanium
TMP	Thermomechanical processing
uvw	Miller indices of crystal direction
V	Vanadium
VAR	Vacuum Arc Remelting
VF	Volume Fraction

Z	Longitudinal billet axis
Zn	Zinc
Zr	Zirconium
α	Alpha phase of titanium
α'	Martensitic alpha morphology
α''	Orthorhombic martensite alpha morphology
α_p	Primary Alpha grain morphology
α_s	Secondary (transformed) Alpha morphology
β	Beta phase of titanium
θ	Angle between the incident ray and the scattering planes (radians)
φ_1, ϕ, φ_2	Euler angles
σ_o	Constant for the friction stress for dislocation movement (MPa)
σ_y	Yield stress (MPa)
τ	Shear stress (MPa)

AKNOWLEDGEMENTS

The realisation of this project would not have been possible without the help of many individuals, the majority of whom I did not even know before I embarked on this project.

My special thanks go to **Dr Brad Wynne** who assisted me at every step. He helped me with research which I could not do myself. On more than one occasion he saved me from what could have been important oversight and omission. I am also very grateful to **Prof Mark Rainforth** for his encouragements during my PhD and for his assistance. I wish to acknowledge TIMET UK. More specifically, thanks to **Dr Andrew Wilson** for providing me with research material and his contribution in terms of technical and industrial information. I wish to thank **IMMPETUS** and the **EPSRC** for their research project and financial support. I would like to express my gratitude to the **technical staff** of the Engineering Materials. I would like to thank to my close family and friends, who throughout these long three years have provided much needed entertainment and enjoyment. Special thanks to my **colleagues in D1**, for the friendly and enjoyable atmosphere. Matt, Pete, Mohammad who helped me with my work; Oliver and Moi who helped me with my modelling; Ollie and Simon my lunch buddies; Sinan, Nelson, Rahul, Magda, Mike, John, Mohammad, Rob, Lin, Jody, Dave and John who assisted with a wide variety of things and to Quake, Kdice, Worms and Miniclip games for providing me with no end of distractions from my research. I would like to thank my partner, **Esther**, who gave me peace of mind in a time of uncertainty and when I needed it the most. She patiently put up with my anxieties of odd hours of the day and night over the three years of my research, and who read the whole manuscript. I would like to thank her for her constant presence and for helping with every word on every page. And finally I would like to express my most special tribute to **Mehdi** my father, teacher and friend who taught me moral values and **Mitra** my mum who taught me compassion and courage. I would like to thank them for giving me what I needed in life to learn and grow into the person I am today and I will always be grateful for giving me time to dream and reason to believe in myself.

I would like to dedicate this thesis to the wonderful memories of two remarkable people, **Morteza** and **Mostafa**, my grandfathers.

God bless you all....

Chapter 1

INTRODUCTION

The breakdown of vacuum arc remelted (VAR) titanium alloy ingot to billet involves a number of thermomechanical processing stages via open die forging. Typically the forging is carried out using a cogging press in which the metal is forged incrementally along its length between two radiused tools during which it may be rotated by various amounts to generate cross-sectional shape change from the initial round ingot though to squares, octagons etc. to produce the finished round bar [1]. Such a process route inherently produces a non-uniform strain distribution from the surface to the centre and a complicated deformation symmetry history to the final product [2, 3]. It is, however, unclear due to a lack of systematic studies to what extent the final microstructure and crystallographic texture varies through the cross section of the billet due to the process route. Of the data available, the majority does not clearly state where the analysis took place in terms of the location within the billet cross-section and/or does not have any knowledge of the prior deformation history [4-7]. In this work the deformation axes have been noted at an intermediate stage of processing and these were retained on the final billet. Hence, all analysis of the microstructure and texture can be investigated with respect to these critical axes.

The work itself was done in collaboration with Timet UK as part of on-going work to identify and quantify the critical process parameters and microstructure features of aerospace titanium billet which determine subsequent forging or in-service performance.

1.1 Project aim

The aim of this work is to investigate the microstructure and crystallographic texture evolution of two different sized billets of the same forging process route and one alternatively forged billet of the $\alpha+\beta$ alloy TIMETAL® 6Al-2Sn-4Zr-6Mo taking their industrial process history into account.

1.2 Project objectives

- Using optical metallography and image analysis techniques, microstructure of the α+β alloy TIMETAL® 6Al-2Sn-4Zr-6Mo will be analysed taking its process history into account.
- Using established texture determination techniques, in particular electron backscattering diffraction, the crystallographic texture evolution of the α+β TIMETAL® 6-2-4-6 will be investigated under conditions applicable to the manufacture of billet materials via hot working (taking process history into account).
- Using heat treatment to build a thin layer of oxide film on a well polished surface of titanium, investigate the potential of correlating the optical metallographic contrast generated by the oxide to the underlying crystallographic texture . This is to see if a quick and cheap method can be found to identify texture or at least large regions of similar texture within large scale billet.

1.3 Thesis outline

The following thesis will document the achievement of said aim using said objectives and shall be structured in the following way in seven chapters;

Chapter two provides background information about titanium alloys, introducing why titanium is so widely used in many industries in particular the aerospace industry, the microstructures of titanium alloys and an understanding of their relationships with mechanical properties. This is to gain an understanding and appreciation of the theoretical background behind the major issues of this work, i.e. metallurgy, classification, microstructure, crystallographic texture etc.

Chapter three outlines the production of the α+β alloy TIMETAL® 6Al-2Sn-4Zr-6Mo from the point of sourcing raw materials through to the supplying of the billet to the component manufacturer. This was necessary in order to understand the effects of the process history on the final products. The chapter then describes the experimental techniques used in this work in detail. And finally the proportion, size and shape distribution of primary α (α_p) within the cross section of two different diameter billets of the α+β TIMETAL® 6Al-2Sn-4Zr-6Mo alloy were analysed. This

is undertaken with a specific aim to determine if the prediction of this critical microstructure feature requires taking process history, e.g. strain path, into account or that simpler relationships, e.g. using total equivalent tensile strain, can be used for microstructure models for the prediction of the size, shape and distribution of the α phase.

Chapter four consists of concise background information about the crystallographic texture in titanium alloys. It then investigates the texture evolution of the α+β TIMETAL® 6Al-2Sn-4Zr-6Mo during billet manufacture. Textures were analysed in four longitudinal slices at the centre and edge of each billet. The aim was to find out if any texture variation within the billet cross-section can be related back to deformation history during breakdown from the VAR ingot. The EBSD results gained were presented as Euler and IPF colouring, Orientation Image Maps and pole figures.

Chapter five discusses the microstructure and texture evolution of an alternative α+β forging route for TIMETAL® 6Al-2Sn-4Zr-6Mo during billet manufacture. The major difference in the production route of this billet compared to those in previous chapters was the absence of an intermediate prestrain and recrystallisation stage. Unfortunately, unlike the previous billets, deformation axes had not been noted at an intermediate stage; therefore, samples were picked randomly and they are not linked to any specific forging directions. The objective of this chapter was to determine the microstructure and texture variation within the billet cross-section to observe the effects of the alternative α+β forging route on the TIMETAL® 6Al-2Sn-4Zr-6Mo billet.

In **Chapter six** a new technique (heat tinting) is introduced in order to qualitatively identify texture. Heat tinting is acknowledged as being a very simple metallographic method that can provide a certain degree of orientation information both easily and inexpensively on a larger scale than the EBSD method. In this chapter heat tinting results were compared to those of other characterisation techniques (EBSD) to show that features such as texture bands (macrozones) can be detected both easy and fast without employing expensive techniques such as EBSD.

Chapter seven summarises the principal observations and draws some conclusions from this work and also suggests some key areas that would be usefully investigated if any further work was undertaken.

Please note, a combined results and discussion section has been included at the end of each chapter due to the large number of similar graphs, figures, crystal

orientation maps and pole figures etc within this thesis. It was deemed more suitable to include the discussion at the end of each chapter in order to fully evaluate each section thus reducing any confusion and creating a more understandable argument.

Chapter 2

BACKGROUND AND LITERATURE REVIEW

2.1 The key concepts of titanium metallurgy

2.1.1 History

For at least 200 years titanium has been known as an element (Symbol Ti; atomic number 22; and atomic weight 47.9). Yet, its commercial production did not start until the 1950s. At the time, titanium was used for critical high-performance aircraft components, such as jet engines and airframes because of its strategic importance as a high strength, lightweight material. The worldwide production of this metal and its alloys has since grown to more than 50 million pounds (22679 tonnes) annually. Today, titanium alloys are common, readily available engineered metals that compete directly with other metals such as stainless steels, copper alloys, nickel based alloys and composites and are gaining increased interest by other markets such as architecture, chemical processing, medicine, power generation, sports and leisure, transportation and military [8].

Titanium is the ninth most plentiful element and the fourth most abundant structural metal in the Earth's crust, exceeded only by aluminium, iron, and magnesium. However, it is rarely found in high concentrations and never found in a pure state. Consequently, the difficulty in processing the metal makes it expensive [9].

2.1.2 Production of titanium

Rutile is a major mineral source of the element titanium, which typically consists of approximately 97 to 98 % titanium dioxide (TiO_2). The titanium oxide in the rutile is first chemically converted to pure titanium tetrachloride ($TiCl_4$). The two primary processes for creating raw titanium from $TiCl_4$ are shown below [10];

1) The Kroll process in which $TiCl_4$ is reacted with magnesium in a closed stainless-steel vessel. The end products of this high temperature reaction are titanium

sponge, magnesium chloride ($MgCl_2$), and some excess magnesium. The chemical reaction is shown below;

$TiCl_4$ (gas) + 2Mg (liquid) → Ti (Solid) + $2MgCl_2$ (liquid) [Temperature 773 to 873°C] (2.1)

2) Hunters process where $TiCl_4$ is reacted with sodium instead of magnesium. In this process the reduction of $TiCl_4$ can be carried out in two steps resulting in very high quality titanium. The chemical reaction for step one is shown below;

$$TiCl_4 + 2Na \rightarrow TiCl_2 + 2NaCl \quad (2.2)$$

In the second step the melt containing the $TiCl_2$ and NaCl is reacted with additional sodium in a sinter pot which has an upper atmosphere of argon gas (Figure 2.1). The reaction is carried out at temperatures below 1037°C and is shown below;

$$TiCl_2 + 2Na \rightarrow Ti + 2NaCl \quad (2.3)$$

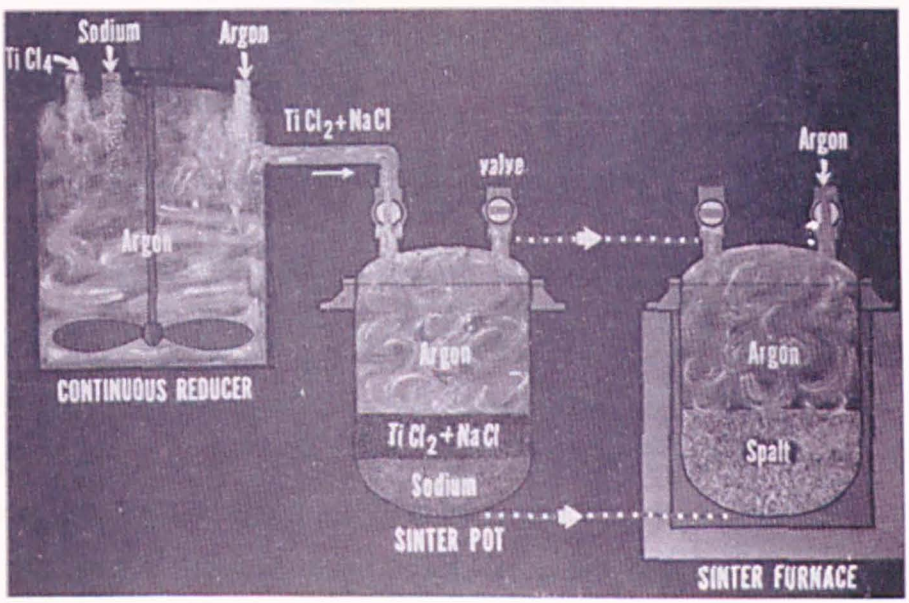

Figurer 2.1 Processing steps in the production of titanium sponge from $TiCl_4$ and Na by the Hunter process [10].

2.1.3 Preparation of titanium ingots

Titanium sponge is crushed and compressed into electrode compacts which are welded together to form a long consumable electrode for vacuum arc remelting (VAR) (Figure 2.2). VAR has many advantages including high purity, good control and reproducibility in the product. Also since molten titanium reacts with oxygen and nitrogen in air, VAR is necessary to prevent the molten titanium from reacting with the oxygen and nitrogen in the air. Care, however, must be taken to keep the electrodes off the floor as they can pick up contaminants which will also affect the chemistry of the product if carried into the furnace.

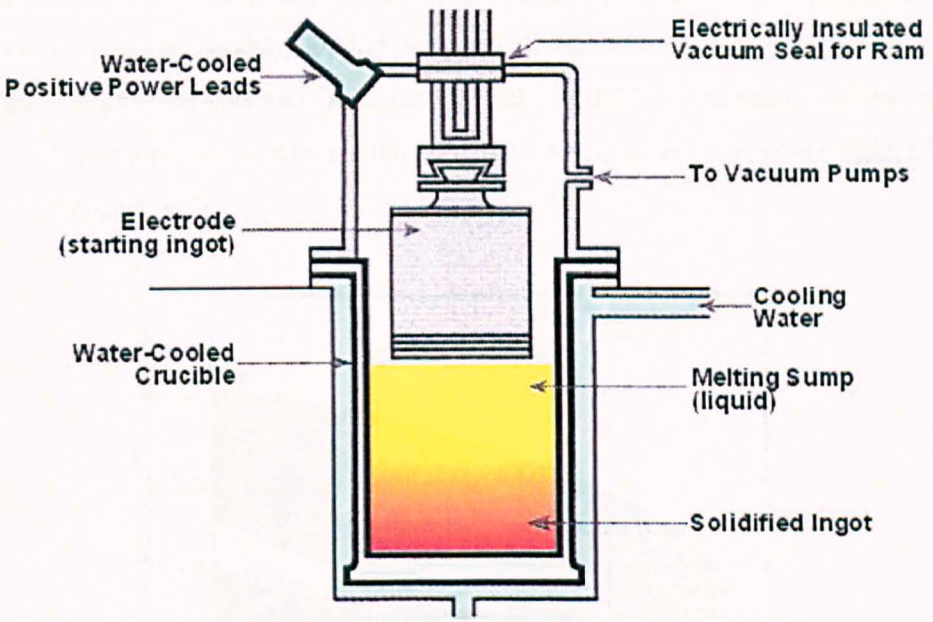

Figure 2.2 A schematic of a typical Vacuum Arc Remelting unit [11].

In the VAR process the consumable compacted electrode (anode) is placed within a water or sodium cooled copper crucible (cathode). An arc is then initiated between the electrode and the copper crucible causing the electrode to melt. Therefore, the molten metal collects and solidifies in the copper crucible. Any slag etc. will rise to the top and can be scalped on solidification leading to a high purity and homogeneous final product.

For alloy ingots the alloying materials are mixed with the crushed titanium sponge before compacting. Alloying additions must be uniformly distributed throughout the long consumable electrode. Double or even triple melting is then used for alloy

ingots to ensure maximum homogeneity of the ingots. In this process, the ingot from the first melting serves as the electrode for the second melting. After each melt the electrode is inverted so that any solidification induced segregation is distributed and broken up slightly [10, 12]. A much more detailed explanation of the VAR process and alloy development for alloys such as TIMETAL® 6Al-2Sn-4Zr-6Mo is given in more detail in Chapter 3 Section 3.1.3.

2.1.4 Introduction to titanium and its applications

The fast growth of the titanium industry is evidence to the metal's high specific strength and corrosion resistance. With density about 55% that of steel, titanium alloys are widely used for highly loaded aerospace components that operate at low to reasonably high temperatures of approximately 600°C[13]. Examples of the relative strength of titanium alloys when compared with steel, nickel and other light alloys is shown in Figure 2.3 [14].

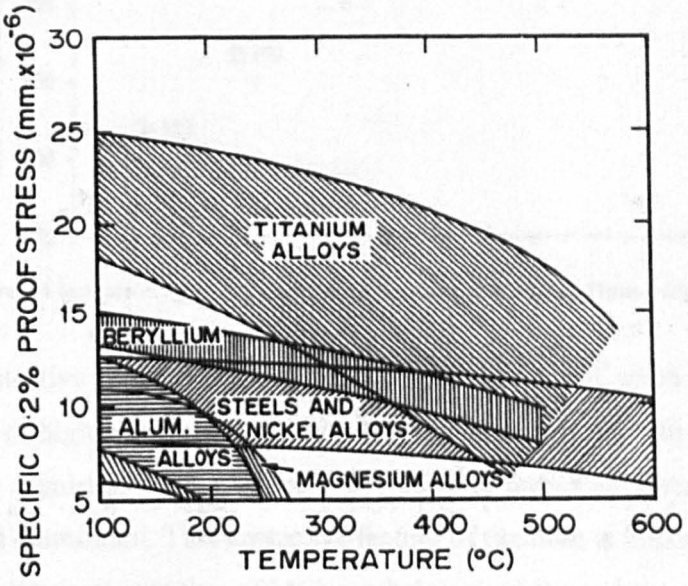

Figure 2.3 Plot of proof stress vs. temperature for light alloys, steels and nickel alloys [14].

The potential of titanium to the aerospace industry can be seen in a comparison of an aero-engine compressor rotor; compared to a rotor of hybrid titanium/nickel assembly an all titanium rotor can save 20% total weight [13]. Additional problems such as thermal expansion and modulus mismatches that can generate considerable stresses

and in extreme cases lead to the failure of a component, may also be eliminated by the use of an all titanium rotor.

The reasonably high in-service temperatures that can be obtained are based on the formation of a highly adherent, non-porous, stable oxide on its surface which protects the base metal from a number of aggressive environments up to temperatures as high as approximately 600° C [15]. Formation of this protective oxide layer can be an important design aspect. This passive behaviour also makes the metal ideal for use in other aggressive environments such as salt water as well as in the production of chemical processing equipment, surgical implants and prosthetic devices [16, 17]. The operating temperatures for various titanium alloys are shown in Figure 2.4.

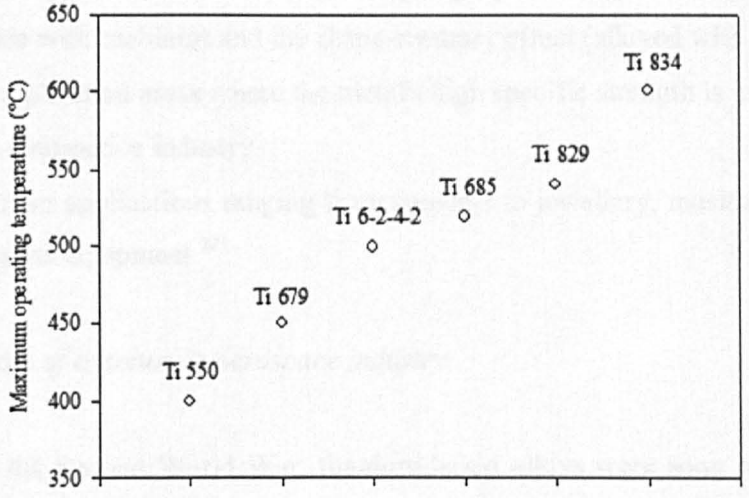

Figure 2.4 Increase in maximum operating temperatures for various Timetal alloys [15].

The protective oxide layer also protects the base metal when in direct contact with a material of higher electro-potential (carbon fibre composites for example), which could generate a galvanic corrosion cell and corrode untreated metals such as steel, magnesium and aluminium. This protective feature of titanium is important as more and more polymer matrix composites (PMC) are being used throughout aircraft structures [18].

Other advantages of titanium include: low coefficient of thermal expansion, low magnetic permeability, high toughness, and low heat-treating temperature during hardening [19, 20, 21].

The unique properties of titanium make it attractive to designers in a variety of applications. Compared to steel and aluminium, titanium is still fairly expensive but increasing use of the metal is expected to accelerate cost reductions, resulting in still more growth in application diversity. Some of these applications, which were taken from *ASM Handbook* Volume 2, are shown below [16]:

- Applications where titanium is used for its resistance to corrosion, such as chemical processing, the pulp and paper industry, marine applications, and energy production and storage
- Biomedical applications that take advantage of the metal's inertness in the human body for use in surgical implants and prosthetic devices
- Special applications that exploit unique properties such as superconductivity (alloyed with niobium) and the shape-memory effect (alloyed with nickel)
- New application areas where the metal's high specific strength is important, such as the automotive industry.
- Consumer applications ranging from cameras to jewellery, musical instruments, and sports equipment [22].

2.1.5 The role of titanium in aerospace industry

After the Second World War, titanium-based alloys were soon considered key materials for aircraft engines. As mentioned before, the exceptional properties of titanium alloys include high specific strength and excellent corrosion resistance. Thus, titanium alloys are found in aerospace applications where the combination of weight, strength, corrosion resistance and/or high temperature stability of aluminium alloys, high strength steel, or nickel based super alloys are insufficient. The main drivers for titanium's use in aerospace applications are:

- Weight saving (primarily as a steel replacement)
- Application temperature (aluminium, nickel, steel alloys replacement)
- Corrosion resistance (replace aluminium and low alloy steels)
- Composite compatibility (replace aluminium alloys)
- Space limitation (replace aluminium alloys)

The gas turbine engine is the main area of application for aerospace titanium alloys. Roughly one third of the structural weight of modern turbine engines is made up of titanium. It is the standard engine material alongside nickel-based super alloys and without a doubt, the titanium content in the gas turbine engine has steadily increased since its first introduction at the beginning of the 1950s by Pratt & Whitney in the USA and Rolls-Royce in England [9, 17].

The first engine components to be made from titanium were compressor blades, with titanium compressor disks being introduced next. Fan disks and the large front fan blades of modern jet engines are now often made from titanium alloys too. Figure 2.5 a) and b) illustrates the scale of such components [9, 17].

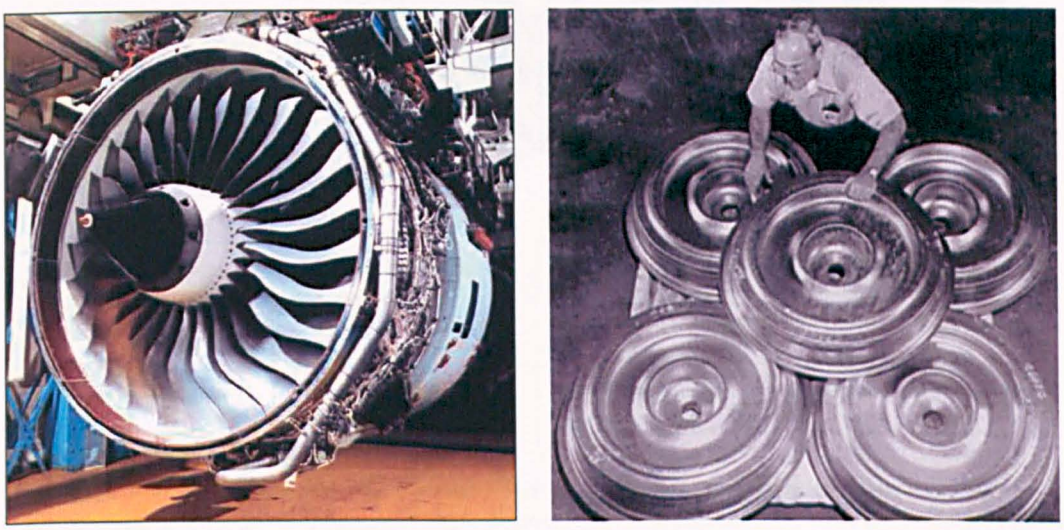

a) b)

Figure 2.5 a) Front fans of commercial Rolls Royce Trent engines made of Ti-6Al-4V **b)** Forged Ti-6Al-4V jet engine fan disks (890 mm in diameter and weigh 249 kg) [22, 23].

2.1.6 Titanium alloys in today's engine and future needs

Figure 2.6 shows the volume fractions of titanium alloy classes in a modern aero-engine plus the future requirements going beyond the potential of today's alloys. Because of its low cost and manufacturers' long experience with the alloy, Ti-6Al-4V is used where the service temperature allows it. Ti-6Al-2Sn-4Zr-2Mo is another standard material which is used for higher temperature. Ti-6Al-2Sn-4Zr-6Mo and IMI834 are materials for special purposes (i.e. higher strength at higher temperature, although they cost more) [24].

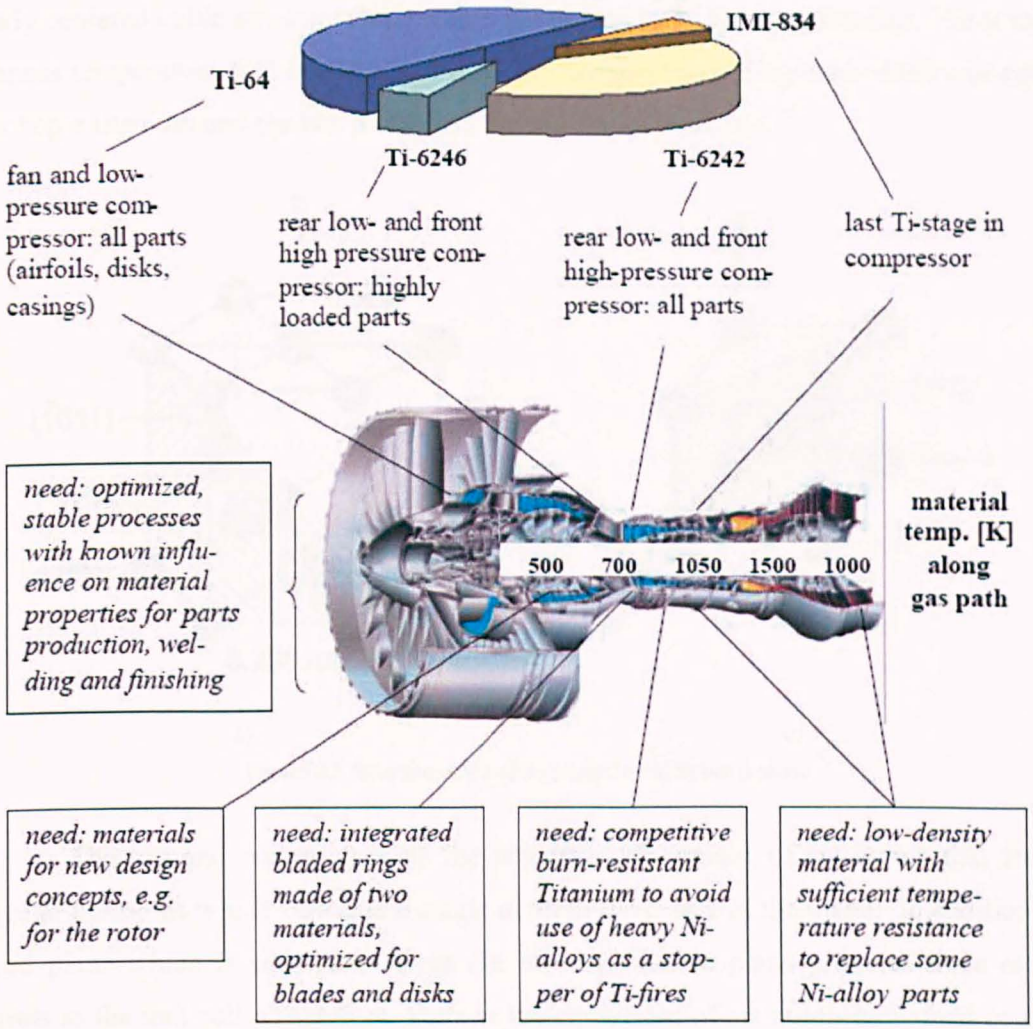

Figure 2.6 Upper diagram: today's volume fractions of Ti-alloy classes in an aero-engine. Immature materials are not included. In lower part of the figure example for titanium made engine parts and some future requirements beyond the standard materials are given [24].

2.2 Metallurgy of titanium alloys

2.2.1 Crystal structure

Titanium can crystallise into various crystal structures like a number of other metals (e.g. iron, zinc, tin). But, each allotriomorph is only stable within particular temperature ranges. The complete transformation from one into another crystal structure is called an allotropic transformation; the respective transformation temperature is called the transus temperature.

Pure titanium crystallises at a low temperature in a hexagonal close packed structure (hcp), recognised as alpha (α) titanium. At high temperature however, it has a

body centered cubic structure (bcc) which is referred to as beta (β) titanium. The α to β transus temperature for pure titanium is 882±2°C. Schematic diagrams of the unit cells for hcp α titanium and the bcc β titanium are shown in Figure 2.7 [9].

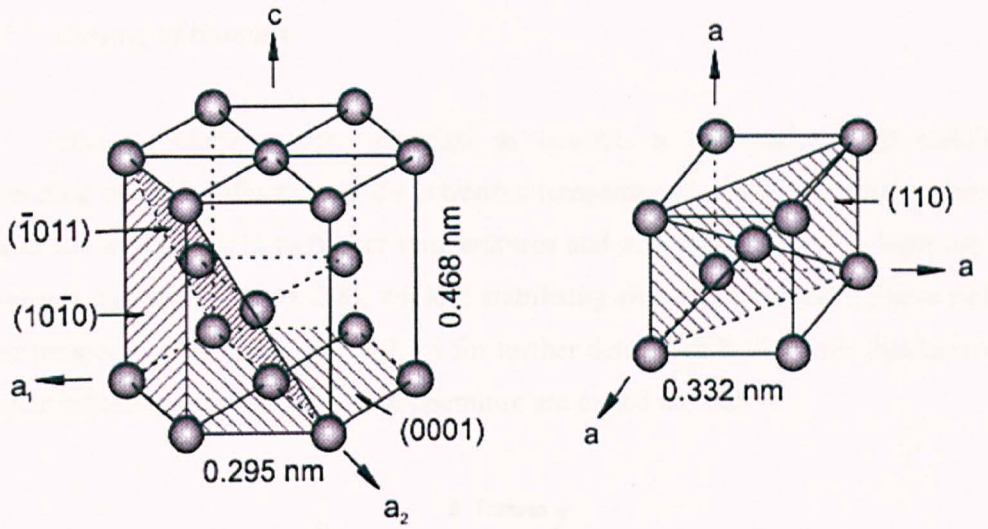

Figure 2.7 Structure of the **a)** hcp α phase and **b)** bcc β phase [9].

The top and bottom face of the hcp unit cell consist of six atoms that form regular hexagons which surround a single atom in the centre of the plane. In addition, a third plane which is situated between the top and bottom plane provides three extra atoms to the unit cell. Therefore, there is the equivalent of six atoms contained in one unit cell: one-sixth of each of the 12 top and bottom face corner atoms, one half of each of the 2 centre face atoms and all 3 mid plane atoms (Figure 2.7 a).

Figure 2.7 a) also highlights the two lattice parameters required to define the unit cell. *a* and *c* represent, respectively, the short and long unit cell dimensions. For α titanium the lattice parameters of hcp crystal structure are a=0.295nm and c=0.468nm, resulting in a *c/a* value of 1.587. For an ideally close packed hexagonal lattice the *c/a* ratio is 1.633. The figure also illustrates the three most close packed planes of the hexagonal unit cell, the (0001) plane, also called the basal plane, $\{10\bar{1}0\}$ planes, known as prismatic planes and $\{\bar{1}011\}$ planes, known as pyramidal planes.

The bcc unit cell consists of a cube with atoms located at all the corners and a single atom at the centre of the cube. Consequently, there is the equivalent of two atoms in one unit cell: one atom from the eight corners and the single atom in the centre. To completely define the unit cell only one lattice parameter, *a*, is required as

shown in Figure 2.7 b). For β-titanium the value of *a* is 0.332 nm. Figure 2.7 b) also shows the six most densely packed lattice planes of the bcc structure which are the {110} planes [9, 12, 25] (See Section 2.4 for further detail).

2.2.2 Alloying of titanium

Alloying elements are classified as neutral, α stabilisers, or β stabilisers (depending on their influence on the β transus temperature). The α stabilising elements expand the α phase field to higher temperatures and also allows the development of a two-phase α+β field (Figure 2.8), while β stabilising elements shift the β phase field to lower temperatures (See Section 2.2.3.4 for further detail) while elements that have only a minor influence on the β transus temperature are called neutrals [9].

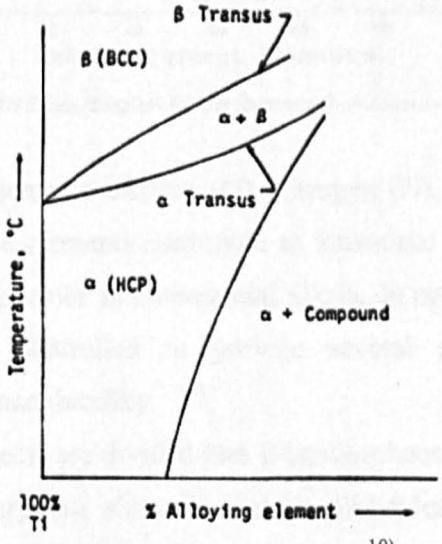

Figure 2.8 Alpha stabilised system [10].

Aluminium is the most widely used α-stabilising element in titanium alloys as it is the only common metal that raises the β transus temperature and has a large solubility in both the α and β phase [26]. The strong effect of aluminium in raising the β transus of titanium is shown in the Ti-Al phase diagram of Figure 2.9.

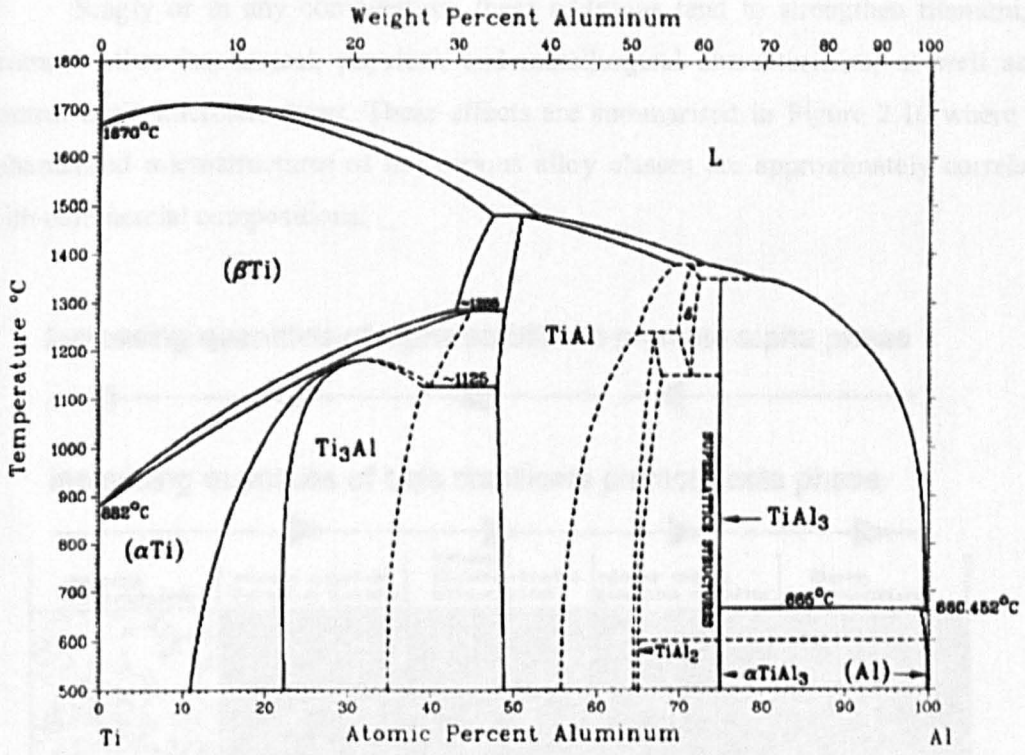

Figure 2.9 Phase diagram for the titanium-aluminium system [10].

The interstitial elements oxygen (O), nitrogen (N), and carbon (C) are also strong α-stabilising. These elements contribute to interstitial hardening of α phase and are usually present as impurities in commercial alloys. In commercially pure titanium, the oxygen content is controlled to provide several grades offering different combinations of strength and ductility [9, 14].

β-stabilising elements are divided into β-isomorphous and β-eutectoid elements. Commonly used β-isomorphous elements include molybdenum (Mo), vanadium (V), tantalum (Ta) and niobium (Nb). As well as stabilising the β phase, these elements solid solution harden the β phase. On the other hand, even a very low volume fraction of β eutectic elements, e.g. iron (Fe), manganese (Mn), chromium (Cr), cobalt (Co), nickel (Ni), copper (Cu), silicon (Si), and hydrogen (H), can lead to the formation of intermetallic compounds [9].

tin (Sn) and zirconium (Zr) are considered neutral elements since they have (nearly) no influence on the α+β phase boundary but as far as strength is concerned, they are not neutral since they tend to lower the β transus temperature and strengthen the α phase slightly [9].

Singly or in any combination, these additions tend to strengthen titanium, to promote other mechanical, physical, and metallurgical characteristics, as well as to control basic microstructures. These effects are summarised in Figure 2.10 where the schematised microstructures of the various alloy classes are approximately correlated with commercial compositions.

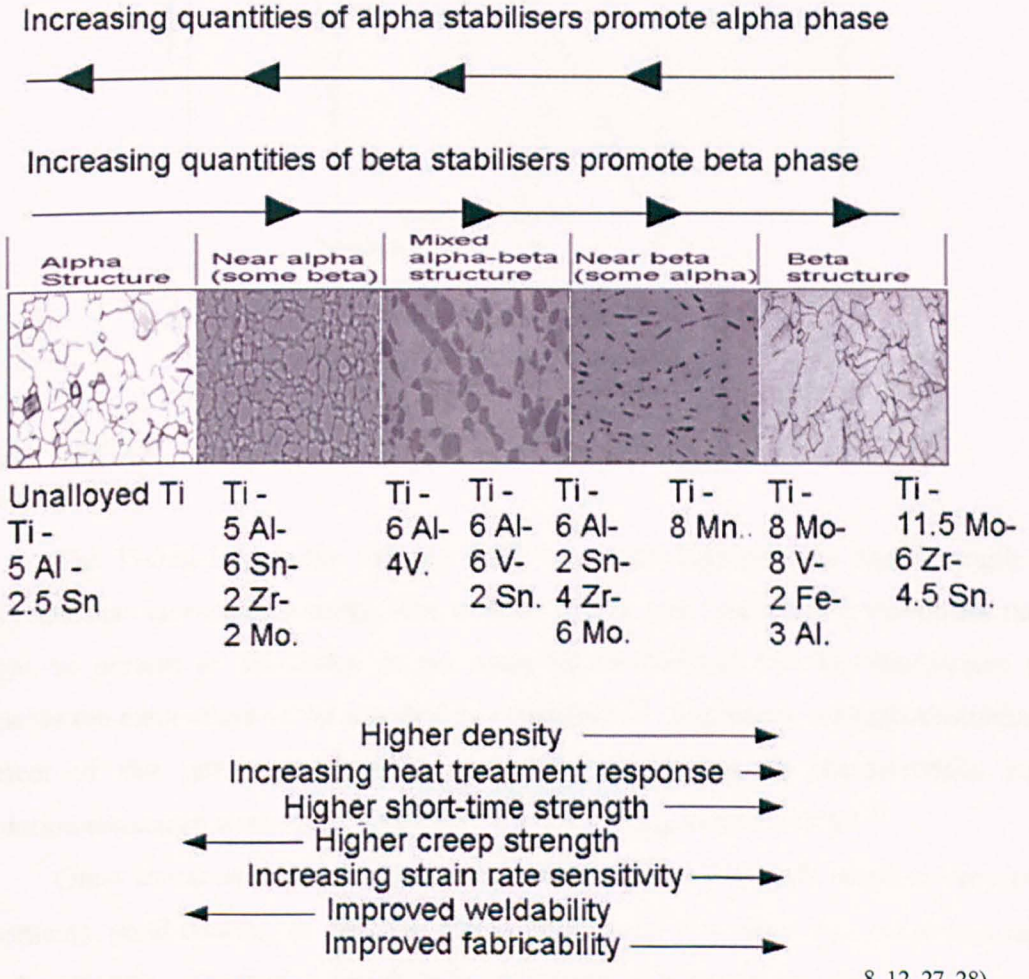

Figure 2.10 Titanium alloying effects on the mechanical characteristics and the microstructure [8, 12, 27, 28].

2.2.3 Classification of Titanium Alloys

Titanium alloys can be classified by the phase present at room temperature as either α alloys, near α alloys, α+ β alloys, near β alloys (or metastable β alloys) and β alloys. The regions in the phase diagram which relate to these types of alloys are schematically shown in Figure 2.11.

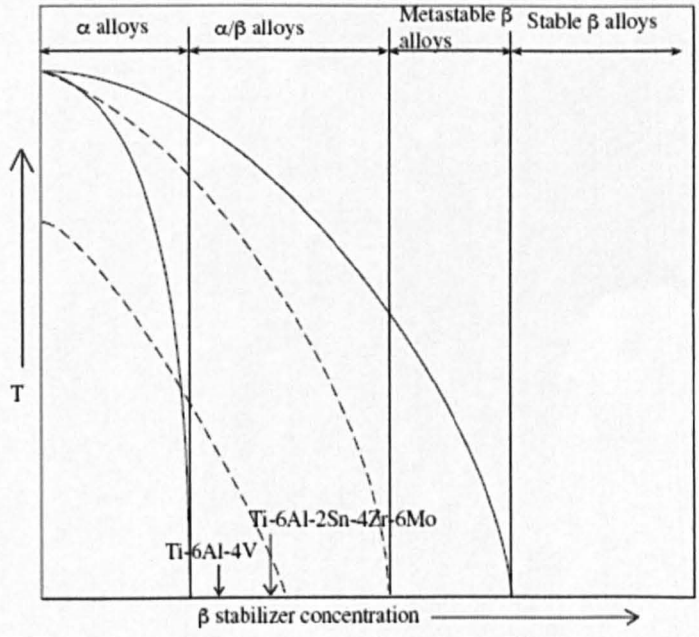

Figure 2.11 Titanium phase diagram [12].

2.2.3.1 α alloys

The Ti-5Al-2.5Sn alloy (Figure 2.12) is a good example of a high strength α alloy that has commercial status. The amount of tin, iron and other β stabilisers that might be present as impurities in the make up of Ti-5Al-2.5Sn are insufficient to override the main effect of the aluminium α stabiliser [20]. In general, the high aluminium content of this group of alloys guarantees excellent strength characteristics and oxidation resistance at elevated temperatures (in the range of 316-593°C) [8].

Other characteristics of α alloys are: very good creep strength (none or very low β content), good ductility at elevated temperature under low strain rate conditions and good weldability. The high strength feature at elevated temperatures of the more highly aluminium alloyed α compositions can be somewhat unfavourable due to its limited fabricability when compared to the mixed two phase α+β alloys and β compositions. This difficulty, however, can be eased by additions of neutral stabilisers and small amounts of β stabilizers [20].

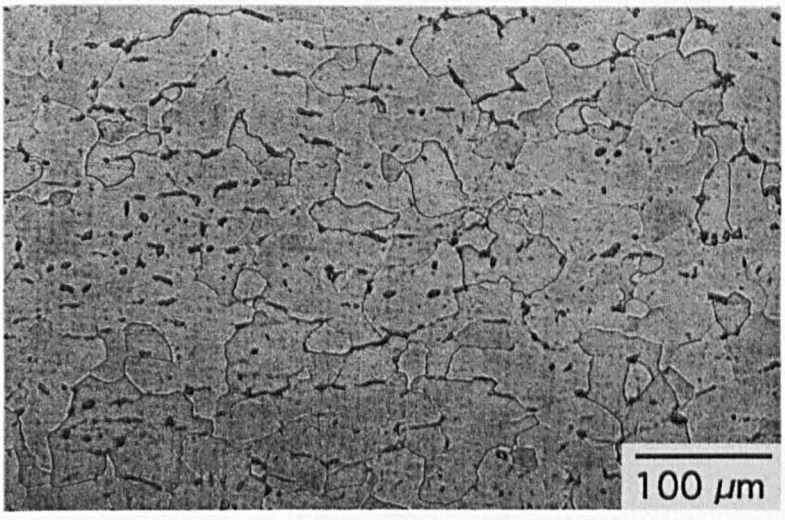

Figure 2.12 Microstructure of Ti-5Al-2.5Sn ELI alloy in a 160 mm diameter billet (National Institute for Materials Science, Japan). It consists mostly of α with a small amount of β [29].

2.2.3.2 Near-α alloys

α alloys which are modified with relatively small amounts of β stabilisers are referred to as near α alloys. Addition of β stabilisers to an α stabilised base results in the presence of larger quantities of the β phase in the predominant α structure. Such additions not only promote a small amount of β phase retention, but alter the mechanical characteristics of the alloy as well. Depending upon the amount and type of β stabilisers used, strength, stability, and fabricability may be improved in comparison with all α compositions of the same α stabilised base. The creep resistance properties of the alloy are, however, reduced [20].

2.2.3.3 α + β alloys

The mechanical characteristics of α+β titanium alloys depends upon the combination of α and β stabilisers used in their make up as well as their processing history. Aluminium is often used as the α stabiliser which contributes to the strength of the alloy over the full service temperature range. Commercial α+β alloys usually contain significant quantities of the β isomorphous elements (molybdenum or vanadium), which impart stability as well as strength at high temperatures. The addition of β eutectoid stabiliser (iron, manganese, chromium, nickel etc.) also contributes to the strength of the alloy although their use in large quantities can result in instability due to

the precipitation of unwanted compounds [20]. In general terms, the amount of alloy addition in α+β alloys is related to strength level. For example, the Ti-6Al-4V alloy is considerably stronger than the Ti-3Al-2.5V alloy [8, 20].

Similarly, α+β alloys with increasing amounts of β stabilising addition are inherently stronger in short time tensile testing and due to the larger β content can be heat treatable to a higher strength. For example, the short time strength and the heat treatability of the Ti-6Al-6V-2Sn alloy is greater than Ti-6Al-4V. Also, Ti-6Al-2Sn-4Zr-6Mo is stronger and more responsive to heat treatment than Ti-6Al-2Sn-4Zr-2Mo. However, if the low strain rate performances of these materials are compared, as in creep for example, the Ti-6Al-4V alloy is shown to be better than Ti-6Al-6V-2Sn and the Ti-6Al-2Sn-4Zr-2Mo outperforms Ti-6Al-2Sn-4Zr-6Mo. An example microstructure of α+β TIMETAL® 6Al-2Sn-4Zr-6Mo alloy is shown in Figure 2.13.

In addition to the strength and heat treatability features characteristic of α+β alloys, this group can be considered as having good fabricability, good ductility and stability commensurate with preferred strength levels and exposure conditions, and marginal weldability except when the β stabilising content is low [20].

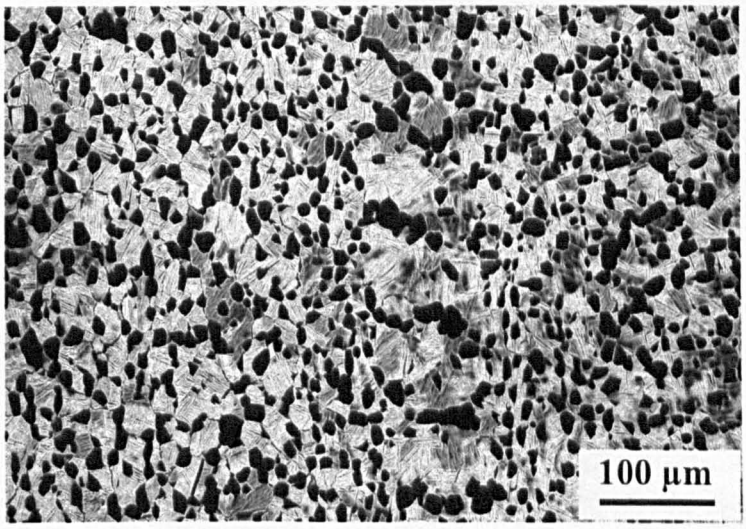

Figure 2.13 Microstructure of Ti-6Al-2Sn-4Zr-6Mo (material was provided by TIMET, UK)

2.2.3.4 Near β and β alloys

Increasing quantities of the β stabilising elements in this group of titanium alloys, raises the amount of β phase in the microstructure at room temperature,

producing a metastable microstructure. Strengthening can occur by the precipitation of α during aging.

Metastable β titanium alloys have been used in airframes, springs (e.g. Ti-3Al-8V-6Cr-4Zr-4Mo) and fasteners [8].

In addition to the heat-treatable high strength characteristic of β alloys, the excellent ductility of the non-heat treated β is a notable feature in this group. The highly ductile β phase has great cold workability which allows excellent room temperature formability. The alloys can also be easily formed at elevated temperatures where their deformation resistance is very low when the strain rate is low. However, deformation resistance is high when strain rate is high, thus indicating a high strain rate sensitivity. The β alloys usually have higher density and lower creep strength when compared to α and α+β alloys [20].

There are two types of β alloys as previously mentioned: a) β isomorphous and b) β eutectoid. In the β isomorphous system the alloying element is completely miscible in the β phase, decomposition of the β phase to α plus another phase or compound does not occur and the β transus temperature decreases as the amount of alloying element is increased as shown in Figure 2.14 [10].

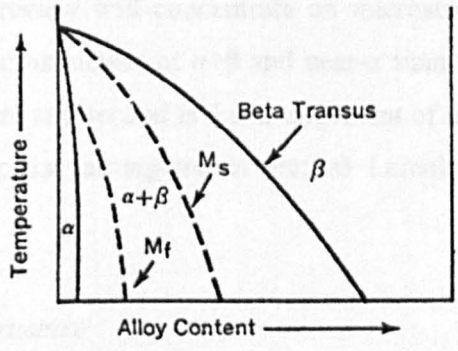

Figure 2.14 β isomorphous system [10].

In the β eutectoid system the alloying element stabilises the β phase and the β phase can transform to α plus another phase compound but only under very slow cooling conditions (Figure 2.15) [10].

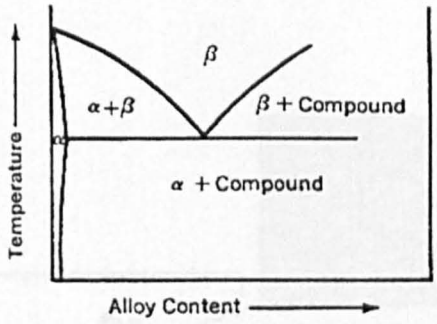

Figure 2.15 β eutectoid system [10].

2.2.4 Microstructure of titanium alloys

One of the most important aspects in the investigation and understanding of titanium alloys is microstructural characterisation as the properties of titanium alloys are strongly dependent on their microstructures, which in turn mainly depend on heat treatment and thermomechanical processing history.

A vast array of microstructures can be produced in titanium alloys; however, as this thesis is focussing on the α+β alloy Ti-6Al-2Sn-4Zr-6Mo and its application to the aerospace industry this review will concentrate on microstructure in α+β and near-α alloys. In general the microstructure of α+β and near-α titanium alloys is described by two factors; first is the size and second is the arrangement of the α and β phase [9, 30]. The two extreme cases of phase arrangements are: a) Lamellar microstructure and b) Bimodal microstructure.

2.2.4.1 Lamellar microstructure

The lamellar microstructure is formed by heat treating or working above the β transus temperature. When cooling the alloy slowly from the high temperature β region, α phase begins to nucleate at β grain boundaries. Then due to the low interfacial energy of certain atomic planes, the α phase grows faster along these planes away from the β grain boundaries and slowly thickens perpendicular to them. As a result, α plates are developed. The formation of this microstructure (Widmanstätten structure) is illustrated in Figure 2.16 [31]. Widmanstätten structure has a relatively large grain size which is

known to give intermediate strength and low ductility, but excellent fracture toughness and creep resistance [31].

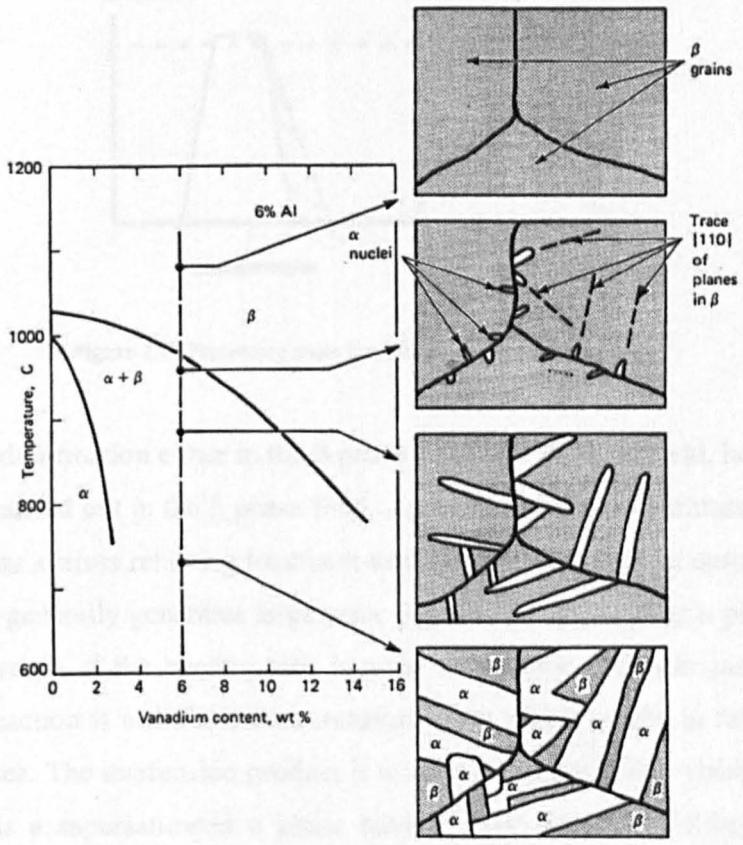

Figure 2.16 Widmanstätten structure in Ti-6Al-4V [31].

An example of lamellar microstructure for Ti-6Al-4V alloy in a high temperature microscopy sequence is shown in Figure 2.17.

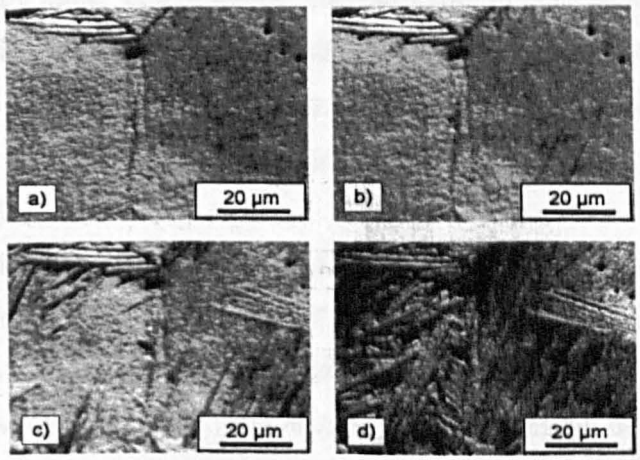

Figure 2.17 Cooling from the β phase field of Ti-6Al-4V (High temperature microscopy) [9].

The processing route for obtaining these fully lamellar microstructures is shown in Figure 2.18.

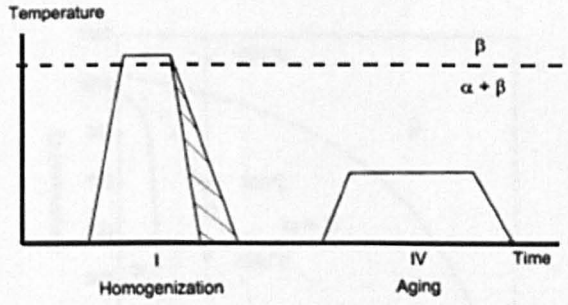

Figure 2.18 Processing route for fully lamellar microstructure [30].

After deformation either in the β phase field or α+β phase field, homogenisation treatment is carried out in the β phase field. Aging at a lower temperature for improved properties or as a stress relieving treatment usually follows. Note that deformation in the β phase field generally generates large prior β grains where lamellar α phase grows on cooling. However, if the cooling rate is rapid martensitic products can form[32]. The martensitic reaction is a diffusionless transformation which results in the formation of unstable phases. The martensitic product is usually a hcp structure, which is designated α'. α' phase is a supersaturated α phase having a fine lath (needlelike) morphology. There is also an orthorhombic martensite, designated α", which is another non-equilibrium phase formed by diffusionless transformation in certain alloys (particularly those containing refractory elements such as Mo, Ta or Nb, which are β-stabilising elements) [33].

Lamellae are either fine or coarse depending on the cooling rate. Pure lamellar microstructure (Figure 2.19 a) is the result of slow cooling from the β phase field. Lamella becomes coarser by reducing the cooling rate. Needle-like microstructure (Figure 2.19 b) is formed by rapid quenching which leads to a martensitic transformation of β.

The metallographic figures of all slowly cooled specimens show β as a small layer around the coarse and light coloured α lamellae. With high cooling rates from temperatures above the martensitic start temperature (M_S) and through the two phase field, β transforms into martensite (Figure 2.19 d). Depending on the starting structure and the homogeneity of the microstructure, the martensitic start temperature differs. The

β volume fraction further decreases at low temperature and no longer transforms to martensite at temperatures below M_S (Figure 2.19 f) [9].

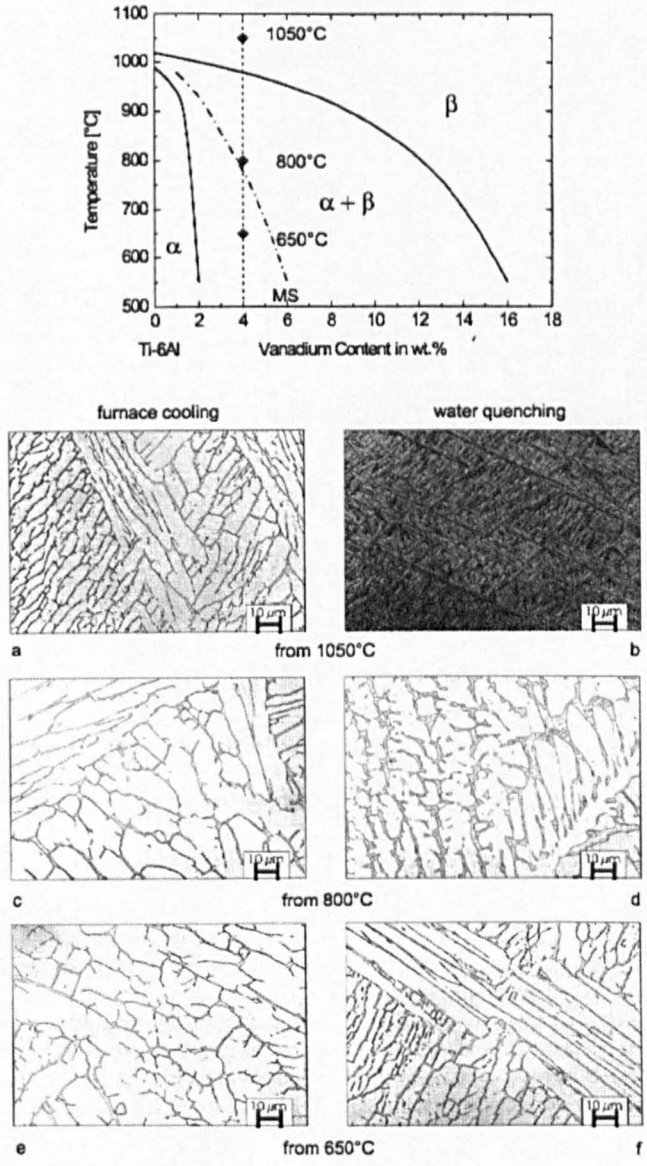

Figure 2.19 Microstructure of Ti-6Al-4V after slow cooling (50° C/h) and water quenching from 1050° C, 800° C and 650° C [9].

The amount of β stabilisers can also affect the microstructure in addition to the cooling rate [34, 35, 36]. For example, comparison of the lamellar microstructures of an IMI 550 alloy (Ti-4Al-4Mo-2Sn-0.5Si), a heavily β stabilised alloy, and a Ti-6Al-4V alloy, a much leaner alloy, have shown that the IMI 550 exhibits both a thinner grain boundary α layer and α lamellar structure for the same process condition [34].

2.2.4.2 Bimodal microstructure

The bimodal microstructure is formed by working and annealing below the β transus (in the α+β phase field) temperature. By heat treating and deforming in the α+β region the grain sizes get much smaller and finer due to the primary α (α_p) limiting β grain growth. Figure 2.20 shows a comparison of typical lamellar and bimodal microstructures.

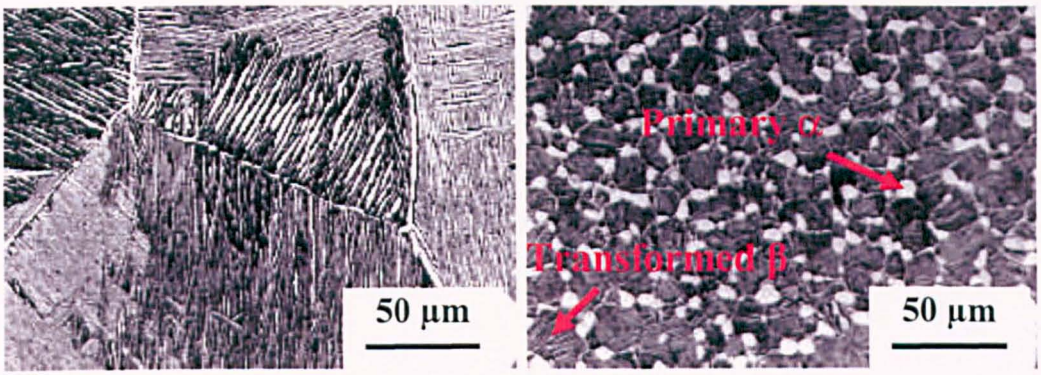

a) b)

Figure 2.20 Typical SEM images of the **a)** lamellar microstructure, and **b)** bimodal microstructure [37].

A typical processing route for obtaining a bimodal microstructure is shown in Figure 2.21. The general processing route can be divided into four different steps:

(I) Homogenisation in the β phase field,

(II) Deformation in the α+β phase field,

(III) Recrystallisation in the α+β phase field,

(IV) Aging at lower temperatures.

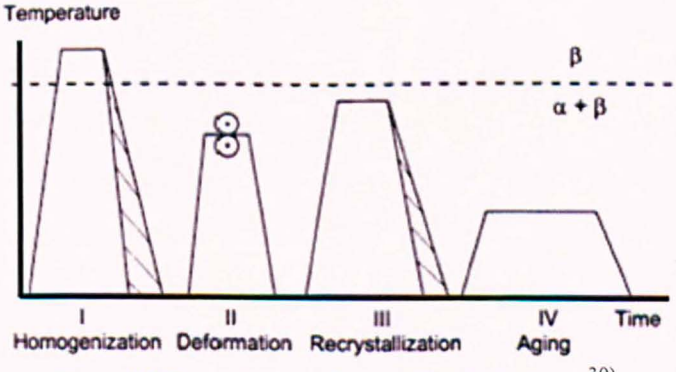

Figure 2.21 Processing route for bimodal microstructures [30].

Cooling rates are very important factors determining the microstructural features in the final bimodal microstructure [37]. The cooling rate from the homogenisation temperature determines the width of the α lamellae in the lamellar structure within the β grains and the extent of the continuous α layer at β grain boundaries. Figure 2.22 shows examples for cooling rates of 1°C min^{-1}, 100°C min^{-1}, and 8000°C min^{-1} [30].

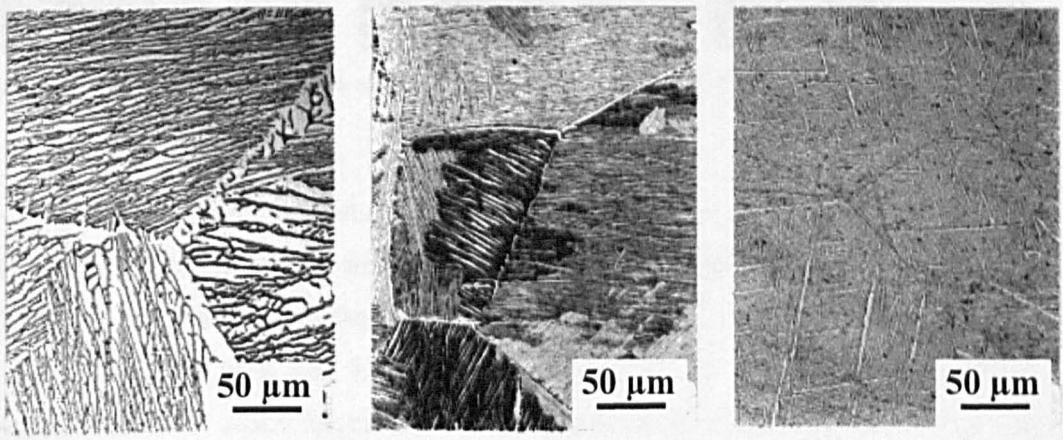

a) b) c)

Figure 2.22 Effect of cooling rate from the β phase field on lamellar microstructures (Ti-6242). **a)** 1°C min^{-1}, **b)** 100°C min^{-1}, **c)** 8000 °C min^{-1} [30].

After homogenisation treatment in the β phase field, the material is deformed in the α+β phase field. During the deformation process, crystallographic textures in the hexagonal α phase and in the bcc β phase can be developed depending on the deformation temperature, the degree of deformation and deformation mode [30]. A recrystallisation step is then applied. This is followed by the final aging step to further improve properties or relieve residual stress.

The other major factor influencing the microstructure features in the bimodal microstructure is temperature. The volume fraction of the α_p phase can be affected by the temperature of the recrystallisation or solution heat treatment after the forging procedure (step III). It is possible to obtain different volume fractions of the primary α phase by varying the temperature of solution heat treatment. Examples of bimodal microstructures in IMI 834 alloys with different volume fractions of the α_p are shown in Figure 2.23 [38].

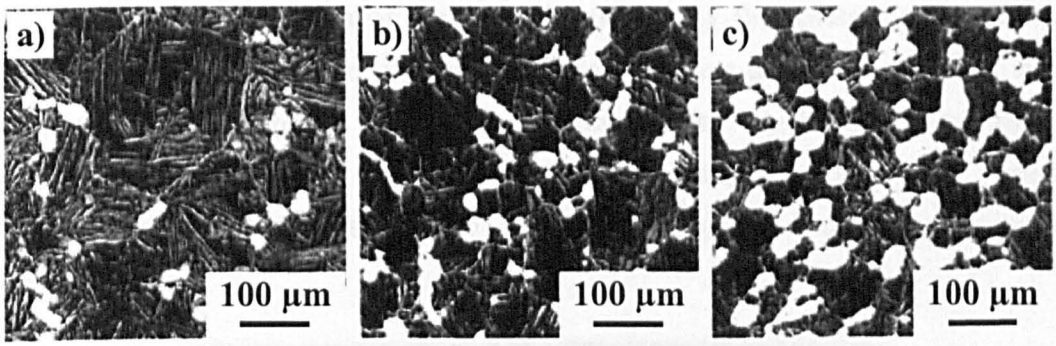

Figure 2.23 Bimodal microstructures of IMI 834 alloys with different volume fractions of the primary phase: **a)** 5%, **b)** 15%, and **c)** 25% [38].

The best combination of mechanical properties, i.e. creep and fatigue resistance, for bimodal microstructure are achieved when the volume fraction of α_p is limited to 10-30 % and the prior β grain size is between 20 and 40 µm [39].

For both α+β and near- α alloys [30, 37, 40] the grain size in the lamellar microstructure is much larger than that in the bimodal microstructure. This is due to rapid grain growth above β transus temperature. However, in bimodal microstructures because the heat treatment temperature is below the β transus temperature, the β grain size is limited by the α_p (i.e. β grain growth is pinned by the α_p) , therefore it shows much finer grain size than the lamellar microstructure. As a result, the bimodal microstructure generally shows higher yield strength due to its finer grain size. The tensile properties of the lamellar and the bimodal structure have been compared by Sauer and Lütjering [34]. They too demonstrated that bimodal microstructures exhibit higher yield stress and ductility in comparison to the lamellar microstructure due to slip being transferred easier within colonies of the lamellar structure and also because of the extra strengthening effect of the small grain size in the bimodal structure.

2.2.4.3 Equiaxed microstructure

The process of recrystallisation results in equiaxed microstructures. For this reason the alloy, must be highly deformed in the α+β field to introduce enough work into the material. Upon subsequent solution heat treatment at temperatures in the two-phase field, a recrystallised and equiaxed microstructure is generated (Figure 2.24 a). The equiaxed microstructure may be coarsened by extended annealing (Figure 2.24 b).

The volume fraction of the α_p is determined by the solution heat treatment temperature itself. As previously mentioned, solution heat treatment just below the β transus temperature results in bimodal microstructures which consist partially of equiaxed (primary) α in a lamellar α+β matrix (Figure 2.24 c, d). Bimodal microstructure can be considered to be a combination of lamellar and equiaxed microstructure [9].

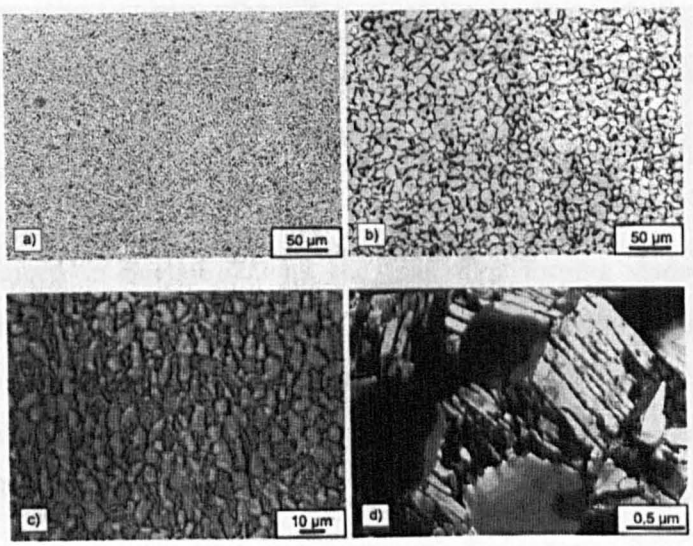

Figure 2.24 Equiaxed microstructures of Ti-6Al-4V via recrystallisation: **a)** Fine equiaxed **b)** coarse quiaxed **c, d)** bimodal (OM, TEM) [9]

The various microstructures have strong influence on the mechanical behaviour of the titanium alloys. Table 2.1 shows the effects of the size (fine or coarse) and the arrangement of the phases (lamellar or equiaxed) on some important mechanical properties.

For example, fine-scale microstructure increases strength and ductility in addition to delaying crack nucleation. Coarse microstructures, however, are more resistant to creep and fatigue crack growth. Equiaxed microstructures are preferred for superplastic deformation and often have high ductility and fatigue strength. Lamellar structures, however, has high fracture toughness and show superior resistance to creep and fatigue crack growth.

Bimodal microstructure on the other hand, exhibits a well balanced property profile because it combines the advantages of lamellar and equiaxed structures [9].

Table 2.1 Influence of microstructure on selected properties of titanium alloys [9].

fine	*coarse*	*Property*	*lamellar*	*equiaxed*
○	○	Elastic modulus	○	+/– (texture)
+	–	Strength	–	+
+	–	Ductility	–	+
–	+	Fracture toughness	+	–
+	–	Fatigue crack initiation	–	+
–	+	Fatigue crack propagation	+	–
–	+	Creep strength	+	–
+	–	Superplasticity	–	+
+	–	Oxidation behavior	+	–

2.2.4.4 Globularization

As explained in Section 2.2.4.2 the final α+β forging stage takes place at temperatures below the β transus (α+β phase field) which results in the breakdown of the transformed microstructure, developing an equaxed α microstructure. This process is referred to as globularization or spherodisation. Globularization is the direct result of the amount of prior deformation, working temperature and the mode of deformation applied [41].

Techniques which convert the colony of α phase to a globular morphology during deformation and post-deformation annealing of α+β titanium alloys have been studied by various researchers. Weiss et al.[41] suggested that globularization of the lamellar structure occurs by the shearing of α platelets followed by a penetration of β phase to complete the separation.

The work of Semiatin et al. [42] and Weiss et al.[41] revealed the importance of strain as an attribute to the initiation of the globularization process. It was also found that strain path can also have a major influence on globularization kinetics[42].

Microstructural observations indicated that the globularization process can be divided into two broad regimes. The first includes changes that take place during deformation and the initial stages of annealing. Whilst the second stage proceeds until the microstructure has been fully globularized and comprises essentially a coarsening process [43].

2.3 Thermomechanical Processing of Titanium

2.3.1 Introduction

Different microstructures are normally generated by thermomechanical treatments. These are considered as a complex series of solution heat treatments, deformation, recrystallisation, etc. β transus temperature is a central point for thermomechanical treatment because it separates the single β phase field from the two-phase α+β field. Thermomechanical processing (TMP) is associated with two major requirements:

1) The production of usable shapes through ingot breakdown and secondary mill operations (forging, hot rolling, etc.).
2) The optimisation of mechanical properties through microstructure control (controlling α and β phases through alloying additions) during the different stages of the thermomechanical process [44].

2.3.2 Forging and forming

Forging may refer to different processes in which the deformation is induced by localised compressive forces. The tools can be manual, power hammers, presses, or special forging machines. The term forging usually implies to hot forging above the recrystallisation temperature although deformation can be done in the hot, warm or cold mode [45].

2.3.2.1 Forging methods

Titanium alloy forgings are produced by a variety of different forging methods such as open-die forging, closed-die forging, upsetting, roll forging, etc. depending on the desired forging shape, cost, and the desired mechanical properties and microstructure. There are two major metallurgical approaches to the forging of titanium alloys:

- Conventional α+β forging (Forging the alloy predominantly below the β transus temperature) and

- β forging (Forging the alloy predominantly above the β transus temperature)

In some cases the above approaches can be combined in order to achieve a controlled microstructure for specific requirements or future service applications.

Conventional α+β forging: most or all of the forging deformation is carried out at temperatures below the β transus of the alloy. Thus forging involves working the material at temperatures where both α and β phases are present. The resultant as-forged microstructure is characterised by deformed or equiaxed α_p in a transformed β matrix; the volume fraction of α_p is dictated by the alloy composition and the actual work history and temperature (Figure 2.25 a). α+β forging is typically used to develop optimal strength/ductility combinations and optimal high/low cycle fatigue properties. The effects of working on microstructure (particularly α morphology changes) with conventional α+β forging are cumulative. Structural changes achieved in earlier operations are therefore enhanced with each successive α+β working operation [46].

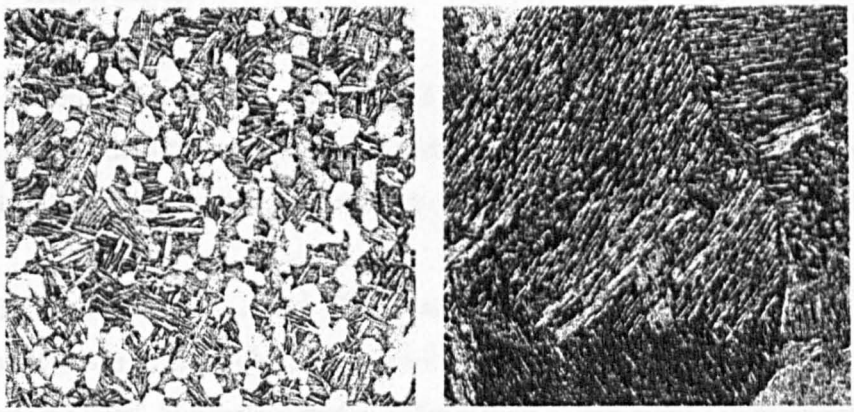

a) b)

Figure 2.25 Microstructure of forged titanium alloys. **a)** α+β forging of alloy Ti-6Al-4V (Equiaxed primary alpha in transformed β. 200×). **b)** β forging of alloy Ti-6Al-4V (acicular primary α in transformed β. 200×)* [46].

β forging: most or all of the forging work is done at temperatures above the β transus of the alloy. In general β forging techniques involve supertransus forging in the early and/or intermediate stage with controlled amounts of final deformation below β transus of the alloy. The final work at subtransus temperature depends on the alloy, the forging design, and the required mechanical property combinations. Unlike α+β forging the working influences on microstructure are not fully cumulative. With each working, cooling and reheating sequence being above the β transus temperature, the effects of the previous working operations are partially lost.

* No scale bar was indicated in the original document.

β forging techniques are used in order to develop acicular α morphology in a transformed β matrix (Figure 2.25 b) or microstructures characterised by Widmanstätten [46].

This forging process is typically used to improve the fracture related properties (e.g. fracture toughness and fatigue crack propagation resistance) and the creep resistance of α and α+β alloys. There is often a loss in strength and ductility with β forging as compared to α+β forging.

Also β forging of α and α+β alloys, has the advantages of reducing the forging unit pressures and cracking tendency. In addition the forging process must be done under carefully controlled conditions in order to avoid non uniform working, excessive grain growth, and/or poorly worked structures, all of which can result in final forgings with unacceptable or widely variant mechanical properties within a given forging [46].

2.3.2.2 Heat treatment

As mentioned before a final heat treatment is given to produce the best combination of ductility, machinability, stability in the final products, reduce residual stresses developed during fabrication and to increase strength by solution treatment and aging [15].

The α and near-α titanium alloys can be stress relieved and annealed, but only moderate increases in strength can be developed in these alloys by heat treatment. The commercial β alloys, however, contain metastable β which allows strengthening during aging as the retained β decomposes. They also demonstrate a great potential for age hardening and make use of the stability of their β phase to provide large section hardenability.

The α+β alloys display a mixture of heat treatment characteristics of both α and β alloys. Similar to β alloys, α+β alloys can exhibit age hardening from the decomposition of β but due to the lesser amounts of retained β in these alloys they do not exhibit the same section size hardenability as the β alloys.

An overview of the general effects of β or α+β processing on the properties of α+β alloys are shown in the Table 2.2 [22].

Table 2.2 effects of β or α+β processing of α+β alloys [22)]

Property	β processed	α+β processed
Tensile strength	Moderate	Good
Creep strength	Good	Poor
Fatigue strength	Moderate	Good
Fracture toughness	Good	Poor
Crack growth rate	Good	Moderate
Grain size	Large	Small

It should be noted that β transus temperature is the key to successful forging and heat treatment. The effects of heat treatment and forging temperatures on properties of a typical α+β alloy such as Ti-6Al-4V are shown in Figure 2.26. It can be noticed that the percentage of β increases by increasing the processing temperature in the α+β region therefore more β is available to transform upon cooling. Upon quenching from above the β transus, a completely transformed, acicular structure arises.

Depending on the exact location of the β transus (which varies for a given alloy), the degree and nature of deformation, the form of the transformed β structures changes [22)].

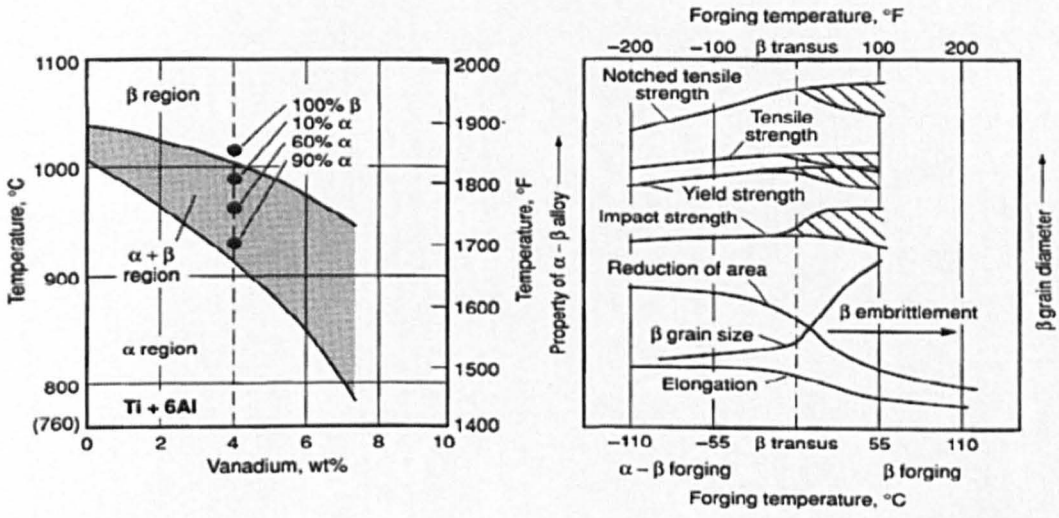

Figure 2.26 Effects of forging and heat treating temperatures on properties of titanium alloys. **a)** Phase diagram of α+β contents with a base composition of titanium + 6 wt% Al. **b)** Generalised effect of processing temperature on β grain size and room temperature mechanical properties of an α+β alloy [22].

2.3.2.3 Cooling methods

Different cooling methods and cooling rates are important parameters in heat treatment. For α+β titanium alloys the effects of the cooling rate from the β and the α+β region has been studied by a number of authors [47, 48, 49, 50, 51].

The cooling rate determines the microstructural morphologies caused by different mechanisms of phase transformations. High cooling rates are frequently used in order to produce higher strength materials. Martensitic transformation is the dominant mechanism at fast cooling rates, whilst diffusional phase transformation is dominant at slow cooling rates [48, 52].

Figures 2.27 a) and b) shows by the comparison the effects of cooling from the β homogenisation (Figure 2.21) heat treatment on the α_p phase of IMI 834 alloy [30]. Note that the only difference in the processing route is the cooling rate after the β homogenisation heat treatment during a compressor disk fabrication process [30].

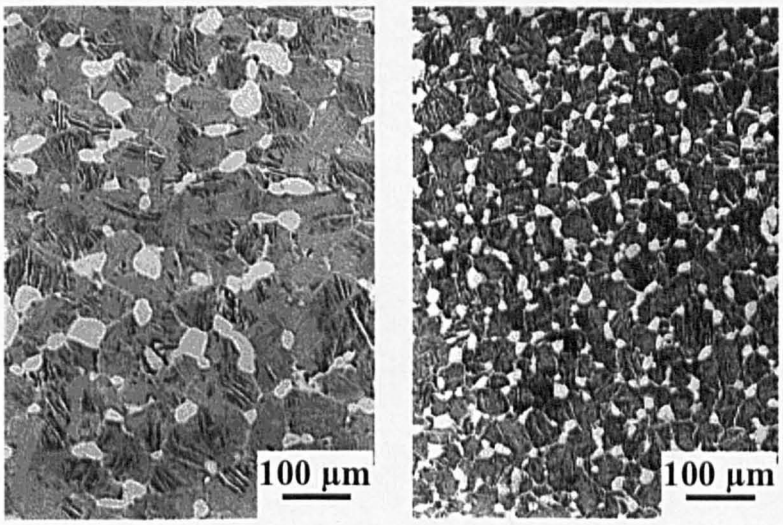

Figure 2.27 Bimodal microstructures of IMI 834 alloys with different cooling rate after β homogenisation heat treatment: **a)** slow and **b)** fast [30].

Microstructural features such as the dimension of lamellar α and β within the transformed β region in the bimodal microstructure, are also affected in a similar way to lamellar microstructure when subjected to different cooling rates from the solution heat treatment. Due to martensitic transformation, very high cooling rates display very fine lamellae and slower cooling rates show much wider lamellae originated by a diffusion controlled process [38]. From Figure 2.28 it can be observed that by decreasing the cooling rate, the thickness of α laths in the transformed β region increases significantly.

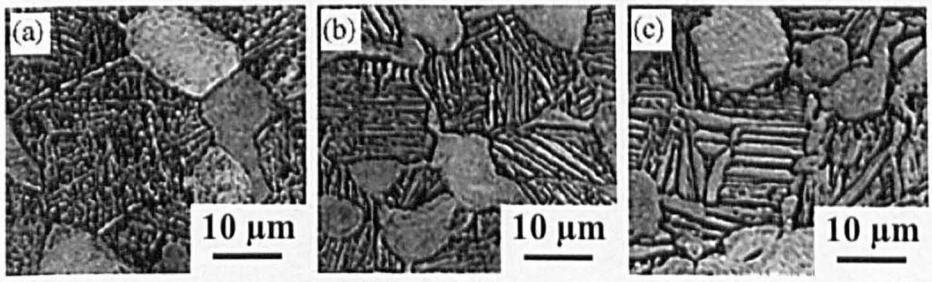

Figure 2.28 Bimodal microstructures of Ti-6Al-4V alloys with different cooling rates, **a)** 2000°C min^{-1}, **b)** 500°C min^{-1}, and **c)** 50°C min^{-1} [38]

Furthermore, a forced cooling rate along with the material's transformation and phase growth kinetics controls the development of the required mechanical properties [49, 50, 51, 52]. By increasing the cooling rate the tensile strength and yield strength usually increases. For example, in the lamellar microstructure the size of α colonies is thought to be the most dominant microstructural parameter on the mechanical properties

because it determines the effective slip length [30]. By increasing the cooling rate the α colony size usually decreases, therefore the effective slip length is decreased. As a result, the yield strength is increased with increasing cooling rate as shown in Figure 2.29 [30].

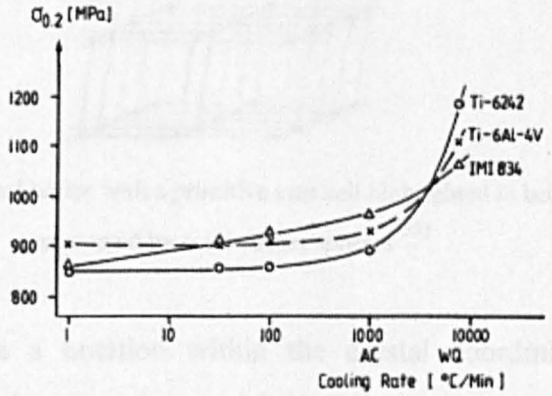

Figure 2.29 Effect of cooling rate from the β phase region on yield strength of the lamellar structure [30].

When selecting the cooling rates and methods there are additional factors to consider other than mechanical properties. Large variations in cooling rate will cause both very large thermal stresses, and consequently very high residual stresses. This can cause problems such as machining distortion, quench cracking, unexpected mechanical properties and poor performance in the final component [52].

2.4 Crystallography and deformation modes

In order to be able to explain the crystallography of titanium is important to have a good knowledge of the Miller and Miller-Bravais indices notation.

2.4.1 Miller and Miller-Bravais Notation

A crystal is a homogenous solid formed by a repeating, three-dimensional pattern of atoms, ions or molecules. In order to visualise the structure of a crystal it is often helpful to focus on the geometry of periodic arrays and to ignore the actual atoms, ions or molecules. The crystal is then represented as a lattice - a three dimensional array of points (lattice points), with each point having identical surroundings (Figure 2.30) [53].

A Cartesian coordinate frame is tied to the lattice, *x, y, z* aligned with the unit cell vectors *a, b* and *c* in crystals consisting of cubic, tetragonal or orthorhombic lattice structures.

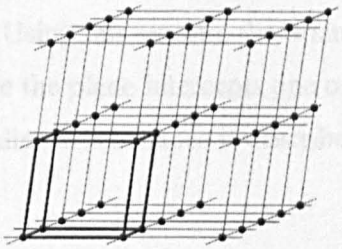

Figure 2.30 Three dimensional lattice with a primitive unit cell highlighted in bold. Lattice points are represented by solid circles/spheres [53].

Miller indices are a notation within the crystal coordinate system which describes the crystallographic directions and lattice planes in terms of integer indices which are derived as follows [54]:

$$r = ua + vb + wc \tag{2.4}$$

A crystallographic direction is given by the vector *r* in the crystal. *a, b, c,* are the three axes in crystallographic system and, thus, the direction is described by a set of 3 integer numbers, *u*, *v*, and *w*. In some cases the Miller indices are best multiplied or divided through by a common number in order to simplify them for example, $[\frac{1}{2}\ \frac{1}{2}\ 1]$, [112] and [224] all represent the same direction and should be written [112]. This simply generates a parallel plane which is at different distance from the origin of the particular unit cell (Figure 2.31) [53].

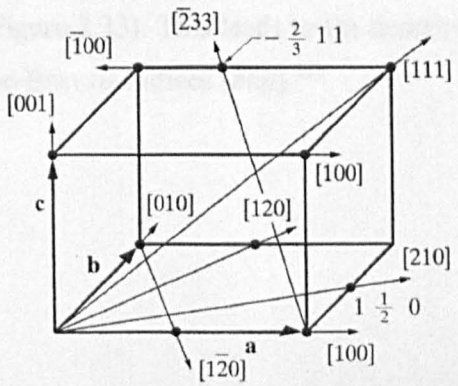

Figure 2.31 indices of directions [53].

The orientation of a crystal plane may be defined by considering how the lattice plane or any parallel plane intersects the main crystallographic axes of the solid. According to a system popularised by Miller the orientation of the planes in a lattice can be represented symbolically. Using this system, the orientation of the plane is described by expressing the point where the plane intercepts one of the three axes as a fraction of the axial length. A set of parallel lattice planes is described according to the equation;

$$h\frac{x}{a}+k\frac{y}{b}+l\frac{z}{c}=1 \tag{2.5}$$

Coordinates of any point on a particular plane are represented by x, y, and z. The miller indices (hkl) refer to the reciprocal multiples of the axis intercepts, again reduced to the smallest integers that have the same ratios, examples of which can be seen in Figure 2.32 [53].

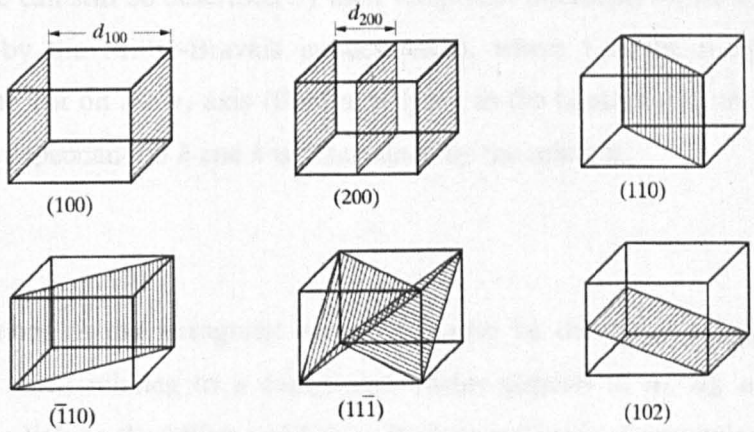

Figure 2.32 Miller indices of lattice planes. The distance d is the plane spacing [53].

Though directions and planes can be described by the Miller indices in all crystal structures, for hexagonal crystals it is more conventional to use a coordinate system with four axes (Figure 2.33). This leads to the description of directions by a four index notation, the Miller-Bravais indices ($hkil$) [53].

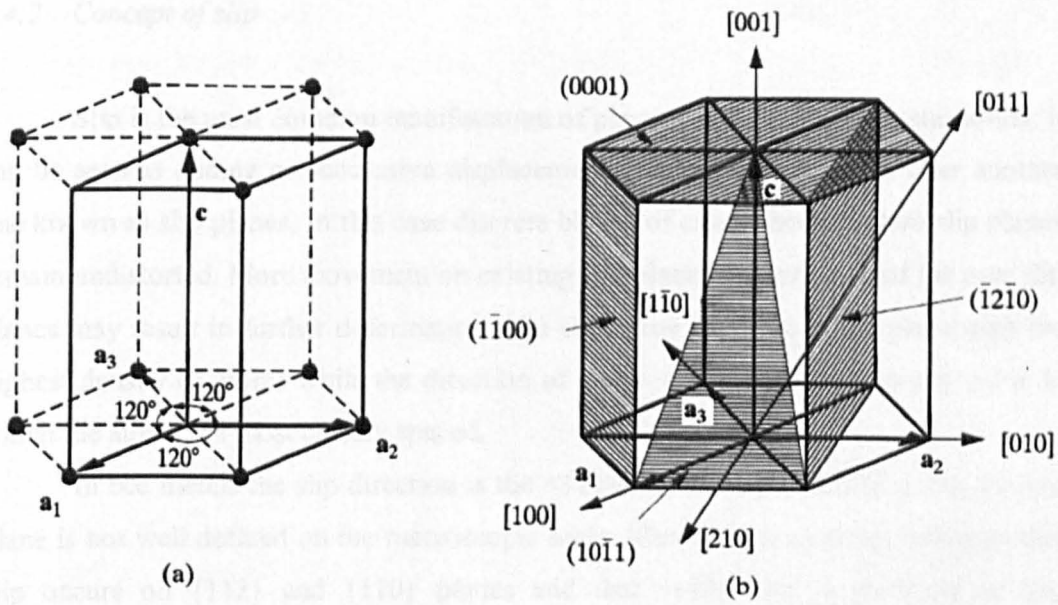

Figure 2.33 a) The hexagonal unit cell (heavy lines) and **b)** indices of planes and directions [53].

Lattice can still be described by their reciprocal intercepts on all four axes; they are denoted by the Miller-Bravais indices (*hkil*), where *i* is the reciprocal of the fractional intercept on the a_3 axis (third axis lying in the basal plane, see Figure 2.33) and its value, dependant on *h* and *k* is determined by the relation;

$$h + k + i = 0 \tag{2.6}$$

Directions in the hexagonal system can also be described using four indices [*uvtw*], each index relating to a component vector parallel to a_1, a_2, a_3 and *c*. The transformation linking the Miller and Miller-Bravais indices is shown below [54]:

For planes, i.e. (*hkil*) => (*HKL*)

$$H = h; \quad K = k; \quad L = l$$
$$h = H; \quad k = K; \quad I = -H - K; \quad l = L \tag{2.7}$$

For directions, i.e. [*uvtw*] => [*UVW*]

$$U = u - t \; ; \quad V = v - t; \quad W = w$$
$$u = 2U - V; \quad v = 2V - U; \quad t = -U - V; \quad w = 3W \tag{2.8}$$

2.4.2 Concept of slip

Slip is the most common manifestation of plastic deformation in crystal solids. It can be seen as sliding or successive displacement of one plane of atoms over another one known as slip planes. In this case discrete blocks of crystal between two slip planes remain undistorted. More movement on existing slip planes or formation of the new slip planes may result in further deformation. The slip plane is normally the plane with the highest density of atoms while the direction of slip is the direction in the slip plane in which the atoms are most closely spaced.

In bcc metals the slip direction is the <111> close packed direction, but the slip plane is not well defined on the macroscopic scale. Microscopic evidence suggests that slip occurs on {112} and {110} planes and that {110} slip is preferred at low temperatures [55].

The close-packed directions for easy crystallographic slip in hcp single crystals are the three (11-20) or <a> directions. The three most dominant sets of planes which contain this slip direction are: 1) the (0001) basal plane, 2) the three {10-10} prismatic planes and 3) the six {10-11} pyramidal planes; see Figure 2.34.

It is now well established that in hcp single crystals, prismatic and basal slip is always the easiest slip mode at low temperature. The activation of the pyramidal slip systems in polycrystalline aggregates occurs primarily due to the large stresses generated in grain-boundary regions because of the misorientation between neighbouring grains [56].

A grain in a polycrystal is not free to deform plastically as though it were a single crystal, for it must remain in contact and accommodate the shape change of its neighbours. It requires five independent shear systems to satisfy Von Mises condition that every grain should be able to undergo homogeneous strain to meet the shape changes imposed by its neighbours. A shear system is independent of others if its operation produces a change in shape that cannot be produced by a combination of strains on those other systems [55, 56].

All of the easy <11-20> slip directions that were mentioned before are perpendicular to the c-axis, and therefore slip on these systems can not produce any elongation or shortening parallel to the c-axis. In order to accommodate straining in the c-direction, slip systems with <c+a> slip directions must be operative which are not

operational at room temperature. Thus deformation twinning (section 2.4.4) is the dominant mechanism of strain in the c-direction at low homologous temperatures. However, at high homologous temperatures, slip in the <11-23> directions becomes possible, and the slip planes containing this slip direction are the first-order pyramidal {10-11} and the second-order pyramidal {11-22} planes; see Figure 2.34 [55, 56].

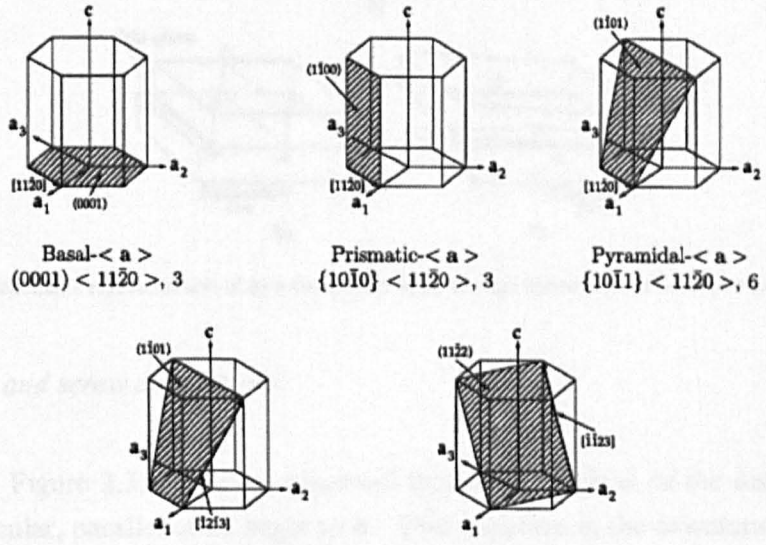

Figure 2.34 Basal, prismatic, pyramidal slip systems and first and second order pyramidal slip systems in hcp materials [56].

2.4.3 Dislocations

A dislocation is a crystallographic defect or irregularity which runs throughout the crystal structure or in other words is a linear or one dimensional defect around which some of the atoms are misaligned. Deformation occurs by passage of such dislocations along the slip plane which may be divided into two regions, one where slip has occurred and the other which remains unslipped. Between these two regions the structure will be dislocated. This is shown in Figure 2.35. Three simple properties of dislocation are evident: (1) line discontinuity, (2) formation of a closed loop positioned within the crystal or emerging at the surface and (3) variation in slip across the dislocation line is constant. This third property is possibly the most important, given that a dislocation is characterised by the magnitude and direction of the slip movement

associated with it. This is called the Burgers vector ***b***, which for any given dislocation line is the same along its entire length [26, 57].

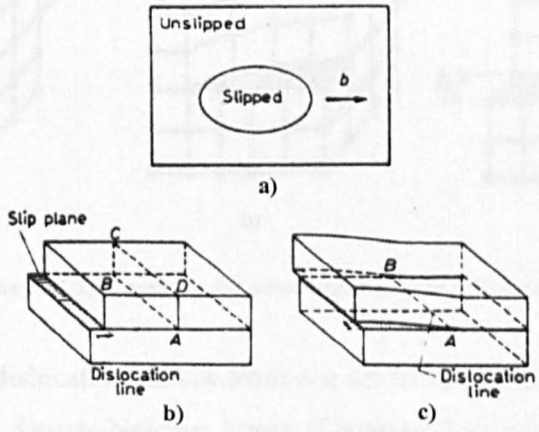

Figure 2.35 Schematic representation of **a)** a dislocation loop, **b)** edge dislocation and **c)** screw dislocation [57].

2.4.3.1 Edge and screw dislocations

From Figure 2.35 it can be observed that some sections of the dislocation line are perpendicular, parallel at an angle to ***b***. This variation in the orientation of the line with respect to Burgers vector gives rise to a difference in the structure of dislocations. When the dislocation line is normal to the slip direction it is called an edge dislocation and when parallel to the slip direction it is known as a screw dislocation. However in reality dislocation lines are rarely pure edge or screw dislocations lines, but it is convenient to use these ideal dislocations as any dislocation can be resolved into edge and screw components. The atomic structure of a simple edge and screw dislocation is shown in Figures 2.36 and 2.37 [57].

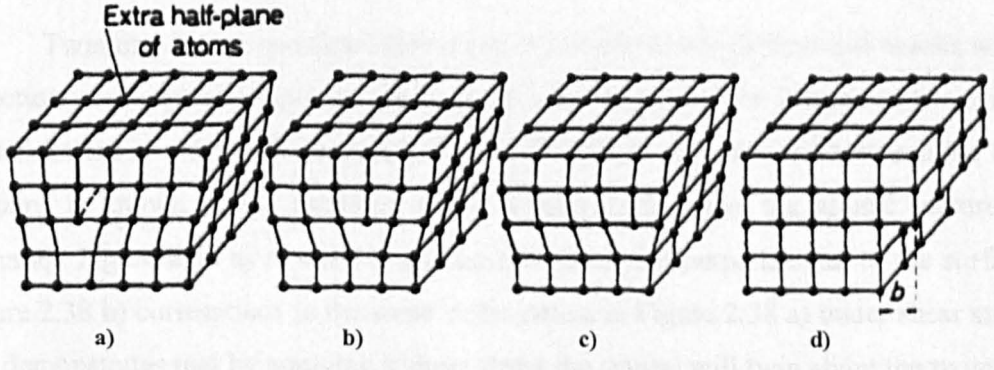

Figure 2.36 Slip caused by the movement of an edge dislocation[57].

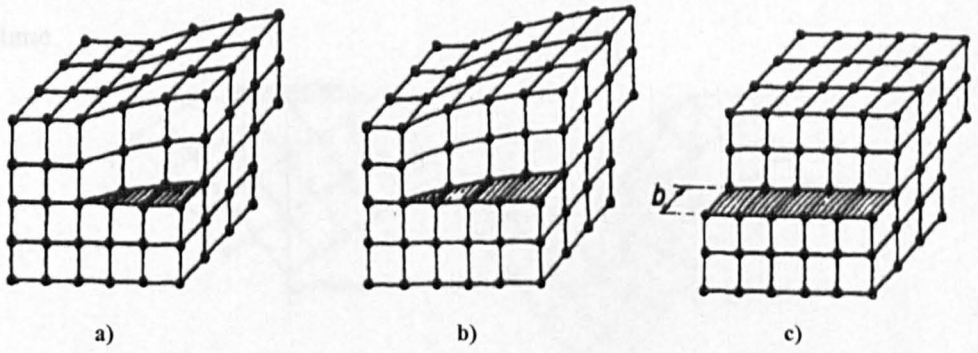

Figure 2.37 Slip caused by the movement of a screw dislocation [57].

During slip a dislocation moves from one set of surroundings to an identical set of surroundings. The Peierls-Nabarro stress (Equation 2.9) is required to move the dislocation from an equilibrium location to another,

$$\tau = c\exp(-kd/\mathrm{b}) \tag{2.9}$$

Where τ is the shear stress required to move the dislocation, d is the interplanar spacing between adjacent slip planes, $\boldsymbol{b}$ is the Burgers vector and both c and k are constants for the material [62].

From Equation 2.9 it can be observed that the stress required to cause the dislocation to move, increases exponentially with the length of the Burgers vector and decreases exponentially with the interplaner spacing of the slip planes [58].

2.4.4 Twinning

Twinning is an important mechanism by which metals deform and results when a section of a crystal adopts the exact same orientation (mirror image) of the parent crystal lattice in a defined symmetrical way. The plane of symmetry between the two portions is known as the twinning plane. Figure 2.38 shows the atomic picture of twinning. Figure 2.38 a) represents a cubic lattice section perpendicular to the surface. Figure 2.38 b) corresponds to the same cubic lattice in Figure 2.38 a) under shear stress and demonstrates that by applying a shear stress the crystal will twin about the twinning plane [59]. The region to the right of the twinning plane is undeformed. To the left of this plane, the planes of atoms have sheared in such a way as to make the lattice a mirror image across the twin plane. In simple lattice such as this, each atom in the twinned

region moves by a homogeneous shear a distance proportional to its distance from the twin plane.

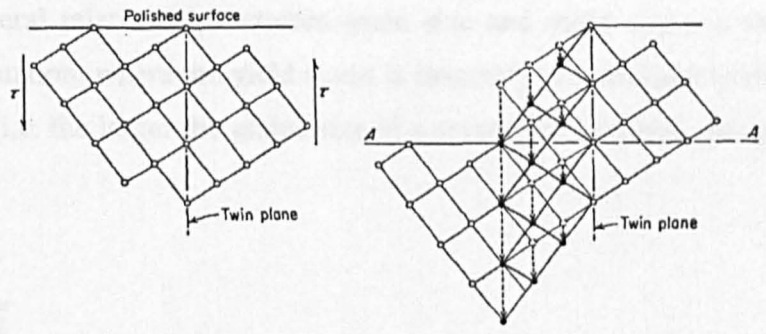

a) b)

Figure 2.38 Classical picture of twinning. **a)** Represents a cubic lattice section perpendicular to the surface, **b)** corresponds to the same cubic lattice under shear stress [59].

Twinning differs from slip in several specific respects. In slip, after deformation the orientation of the crystal above and below the slip plane is the same as before deformation occurred whereas twinning results in an orientation difference across the twin plane. Slip is usually considered to occur in separate multiples of the atomic spacing, while in twinning the atom movements are much less than an atomic distance. Slip takes place on relatively wider spread planes, however, in the twinned region of a crystal every atomic plane is involved in the deformation. Twins may be produced by mechanical (mechanical twins) or as the result of annealing (annealing twins) following plastic deformation. Mechanical twins are produced in bcc or hcp metals under conditions of decreased temperature, high strain rate and quick rate loading e.g. shock loading [59]. The common twin planes and directions have been documented by a number of authors [59, 57]. This is shown in Table 2.3.

Table 2.3 Twin planes and directions [59]

Crystal structure	Typical examples	Twin plane	Twin direction
bcc	α-Fe, Ta	(112)	[111]
hcp	Zn, Cd, Mg, Ti	$(10\bar{1}2)$	$[\bar{1}011]$

Twinning is not a dominant deformation mechanism in metals which possess many possible slip systems. Twinning generally occurs when the slip systems are restricted or when a factor causes an increase in the critical resolved shear stress so that the twinning stress is lower than the stress for slip [59].

2.4.5 *Dependency of grain size on yield stress*

A general relationship between grain size and yield stress is the well known Hall-Petch equation, where the yield stress is inversely proportional to the grain size to the power ½ (i.e. the larger the grains size of a crystalline material, the smaller its yield strength) [60].

$$\sigma_y = \sigma_0 + \frac{k_y}{\sqrt{d}} \tag{2.10}$$

Normally at the grain boundaries the crystallographic orientation changes rapidly. Therefore due to this orientation change, the movement of dislocations on a slip plane is delayed at the grain boundary. Thus the movement of another dislocation on the same slip plane requires more stress due to the interaction between two dislocations. As a result, an increasing stress is necessary to continue to generate dislocations from a source [31]. Given that the grain size is the maximum slip length, it can be expected that strength is inversely proportional to the grain size. As a result, the bimodal microstructure generally shows higher yield strength due to its finer grain size. The relationship between yield stress and grain size is shown in Figure 2.39 [60].

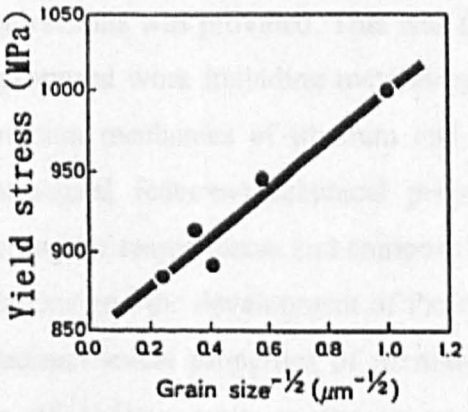

Figure 2.39 Relationship between yield stress and grain size [60].

Flower [32] also confirmed that reduction in microstructural feature such as grain size and the thickness of grain boundary α, promoted the ductility. This is due to the fact that by reducing the grain size, the effective length of the continuous grain boundary α layer is reduced therefore ductility can be increased [34, 37]. Sauer and Lütjering [37] were

also able to increase the ductility from RA=3.7 % to RA=17.1 % by reducing the grain size in the lamellar microstructure from 400 to 200 μm.

From Figure 2.40 it can be observed that by increasing the yield stress, elongation tends to decrease (grain sizes 16 to 3 μm). However grain sizes 1 to 3 μm tend to have higher elongation value as well as high strength. Therefore the ductility is improved in the ultra fine grain structure with a grain size of about 1 μm[60].

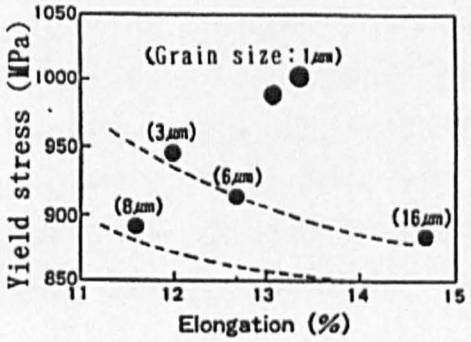

Figure 2.40 Relationship between yield stress and elongation [60].

2.5 Summary

Within this literature review the background information about titanium's history, production and preparation, application and rolls especially in the aerospace industry and its future requirements was provided. This was followed by the review of fundamentals behind the proposed work including metallurgy, classification, alloying, microstructure and deformation mechanics of titanium and titanium alloys plus the overall trends of microstructural features/mechanical properties relationships. The differences in phases including the temperatures and composition regimes in which they exist, the phase transformations and the development of the microstructures have been discussed. Next the thermomechanical properties of titanium including forging, heat treatment and the effects of cooling rates on the microstructure were examined. Research established that the geometrical parameters of the microstructure are influenced by the cooling rate from the β phase field and the heat treatment conditions. Finally a detailed analysis of titanium's crystallographic structure was included.

Chapter 3

MICROSTRUCTURAL ANALYSIS

3.1 Introduction

This chapter analyses and interprets the microstructure developed in TIMETAL® 6Al-2Sn-4Zr-6Mo during thermomechanical processing as a function of process history. Firstly, however, the chapter begins with an overview of the typical production routes used by Timet UK to produce titanium billet fit for aerospace applications. This is then followed by a description of the specific process route used for the Timetal 6-2-4-6 used in the work and an explanation of the experimental procedures used.

3.1.1 Typical thermomechanical treatment of α+β titanium alloys

For the most demanding applications such as compressor disks, the primary forging of α+β titanium alloys, is concerned with reaching a certain level of microstructure development in the most cost effective way. In general, the final forging for conventional α+β forged alloys can affect only modest development of the α+β structure. For this reason, obtaining a fine uniform structure in a forged and heat treated disk, for example, is dependant upon having an optimum structure in the as-received billet. For high quality compressor disk applications the ingot to billet conversion practice may consist of several stages as illustrated in Figure 3.1 [1]. The key aspects of each stage are reviewed in the following section.

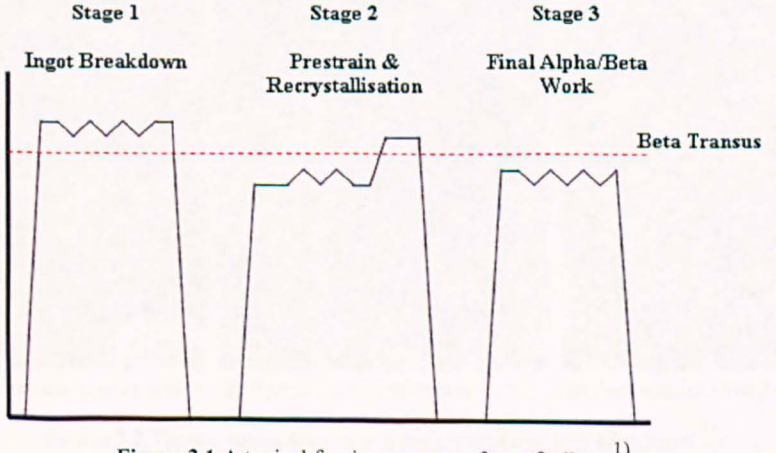

Figure 3.1 A typical forging sequence for α+β alloys [1].

Stage 1 (Ingot breakdown above β transus): The purpose of this stage is firstly to break up the coarse ingot structure produced by the VAR process, and secondly to provide large cross-sectional shape change at relatively low loads. Temperatures used during this stage are normally in excess of 1100°C thus quite large reductions can be achieved quickly. After forging the billet is generally allowed to cool in air and because its diameter is still relatively big, the cooling rate experienced within the billet is slow thus producing a very coarse acicular structure.

Stage 2 (Prestrain in the α+β region followed by β recrystallisation): The idea behind this stage is to render sufficient plastic strain into the billet (usually at a temperature below the β transus) so as to drive complete recrystallisation of the β phase during a subsequent thermal treatment (normally above the β transus). The recrystallisation is thought to be completely static and important parameters are the total plastic strain and the temperatures of both the prestrain and recrystallisation operation, all of which affect grain size after the recrystallisation treatment. However, minimising the time of the recrystallisation treatment is the most critical factor as β grain growth in titanium alloys is generally rapid. The billet is then quenched which produces again a coarse acicular structure but with much reduced lath length due to the final β grain size (Figure 3.2a).

Stage 3 (Final α+β forging): This is the most important stage and takes place below the β transus (i.e. within the α+β phase field). The reason behind this stage is to break up the coarse acicular structure to produce a uniform equiaxed α (i.e. produce the α_p) structure (Figure 3.2b, c) [1].

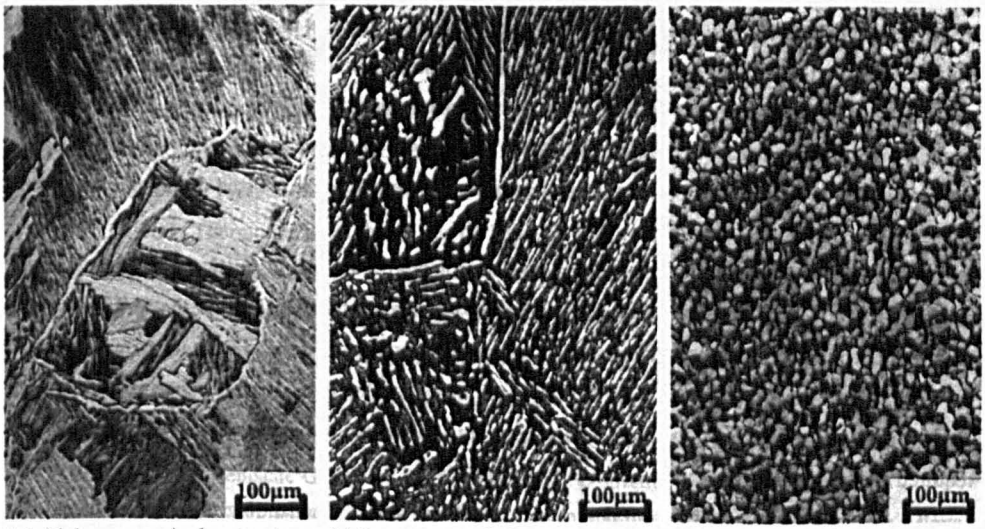

a) Initial coarse acicular structure **b)** Part processed structure **c)** Final equiaxed α+β structure

Figure 3.2 Typical structures found during processing α+β alloy billet [1].

3.1.2 High strength intermediate temperature alloy Ti 6Al-2Sn-4Zr-6Mo

Ti 6Al-2Sn-4Zr-6Mo is a heat treatable, α+β alloy which was mainly designed for high temperature applications. It's normally selected over its major competitor, Ti 6Al-2Sn-4Zr-2Mo because of its higher strength at higher temperatures. It combines good strength and corrosion resistance and it can be found in gas turbine engines (particularly in compressor disks and fan blades) and impellers and has been evaluated for use in deep sour well applications [12, 17].

Ti-6-2-4-6 aerospace components are fabricated by hot die and isothermal forging techniques, resulting in cost effective near net shape forgings, due to reduced final machining. As component complexity increases, improved accuracy of microstructural predictions is required, due to the inevitable variation in TMP parameters, even under isothermal conditions [18].

Ti-6-2-4-6 alloys are similar to Ti-6-4 in forgeability and crack sensitivity, but are stronger and more readily heat treated than Ti 6-4. These features are due to the increased solid solution strengthening provided by the addition of tin and zirconium which have relatively small effects on the transformation temperature, as well as the large molybdenum additions which result in an increased amount of β phase [12, 17]. Martensite does not form in ordinary situations in Ti 6-2-4-6[12].

The high elevated temperature strength of Ti 6-2-4-6 has been one of the most attractive features of this material. More recently, their high low-temperature strength has also been exploited. Figure 3.3 shows the yield strength range of the α+β Ti 6-2-4-6 alloy at the low to high temperatures commonly encountered in various applications. It is quite apparent that the higher temperature usefulness for Ti-6-2-4-6 is limited by a rapid decrease in tensile yield strength above about 555° C (1032 F).

In general, the upper service temperature limit for titanium alloys is 537°C (1000 F). However, the limit for any one alloy depends largely on composition, mill product form, heat treatment condition, and the time, temperature, and stress combinations of the application [9].

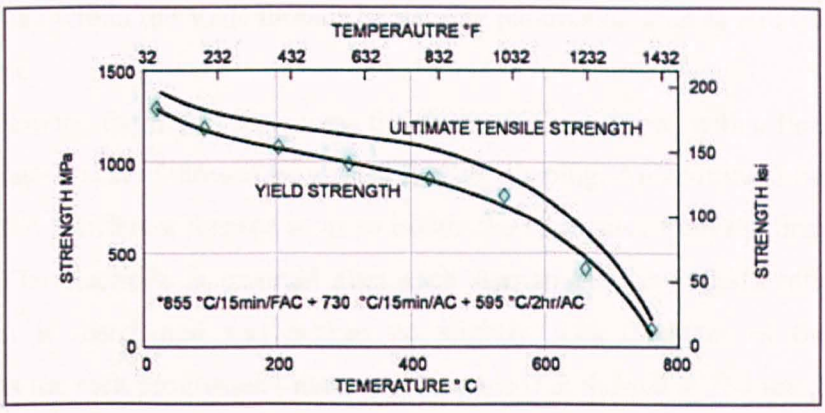

Figure 3.3 Typical range in tensile yield strength found for TIMETAL® 6Al-2Sn-4Zr-6Mo alloy due to variation in chemistry, structure, mill product form, heat treatment and test conditions [17].

3.1.3 TIMETAL® 6Al-2Sn-4Zr-6Mo production route

A typical billet manufacturing process route for TIMETAL® 6Al-2Sn-4Zr-6Mo begins with mixing the raw materials. At this stage the raw materials (Ti sponge, scrap, elementals....) are mixed together in groups of 3 tonnes which then are separated into six half Tonne lots. Batches are then broken down into 14 equal 43kg lots to ensure a homogenous distribution of alloying elements.

For better handling each 43kg lot is then compressed into D-shaped solids (Figure 3.4 b). These compressed D-shaped solids (compacts) are then used to build up the electrode (84 compacts are used to piece together a 483 mm diameter electrode) that will be used in the VAR furnace later in the process.

The compacts are plasma welded together and then are ready for the first VAR melt. Care is taken in order to stop the electrodes from coming into contact with contamination, such as dust, which can affect the chemistry of the product if carried into the furnace.

Once the electrode is prepared, it is placed within the copper crucible of the VAR furnace. A stub is used to spark an initial contact, causing a small melt pool on the top of the electrode.

Next, the stub, held by a ram, is forced into the melt pool which then solidifies producing a join between the stub and the electrode. The ram is then moved up and the electrode is lifted off the ground. A spark is then initiated between the electrode and the copper crucible causing the electrode to melt. The spark is maintained between the top of the melt pool and the electrode until the electrode is consumed. Control of the melt

pool is gained within the VAR furnace by varying parameters such as Arc Coil, Stirring, Vacuum, etc.

Following the first melt process the electrode is machined with a floating tool in order to remove scale followed by a fixed tool for shaping. An additional two melts are carried out in a different furnace so as to isolate the impurities from the first step of the process. The electrode is inverted after each step so that any solidification induced segregation is distributed and broken up slightly. The diameter of the electrode increases as the melt progresses (diameter of the ingot at the end is 760 mm). Figure 3.4 shows some of the production of titanium alloy ingot.

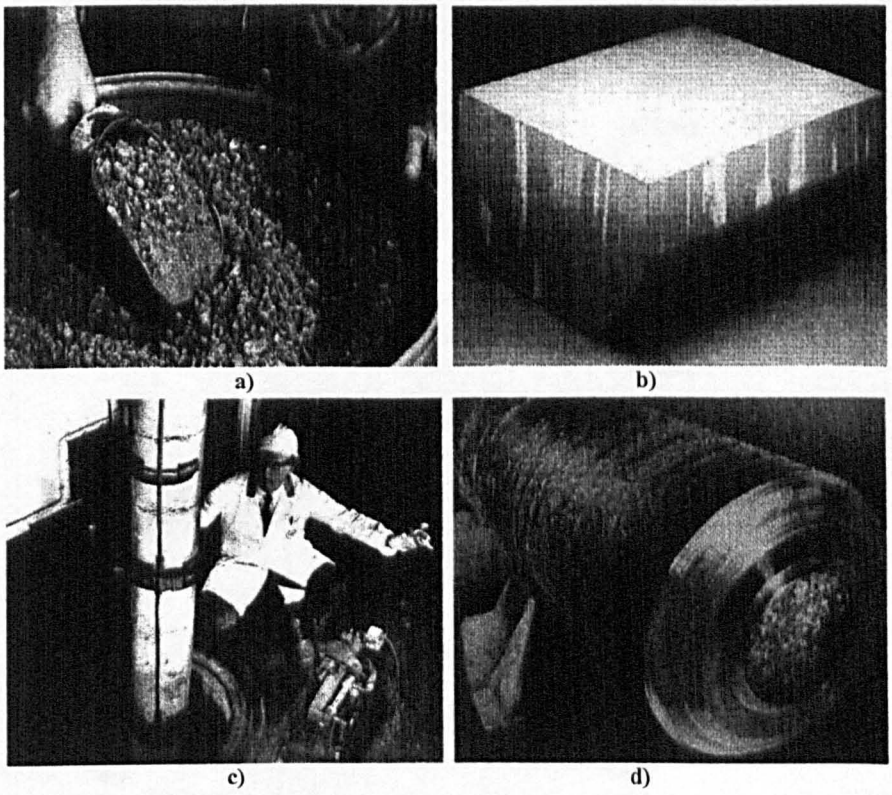

Figure 3.4 Titanium ingot production **a)** Granules **b)** D-shaped compact **c)** Lowering electrode into furnace **d)** Final ingot [12].

Following ingot production, to break up the microstructure and create a desired shape, hot forging is necessary. The process is shown schematically in Figure 3.5, based on private communications with TIMET, UK.

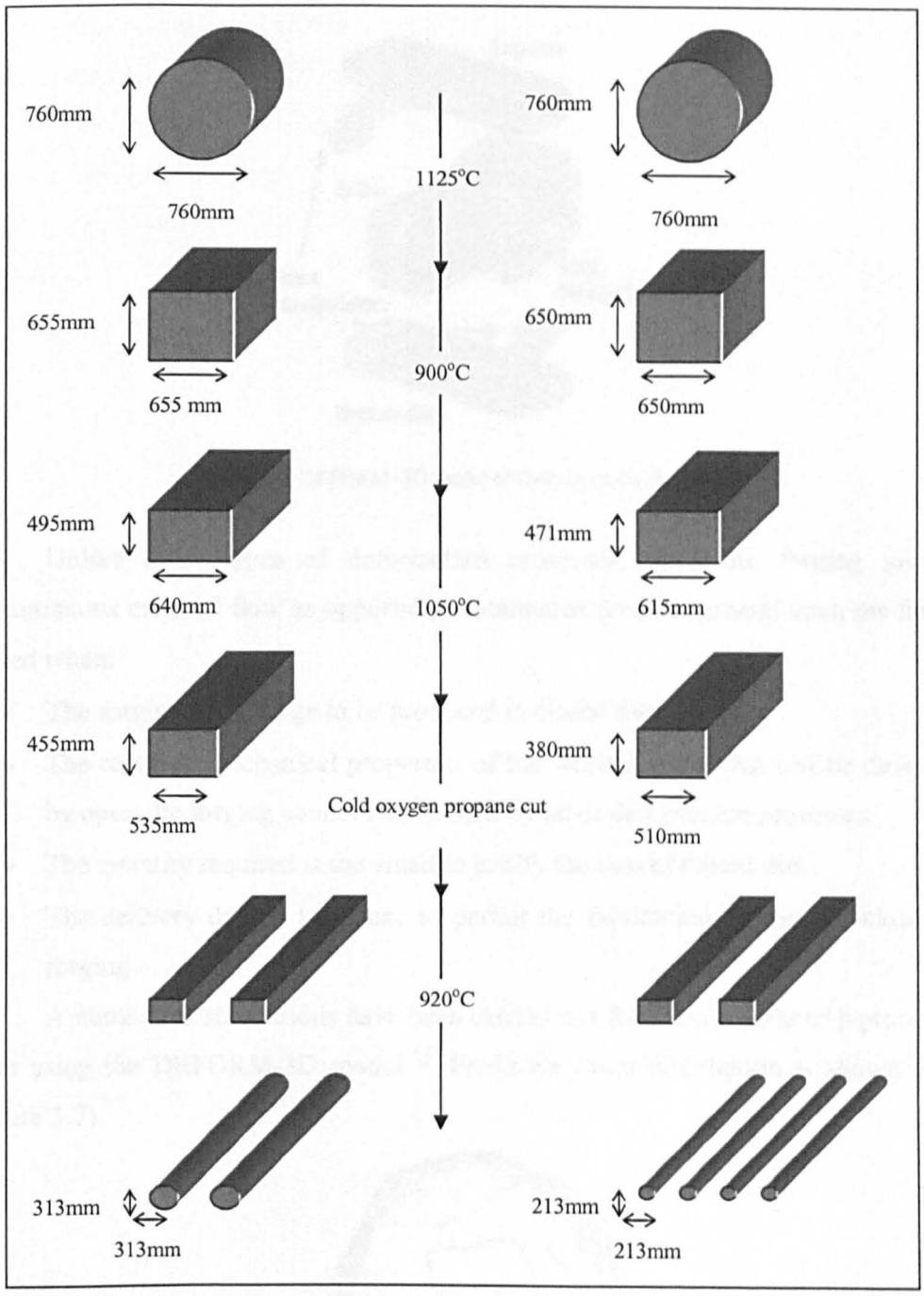

Figure 3.5 Schematic of TIMETAL® 6Al-2Sn-4Zr-6Mo billet process route.

The manufacture of the TIMETAL® 6Al-2Sn-4Zr-6Mo billet used in this work was carried out using an 1800 Tonne Davy hydraulic uniaxial open die press (Figure 3.6), forging a triple vacuum arc remelted ingot to produce finished diameters of 213 and 313 mm.

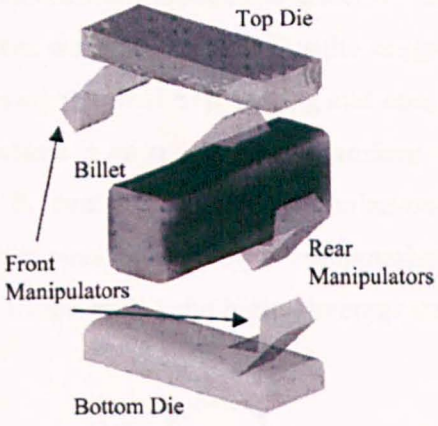

Figure 3.6 DEFORM -3D model of Davy open die forging [3].

Unlike other types of deformation processes, open die forging provides discontinuous material flow as opposed to continuous flow. In general open die forging is used when:

- The forging is too large to be produced in closed dies
- The required mechanical properties of the worked metal that can be developed by open-die forging cannot be obtained by other deformation processes
- The quantity required is too small to justify the cost of closed dies
- The delivery date is too close to permit the fabrication of dies for closed die forging

A number of simulations have been carried out for the complete α+β processing route using the DEFORM-3D model [3]. Predicted strain distribution is shown below (Figure 3.7).

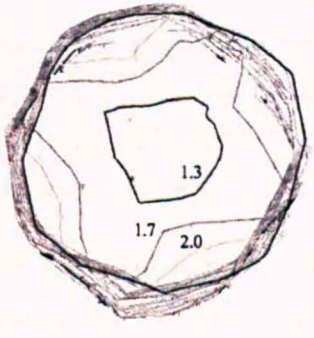

Figure 3.7 Transverse slice showing predicted strain distribution in Davy press [3].

From the above model it can be observed that the strain levels are not radially uniform and strain distribution decreases from about 2 near the surface to about 1 in the centre.

Using α phase globularization model, the effect of time, temperature and strain on microstructure refinement was also studied. Results suggest a significant amount of α phase globularization during the final α+β forging and ensuing heat treatment (Figure 3.8). The Davy process resulted in an approximately uniform fraction of globularized α, which ranged from 70-99 %, centre having less globularization. A significantly larger fraction of α globularization was caused by a combination of a greater number of reheats (i.e. longer time at temperature) and higher average strain levels in the Davy bar [3].

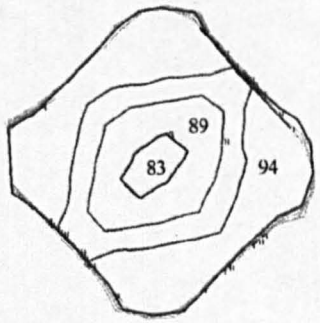

Figure 3.8 Transverse slice showing predicted volume fraction of globularized alpha distribution in Davy press, following final α+β forging and heat treatment [3].

3.2 Experimental work

The chemical composition of as-received TIMETAL® 6Al-2Sn-4Zr-6Mo billet material, originating from Timet UK is shown in Table 3.1. The β transus was found to be 990 ± 5 C°.

Table3.1 chemical composition of Ti 6Al-2Sn-4Zr-6Mo.

Element	Al	Sn	Zr	Mo	Fe	Si	C	N_2	O_2
Weight%	6.14	1.97	4.03	6.08	0.06	0.06	0.008	0.002	0.09

At an intimidate stage of the processing when the billet was rectangular, two orthogonal marks on the long and short axes of the rectangle were placed on the billet. These marks stayed orthogonal and remained on the sample during the process and were designated as R1 (long) and R2 (short) as shown in Figure 3.9. A section for microstructure investigation was then cut from the middle of the billet to avoid any end effects. Microstructure investigation, using scanning electron microscopy, was then

undertaken within four slices of this section. Slices S1 and S4, from the small billet and LS1 and LS4 from the larger billet were in planes parallel to R1 and R2, respectively whilst slices S2 and S3 (from the small billet) and LS2 and LS3 (from the large billet) were at approximately 30° and 60° from R1, respectively. In all cases the microstructure was analysed in the plane containing the longitudinal axis of the billet, Z.

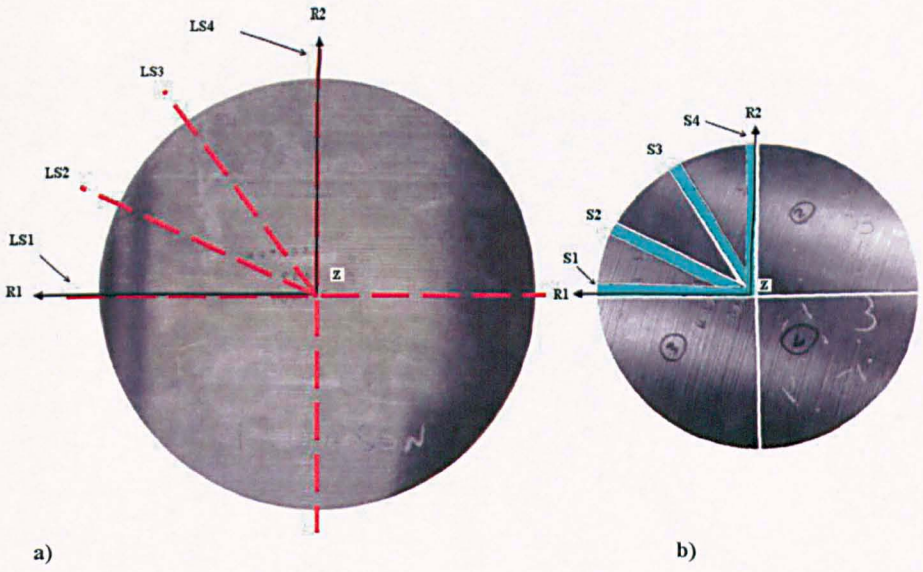

Figure 3.9 Cross-section of the as-forged billets, **a)** 313 mm and **b)** 213 mm a diameter with reference axes R1, R2 and Z defined. S1 to S4 and LS1 to LS4 represent locations of microstructure analysis.

3.2.1 Preparation

Due to its high ductility, titanium produces long chips when machined or cut, which makes metallographic cutting with regular aluminium oxide cut-off wheels very ineffective. Heat damage can occur easily and therefore special silicon carbide cut-off wheels have been used specifically for cutting of titanium.

Once sectioned and mounted each specimen was ground then polished using a Struers grinding system and a Struers MD-Largo honeycomb pad with 9μm diamond suspension respectively. The aim of these processes was to create a flat, smooth clean surface ready for etching. The best results were obtained when using a disc speed of 150 rpm with loads of approximately 100N.

The final step was a chemical-mechanical polishing with colloidal silica (Silco of 0.05μm), which led to an improved surface finish. If this chemical-mechanical polish is not used, the surface of the titanium sample displays a more scratched surface as it is almost impossible to achieve a good polish with diamond only.

3.2.1.1 Etching

Once fully polished the specimen was etched in order to show up the microstructure for optical analysis. Etching of the samples was carried out using Kroll's reagent (100 ml water, 1-3 ml hydrofluoric acid, 2-6 ml nitric acid). The concentration can vary depending on the alloy and can be adjusted individually. Each sample was submerged in the Kroll's reagent for a period of 8-12 seconds. This was followed by soaking the sample in a lime solution for 30 seconds and then by holding it in water for 60 seconds. Once etched the specimen's microstructure was ready for optical examination using reflected light microscopy. Figure 3.10 illustrates the cross section of two samples after etching.

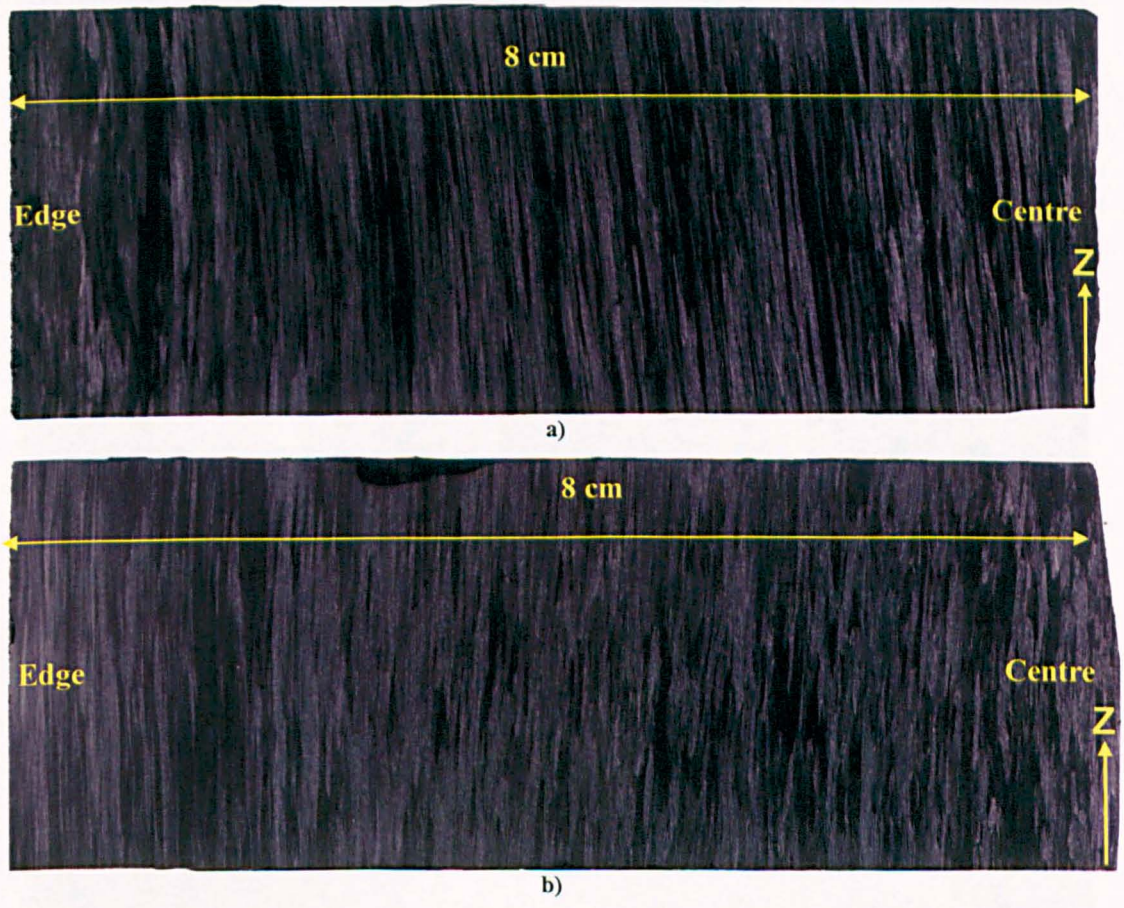

Figure 3.10 Cross section of samples **a)** S2 and **b)** S3 after etching.

3.2.2 Scanning Electron Microscopy (SEM)

The Camscan series 2 SEM was used for imaging. The SEM images were taken using secondary-electron (SE) imaging.

Throughout the whole cross-section of the billet analysed, a bimodal microstructure consisting of relatively equiaxed α_p within an acicular transformed β matrix was observed, examples of which are shown below.

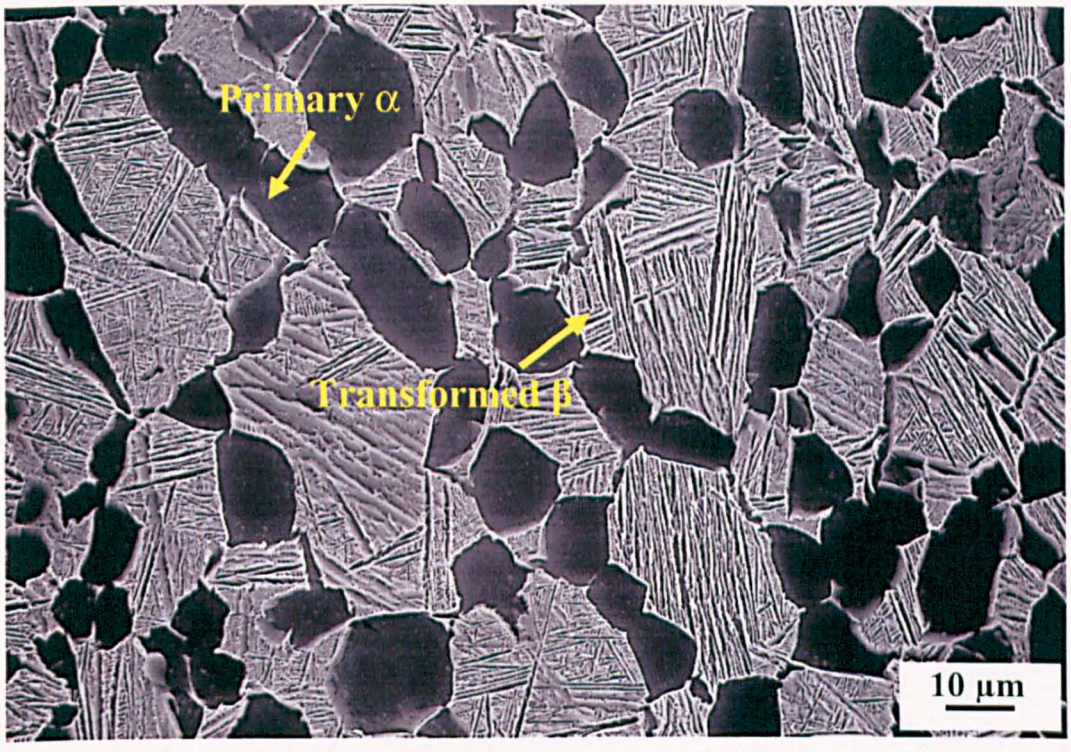

a) Secondary electron image of TIMETAL® 6-2-4-6 containing 30% α_p in a matrix of transformed β

b) Large scale secondary electron image of sample S4 near the billet centre

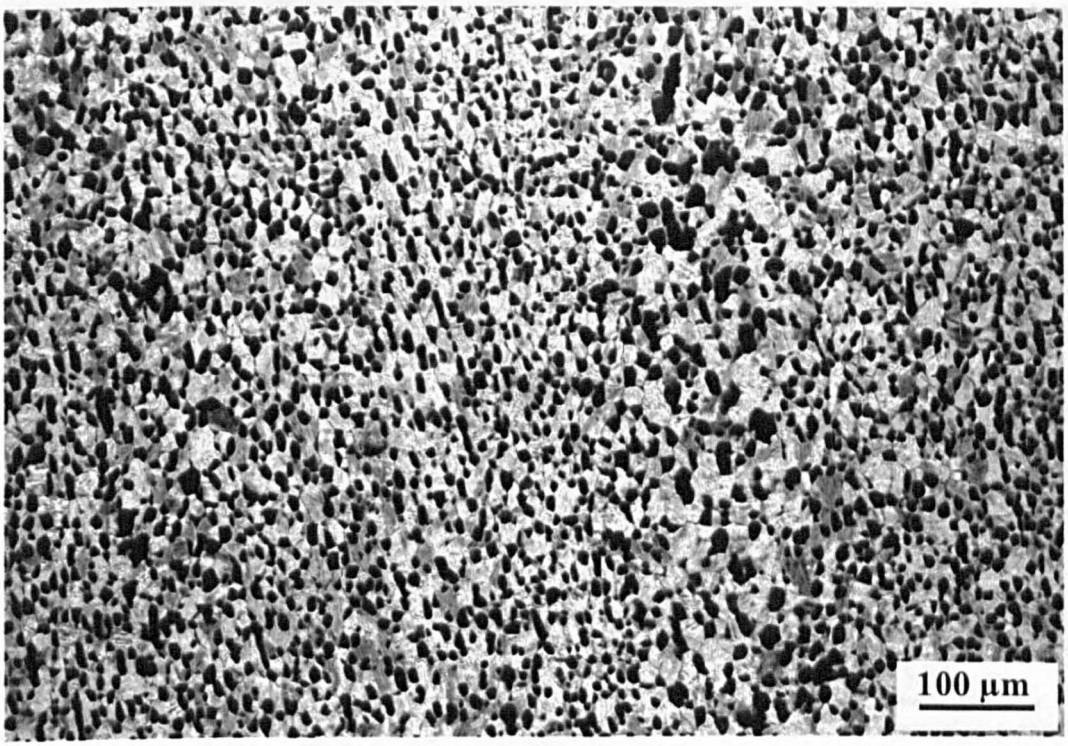

c) Large scale secondary electron image of sample S4 near the billet centre

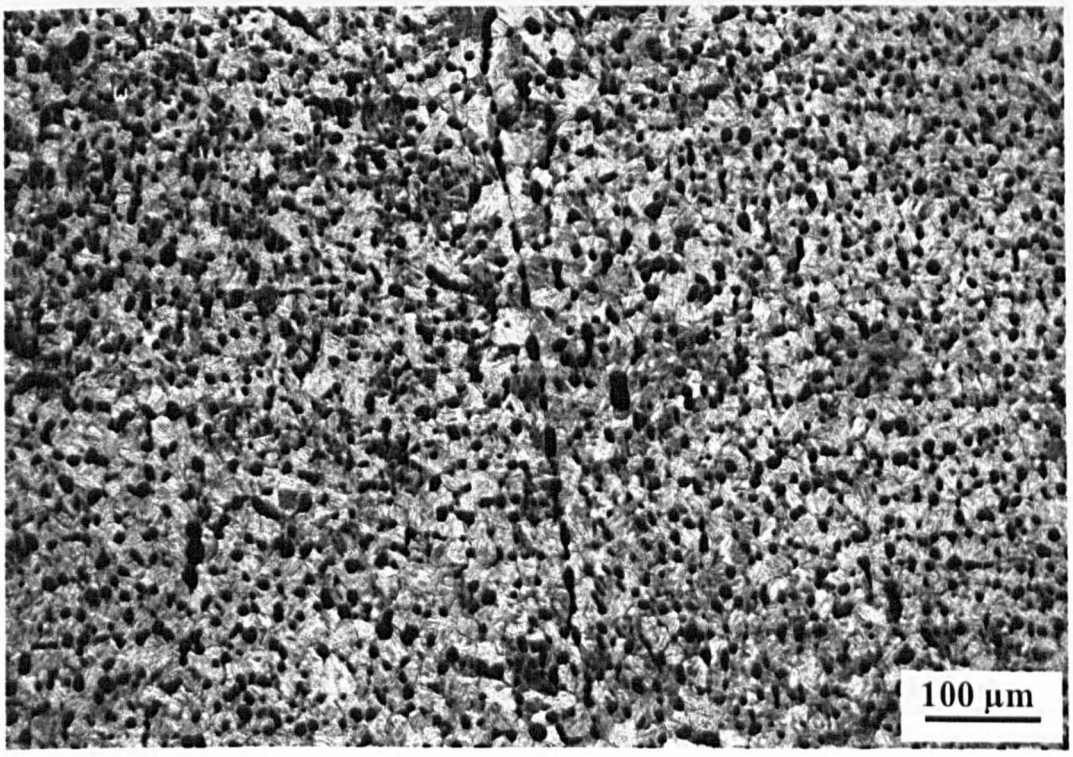

d) Large scale secondary electron image of the large billet near the billet centre

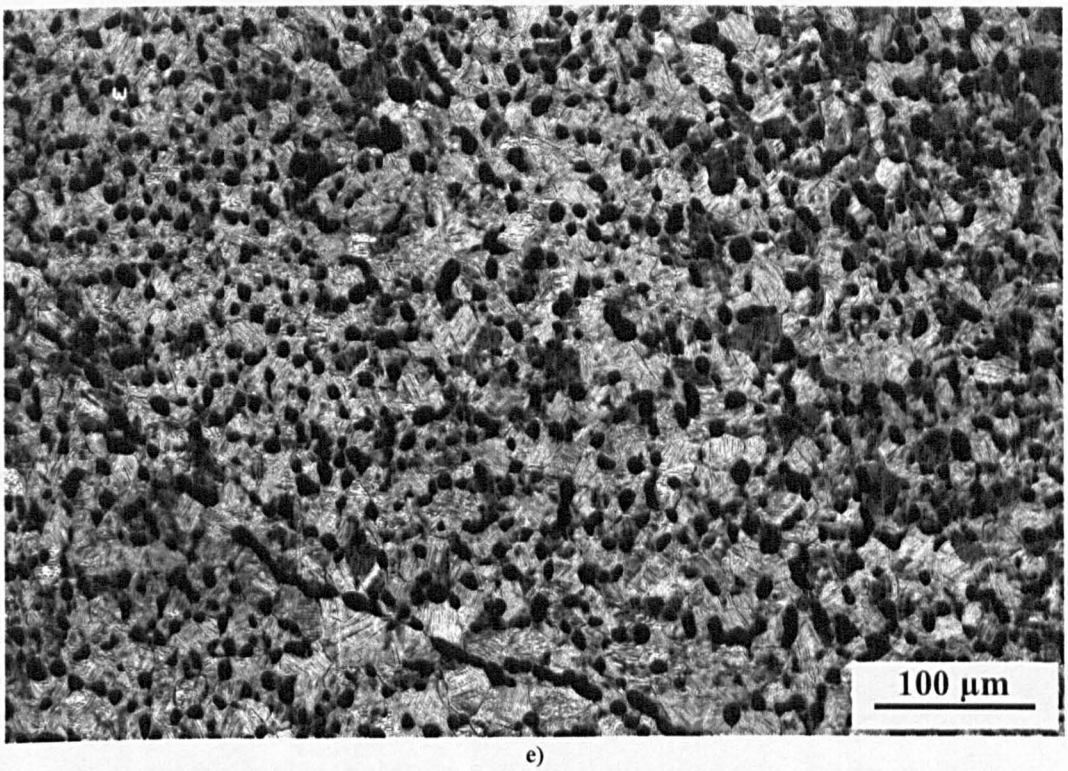

e)

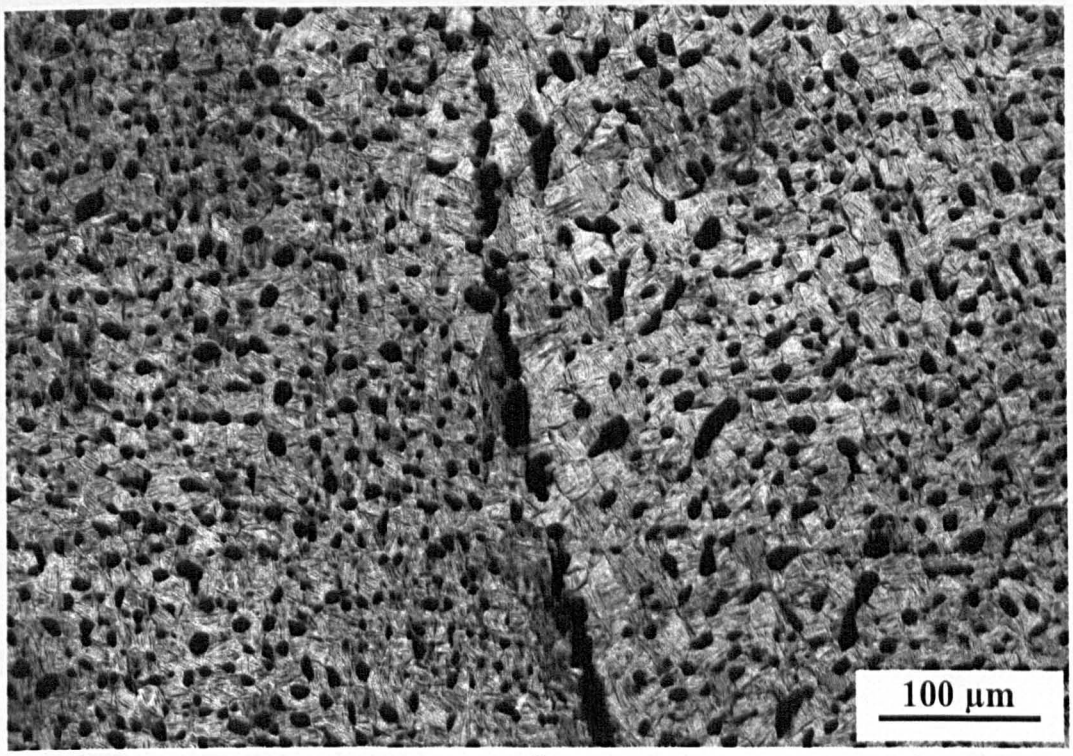

f)

Figure 3.11 a) Secondary electron image of TIMETAL® 6-2-4-6 containing 30% α_p in a matrix of transformed β, **b, c)** large scale secondary electron image of sample S4 near the billet centre **d, e, f)** large scale secondary electron image of the large billet near the billet centre.

Detailed analysis of slices S1 through to S4 and LS1 to LS4 was performed at two locations: 1) near the edge of the billet to a depth of approximately 30 mm and 2) at the centre of the billet up to a radius of roughly 30 mm (Figure 3.12). For all cases, a series of slightly overlapping micrographs, each covering 550 μm x 550 μm was taken to cover the whole 30 mm.

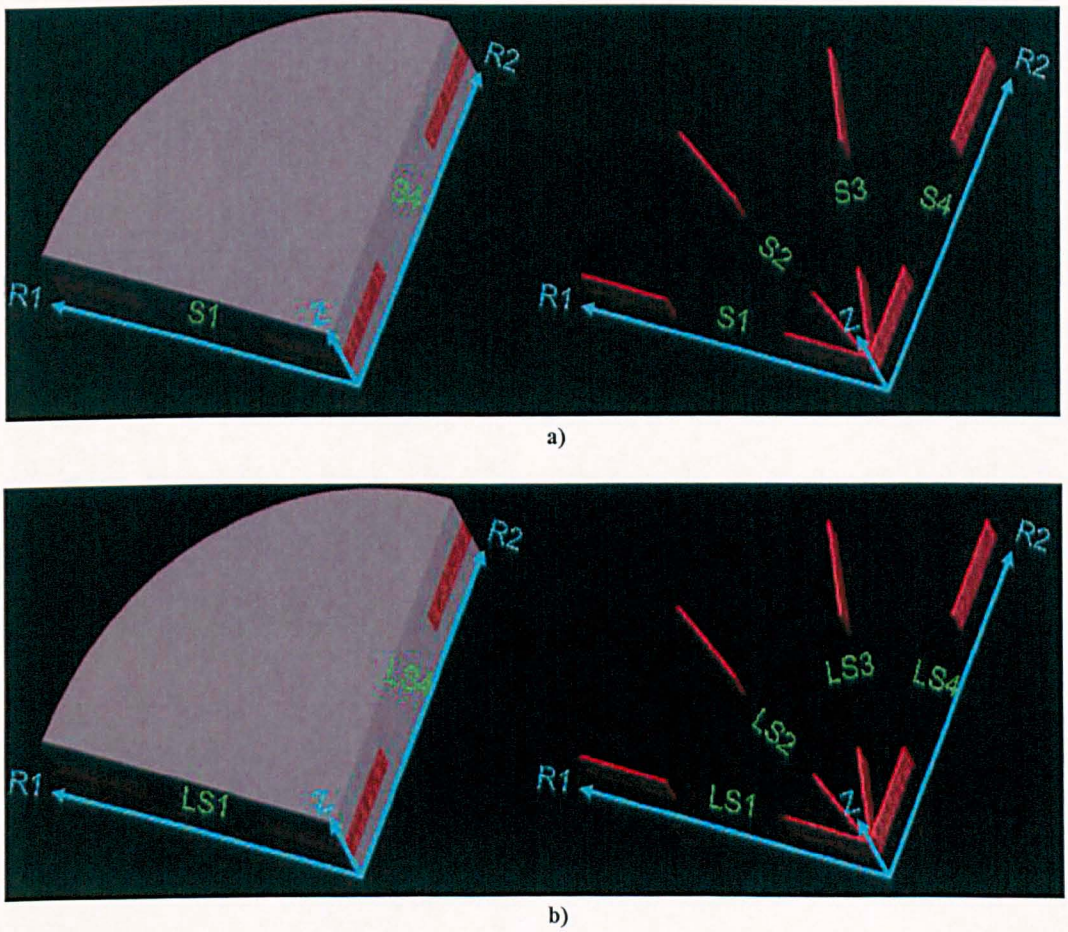

Figure 3.12 a) Slices S1 to S4 in the small billet (213 mm a diameter) **b)** Slices LS1 to LS4 in the large billet (313 mm a diameter).

An example of the series of micrographs from sample S2 edge each covering approximately 550 μm x 550 μm for the whole 30 mm is shown below in Figure 3.13.

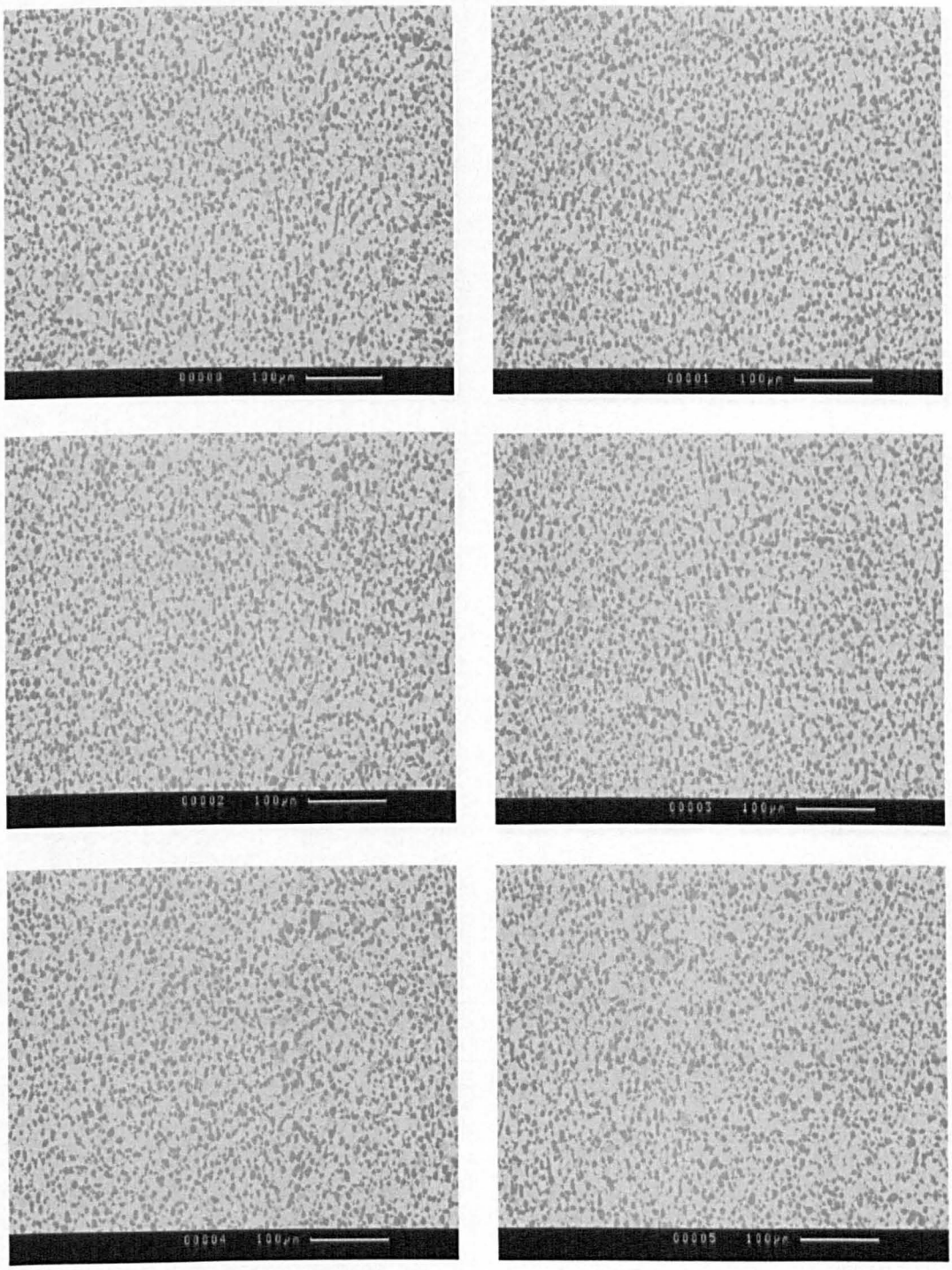

a) Micrographs from 0 to 3300µm

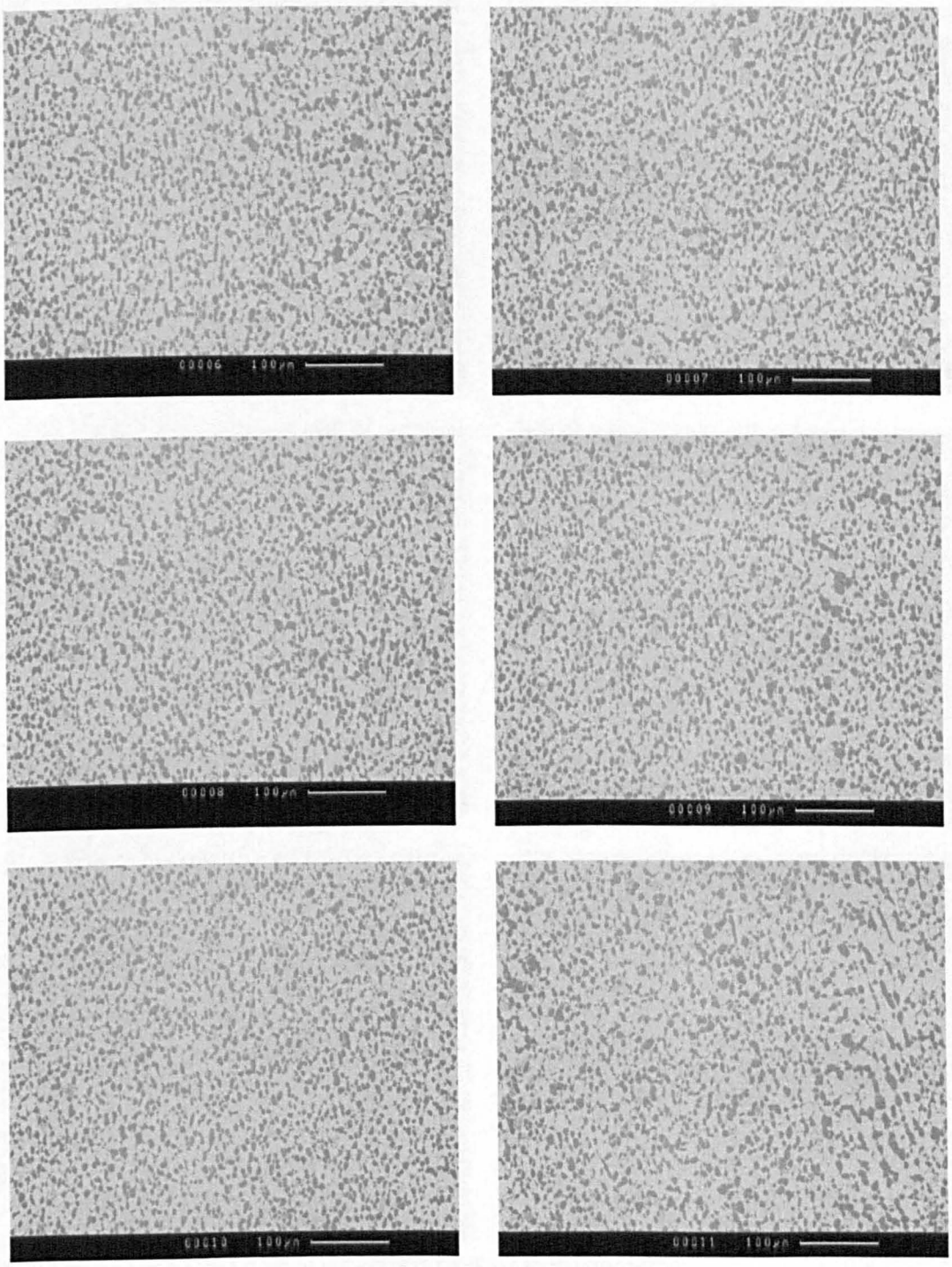

b) Micrographs from 3300 to 6600µm

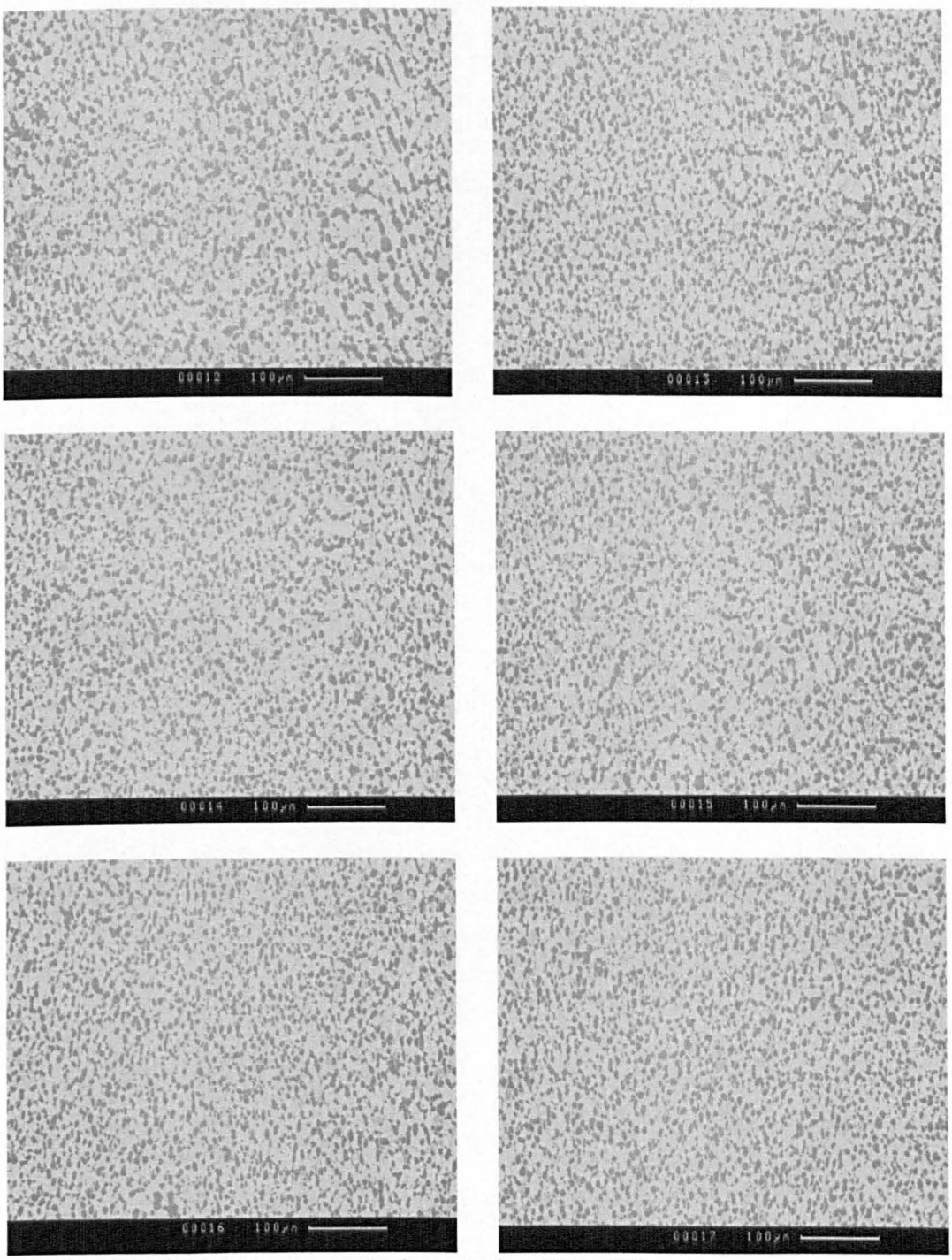

c) Micrographs from 6600 to 9900μm

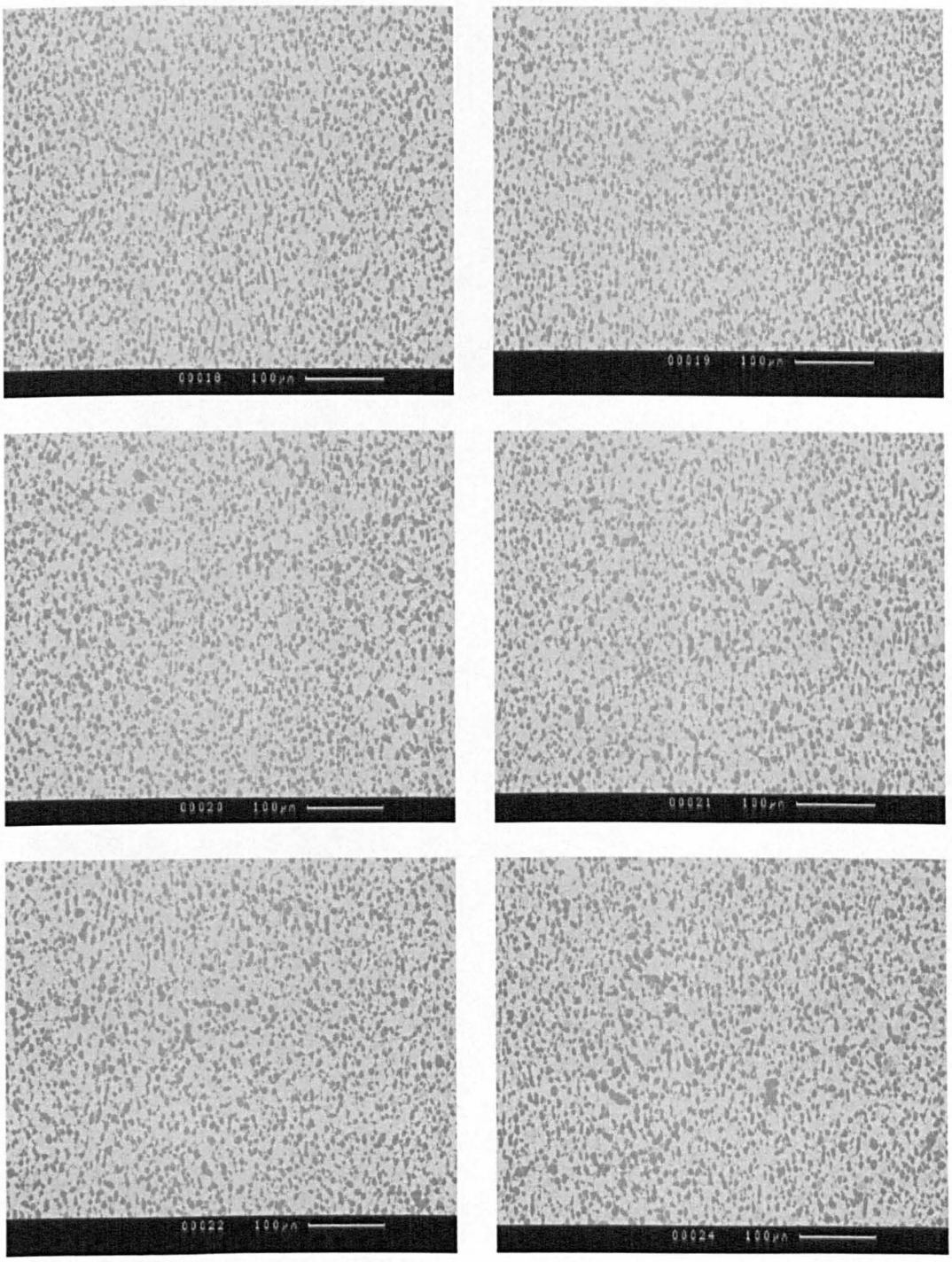

d) Micrographs from 9900 to 13200μm

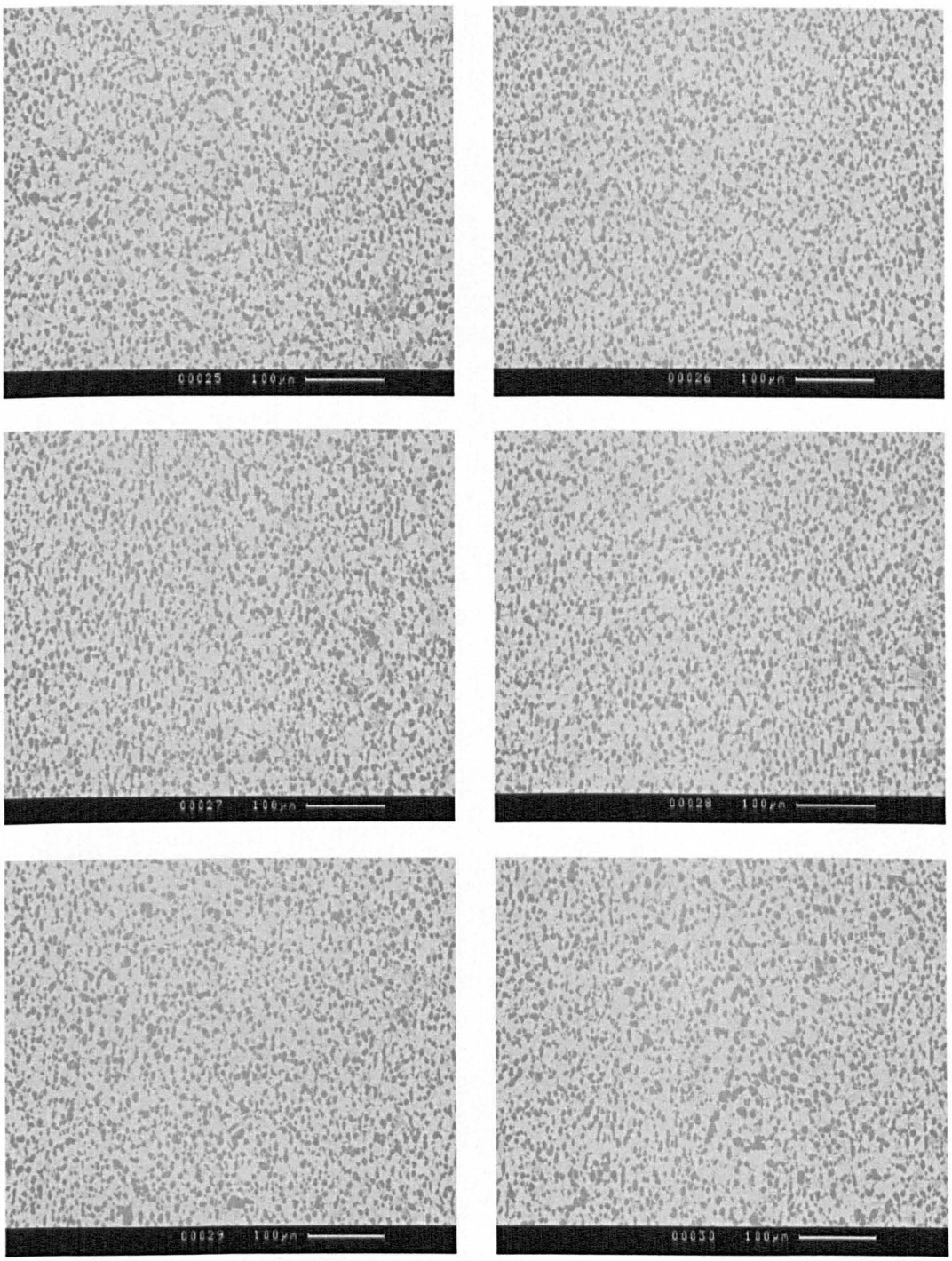

e) Micrographs from 13200 to 16500µm

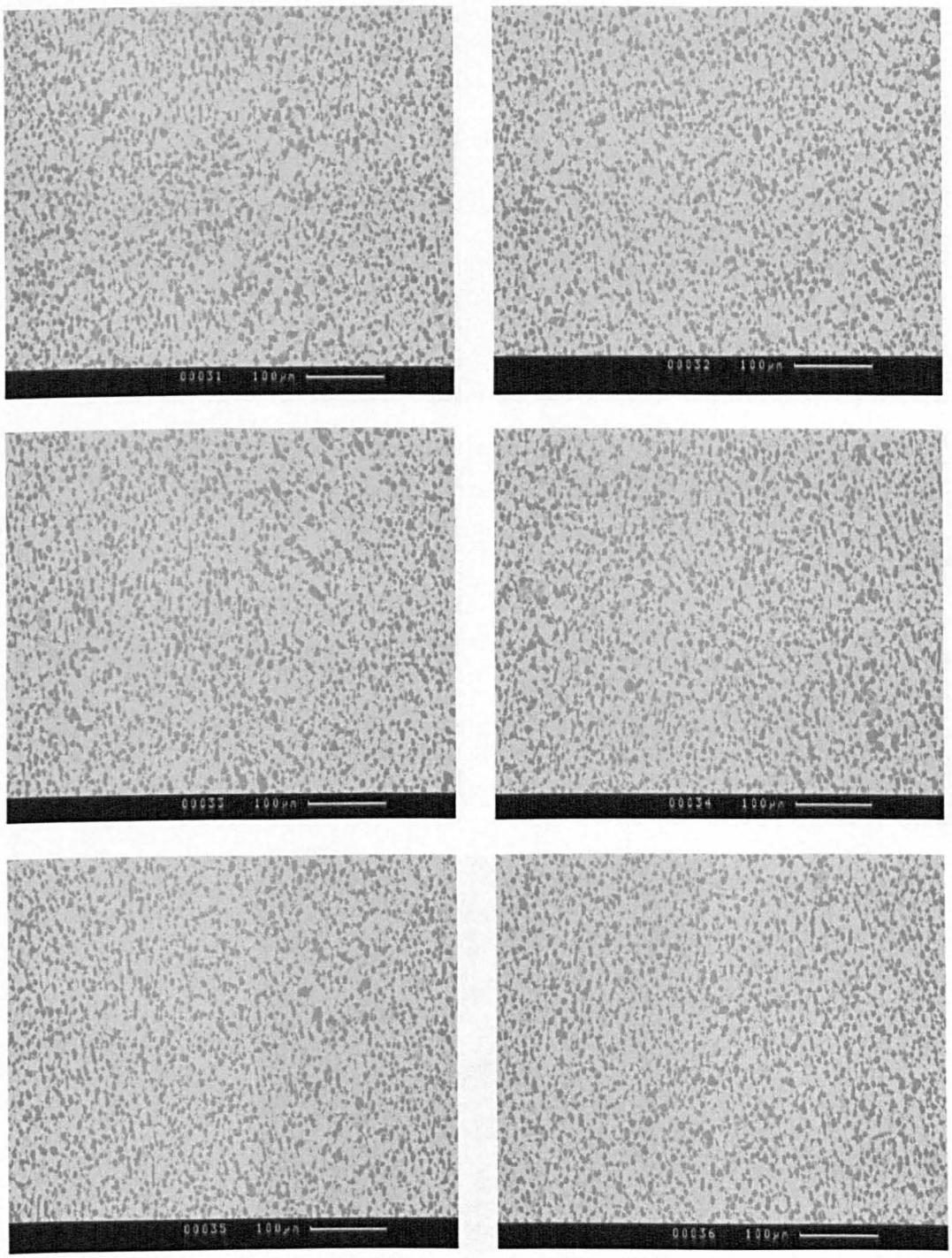

f) Micrographs from 16500 to 19800µm

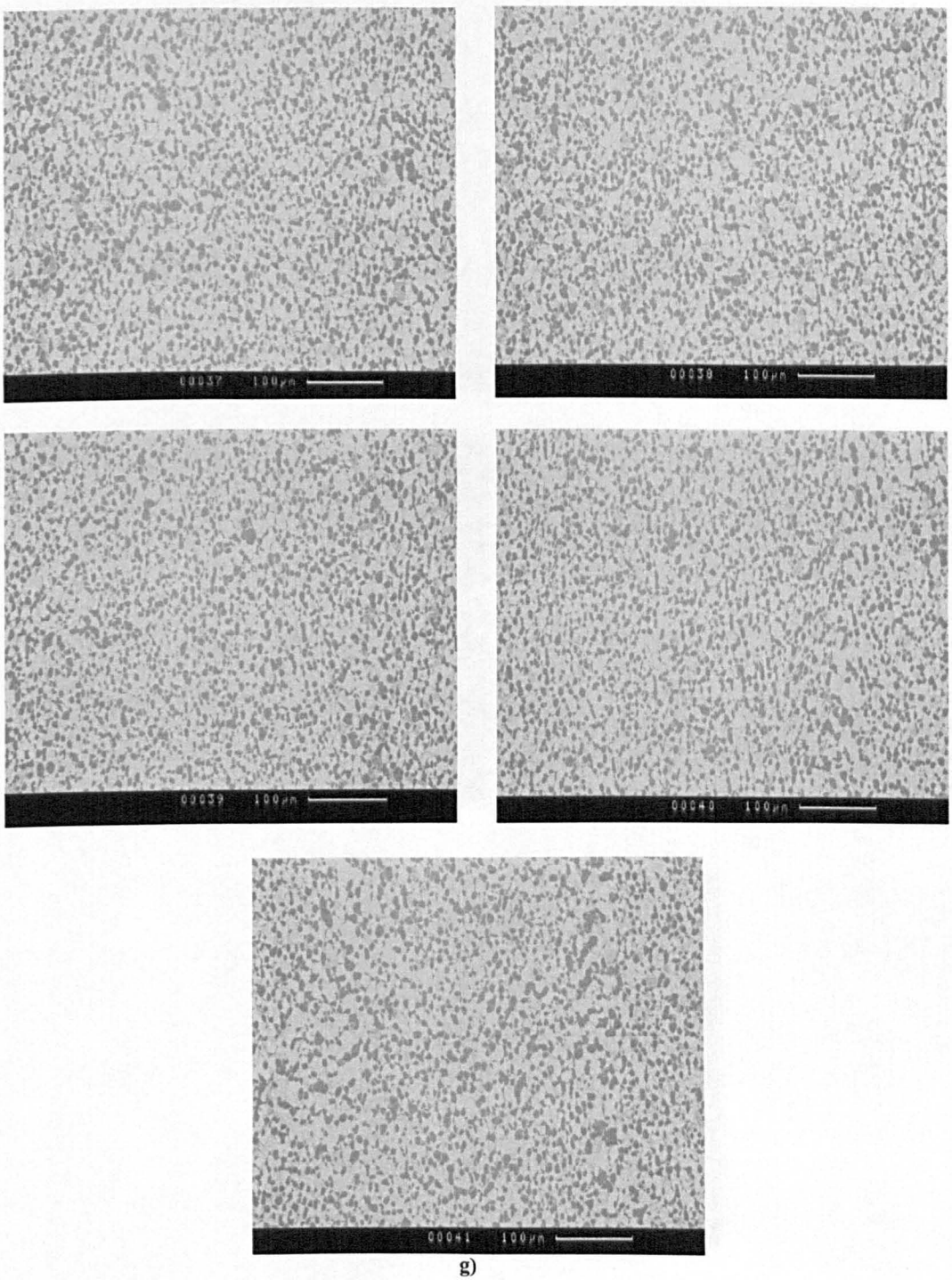

g)

Figure 3.13 Series of micrographs, each covering 550 μm x 550 μm covering approximatly 30 mm (S2 at the edge)

Digital image analysis software KS400 was then used to determine the volume fraction of α_p, its size distribution and its aspect ratio distribution. Note that within each micrograph, the majority of α_s was eliminated in order to obtain accurate results. This was achieved using Camscan series 2 SEM. Figure 3.14 illustrates schematically the principals behind the KS400 software.

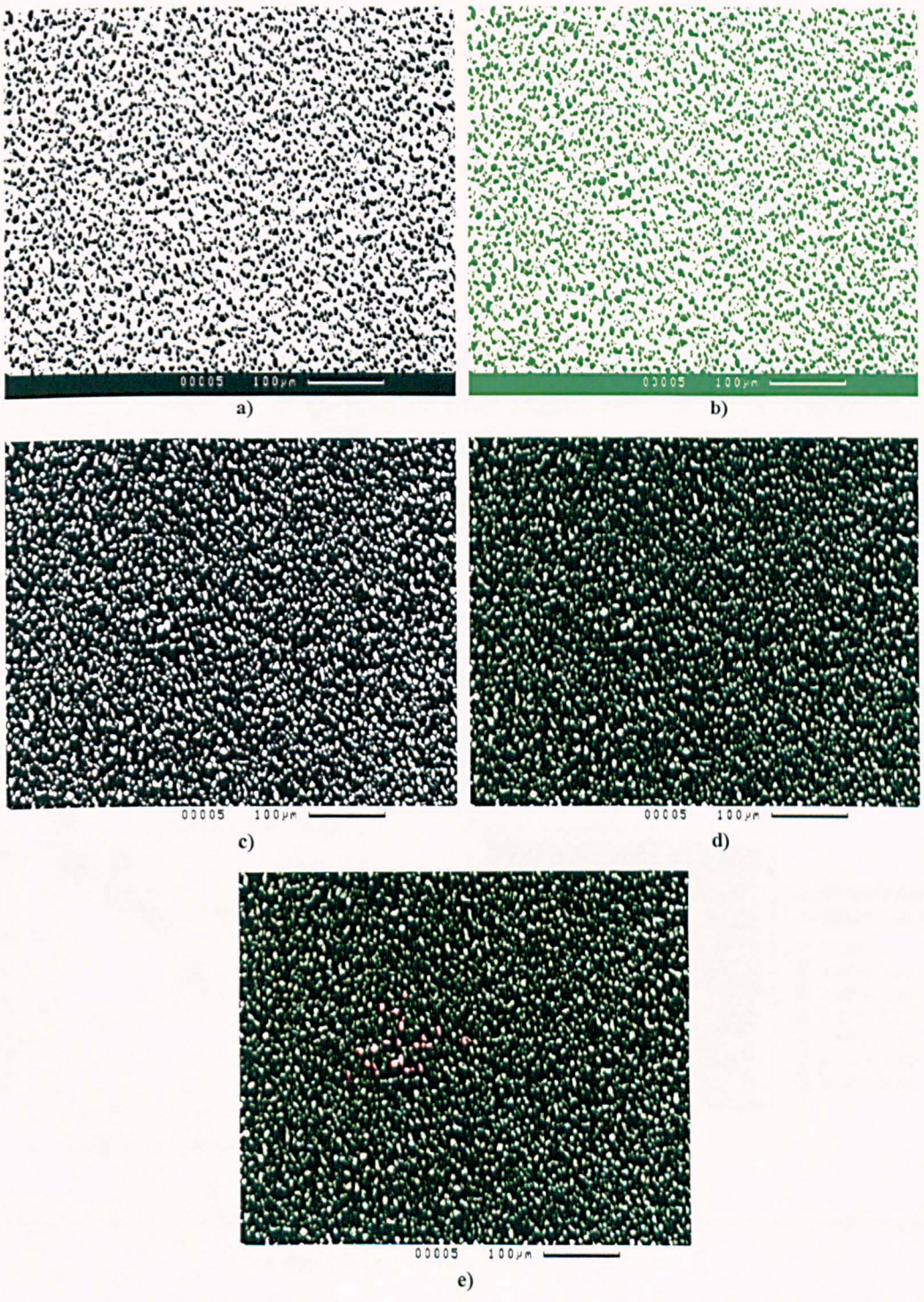

Figure3.14 a) Modified micrograph, using ks400 (majority of secondary alpha having been omitted) with increased contrast between dark and light greys **b)** selecting all the black features within the micrograph **c)** setting the frame (in order to prevent counting of unwanted black areas at the bottom edge of each micrograph) **d)** measuring the required dimensions of selected areas (e.g. area of primary alpha) **e)** red lines around some grains illustrate that single wanted grains can be select or deselected.

Any misidentification between primary and existing secondary α can be rectified at a later stage in this process using Microsoft excel. Using KS400 software the width and length of individual α_p grains, total area of the frame, total area of α_p and total percentage of α_p within each micrograph was measured.

3.3 Results and discussions

Major differences between the large and small billet were observed at the centre of each billet when the corresponding micrographs were compared (Figures 3.11). Continuous α grains were observed (grain boundary α) at the centre of the larger billet. Grain boundary α is formed along the β grain boundaries (as shown by SEM micrographs Figures 3.11 d, e, f) due to slower cooling rates at the centre in comparison to the edge of the larger diameter billet.

The work done by Fox and Neal [1] also showed that following the recrystallisation stage, the rate of cooling dictates the scale of the transformation product and the thickness of grain boundary α. This is revealed in Figure 3.15.

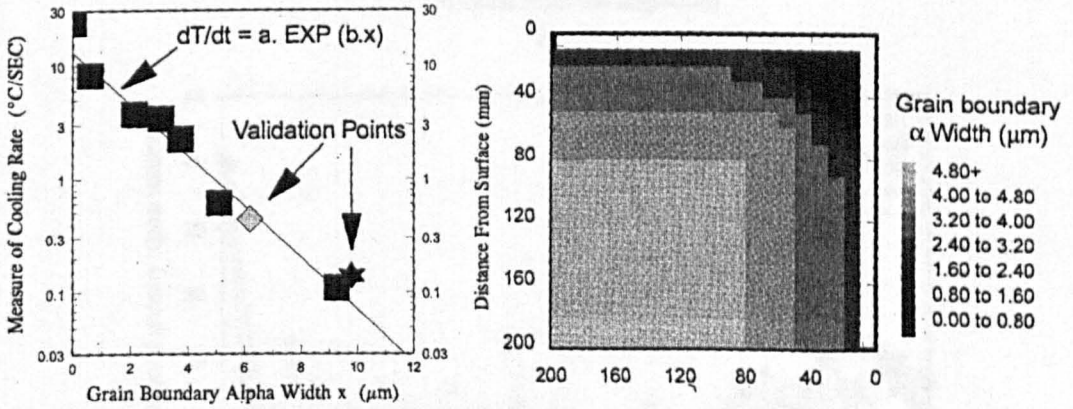

Figure 3.15 a) Relationship between the cooling rate and the grain boundary α thickness and **b)** variation in grain boundary α width with location for an IMI 318 billet [1].

By calculating the ratio of the cross section area of the billets after the recrystallisation stage to the final cross section area of the billets, it can be revealed that the amount of strain being applied to the smaller billet is twice as much as the strain being applied to the larger billet. It can therefore be argued that there is more penetration of strain at the centre of the smaller billet causing the grain boundary α to break up.

3.3.1 *Total percentage of α_p volume fraction*

The total percentage of α_p volume fraction for each sample was then calculated using both the area of each grain within each micrograph and the total frame area in each calculation. The volume fraction of α_p as a function of location within the small and large size billet is shown in Figure 3.16 a) and b).

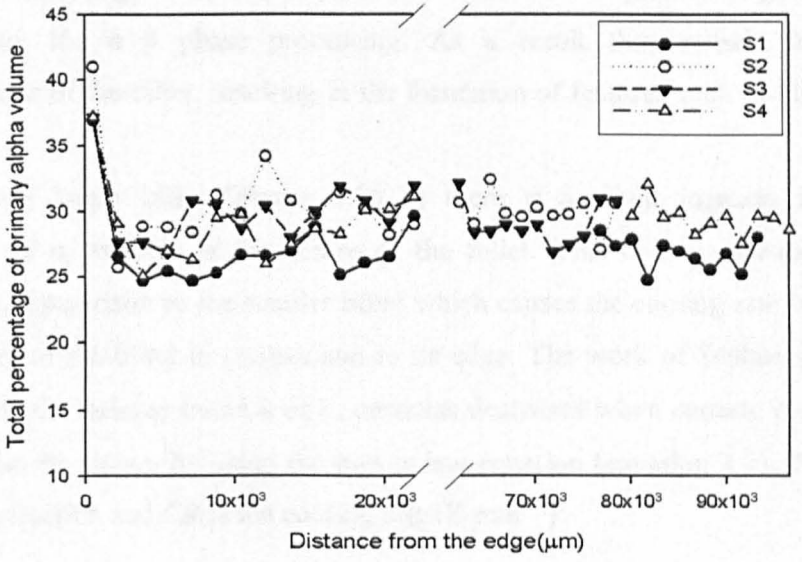

a)

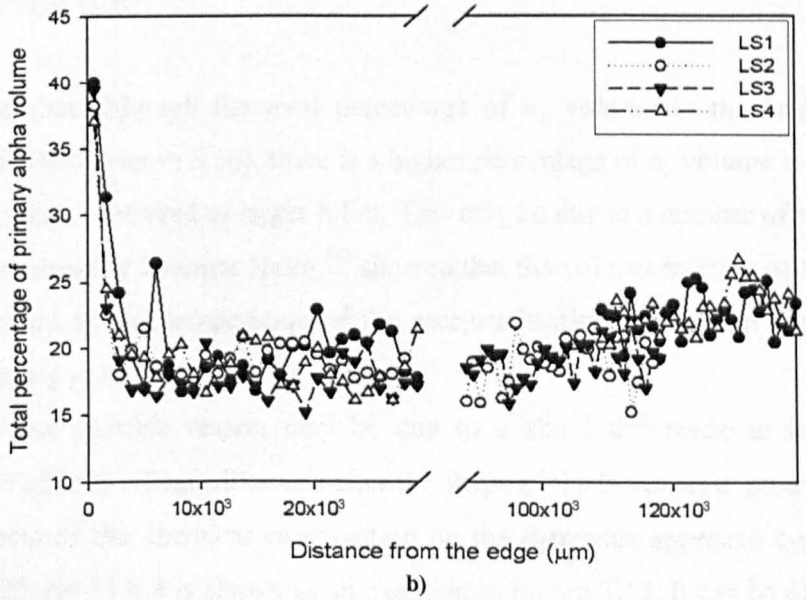

b)

Figure 3.16 The total percentage and the distribution of the α_p at the edge and centre of **a)** small billet **b)** Large billet.

Figure 3.16 a) show that with the exception for the extreme edge (≈ 1 mm), where the α_p fraction is close to 40%, the α_p volume fraction is consistently between 25

and 30% from edge to centre regardless of sample location. However, within this data there is some sensitivity to specimen location with, for example, sample S2 is consistently 2 to 3% higher than sample S1. Possible reasons for this discrepancy become evident when the microstructure is analysed at lower magnifications, e.g. Figure 3.11 c), where clear regions of different α_p morphologies and sizes can be recognised. These regions are equivalent to already well described phenomena such as blocky alpha and aligned alpha colonies. It is difficult to fragment the grain boundary alpha during the $\alpha+\beta$ phase processing. As a result they remain in the final microstructure of the billet, resulting in the formation of features such as blocky alphas [1, 5].

In the larger billet (Figure 3.16 b) there is a slight increase in the total percentage of α_p volume at the centre of the billet. This can be due to its greater diameter in comparison to the smaller billet which causes the cooling rate being slower at the centre of the billet in comparison to its edge. The work of Senkov et al. [50] too revealed that the volume fraction of α_p particles decreases when cooling rate increases. This can also be shown by using the power law equation (equation 3.1). Where *VF* is the volume fraction and *CR* is the cooling rate (K min $^{-1}$):

$$VF = 1.67(CR)^{-0.36} \tag{3.1}$$

Note that although the total percentage of α_p volume in the larger billet is generally uniform (Figure 3.16), there is a higher percentage of α_p volume in the smaller sized billet when compared to larger billet. This may be due to a number of reasons.

Work done by Dietmar Helm [38] showed that the volume fraction of the α_p phase can be effected by the temperature of the recrystallisation or solution heat treatment after the forging procedure.

Another possible reason may be due to a slight difference in the chemical composition of both billets which can alter the shape of the β transus approach curve.

Effects of the chemical composition on the β transus approach curve for IMI 834, IMI 829 and Ti 6-4 is shown as an example in Figure 3.17. It can be observed that the slope of the β transus approach curve for IMI 834 is less than IMI 829 which causes widening of the allowable temperature range to obtain the microstructure containing a small amount of α phase. Therefore, by altering the angle of the β transus approach

curve, the percentage of β phase volume changes consequently changing the percentage of α_p [14, 57].

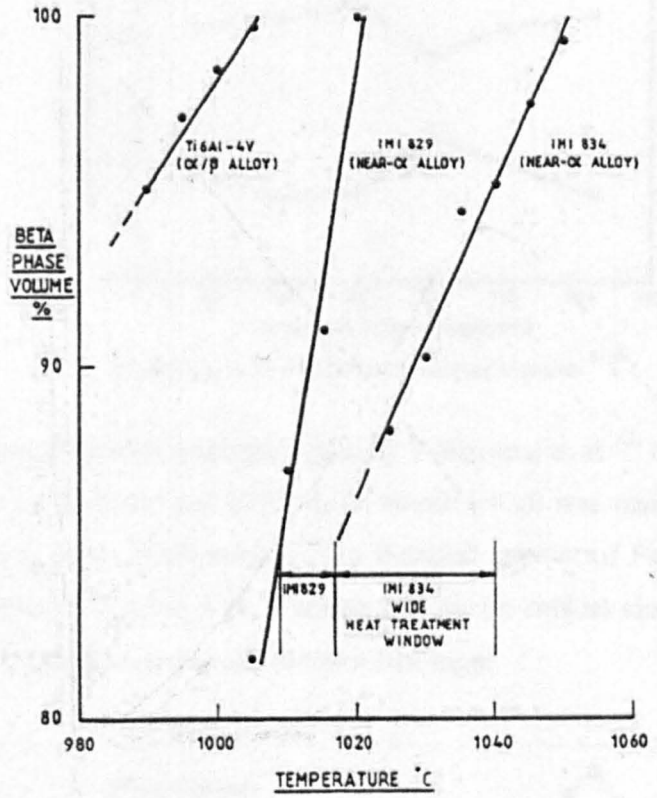

Figure 3.17 β transus approach curve for IMI 834, IMI 829 and Ti-6-4 [57].

Finally the difference in total percentage of α_p volume within the billets may be due to a phenomenon called segregation. VAR is the main method used to produce titanium alloys however, the VAR slow solidification speed causes microstructure defects initiated by segregation of alloying elements and composition etc.[61, 62]. Segregation in titanium ingots can lead to several different types of imperfections that cannot be readily eliminated by homogenising heat treatments or combinations of heat treatment and primary mill processing [12].

It is important to note that segregation tendency is different within different sections of the billet and because the cross section slices taken from the large and small billets may have been cut from different sections within each of the different diameter billets, one could be effected to a greater degree by the different chemical composition e.g. α stabiliser in comparison to the other.

Liu et al. [61] investigated the microscopic composition characteristics of the typical Ti-6-4 alloy ingot. Figure 3.18 shows the change tendency of alloying elements along axial direction. In the middle of the ingot, element V is rich, while Al is lacking.

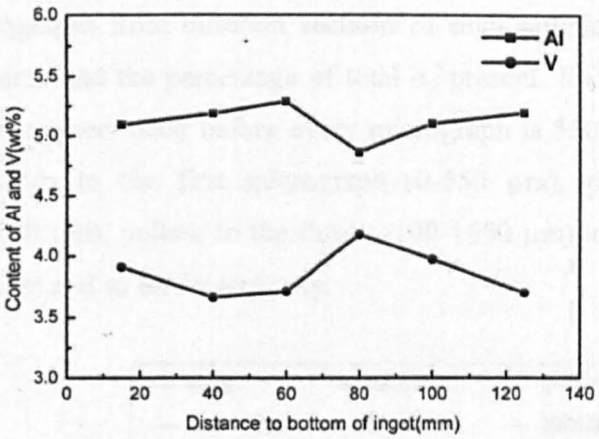

Figure 3.18 Axial distribution of alloying elements [61].

Additional research was undertaken by Yokoyama et al. [62] on a Ti 10V-2Fe-3Al ingot 700 mm in diameter and 1320mm in length which was manufactured following conventional two times VAR method. The detected amount of Fe in the Ti 10V-2Fe-3Al ingot is shown in Figure 3.19. It shows that the Fe content changes largely both in the longitudinal direction and at the centre of the ingot.

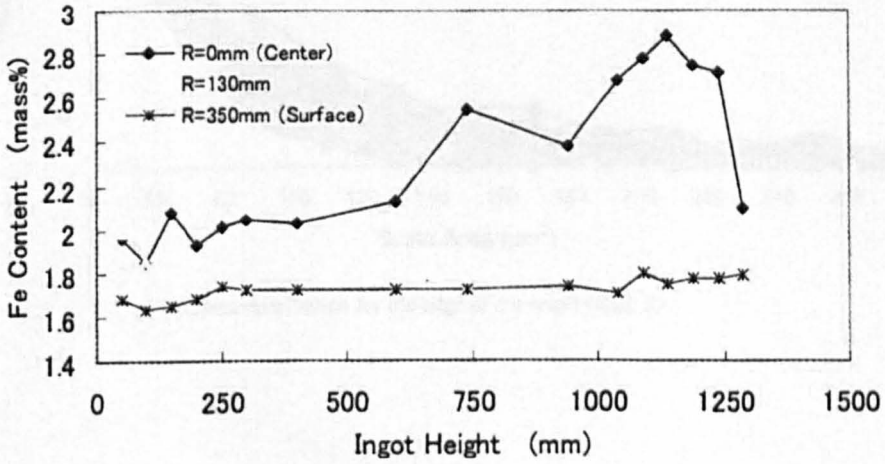

Figure 3.19 Experimental results of Fe content in VAR ingot [62].

3.3.2 *Size distribution of α_p*

To investigate whether there is a prevalence of features such as blocky alpha at certain positions leading to an increased α_p content, a detailed analysis of the α_p size distribution as a function of location was performed. Results are shown in Figure 3.20 and 3.21 for small and large billet respectively.

Using micrographs from different sections of each sample, the graphs below compare the grain area and the percentage of total α_p present. Each colour represents one micrograph and as mentioned before every micrograph is 550 μm x 550 μm e.g. navy blue corresponds to the first micrograph (0-550 μm), pink to the second micrograph (550-1100 μm), yellow to the third (1100-1650 μm) and light blue to the fourth (1650-2200 μm) and so on respectively.

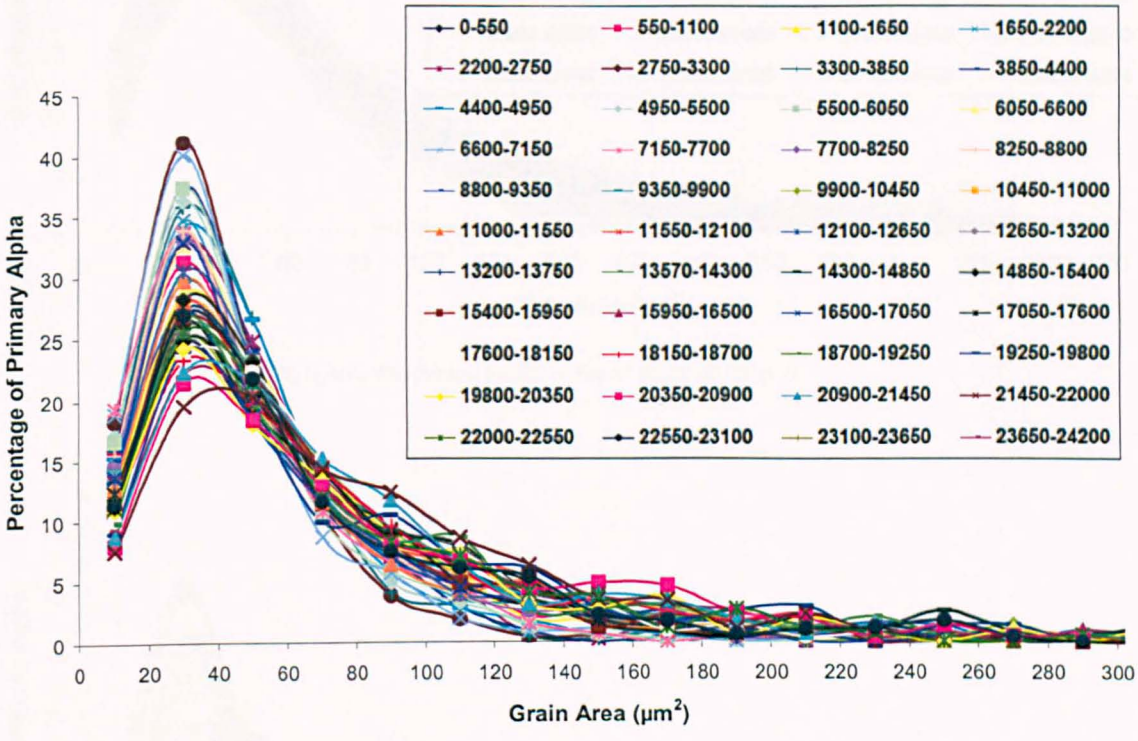

a) α_p area distribution for the edge of the small billet, S1.

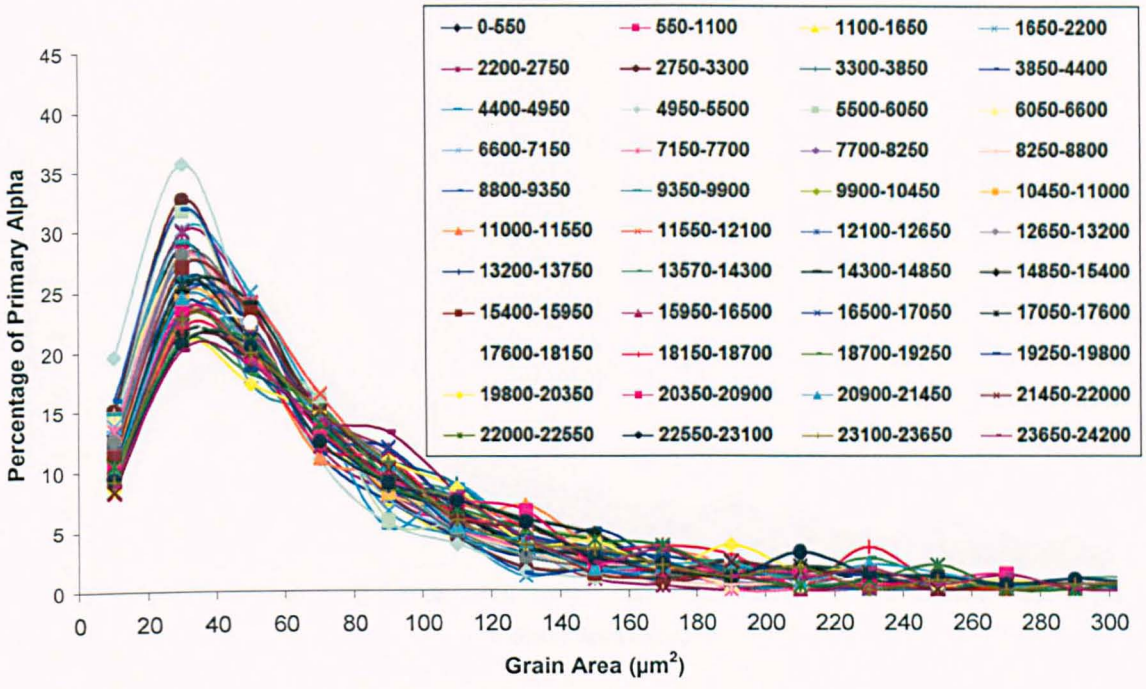

b) α_p area distribution for the centre of the small billet, S1.

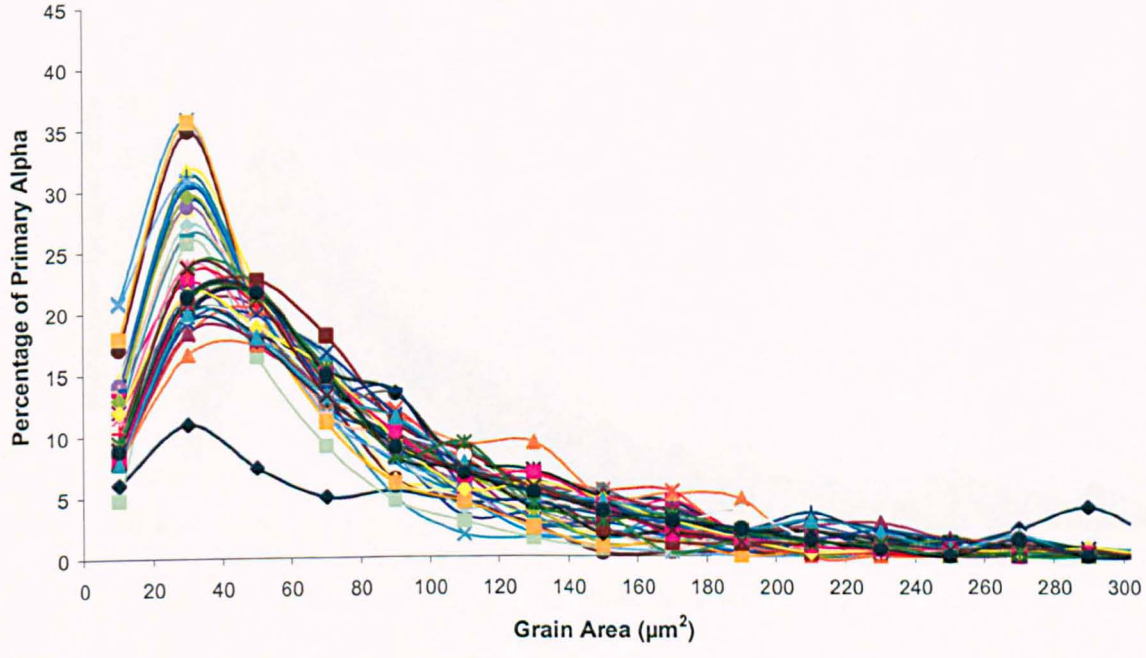

c) α_p area distribution for the edge of the small billet, S2.

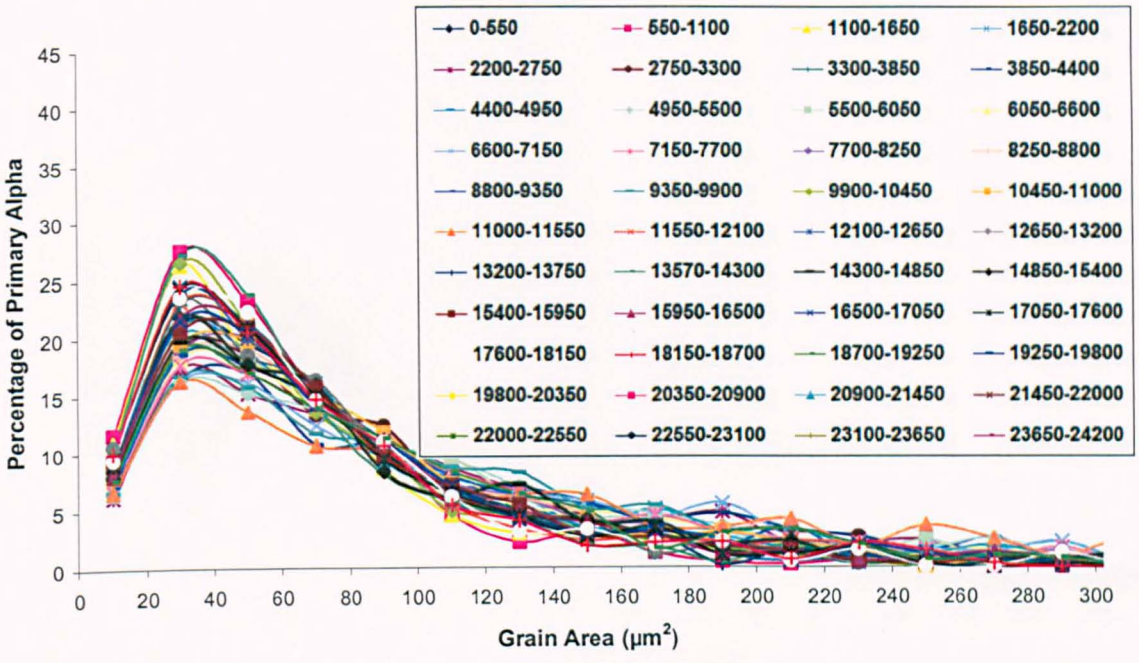

d) α_p area distribution for the centre of the small billet, S2.

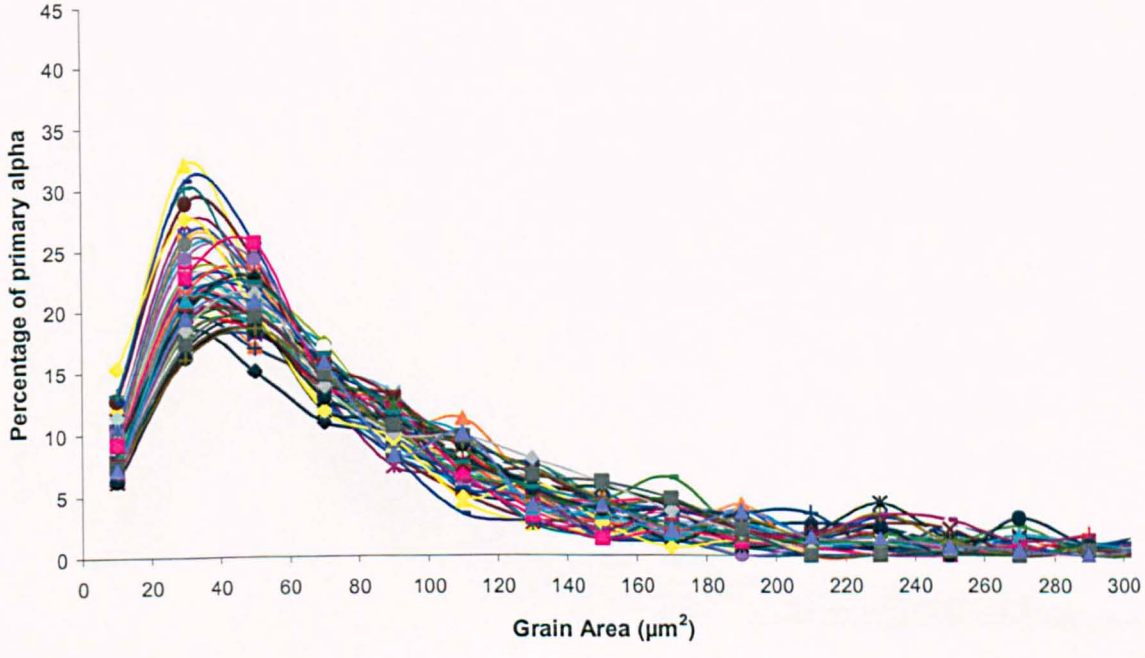

e) α_p area distribution for the edge of the small billet, S3.

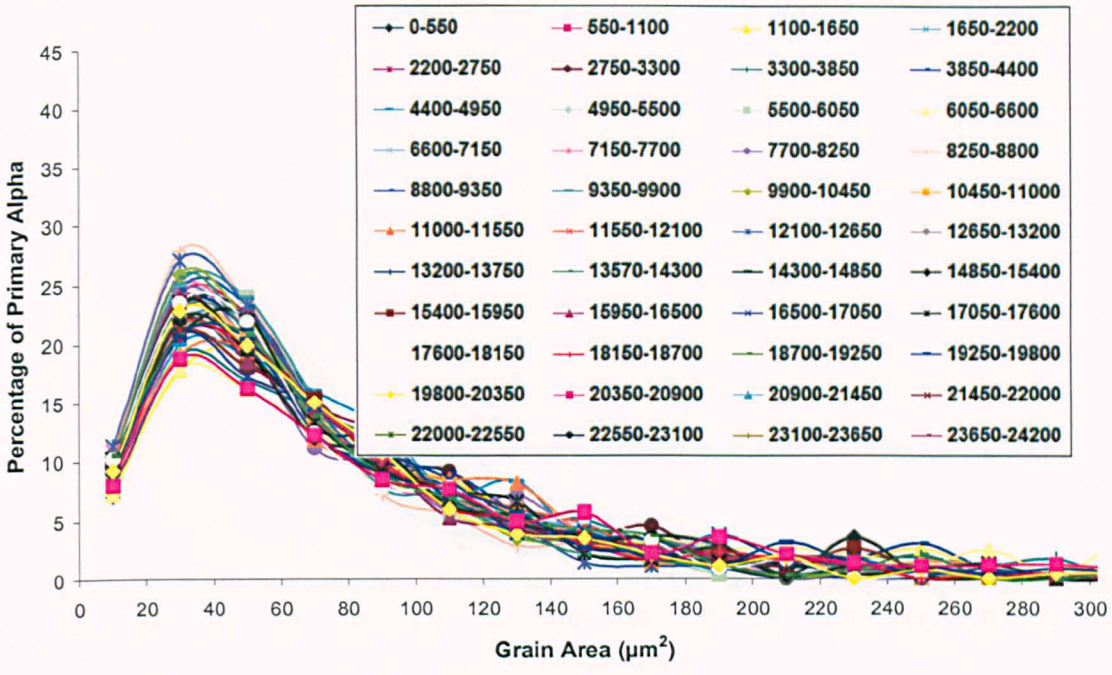

f) α_p area distribution for the centre of the small billet, S3.

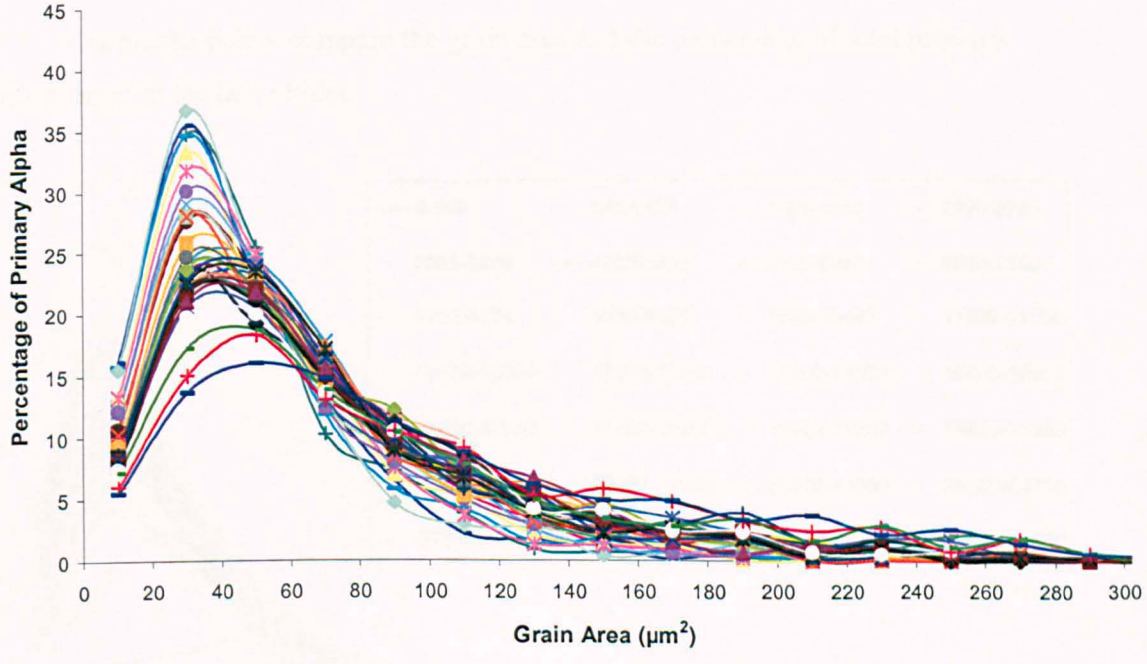

g) α_p area distribution for the edge of the small billet, S4.

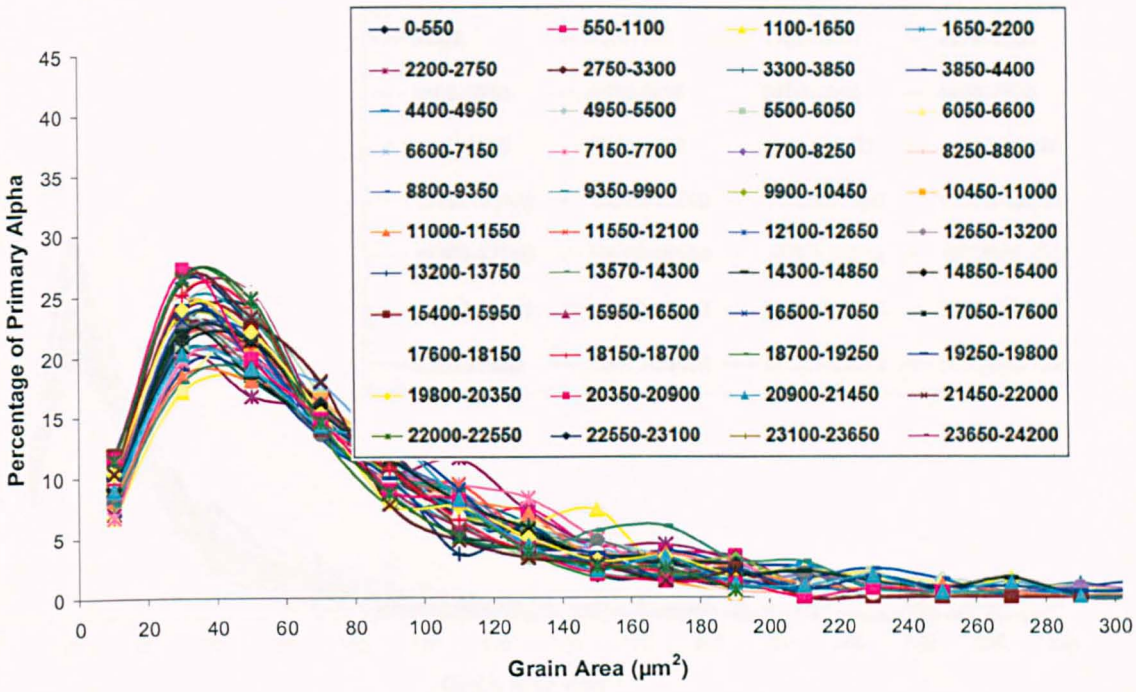

h)

Figure 3.20 α_p area distribution for the edge **(a, c, e, g)** and centre **(b, d, f, h)** of the small billet at selected locations. **a** and **b**; **c** and **d**; **e** and **f**; **g** and **h** are for samples S1, S2, S3 and S4 respectively.

The graphs below compare the grain area and the percentage of total primary alpha present in the large billet.

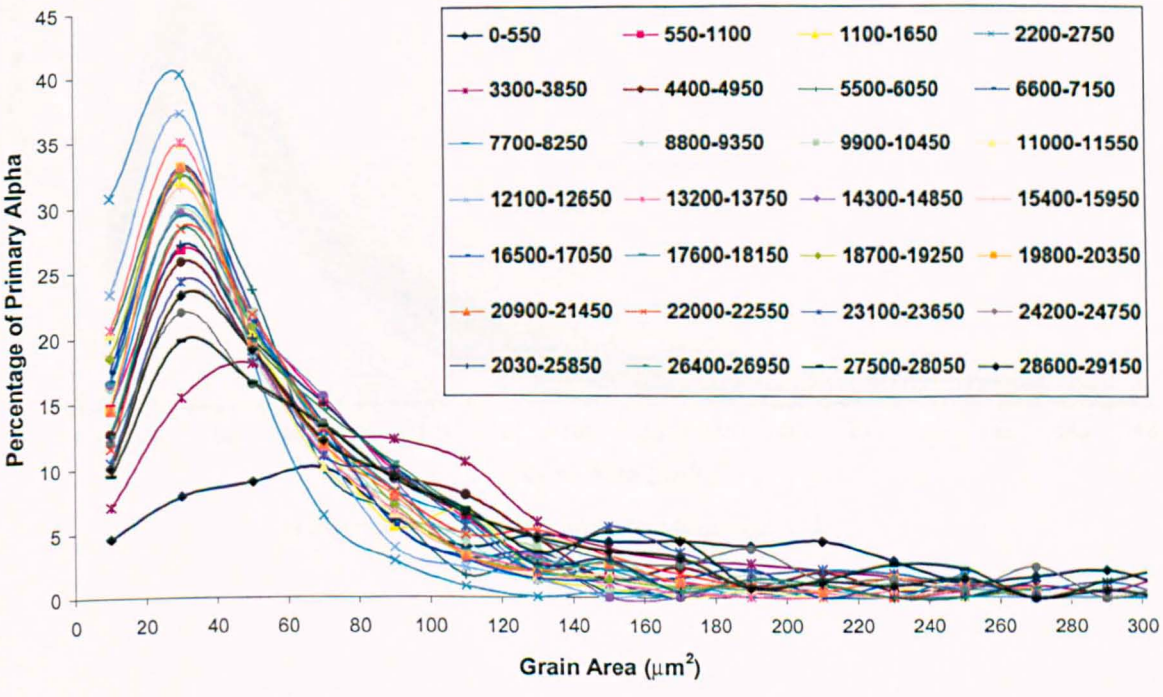

a) α_p area distribution for the edge of the large billet, LS1.

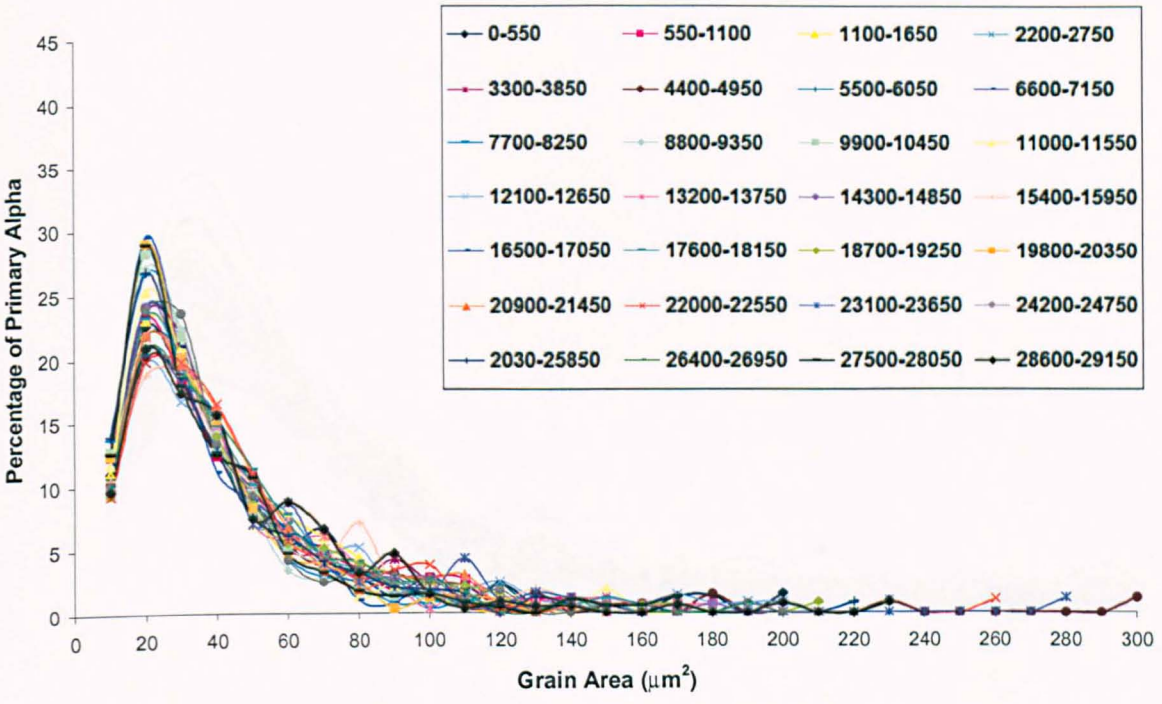

b) α_p area distribution for the centre of the large billet, LS1.

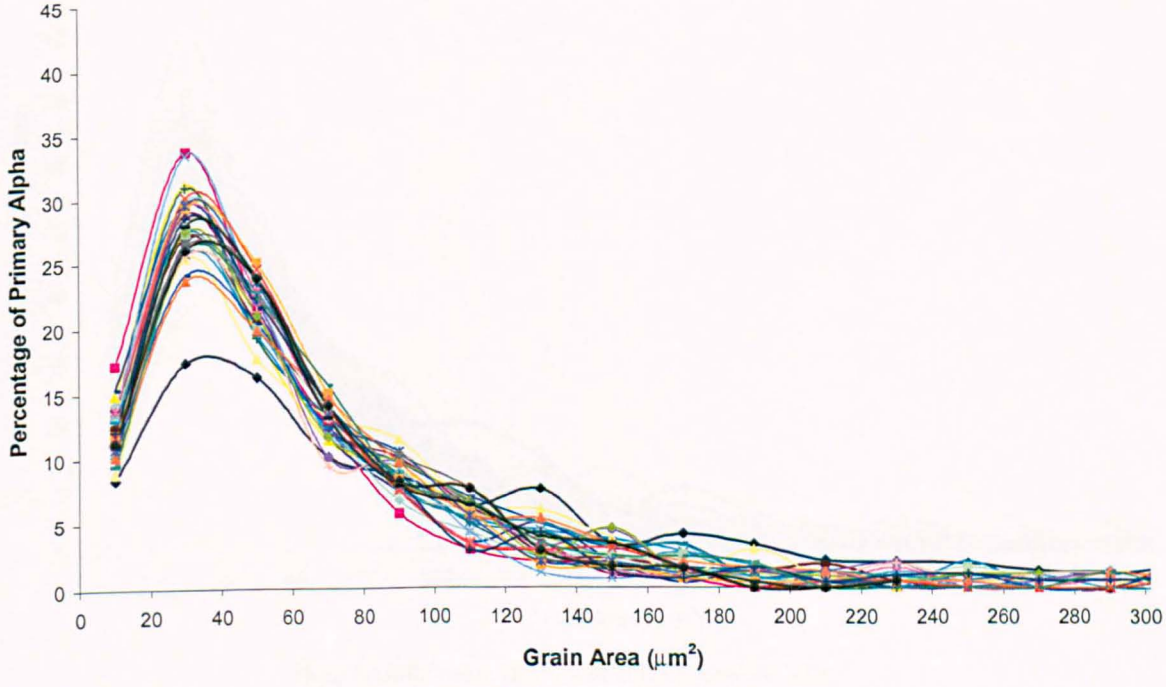

c) α_p area distribution for the edge of the large billet, LS2.

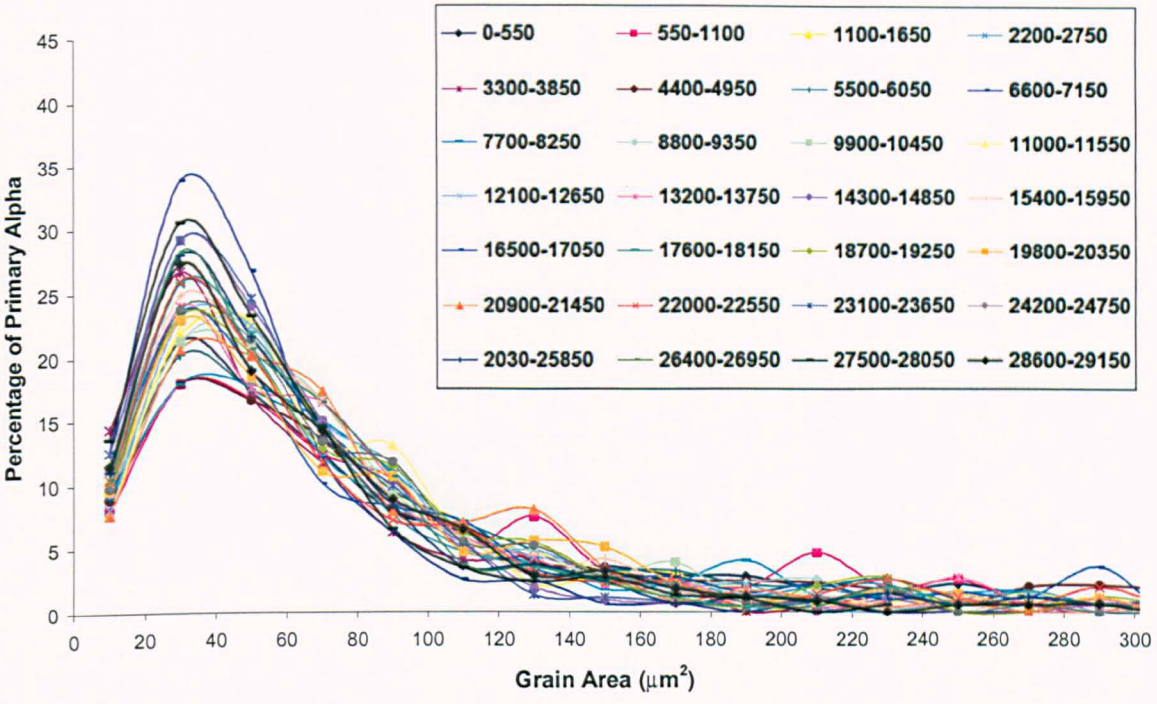

d) α_p area distribution for the centre of the large billet, LS2.

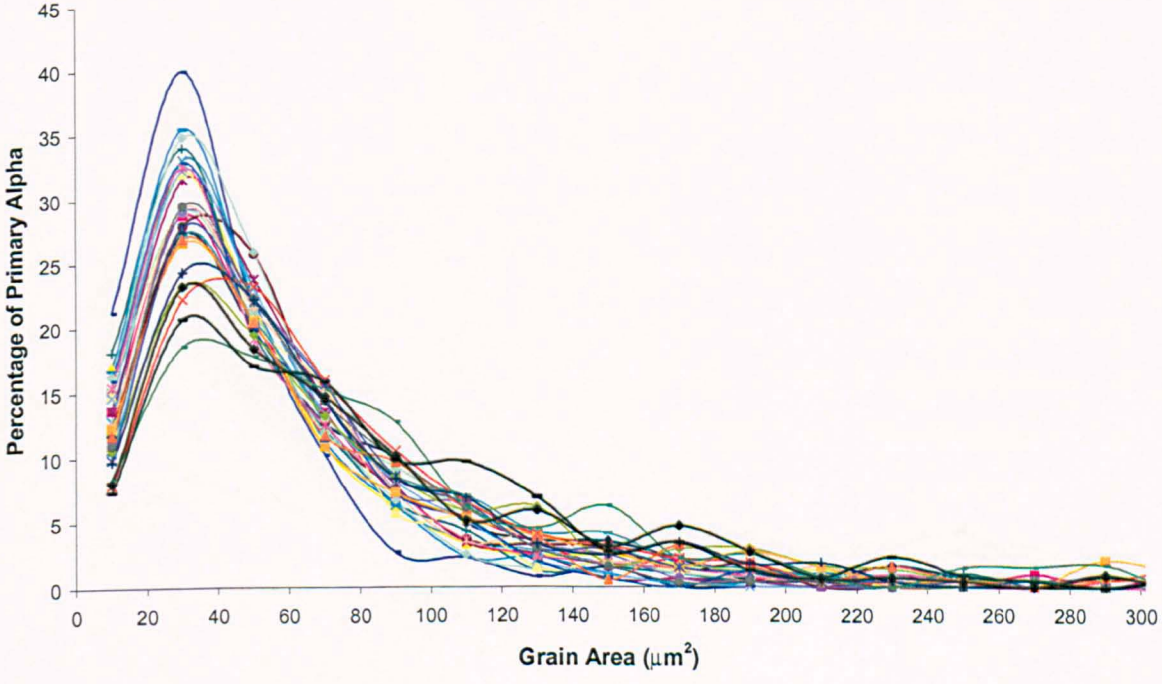

e) α_p area distribution for the edge of the large billet , LS3.

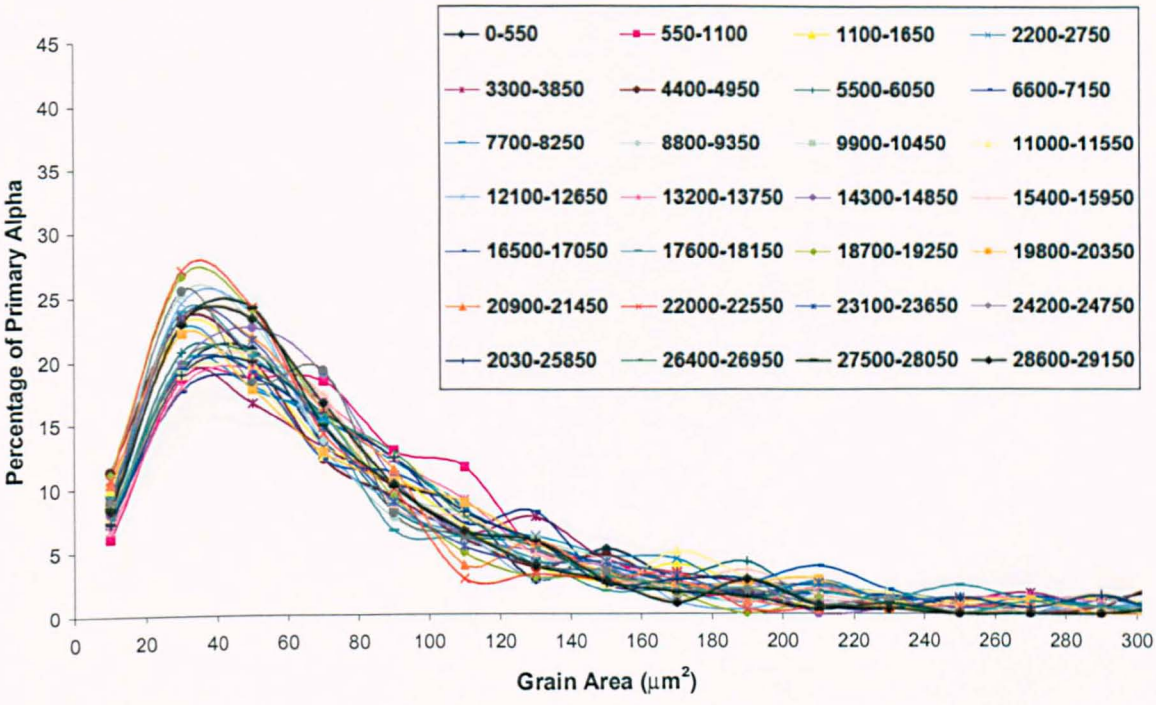

f) α_p area distribution for the centre of the large billet, LS3.

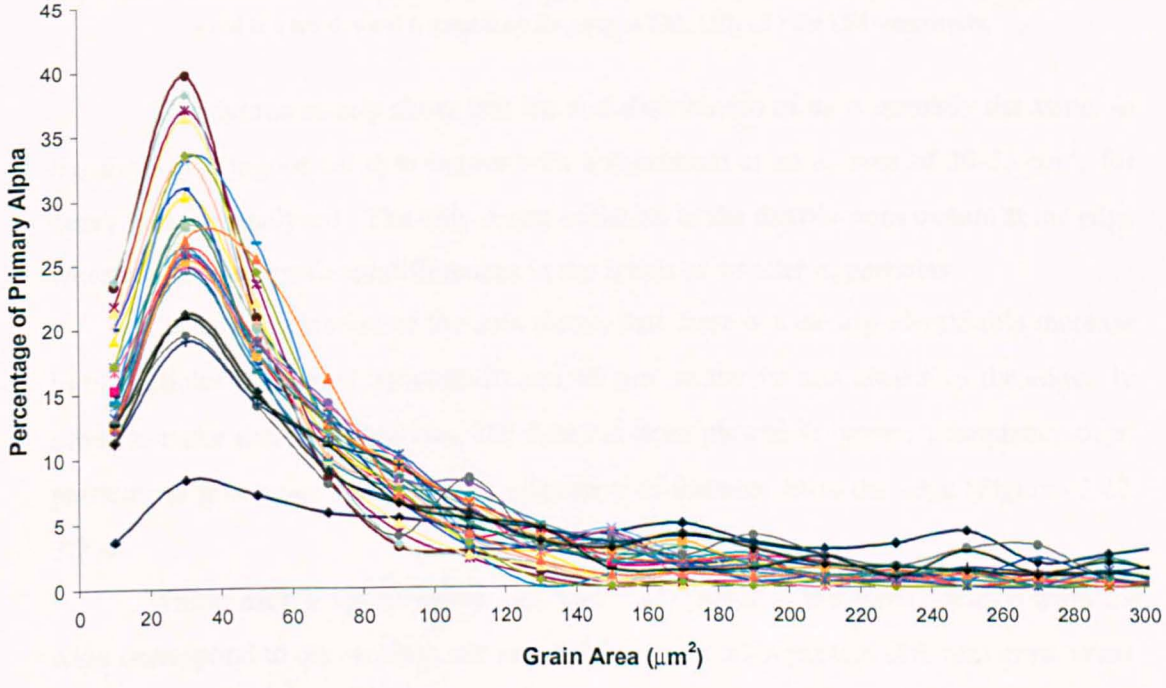

g) α_p area distribution for the edge of the large billet, LS4.

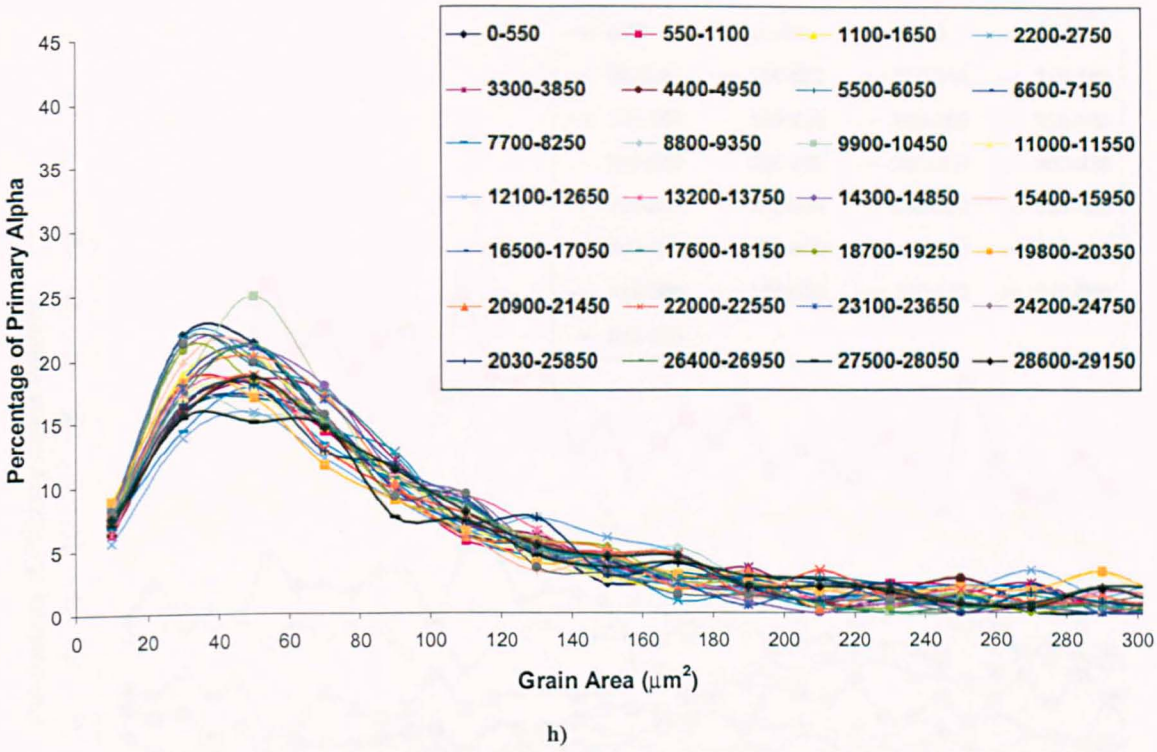

h)

Figure 3.21 α_p area distribution for the edge **(a, c, e, g)** and centre **(b, d, f, h)** of the large billet at selected locations. **a** and **b**; **c** and **d**; **e** and **f**; **g** and **h** are for samples LS1, LS2, LS3 and LS4 respectively.

The figures clearly show that the size distribution of α_p is virtually the same, in the form of a lognormal distribution with a maximum at an α_p area of 30-35 μm^2, for every location analysed. The only major variation in the distributions occurs at the edge where there are significant differences in the levels of smaller α_p particles.

Closer examination of the data shows that there is a clearly identifiable increase in α_p particles with sizes between 20 and 40 μm^2 in the 10 mm closest to the edge. In order to make this more obvious, the data has been plotted in terms of frequency of α_p particles in groupings of 20 μm^2 as a function of distance from the edge (Figures 3.22, 3.23).

Within each graph (Figures 3.22 and 3.23) points at the same distance from the edge correspond to one micrograph and different colours represent different grain areas. For example navy blue represents grains between 0 and 20μm^2, Pink for grains between 20 and 40μm^2, yellow for grains between 40 and 60μm^2, Light blue for grains between 60 and 80μm^2 and so on.

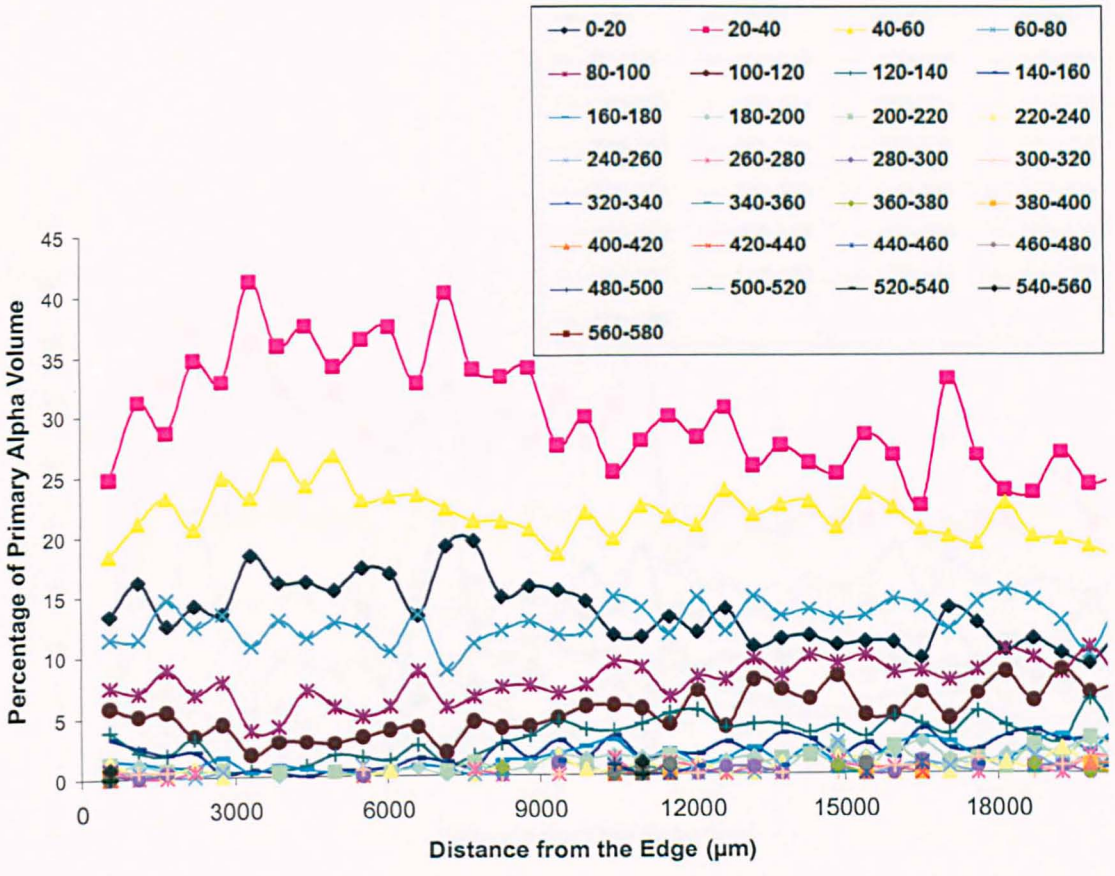

a) The distribution of α_p particle as a function of distance at the edge (small billet, S1).

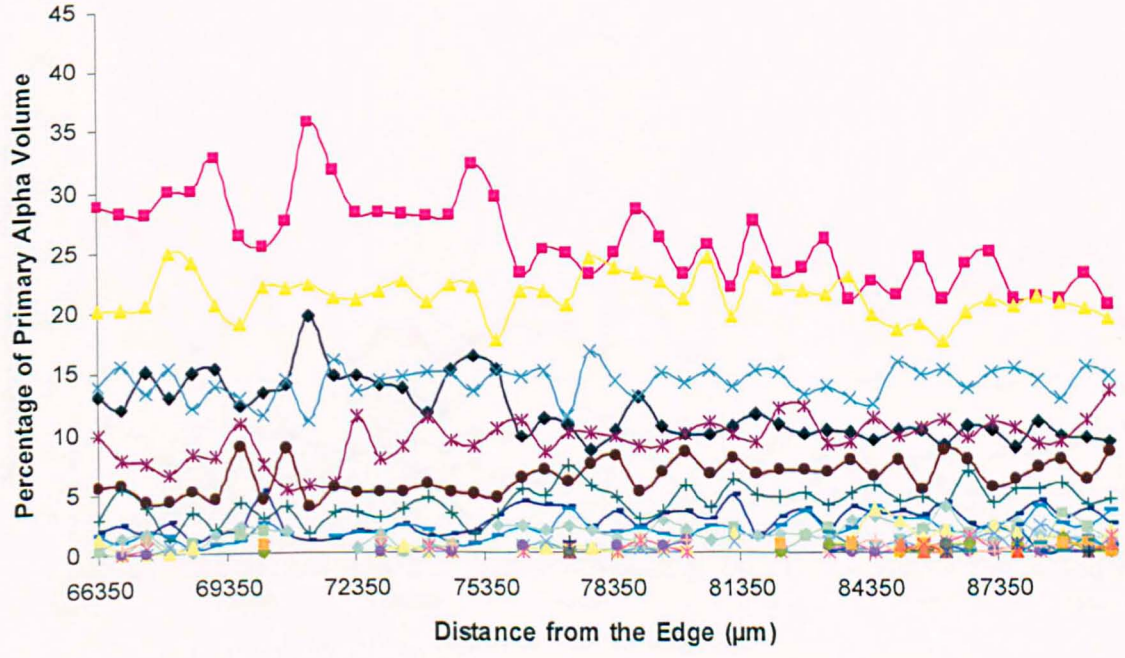

b) The distribution of α_p particle as a function of distance at the centre (small billet, S1).

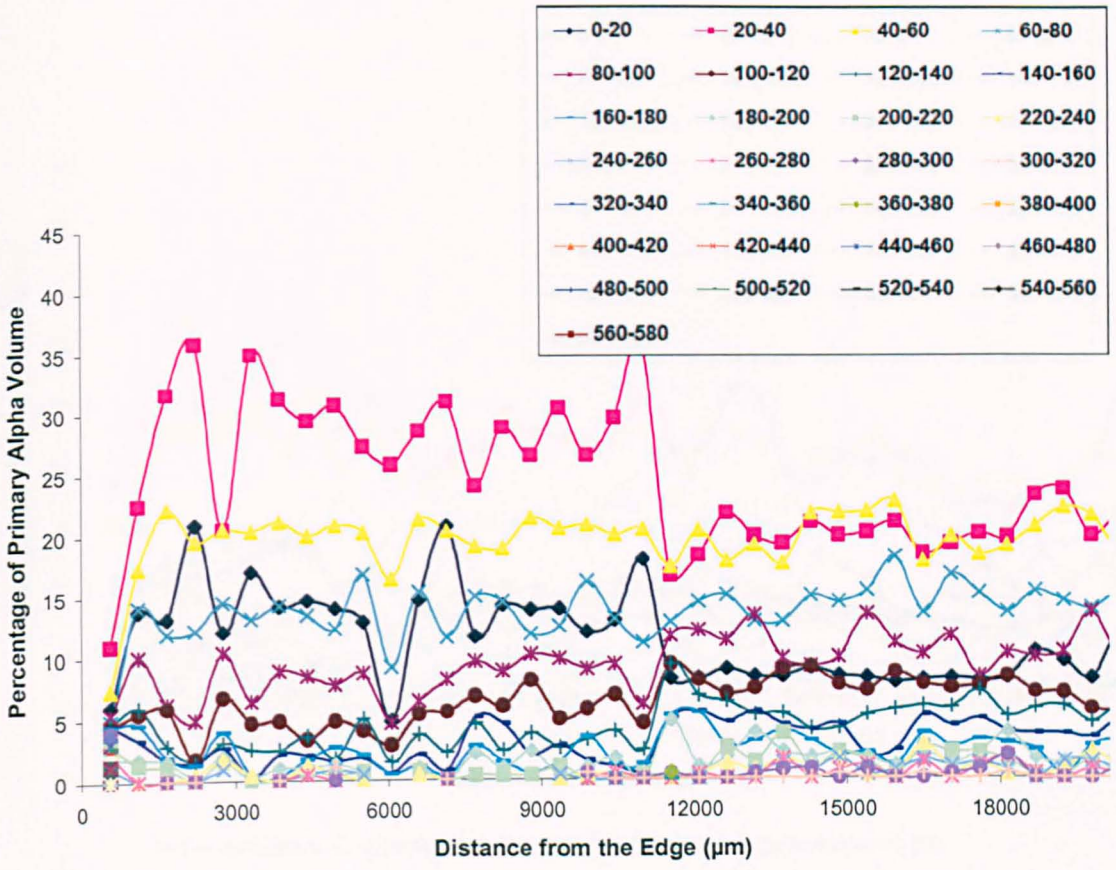

c) The distribution of α_p particle as a function of distance at the edge (small billet, S2).

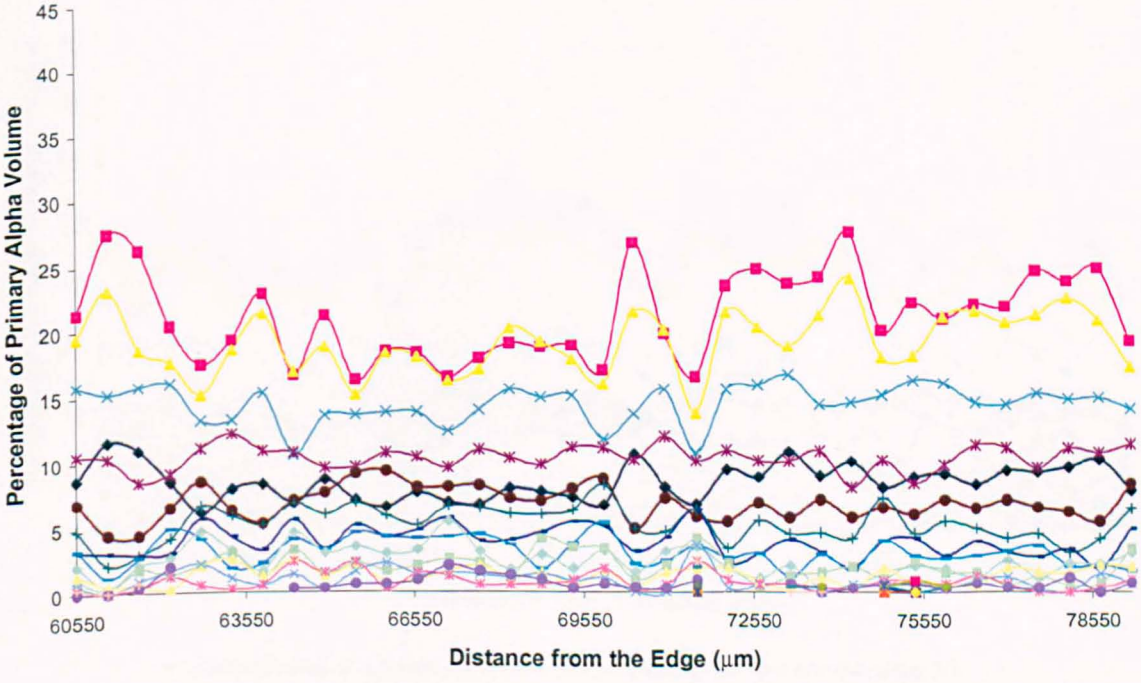

d) The distribution of α_p particle as a function of distance at the centre (small billet, S2).

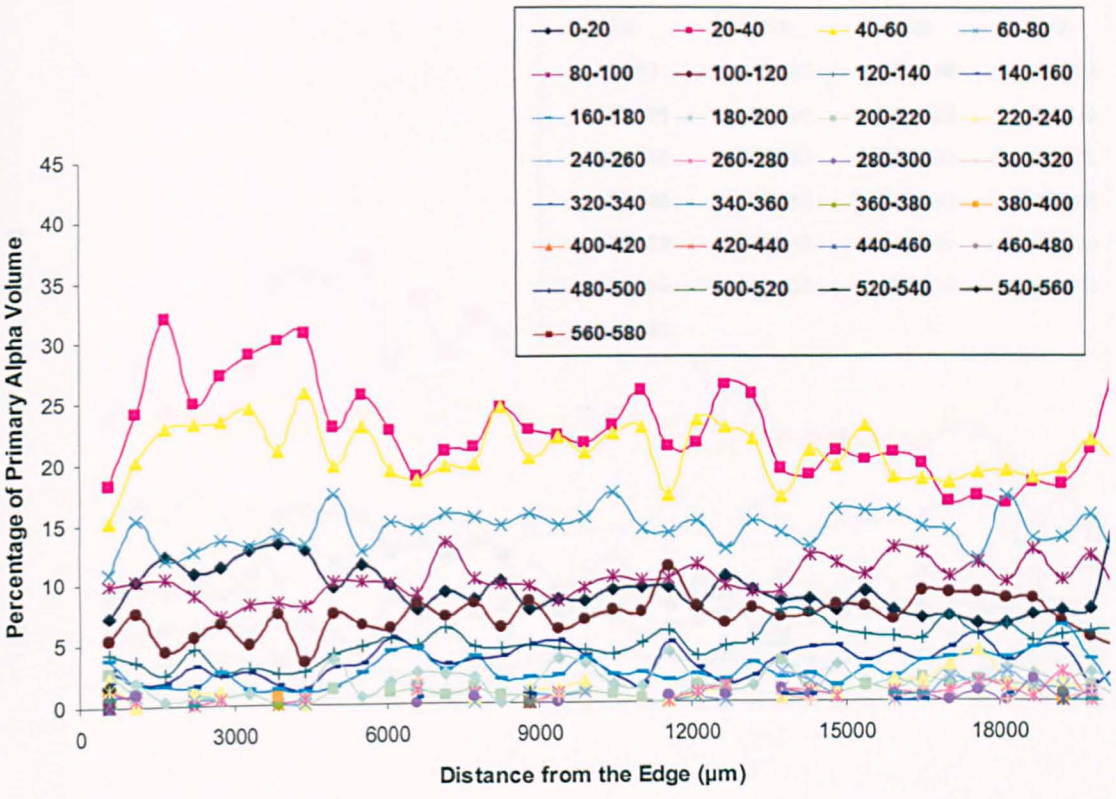

e) The distribution of α_p particle as a function of distance at the edge (small billet, S3).

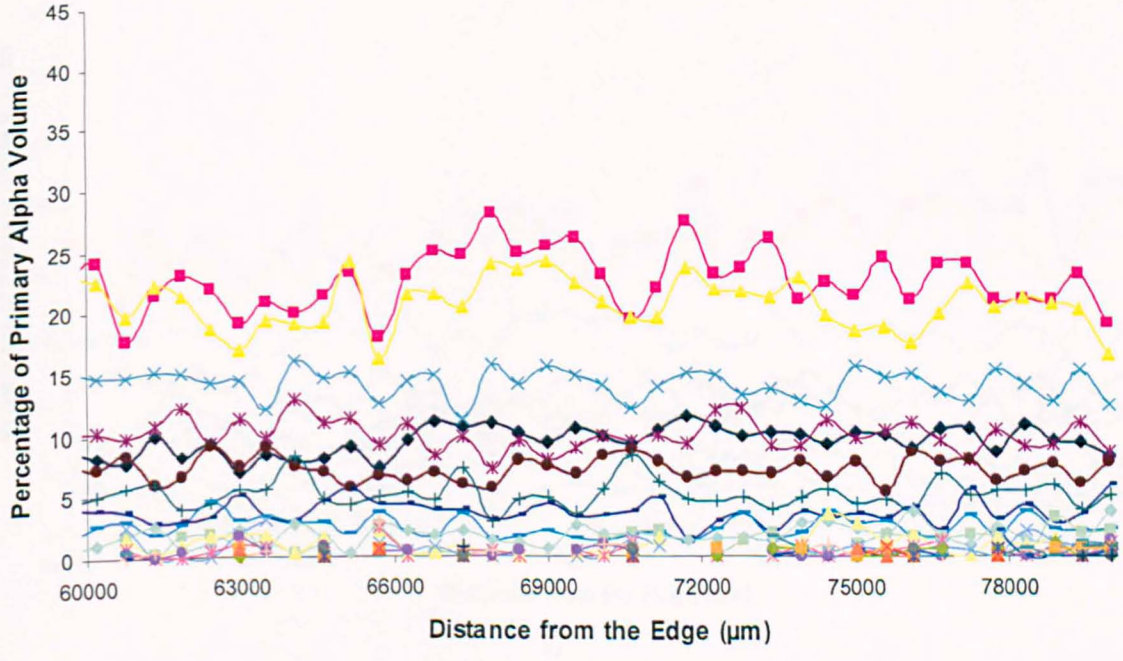

f) The distribution of α_p particle as a function of distance at the centre (small billet, S3).

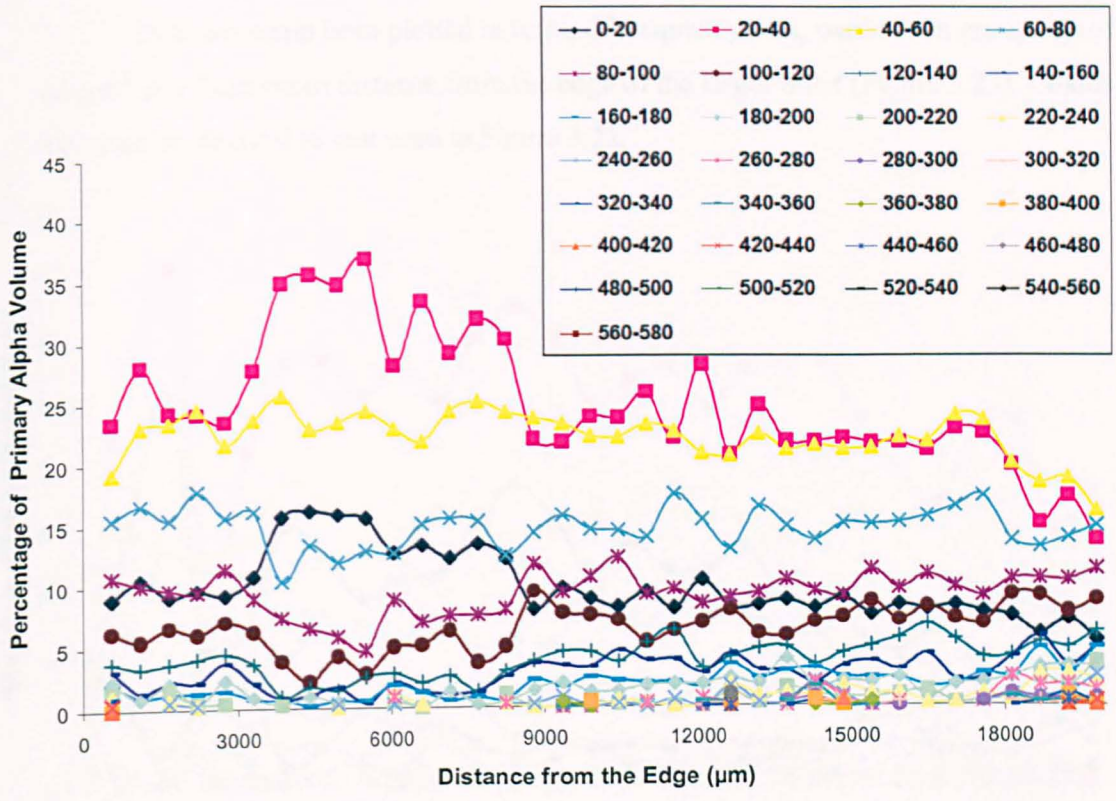

g) The distribution of α_p particle as a function of distance at the edge (small billet, S4).

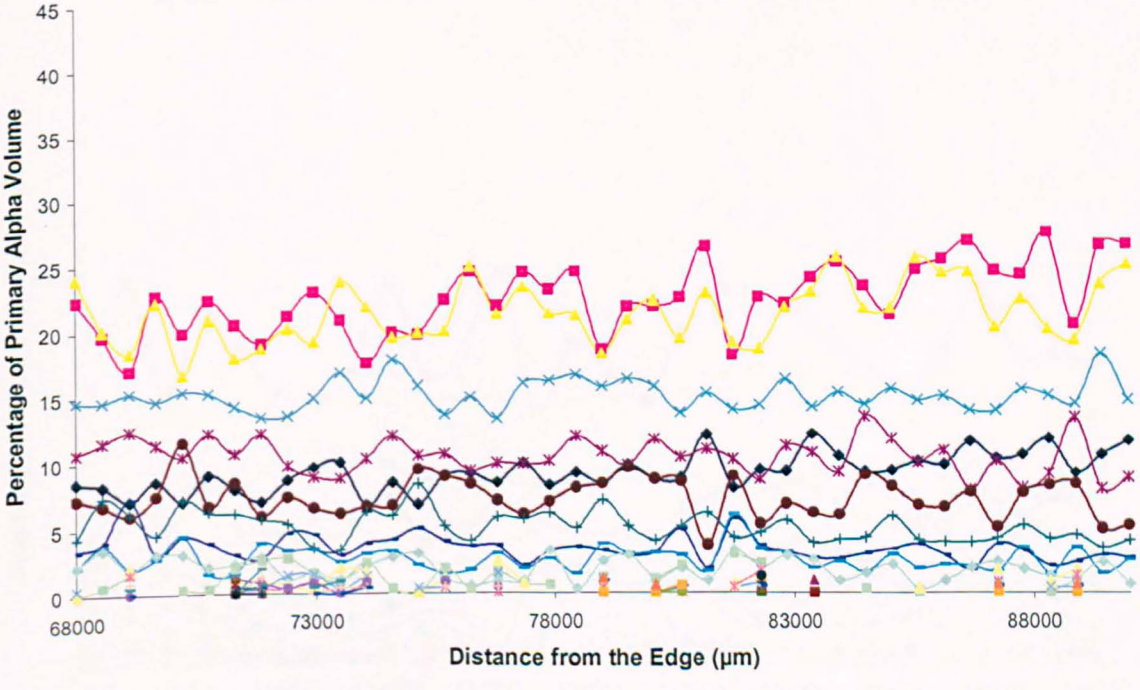

h)

Figure 3.22 The distribution of α_p particle as a function of distance from the edge with **a, c, e, g)** at the edge and **b, d, f, h)** at the centre of the sample (small billet).

Data has again been plotted in terms of frequency of α_p particles in groupings of 20 μm^2 as a function of distance from the edge of the larger billet (Figure 3.23). Colour key used is identical to that used in Figure 3.22.

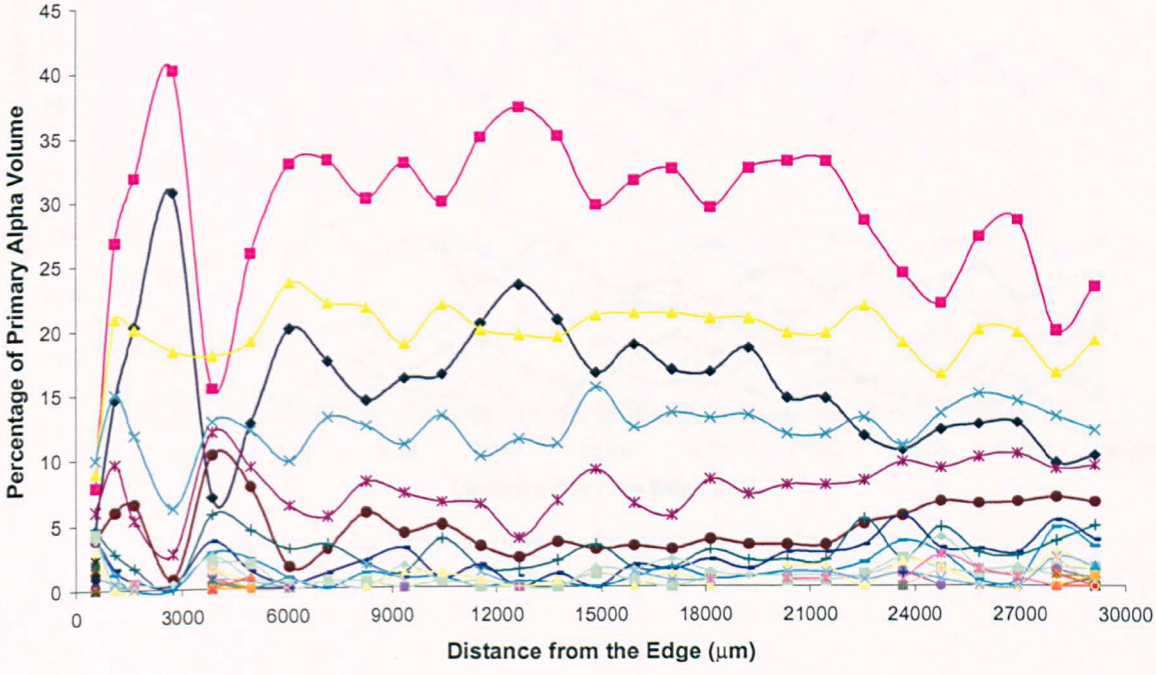

a) The distribution of α_p particle as a function of distance at the edge (large billet, LS1).

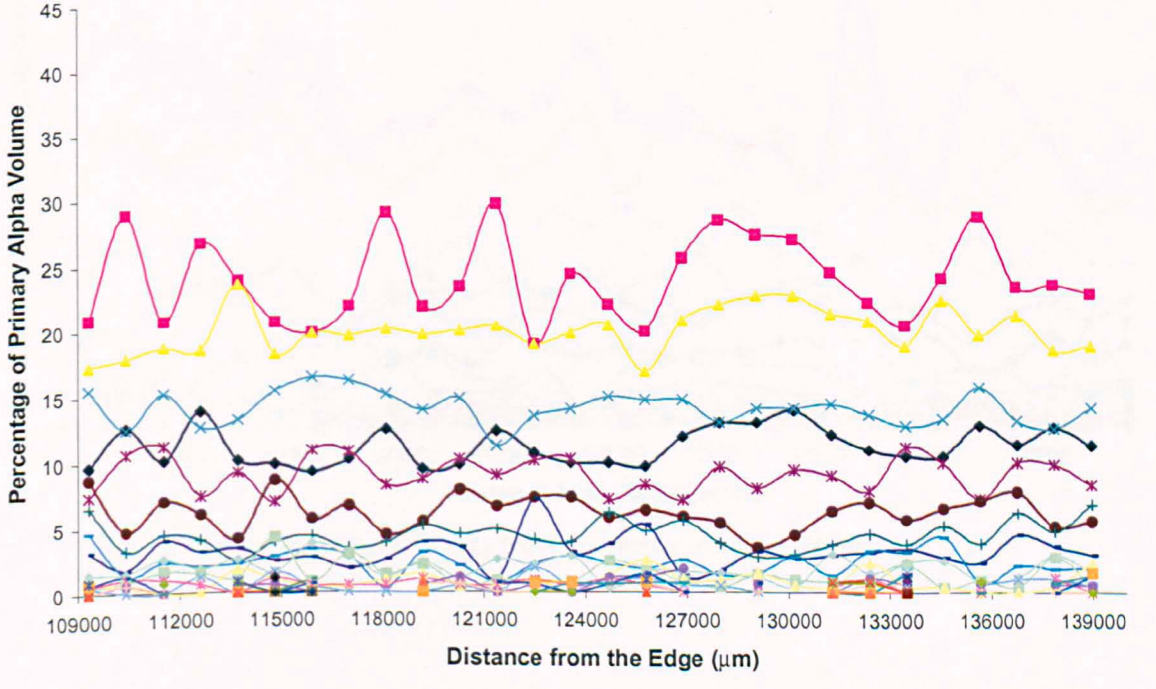

b) The distribution of α_p particle as a function of distance at the centre (large billet, LS1).

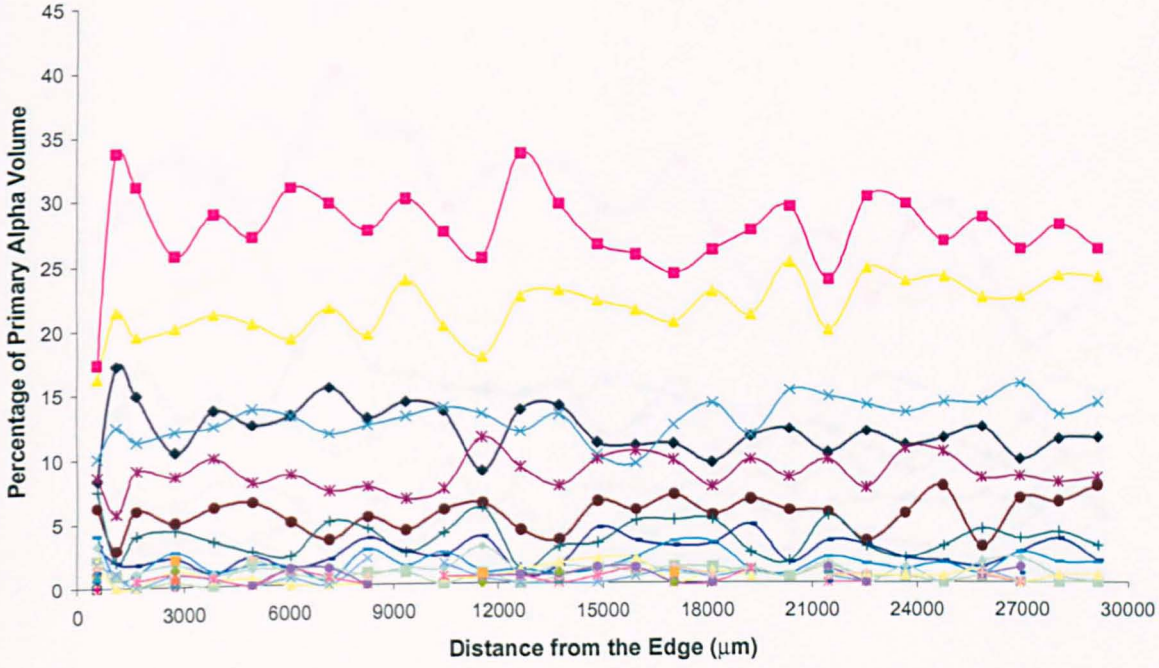

c) The distribution of α_p particle as a function of distance at the edge (large billet, LS2).

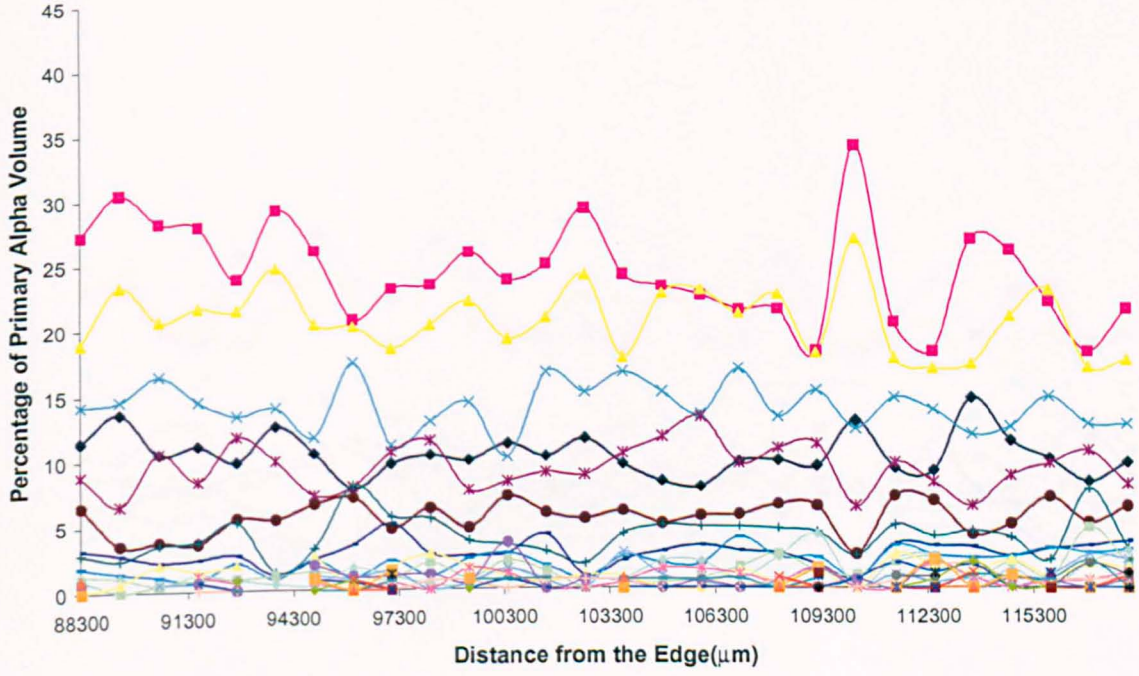

d) The distribution of α_p particle as a function of distance at the centre (large billet, LS2).

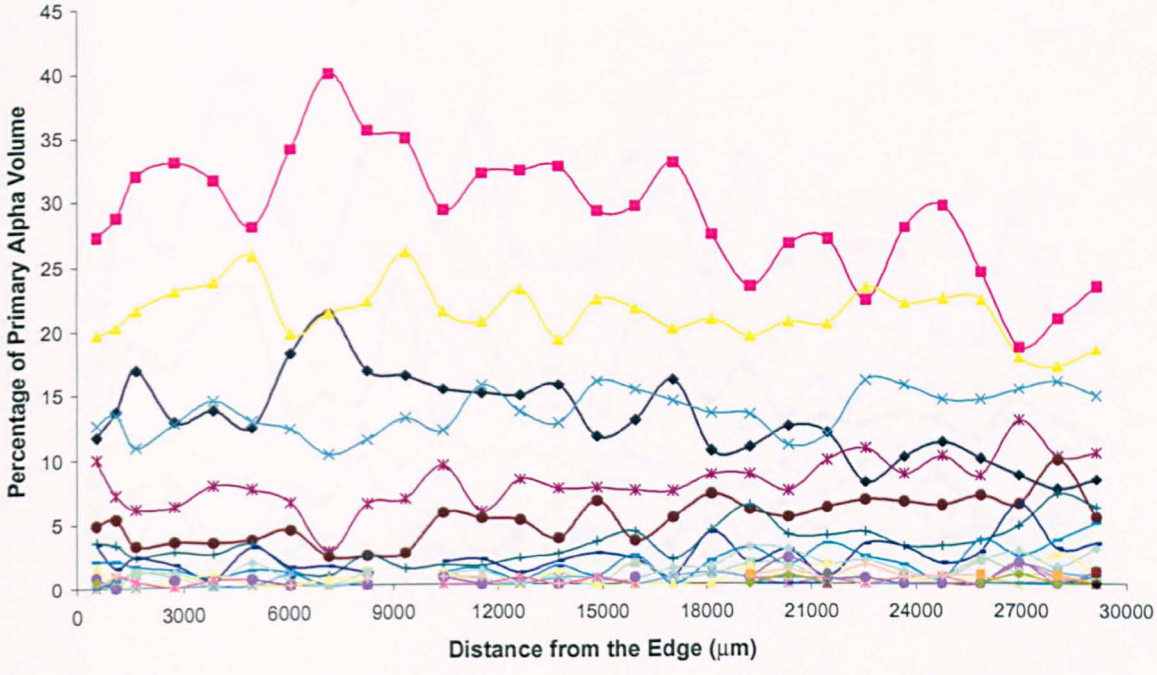

e) The distribution of α_p particle as a function of distance at the edge (large billet, LS3).

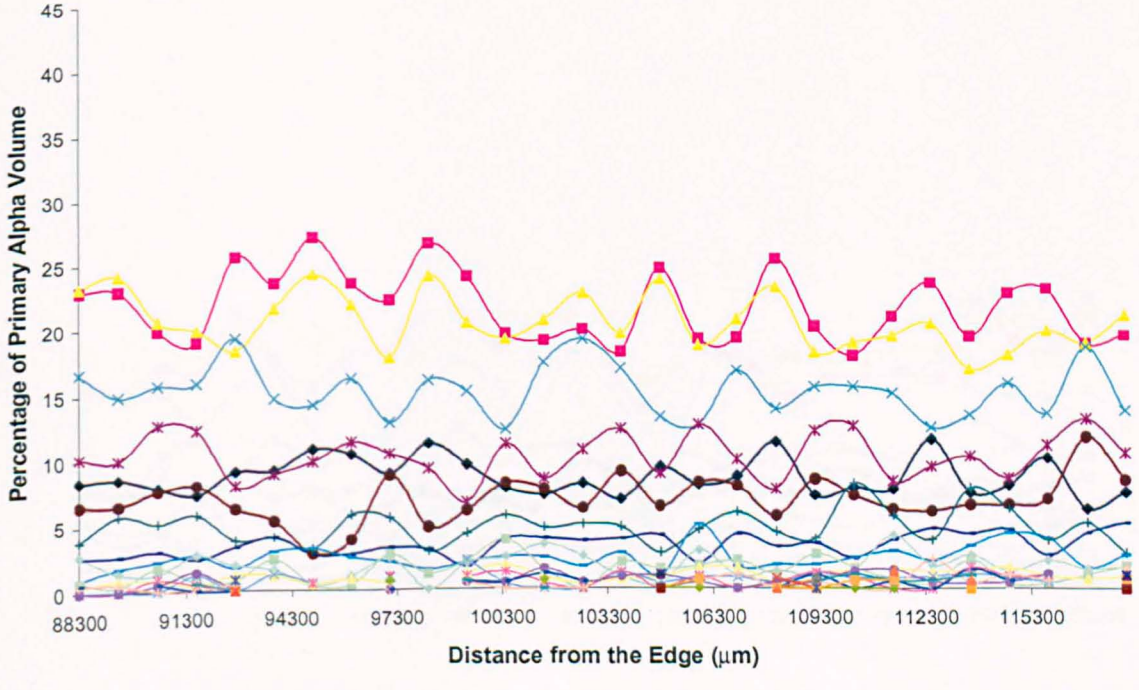

f) The distribution of α_p particle as a function of distance at the centre (large billet, LS3).

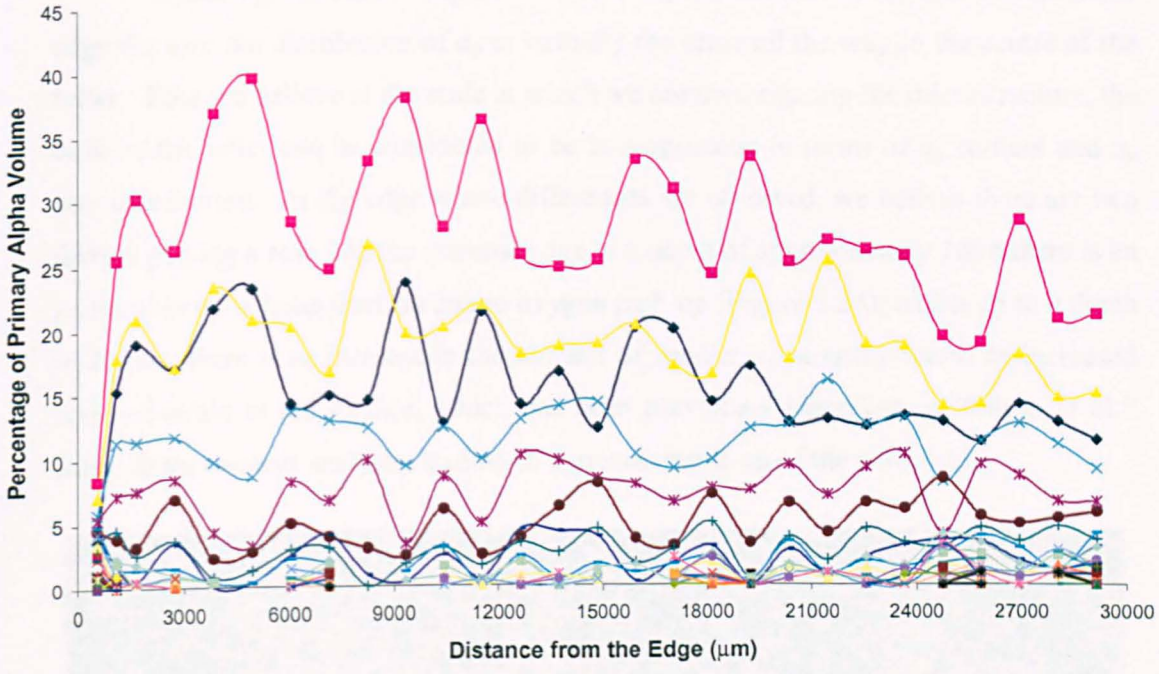

g) The distribution of α_p particle as a function of distance at the edge (large billet, LS4).

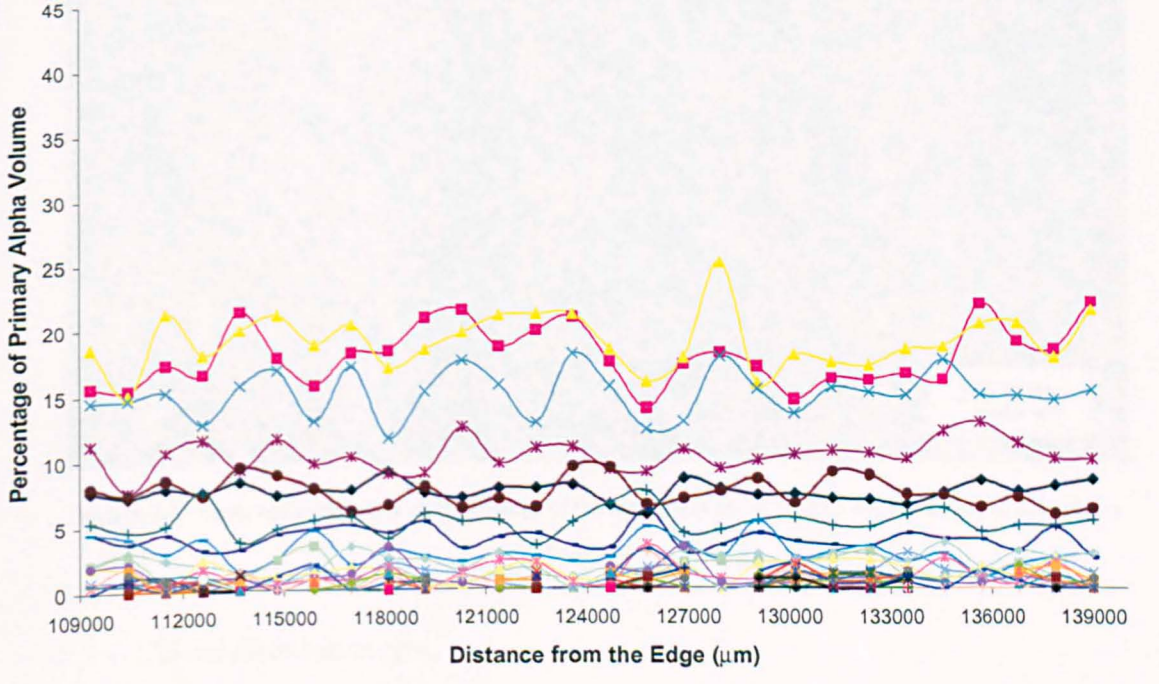

h)

Figure 3.23 The distribution of α_p particle as a function of distance from the edge with **a, c, e, g)** at the edge and **b, d, f, h)** at the centre of the sample (large billet).

These figures makes it quite clear that beyond the first 10-15 mm closest to the edge the size the distribution of α_p is virtually the same all the way to the centre of the billet. Thus we believe at the scale at which we are investigating the microstructure, the bulk of the billet can be considered to be homogeneous in terms of α_p content and α_p size distribution. At the edge where differences are observed, we believe there are two factors playing a role. At the extreme edge to a depth of approximately 1mm there is an increase in α_p volume fraction due to oxygen pick-up (Figure 3.24); whilst up to a depth of 10 mm there is an increase in the number of smaller α_p particles due to an increased level of strain at the surface, which has been previously identified by Wilson et al.[3] using finite element analysis, leading to a greater break-up of the particles.

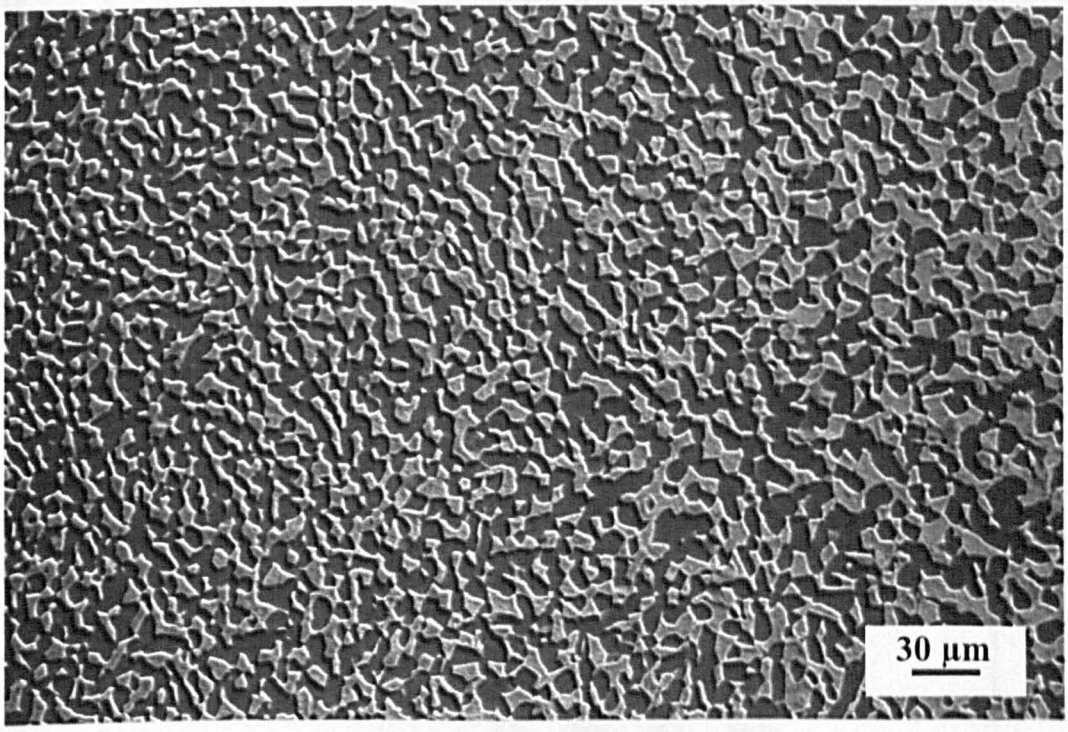

Figure 3.24 Large scale secondary electron image of the small billet at the extreme edge (majority of α_s has been eliminated)

3.3.3 Shape distribution of α_p

The shape of the α_p particles (this is simply the ratio of the width against the length of each individual α_p grains) for each sample within the small and large sized billet was calculated. An analysis of the shape of the α_p particles is shown in Figures 3.25 and 3.26 which compare the aspect ratio distribution of the particles at the edge and centre of the entire area of each of the samples.

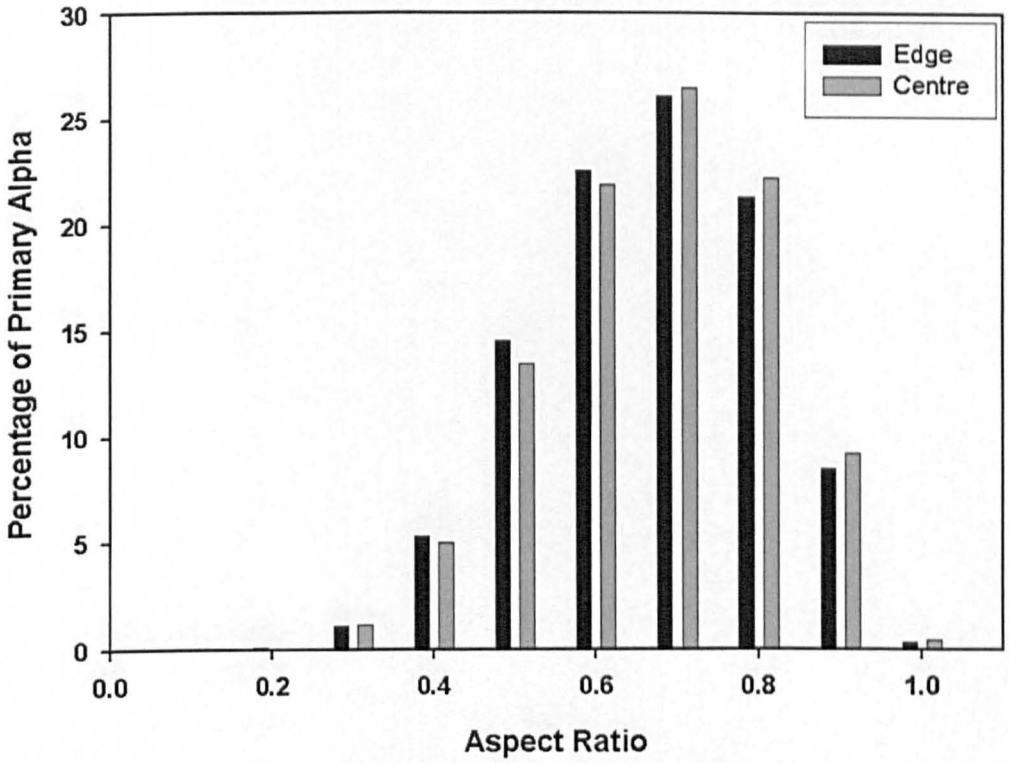

a) The aspect ratio of the α_p particles for S1.

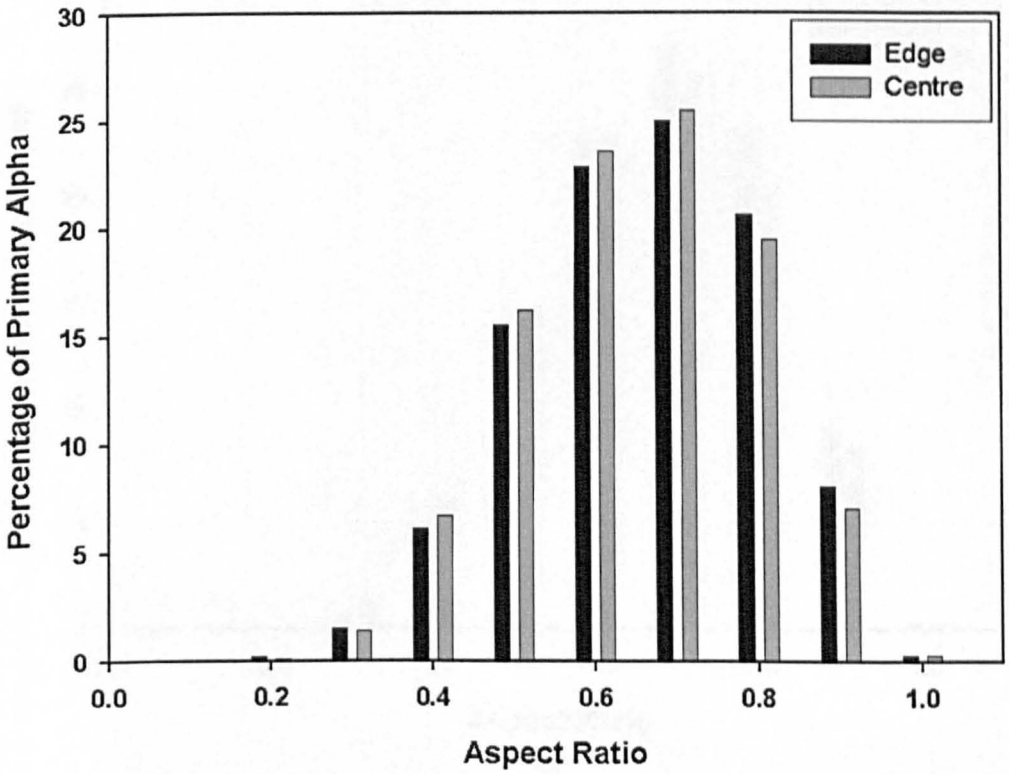

b) The aspect ratio of the α_p particles for S2.

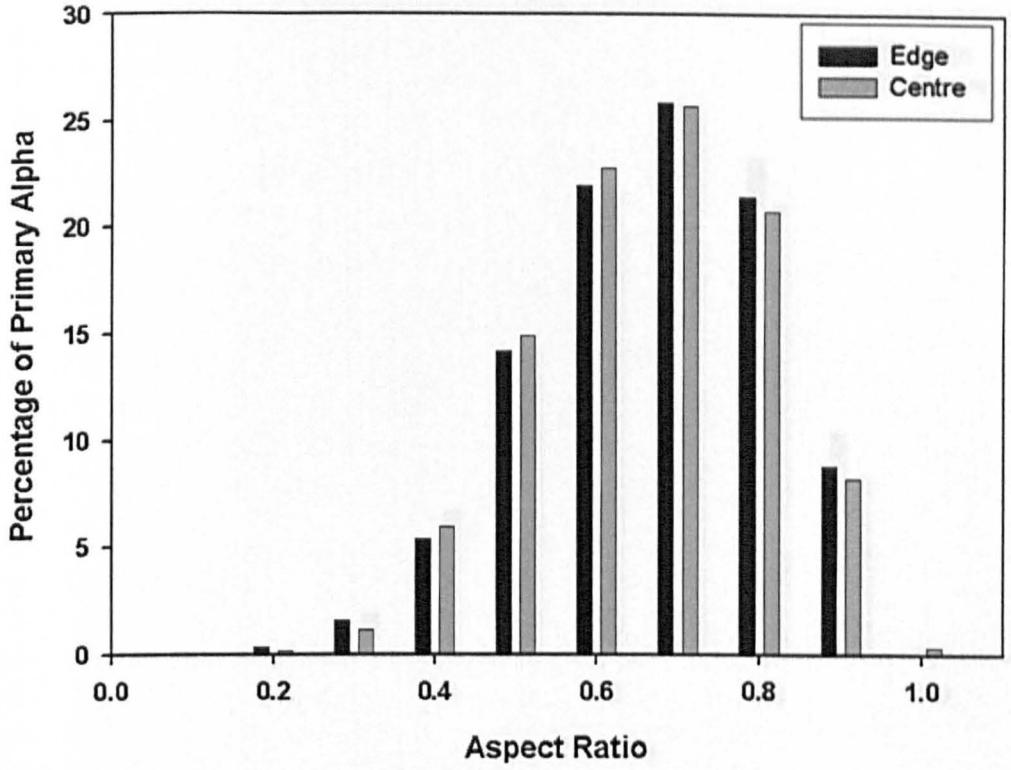

c) The aspect ratio of the α_p particles for S3.

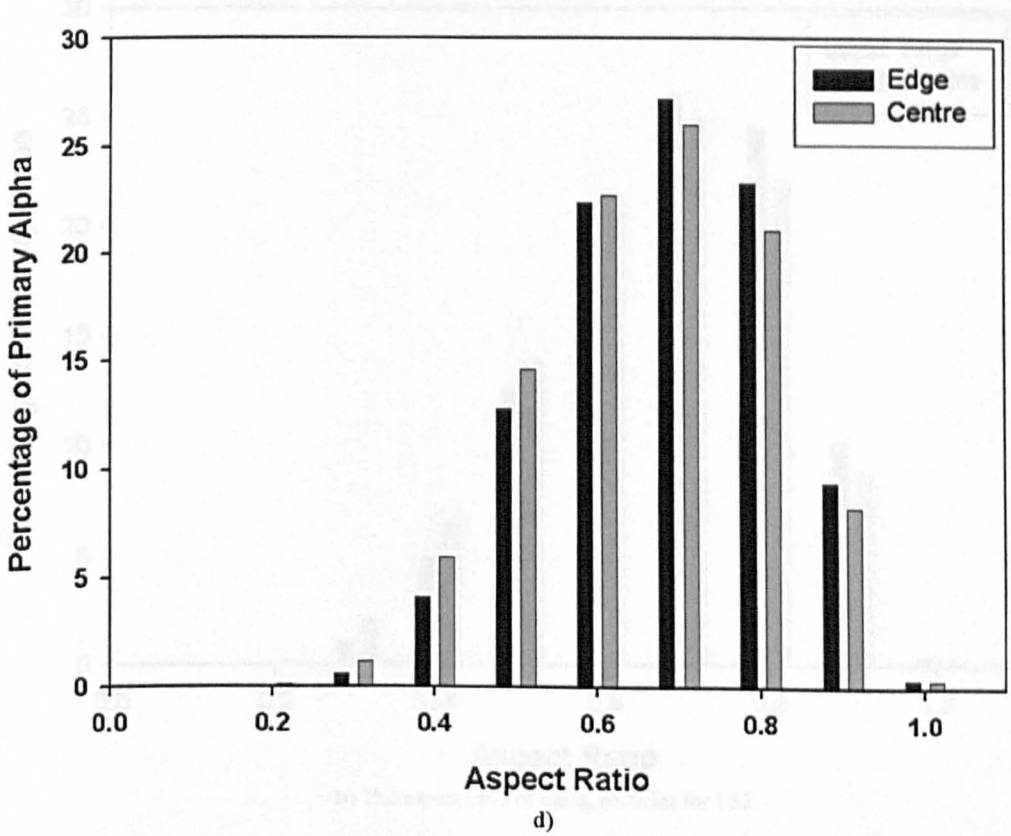

d)

Figure 3.25 The aspect ratio of the α_p particles for the small billet at the edge and centre for samples **a)** S1 **b)** S2 **c)** S3 **d)** S4.

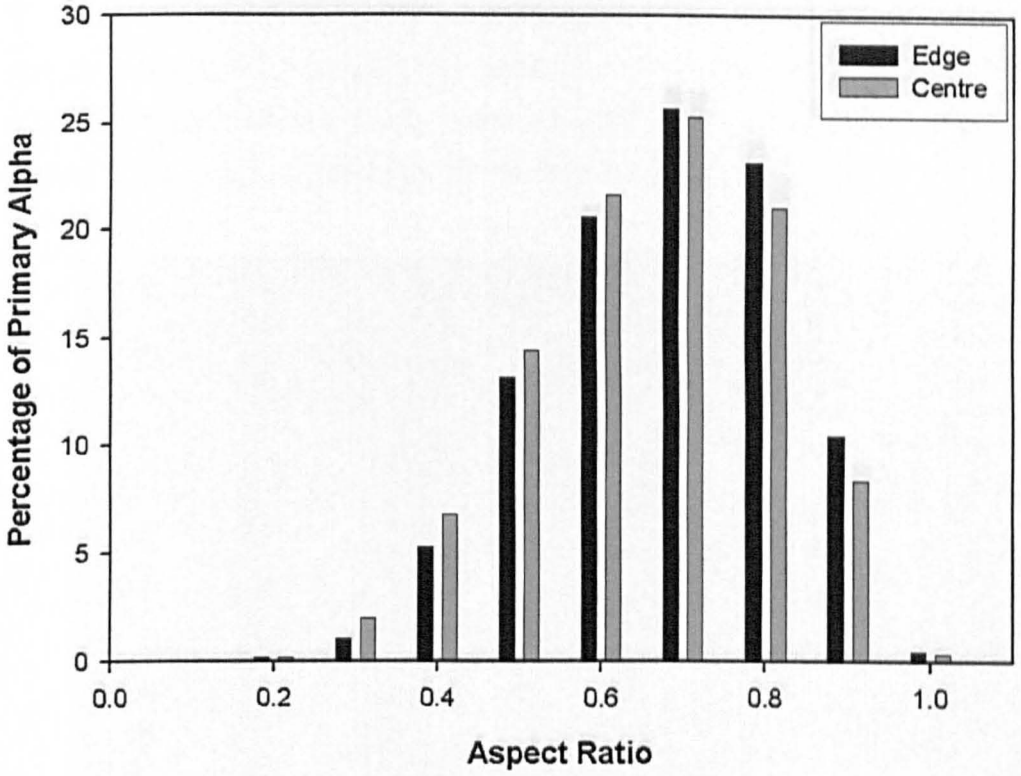

a) The aspect ratio of the α_p particles for LS1.

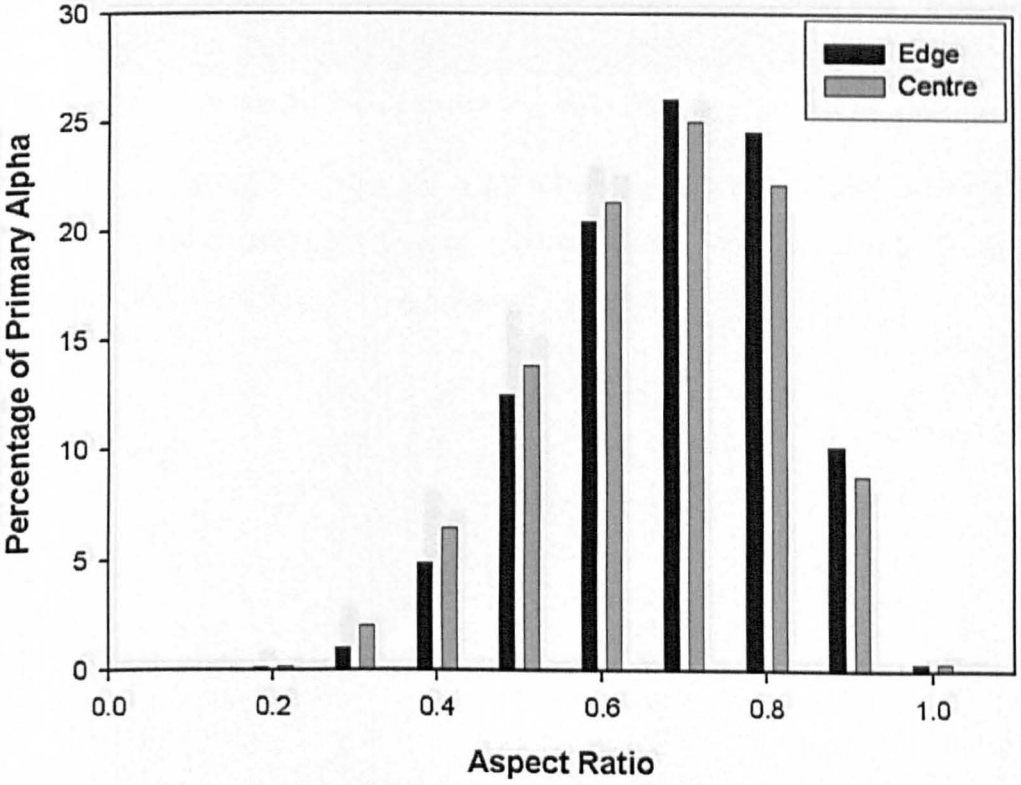

b) The aspect ratio of the α_p particles for LS2.

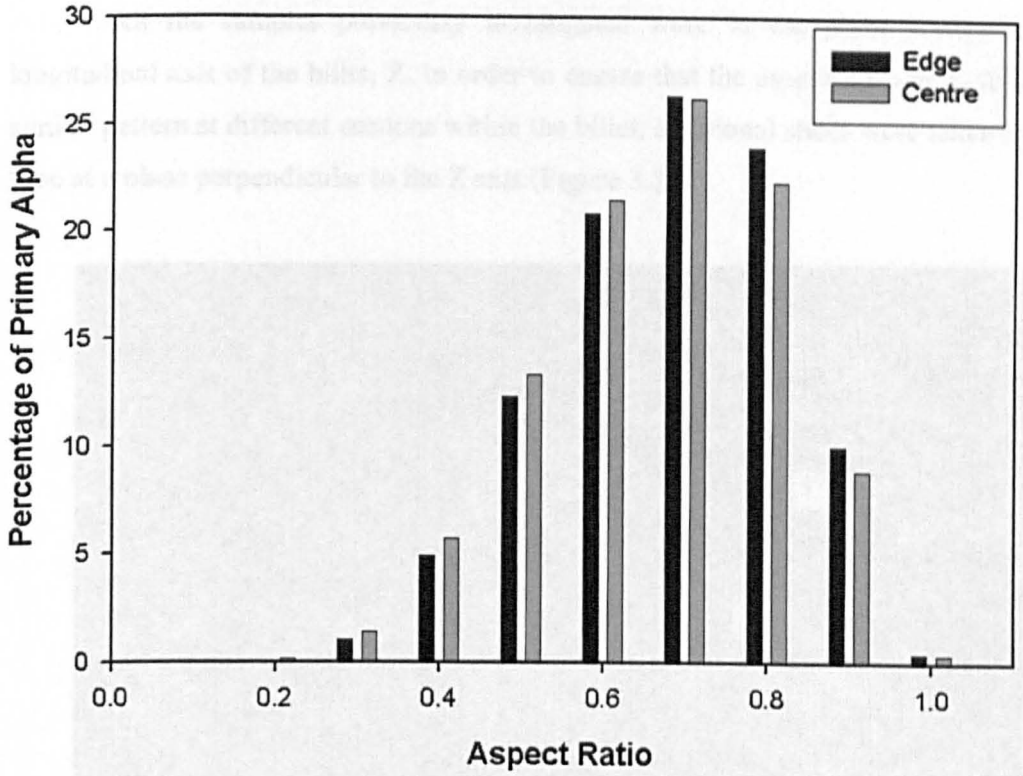

c) The aspect ratio of the α_p particles for LS3.

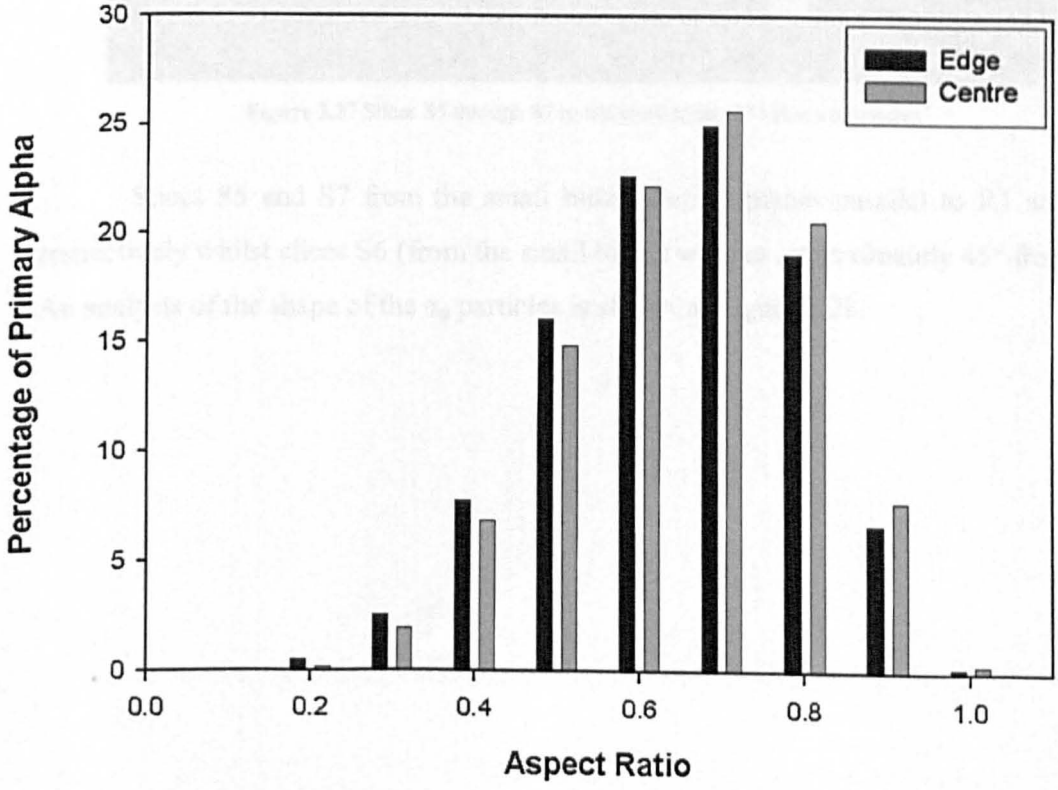

d)

Figure 3.26 The aspect ratio of the α_p particles for the large billet at the edge and centre for samples **a)** LS1 **b)** LS2 **c)** LS3 **d)** LS4.

All the samples previously investigated were in the plane containing the longitudinal axis of the billet, Z. In order to ensure that the aspect ratio of α_p follows a similar pattern at different sections within the billet, additional slices were taken but this time at a plane perpendicular to the Z axis (Figure 3.27).

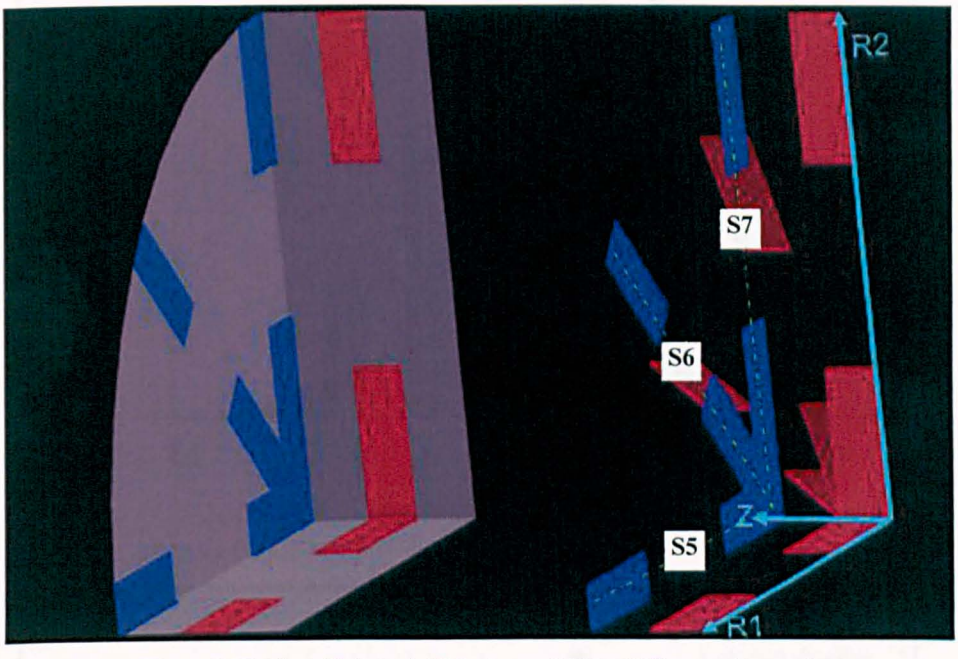

Figure 3.27 Slices S5 through S7 in the small billet (213 mm a diameter).

Slices S5 and S7 from the small billet were in planes parallel to R1 and R2, respectively whilst slices S6 (from the small billet) were at approximately 45° from R1. An analysis of the shape of the α_p particles is shown in Figure 3.28.

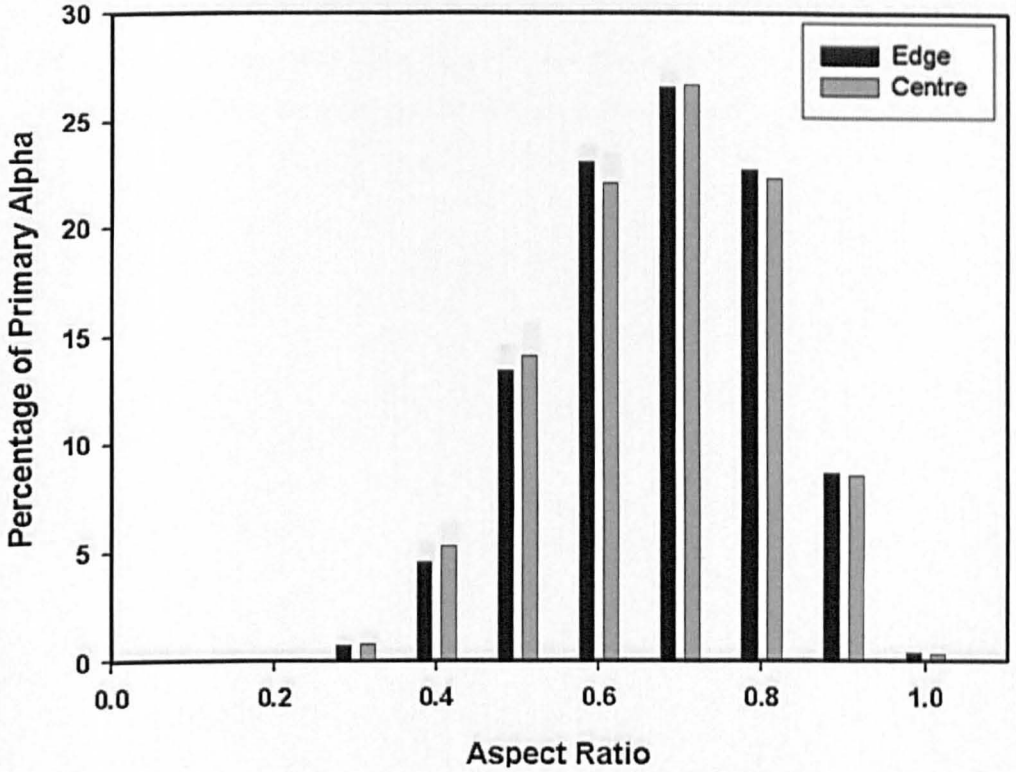

a) The aspect ratio of the α_p particles for the small billet, S5.

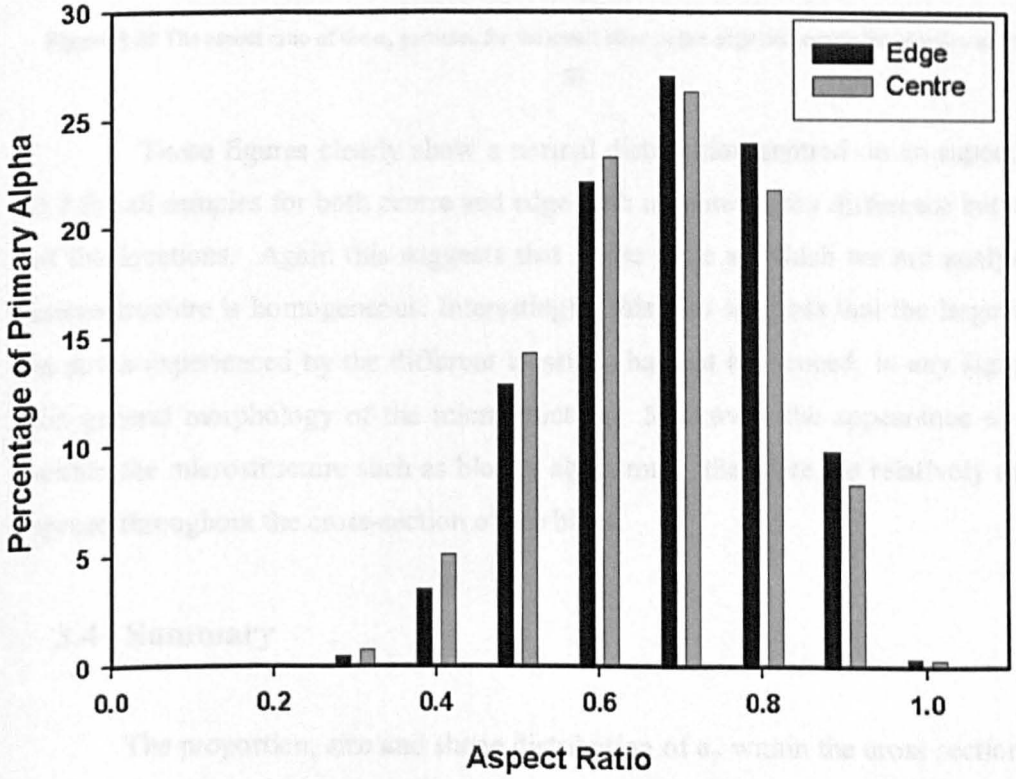

b) The aspect ratio of the α_p particles for the small billet, S6.

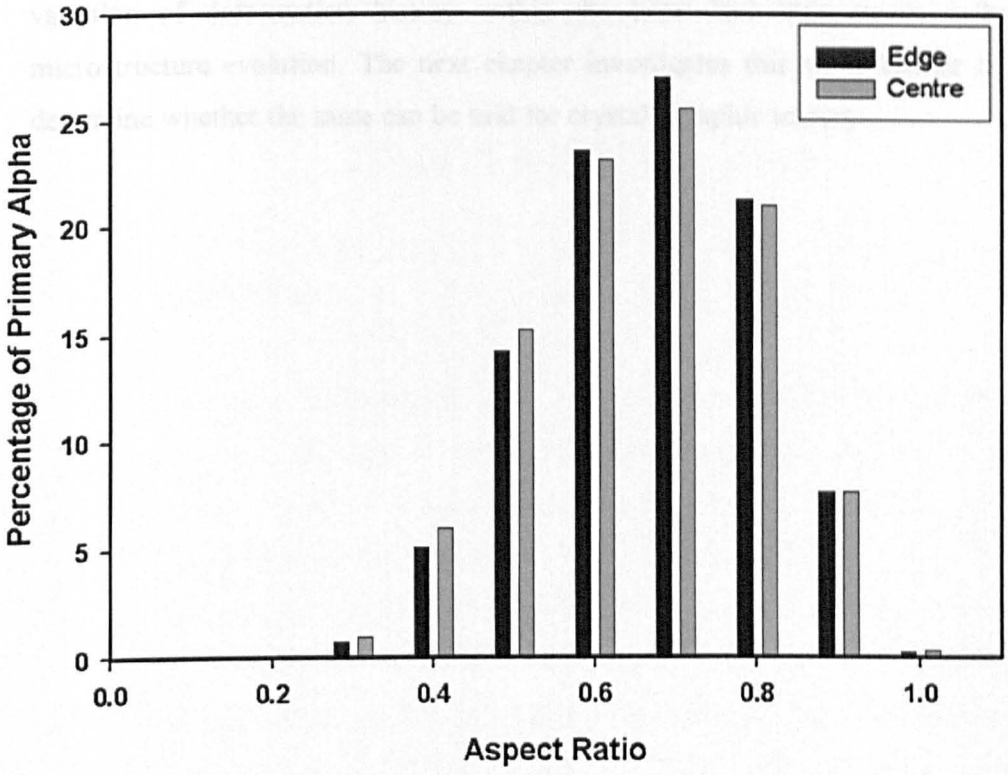

c)

Figure 3.28 The aspect ratio of the α_p particles for the small billet at the edge and centre for samples **a)** S5 **b)** S6 **c)** S7

These figures clearly show a normal distribution centred on an aspect ratio of 0.7 for all samples for both centre and edge with no noteworthy difference between any of the locations. Again this suggests that at the scale at which we are analysing, the microstructure is homogeneous. Interestingly, this also suggests that the large variation in strain experienced by the different locations has not influenced, in any significance, the general morphology of the microstructure. Moreover, the appearance of features within the microstructure such as blocky alpha must, therefore, be relatively uniformly spread throughout the cross-section of the billet.

3.4 Summary

The proportion, size and shape distribution of α_p within the cross section of both 313 and 213 mm diameter billets of the $\alpha+\beta$ alloy TIMETAL® 6-2-4-6 has been analysed. For all three parameters investigated there was no variation throughout the cross-section except for the extreme edge of the samples to a depth of 10 mm. This leads to the conclusion that on the scale that we observed the microstructure any

variation of deformation history within the billet had little or no influence on microstructure evolution. The next chapter investigates this work further in order to determine whether the same can be said for crystallographic texture.

Chapter 4

TEXTURE ANALYSIS

4.1 Introduction

This chapter analyses and interprets the crystallographic texture developed in TIMETAL® 6Al-2Sn-4Zr-6Mo during thermomechanical processing as a function of process history. Firstly, however, the chapter begins with an overview of crystallographic texture, with particular reference to titanium, and methods of its analysis. This is then followed by an explanation of the experimental procedures used.

Texture refers to the distribution of the orientations of individual grains within a polycrystalline material. Texture development is a complex function of mechanical and thermal treatments as well as the material itself, i.e. crystal structure, stacking fault energy, alloy content. The importance of texture to materials lies in the fact that many material properties are texture specific. Some examples of properties which depend on the average texture of a material are Young's modulus, ductility, thermal expansion coefficient and toughness etc [54, 63]. In this section background information about crystallographic texture such as techniques used in its measurement, methods of representation, texture in titanium alloys and orientation relationships between α and β phases are presented. It also illustrates how an important parameter to aeroengine component design, dwell fatigue, is dependant on the crystallographic texture of titanium.

4.1.1 Techniques used in the measurement of texture

Texture can be determined and quantified by simple X-ray diffraction, neutron diffraction or the electron backscatter diffraction (EBSD) method (Figure 4.1). X-ray diffraction is frequently used for macrotexture determination and EBSD is used to obtain higher resolution microtextures where orientation and spatial location of data can be obtained.

In order to obtain microtextural information it is important that the probe size formed by the exploring radiation (i.e. X-ray, neutrons or electrons) is smaller than the size of the microstructural units themselves. For this reason X-ray diffraction is not suitable for microtexture determination, thus EBSD techniques are typically used [55, 64].

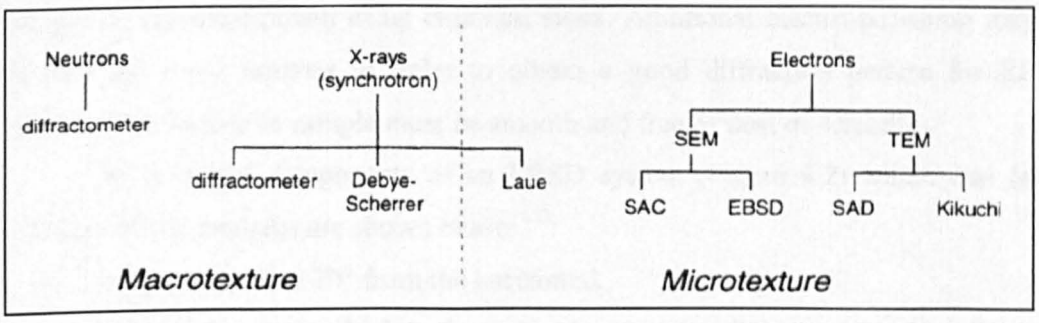

Figure 4.1 Mainstream techniques for texture determination [54].

4.1.1.1 Electron Back Scatter Diffraction (EBSD)

Electrons are ideal for combined microstructural/crystallographic studies. Back scattered electrons (BSE) are emitted when an electron beam incises on a sample. The number of back scattered electrons collected from each point is dependent on the atomic number (Z) of the material and the crystallographic orientation in the case of a crystalline sample in addition to the current and accelerating voltage applied. Until the 1980's Transmission electron microscopy (TEM) was the major technique used for this type of work, with some involvement from selected area channelling in an SEM. Since then a more suitable SEM-based technique for micro-texture has been developed, known as electron back-scatter diffraction (EBSD). EBSD is now the most important component of most microtexture research [54].

Since its launch, EBSD has revolutionised texture investigations both in research and industry. The technique has passed through various stages of development, and in its most advanced form provides the tool for a totally synthesised approach to orientation and microstructure [54].

In EBSD, a fixed electron beam hits a tilted sample and the diffracted electrons form a pattern which is recorded and the crystal orientation of the microstructure is calculated. When the beam is scanned in a grid across a polycrystalline sample and the crystal orientation measured at each point, the resulting map reveals the constituent grain morphology, orientations and the location of boundaries etc on the specimen's

surface. Also from these data, the preferred crystal orientations (microtexture) present in the material can be quantified.

Depending on the material, the sample preparation for EBSD analysis varies. In general it consists of a combination of mechanical grinding using silicon carbide papers or equivalent, mechanical polishing using diamond paste on the appropriate pads and a mechanical/chemical polish using colloidal silica. Additional electro-polishing may be required for some samples in order to obtain a good diffraction pattern for EBSD analysis. The surface of sample must be smooth and free of dust or scratches.

The principal components of an EBSD system (Figure 4.2) which was taken from Oxford Instruments are shown below [65]:

- Sample is tilted at 70° from the horizontal.
- A phosphor screen which is fluoresced by electrons from the sample to form the diffraction pattern.
- A sensitive charge coupled device (CCD) video camera for viewing the diffraction pattern on the phosphor screen.
- A vacuum interface for mounting the phosphor and camera in an SEM port. The camera monitors the phosphor through a lead glass screen in the interface and the phosphor can be retracted to the edge of the SEM chamber when not in use.
- Electronic hardware that controls the SEM, including the beam position, stage, focus, and magnification.
- A computer to control EBSD experiments, analyse the diffraction pattern and process and display the results.
- An optional electron detector mounted below the phosphor screen for electrons scattered in the forward direction from the sample.

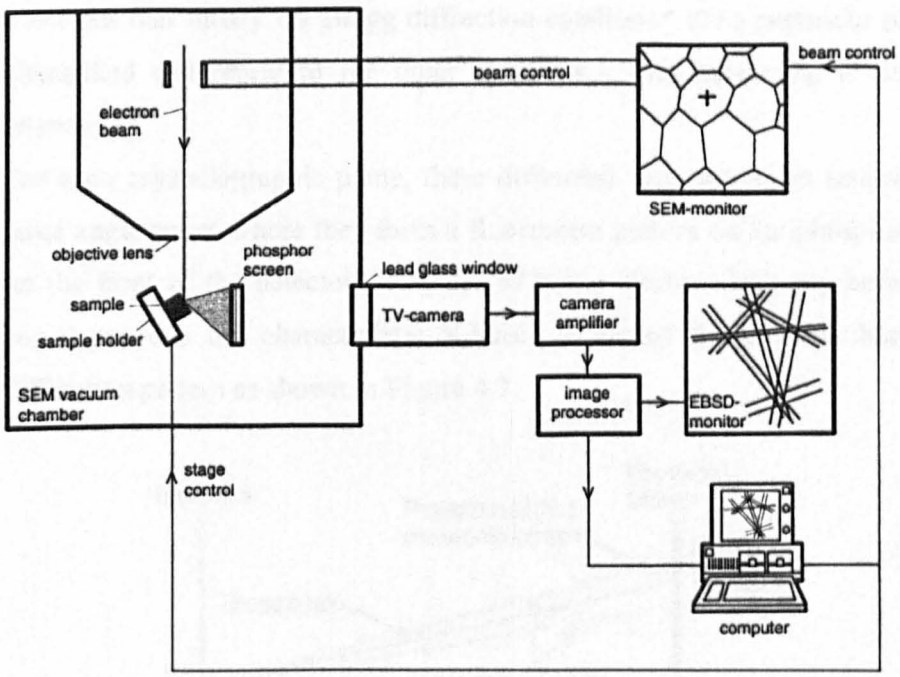

Figure 4.2 Components of an EBSD system [54].

The reason behind tilting the sample is to decrease the path length of the electrons which have been backscatted by lattice planes as they enter the sample therefore allowing a far greater amount of electrons to undergo diffraction and break out from the sample before being absorbed and thus improving the pattern contrast. When the sample is flat (e.g. conventional SEM), the path length is longer therefore absorption of the backscattered electrons is too great to produce detectable diffraction however ,tilting beyond about 80° causes unnecessary anisotropy of the sampled volume and distortion of the uncorrected image.

The principal features by which the diffraction patterns are formed are described below [66].

- The electrons strike the specimen, and within the pattern source point (PSP) [66] they are inelastically scattered, losing small amount of their energy (approximately 1%).
- These scattering events generate electrons travelling in all possible directions in a small volume which is effectively a point source.

- Electrons that satisfy the Bragg diffraction condition* for a particular plane are channelled differently to the other electrons - thus producing a change in intensity.
- For each crystallographic plane, these diffracted electrons form sets of paired large angle cones where they form a fluorescent pattern on the phosphor screen on the front of the detector. Regions of better electron intensity between the cones produce the characteristic Kikuchi bands of the electron backscatter diffraction pattern as shown in Figure 4.3.

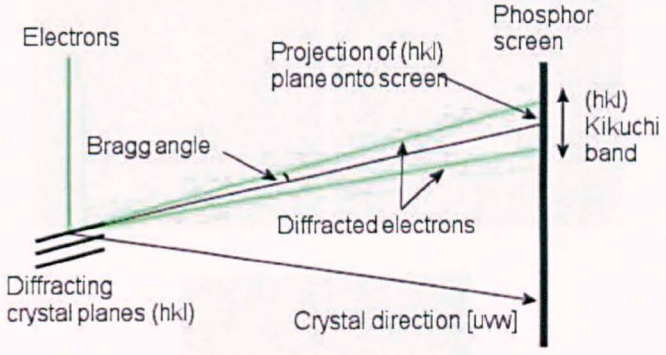

Figure 4.3 shows schematically how features in the diffraction pattern are related to the crystal structure.

The electron backscatter pattern (EBSP) consists of many intersecting Kikuchi bands shown as highlighted strips, brighter than the background, bounded by two edges. This is shown schematically in Figure 4.4.

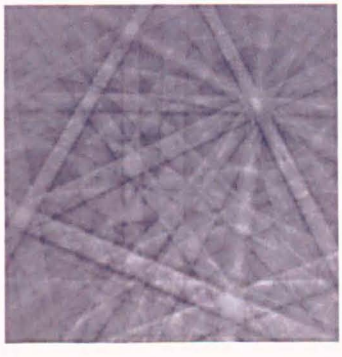

Figure 4.4 Intersecting Kikuchi bands shown as highlighted strips [65].

---

* Diffraction occurs according to Bragg's law which states:

1) The lattice plane *hkl* diffracts if it is in a reflection position between incident and diffracted X-ray.

2) Lattice planes with a spacing d_{hkl} obey the law;

$2d_{hkl} \sin\theta = n\lambda$

Where n is an integer determined by the order of diffraction, λ is the wavelength of the X-ray, d_{hkl} is the spacing between the planes in the atomic lattice, and θ is the angle between the incident ray and the scattering planes.

4.1.1.1.1 Background removal

In general the contrast of the Kikuchi bands of the initial image is weak. In order to improve this visibility of the Kikuchi bands, the background intensity can be removed. This is done by subtraction or division of the image of the background from the original pattern. Note that the background is measured over a relatively large area on the specimen at a low magnification. This is shown schematically in Figure 4.5.

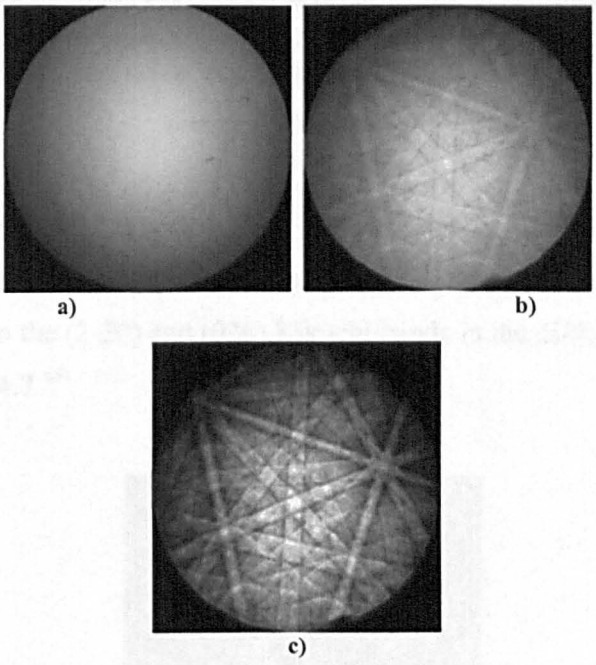

Figure 4.5 a) Background **b)** Original pattern **c)** Background subtraction [65].

The subtraction of the background is then followed by indexing the Kikuchi bands using Miller indices of the diffracting crystal plane which has generated them. Each point on the phosphor screen corresponds to the intersection of a crystal direction with the screen. In particular, the intersections of the Kikuchi bands correspond to the intersection of zone axes in the crystal with the phosphor screen. These points can be labelled by the crystal direction for the zone axis. The indexing of the diffraction pattern is shown in Figure 4.6.

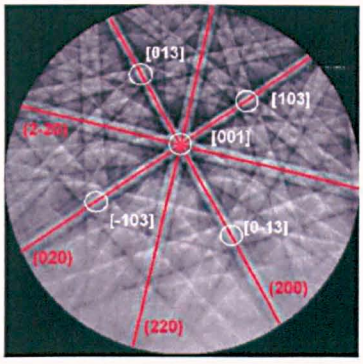

Figure 4.6 Kikuchi bands are labelled with the Miller indices of the crystal planes that generated them (red). The planes project onto the screen at the centre of the bands. Kikuchi band intersections are labelled with crystal direction that meets the screen at this point (white). This direction is the zone axis of the planes corresponding to the intersecting Kikuchi bands [65].

As an example, a nickel crystal unit cell has been placed over on the diffraction pattern in the orientation which generates this pattern. The crystal planes are labelled which correspond to the (2-20) and (020) Kikuchi bands in the diffraction pattern. This is shown in Figure 4.7 [65].

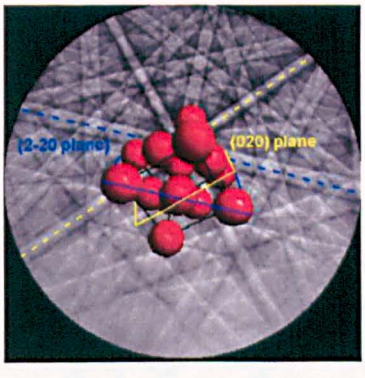

Figure 4.7 Nickel crystal unit cell being placed over on the diffraction pattern in the orientation which generates this pattern [65].

4.1.1.1.2 Automated indexing and orientation measurement

The crystal orientation is calculated from the Kikuchi band positions by the computer processing the digitised diffraction pattern collected by the CCD camera. The Kikuchi band positions are found by calculating the average intensity along lines inclined at an angle θ and displaced from the centre of the image by ρ using the Hough transform (Figure 4.8).

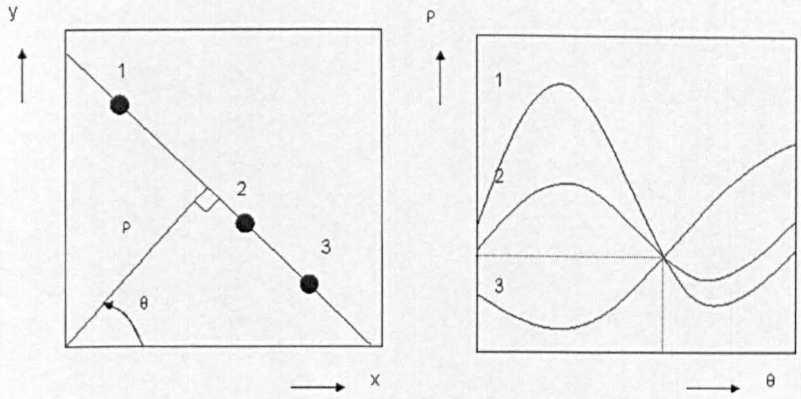

Figure 4.8 The Hough Transform transforms lines into points in Hough space [65].

The transformation between the coordinates (x, y) of the diffraction pattern and the coordinates (ρ, θ) of Hough space is given by Equation 4.2.

$$\rho = x \cos\theta + y \sin\theta \tag{4.1}$$

Based on Hough space a straight line is characterised by ρ, the perpendicular distance from the origin and θ the angle made with the x-axis and so is represented by a single point (ρ, θ) in Hough space. Figure 4.9 illustrates schematically the principals behind finding the position of the Kikuchi bands in the diffraction pattern using the Hough transform

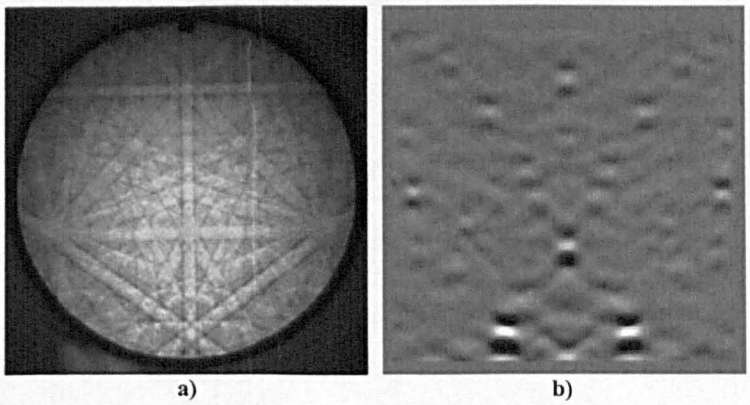

a) **b)**

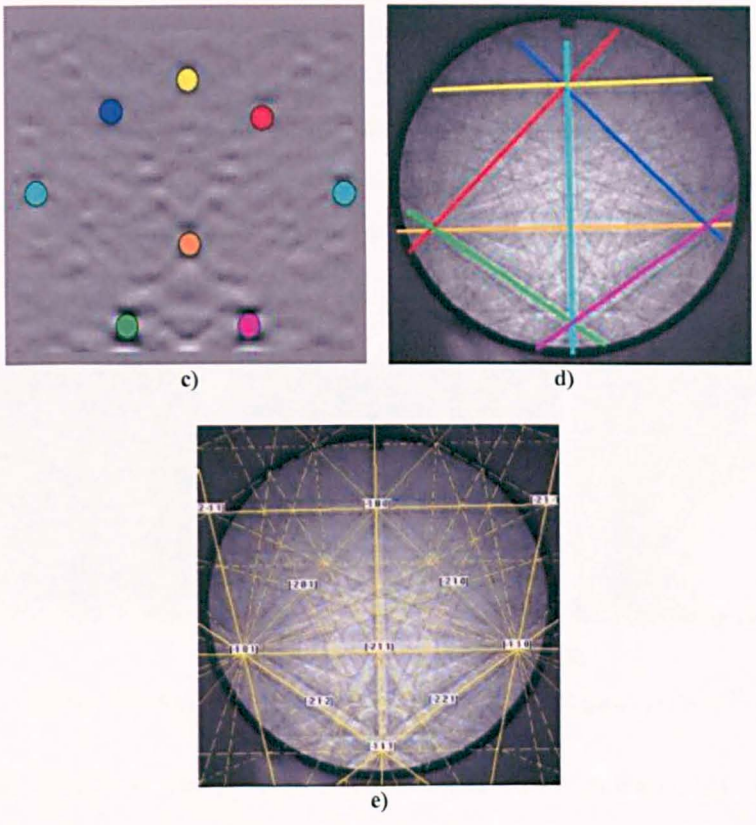

Figure 4.9 a) Diffraction pattern collected from germanium at 20kV accelerating voltage, **b)** The Hough transform of this diffraction pattern, **c)** The peaks in the Hough transform identified and coloured, **d)** The lines in the original diffraction pattern corresponding to the peaks found in the Hough transform and coloured similarly, **e)** The indexed diffraction pattern [65].

4.1.1.1.3 Parameters for EBSD analyses

One of the major factors affecting the EBSD run is the time and quality of the patterns produced for mapping. Time taken to index a Kikuchi pattern can be effected by number of parameters.

Step size is an important variable since it obtains sufficient amount information on the desired area. By decreasing the step size the accuracy is increased, but this increases the run time to a great extent. However by increasing the step sizes, there is an increased chance that microstructural features such as grain boundaries will be misplaced.

Frame average is the average of the numbers of frames taken to produce the pattern for that particular area. In general increasing the number of frames increases the clarity of the pattern, but this also increases the run time. The background pattern (taken

prior to the run) is subtracted from this averaged frame and the diffraction pattern is then indexed and saved using the software [66].

Timing per a frame is the time used to obtain a frame. Insufficient signal in the image (too dark) is the results of time per frame being too low, while if the time is set too high , then part of the image will be over-saturated forming a white area [66]. These are shown in Figure 4.10.

a) b) c)

Figure 4.10 Example of time per a frame being **a)** to low **b)** good **c)** to high [66].

Other important factor which effects the time considerably is the camera binning. The digital camera allows users to adjust the quality of diffraction pattern in order to suit each particular analysis. The camera has a high resolution which allows the acquisition of good quality EBSPs. However, by binning (clustering groups of pixels together), it is possible to collect different resolution EBSPs at different speeds. Figure 4.11 shown as an example.

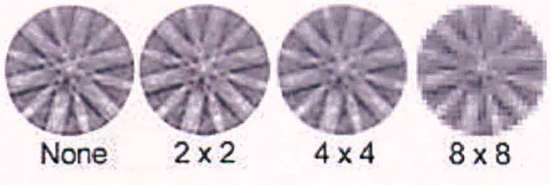

Figure 4.11 different binning levels on a small part of an EBSP [66].

When analysing the texture if accuracy is more important than speed for example phase identification, 2x2 Regular EBSD analyses is used. Whereas if slight loss in accuracy is not an issue for example large texture analyses, 8x8 High speed analyses can be used [66].

4.1.2 Methods of representation of texture

- **Pole figures**: are graphical representations of the strength of orientation distribution of crystallographic lattice planes or directions on a stereographic projection with respect to the coordinate system of a sample. Pole figures represent the orientation of the crystal coordinate system in the sample coordinate system. The colours and contour lines applied to each pole figure illustrate the strength of the texture as the number of magnitude random occurs. Pole figures for hexagonal materials are normally presented in three {0001}, {10-10} and {11-20} planes. An example of the construction of a pole figure is shown in Figure 4.12 [63, 66].

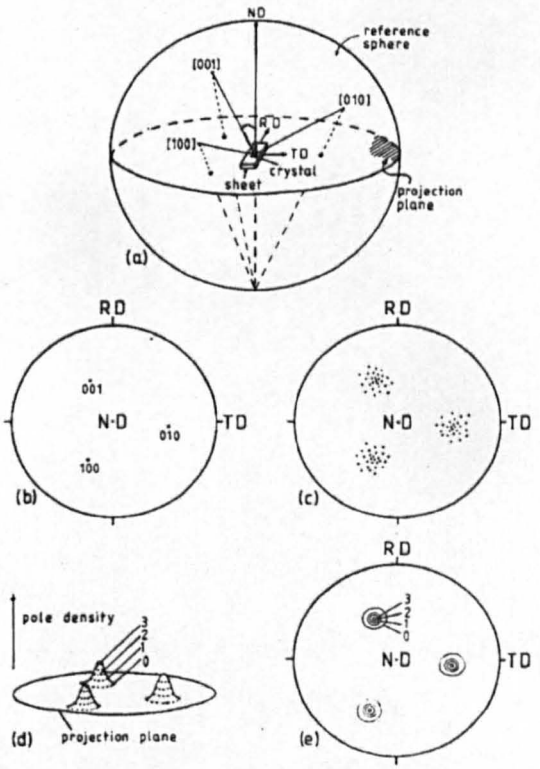

Figure 4.12 Illustrating **a)** projection sphere and reference direction, **b)** projection of poles for a single grain, **c)** projection of poles from textured grains **d)** pole density distribution and **e)** contour map of pole density [63].

- **Inverse pole figures**: Unlike pole figures (representing the orientation of the crystal coordinate system in the sample co-ordinate system) the orientation of the sample coordinate system can be projected into the crystal co-ordinate system. This representation is called the inverse pole figure (IPF). This system although being the

simplest way of showing the texture in a material has one key disadvantage. It only shows the orientation of one reference axis but rotations about this axis are ignored. Typically for cubic phases, red, green, and blue are assigned to grains whose <100>, <110> and <111> axes, respectively, are parallel to the projection direction of the IPF (typically the surface-normal direction). For hexagonal phases however, full red, green, and blue are assigned to grains whose <0001>, <-12-10> <01-11> axes, respectively, are parallel to the projection direction of the IPF. Orientations in the middle are coloured by an RGB mixture of the primary components. The colour scheme in IPF colourings for cubic face is shown in Figure 4.13 [54, 67].

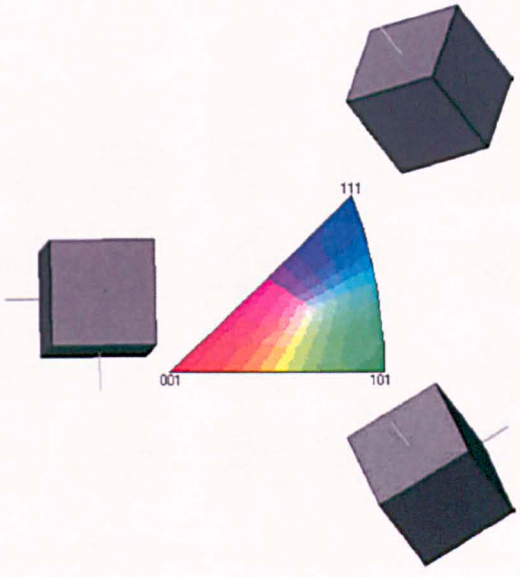

Figure 4.13 Legends illustrating the colour schemes in IPF colouring [67].

- **Euler angles:** The Euler angles refer to three rotations which are used to describe the sample orientation relative to the crystal or vice-versa. This involves rotating one of the coordinate systems about various axes until it comes into coincidence with the other. There are different possibilities concerning the selection of the axes and the order of which they function. The most commonly used rotations for expressing Euler angles and that which is also used by the Channel 5 EBSD software is called the Bunge rotation. The three Euler angles $\varphi_1, \phi, \varphi_2$ represent the following rotations are shown schematically in Figure 4.14:

1) A rotation of φ_1 about the z-axis followed by,
2) A rotation of ϕ about the rotated x-axis followed by,
3) A rotation of φ_2 about the rotated z-axis.

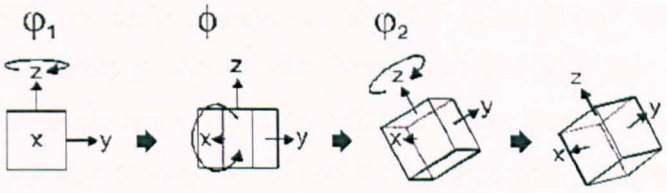

Figure 4.14 Euler angle rotations according to Bunge's convention [66].

In order to show the three rotations in a simple arrangement, by setting φ_2 to zero, it is possible to demonstrate the effects of φ_1 and ϕ. The following schematic (Figure 4.15) shows a silicon unit cell (Si atoms shown as black circles) being rotated.

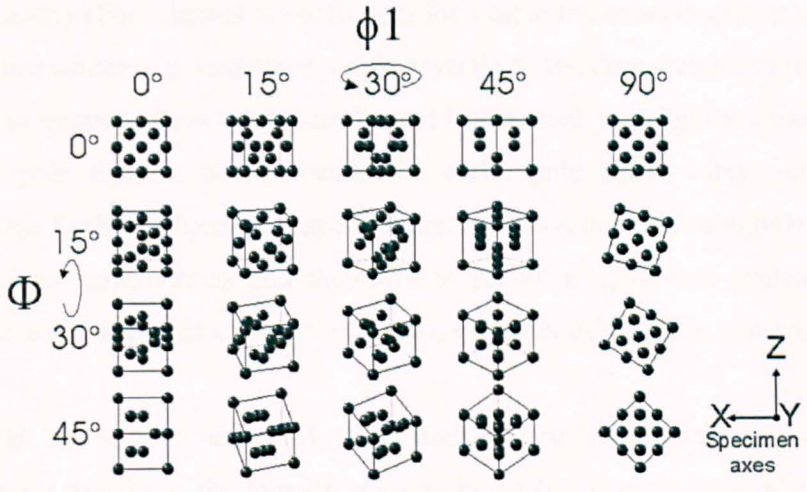

Figure 4.15 The effects of φ_1 and ϕ Euler angles on a silicon unit sell (φ_2 is set to zero) [66].

When using Euler angles to describe metalworking textures, it is common to relate the sample coordinate system *X,Y*, and *Z* to directions defined by the forming process such as rolling direction (RD), Transverse direction (TD), Extrusion direction (ED) and normal direction (ND) [54, 66].

In Euler colouring maps, each pixel is a combination of the 3 colours depending on the magnitude of each Euler angle seen in Figure 4.16.

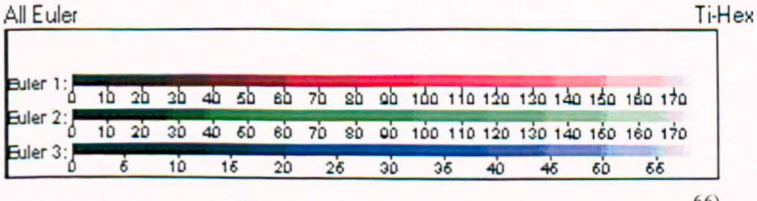

Figure 4.16 Legends illustrating the colour schemes in Euler colouring [66].

Unlike IPF in Euler colouring all the information about a particular crystallographic direction is shown. But because of the way that Euler angles are defined they can generate two completely different colour for two close orientation e.g. two neighbouring grains having 179.5° and 0.5° degree of miss-orientation will have completely different colouring despite being only a degree missorientated. Thus care must be taken in interpreting results.

- **Orientation distribution function (ODF)**: the projection of a three dimensional orientation distribution onto a two dimensional projection plane makes it difficult to define the complete orientation of the crystals orientation, therefore the calculated pole figure from a three dimensional orientation (texture for example), might result in reduced accuracy (Pole figures are sufficient for simple textures consisting only a small number of orientation e.g. texture of single crystals or the cube texture in recrystallised aluminium or copper). Also most experimentally obtained pole figures from X-rays are incomplete pole figures, which means the entire pole figure range has not been recorded. This further reduces the texture information available in such pole figures. To overcome these uncertainties and therefore to permit a quantitive evaluation of the texture, it is necessary to describe the orientation density of grains in a polycrystal using ODF [54].

The ODF is a four dimensional object and is a method of representing preferred orientations for materials, the four dimensions being the three Euler angles (The three Euler angles are used to form a three dimensional coordinate system) and a density value corresponding to how strongly a particular orientation appears. This strength is expressed as a ratio to that expected for a completely random distribution of orientations [66].

Figure 4.17 shows a general case of triclinic crystal symmetry and no sample symmetry. The Euler angles are defined in range of $0° \leq \varphi_1, \varphi_2 \leq 360°$ and $0° \leq \phi \leq 180°$ which in turn defines the maximum size of the Euler angle space, the so called asymmetric unit.

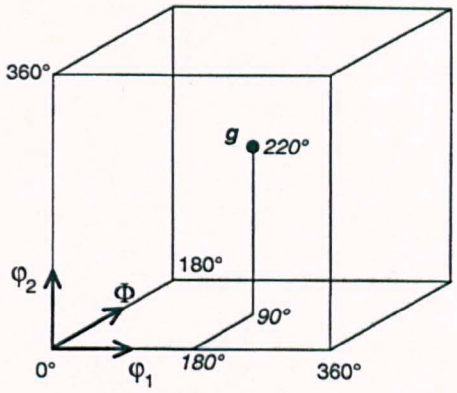

Figure 4.17 Representation of orientation in a three –dimensional orientation space defined by the Euler angles. Each orientation g correspond to a point in the Euler space whose coordinate are given by the three Euler angles φ_1, ϕ, φ_2 describing the orientation (Bunge's convention) [54].

A representation of an ODF in a three dimensional space is shown in Figure 4.18 a). This type of representation is not generally suitable for publication on the printed page. Therefore, it is common practice to represent ODFs in the form of sections through the orientation space. The intensity distribution in the individual sections can be displayed by different colours, different gray values or most commonly by contour lines. This is shown in Figure 4.18 b) [54].

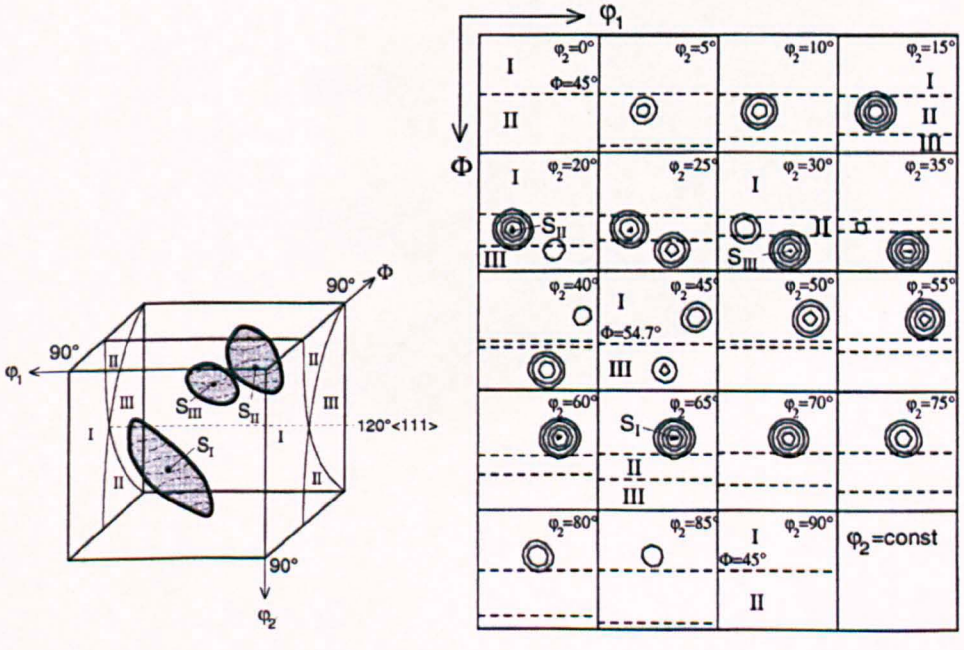

Figure 4.18 a) An ODF in a three dimensional space **b)** same texture as in (a) plotted using contour lines in φ_2 section ($\Delta\varphi_2$=5°) through the Euler space [54].

- **Orientation maps**: Orientation maps are used in order to express the basic characters of the material's microstructure in 2D (grain size, shape, overall preferred orientation and etc.). Using Orientation Imaging Microscopy (OIM), regions with the same Euler angles can be mapped using the same colour (Figure 4.19) showing correspondence with the microstructure in the region and thus distinguishing regions of different orientations [63].

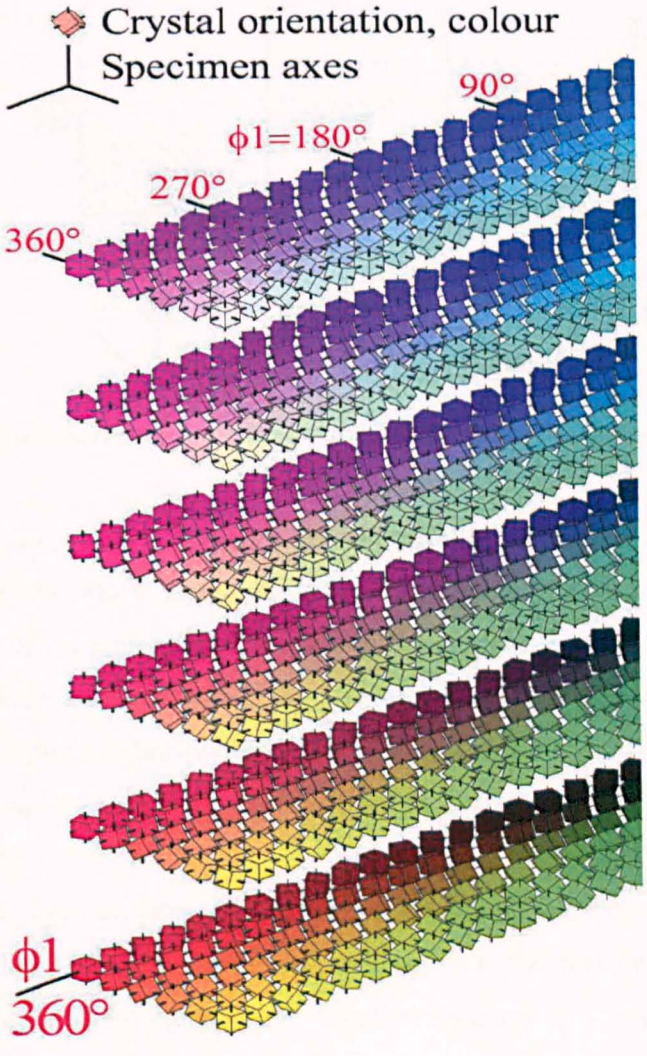

Figure 4.19 A simple illustration of Orientation Imaging Microscopy (OIM) in Euler colouring [66].

4.1.3 Texture in Titanium alloys

Titanium alloys can have a pronounced anisotropy of properties, which can be directly related to the inherent anisotropy of the hexagonal crystal structure of α. These crystallographic textures develop during solidification and deformation and can be

further pronounced by a subsequent recrystallisation and/or annealing. Crystallographic textures also normally depend on the degree, the mode and the temperature of deformation. Generally the intensity of the texture is directly affected by the deformation degree, i.e. the total strain imposed on the material and strain path history.

Figure 4.20 shows the influence of temperature and deformation on (0001) pole figures in a basic deformation mode (upset forging).

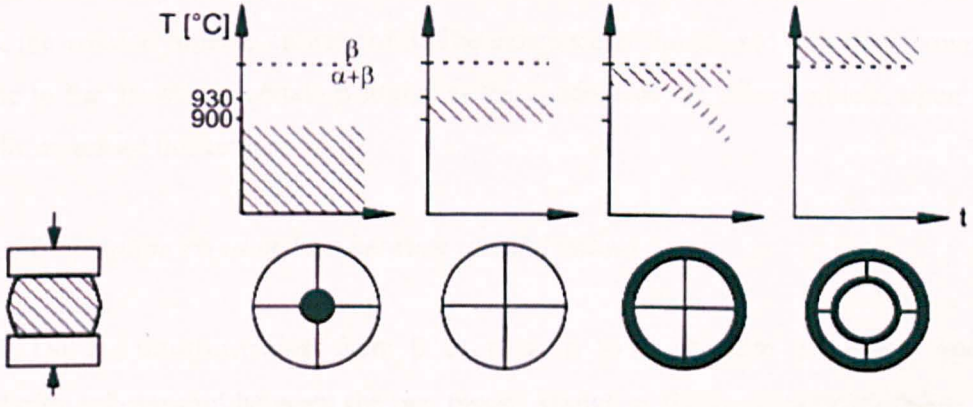

Figure 4.20 Influence of forging on texture of Ti 6-4 during different temperature periods [9].

Within the α+β Ti 6Al-4V alloy, four temperature regions can be distinguished. At temperatures below 900° C, where the structure is predominately hcp, a basal texture perpendicular to the compression direction is developed. At this point the volume fraction of α is much higher compared to β therefore material deforms like a single α phase with a hcp structure. Between 900 and 930° C, the volume fraction of α and β is generally the same therefore no preferential texture is observed (independent of deformation mode).

If EBSD is used however, both α and β texture should be visible. If an equal volume of α and β is present, when strain is applied, the majority of the strain is accommodated by the softer cubic phase therefore resulting in a larger deformation in the β phase. By having deformation in the β phase, on cooling β transforms by the Burgers orientation relationship (Section 4.1.3.1) to α_s therefore resulting in a strong α_s texture at the edge and a very defined α texture at the centre of the pole figure.

Just below β transus temperature, there is a high volume fraction of β. At this temperature a very strong β texture is generated meaning a commensurate α texture in α_s should be seen. If the the β grain has a very strong texture then a very strong texture in the α_s will subsequently be noted due to the Burgers orientation relationship. Therefore

due to the large volume of β texture, a reflection of the β texture in the α_s should be seen. Above β transus temperatures structure consists entirely of β phase, however within the pole figure observed in Figure 4.20, in addition to the outer ring seen at temperatures just below transus a second inner ring is noted. The outer ring positioned at the edge must be α_s (because there is such little α_p) as was seen at temperatures just below transus due to the volume consisting of virtually all β. The existence of the second inner ring seen at temperatures above β transus is not understood as, at this point, the volume consists entirely of β. The existence of the second ring may, however, be due to the growth of certain β grains at the expense of the others which, when they transform, create this texture [9].

4.1.3.1 Orientation relationships between α and β phases

During transformation from β to α or α to β titanium exhibits a special orientation relationship between the two phases known as the Burgers relationship. The Burgers orientation relationship is the major orientation relationship between the α and the β phases, in which the basal plane $(0\ 0\ 0\ 1)_\alpha$ is parallel to the $(1\ 1\ 0)_\beta$ and the $[11\bar{2}0]_\alpha$ direction is parallel to the $[1\bar{1}1]_\beta$ direction [68, 69]. Burgers relationship is generally shown as:

$$(110)_\beta \parallel (0001)_\alpha$$
$$[1\bar{1}1]_\beta \parallel [11\bar{2}0]_\alpha$$

The Burgers orientation relationship is show diagrammatically in Figure 4.21

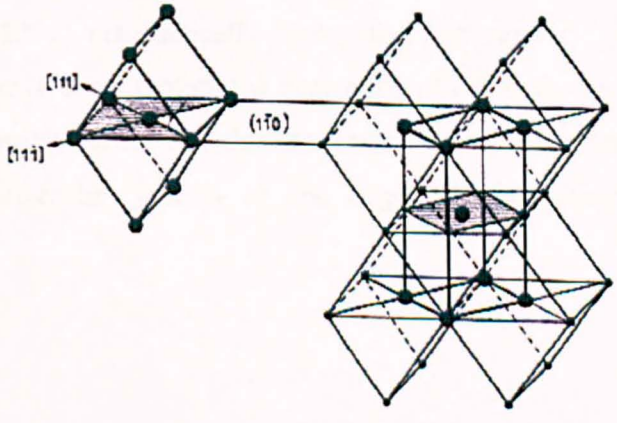

Figure 4.21 Illustration of mechanism proposed by Burgers for transformation of bcc lattice to hcp lattice [70].

According to the Burgers relationship during $\beta \longrightarrow \alpha$ transformation the individual β grains can potentially transform into 12 daughter variants (6 planes with 2 directions) of the α phase. Also each (0001) plane of α phase can be parallel to one of six (1 1 0) planes in β phase when $\alpha \longrightarrow \beta$ [71, 72].

4.1.3.2 Variant selection

In most diffusional phase transformation and precipitation processes, nucleation of the product phase occurs heterogeneously at some preferential nucleation sites in the matrix such as a grain boundary, dislocation etc. As mentioned previously, the refinement of grain size is the most efficient method of obtaining metallic materials with high strength and high toughness. The introduction of lattice defects into the matrix by thermomechanical processing increases such nucleation sites and subsequently raises the nucleation rate of the product phase. This product phase maintains coherency with its matrix phase as much as possible to reduce the activation energy for the nucleation. Under such a situation, a specific, rational orientation relationship is held between the two phases. When the crystal structure is dissimilar between these phases, there are a number of equivalent orientations of the product phase for a given orientation relationship, which are called variants.

Figure 4.22 a) schematically shows the situation in which the formation of the variant occurs randomly and adjacent nuclei are of different variants. In this situation, each nucleus becomes a grain after the growth and coalescence and a fine grain structure is formed. In the heterogeneous nucleation on lattice defects, however, the variant formation of the product phase is extremely restricted by the nature of the defects. Figure 4.22 b) schematically shows that the variants formed are severely selected in local areas. Even though the nucleation rate is high, the number of variants formed within a matrix grain is reduced. When neighbouring nuclei with the same variant are coalesced, they emerge to one large grain, resulting in a coarse grain structure [73].

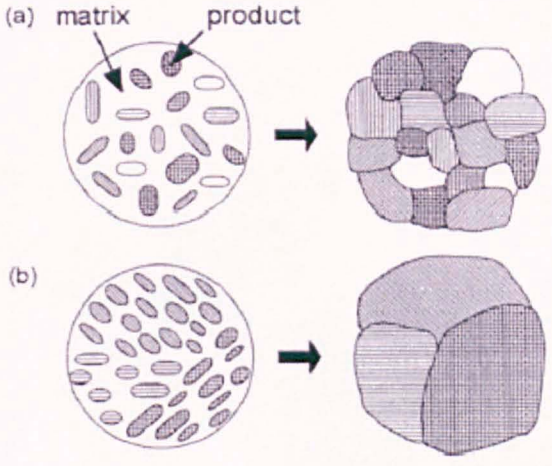

Figure 4.22 Microstructure development by diffusional phase transformation: **a)** with no variant selection and **b)** with severe variant selection which occurs locally [73].

Due to variant selection some orientation variants are preferentially selected during $\alpha \longrightarrow \beta \longrightarrow \alpha$ phase transformation in titanium [72]. For example, it has been reported that hot rolling above β transus and heavy cold rolling before β annealing in titanium alloys leads to variant selection during $\beta \longrightarrow \alpha$ [71]. Some other work done on Ti 6-2-4-6 states that there is a tendency for a prior β/β grain boundary to have α product on either side with close alignment of their (0001) poles. Also other authors have shown variant selection is the result of preferential nucleation of certain α orientation between β grains having nearly parallel (110) planes [72, 74].

4.1.4 Dwell fatigue

During service, compressor disks are under severe operating conditions due to high cyclic loads. Conditions such as fatigue, creep oxidation and corrosion are important factors in determining the life of the component. Resistance to fatigue crack initiation for titanium alloys is generally reduced as the microstructure coarsens [75].

Dwell fatigue is of particular importance to aeroengine components, as maximum stresses may be sustained over lengthy periods. Dwell fatigue life is much shorter than for simple sinusoidal cyclic loading when a particular maximum stress, or stress intensity factor is reached (Figure 4.23) [75].

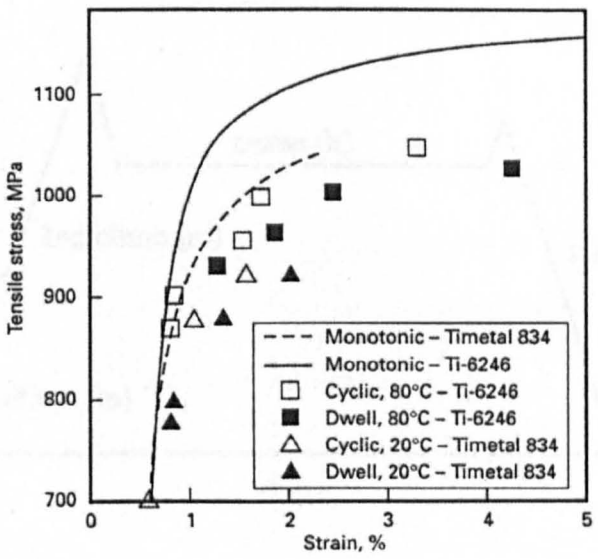

Figure 4.23 effect of dwell fatigue loading on titanium alloys [75].

Dwell fatigue was first recognised in late 1972 due to an unexpected failure of two titanium alloy fan disks in Rolls-Royce RB211 engines. The fan disks were manufactured from the near α alloy IMI 685. These disks had passed all the fatigue criteria of that era. Therefore the early service failures were indicative that additional factors were affecting the fatigue response. This was soon followed by an agreement that fatigue in titanium alloys at ambient temperatures could no longer be described by simple load on/load off cycles [76].

Figure 4.24 shows a typical flight operation, broken down in simplistic terms into a sequence comprising take off, cruise and landing. It can be observed that the stress cycle cannot be modelled as single low cycle fatigue (LCF) and the relatively long term hold or "dwell" at high mean stress during the cruise stage must be considered.

As a reaction to the above events, the IMI 685 disks were replaced with a finer grained variant Ti 6Al-4V due to the fact that this alloy had already gathered significant service experience [76].

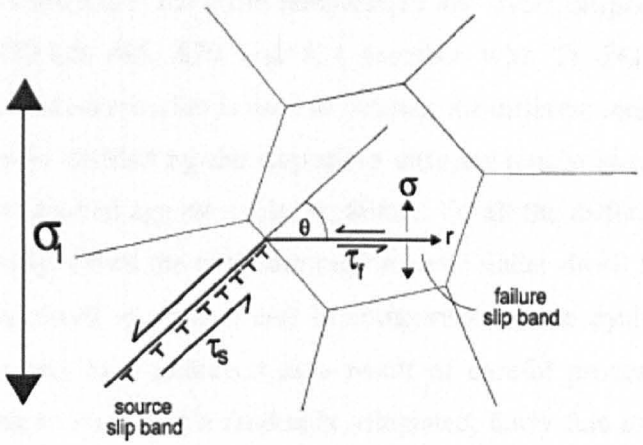

Figure 4.25 The Stroh model for planar slip [76)]

An example of faceted initiation in support of the above model is shown in Figure 4.26 for a relatively coarse grained alloy TIMETAL® 685 tested under torsional fatigue loading. The metallographic section is shown through the grain containing the facet (inclined to the left hand side). Evidence of the original shear deformation that preceded the facet formation is included in the right hand neighbouring grain. The principal tensile stress axis is inclined at 45 degrees and is therefore perpendicular to the facet. The weak grain has undergone slip on a plane of maximum shear. Secondary cracking has been caused by the complexity of the stress state as the pile-up intersects the grain boundary. Discrete electron backscatter diffraction (EBSD) measurements evaluating the crystallographic orientation of the two individual grains confirms that the slip and facet planes both have near basal orientations [81)].

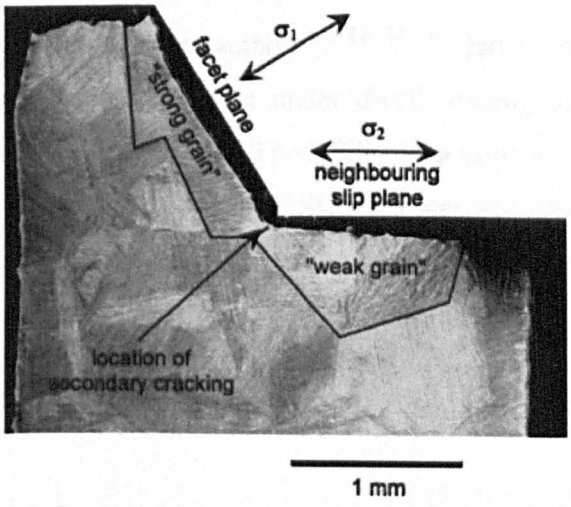

Figure 4.26 Vertical section taken through facets developed under cyclic torsion LCF in TIMETAL® 685 [81)].

Figure 4.27 illustrates the room temperature low cycle fatigue (LCF) data from the alloys TIMETAL® 685, 829 and 834 together with Ti 6Al-2Sn-4Zr-6Mo. A normalised applied stress criterion is used to account for different strengths between the alloys (applied stress divided by the respective ultimate tensile stress for the specific alloys). Results are plotted against cycles to failure. Of all the different alloys, Ti 6Al-2Sn-4Zr-6Mo clearly shows the optimum performance under dwell loading conditions (again two minute dwell at peak stress) in comparison to the cyclic performance of other alloys. This has been achieved as a result of careful processing above the β transus temperature to guarantee a randomly orientated, fairly fine scale microstructure (i.e. the microstructure is fully transformed) [81].

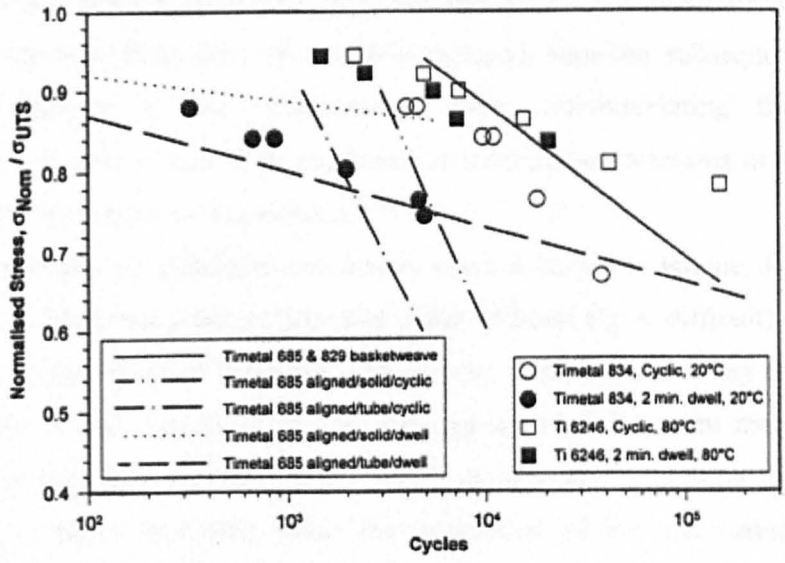

Figure 4.27 Combined LCF data for the alloys TIMETAL® 685, 829 and 834 together with Ti 6-2-4-6 [81].

In addition several different authors [5, 82, 83, 84] have reported that the poor performance of TIMETAL® 834 billet under dwell loading conditions are due to regions of similar orientated α_p grains. The EBSD map done by Germain et al. [5] is a good example (Figure 4.28). The large EBSD map was acquired in the longitudinal plane using a step size of 15μm. Red colour represents the basal planes (0001) having their c-axis aligned with the billet axis. In the OIM shown in Figure 4.28 band-like regions with sharp local textures, commonly called macrozones, can clearly be revealed.

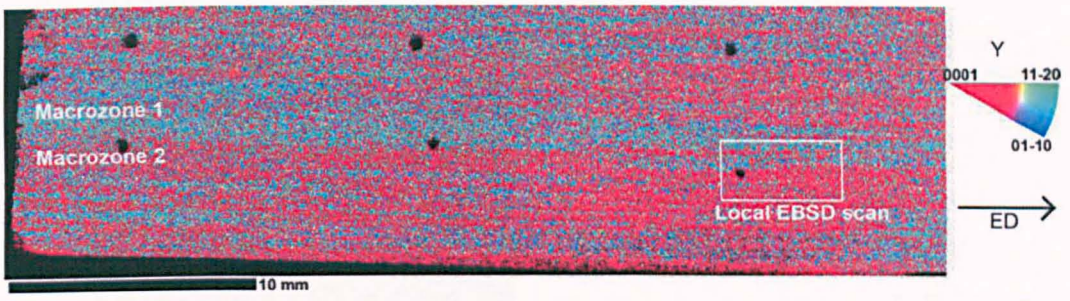

Figure 4.28 Low magnification IPF map of the reference sample revealing sharp texture heterogeneities [5].

Macrozones are the result of a pronounced variant selection mechanism, often reported after severe deformation in β. As mentioned before, the coarse α_p lamellae is the result of $\beta \longrightarrow \alpha$ phase transformation after primary ingot breakdown in β. It is very likely that upon cooling large sets of α variants with close orientations have been generated therefore these sets of similarly oriented lamellae subsequently undergo heavy deformation at high temperature, each accommodating the strain in approximately the same way. This maintains or strengthens variations in local textures and causes the formation of macrozones [5, 85].

Macrozones are important parameters when it comes to fatigue. Fatigue cracks are initiated on the basal plane or prismatic plane (if basal slip is difficult). Therefore in macrozones where basal or prismatic slip is easy, many adjacent tiny cracks (which have the size of the primary α_p grains) can appear over the entire macrozone. This contributes to the crack growth over the whole macrozone [86]. In order to improve the fatigue life of the components either the orientation of the macrozones should be modified or the size of the macrozones could be reduced to ensure that slip is difficult and to reduce the initial flaw size respectively. This could significantly improve the fatigue life of various titanium alloys in which the existence of macrozones is expected [86].

Bache et al. [87] used EBSD to investigate the orientation of fracture facets of IMI685 and IMI834 (TIMETAL® 834) produced by fatigue failures generated in the laboratory. Figure 4.29 shows these facets at the initiation site in TIMETAL® 834. EBSD analysis was then carried out on the facets resulted in the observation of a near-basal orientation of the facet. This is shown in Figure 4.29 using IPF colouring.

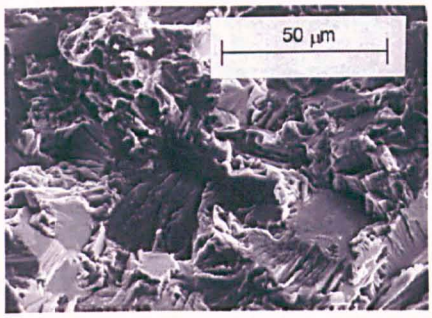

a)

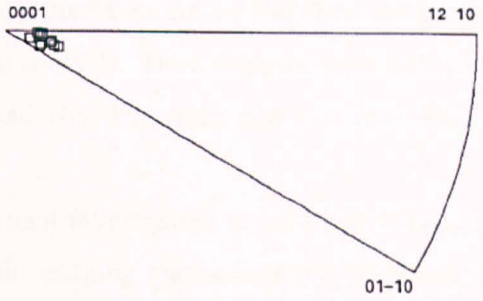

b)

Figure 4.29 Illustrates **a)** Facets at the initiation site in Timetal 834 and **b)** inverse pole figure for EBSD measurements taken of the fracture site facets [87].

4.1.5 Summary

Within this section the background information regarding the crystallographic texture in titanium alloys and the techniques used in the measurement of texture was provided.

The next section contains experimental work which will investigate the texture evolution of the α+β TIMETAL® 6-2-4-6 during billet manufacture. Textures will be analysed in longitudinal slices at different parts of the billet. The aim of this experimental section is to find out if any texture variation within the billet cross-section can be related back to deformation history during breakdown from the VAR ingot.

4.2 Experimental work

In Chapter 3, the size and shape distribution of spheroidised α within the cross section of a billet of the α+β alloy TIMETAL® 6-2-4-6 under conditions applicable to the manufacture of billet materials via hot working was investigated. Interestingly, the results suggested that the large variation in strain experienced by the different locations within the cross section of the billet has not influenced, in any significance, the general morphology of the microstructure.

This Chapter investigates the texture evolution of the α+β alloy TIMETAL® 6Al-2Sn-4Zr-6Mo under conditions applicable to the manufacture of billet materials. This investigation is necessary in order to determine whether any texture variation within the billet cross-section can be related back to its deformation history of the billet.

Note that the samples used for texture investigation are the same samples used in the previous chapter for the microstructural analysis. Here samples were polished again but this time with colloidal silica (silco) and 10% hydrogen peroxide mix. This was to prevent etching from the silco.

The local texture of the billet was then investigated using the EBSD technique. As described before, EBSD is an orientation imaging microscopy (OIM) where the data is saved as a series of mapped orientations in a grid determined by the step size. For analysing large surfaces, maps are taken individually and stitched together. EBSD analysis was carried out on a Sirion FEGSEM equipped with Channel 5 software, operating at 15 KV. One of the major factors when using the FEGSEM is the time and quality of the patterns produced for mapping. The Parameters used for EBSD pattern acquisition in this investigation are given in Table 4.1.

Table 4.1 Parameters used in the Sirion FEGSEM

EBSD Parameters for the FEI Sirion	**Values Used**
Magnification	200-400X
Beam spot size	3-4
Beam voltage	15KV
No. of background frames	64
No. of averaged frames	4 – 8
Timing per frame	10ms
Step size	0.3μm – 3μm
Mapping Rate	0.8-1.2 s^{-1}
Camera binning	4x4 or 8x8

4.2.1 Billet co-ordinate system

The billet macroscopic coordinate system used for the texture analysis is the same as that for microstructural analysis as shown in Figure 3.9 in Chapter 3 (Z: longitudinal axis of the billet, R1 and R2: two orthogonal marks that were placed on the billet when having a rectangular cross section). The reference directions used by Channel 5 software is shown in Figure 4.30. Note that in order to present and analyse

the data based on the billet macroscopic co-ordinate system (i.e. perpendicular to the longitudinal axis of the billet Z), the reference directions must be edited.

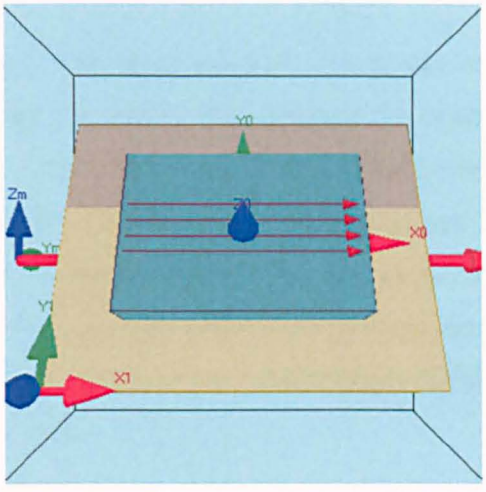

Figure 4.30 A schematic of virtual chamber with the major reference axes illustrated.

Figure 4.31 describes the billet and sample co-ordinate system in green and blue respectively. This figure demonstrates that the co-ordinates of sample S1 (X, Y, Z) are parallel to R1, Z and R2 respectively of the billet's co-ordinate system while the co-ordinates of sample S4 (X, Y, Z) are parallel to R2, Z and R1 respectively.

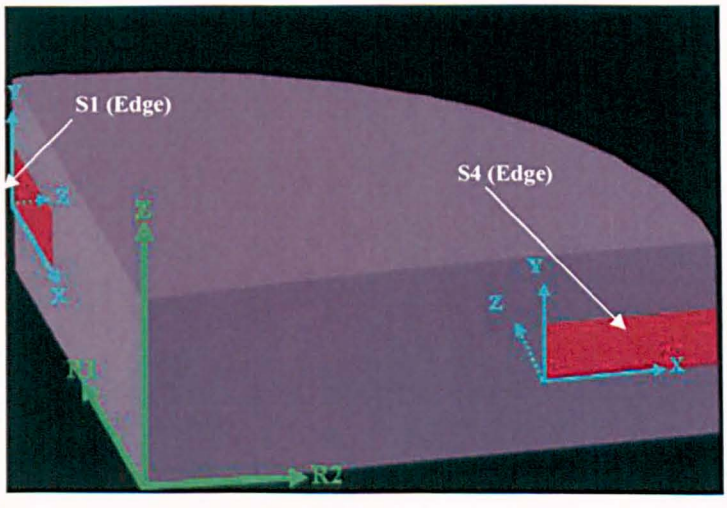

Figure 4.31 Billet and samples coordinate system in green and blue respectively.

4.3 Results and discussions

4.3.1 Small billet

Large EBSD maps were acquired with a step size of 3 μm on the reference samples (samples S1 edge, S1 centre, S4 edge and S4 centre). Figures 4.32 to 4.35 present the texture of samples S1 edge, S1 centre, S4 edge and S4 centre in Euler and IPF colouring with their corresponding pole figures. One can clearly observe band like regions, with significantly different colours, elongated over a few hundreds of μm.

Note that within the pole figures the axes of projection sphere are aligned with the axes of the billet and the colours display the strength of the texture as the number of magnitude random occurrence.

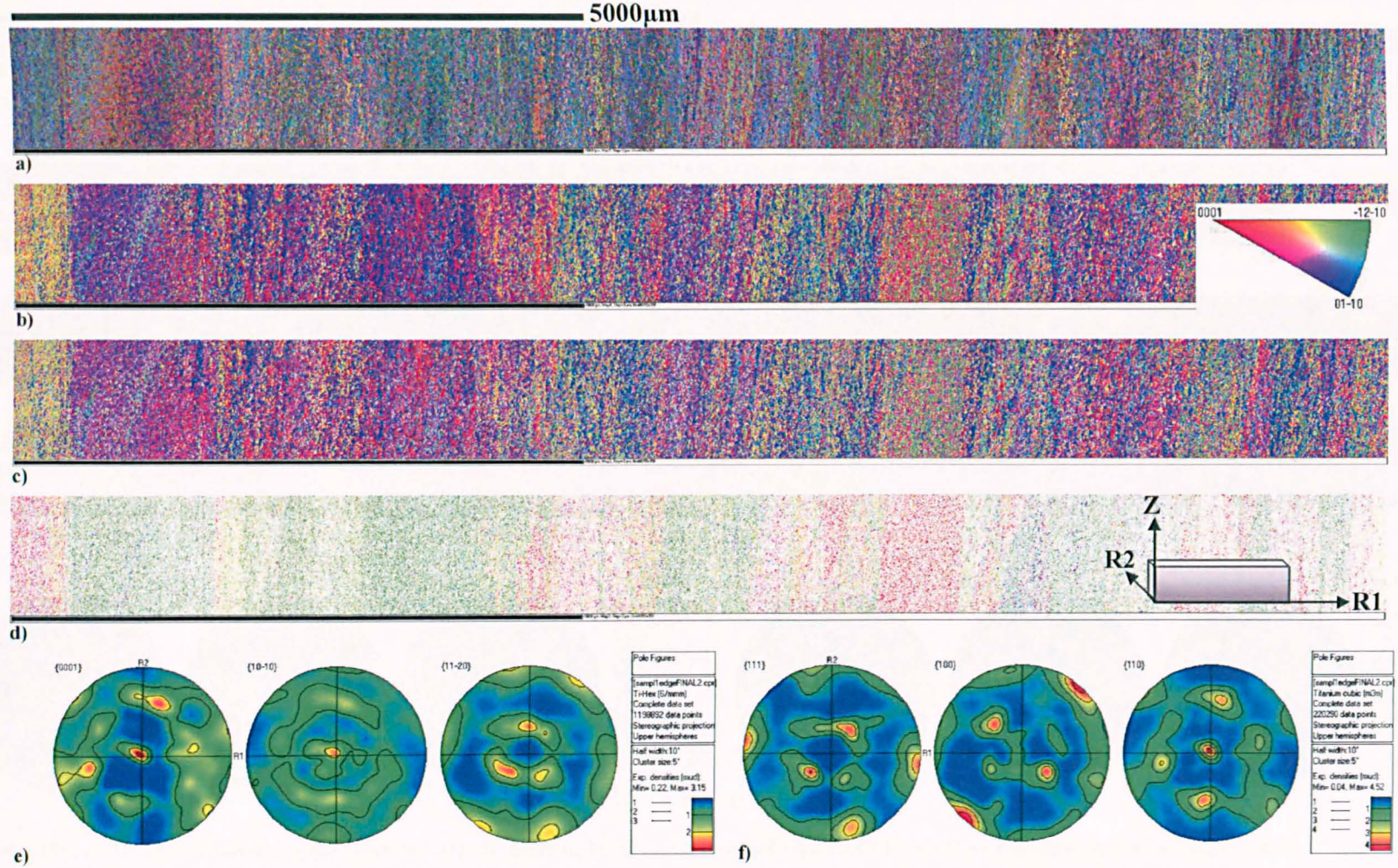

Figure 4.32 Crystal orientation map for sample S1 edge. **a)** Euler colouring **b)** IPF colouring **c)** alpha phase only **d)** beta phase only and **e)** alpha **f)** beta phase pole figure from Sample S1 edge.

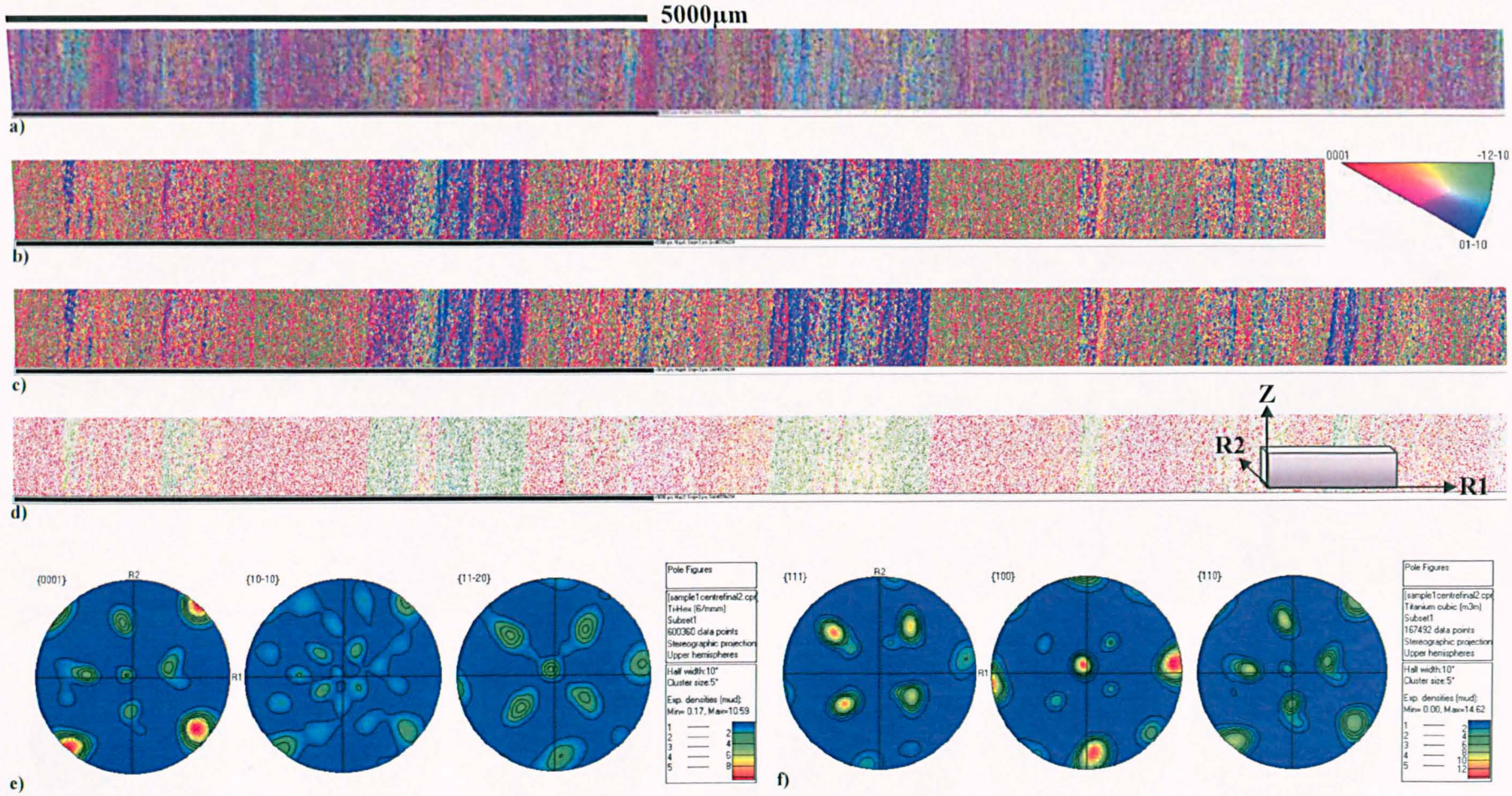

Figure 4.33 Crystal orientation map for sample S1 centre. **a)** Euler colouring **b)** IPF colouring **c)** alpha phase only **d)** beta phase only and **e)** alpha **f)** beta phase pole figure from Sample S1 centre.

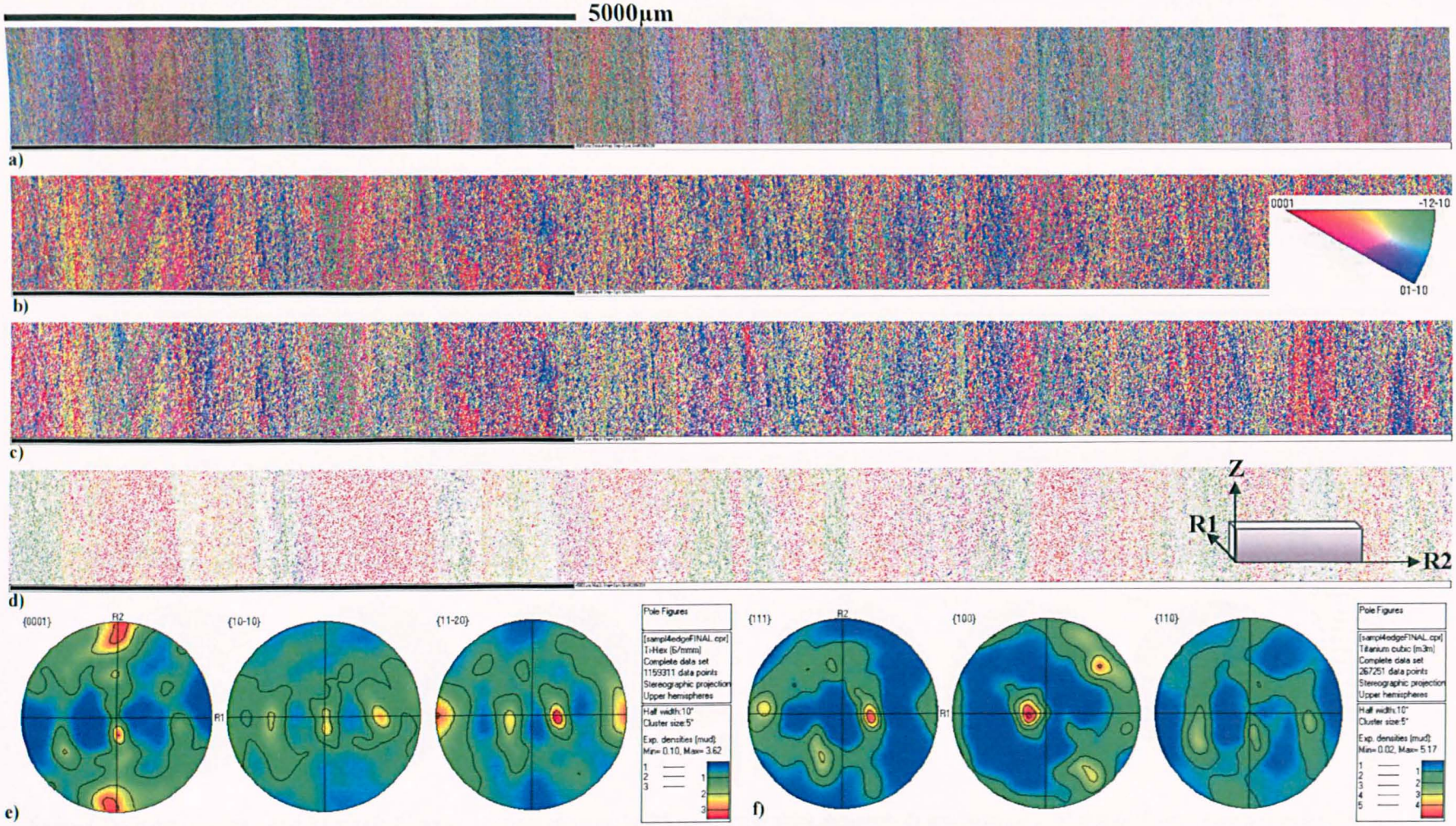

Figure 4.34 Crystal orientation map for sample S4 edge. **a)** Euler colouring **b)** IPF colouring **c)** alpha phase only **d)** beta phase only and **e)** alpha **f)** beta phase pole figure from Sample S4 edge.

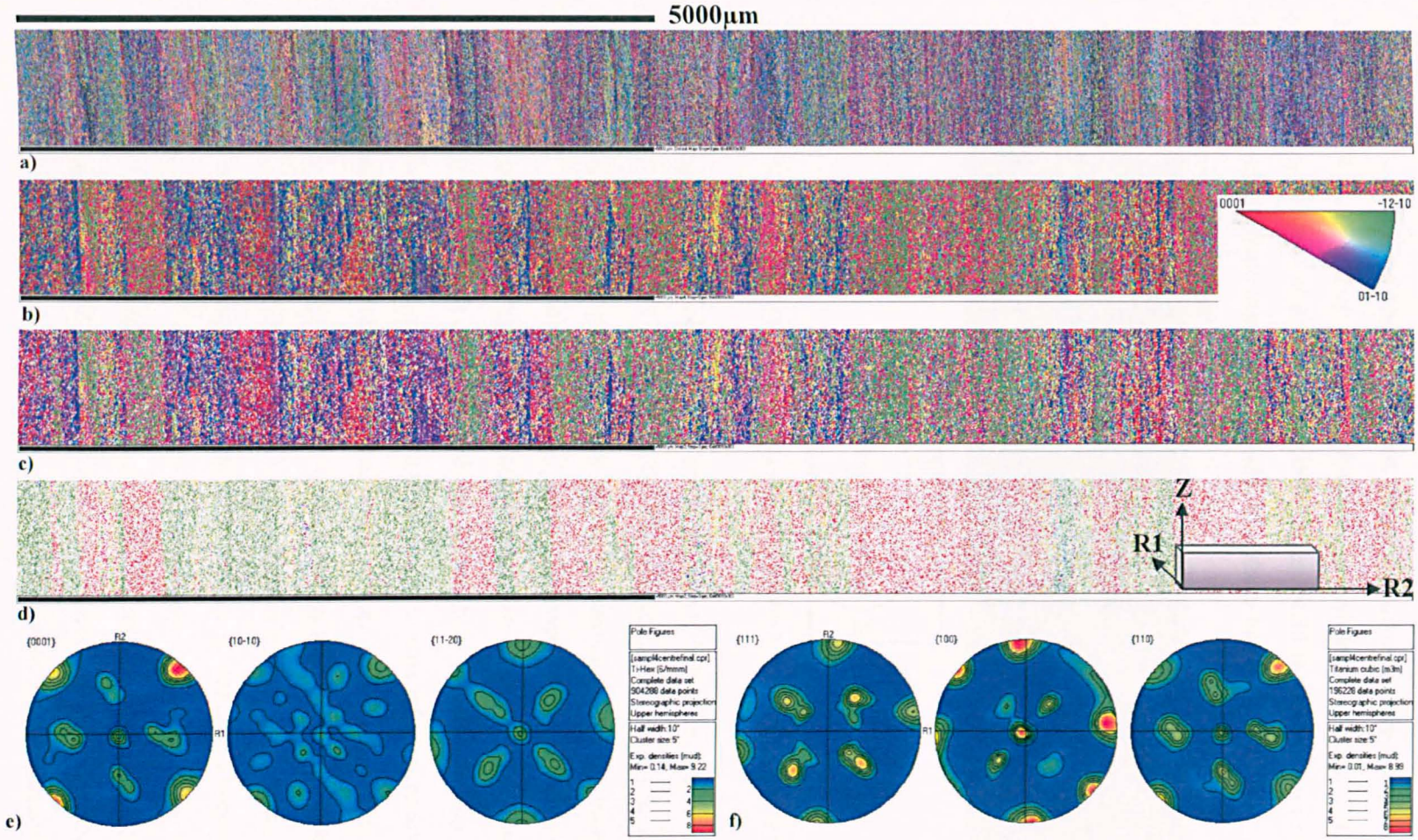

Figure 4.35 Crystal orientation map for sample S4 centre. **a)** Euler colouring **b)** IPF colouring **c)** alpha phase only **d)** beta phase only and **e)** alpha **f)** beta phase pole figure from Sample S4 centre.

Macrozones, are clearly revealed in all the OIMs in Figures 4.32 to 4.35. These macrozones are all aligned along the longitudinal axis of the billet, Z and stretched out over a few hundreds of μm. Each region presents a main texture component, different from the adjacent regions. The OIM from the tested samples showed that the billet contained macrozones at all these locations. Figure 4.36 is shown as an example as to how a randomly chosen macrozone consists of a sharp local texture.

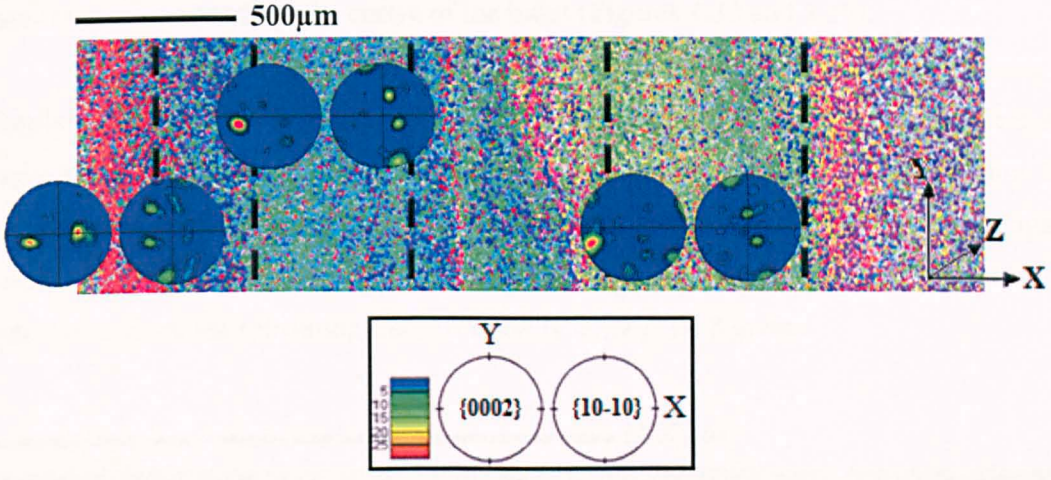

Figure 4.36 OIM map in IPF colouring revealing sharp local textures with their corresponding pole figures.

Macrozones were observed and analysed in details by Germain et al. [5, 88] in hot deformed near α titanium alloy IMI 834. The microtextures of the α_p grains, the α_s inherited colonies and the parent β phase for each macrozone were determined and their contribution to the local texture sharpness discussed. Germain et al. [5] defined microzones initially as a group of α_p grains oriented around a single texture component with about 20° spread and demonstrated that although α_p grains represent only 30% of the volume, they significantly contribute to the sharp texture of a macrozone. They then studied α_s and determined that although α_s texture components are significantly different from one zone to the other, they match the corresponding main α_p orientation. The authors then determined that the sharp local texture of a macrozone is the result of the overlapping of an α_p single component and a main α_s texture component. In their research, Germain et al. [5] also discovered that groups of β grains in the same vicinity can locally share close orientations. These β grains are either adjacent or separated by primary α_p grains and form volumes known as clusters of different orientations and sizes. Within these clusters, some β grains with differing orientations were also observed.

By monitoring the pole figures from Figures 4.32 to 4.35 it can be noticed that the general billet texture is quite weak. Despite this, there are some noticeable differences in the texture when moving from the edge towards the centre of the billet.

The samples appear to follow a symmetric pattern. This can mainly be due to the forging process of the billet from the primary/original ingot (Billet was forged from a rectangular cross-section to a circular cross-section). This symmetric pattern can be observed more clearly at the centre of the billet (Figures 4.33 and 4.35).

The corresponding orientation maps for the β phase of sample S1 centre is displayed in Figure 4.37(α grains are not represented). It can be noticed that there are only three clearly different oriented β within this region (With one orientation the strongest), elongated perpendicular to Z and approximately 45° to R1 which again confirms the result of the process history on the texture of the billet. These β macrozones are the remaining trace of initially large prior β grains.

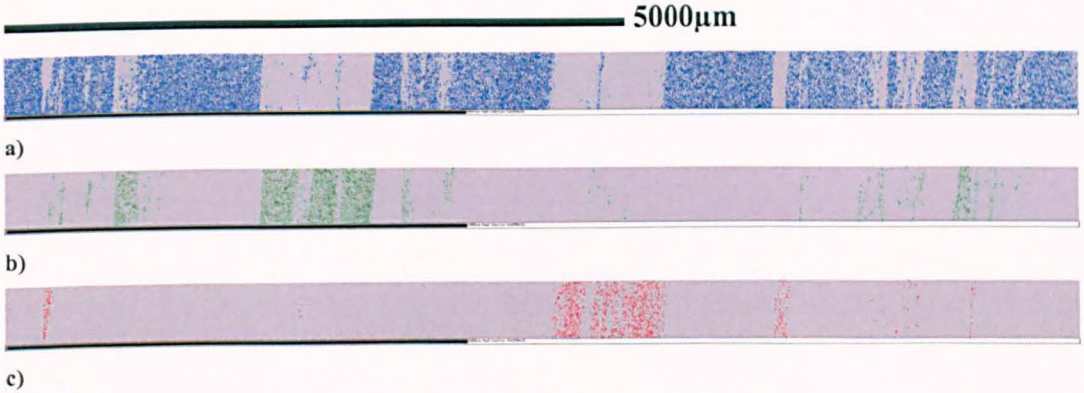

Figure 4.37 a, b, c) The only three existing beta crystal orientation map for sample S1 centre in Euler colouring.

As mentioned before, IPF colouring does not describe the texture completely because it only shows the orientation of one reference axis. In order to truly describe the nature of the texture the orientation of two reference axes would be required. Therefore in order to confirm the result, texture was represented in terms of its ODF. This strength was expressed as a ratio to that expected for an entirely random distribution of orientations [67].

Figures 4.38 and 4.39 show a) the 3D view of the orientation distribution function coefficient, showing the strongest texture on the ϕ-φ_2 plane and elongated parallel to the φ_1 Euler angle, b) the strongest texture on ϕ-φ_1 cross section, which is a

single slice along the length of the cuboids and c) the density profiles of a chosen slice at both the edge and centre of samples S1 and S4.

The complete ODF of the samples plotted in sections through the three dimensional Euler space is shown in Figures 4.40 and 4.41. Each contour line is representative of an additional multiple of times random. It is important to note that the value of Gaussian distribution (spread of orientations around an ideal orientation) used is 5°.

Although the general texture features are consistent throughout both edge and both centre samples, the results show a large variation in the intensity of the texture when comparing results from samples taken at the edge of the billet to those from the centre. Even though the process route inherently produces a non-uniform strain distribution from the surface to the centre, the texture at the centre is similar through each incremental 5° slice of the sample.

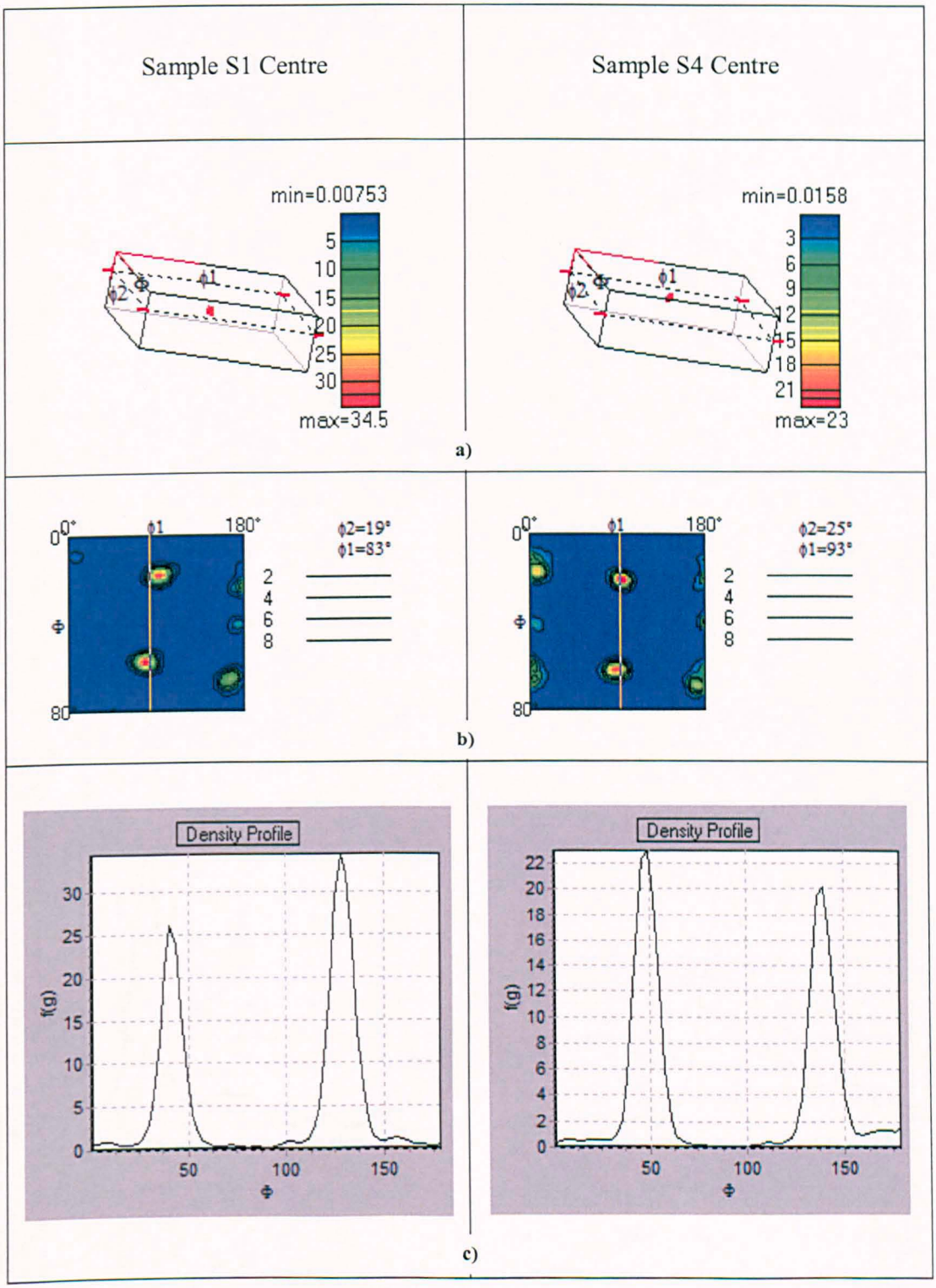

Figure 4.38 Illustrates the **a)** Orientation distribution function coefficient **b)** ϕ-φ_1 parallel slice through ODF at φ_2 = 19° and φ_2 = 25° for samples S1 Centre and S4 Centre respectively **c)** the density profiles of a chosen slice.

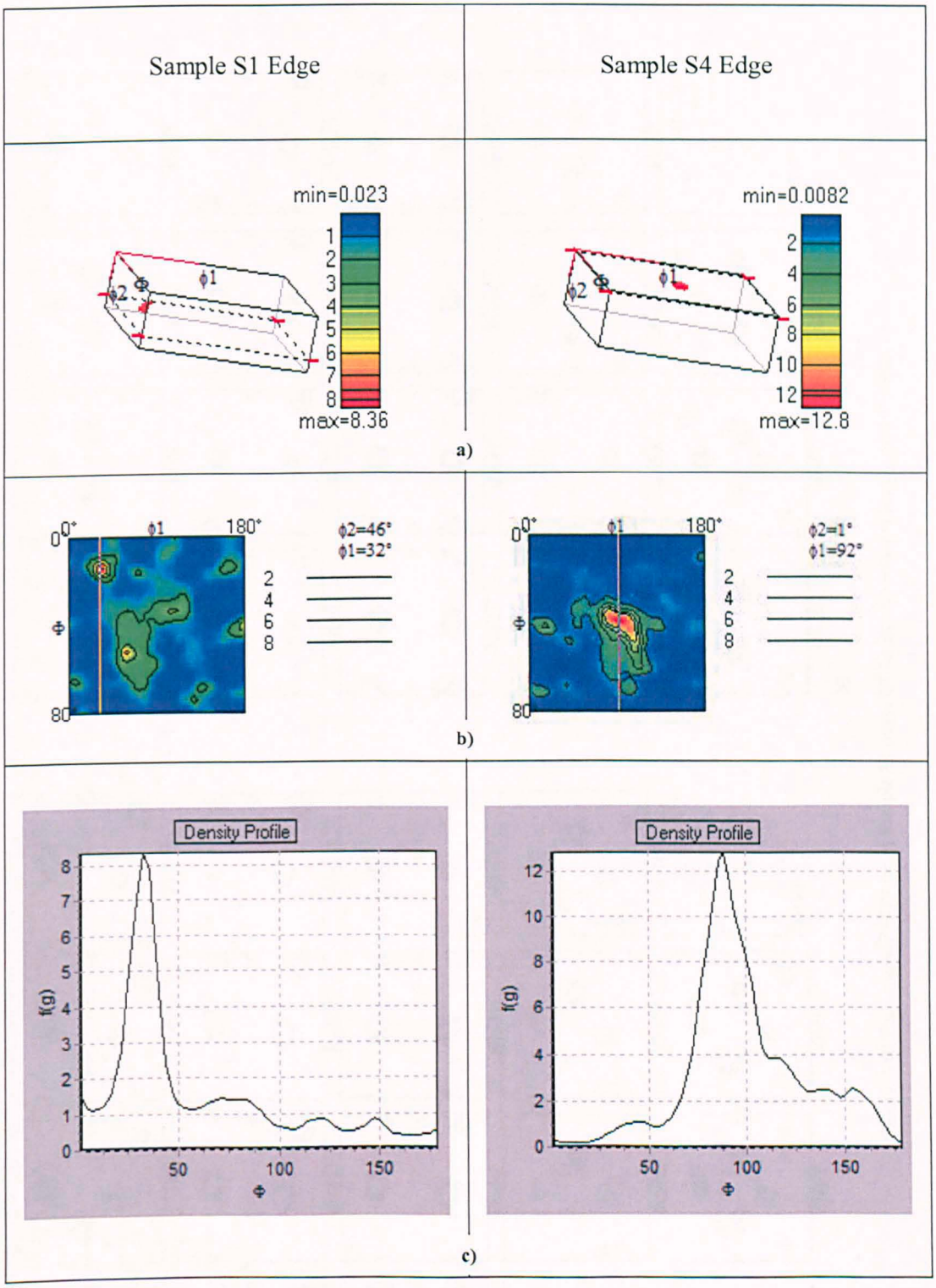

Figure 4.39 Illustrated the **a)** Orientation distribution function coefficient **b)** ϕ-φ_1 parallel slice through ODF at φ_2 = 46° and φ_2 = 1° for samples S1 Edge and S4 Edge respectively **c)** the density profiles of a chosen slice.

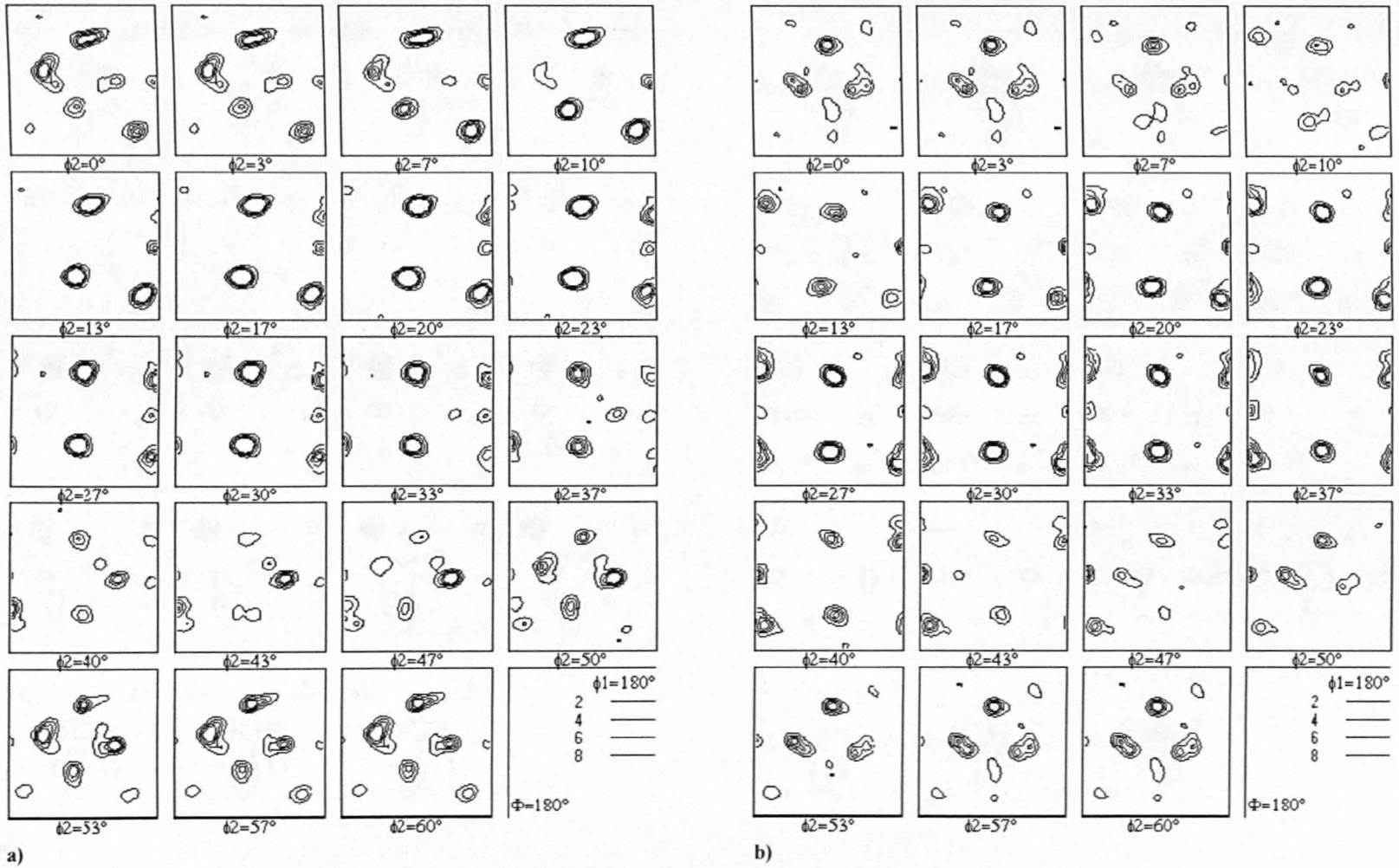

Figure 4.40 The complete ODF for **a)** Sample S1 centre **b)** Sample S4 centre at incremental 5° slices.

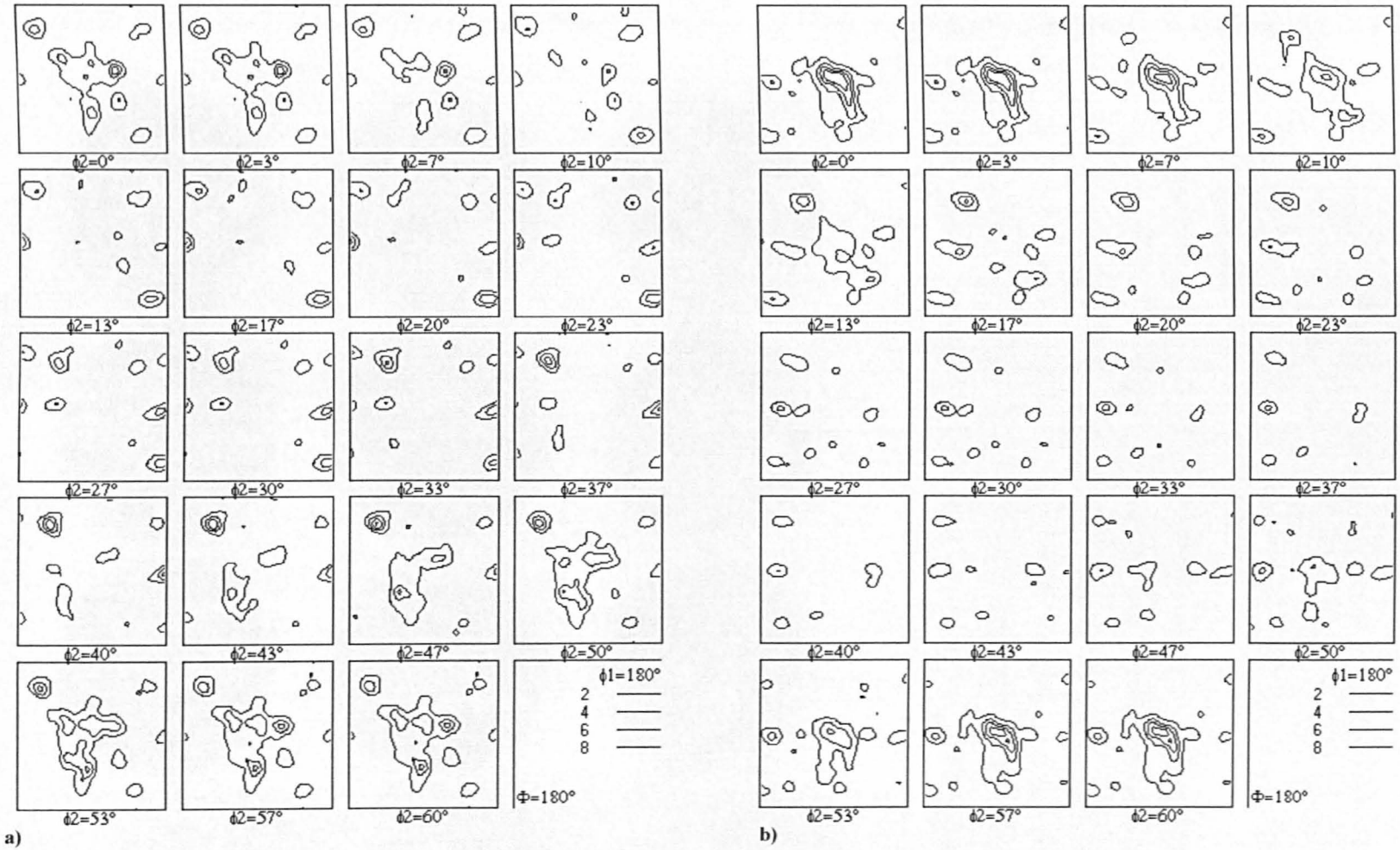

Figure 4.41 The complete ODF for **a)** Sample S1 edge **b)** Sample S4 edge at incremental 5° slices.

To this point, α (which is a mixture of α_p and α_s) and β phase were measured experimentally using EBSD (Figures 4.32 to 4.35).

According to the Burgers orientation relations, the α_s orientations are inherited from the parent β one, possibly with some variant selection [5, 88]. Therefore using Burgers relations, α_s texture was calculated from the existing β texture (using software written by Dr Brad Wynne).

The software uses the existing β texture and creates an α_s pole figure which shows the texture with no variant selection. The expected results would thus give the α_s pole figures of the experimental material only. But in some cases, especially at the centre, the texture calculated from the β produced a similar texture as the total experimental α texture. This raised the question of the significance of the α_p within the texture. Pole figures for the experimental and theoretical data are shown in Figures 4.42 and 4.43.

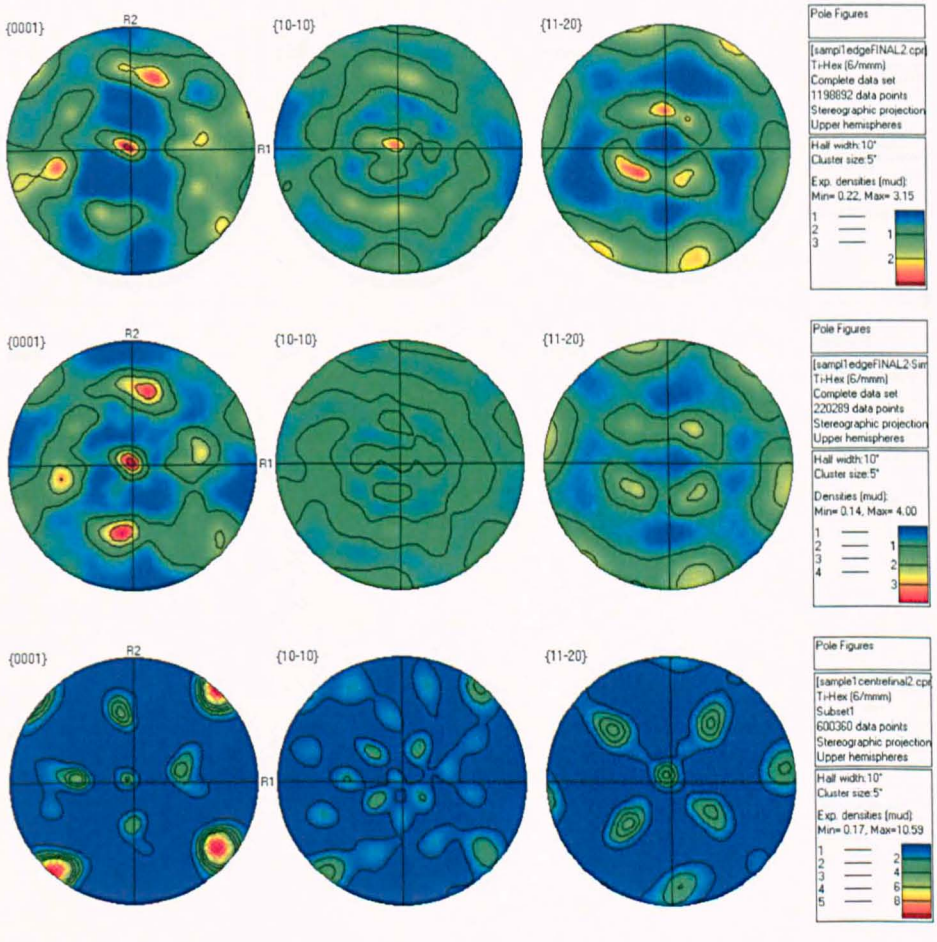

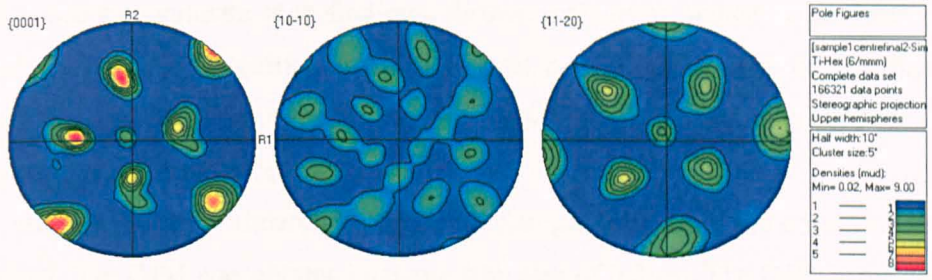

d)

Figure 4.42 Comparison of the experimental data **(a, c)** to the theoretical (non variant selection) data **(b, d)** for sample S1 edge **(a)** and centre **(c)**.

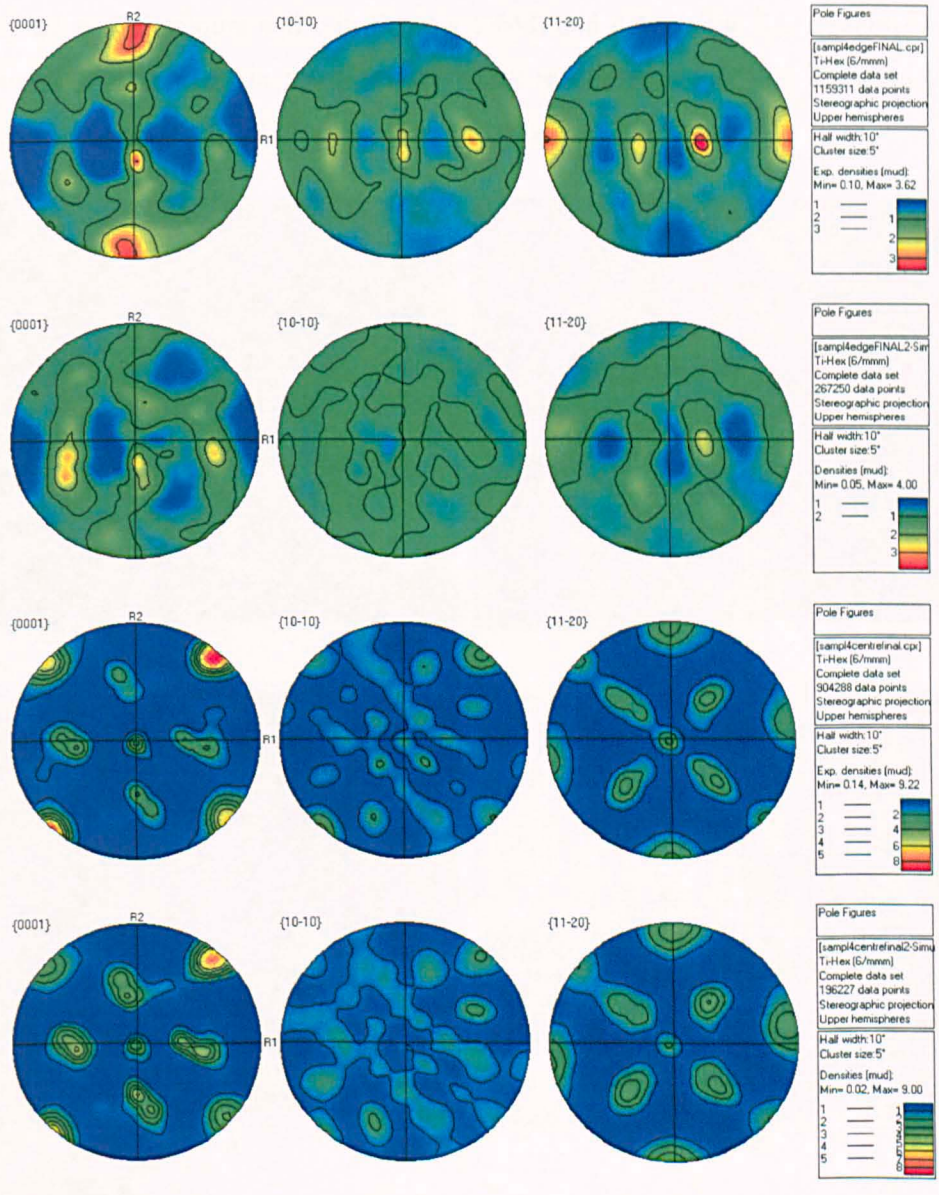

a)

b)

c)

d)

Figure 4.43 Comparison of the experimental data **(a, c)** to the theoretical (non variant selection) data **(b, d)** for sample S4 edge **(a)** and centre **(c)**.

In order to validate such findings, further analysis at higher magnification were required. The higher magnification of the local map allows easier differentiation of individual α_p and α_s orientations. The contribution of each type of grain to the sharp local texture can therefore be estimated.

An area of approximately 300mm^2 on Sample S1 centre and edge was scanned using OIM. The OIM was obtained using a step size of 0.3μm. The OIM maps obtained from the scan are shown in Figures 4.44 and 4.45 for sample S1 centre and edge respectively. Figures 4.44a, b) and 4.45a, b) show the α and the β phase in Euler and IPF colouring respectively. In Figures 4.44c) and 4.45c) the α_p and α_s phases are highlighted in IPF colours while in Figures 4.44d) and 4.45d), the β is also highlighted in IPF colours as shown in the legend. Finally in 4.44e) and 4.45e) the α and the β phases are shown in red and blue colours respectively.

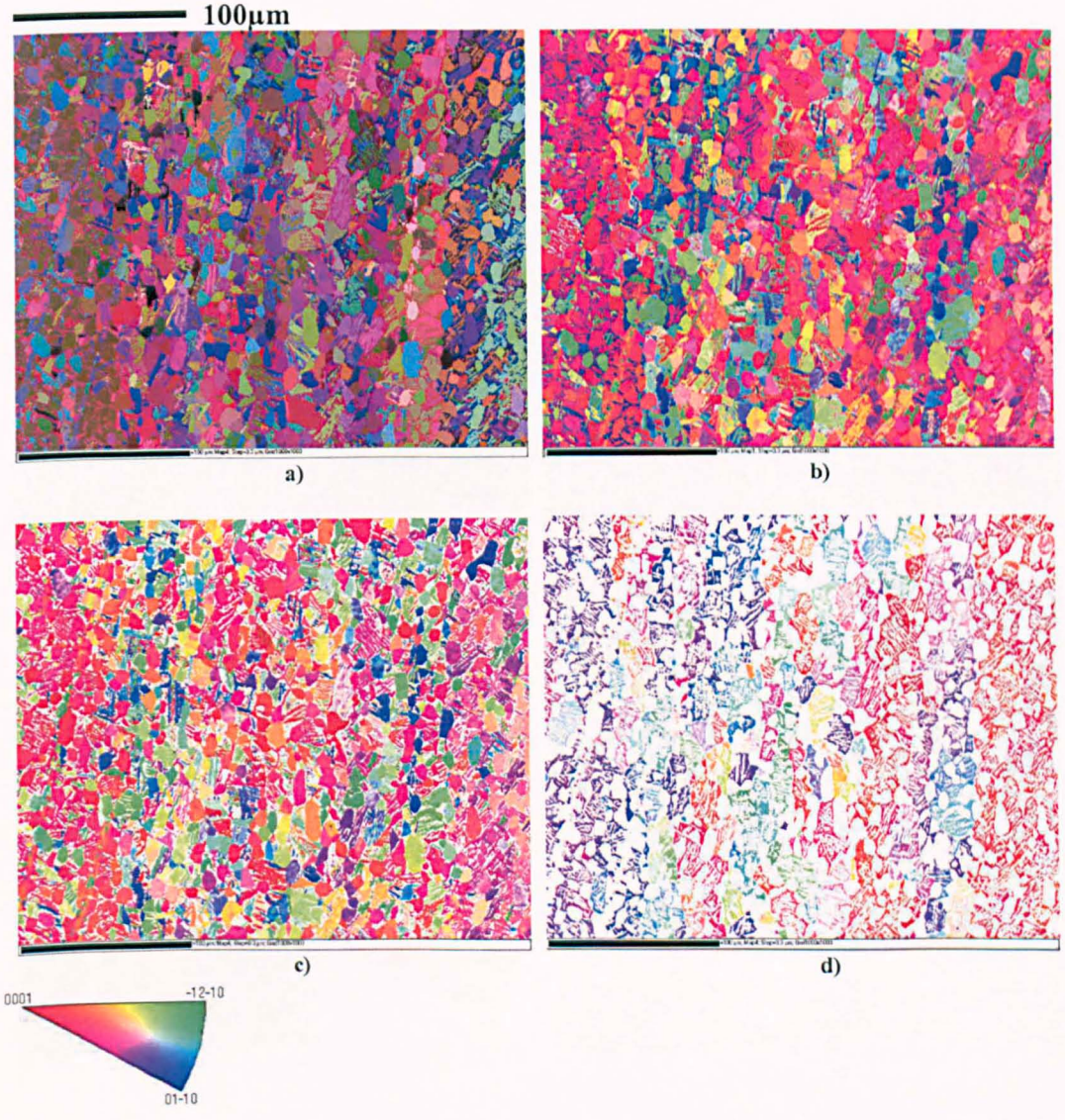

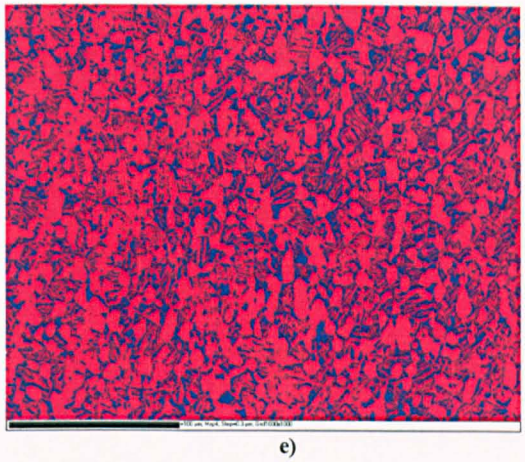

e)

Figure 4.44 Crystal orientation map for sample S1 centre at higher magnification (using a step size of 0.3μm). **a)** Euler colouring **b)** IPF colouring **c)** alpha phase only **d)** beta phase only **e)** Phase map (colour Red corresponds to the alpha phase and colour blue represents the beta phase).

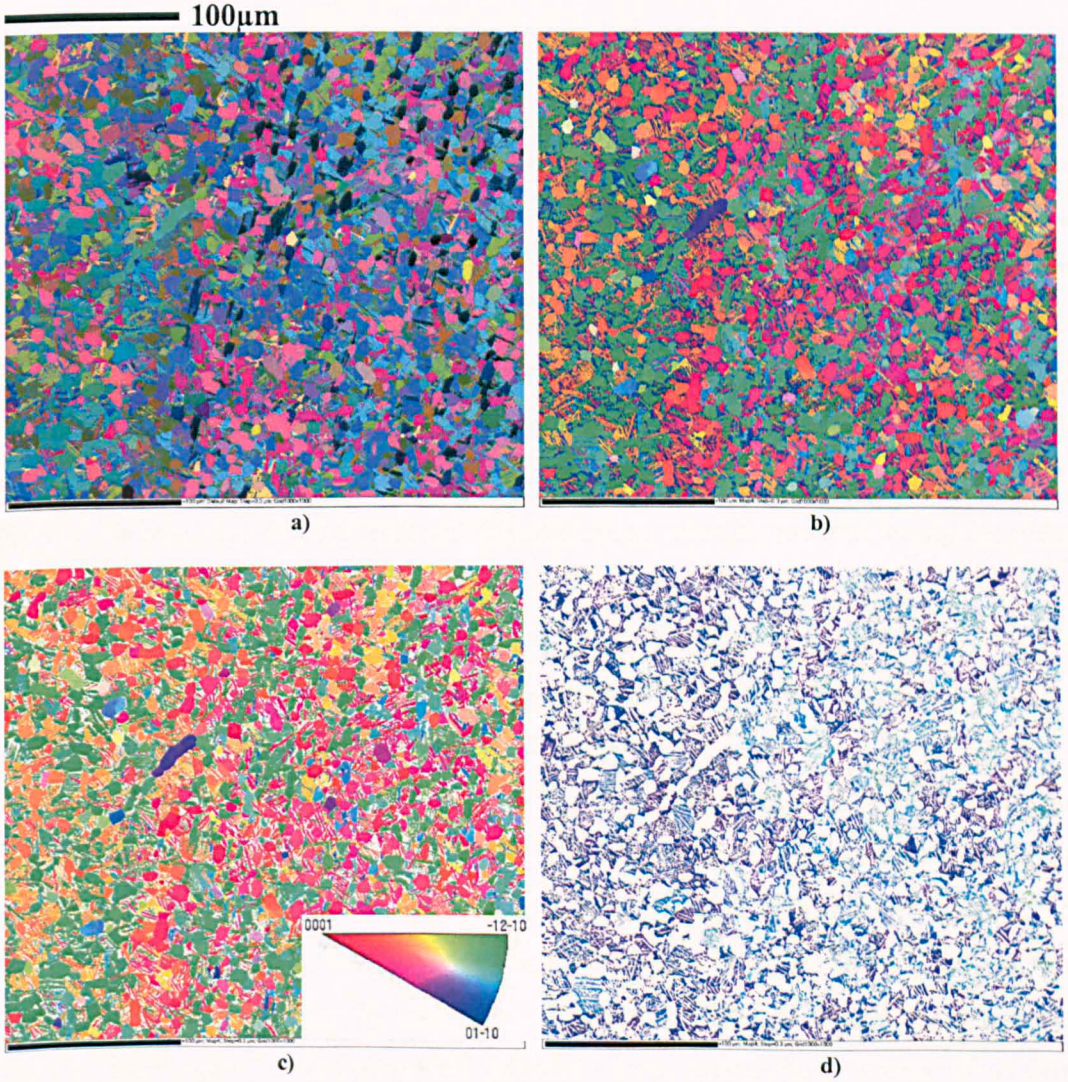

a) b)

c) d)

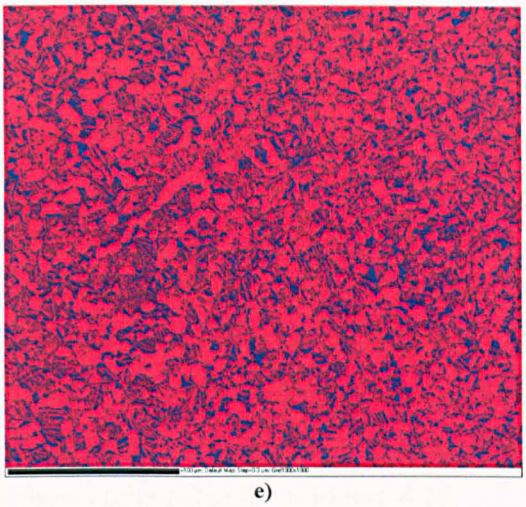

e)

Figure 4.45 Crystal orientation map for sample S1 edge at higher magnification (using a step size of 0.3μm). **a)** Euler colouring **b)** IPF colouring **c)** alpha phase only **d)** beta phase only **e)** Phase map (colour Red corresponds to the alpha phase and colour blue represents the beta phase).

Figures 4.44 and 4.45 demonstrate that α_s colonies are also strongly textured around the same texture component as the α_p grains. The scale at which analysis of the texture is performed shows there is a close orientation among the α_p grains and α_s colonies which contributes to the sharp local texture. This result is unexpected as the formation of each grain type results from entirely different mechanisms. As was shown by various researchers [5, 88] α_p grains are formed by deformation and globularization of originally coarse α lamellae, in comparison to α_s colonies which are a direct product of the transformation of β phase, present during the last α+β treatment [5]. The similarity in α_p and α_s orientation can be due to the orientation variant selection criteria, by which some orientations developed preferentially and others were suppressed during the phase transformation.

Similar results were reported by Germain et al. in the analysis of TIMETAL 834 samples. In order to determine and understand the formation of the α_s texture, they reconstructed the parent β orientation map from the α_s [5].

As mentioned previously, before any deformation at high temperatures the orientation relationship between the α_p grains and surrounding β phase follows the Burgers orientation relationship. It is only after deformation at high temperature which the crystal lattices of α_p and β grains starts to rotate. However further analysis by Germain et al. showed that the majority of the grains maintain their Burgers relations (or at least common crystallographic planes). As a result, the β grains of a sharp textured α_p region, can change into α_s colonies with orientations close to those of the

surrounding α_p grains even if they have different orientations. In addition this demonstrates that the inherited orientations were less numerous than Burgers orientation relations allow and that colonies were preferentially selected during the transformation [5].

In order to characterise such texture over larger and therefore more representative surface, additional samples (edge and centre of both samples S2 and S3) were analysed from different locations of the billet (Figures 4.47 to 4.50).

Note that in order to be able to compare the result with respect to R1 and R2 the sample's co-ordinate system must be rotated about the Y axis by 30° and 60° for S2 and S3 respectively. This is shown schematically in Figure 4.46.

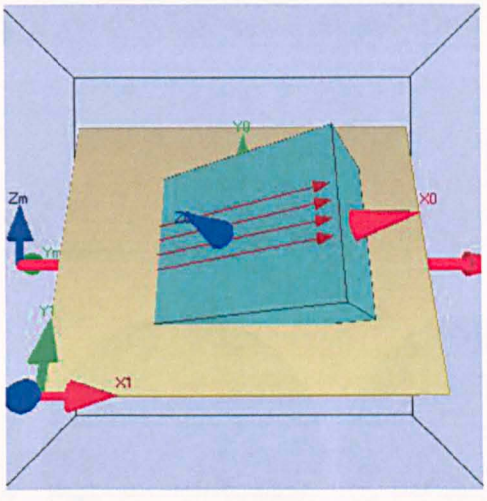

Figure 4.46 A schematic of virtual chamber being rotated 30° around Y axis

Large EBSD maps for samples S2 edge and centre (Figures 4.47 and 4.48) covering approximately an area of 6.5mm x 1mm and 8.5mm x 1mm respectively and for samples S3 edge and centre (Figures 4.49 and 4.50) covering approximately an area of 7.5mm x 0.8 mm and 8.5mm x 7.5mm respectively were acquired using a step size of 3 μm.

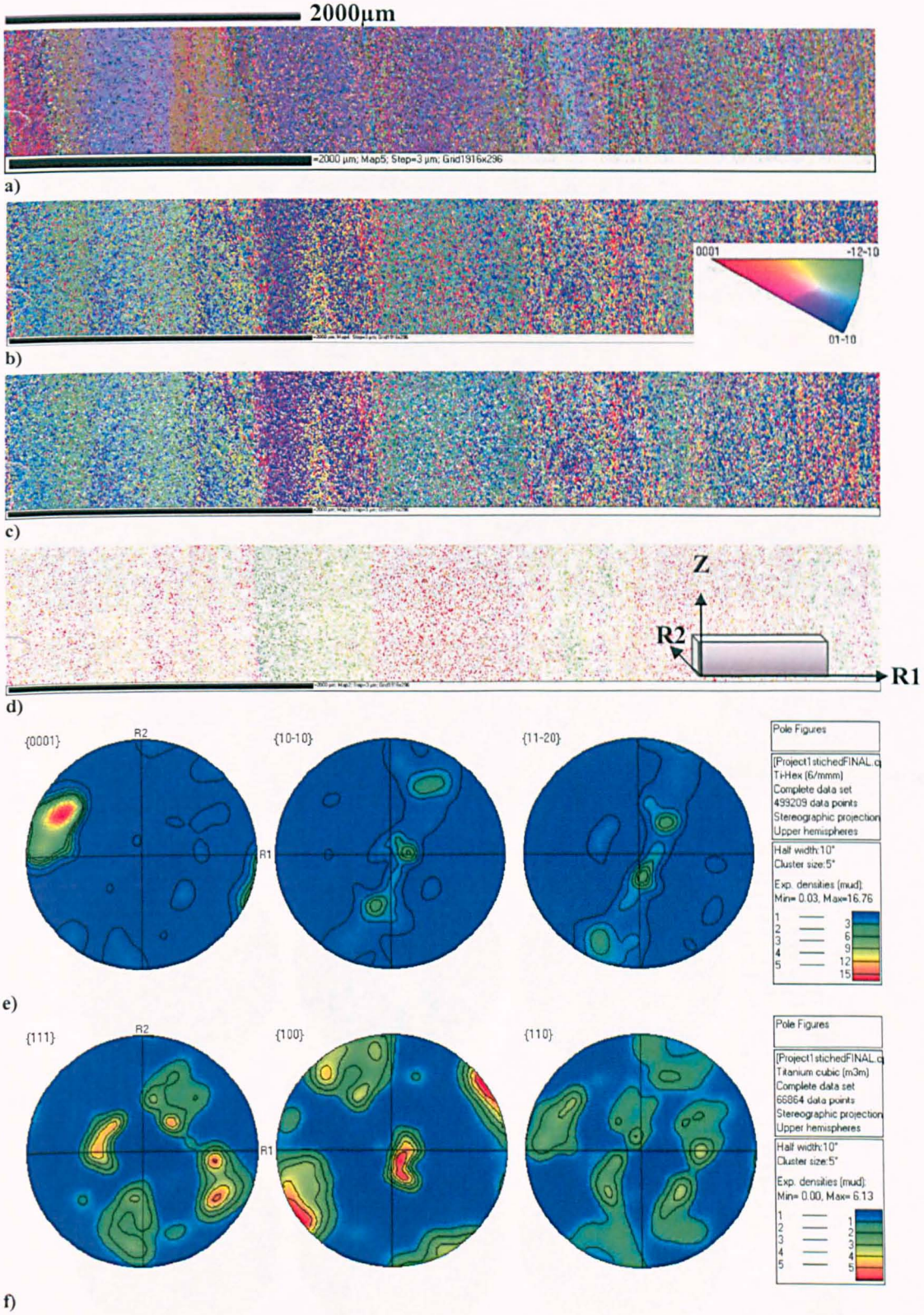

Figure 4.47 Crystal orientation map for sample S2 edge. **a)** Euler colouring **b)** IPF colouring **c)** alpha phase only **d)** beta phase only and **e)** alpha and **f)** beta phase pole figure from Sample S2 edge.

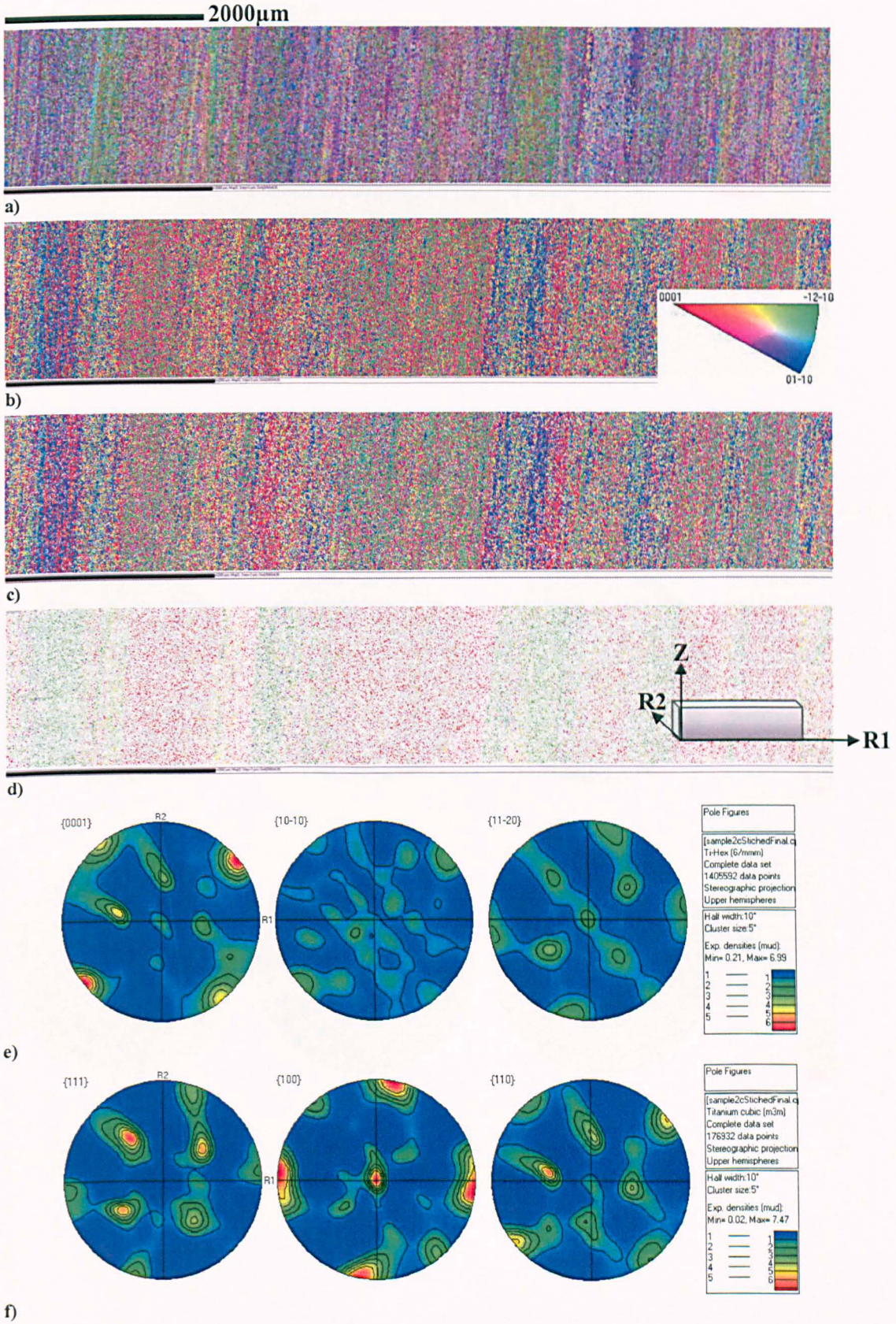

Figure 4.48 Crystal orientation map for sample S2 centre. **a)** Euler colouring **b)** IPF colouring **c)** alpha phase only **d)** beta phase only and **e)** alpha and **f)** beta phase pole figure from Sample S2 centre

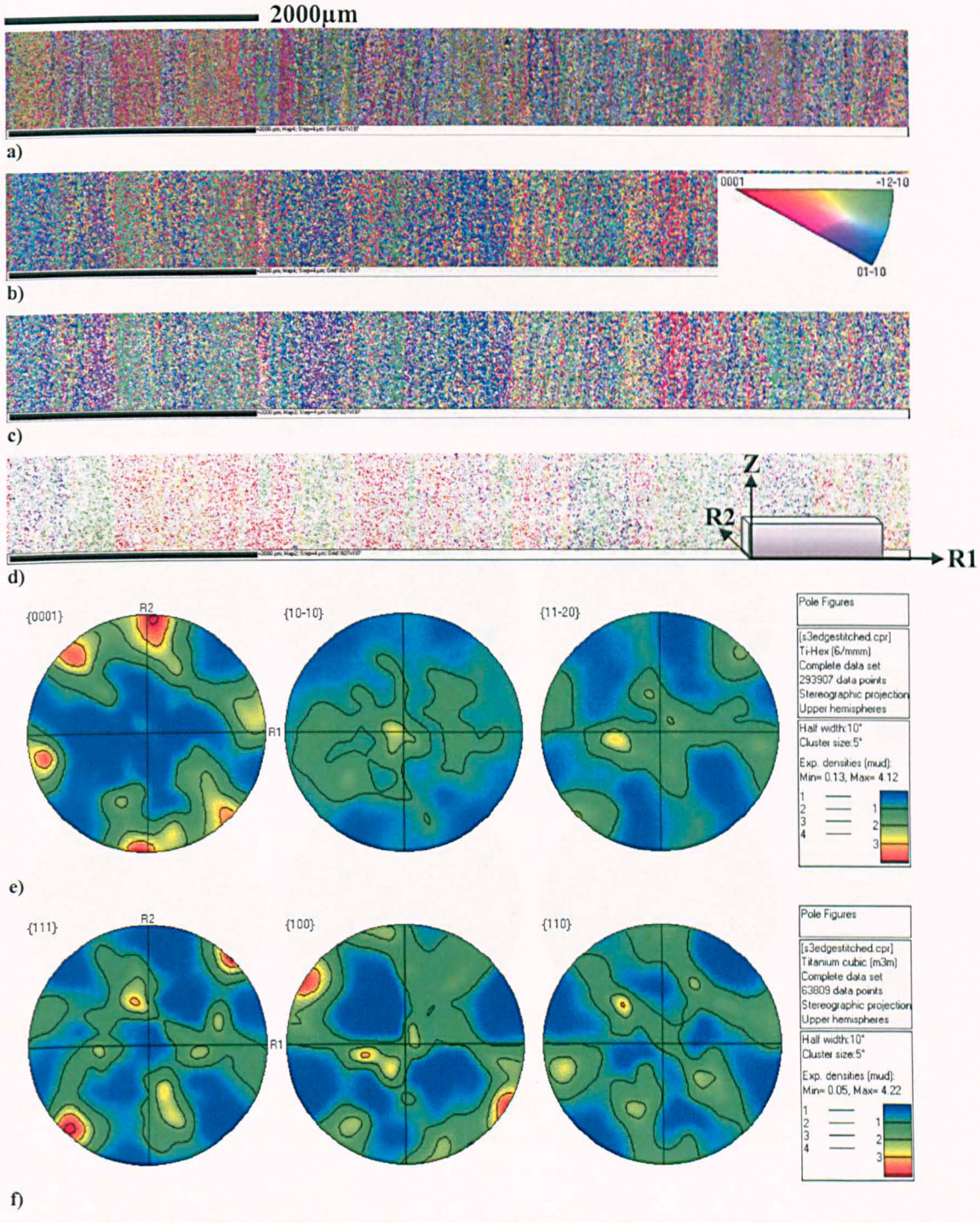

Figure 4.49 Crystal orientation map for sample S3 Edge. **a)** Euler colouring **b)** IPF colouring **c)** alpha phase only **d)** beta phase only and **e)** alpha and **f)** beta phase pole figure from Sample S3 Edge.

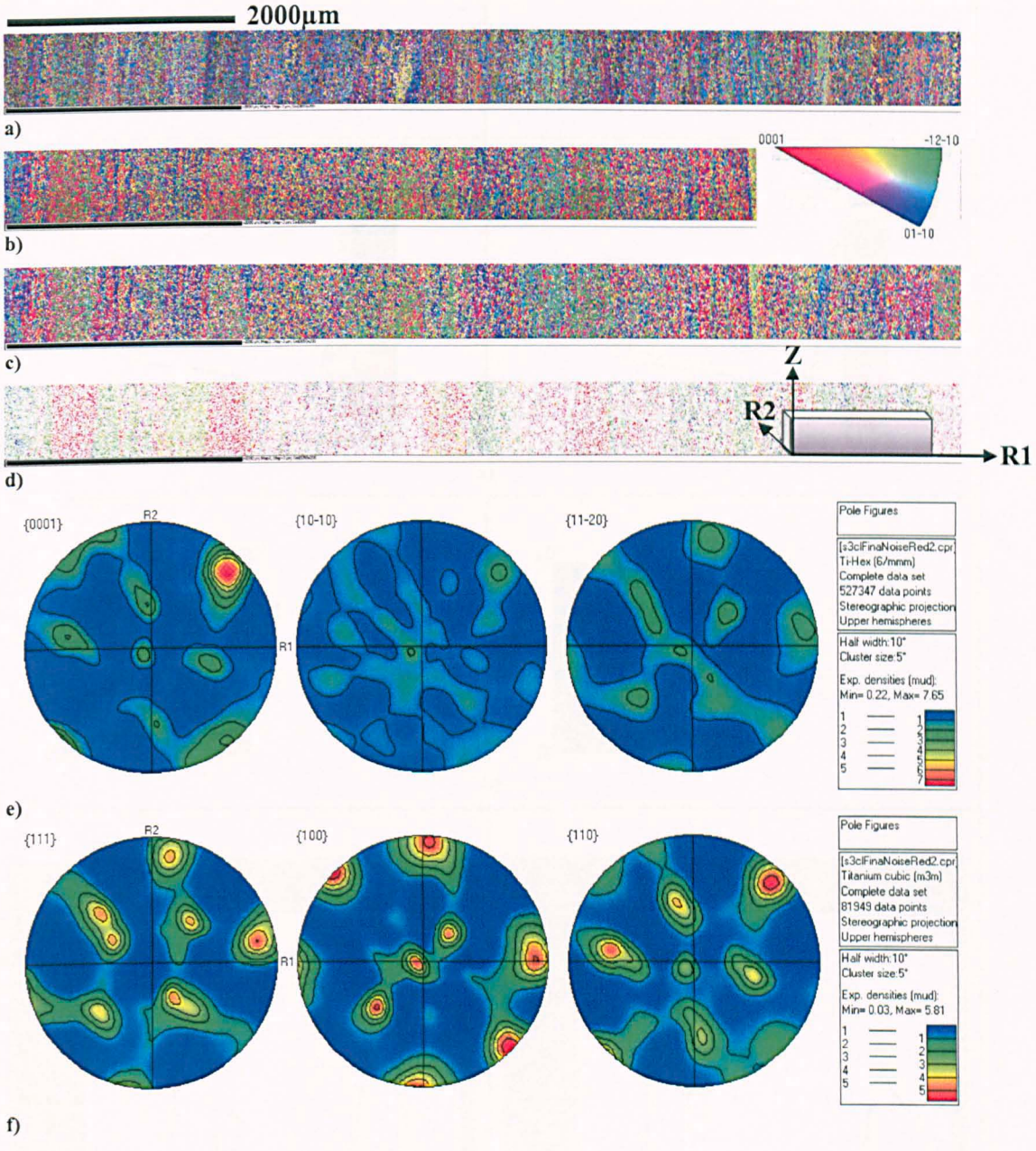

Figure 4.50 Crystal orientation map for sample S3 centre. **a)** Euler colouring **b)** IPF colouring **c)** alpha phase only **d)** beta phase only and **e)** alpha and **f)** beta phase pole figure from Sample S3 centre.

The ODF coefficient for samples S2 and S3 showing the strongest texture on ϕ-φ_2 and ϕ-φ_1 cross section, the density profiles of corresponding planes and the complete ODF through each incremental 5° slice are shown below (Figures 4.51, 4.52 and Figures 4.53, 4.54).

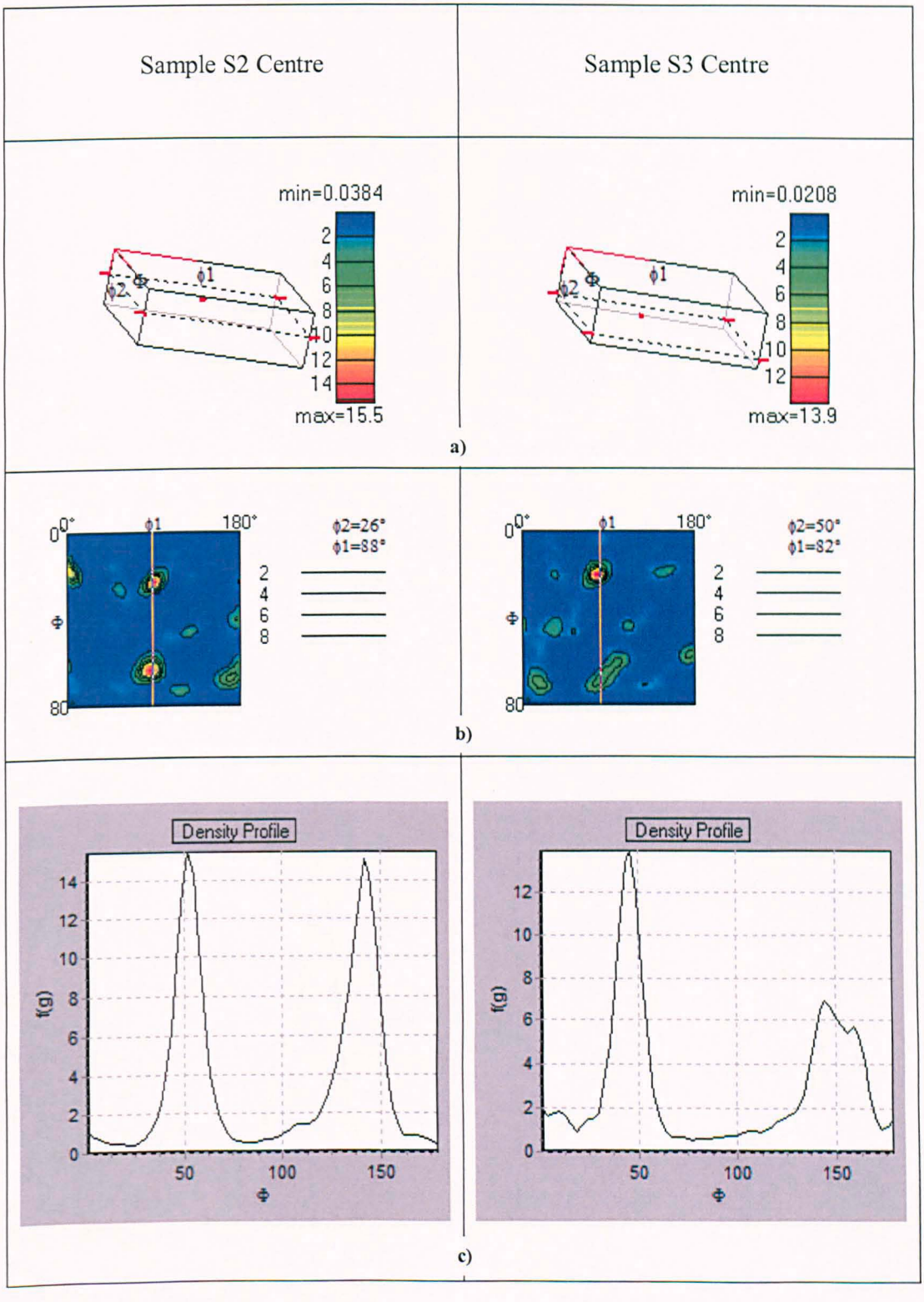

Figures 4.51 Illustrates the **a)** Orientation distribution function coefficient **b)** ϕ-φ_1 parallel slice through ODF at φ_2 = 26° and φ_2 = 50° for samples S2 Centre and S3 Centre respectively **c)** the density profiles of a chosen slice.

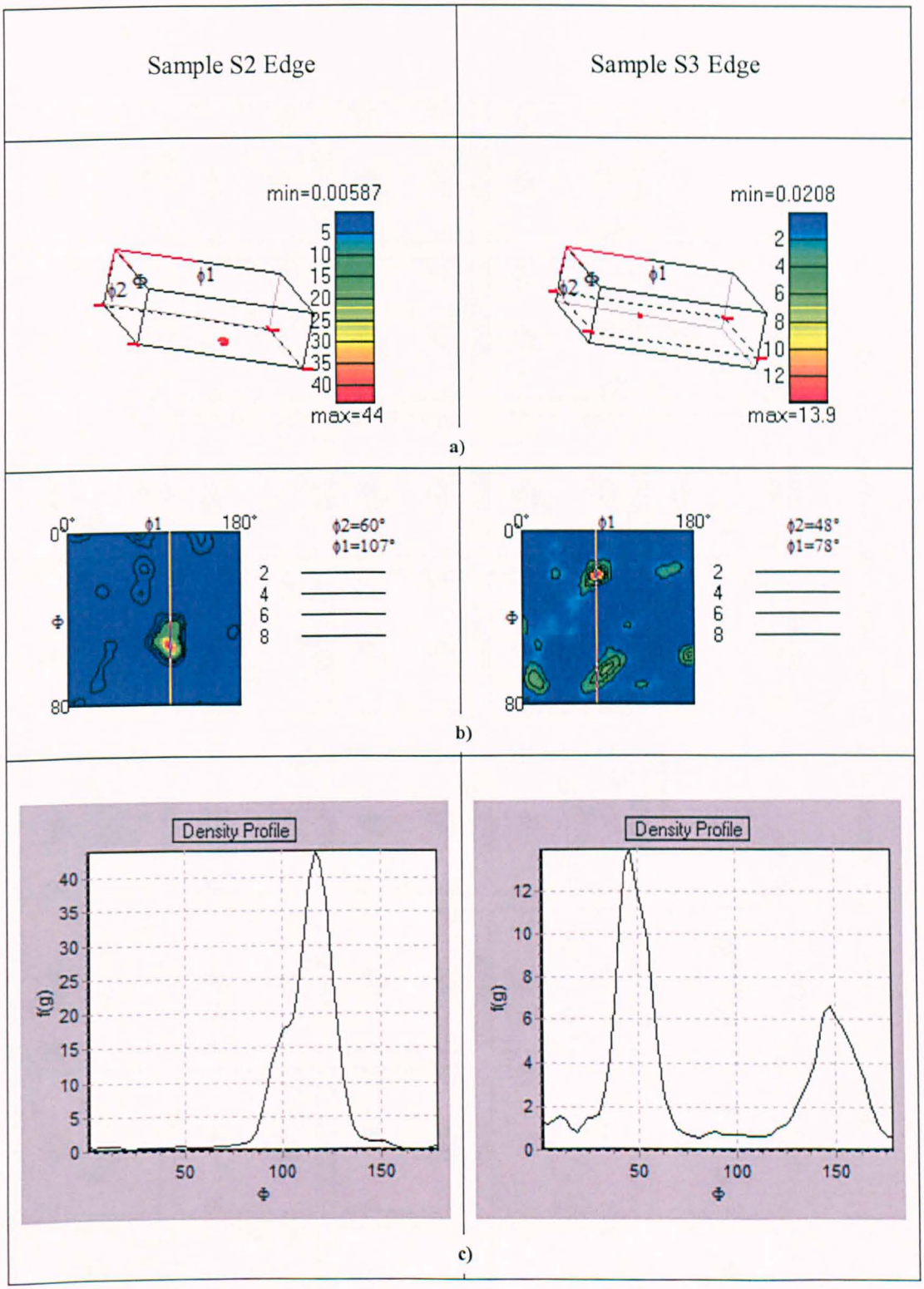

Figures 4.52 Illustrated the **a)** Orientation distribution function coefficient **b)** ϕ-φ_1 parallel slice through ODF at φ_2 = 60° and φ_2 = 48° for samples S2 Edge and S3 Edge respectively **c)** the density profiles of a chosen slice.

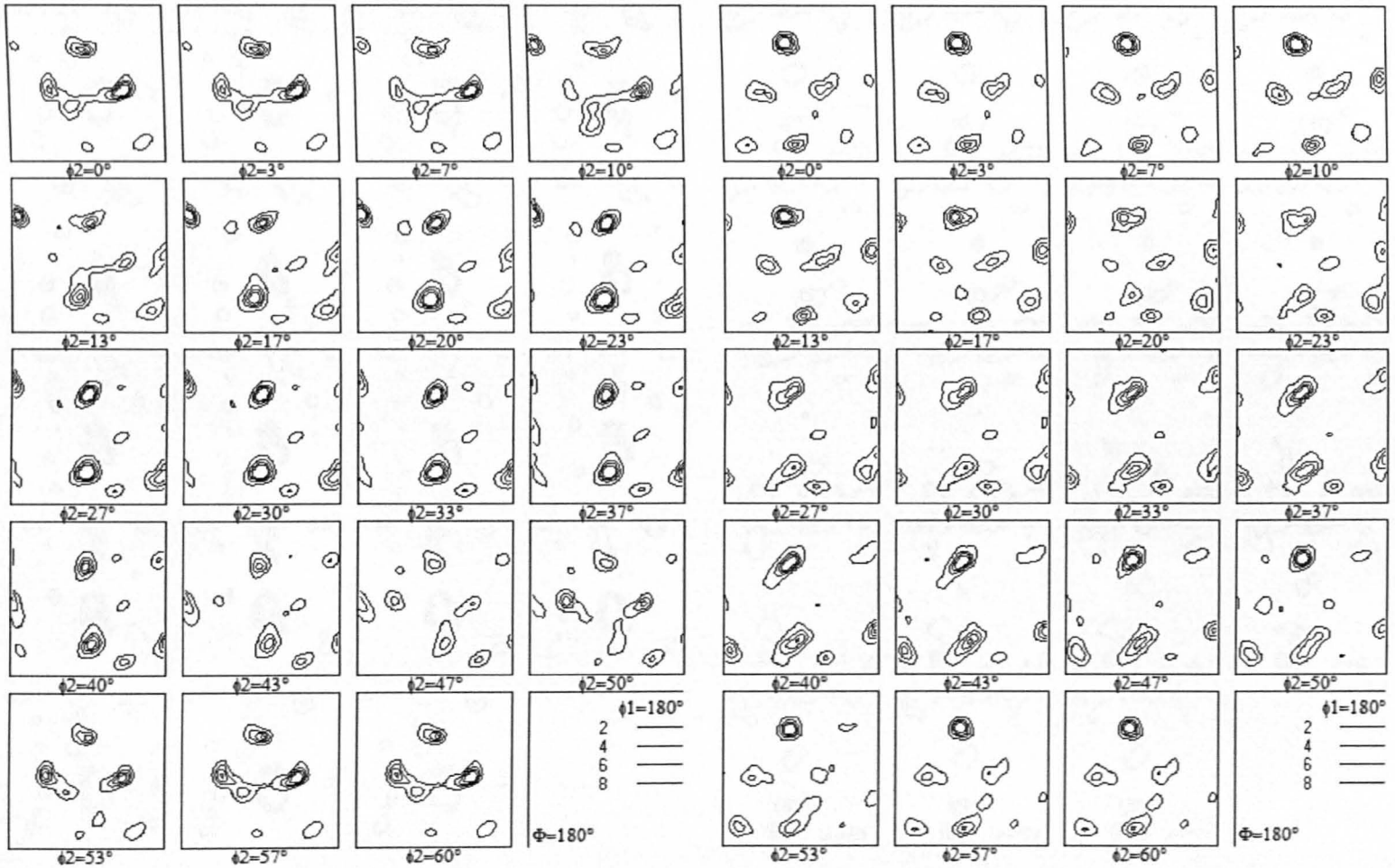

Figure 4.53 The complete ODF for **a)** Sample S2 centre **b)** Sample S3 centre at incremental 5° slices.

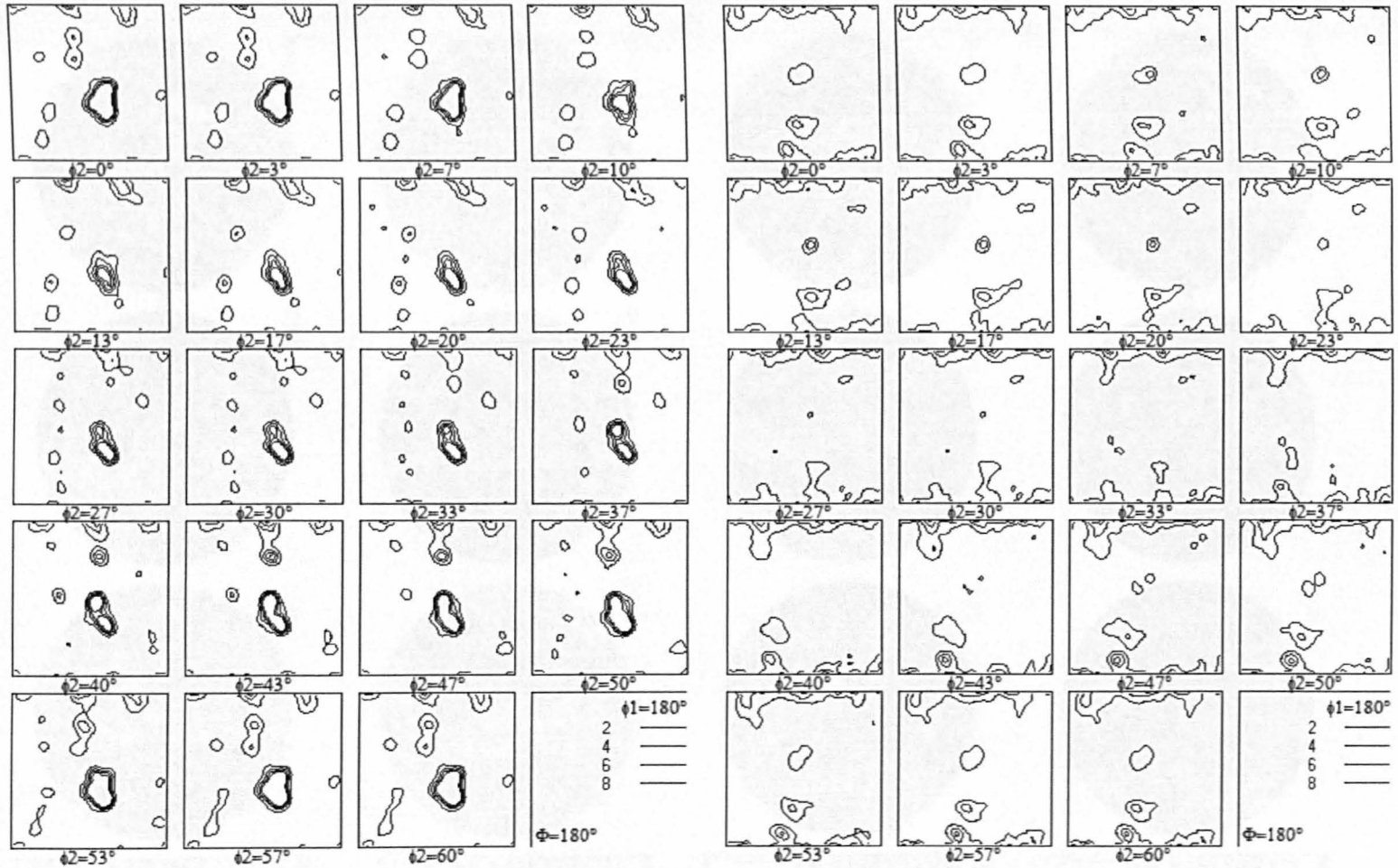

Figure 4.54 the complete ODF for a) Sample S2 edge b) Sample S3 edge at incremental 5° slices.

Using software written by Dr Brad Wynne the α_s texture for samples S2 and S3 was calculated from their existing β texture. The results are shown in Figures 4.55 and 4.56.

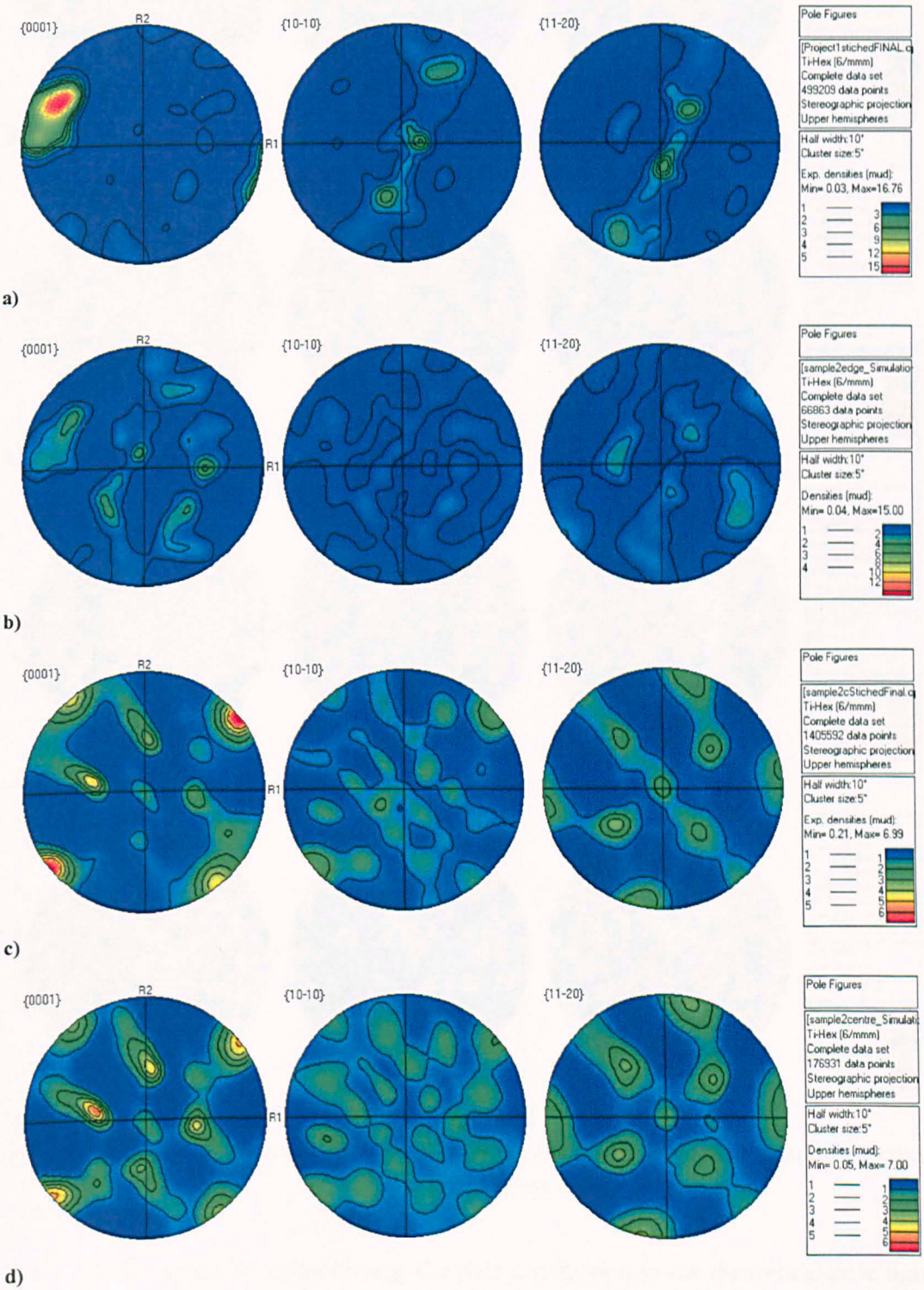

Figure 4.55 Comparison of the experimental data **(a, c)** with theoretical (non variant selection) data **(b, d)** for sample S2 edge **(a)** and centre **(c)**.

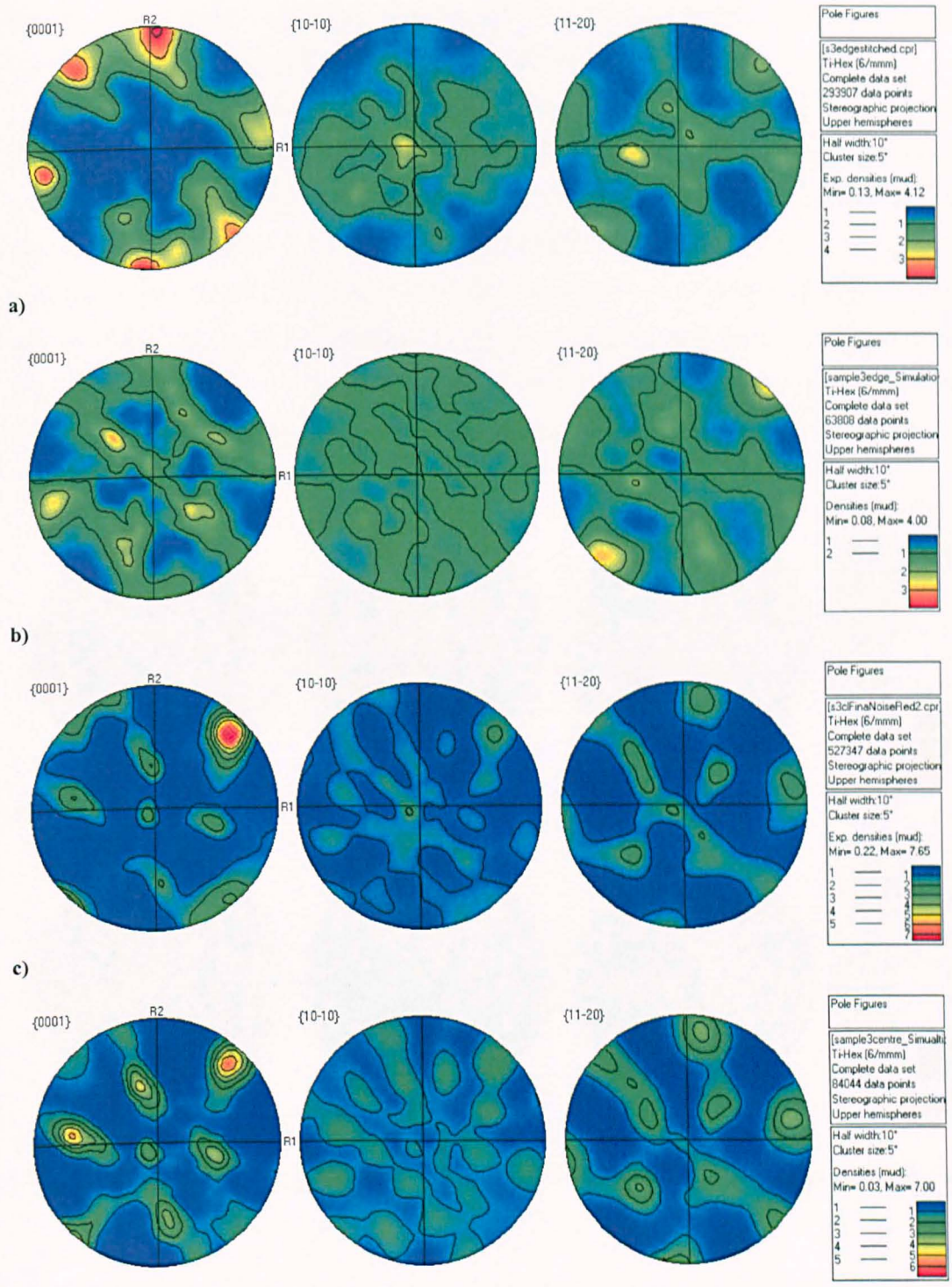

Figure 4.56 Comparison of the experimental data **(a, c)** with theoretical (non variant selection) data **(b, d)** for sample S3 edge **(a)** and centre **(c)**.

If no variant selection occurs, the pole distribution in the theoretical pole figure should be similar to that of the experimental ones. The comparison of the corresponding pole figures for samples S2 and S3 edge clearly shows that pole intensities are not

similar. This clearly demonstrates the strong influence of the variant selection mechanism on the local texture sharpness of the billet.

The initial observation when comparing the experimental and theoretical pole figures at the edge of the billet (samples S2 and S3 edge) would be that the textures are completely different. However, when the intensity contour bar of the experimental pole figure is adjusted and the resulting figure compared to that of the theoretical figure, it can clearly be seen that the texture of α_s which has been produced theoretically is seen at a lower intensity in the background of the experimental pole figure (green coloured areas). This demonstrates the strong influence of the variant selection mechanism on the local texture sharpness of the billet at the edge. Figure 4.57 is shown as an example.

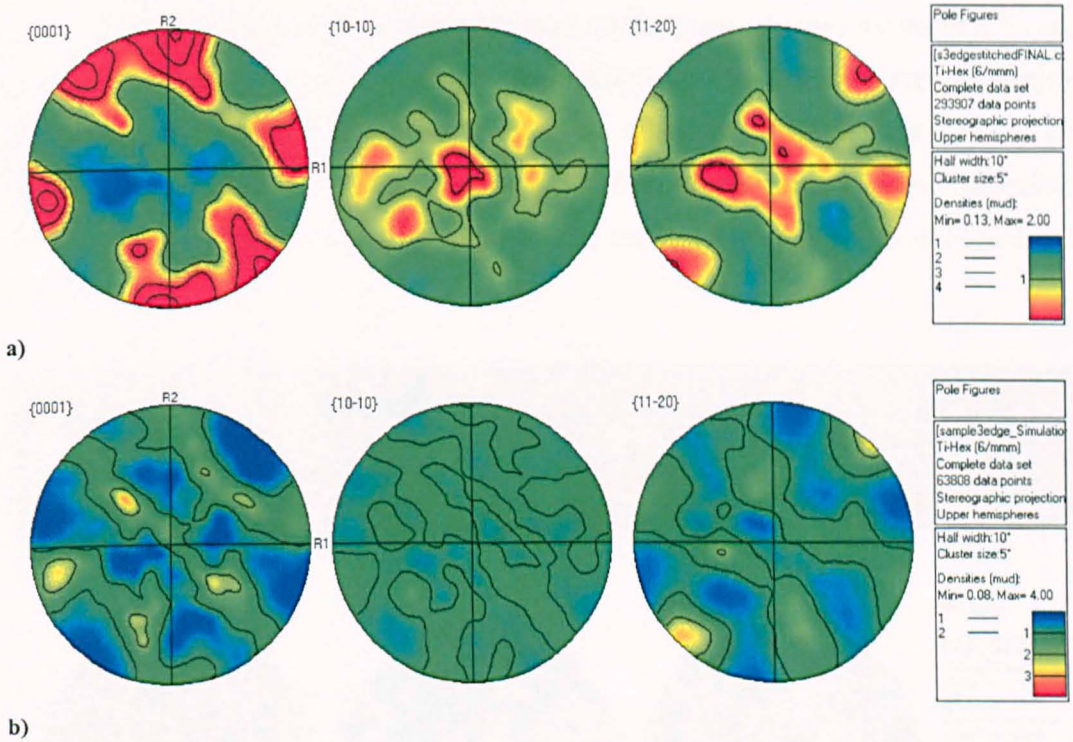

Figure 4.57 Comparison of the **a)** experimental data with **b)** theoretical (non variant selection) data for sample S3 edge.

Based on the finding above, the initial observation would be that the difference between the theoretical pole figures and the experimental pole figures would be the α_p texture (points with higher intensity represent the texture of α_p). For example, the strong texture observed in sample S2 edge would be mainly due to the strong orientation of α_p under the influence of an enormous variant selection mechanism.

However, from all the results above it is almost impossible to distinguish between the α_p and α_s. As shown in Chapter 3 Section 3.3.1, the volume fraction of α constitutes approximately 25-30% of the total billet volume. By examining the previous α phase OIM it can be seen that the total percentage α is much greater than 30% meaning a high percentage of α_s exists within the macrozones. Also, as previously discussed, α_s colonies are direct products of the transformation of β phase, therefore as β texture at the edge is very strong, α_s may consequently be the strongest texture.

Ideally, it is necessary to separate the α_p and α_s, however this would not be straightforward due to the fact they both have very similar orientations (Figures 4.44 and 4.45) throughout the whole billet. It is therefore not possible to draw any final conclusion as to whether the strong texture within the pole figures is due to the α_p or α_s.

More detailed analysis was performed on the β macrozones for sample S2 edge (Figure 4.47 d)). It is evident from the orientation map that there are only two major β orientations (highlighted in red and green). Two subsets were taken from the OIM map in areas where the green and red colour orientation grains exist. The corresponding α and β phase pole figures were then plotted. The results are shown below in Figures 4.58 and 4.59.

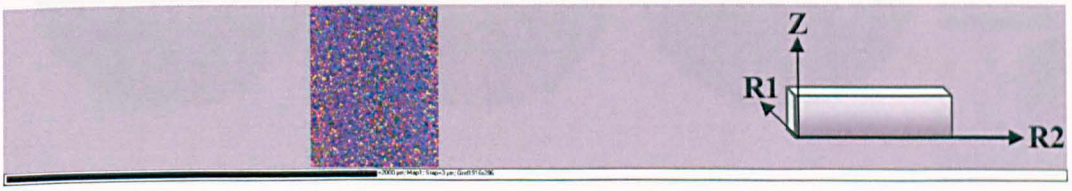

a)

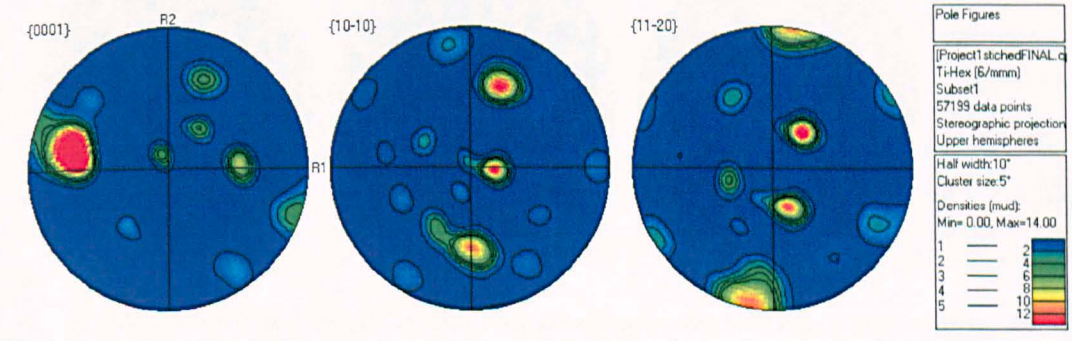

b)

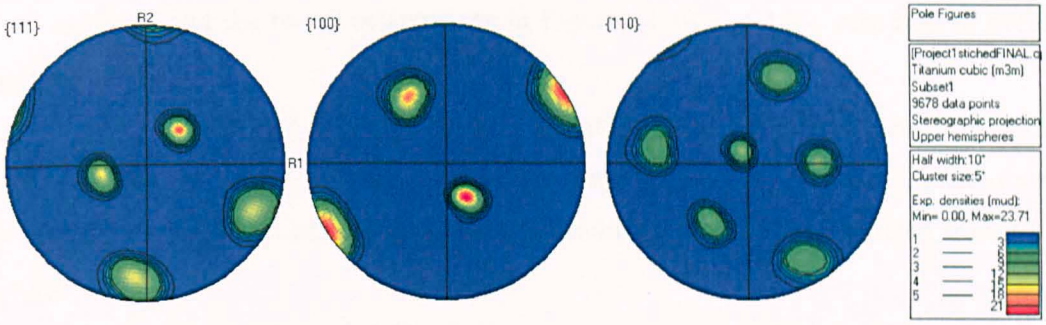

c)

Figure 4.58 Subset taken from the **a)** Crystal orientation map for sample S2 edge in Euler colouring .The corresponding **b)** alpha **c)** beta phase pole figure from Sample S2 edge.

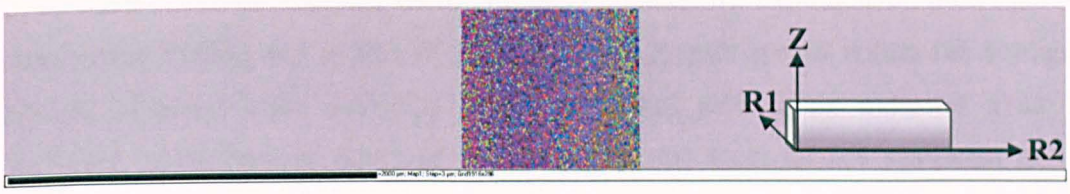

a)

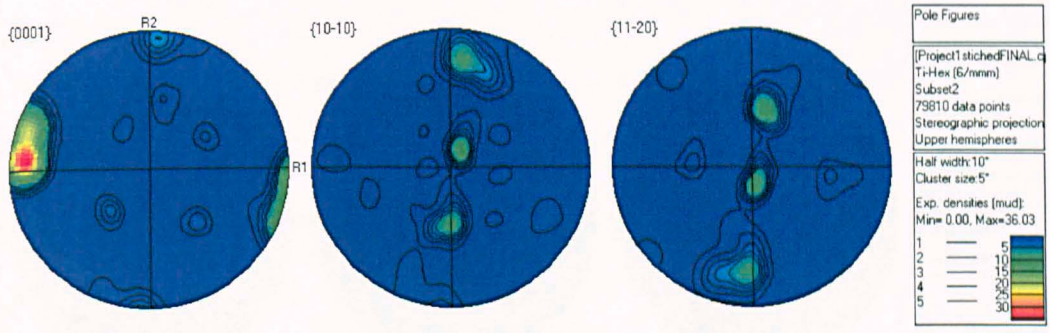

b)

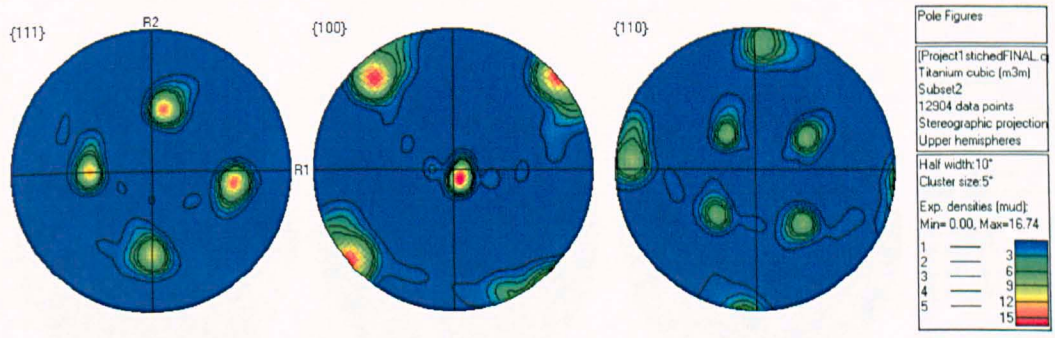

c)

Figure 4.59 Subset taken from the **a)** Crystal orientation map for sample S2 edge in Euler colouring. The corresponding **b)** alpha **c)** beta phase pole figure from Sample S2 edge.

It can clearly be seen that the pole figure shown in Figure 4.47 e) is the combination of two major orientations shown in Figures 4.58 and 4.59. The result shows that there is only a 21 degree rotation between the two α orientations in Figures

4.58 and 4.59 and the two β orientations in Figures 4.58 and 4.59, resulting in perfect Burgers relations.

Figures 4.58 and 4.59 clearly demonstrate there is only one orientation within each pole figure therefore by taking a subset of the existing β texture and using software written by Dr Brad Wynne, it is possible to calculate α_s texture (as expected from the β grains).

By observing Figures 4.60 a) and b) it can be seen that the theoretical pole figures have peaks of equal orientation therefore no variant selection has occurred and perfect Burgers relationship exists. However when this is compared to the experimental pole figure it can be seen that the strong texture within the experimental pole figure is much more diffuse and differs in intensity. The greater spread within the strongest texture observed when analysing the experimental pole figure indicates a strong influence of the variant selection mechanism on the local texture sharpness of the sample and therefore suggests that the texture is dominated by α_p.

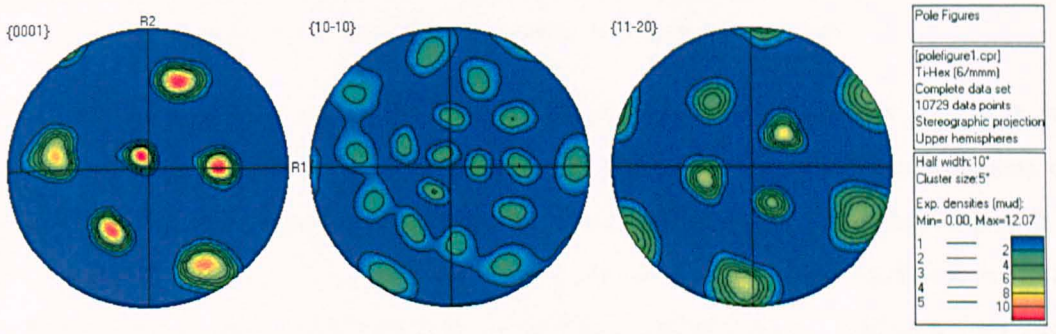

a)

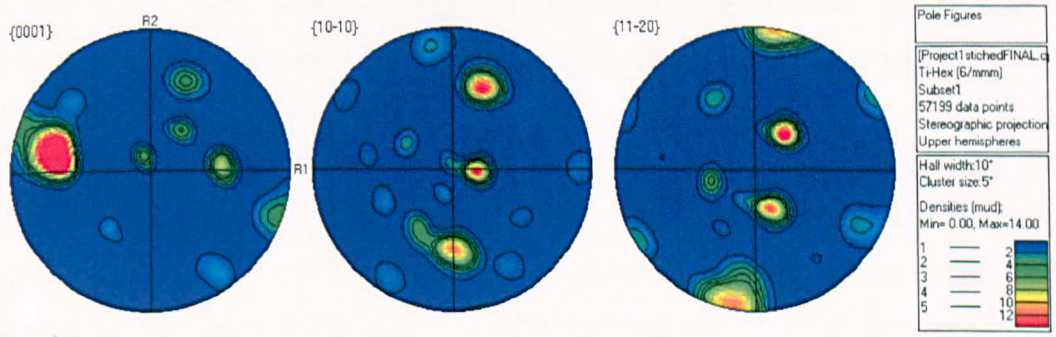

b)

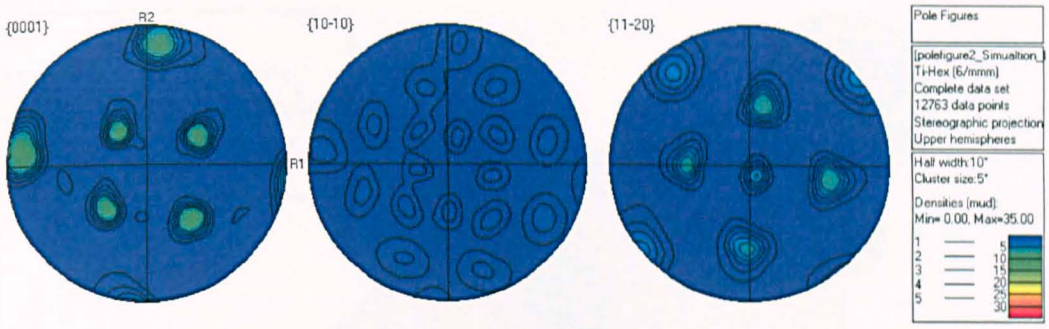

c)

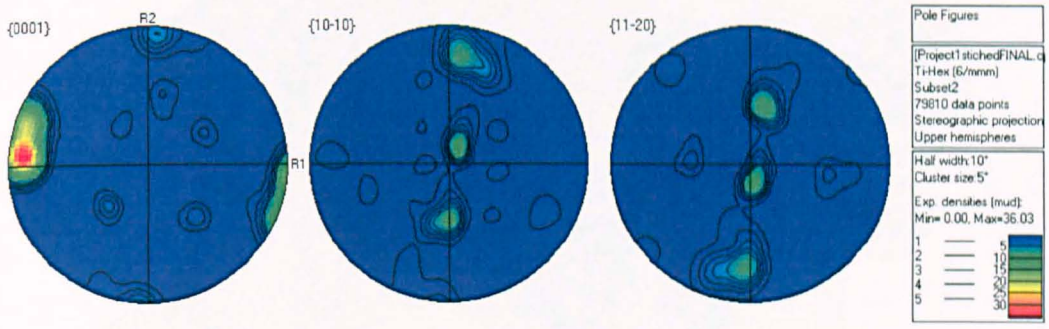

d)

Figure 4.60 Comparison of the experimental data (**b, d**) with their corresponding theoretical (non variant selection) data (**a, c**) respectively (for the subsets taken from sample S2 edge).

Figures 4.60 c) and d) also demonstrate that intensity is much greater in the experimental pole figures than the theoretical pole figures. The majority of variants do exist, however, significantly more spread can be observed. Using Burgers relation, it is not unusual to observe a variation of 2 to 3 degrees however the variation is much greater suggesting that the results must be due to α_p rather than α_s. Unless a very large high resolution map containing sufficient data is obtained, however, it will never be possible to confidently state that the results are due to variant selection and that variants of a certain orientation are selected.

The complete results from the EBSD analysis are presented in Figure 4.61. Each texture measurement is represented by an {0001} and a {100} pole figure. The effects of the strains are apparent in the billet texture and can be explained by the forging history of the billet. A greater strain was imposed between the corners of the billet and subsequently about the billet axis as it was forged from a rectangular to a circular cross section (Figure 4.62).

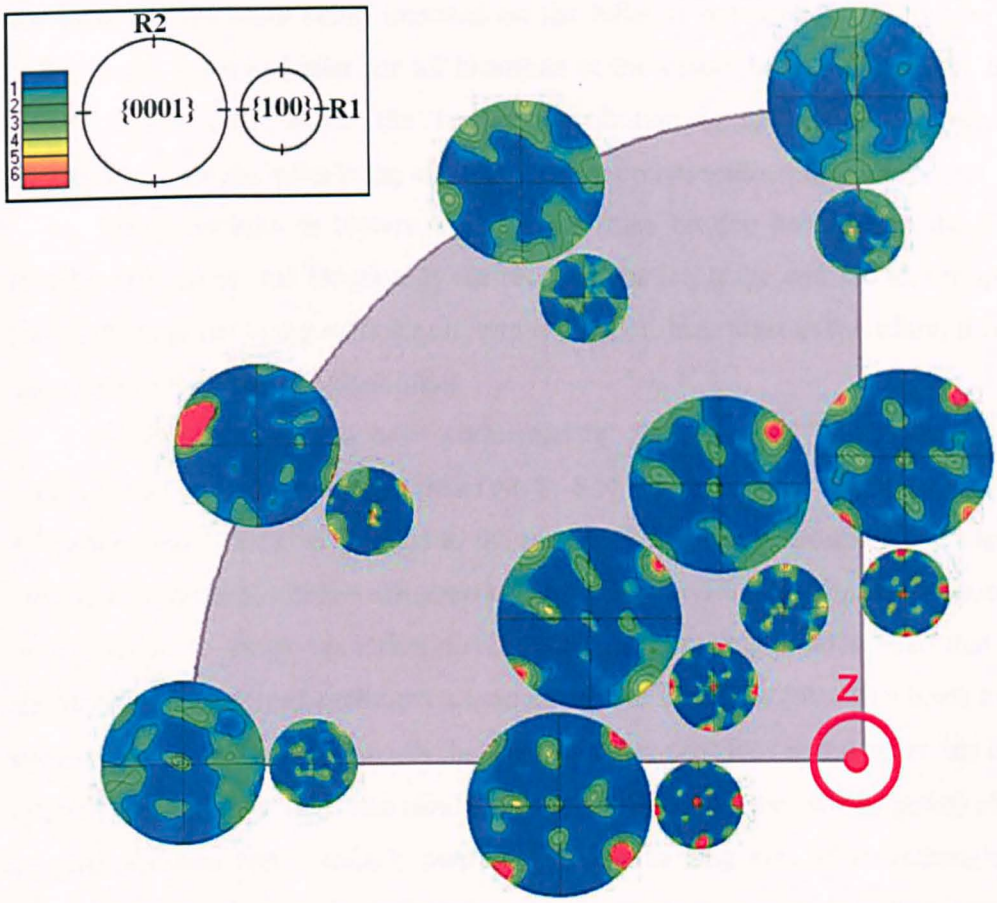

Figure 4.61 Small billet texture results represented by an {0001} and a {100} pole figure.

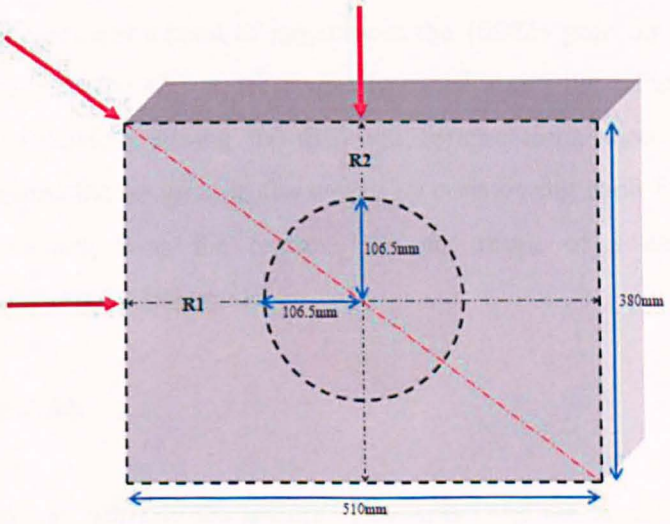

Figure 4.62 Shows the variation of billet cross-section in shape, changing from an initial rectangle to the round billet (small billet).

On examining the billet in Figure 4.61 it can clearly be seen that there are two separate deformation regimes located at the centre and edge of the billet. As previously described, texture is the direct result of deformation history [54]. It is interesting to see

that although the stain being imposed on the billet is not spread equally, the texture arrangement is very similar for all locations at the centre of the billet. This however differs at the edge where the texture distribution is spread radially across the circumference of the billet being aligned with the compression direction.

The similarity in texture at the centre may be due however to the β texture already existing in this location at the recrystallisation stage and the strain applied at final α+β stage not being sufficient to remove it. For these reasons therefore, this texture may have remained in the final billet.

Similar analysis has been performed by Davies et al. [89]. who examined the cross-section of a billet of TIMETAL® 834 using optical microscopy, neutron diffraction and EBSD. In contrast to the results above where texture at the edge of the sample was aligned with the compression direction, Davies et al. found the texture to be perpendicular to the compression direction. Their research demonstrated that there is increasingly a preferred rotational alignment of the fibre like {10-10} planes about the billet axis from the centre towards the edge. In many positions in the billet, the direction of this preferred alignment was similar; with the c axes (i.e. the {0002} poles) aligned in a radial direction approximately perpendicular to the long axis of the rectangle (as the billet was forged from a rectangular cross-section to a circular cross-section). In addition, they noted that from the centre of the billet to the edge, there was also a {0002} component and a band of intensity in the {0002} pole figure, which they stated could be related to the non equal strains imposed about the billet axis (constraint and side spread of material during the different compressions about the billet axis). The authors explained the textures in the centre by considering each forging bite as a plane strain compression, with the texture, the net result of a series of plane strain compressions about the billet axis.

4.3.2 Large billet

In order to compare the texture of the small and the large billet an EBSD texture run was carried out on samples LS1 edge and centre over approximately an area of 7.5mm x 800μm and 4.8mm x 341μm respectively and samples LS4 edge and centre covering approximately an area of 5.5mm x 800μm and 11mm x 400μm correspondingly. The related Euler and IPF maps and the corresponding pole figures are shown in Figures 4.63 to 4.66.

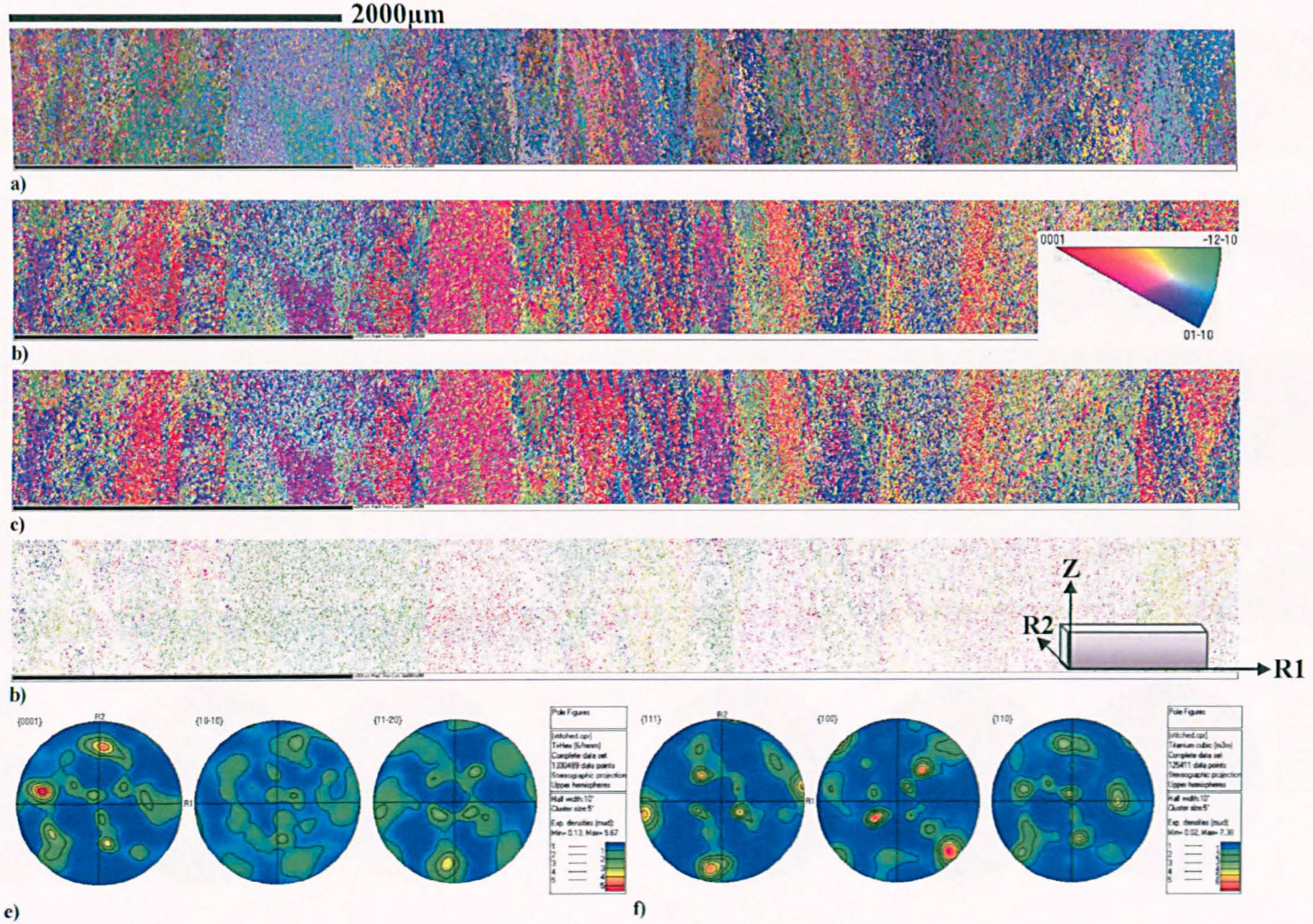

Figure 4.63 Crystal orientation map for sample LS1 edge. **a)** Euler colouring **b)** IPF colouring **c)** alpha phase only **d)** beta phase only and **e)** Alpha **f)** beta phase pole figure from LS1 edge.

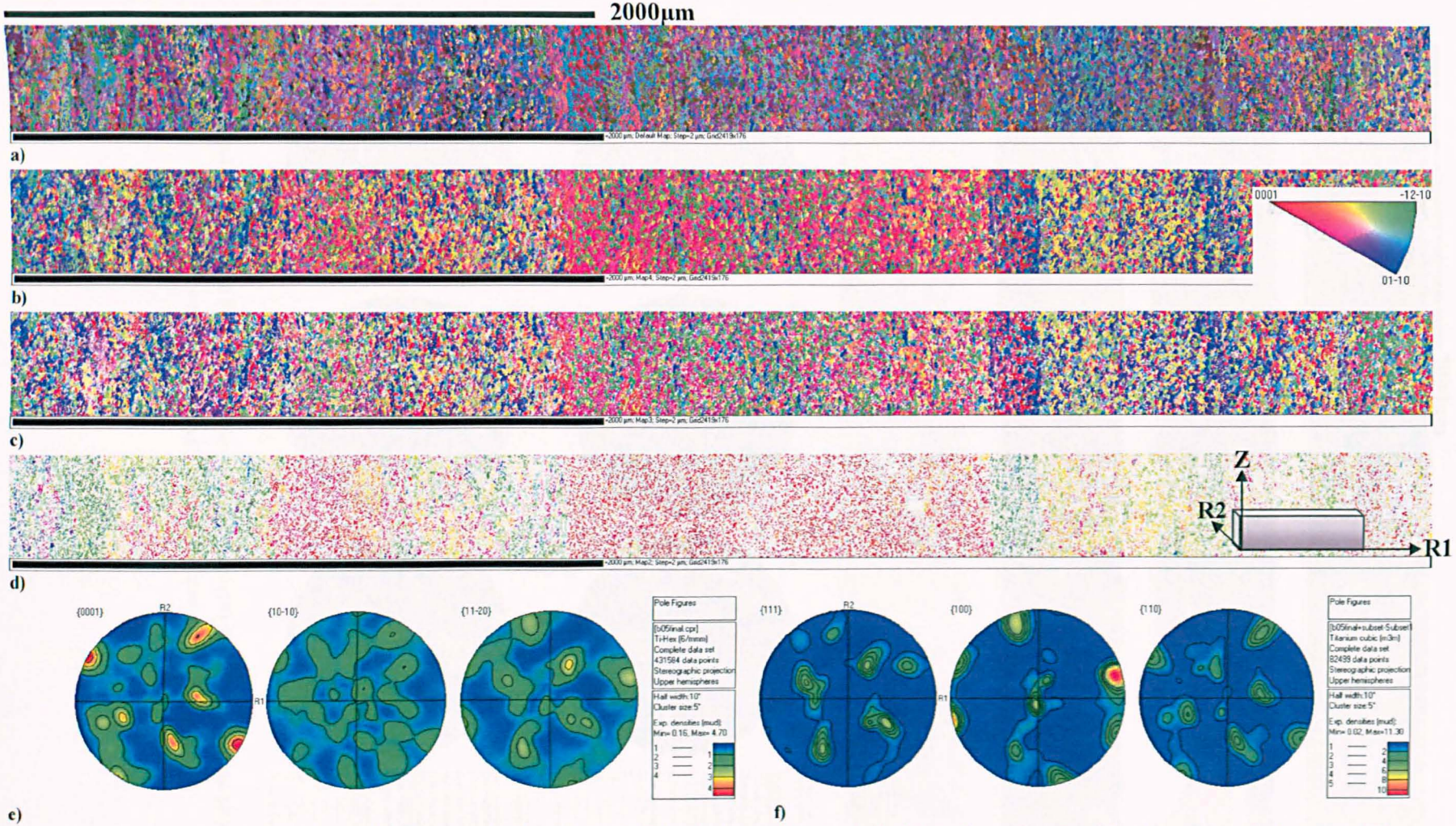

Figure 4.64 Crystal orientation map for sample LS1 centre. **a)** Euler colouring **b)** IPF colouring **c)** alpha phase only **d)** beta phase only and **e)** alpha **f)** beta phase pole figure from LS1 centre.

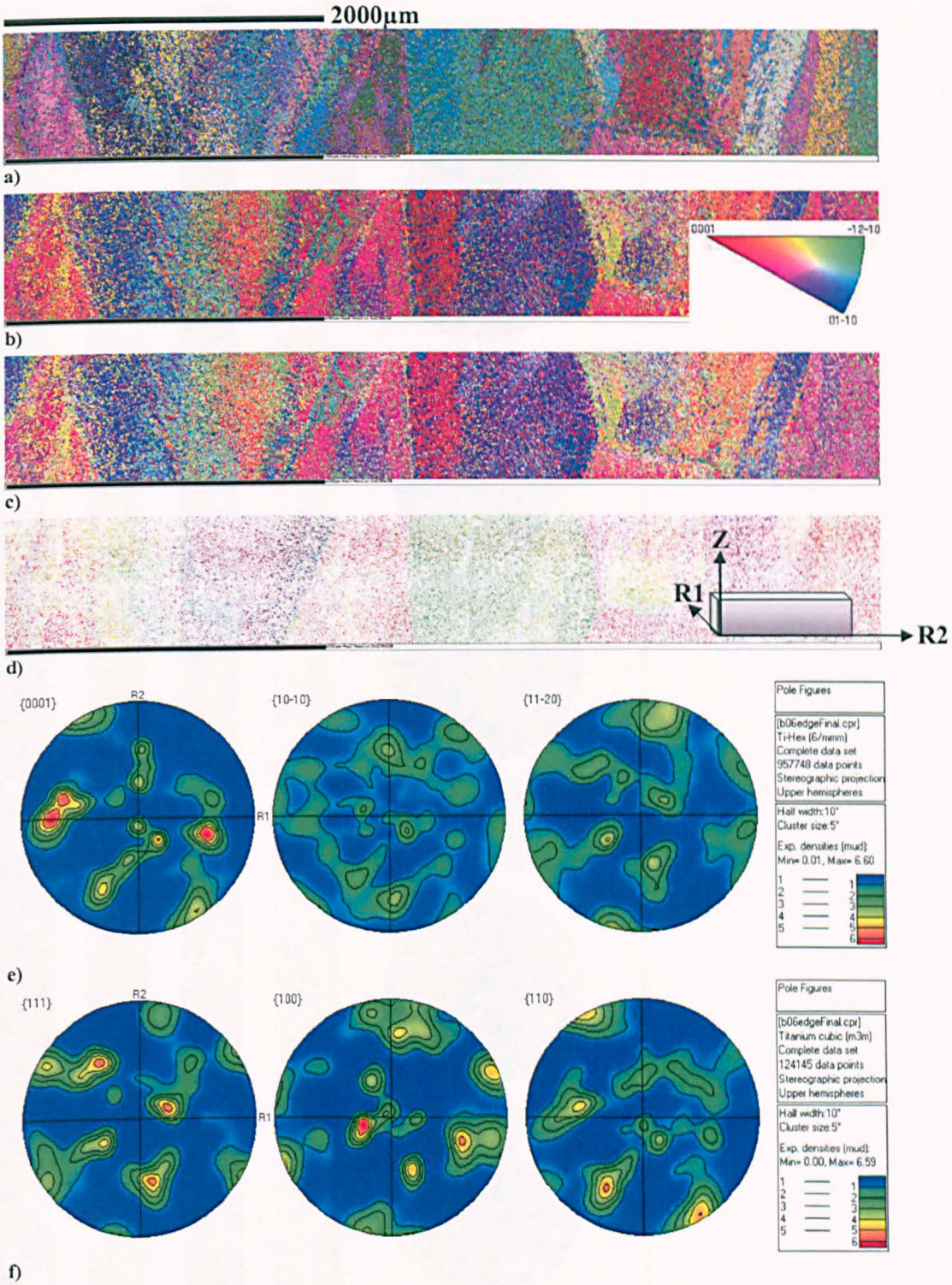

Figure 4.65 Crystal orientation map for sample LS4 edge. **a)** Euler colouring **b)** IPF colouring **c)** alpha phase only **d)** beta phase only and **e)** alpha **f)** beta phase pole figure from Sample LS4 edge.

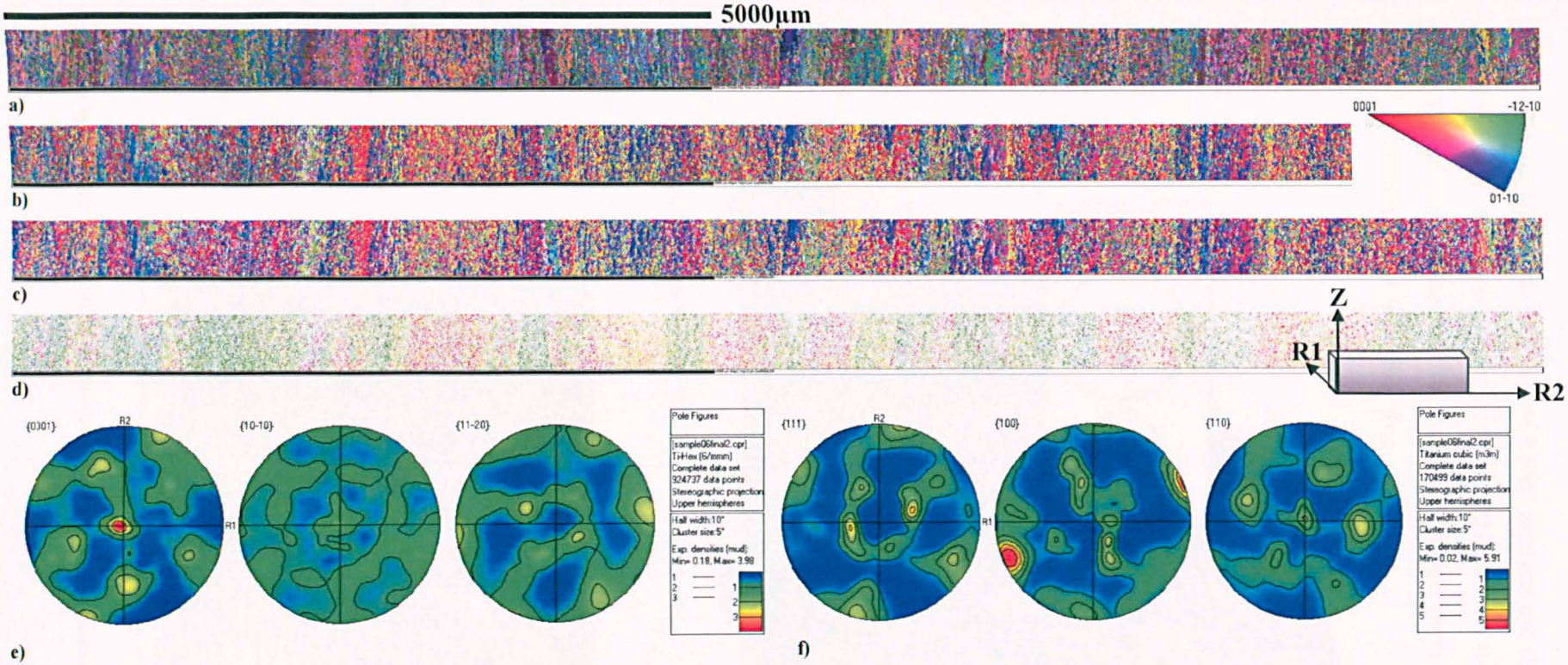

Figure 4.66 Crystal orientation map for sample LS4 centre. **a)** Euler colouring **b)** IPF colouring **c)** alpha phase only **d)** beta phase only and **e)** alpha **f)** beta phase pole figure from Sample LS4 centre.

The complete results from the EBSD analysis are shown in Figure 4.67. Each texture measurement is represented by an {0001} and a {100} pole figure. Figure 4.68 shows the reductions required for the shape change from the initial rectangle to the round billet in the final α+β forging step.

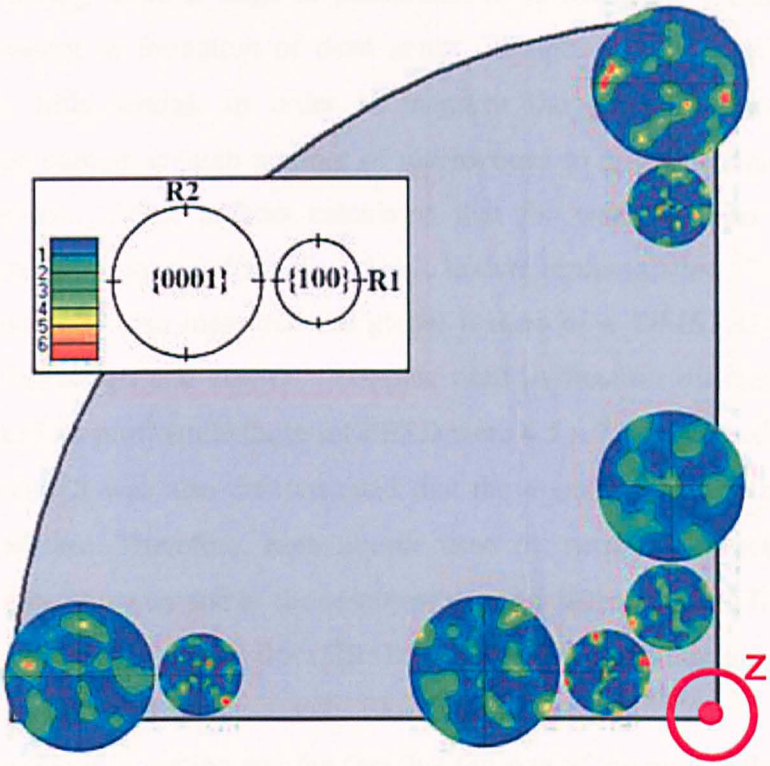

Figure 4.67 Large billet texture results represented by an {0001} and a {100} pole figure.

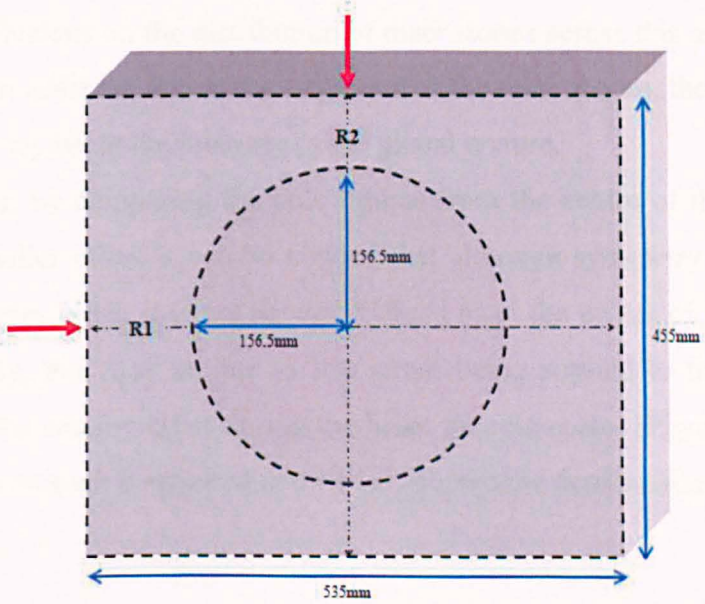

Figure 4.68 Shows the variation of billet cross-section in shape, changing from an initial rectangle to the round billet (large billet).

As was seen in the smaller billet, macrozones were observed throughout the whole billet, aligned along the longitudinal axis, Z of the larger billet. The widths of the macrozones at the edge of the large billet however, were wider in comparison to those of the smaller billet. This may be due to lack of strain being applied to the larger diameter billet during its final stage of production or to resistance formed under the forging tools leading to formation of dead zones (sections of the billet which have undergone very little strain). In order to measure the global textures, the area investigated must contain enough number of macrozones to guarantee that the data is statistically relevant. Some authors calculated that for weak textures up to 2400 orientations are required for a statistically reliable texture representation [54].

Davies et al. [89] also measured the global texture of a TIMETAL® 834 billet using neutron diffraction and EBSD. Samples used in neutron diffraction were of dimensions 15 x15 x8 mm^3 while those for EBSD were 4.5 x 7.5 mm^2 producing results in good agreement. It was also demonstrated that the diameter of each macrozone is approximately 500μm. Therefore, each sample used for neutron diffraction contains several thousand macrozones and as the results of neutron diffraction and EBSD were in good agreement, the results gained from EBSD are good representation of global texture (each EBSD map contained approximately 100-200 macrozones) [89, 90].

Based on this information and the fact that the size of the map at the edge of the sample is small in comparison to the size of the macrozones, it is not possible to draw any strong conclusions on the distribution of macrozones across this area of the sample (lack of data). In addition, due to the large size of the macrozones, the intensity of pole figures may not represent the intensity of the global texture.

However, by comparing the pole figures from the centre of the larger billet to those of the smaller billet, it can be noticed that although symmetry does exist at the centre of the larger billet, it is not as well defined as at the centre of smaller billet. As stated previously, this may be due to less strain being applied to the larger billet in comparison to the smaller billet during the billet process route. (Figures 4.62 and 4.68 illustrate that more stain is required in order to achieve the final smaller sized billet).

4.4 Summary

This chapter provided general information about the texture of titanium alloys and discussed techniques used to measure and represent texture. Detailed EBSD studies were carried out on two different diameter TIMETAL® 6Al-2Sn-4Zr-6Mo billets with similar process histories. It was shown that the texture of both TIMETAL® 6Al-2Sn-4Zr-6Mo billets, were strongly dependent on the strain imposed by the deformation process. Large band like regions with sharp local textures, commonly called macrozones, were observed throughout the whole billets stretching along the billet axis. In this work it was shown that that α_s colonies were also strongly textured around the same texture component as the α_p grains. The scale at which analysis of the texture was performed showed there was a close orientation among the α_p grains and α_s colonies which contributes to the sharp local texture. In general, the billet textures were quite weak but regardless of this weakness, moving from the edge towards the centre of the billet there were some noticeable differences in the textures. Two separate deformation regimes located at the centre and edge of the billets were observed. The texture arrangement was very similar for all locations at the centre of the billet having no variant selection. This similarity in texture was thought to be due to the β texture already existing in this location at the recrystallisation stage and the strain applied at final $\alpha+\beta$ stage not being sufficient to remove it. For these reasons therefore, this texture may have remained in the final billet. This however differed at the edge where strong influence of the variant selection mechanism was observed. The texture distribution at the edge was spread radially across the circumference of the billet being aligned with the compression direction. The samples appeared to have a symmetric pattern which was clearer at the centre of the billet. This symmetry was explained by the non equal strains imposed about the billet axis by the forging process due to the fact that the billet was forged from a rectangular cross section to a circular cross section.

At the edge of the larger billet the widths of the macrozones were wider in comparison to those of the smaller billet. This was thought to be due to lack of strain being applied to the larger diameter billet during its final stage of production. However, because of the size of the map was small in comparison to the size of the macrozones, it was not possible to draw any strong conclusions on the distribution of texture across this area of the sample.

Chapter 5

ALTERNATIVE FORGING ROUTE

5.1 Introduction

This chapter analyses and interprets the microstructure and crystallographic texture developed in an alternatively forged TIMETAL® 6Al-2Sn-4Zr-6Mo billet and makes comparison with results from the previous 2 Chapters from conventionally forged billets.

5.1.1 Alternative production route for TIMETAL® 6Al-2Sn-4Zr-6Mo

Since the microstructure of forged TIMETAL® 6Al-2Sn-4Zr-6Mo is dependent on a large number of process variables, considerable cost saving can be gained through use of the best possible process conditions. TIMET, UK has developed an alternative forging process in which the ingot was forged into a square section at a high β forging temperature (where large shape changes can be achieved using relatively low forces) on the open die press. It was then cooled to room temperature and cut into two equal halves. The two pieces were subsequently α+β forged to produce a polyhedron (hexagonal) using the Davy open die press in a number of reheats. They were then α + β forged to a larger diameter (compared to the final size) on Timets RUMX radial forging (4 die) machine followed by air cooling. Samples were further α+β forged to a diameter of 250mm on the radial forging machine. As previously discussed, this final forging step is utilised to break up the coarse lamellar α+β microstructure and produce a microstructure containing individual α_p grains (globularization). The process is shown schematically in Figure 5.1 a)[91].

By comparing the forging route with those in Chapter 3, one significant difference can be observed. The alternatively forged billet was α+β forged following the ingot breakdown above β transus temperature therefore resulting in termination of the prestrain and β recrystallisation stage. This is illustrated in Figure 5.1 b).

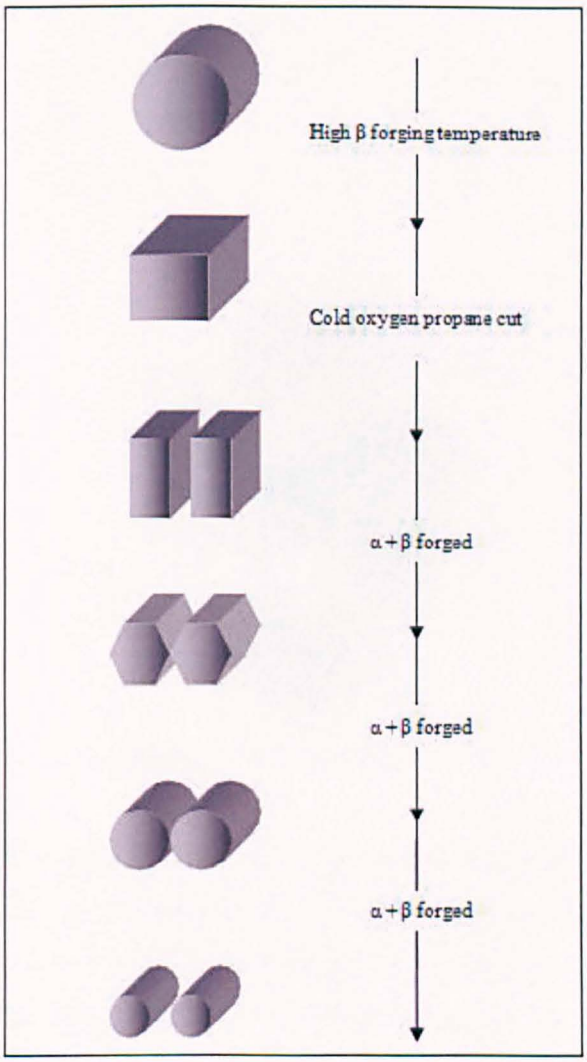

a)

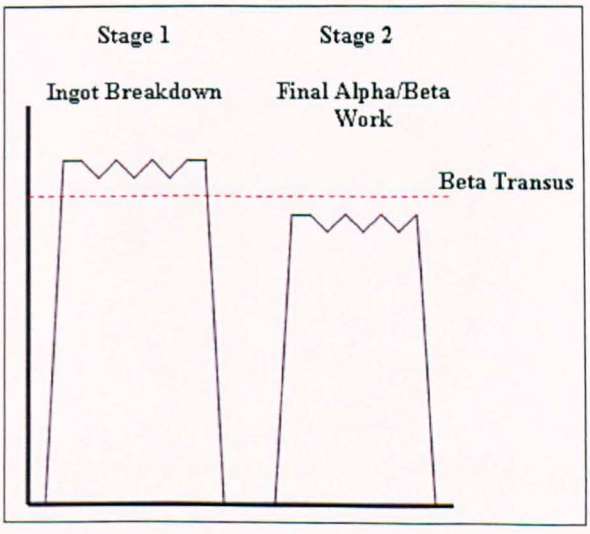

b)

Figure 5.1 a) Process route of the alternatively forged TIMETAL® 6Al-2Sn-4Zr-6Mo billet **b)** forging sequence for the alternatively forged α+β alloys.

Temperatures applied to the alternatively forged billet were approximately equal to those applied to previously analysed billets. The billets examined in Chapter 3 however, were forged entirely on the open die (2 die) press while radial forging (4 die) was used in the final forging stage of the alternatively forged billet as shown in Figure 5.2.

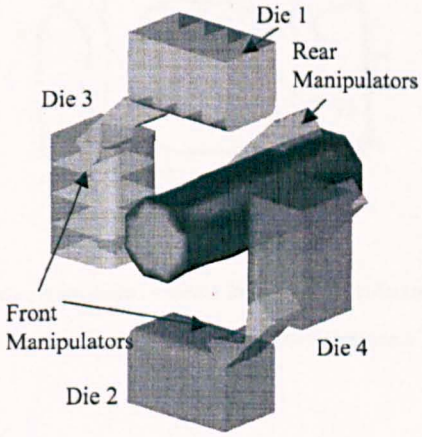

Figure 5.2 RUMX radial forging processes[3].

Differences in predicted strain distribution between the edge and the centre of the radial forged billet can be observed in Figure 5.3. This simulation has been carried out using DEFORM-3D model [3]. From this DEFORM-3D model it can be determined that the RUMX forged billet is uniformly worked circumferentially, with strain levels increasing from 1 near the centre to 2 close to the surface (less strain penetration than the open die press).

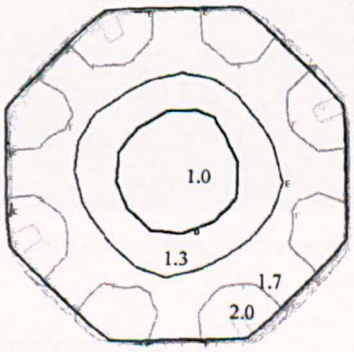

Figure 5.3 Transverse slice showing predicted strain distribution in RUMX forged bar, following final α+β forging [3].

Using the α phase globularization model, the effect of time, temperature and strain on microstructure refinement was also studied [3]. Results showed a major amount

of α phase globularization during the final α+β forging and subsequent heat treatment (Figure 5.4). The RUMX process resulted in a less uniform fraction of globularized α, ranging between 60-95% having less globularization in the centre [3].

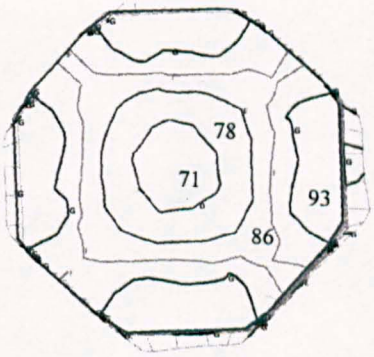

Figure 5.4 Transverse slice presenting predicted volume fraction of globularized α distribution in RUMX press, following final α+β forging and heat treatment [3].

5.2 Experimental work

The cross-section of the alternatively forged billet, 220 mm in diameter with reference axes Z (longitudinal axis of the billet) is shown below (Figure 5.5). Unfortunately unlike the previous billets in Chapter 3, samples were picked randomly and they are not linked to any specific forging directions (e.g. R1, R2) since these were not identified.

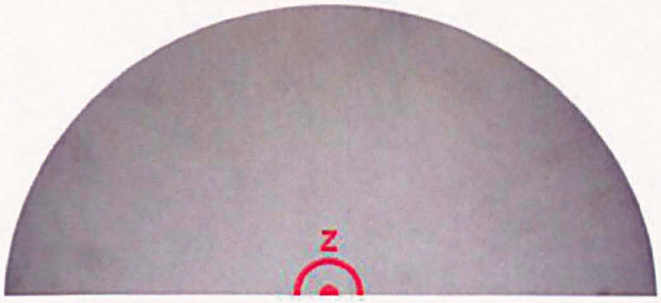

Figure 5.5 Cross-section of the alternatively forged billet, 220 mm a diameter with reference axes Z defined.

5.2.1 Scanning Electron Microscopy (SEM)

The preparation of the samples' surfaces was completed using the same procedure for those in Chapter 3. This was followed by etching the samples using Kroll's reagent. The microstructure at the centre and the edge of the billet was then

observed using Camscan series 2 SEM optical microscopy. A number of examples of the microstructure throughout the whole cross-section of the billet are shown in Figure 5.6.

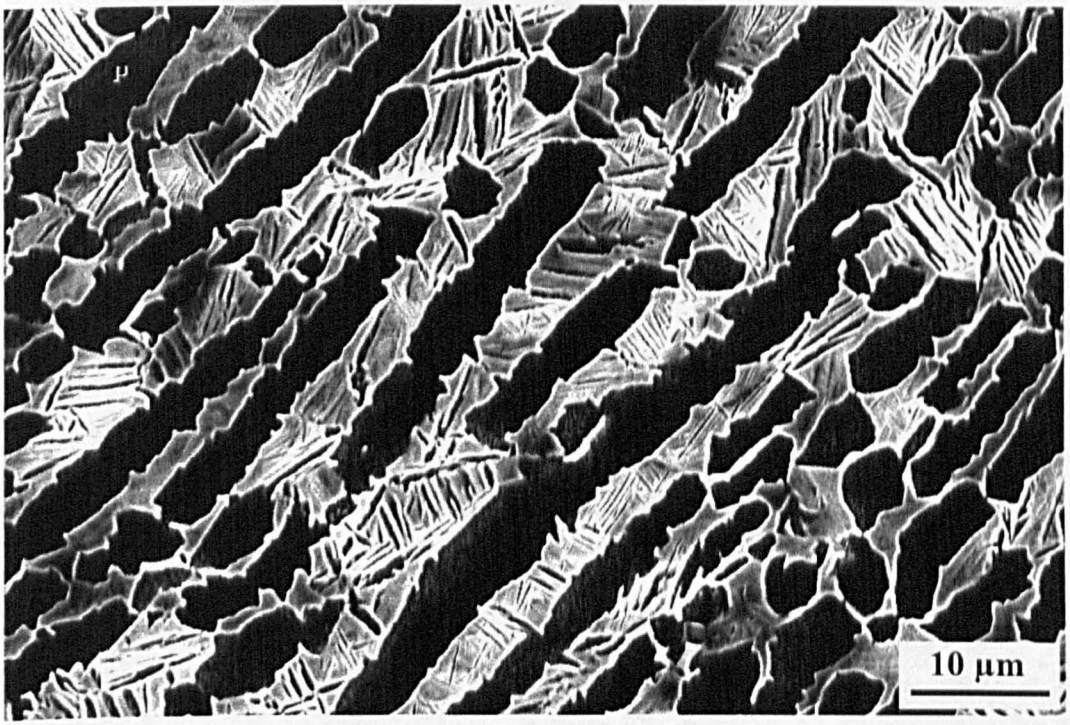

a) Microstructure of the alternatively forged billet.

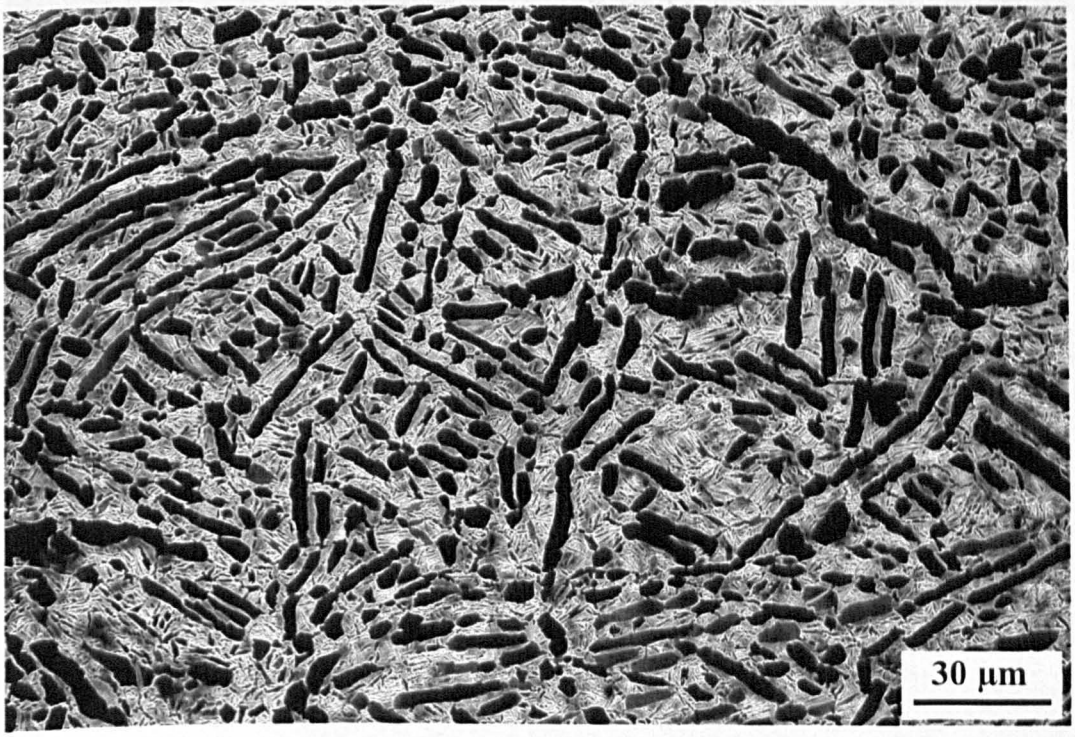

b) Microstructure of the alternatively forged billet.

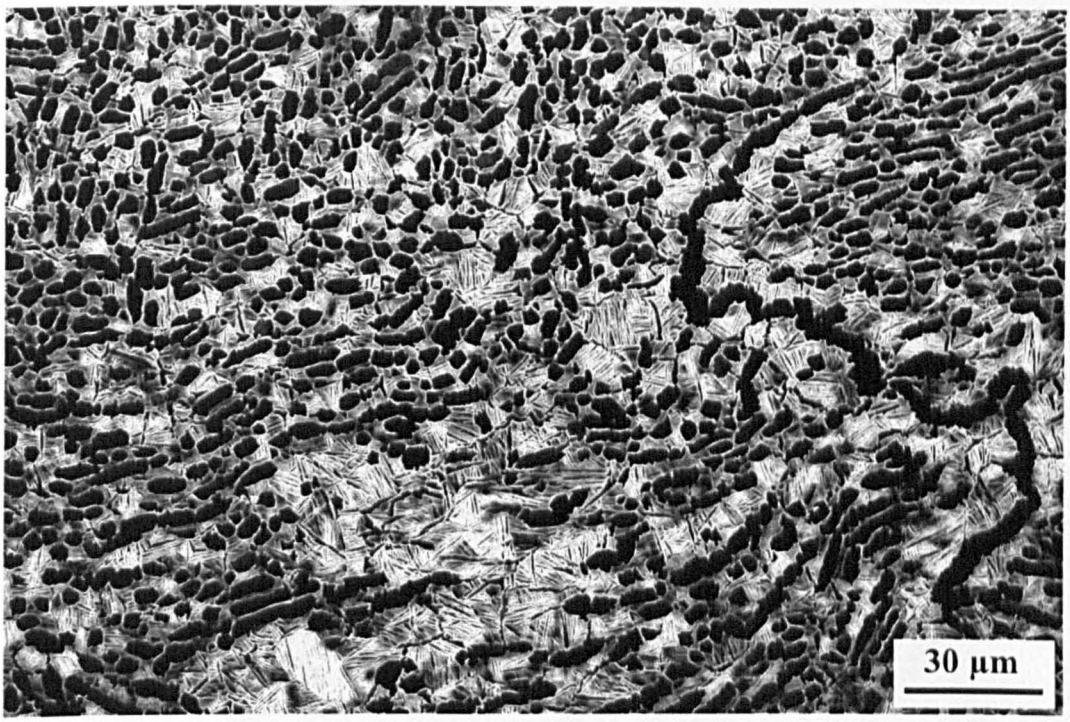

c) Microstructure of the alternatively forged billet.

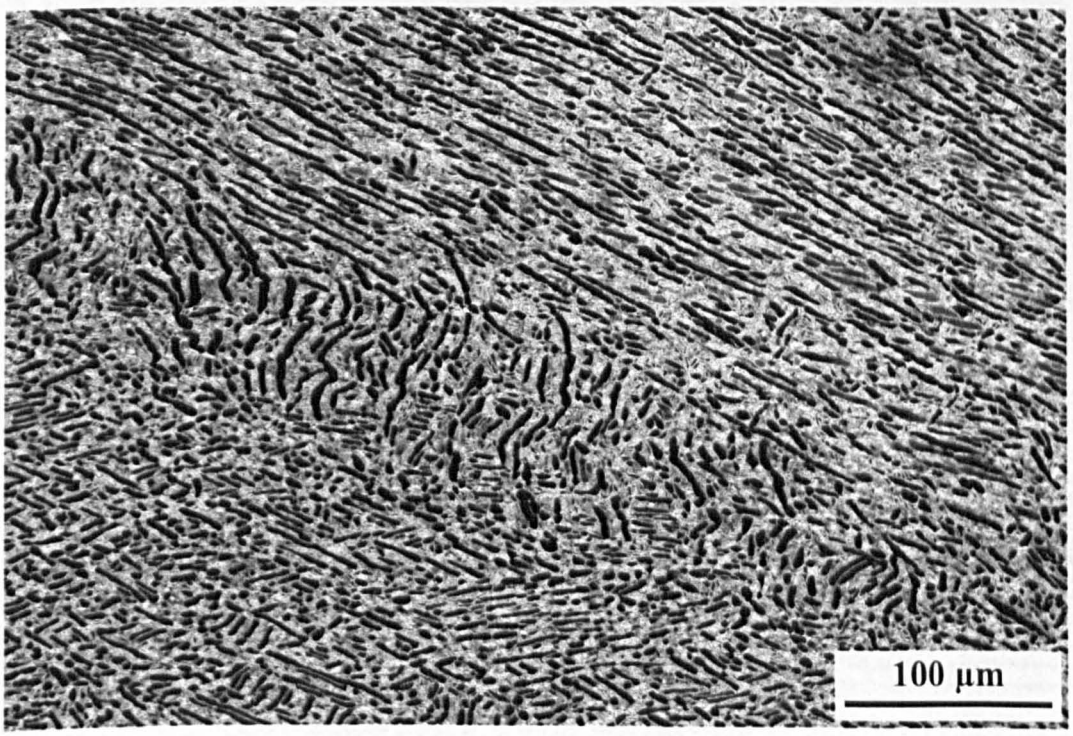

d) Microstructure of the alternatively forged billet.

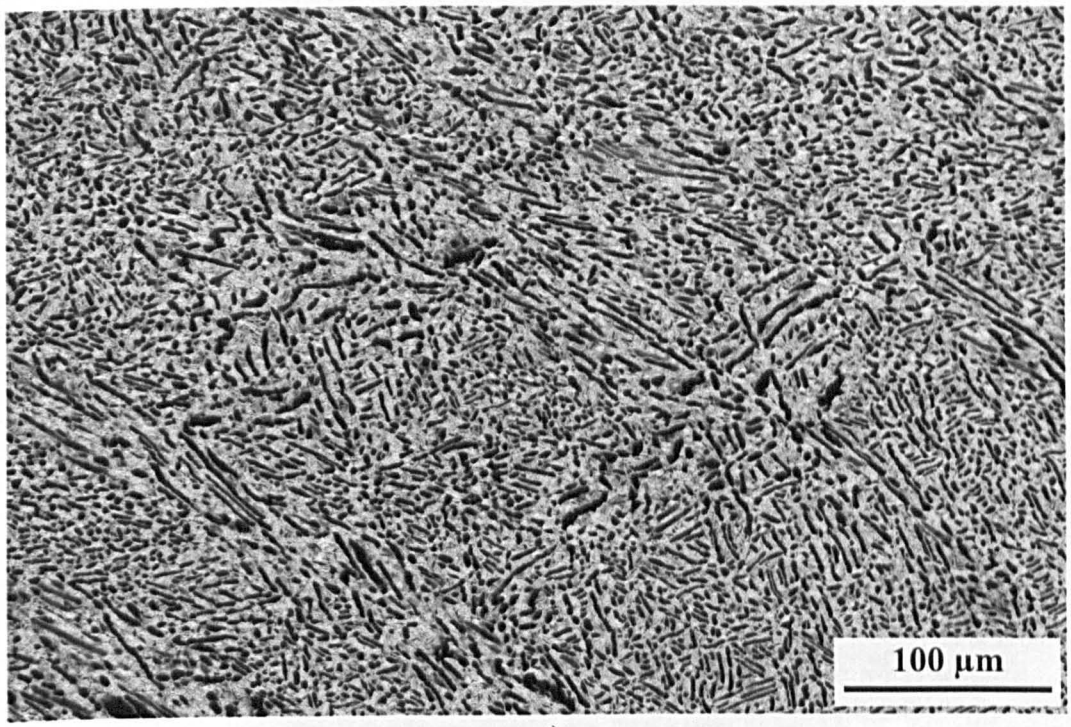

e)

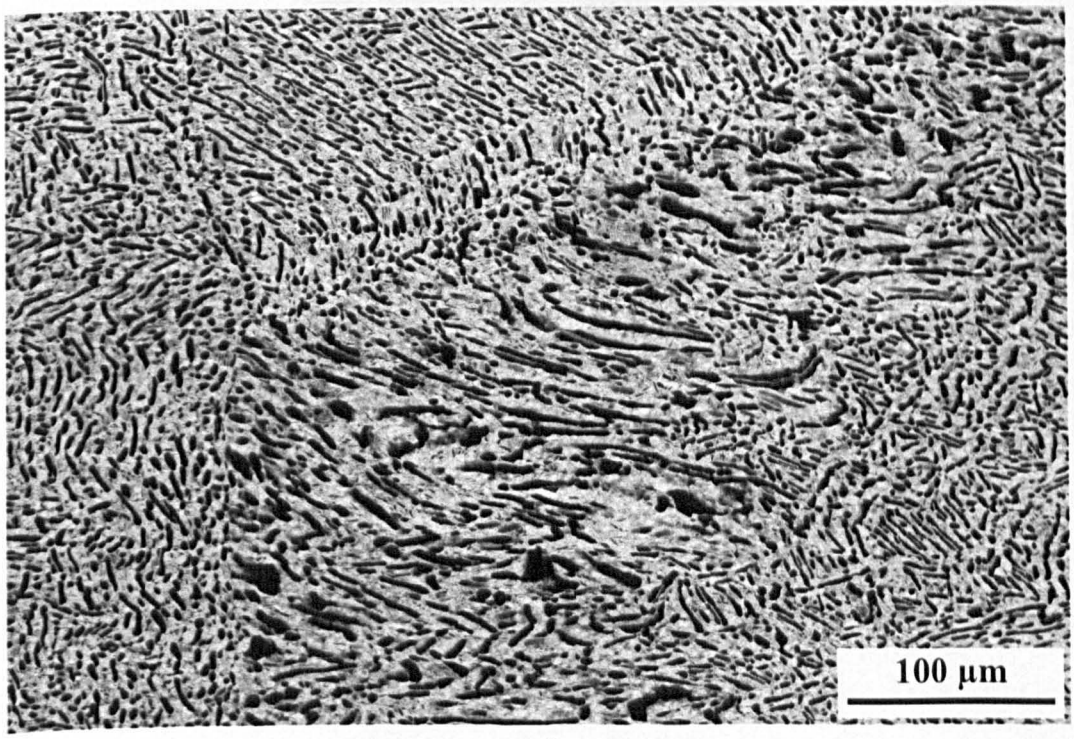

f)

Figure 5.6 Secondary electron images of the microstructure throughout the whole cross-section of the alternatively forged billet.

In order to characterise such microstructure over a larger and therefore more representative surface, detailed analysis of the microstructure was carried out at two main locations: Firstly using samples from up to a maximum of approximately 30mm

from the edge of the billet and secondly at the centre of the billet up to a radius of roughly 30 mm. This is shown in Figure 5.7.

Note that in all cases the microstructure was analysed in the plane perpendicular the longitudinal axis of the billet, Z (transverse plane). This was primarily completed because of the texture analysis in Section 5.3.2.

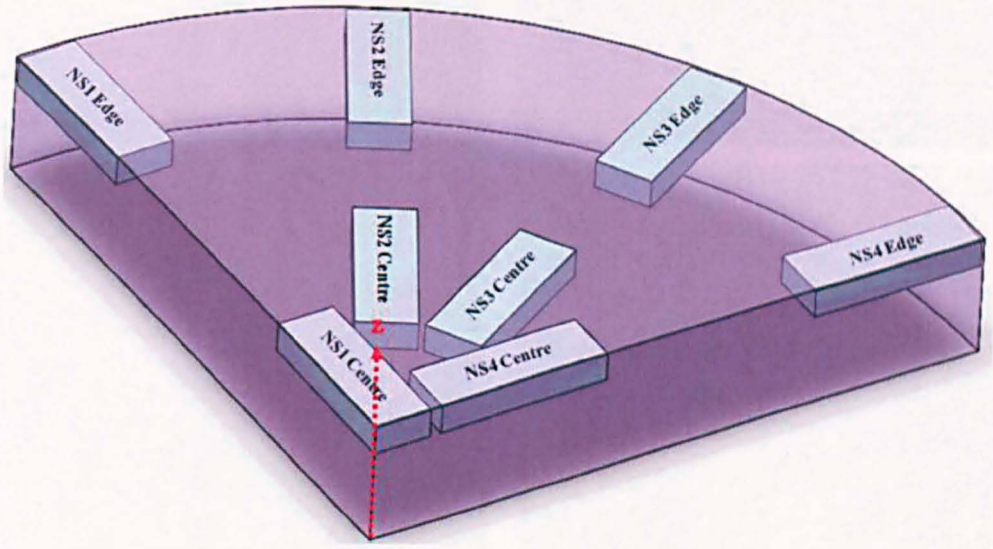

Figure 5.7 Samples NS1 through NS4 in the alternatively forged billet.

The method used in Chapter 3 was employed to analyse the microstructure of each sample. A series of micrographs each measuring 550 μm x 550 μm were taken so as to cover the total surface area of each sample. A selection of micrographs taken from different samples is shown in Figure 5.8 as an example.

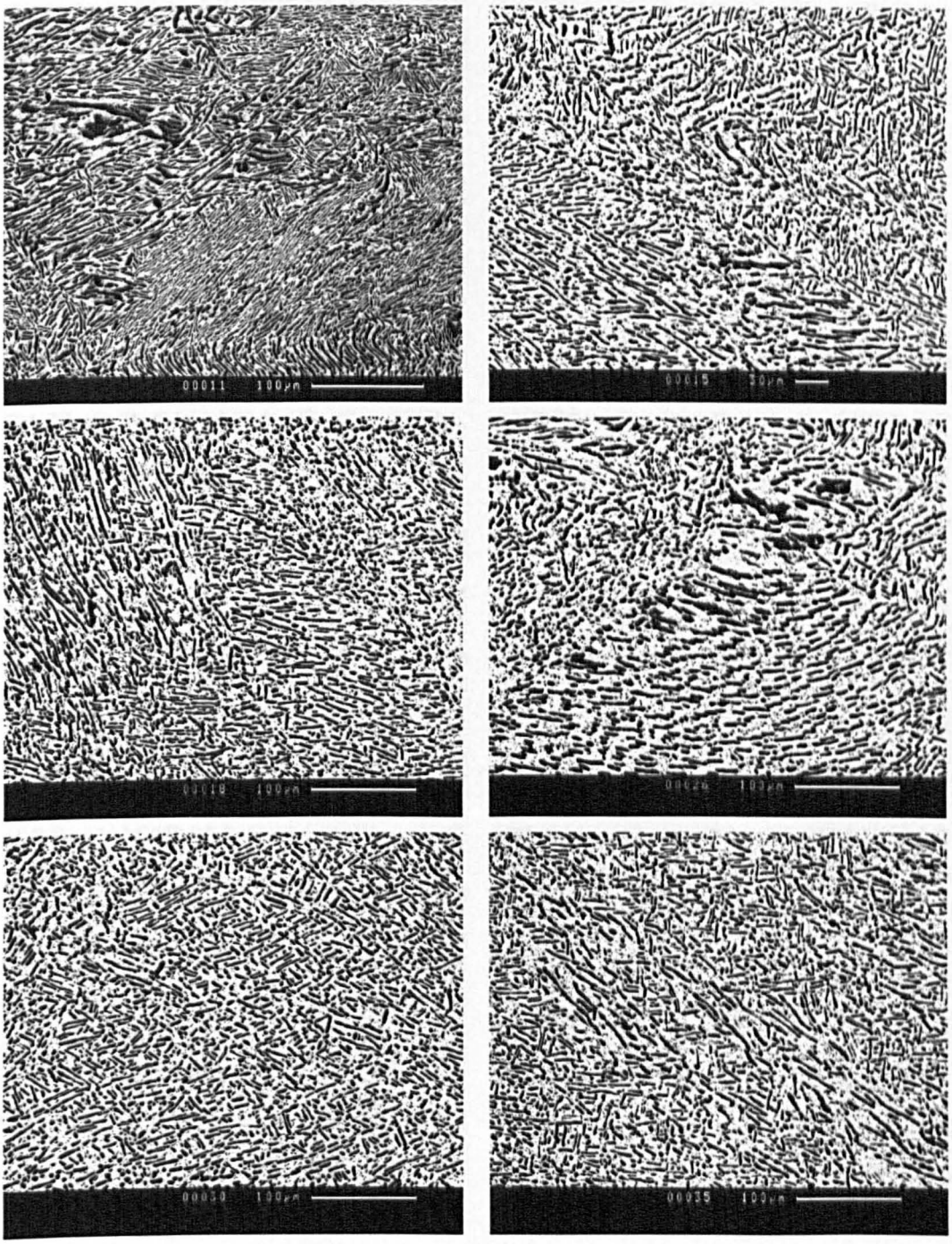

a) NS1 Edge

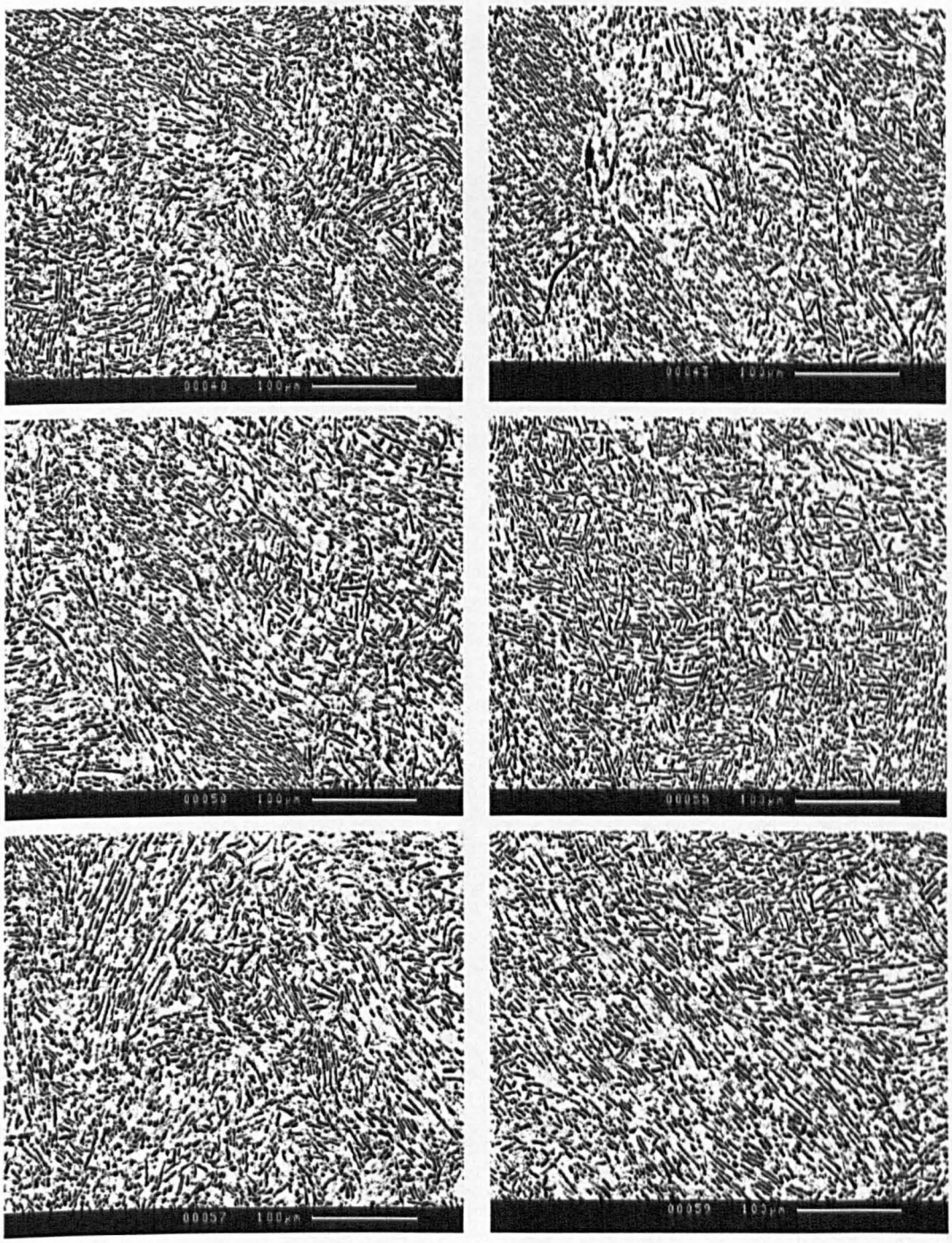

b) NS1 Centre

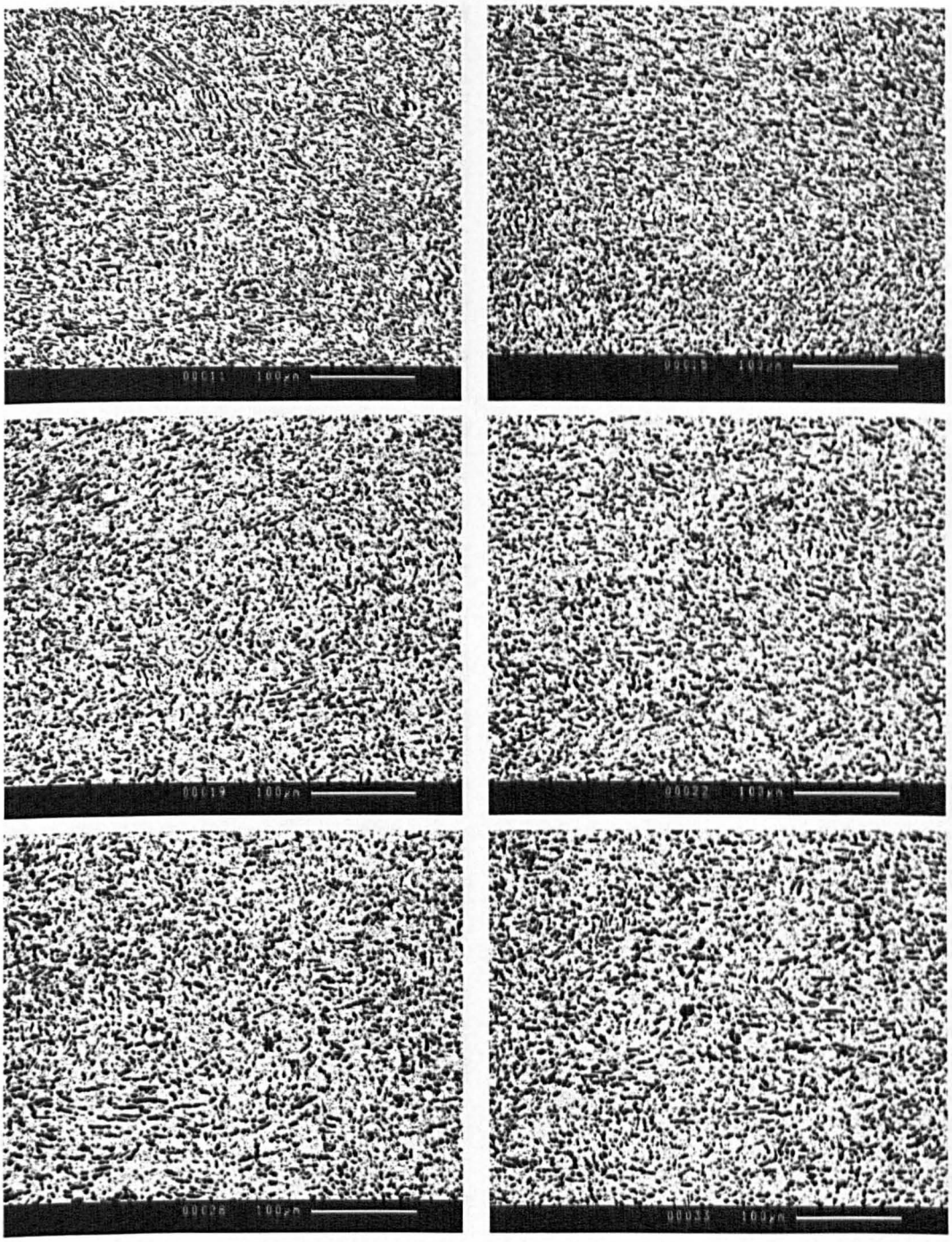

c) NS2 Edge

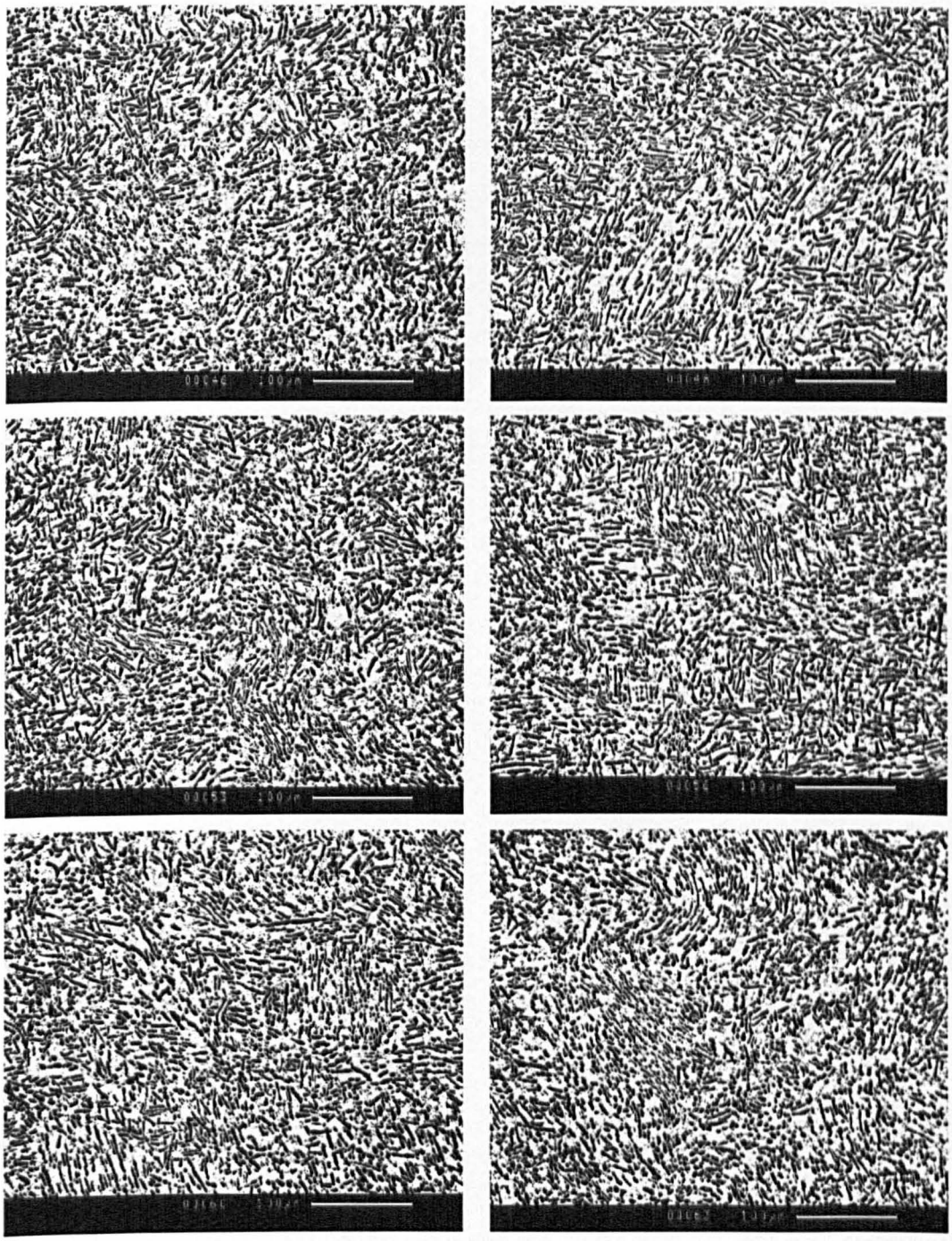

d) NS2 Centre

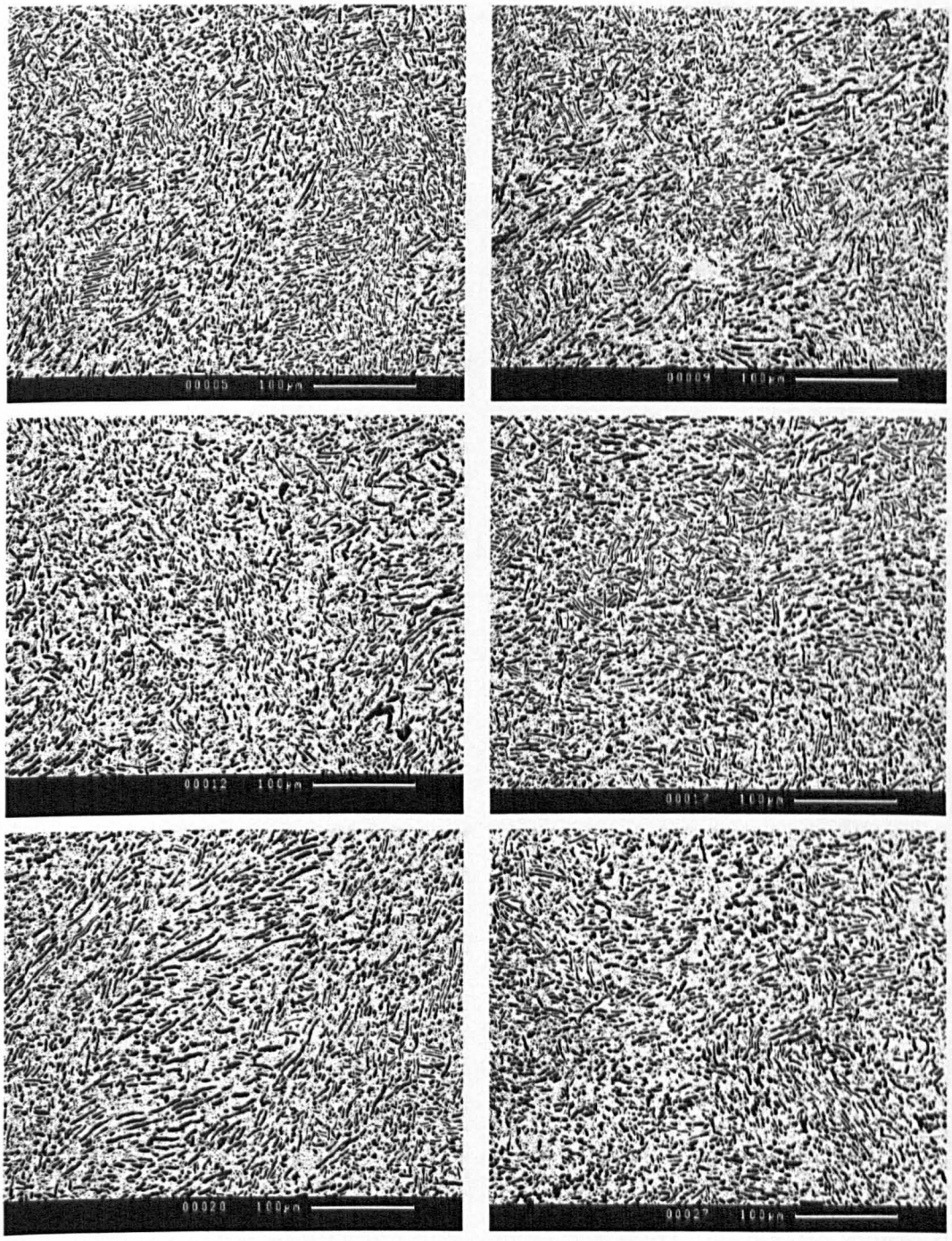

e) NS3 Edge

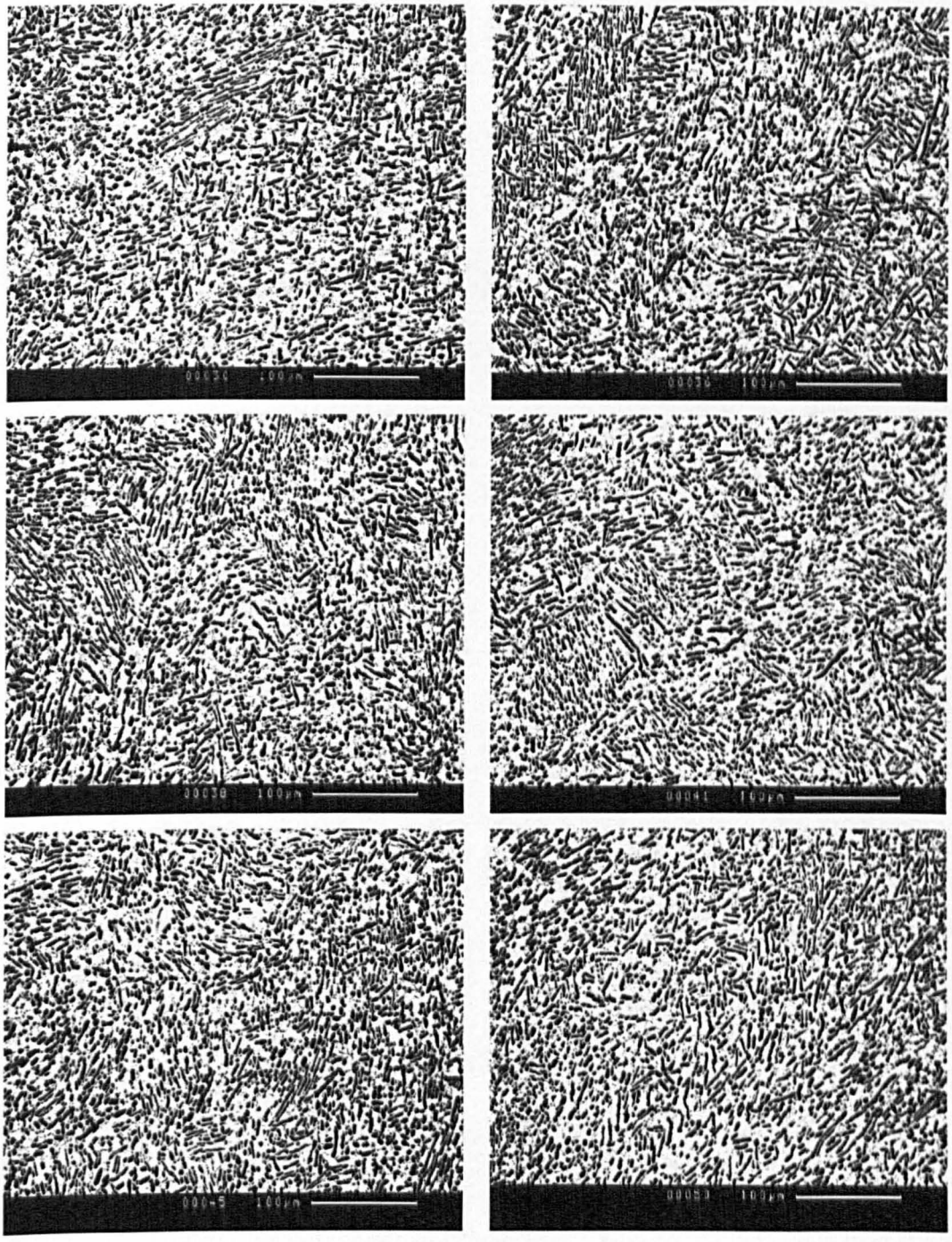

f) NS3 Centre

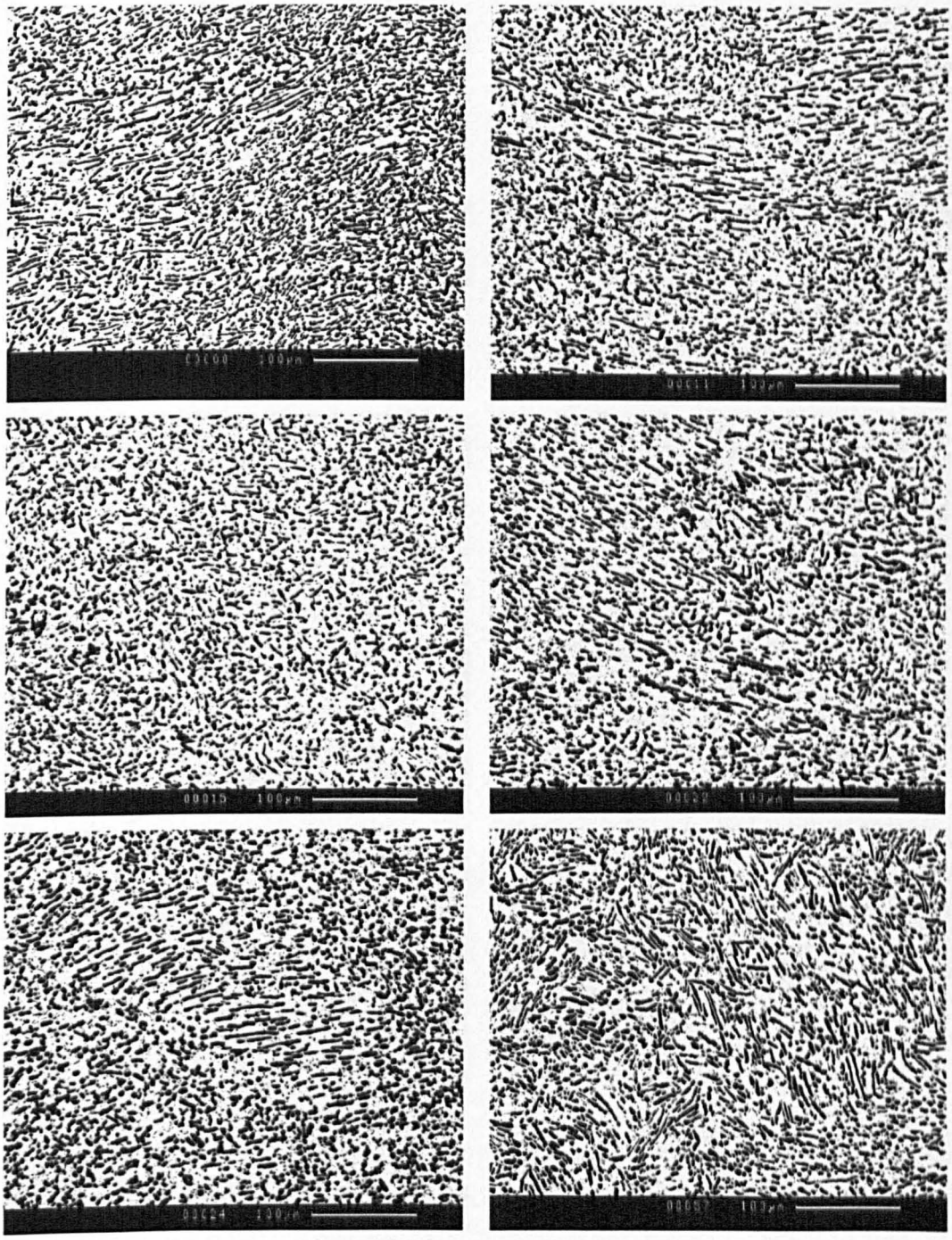

g) NS4 Edge

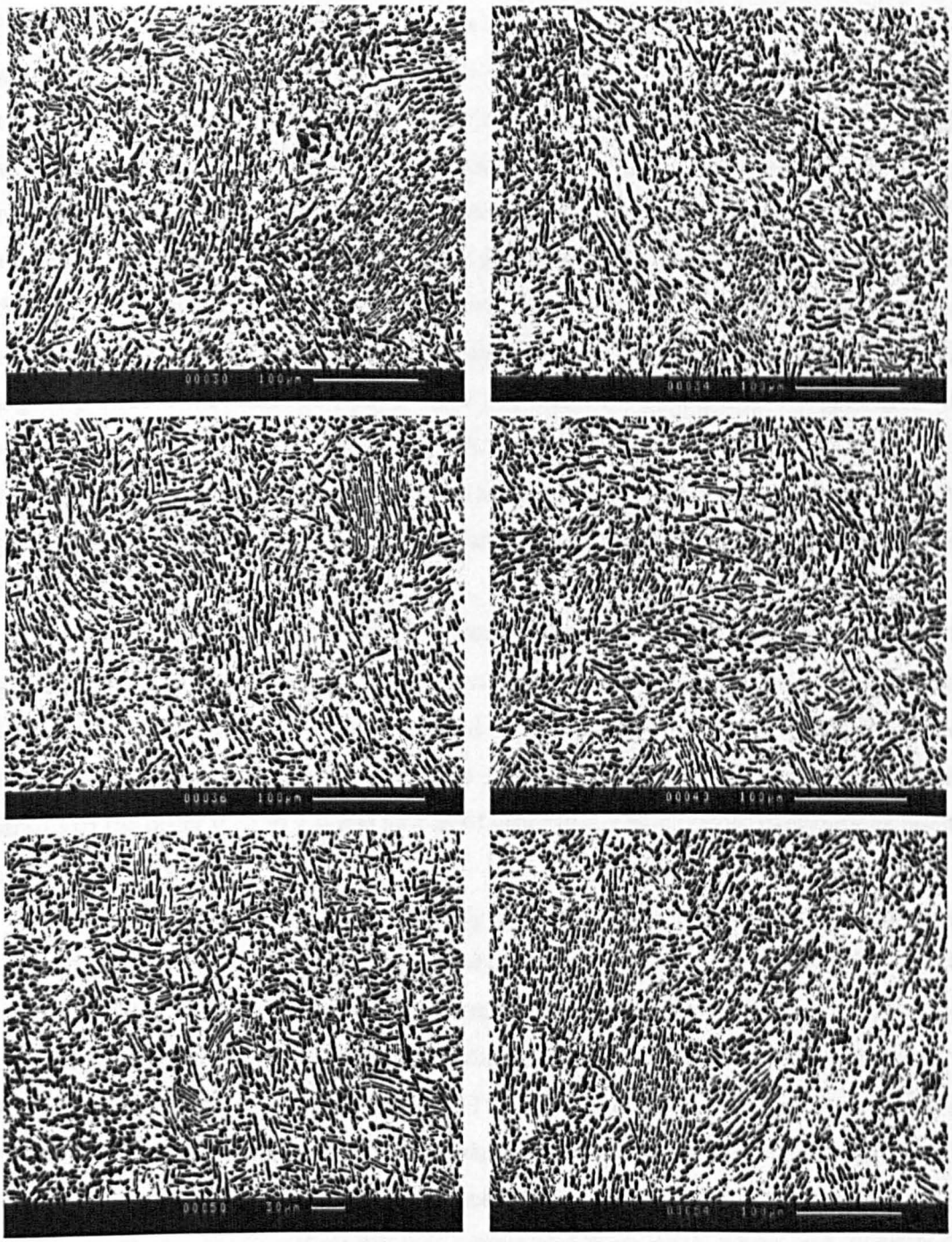

h)

Figure 5.8 Selection of micrographs, each covering 550 μm x 550 μm for samples **a)** NS1 Edge **b)** NS1 Centre **c)** NS2 Edge **d)** NS2 Centre **e)** NS3 Edge **f)** NS3 Centre **g)** NS4 Edge **h)** NS4 Centre.

From Figures 5.6 and 5.8 it can be confirmed that at various points within the billet, the microstructure has not been globularized. This can be due to the insufficient strain being applied to the billet by termination of the β recrystallisation stage [92].

As was observed from the previous billets in Chapter 3, each billet was heated into the α+β phase field and deformation was followed by heat treatment above β transus at the recrystallisation stage. The object of this stage was to impart sufficient strain (plastic deformation) in order to introduce enough dislocations to drive complete recrystallisation of the β phase and to produce a smaller β grain size so that the effective variant size is smaller [1, 3]. Dislocations are effectively stored energy which behave as a driving force for grain growth when heated above β transus. By introducing a large amount of deformation, the level of potential nuclei also increases. Therefore in having a greater number of nuclei as well as more potential driving force for the grain growth more grains would potentially start to grow rapidly until they are effectively pinned by each other and therefore by quenching (rapid cooling) the material quickly, grain growth speed is stopped and recrystallisation will occur hence resulting in a finer grain size.

Work done by Semiatin et al. [93] stated the strain levels needed to achieve a globularized α morphology. This was performed using finite element methods to predict local strain variation found during uniaxial compression of Ti 6Al-4V containing the lamellar α structure. Results showed that dynamic globularization initiated at local strains of the order 0.75 to 1.0 and strains of order of 2.0 to 2.5 were necessary to attain almost full globularization.

Additional work also undertaken by Semiatin [93] on Ti 6Al-4V during forging showed that in order to begin α phase globularization, local strains around 0.5 to 1.0 were required, however, achieving complete α phase globularization depended somewhat on combination of the starting microstructure and deformation temperature. When deformed at temperature around 815°C, materials (containing fine acicular α (0.25 μm)) required local strains of the order of 1.4 to attain complete globularization. However when the temperature was increased to around 955°C material containing the acicular microstructure required the same amount of local strain, of the order of 2.5, in order to reach complete globularization similar to material containing coarser α lamella (5 μm) microstructure [93].

Note that the kinetics of the α phase globularization not only depend on the amount of total strain but also show a strong dependence on the method of deformation used to provide the strain [93].

5.3 Results and discussions

5.3.1 Microstructure analysis

Digital image analysis software KS400 was used to determine the volume fraction of α_p, its size distribution and its aspect ratio distribution (for a more detailed description of the procedure involved see Chapter 3).

The volume fraction of α_p as a function of location within the billet is shown in Figure 5.9.

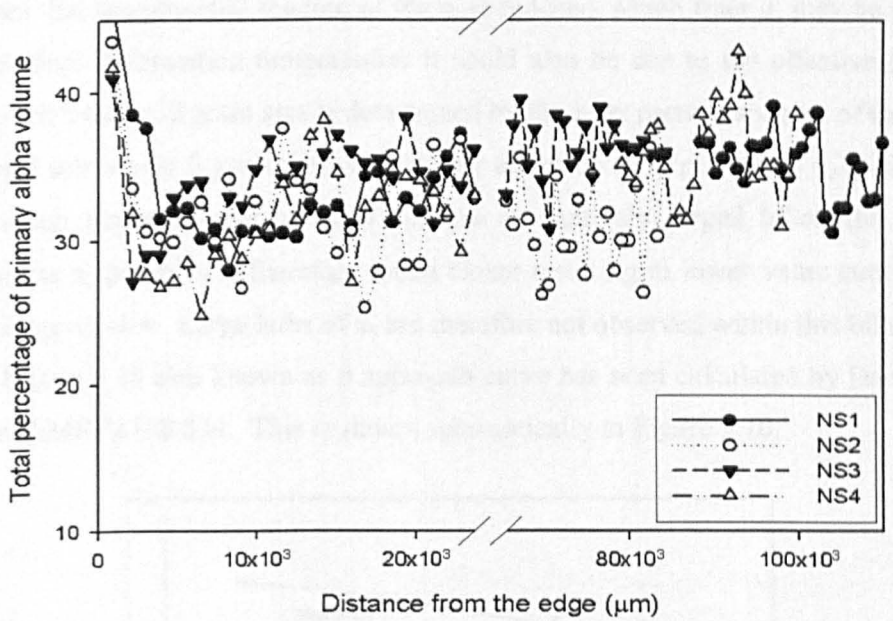

Figure 5.9 The total percentage and the distribution of the α_p at the edge and centre of each sample (alternatively forged billet).

Figure 5.9 shows that the volume fraction of α_p varies from approximately 25 % to 38 % with the exception of the extreme edge (α_p volume fraction is approximately 50% at the edge). Figure 5.9 also clearly shows that microstructure of the alternatively forged billet is not as homogeneous as the previous billets.

The amount of α phase increases rapidly with decreasing temperature especially at temperatures approaching the β transus. Deformation lower than transus temperature (close to the β transus), where volume fraction α is low, means α phase is deformed only to a small extent relative to the total deformation. This therefore results in insufficient strain to start a dynamic or static globularization on the α phase during deformation and during subsequent annealing [94].

A slight increase in the total percentage of α_p volume at the centre of the billet is also observed. This may be due to the cooling rate being slower at the centre of the billet in comparison to its edge.

Deformation temperature has been found to greatly affect the homogeneity of the deformation where lower temperatures invariably lead to more localised deformation for any given strain rate [94]. The globularization process favours areas of high strain or localised deformation, which can result in inhomogeneous globularization during deformation and upon subsequent annealing.

By comparing the micrographs in Figure 5.6 to those in Figure 3.11, Chapter 3, it appears that the potential spacing of the α_s is reduced. Much finer α_s may be due to a different final deformation temperature. It could also be due to the effective β grains being much smaller. β grain size is determined by the inter particle spacing of the α_p. As mentioned previously β grains grow until they are effectively pinned by α_p grains. Due to the much larger content of α_p within the alternatively forged billet, the spacing between the α_p particles is therefore much closer resulting in lower value content of β and small grain size. Large laths of α_s are therefore not observed within this billet.

Figure 5.10 also known as β approach curve has been calculated by Daeubler et al. [13] for TIMETAL® 834. This is shown schematically in Figure 5.10.

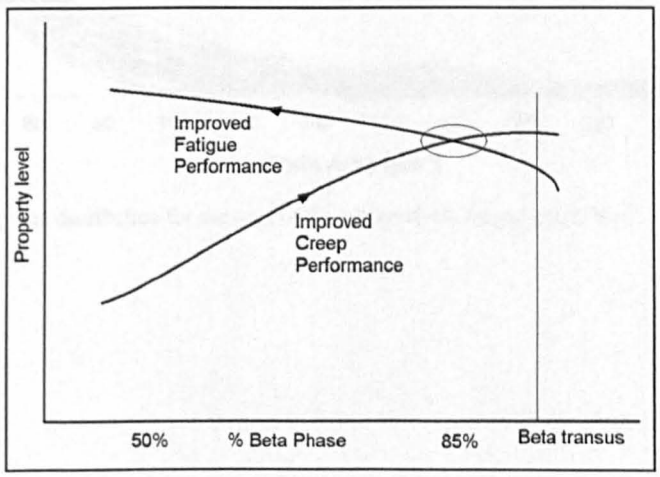

Figure 5.10 Schematic optimal fatigue-creep properties for TIMETAL® 834 [13].

Figure 5.10 shows that the desired optimisation of both fatigue and creep performance is reached when the volume fraction of the α_p phase is between 15-20%. As previously explained in Figure 5.9 it can be acknowledged that the microstructure is not homogeneous within the alternatively forged billet therefore regions with different

contents of α will be present which may result in poor creep resistance (localised creep) locally but improved fatigue. Therefore by having an inhomogeneous microstructure there may be inhomogeneous mechanical properties. This non-uniformity is undesirable within aerospace applications.

As in Chapter 3, a detailed analysis of the α_p size distribution as a function of location was calculated for each sample. This is shown in Figure 5.11. Using micrographs from different sections of each sample, the graphs below compare the grain area and the percentage of total α_p present.

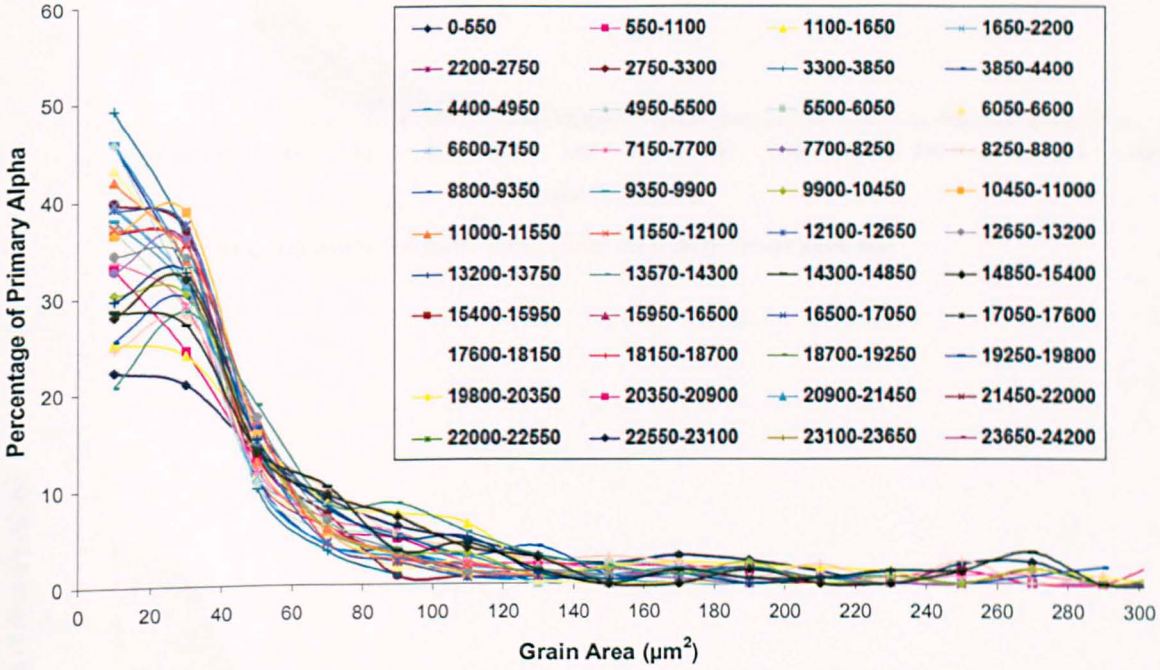

a) α_p area distribution for the edge of the alternatively forged billet, NS1.

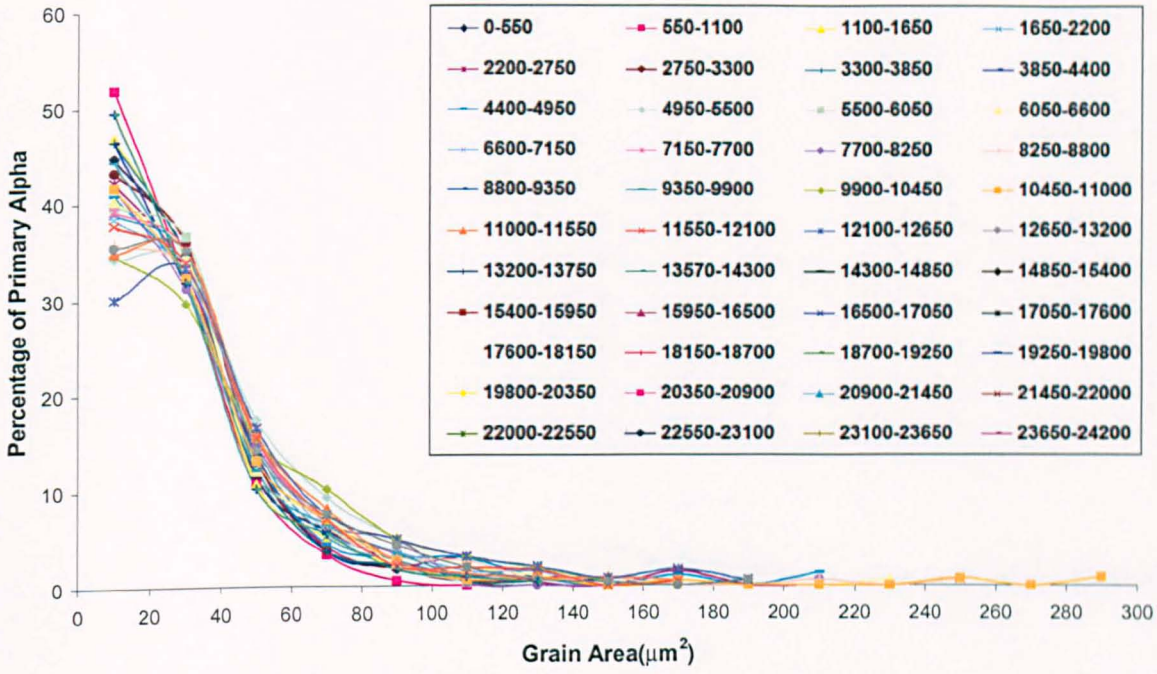

b) α_p area distribution for the centre of the alternatively forged billet, NS1.

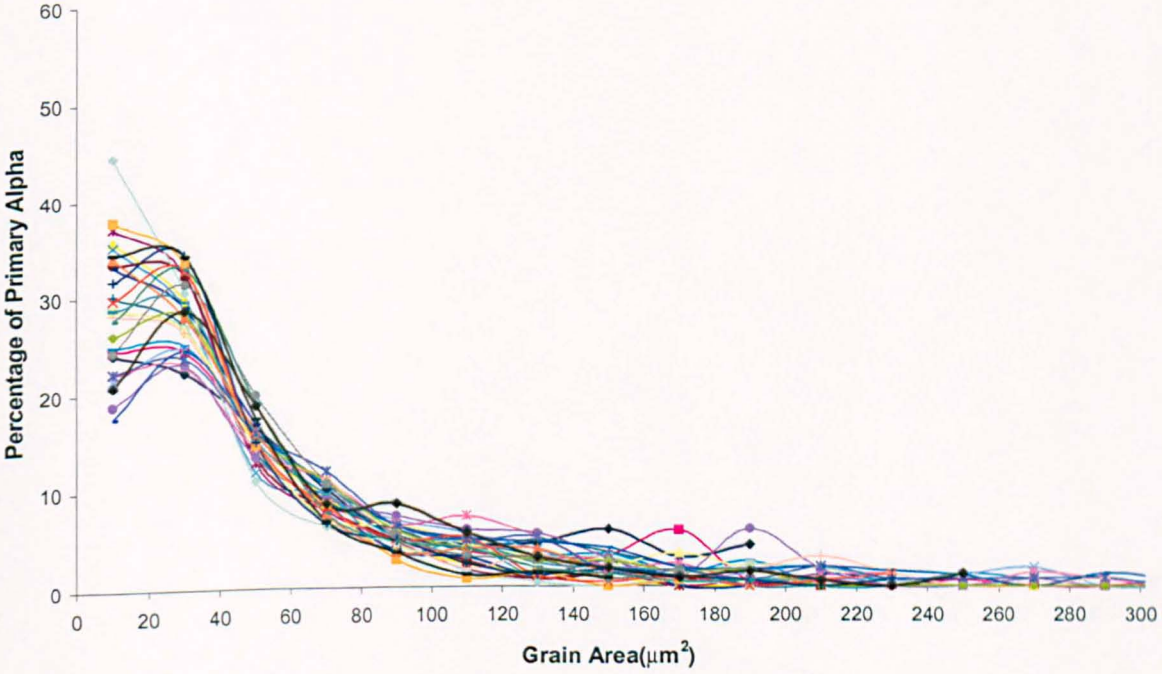

c) α_p area distribution for the edge of the alternatively forged billet, NS2.

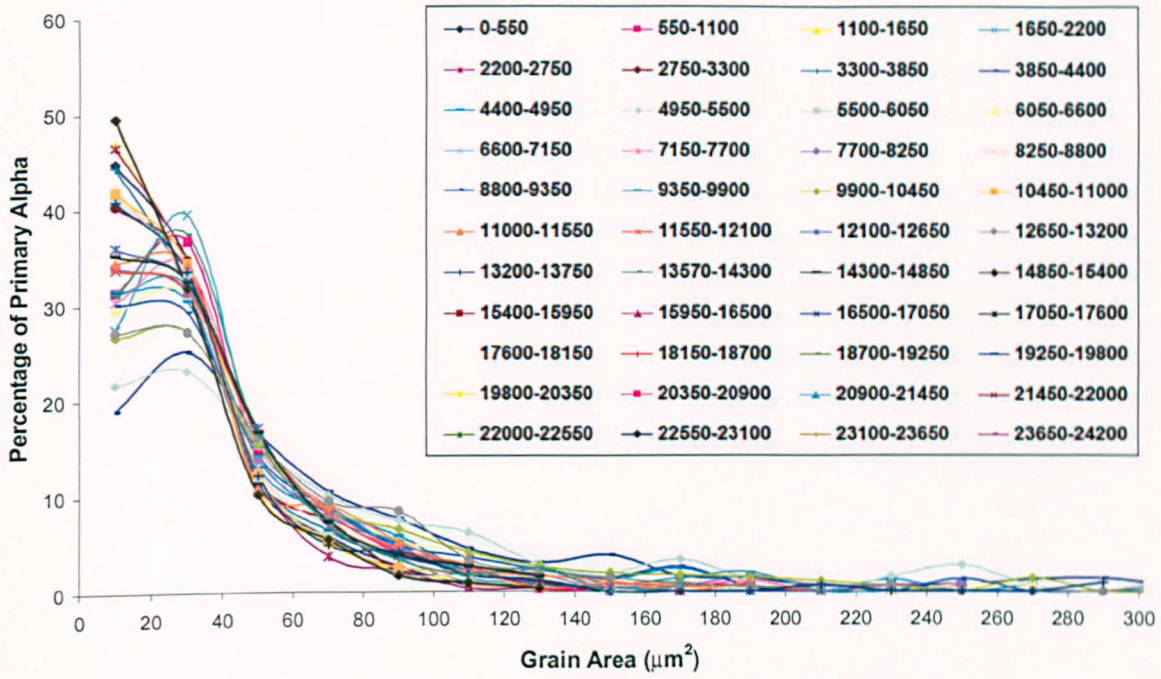

d) α_p area distribution for the centre of the alternatively forged billet, NS2.

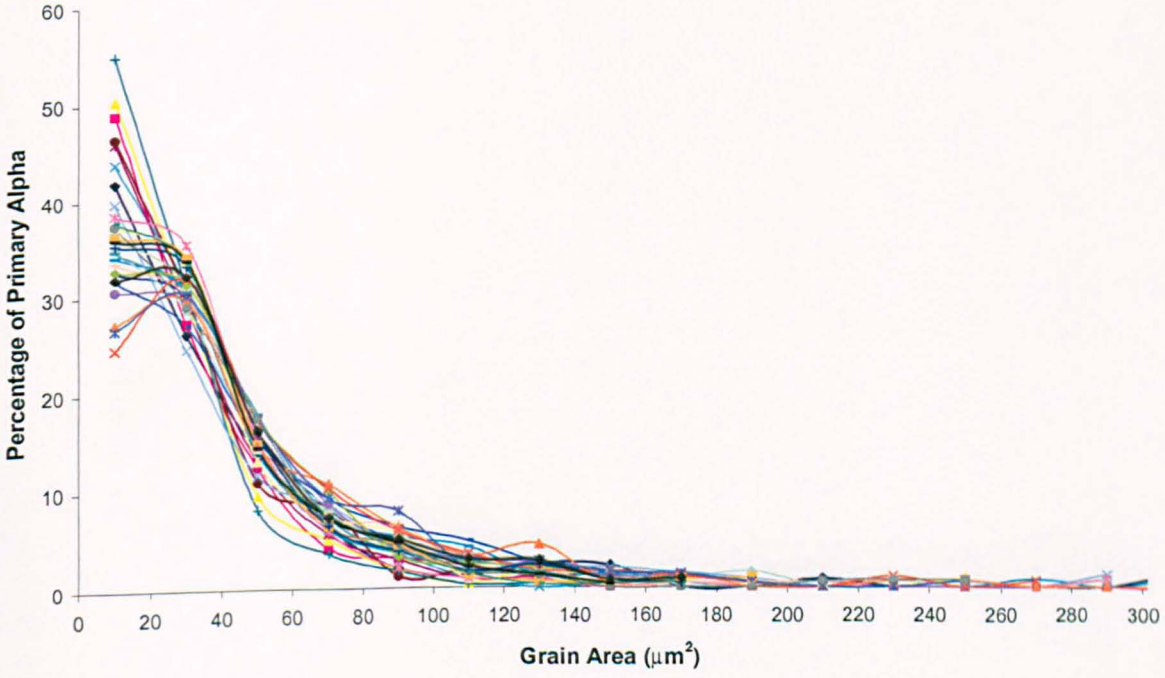

e) α_p area distribution for the edge of the alternatively forged billet, NS3.

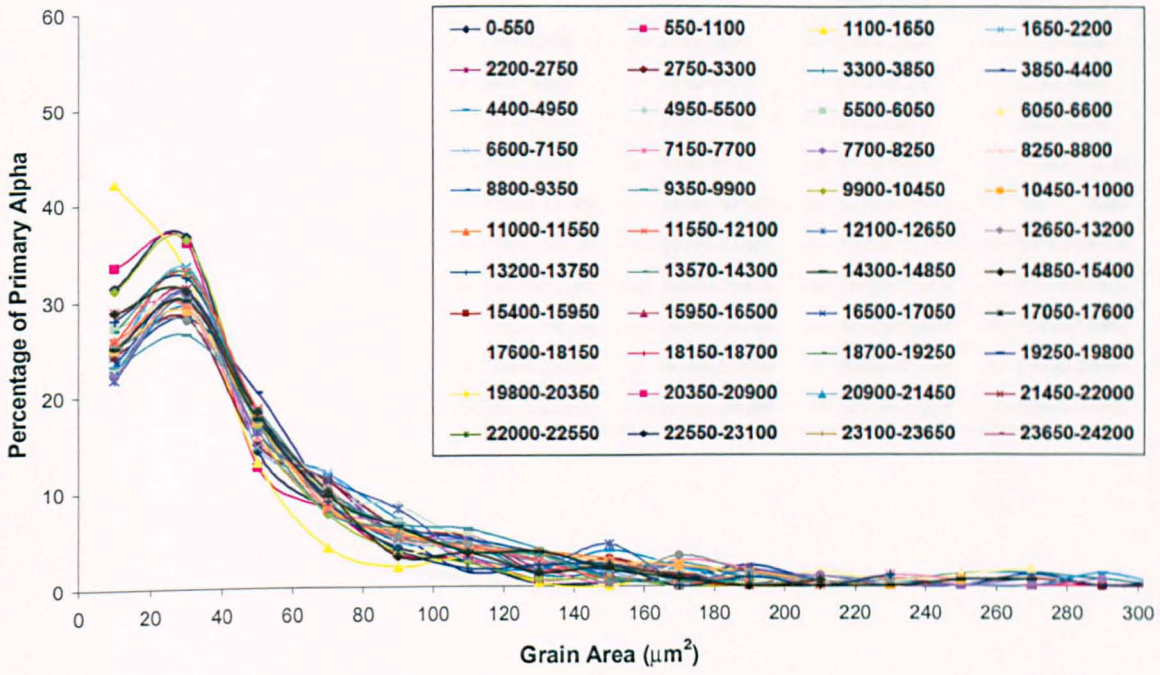

f) α_p area distribution for the centre of the alternatively forged billet, NS3.

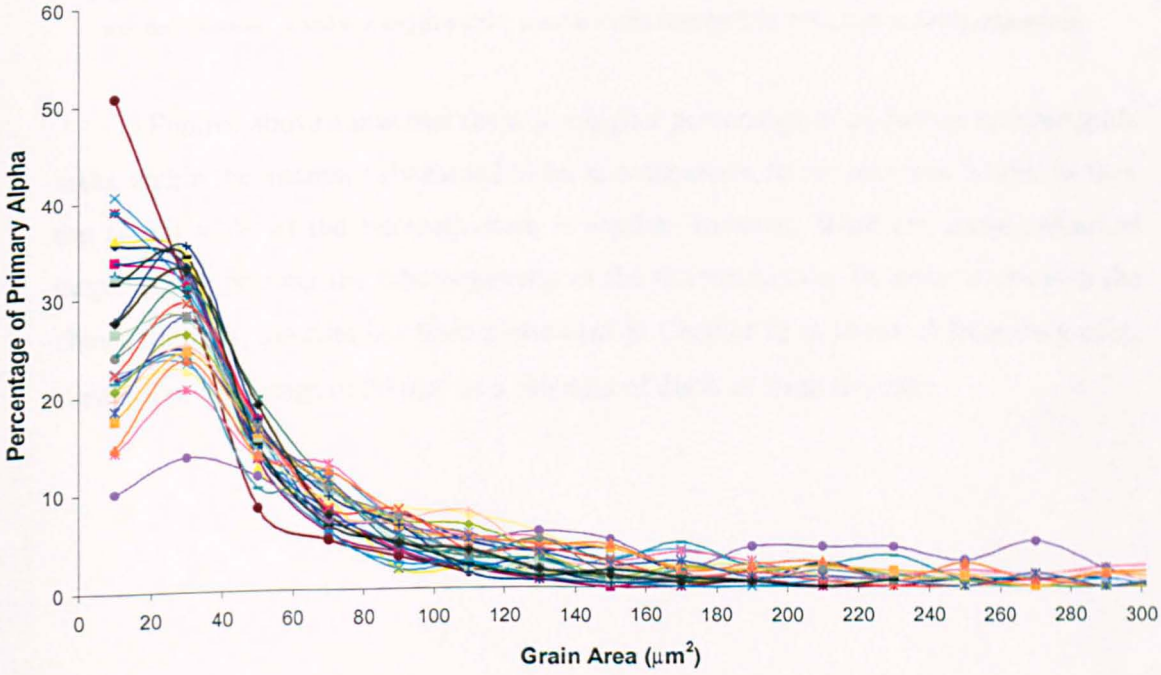

g) α_p area distribution for the edge of the alternatively forged billet, NS4.

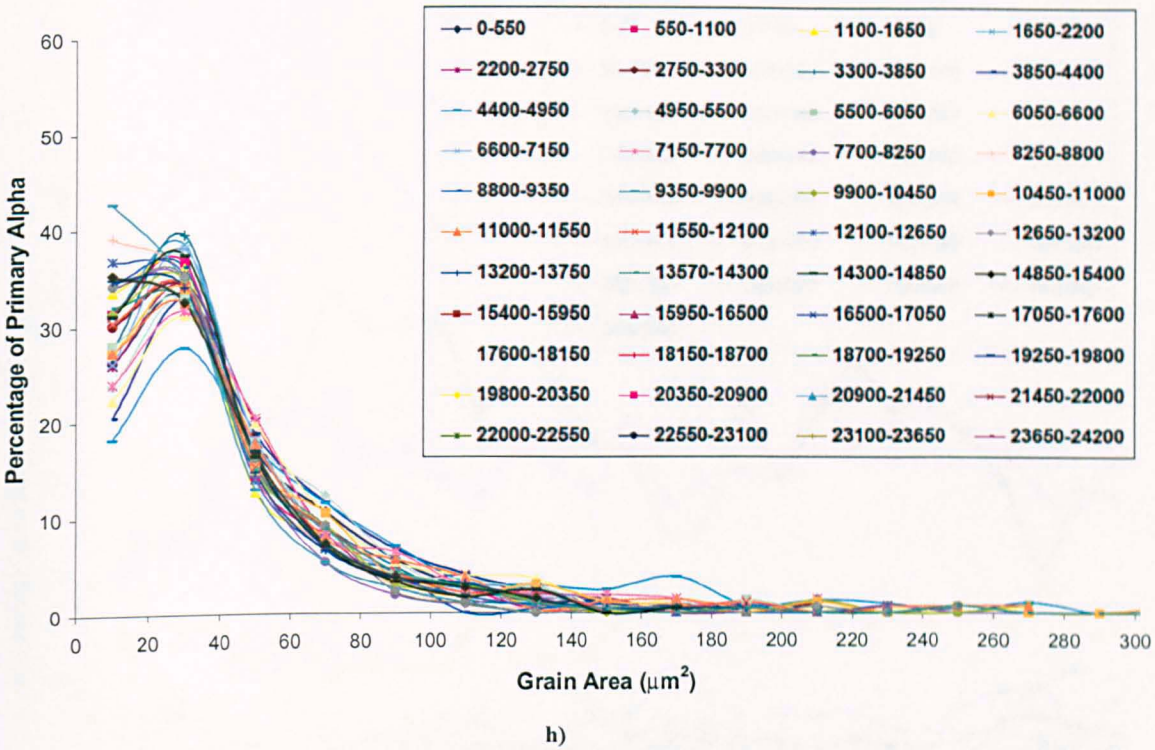

h)

Figure 5.11 α_p area distribution at the edge **(a,c,e,g)** and centre **(b,d,f,h)** of the alternatively forged billet at the selected locations. **a** and **b**; **c** and **d**; **e** and **f**; **g** and **h** are for samples NS1, NS2, NS3 and NS4 respectively.

Figures above show that there is a higher percentage of α_p having smaller grain areas within the alternatively forged billet in comparison to the previous billets. In fact, the actual scale of the microstructure is smaller however, there are some unwanted larger grains proving the inhomogeneity of the microstructure. In order to confirm the above findings, the data has been plotted (as in Chapter 3) in terms of frequency of α_p particles in groupings of 20 μm^2 as a function of distance from the edge.

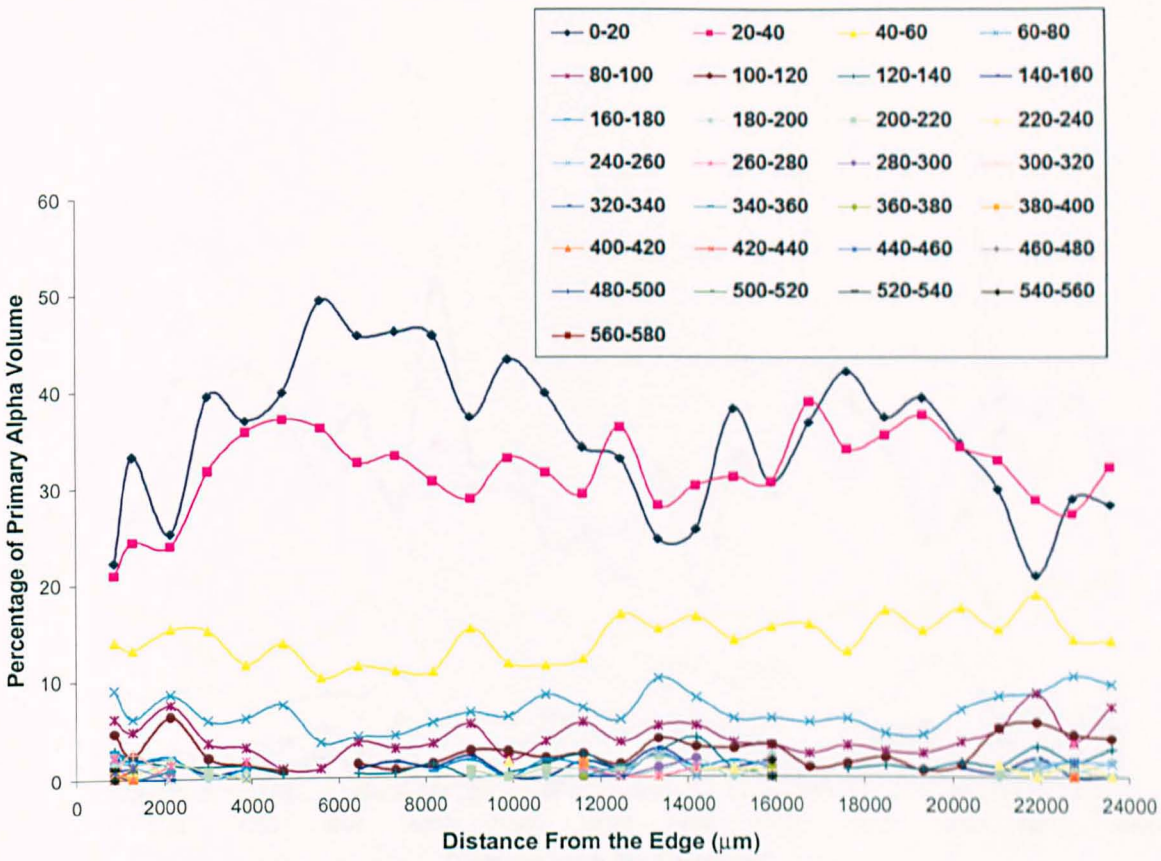

a) The distribution of α_p particle as a function of distance at the edge (NS1).

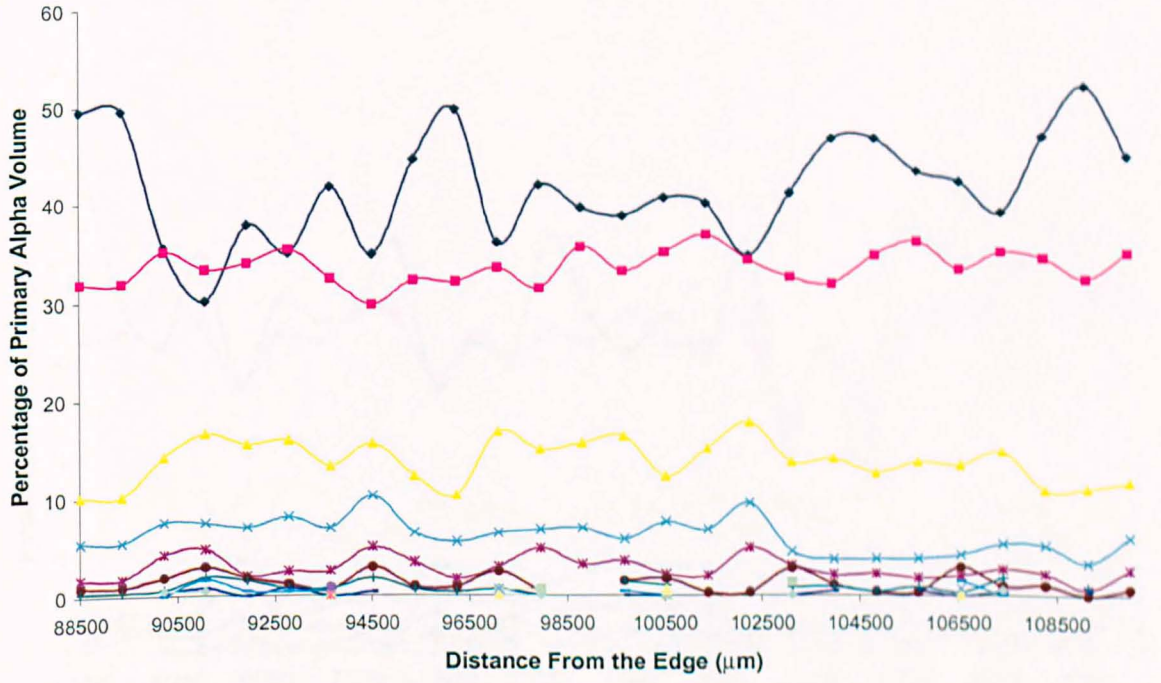

b) The distribution of α_p particle as a function of distance at the centre (NS1).

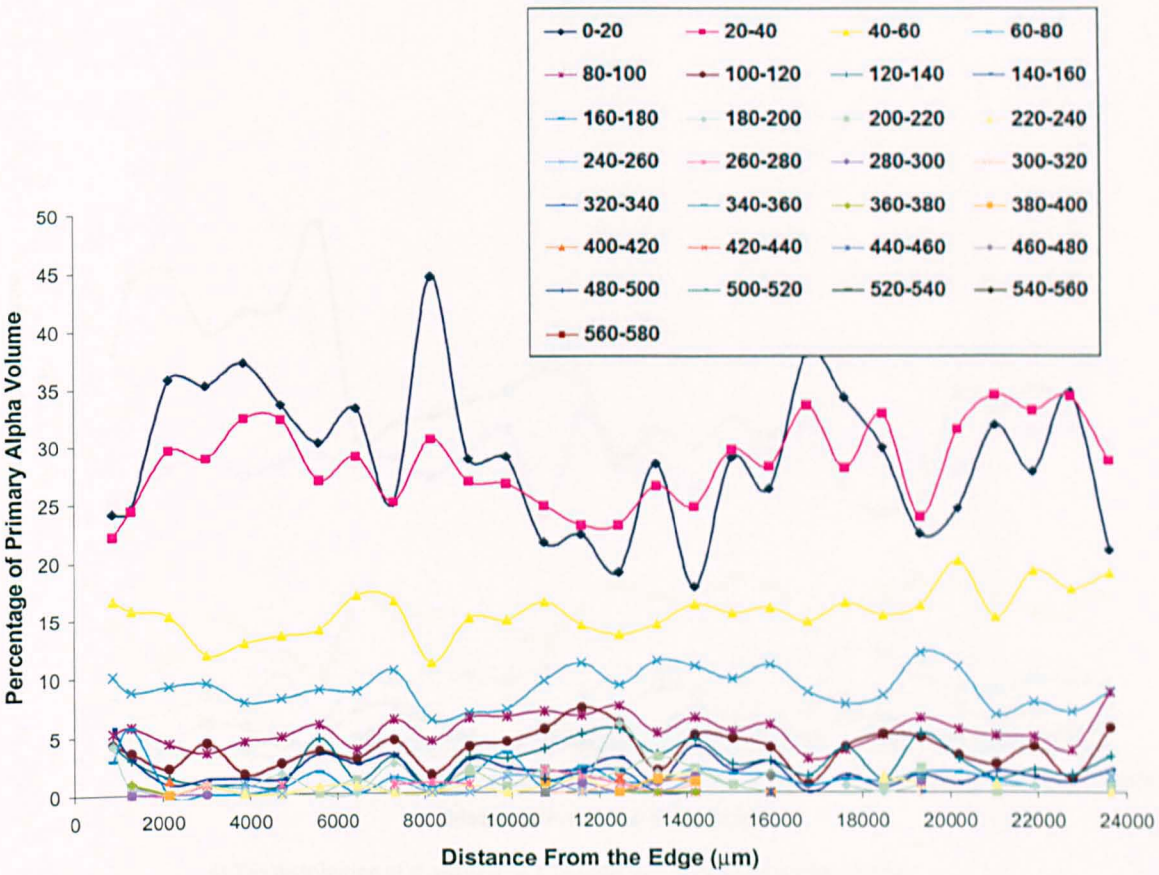

c) The distribution of α_p particle as a function of distance at the edge (NS2).

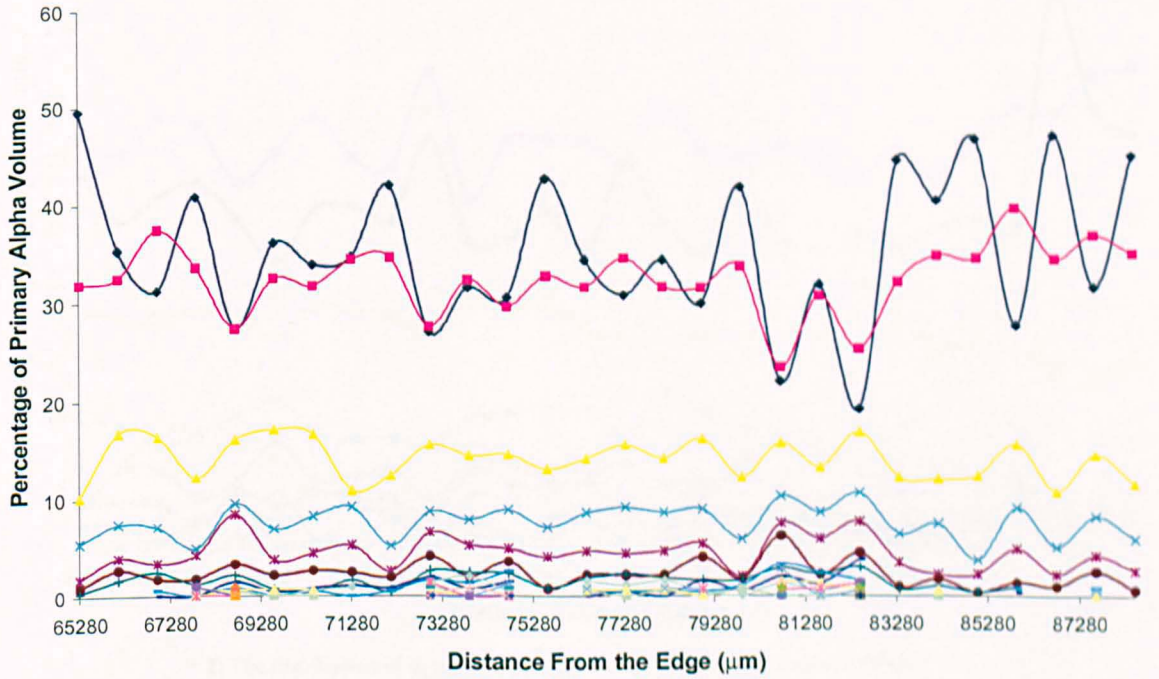

d) The distribution of α_p particle as a function of distance at the centre (NS2).

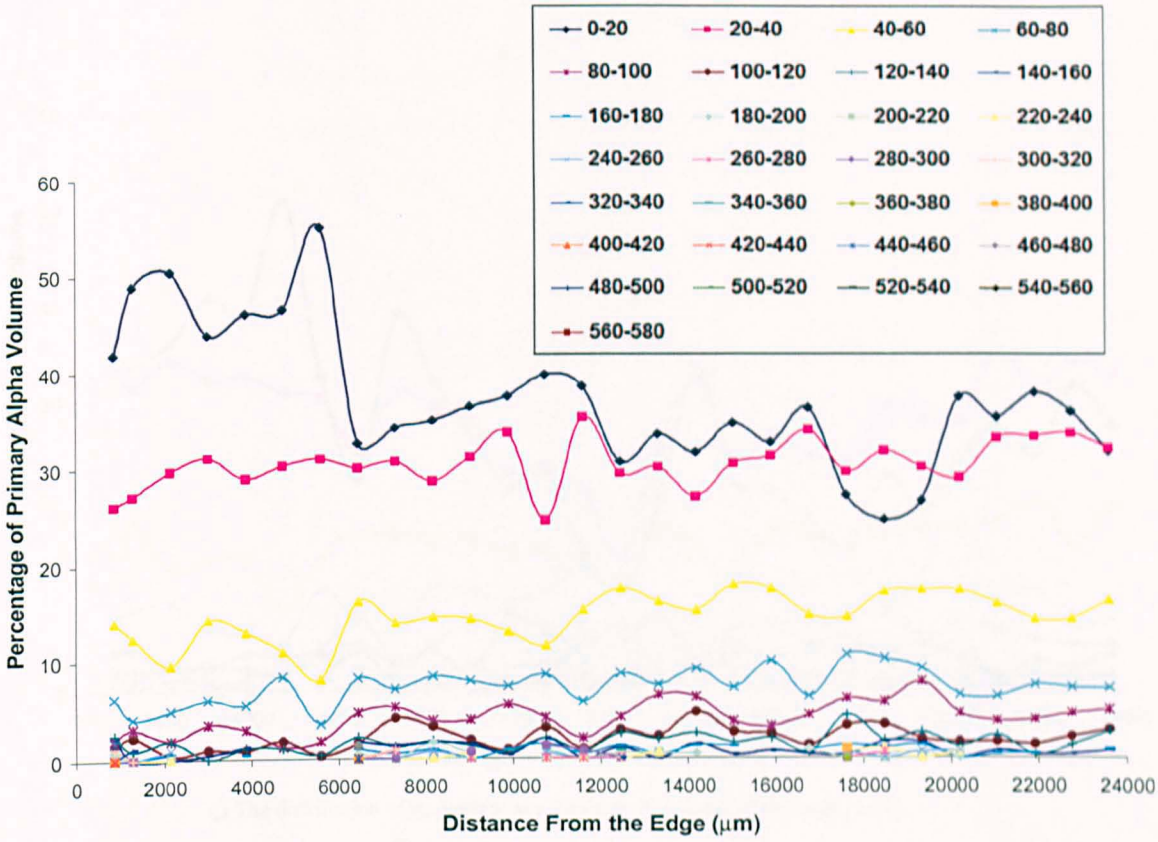

e) The distribution of α_p particle as a function of distance at the edge (NS3).

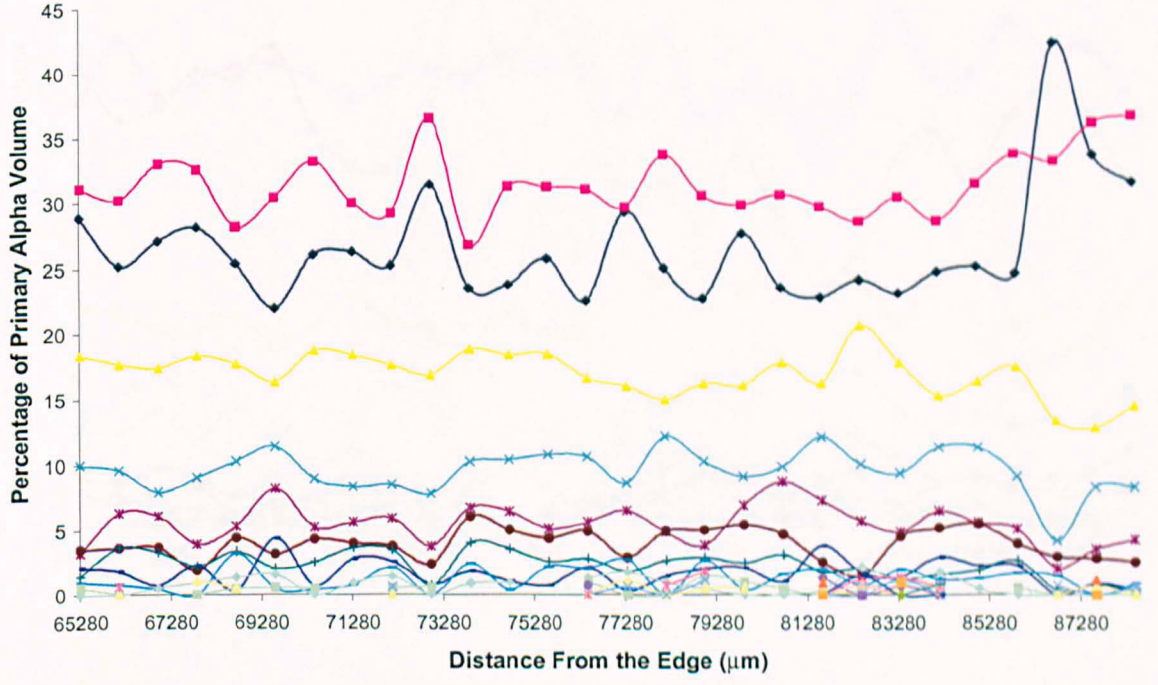

f) The distribution of α_p particle as a function of distance at the centre (NS3).

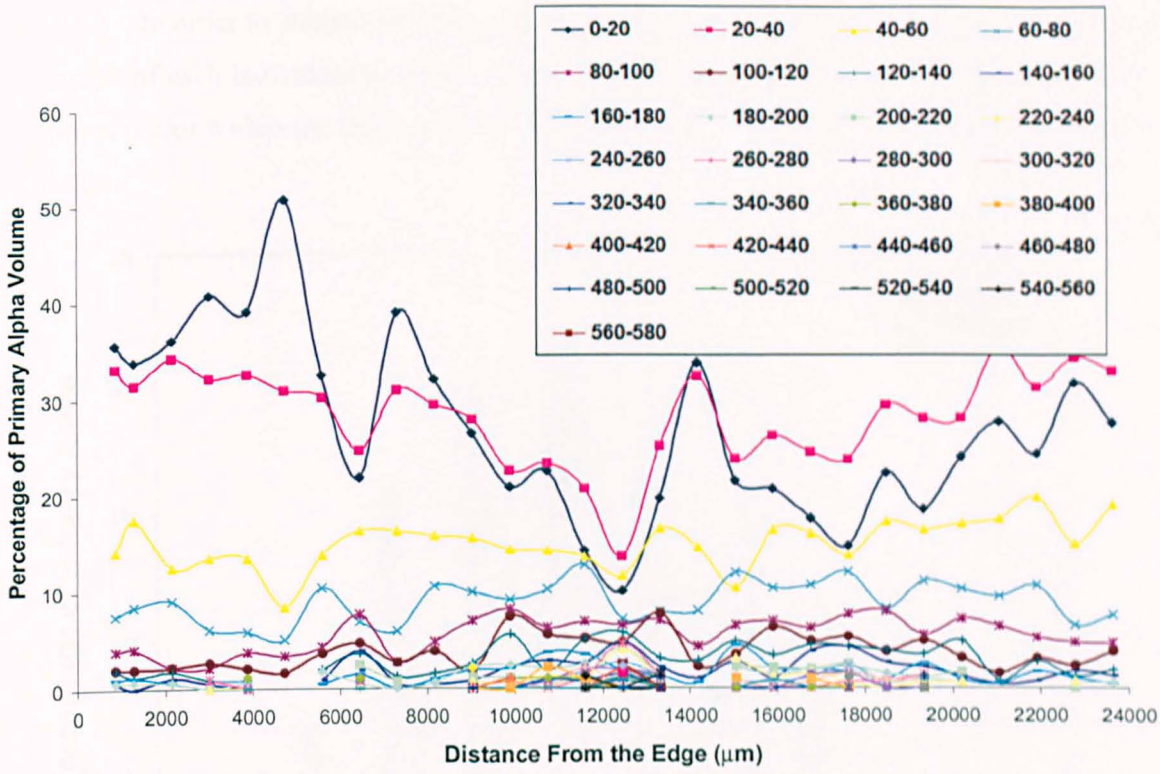

g) The distribution of α_p particle as a function of distance at the edge (NS4).

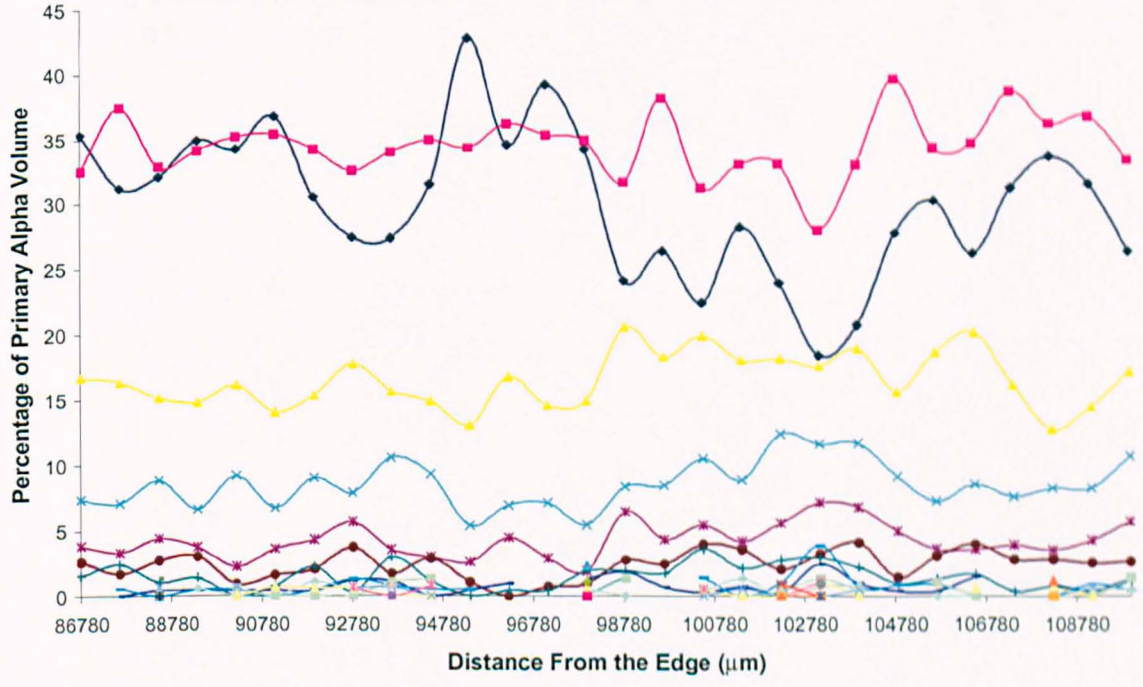

h)

Figure 5.12 The distribution of α_p particles as a function of distance at the edge (**a, c, e, g**) and centre (**b, d, f, h**) of the alternatively forged billet. **a** and **b**; **c** and **d**; **e** and **f**; **g** and **h** are for samples NS1, NS2, NS3 and NS4 respectively.

In order to analyse the shape of the α_p particles (the ratio of the width against the length of each individual α_p grain), Figure 5.13 compares the aspect ratio distribution of the particles within the entire area of each sample taken from the edge and centre of the billet.

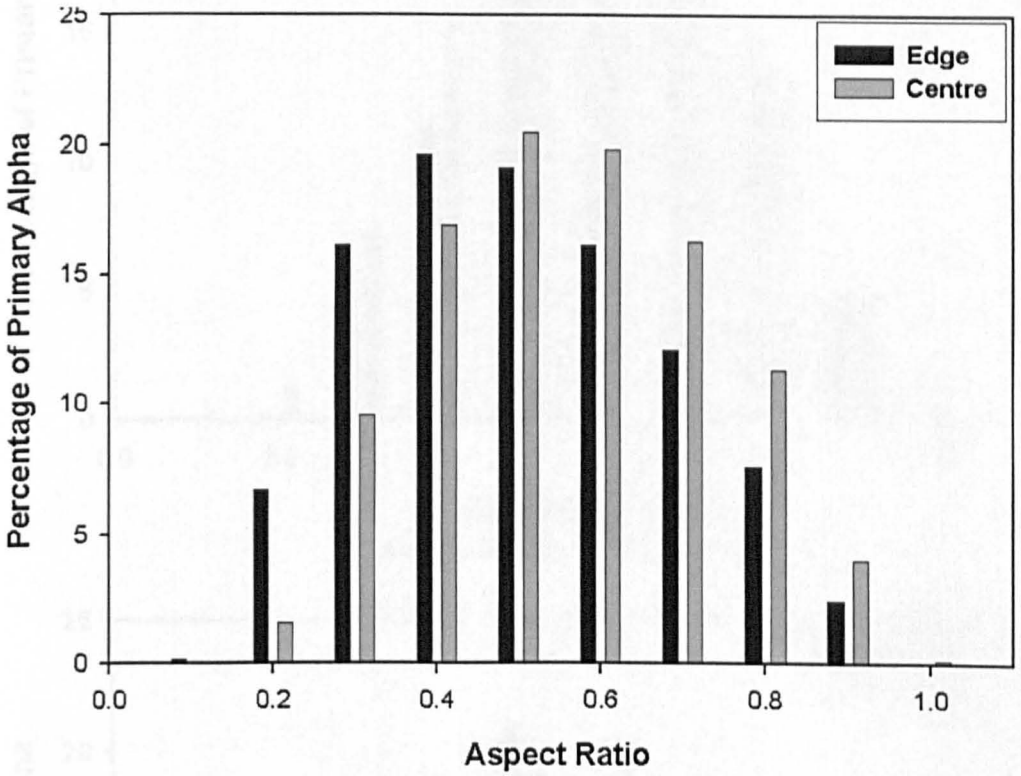

a) The aspect ratio of the α_p particles for NS1.

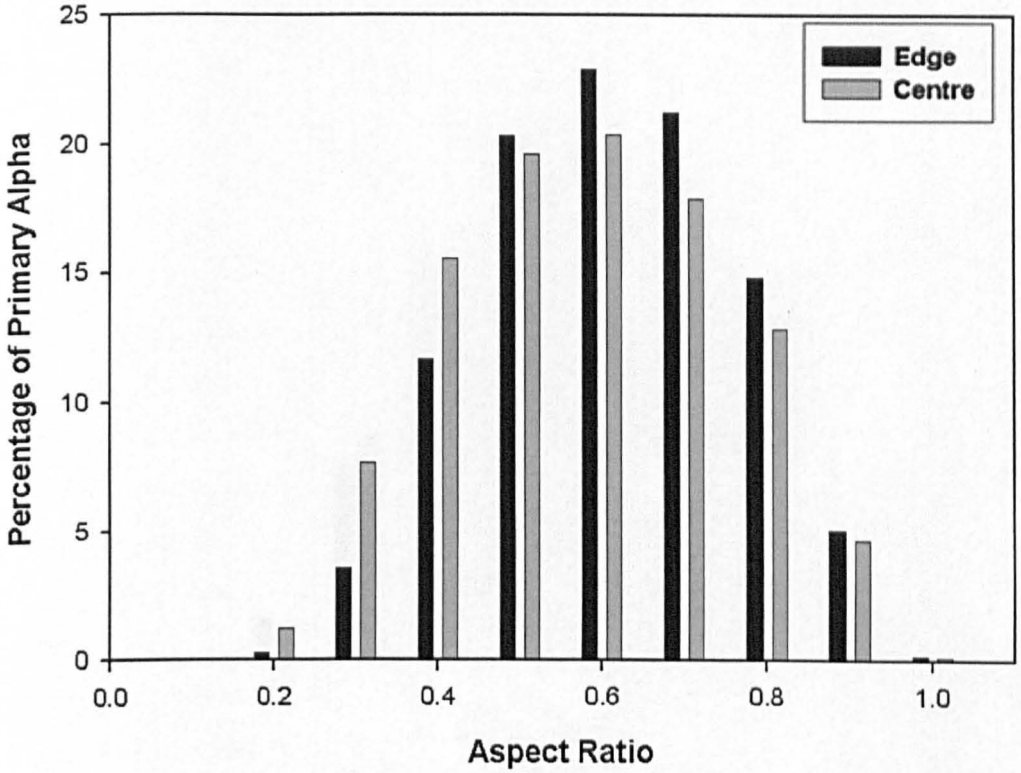

b) The aspect ratio of the α_p particles for NS2.

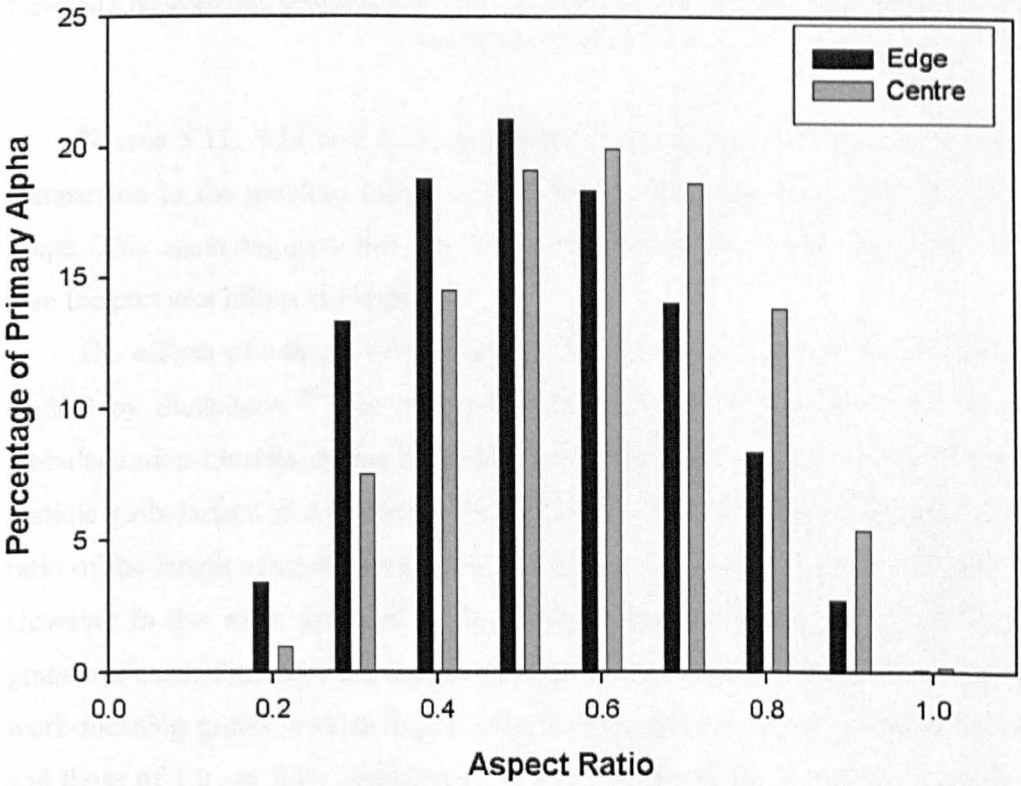

c) The aspect ratio of the α_p particles for NS3.

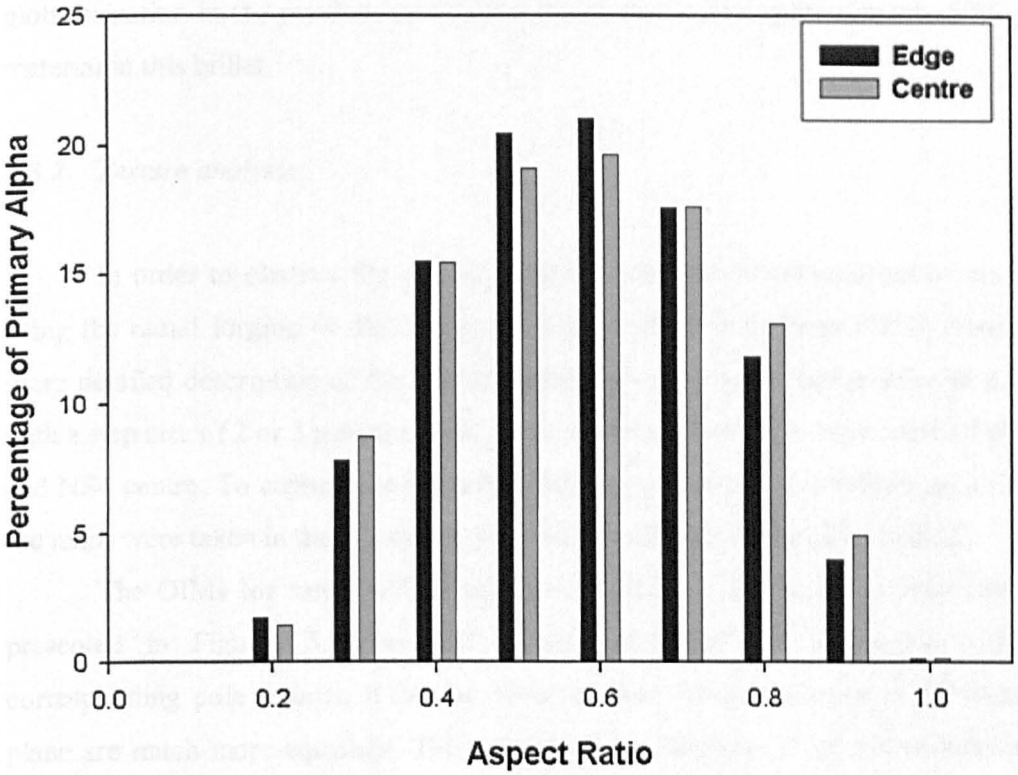

Figure 5.13 The aspect ratio of the α_p particles for the alternatively forged billet at the edge and centre for samples **a)** NS1 **b)** NS2 **c)** NS3 **d)** NS4.

Figures 5.11, 5.12 and 5.13 show that the actual scale of the microstructure in comparison to the previous billets is smaller but the grains are longer and thinner in shape. This again suggests that the level of globularization within this billet is lower than the previous billets in Chapter 3.

The effects of amount of deformation on the static globularization kinetics were studied by Stefansson [93] for material deformed and annealed at 955°C. The static globularization kinetics during annealing was quantified by considering an α plate or particle globularized if it possesses an aspect ratio of 2.0 or less. Stefansson used the ratio of the length against width of each individual α_p grains to determine aspect ratio. However in this work the ratio of the width against the length of each individual α_p grain was used. Therefore the aspect ratio of 2 used by Stefansson relates to 0.5 in this work meaning grains with an aspect ratio of less than 0.5 have not been globularized and those of 1.0 are fully globularized. Therefore, based on Stefansson's definition of globularization, approximately 93% of the material has reached the critical condition for

globularization in the previous two billets in comparison to approximately 59% of the material in this billlet.

5.3.2 Texture analysis

In order to observe the effects of terminating the β recrystallisation stage and using the radial forging (4 die) machine on the texture, four large EBSD maps (for a more detailed description of the EBSD method involved see Chapter 4) were acquired with a step size of 2 or 3 μm on the reference samples, NS1 edge, NS1 centre, NS4 edge and NS4 centre. To capture the maximum number of macrozones within each OIM all the maps were taken in the transverse plane (perpendicular to the billet axis, Z).

The OIMs for samples NS1 edge, NS1 centre, NS4 edge and NS4 centre are presented in Figures 5.14 to 5.17 using Euler and IPF colouring with their corresponding pole figures. It can be observed that the macrozones in the transverse plane are much more equiaxed. The colours of the majority of the macrozones within each OIM are either red or blue indicating that the macrozones have two main orientations (IPF colouring).

Grains are shown in blue when their c-axis is perpendicular to the billet axis, representing the prismatic plane (10-10). However when the grain's c-axis is aligned with the billet axis, the grains are shown in red representing the basal plane (0001). Also present were more scattered groups of green grains having their (10-11) plane lying in the transverse plane.

It appears that there is a difference in the ratio of red and blue macrozones when comparing the centre of the billet to the edge. At the edge of the billet the blue macrozones tend to be greater in number however when moving towards the centre of the billet, blue macrozones start to be replaced by red macrozones.

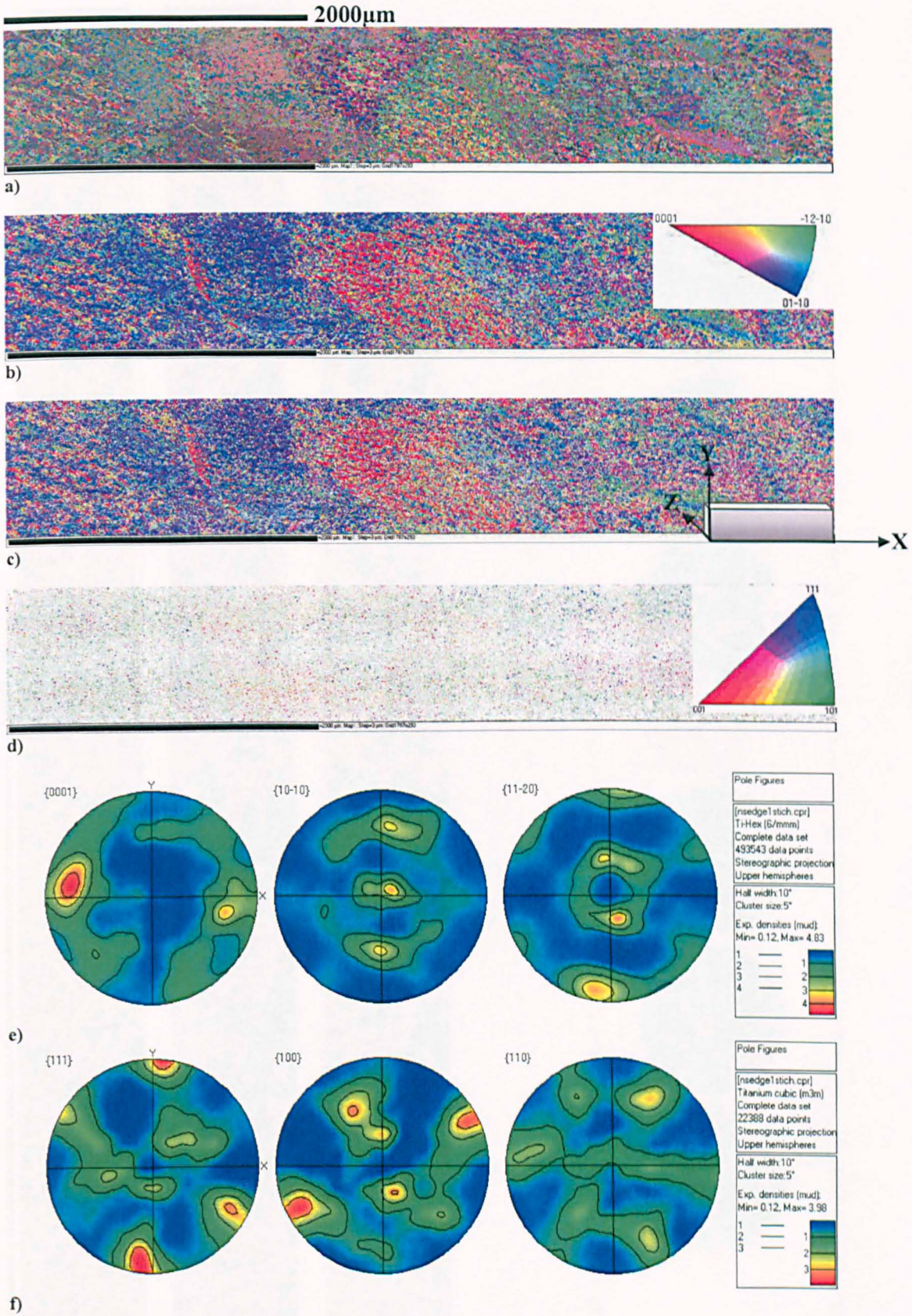

Figure 5.14 Crystal orientation map for NS1 edge. **a)** Euler colouring **b)** IPF colouring **c)** alpha phase only **d)** beta phase only and **e)** alpha **f)** beta phase pole figure from Sample NS1 edge.

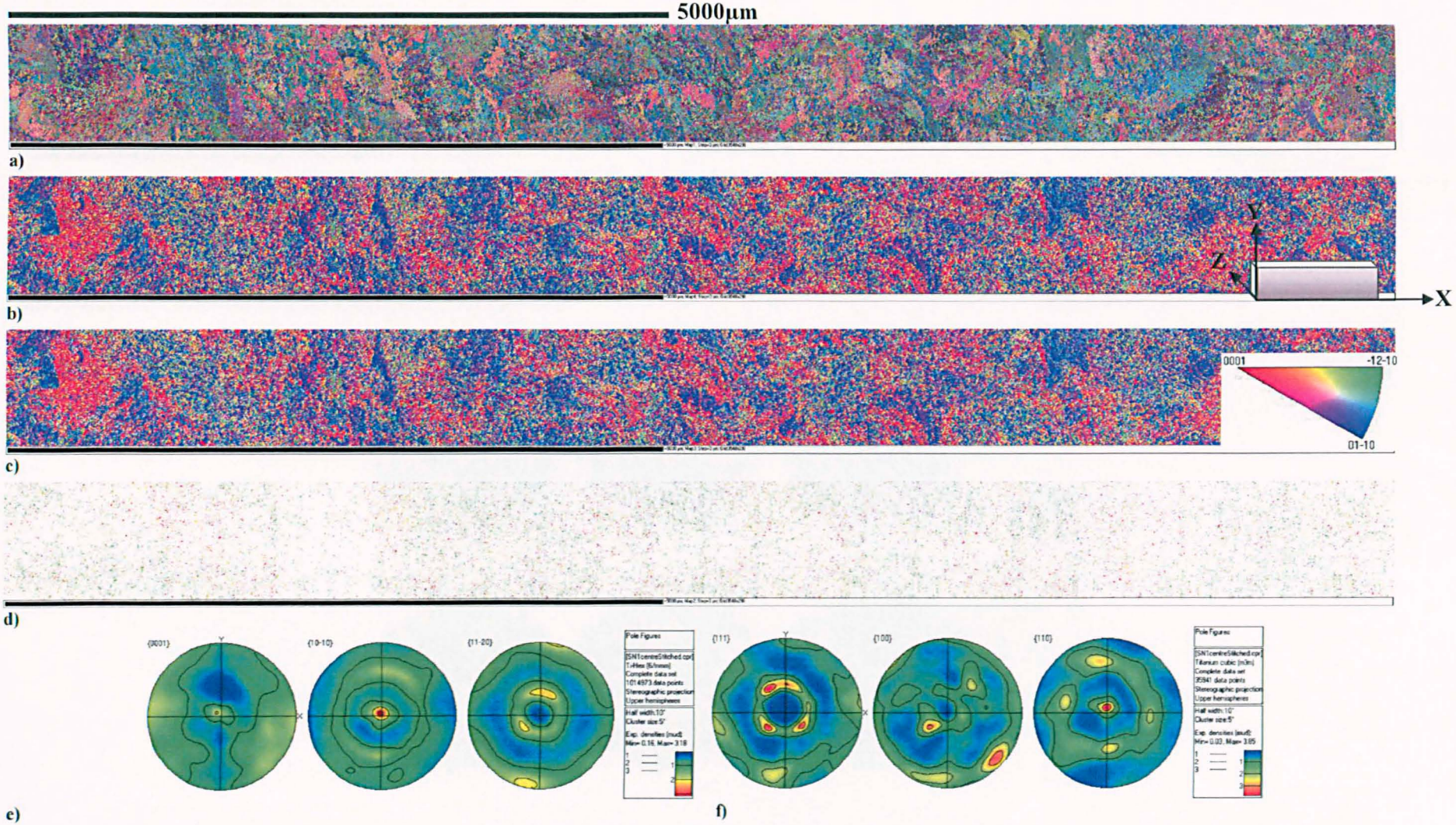

Figure 5.15 Crystal orientation map for NS1 centre. **a)** Euler colouring **b)** IPF colouring **c)** alpha phase only **d)** beta phase only and **e)** alpha **f)** beta phase pole figure from Sample NS1 centre.

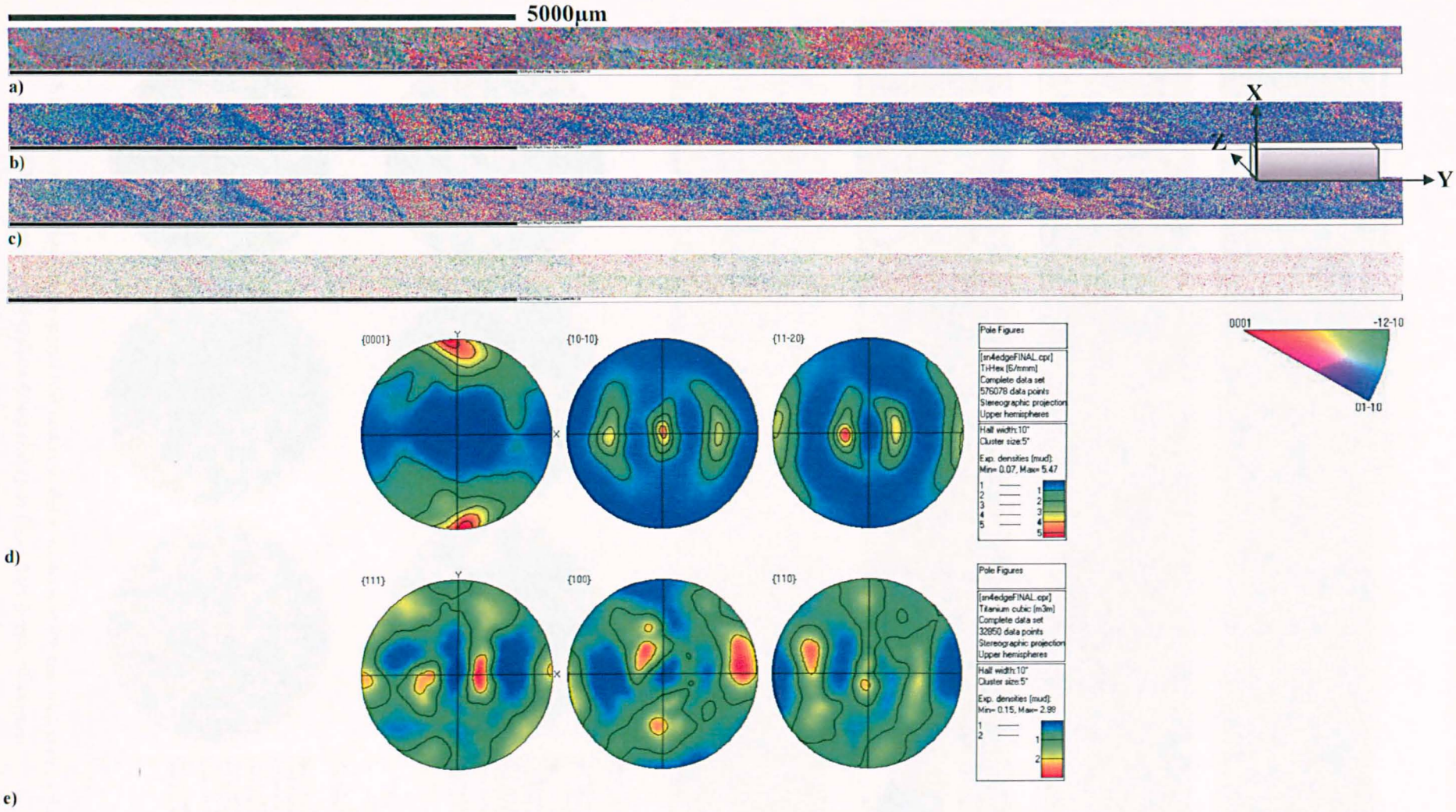

Figure 5.16 Crystal orientation map for sample NS4 edge. **a)** Euler colouring **b)** IPF colouring **c)** alpha phase only **d)** beta phase only and **e)** alpha **f)** beta phase pole figure from NS4 edge.

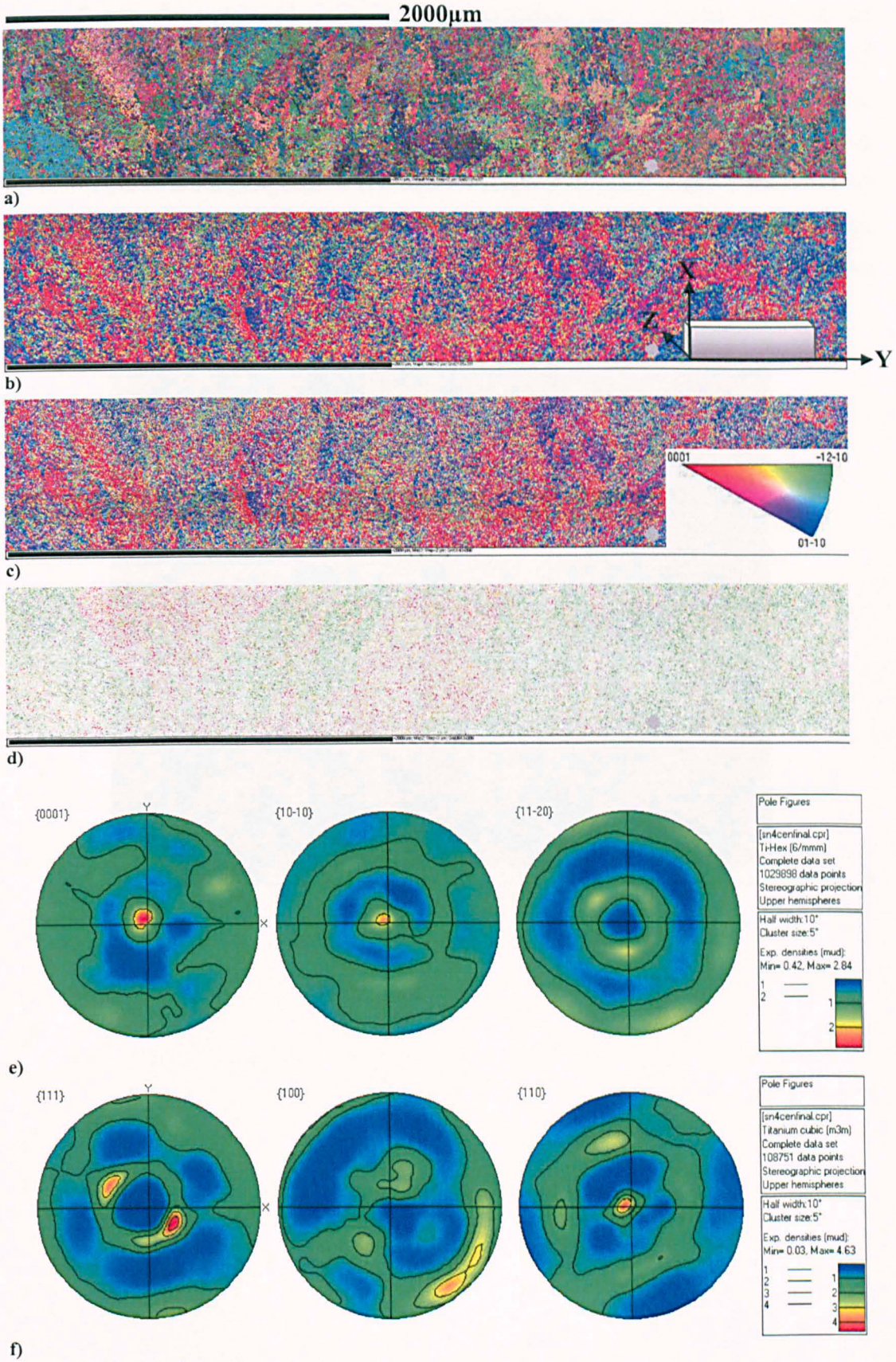

Figure 5.17 Crystal orientation map for sample NS4 centre. **a)** Euler colouring **b)** IPF colouring **c)** alpha phase only **d)** beta phase only and **e)** alpha **f)** beta phase pole figure from Sample NS4 centre.

For a more detailed analysis, high resolution OIM covering an area of approximately 500 x 400 μm^2 was acquired for sample NS4 centre using a step size of 0.3μm. The map is displayed in Figure 5.18. Figures 5.18 a) and b) show the α and the β phase in Euler and IPF colouring respectively. In Figure 5.18 c) and d) the α (α_p and α_s) and β phase are highlighted in IPF colours respectively and finally Figure 5.18 e) represents the α and the β phases in red and blue colours respectively. It can be seen that the majority of the macrozones shown in IPF colours are blue and red with also some diffuse green grains.

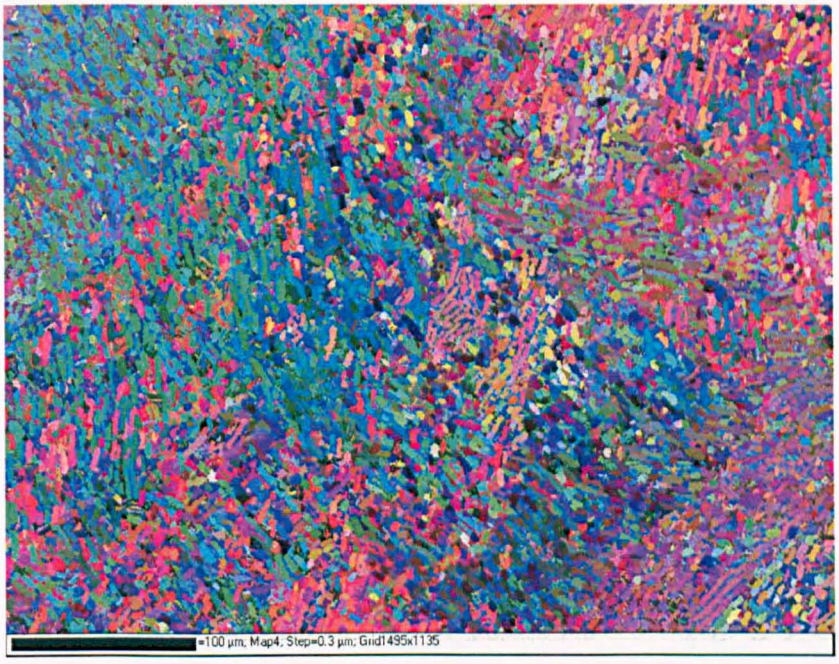

a)

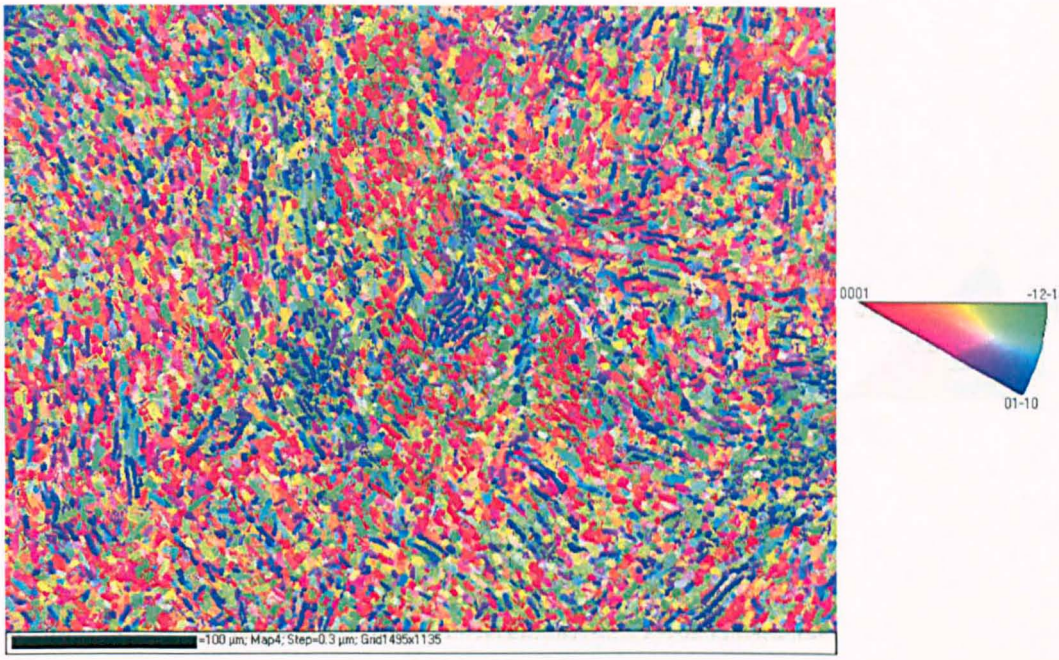
0001
-12-10
01-10
=100 µm; Map4; Step=0.3 µm; Grid1495x1135

b)

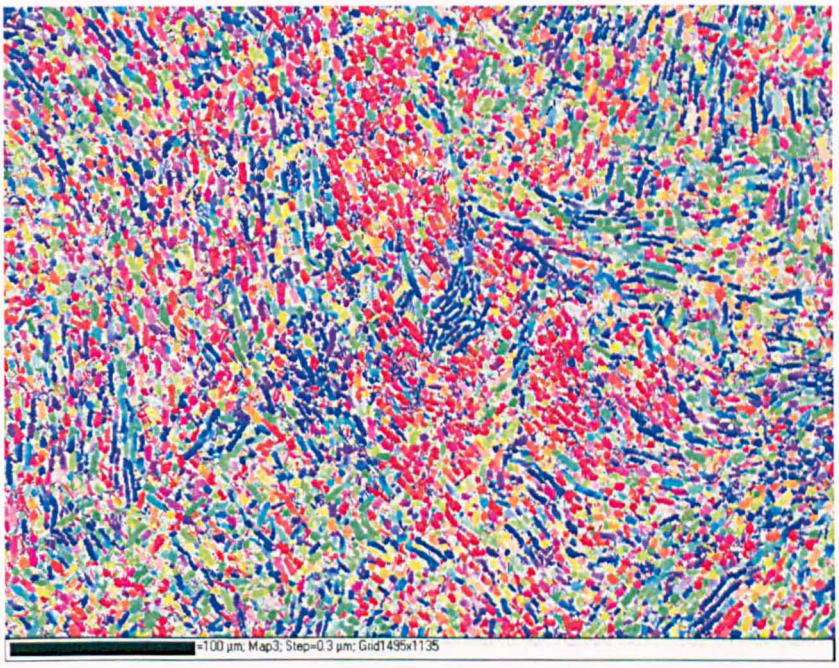
=100 µm; Map3; Step=0.3 µm; Grid1495x1135

c)

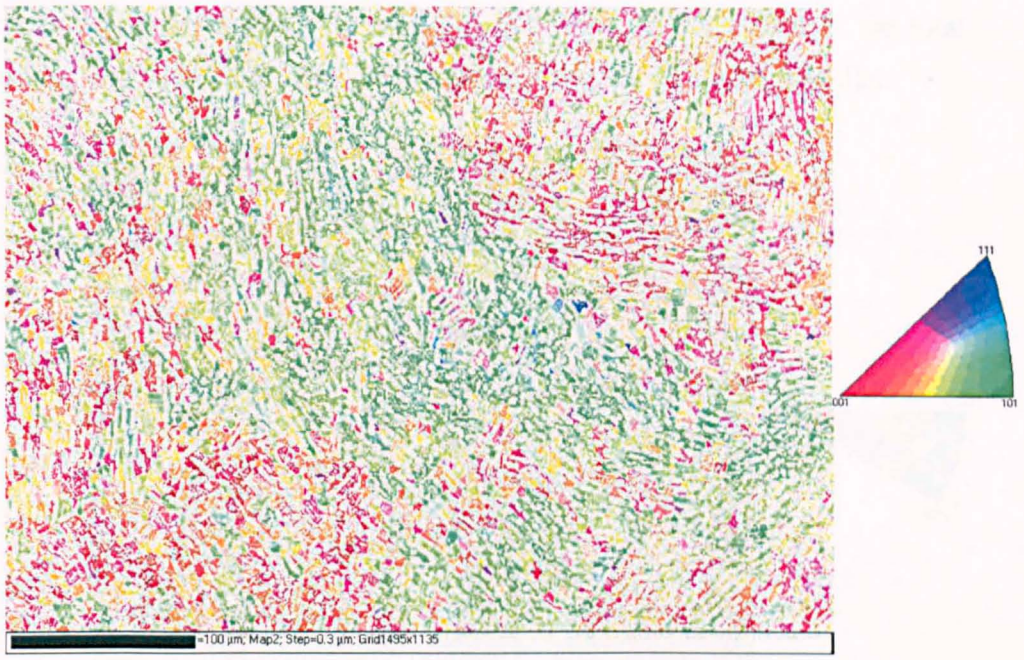

d)

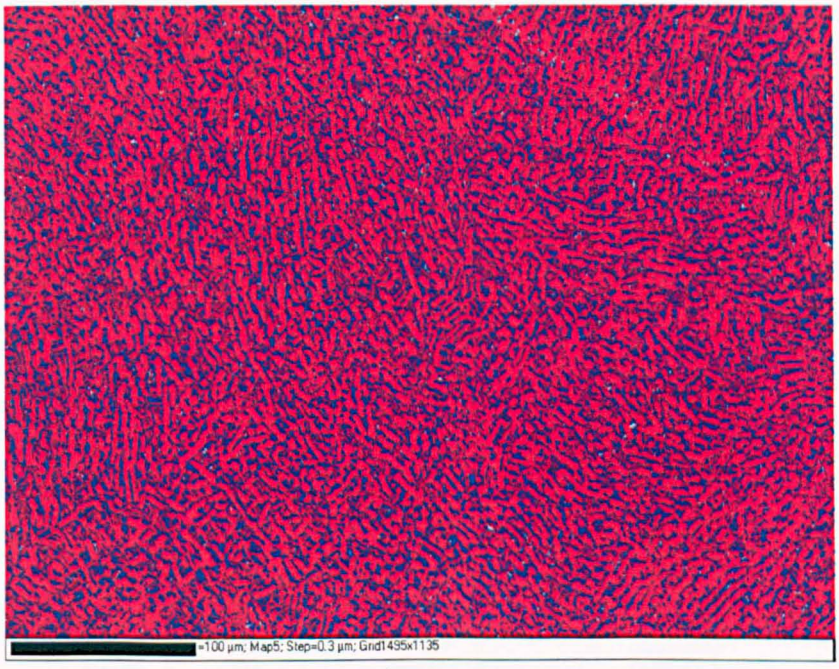

e)

Figure 5.18 Crystal orientation map for sample NS4 centre at higher magnification (using a step size of 0.3µm). **a)** Euler colouring **b)** IPF colouring **c)** alpha phase only **d)** beta phase only **e)** Phase map (colour Red corresponds to the alpha phase and colour blue represents the beta phase).

Two sections taken from the centre of the small billet (Chapter 3) and the alternatively forged billet are shown below in the same scale adjacent to each other (Figure 5.19). By direct comparison it can clearly be seen that the scale of the

microstructure in the alternatively forged billet is smaller. The increase in the total percentage of α_p and finer α_s are also obvious within the alternatively forged billet.

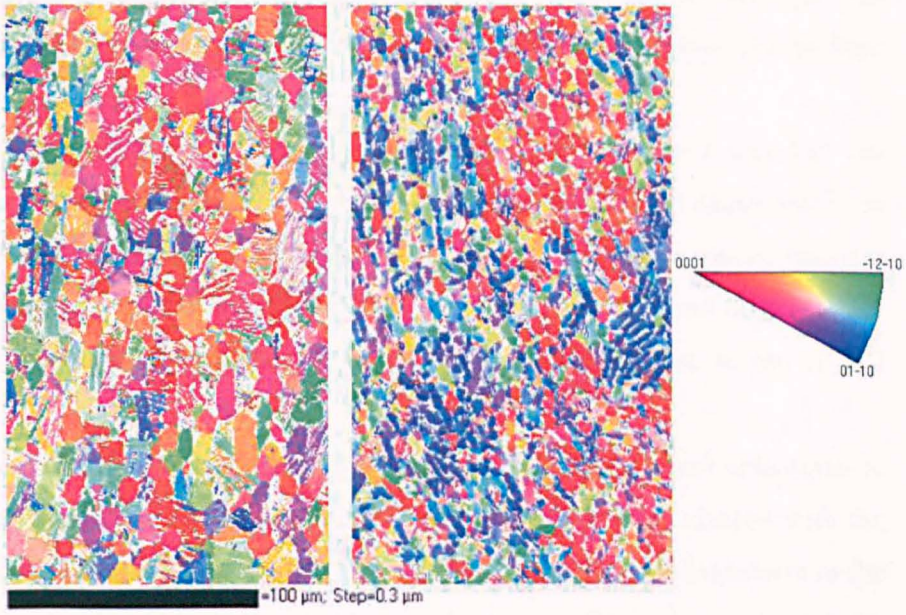

Figure 5.19 Crystal orientation map at the centre of **a)** small billet **b)** alternatively forged billet using a step size of 0.3µm in IPF colouring (alpha phase only).

The complete results from the EBSD analysis are presented in Figure 5.20. Each texture measurement is represented by an {0001} and a {100} pole figure.

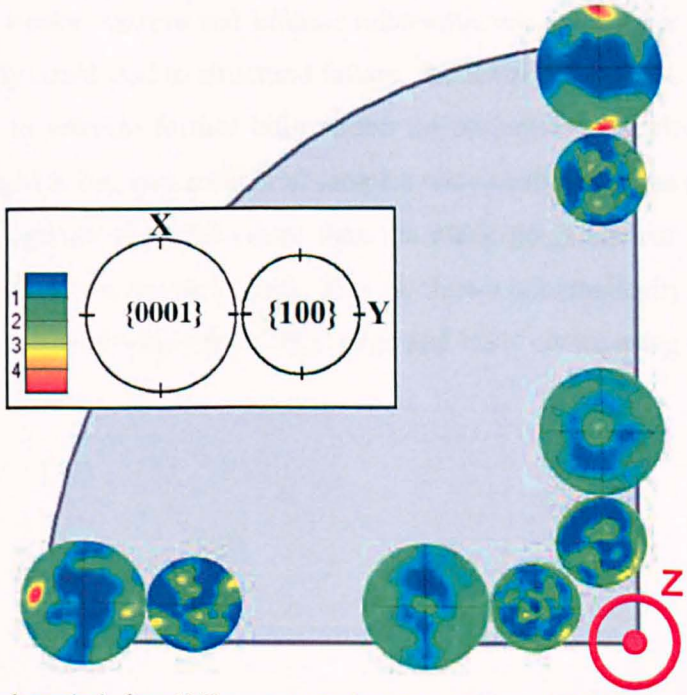

Figure 5.20 The alternatively forged billet texture results represented by an {0001} and a {100} pole figure.

It is interesting to note that although the microstructure within the alternatively forged billet was not homogeneous in comparison to the previous billets analysed, its texture does offer some advantages. It can be seen that the strong texture that was observed at the centre of both previous billets has been replaced by the less intense fibre like texture.

One issue identified with the two previous billets in Chapter 3 was that the majority of the crystals were aligned in a certain direction, which could cause problems if loaded in the wrong direction for dwell fatigue. Therefore if possible, the component should be designed in such a way that the crystals are aligned so that dwell fatigue is not an issue. For this reason the component should be designed relative to the crystal structure.

In the case of this alternatively forged billet, the crystals are not orientated in one direction therefore there will only be a few crystals (macrozones) aligned with the direction of loading. The microstructure however is not as uniform in comparison to the two previously analysed billets meaning if a crack was to occur, it would transfer throughout the whole sample. If structure is uniform however, each time a crack grows it is partially absorbed by another tough ductile α_p before it extends.

The next stage of the manufacture process should also be considered. After the first production stage, billets are then sold to companies such as Firth Rixson who apply further forging processes to the billet. The question as to whether these companies prefer billets of weaker texture and inferior microstructure or stronger texture which if loaded incorrectly could lead to structural failure, should be considered.

In order to provide further information on the crystallographic texture of the alternatively forged billet, two additional samples were analysed in the plane containing the billet axis (longitudinal plane) rather than the plane perpendicular the longitudinal axis of the billet, Z (transverse plane). This is shown schematically in Figure 5.21. EBSD maps were then obtained from NS1' edge and NS1' centre using step size 3 μm.

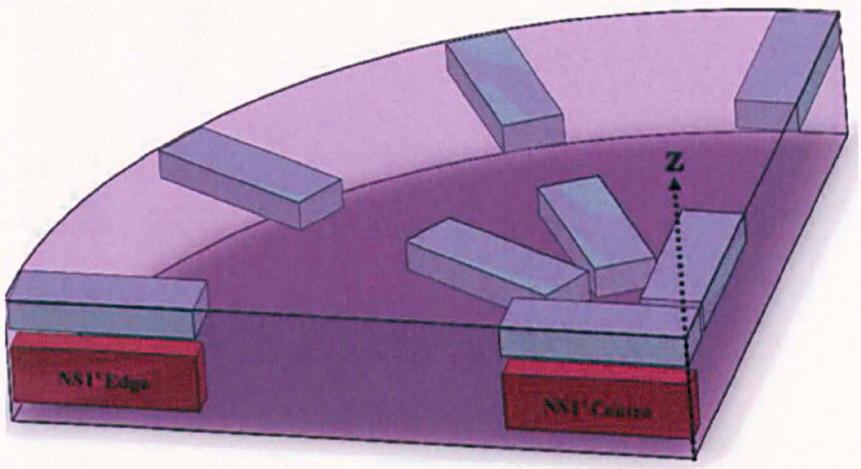

Figure 5.21 Samples NS1' Edge and NS1' Centre.

The OIMs are displayed in Figure 5.22 and 5.23 using Euler and IPF colouring. Similar to the billets in previous chapters the macrozones with sharp local textures are observed throughout the whole billet stretching along the billet axis. At the edge of the billet, the quantity of blue macrozones tends to be great however when moving towards the centre of the billet the blue macrozones start to be replaced by those of red colour. In addition, the pole figures are similar to those in Figures 5.14 and 5.15 therefore confirming these findings.

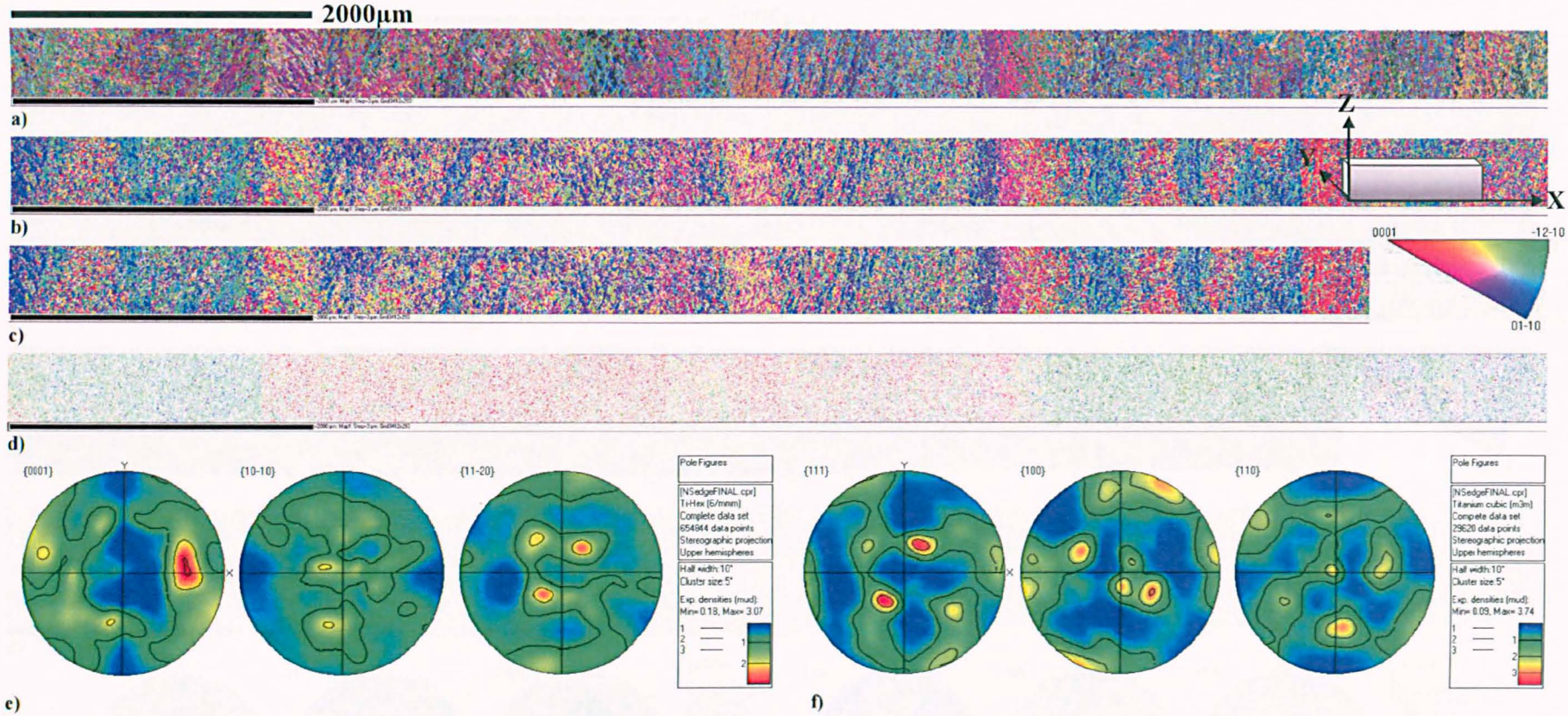

Figure 5.22 Crystal orientation map for NS1' edge **a)** Euler colouring **b)** IPF colouring **c)** alpha phase only **d)** beta phase only and **e)** alpha **f)** beta phase pole figure from Sample NS1' edge.

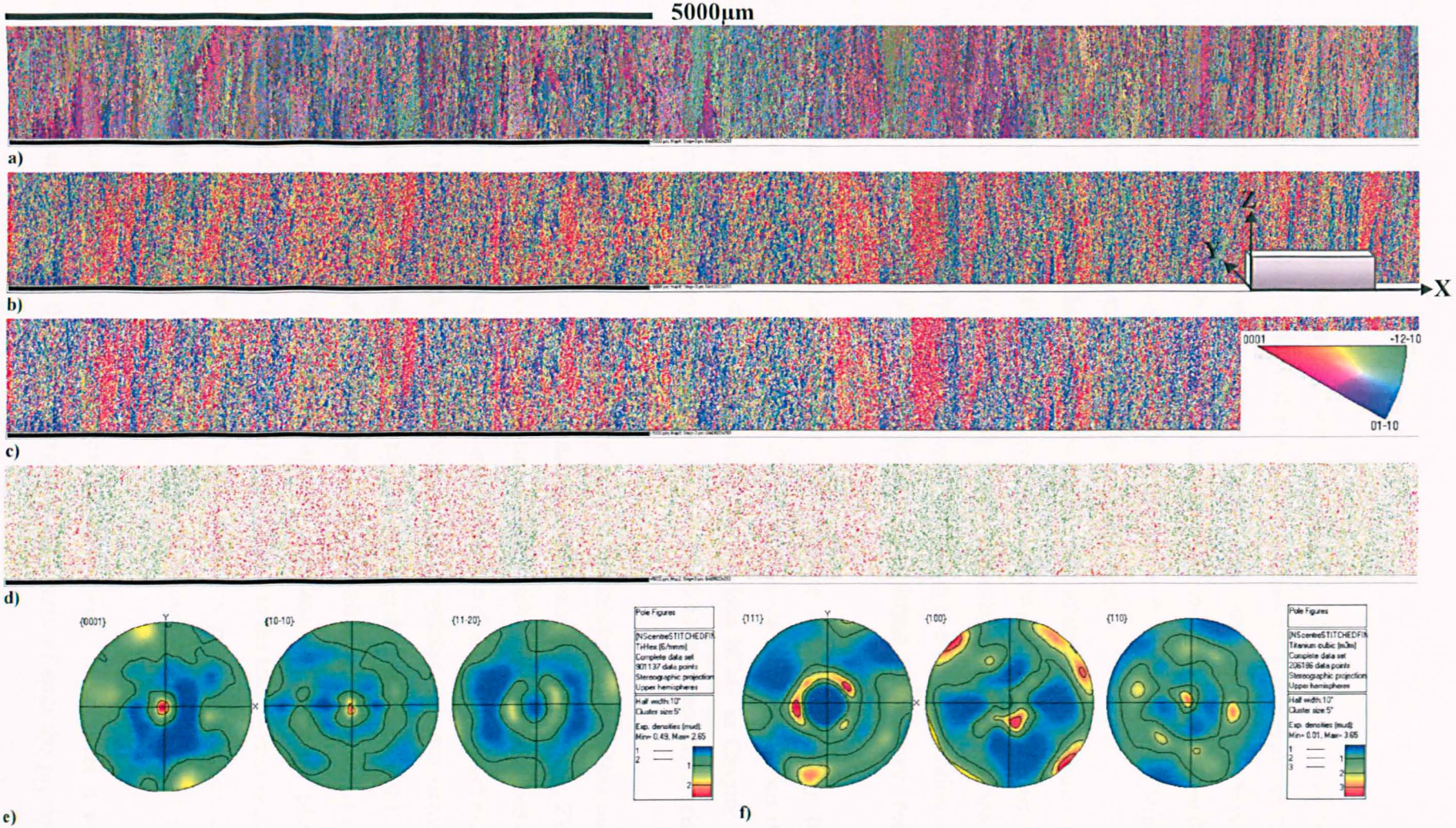

Figure 5.23 Crystal orientation map for NS1' centre **a)** Euler colouring **b)** IPF colouring **c)** alpha phase only **d)** beta phase only and **e)** alpha **f)** beta phase pole figure from Sample NS1' centre.

5.4 Summary

The microstructure (proportion, size and shape distribution of α_p) of the alternatively forged $\alpha+\beta$ alloy TIMETAL® 6-2-4-6 billet has been analysed. All the parameters investigated showed that there was a higher percentage of α_p having smaller grain areas in comparison to the previous billets. In fact the actual scale of the alternatively forged billet microstructure was smaller however there were some larger grains demonstrating the inhomogeneity of the microstructure.

Results also showed that although the actual scale of the microstructure was smaller the shape of the grains changed as they became longer and thinner in dimension. This suggested that the level of globularization within this billet was lower than the previous billets analysed. Based on the definition of globularization by Stefansson approximately 59% of the alternatively forged billet have been globularized.

The study and evaluation of the microstructure was followed by the investigation of texture evolution. Detailed EBSD studies were carried out on the alternatively forged billet. Unfortunately, unlike the previous billets in Chapter 3, samples were picked randomly and they were not linked to any specific forging directions since these were not identified.

In order to capture the maximum number of macrozones possible within each OIM, all maps were taken in the transverse plane (perpendicular to the billet axis, Z). The IPF colour of the majority of the macrozones within each OIM was either red or blue. Grains were shown in blue when their c-axis was perpendicular to the billet axis, representing the prismatic plane (10-10). However when the grains c-axis was aligned with the billet axis, the grains were shown in red, representing the basal plane (0001).

In order to provide further information on the crystallographic texture of the alternatively forged billet, two additional samples were analysed using the plane containing the billet axis rather than the plane perpendicular to the longitudinal axis of the billet, Z (transverse plane). Similarly to the billets in previous chapters the macrozones with sharp local textures were observed throughout the whole billet stretching along its axis.

When analysing the global texture of the alternatively forged billet it was noted that the strong texture that was observed at the centre of both the previous

billets had been replaced by the less intense fibre like texture. Although the texture results were satisfactory, there was clearly not sufficient strain in the $\alpha+\beta$ region to achieve globularization. It was not clear however whether increasing the strain would produce the strong texture dominant in the previous two billets or whether the strong texture of those billets were due to the recrystalisation stage that regenerated the strong β texture which transferred to α texture and could not later be removed.

There is potential regarding the future development of this process route but it is necessary to determine a method to increase the level of globularization within α_p.

Chapter 6

HEAT TINTING

6.1 Introduction

This chapter describes an attempt to correlate optical microstructures of heat tinted titanium with the underlying crystallographic texture. As mentioned in previous chapters X-ray diffraction is often used to measure the macroscopic texture of material. This is useful in determining large-scale orientation differences but it does not give specific information about orientation of particular microstructural features. In addition, X-ray diffraction is limited to a sample size of approximately 25 mm^2. EBSD, on the other hand, uses electron back scatter diffraction to map the orientation of phases in a crystalline material on a microscopic level. This technique can be used to identify the texture at a very specific location. However, this technique requires specialised equipment which can be costly and very time consuming. Also when analysis of titanium alloys products is conducted in a production environment, an assessment of the materials condition is often needed with haste and on a larger scale which EBSD cannot do [54, 95].

Heat tinting, which in effect is oxidation in air, of titanium has been used to create interesting and unusual jewellery for over 35 years due to the variety of colours produced by the oxide (Figure 6.1) [96].

a) b)

Figure 6.1 Titanium jewellery **a)** Stick pin by Debby Moxon (1982), **b)** Annular brooch by Lynne Bartlett (2001) [96].

The use of heat tinting is not widely known for evaluating titanium alloys even though it is a phase identification method and has been included in many metallography handbooks [97, 98, 99]. Heat tinting titanium has been shown to produce good surface coloration (oxide film growth temperatures from 260°C to 704°C have been mentioned) and it is a process that can be carried out using common laboratory equipment [95]. Table 6.1 shows a listing of heat tinting temperatures for different metals and alloys.

Table 6.1 Temperatures for heat tinting [99].

Metal	Temperature and time in air
Beryllium	900 °C (1650 °F) for 30 min
Cast iron	400 °C (750 °F) for 20 min
Stainless steel	500–700 °C (930–1290 °F) for ≤20 min
Nickel	600 °C (1110 °F) for 5–10 min
Rare earth metals	200 °C (390 °F) for minutes to hours
Titanium	400–700 °C (750–1290 °F) for up to 30 min
Zirconium	400 °C (750 °F) for 5 min
Sintered carbides	300–600 °C (570–1110 °F) for 5 min

Recently, however, heat tinting has been acknowledged as a very simple metallographic method that can provide a certain degree of orientation information both easily and inexpensively on a larger scale than X-ray diffraction and EBSD [95]. In this technique the information about microstructural features is collected by the differences in phase composition and crystal structure. This is done using heat treatment to build a thin layer of oxide film on the well polished surface of the sample. Interference of light rays reflecting from the inner and outer film surfaces will then produce colours characteristic of the underlying microstructural features. The thickness and colour of the oxide depends on the oxidation rates [95, 99].

6.1.1 Formation of oxides

Titanium is a very reactive metal. It, however, exhibits a high resistance to corrosion due to the protective effect of its surface oxide film. These films, and in particular TiO_2, are inert to most natural environments and many chemicals [100].

Formation of oxide is regarded as a thermally activated process which means that the oxide formation and the rate at which this process occurs are strongly linked to the temperature of the environment in which the metal is contained. This is shown mathematically (Arrhenius equation) in equation 6.1.

$$k = Ae^{\left(\frac{-Q}{RT}\right)} \quad (6.1)$$

Where k is the rate coefficient, A is a constant, Q is the activation energy, R is the universal gas constant (8.314 x 10^{-3} kJ $mol^{-1}K^{-1}$), and T is the temperature (in Kelvin) [101, 102].

Normally, the rate of oxide formation increases with temperature, however, it is often affected by the purity of the metal, the pressure of the system and the type and amount of defects present in the oxide layer. Once an oxide is formed on the surface of the metal, it operates as a barrier hindering the reaction between the metallic and non metallic ions. Therefore, further growth of the layer will only occur by the migration of the mobile ions across the defects present in the oxide by solid state diffusion mechanisms (Figure 6.2). The rate of reaction between the ions and formation of an oxide during the first stages of the oxidation process is high. This is due to the fact that the barrier is relatively thin. However, as the oxide scale thickens, the distance that metallic ions need to diffuse in order to react also increases, therefore a reduction in the reaction rate and in the oxide scale formation may be seen [102, 103].

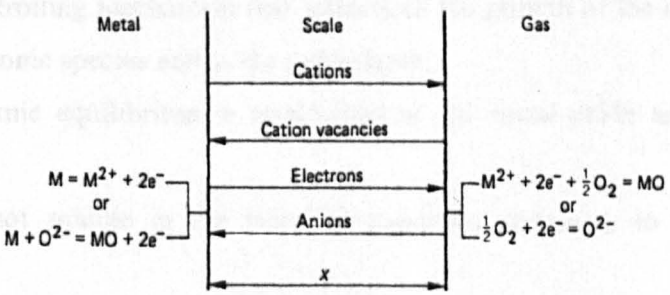

Figure 6.2 Simplified model for diffusion controlled oxidation [103].

A general example was given by Wagner in 1933 [103] of how an oxide grows on the surface of a metal at high temperature. However, due to its complications (many variables and mathematical simplifications used to obtain the final expression) Birks and Meier (1986) [103] presented a simplified approach to this theory which is shown in Figure 6.3.

Figure 6.3 shows two reactions taking place at each interface, the ionization of the reactive ions (metal or oxygen) and the formation of the oxide. Once a small amount

of oxide scale of thickness x has grown, metallic ions travel towards the oxide-gas and oxygen in the opposite direction in order to continue with the oxidation reaction.

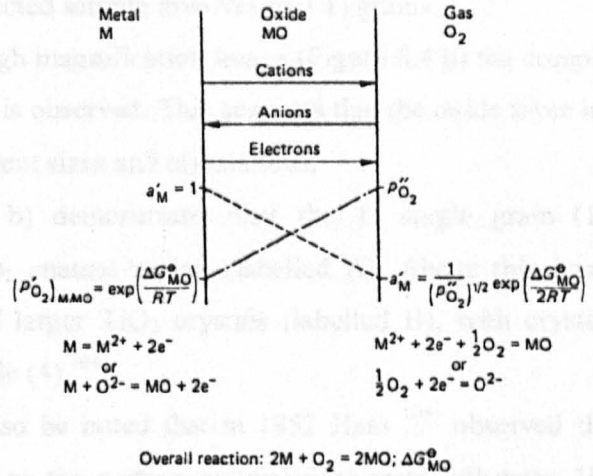

Figure 6.3 Oxide growth according to Wagner's model [103].

Note that the assumptions made in order to develop this theory are summarised as:

1. The oxide scale is free of any major defects such as cracks, etc. and it is perfectly adhered to the metallic substrate.
2. The rate controlling mechanism that influences the growth of the oxide layer is the diffusion of ionic species across the oxide layer.
3. Thermodynamic equilibrium is established at the metal-oxide and the gas-metal interfaces.
4. Oxygen is not soluble in the metal (a condition necessary to develop internal oxidation).
5. The driving force for the occurrence of oxidation reactions is the free energy change of oxide formation. This point suggests that gradients of chemical and electrical potential determined by the activities of metal and the gas will be found across the scale Figure 6.3 [102, 103].

Titanium is classified as a "film-former", i.e. a metal whose surface is always covered with a "natural" oxide film, when exposed to air, water or other oxygen containing media. The "natural" oxide film on titanium varies depending on the composition or purity of the metal, the surrounding medium, the maximum temperature reached during the working of the metal and etc. It has been reported that the oxide film consist of TiO_2 rutile, anatase, or lower amorphous oxides [100]. Figure 6.4 shows a

typical cross-sectional TEM (Transmission Electron Microscopy) image of a Ti/TiO2 specimen at low a) and high b) magnification. The difference in contrast in Figure 6.4 a) implies that the selected sample involves two Ti grains.

From the high magnification image (Figure 6.4 b) the complexity of the contrast in the oxide region is observed. This suggests that the oxide layer is made of crystalline grains having different sizes and orientations.

Figure 6.4 b) demonstrates that the Ti single grain (1) is covered by a polycrystalline TiO_2 anatase region (labelled A). Above this layer there is a thicker layer composed of larger TiO_2 crystals (labelled B), with crystals corresponding to anatase (3) and rutile (4) [104].

It should also be noted that in 1952 Hass [105] observed that rate of oxidation changes depending on the surface quality of the metal substrate. He noted that roughly polished titanium oxidised faster than titanium which had mirror finish surfaces.

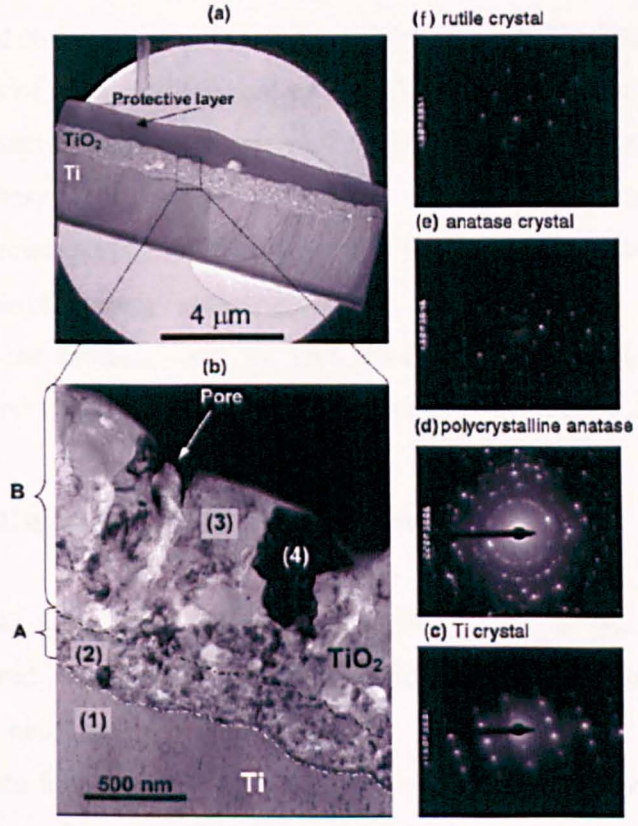

Figure 6.4 Cross-sectional TEM image of the lifted-out Ti/TiO2 specimen at **a)** low and **b)** high resolution; **c), d), e)** and **f)** are selected area diffractions (SAD) corresponding to zones (1), (2), (3) and (4) respectively from **b)**. A and B correspond to the polycrystalline and the oriented crystals region correspondingly. The arrow denotes a cross-sectioned pore [104].

Gueneau de Mussy et al. [104] suggested that an orientation relationship may exist between the Ti substrate and its superficial oxide (using TEM and X-ray measurements). Furthermore, he discovered that it is reasonable to consider that some preferred orientations are formed in the inner oxide region as a result of the underlying textured Ti substrate (by comparing the TiO_2 anatase and rutile pole figures with the Ti substrate pole figure).

Flower and Swann [106] published a paper regarding the correlation between oxide thickness, colour and oxide formation rates. It is generally accepted that a thin layer in the range 10 –500 nm is required to show interference colours [107].

The rate of oxidation varies with the crystallographic orientation of the underlying α and β phases. Polarized light can be used at times to view the heat tinted sample in order to achieve a good colour contrast. This technique cannot reveal detailed orientation information however, it is used as a quick and easy tool to provide additional information to a typical microstructure characterization [95, 108]. While the colours cannot be directly related to a particular crystallographic orientation an idea of the effective structural unit size of similar orientations in the microstructure can be observed.

In this chapter conditions required to obtain the best heat tint results are evaluated and these heat tinting results are then compared to those of other characterization techniques (EBSD) to show that features such as texture bands may be seen without employing costly texture analysis.

Note that the samples used for heat tinting investigation are the same as the samples used in previous chapters for the microstructure and texture analysis.

6.2 Heat tinting experimental procedure

The sample preparation for heat tinting was similar to that for EBSD texture analysis. It required very careful mechanical polishing and a clean surface. Etching, however, was not necessary.

A moderate temperature was required for oxide film growth on the polished surface. A laboratory furnace was used as the heat source since the temperature can be monitored and controlled. A Polyvar optical microscope fitted with a Carl Zeiss high resolution digital camera was then used to capture the images. Heat tinted images of TIMETAL® 6-2-4-6 are shown in Figure 6.5 as an example.

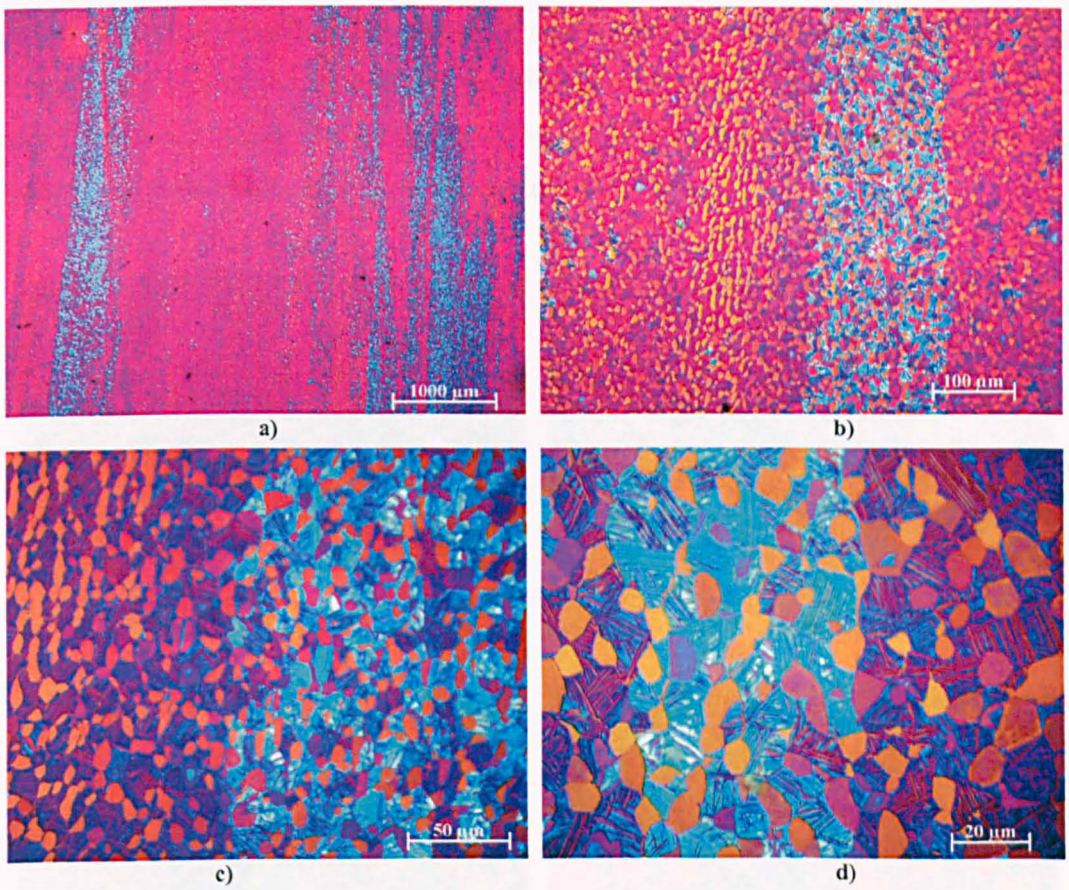

Figure 6.5 Heat tinted images of TIMETAL® 6-2-4-6 containing 30% α_p in a matrix of transformed beta. The oxide layer growth varies depending on the crystallographic orientation of the grains.

A number of sources recommend temperatures of 399°C to 621°C for a short period of time as being suitable for heat tinting of titanium [91].

Based on this information, the first trials using temperatures from 400°C to 600°C for a few minutes did not create a thick enough oxide to produce phase contrast. A sample was then progressively heated firstly using a temperature of 600°C for 10 minutes (which did not develop a pronounced colour) then 620 °C for 10 minutes and finally 630°C for 20 minutes.

Whilst colour image capture may be desirable, the colour image produced was too complicated to analyse due to the wide range and number of colours involved. Thus, in order to simplify the problem and to relate the images to the crystallographic orientation maps (EBSD map) it was essential during evaluation to convert the images from colour to greyscale (256 greyscale levels contain sufficient information for most purposes).

Figure 6.6 a) shows the greyscale map while Figure 6.6 d) is the EBSD map (using a step size of 0.3μm over an area of approximately 55 x 30 μm^2) of the same area. Figures 6.6 b) and c) were produced by merging the greyscale and EBSD maps in order to highlight similarities in microstructure of the sample.

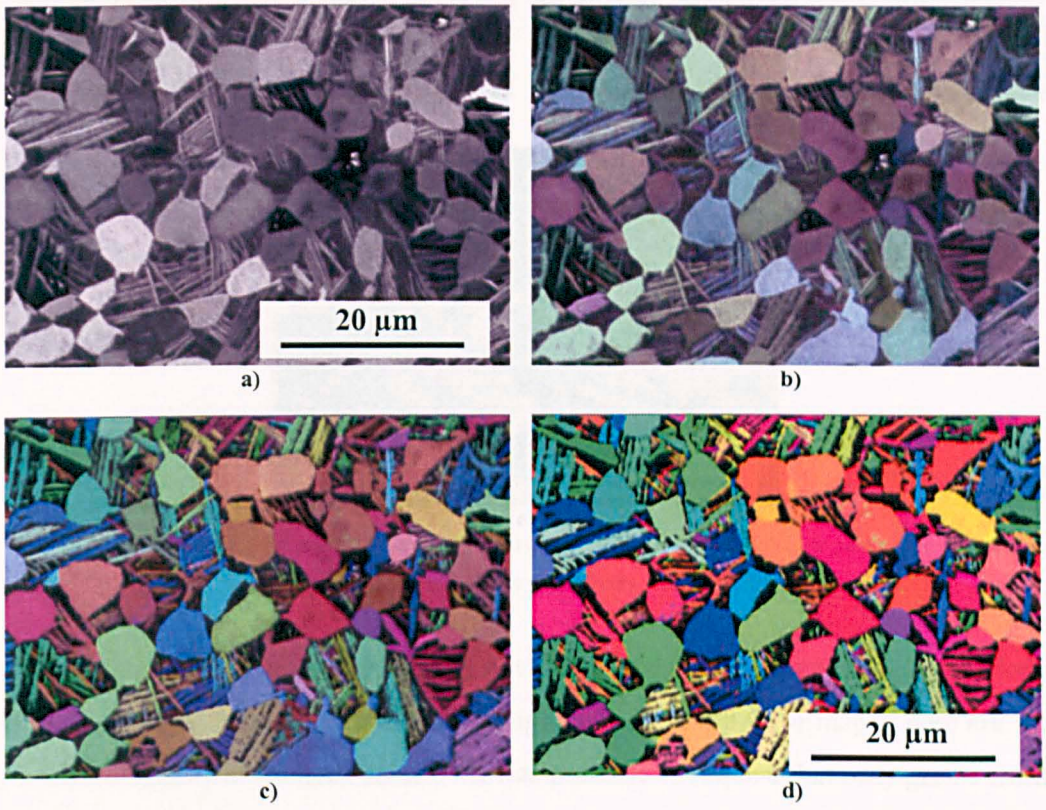

Figure 6.6 TIMETAL® 6-2-4-6 **a)** gray scale image of the heat tinted sample **b, c)** merged images of the greyscale and EBSD map **d)** Crystal orientation map of the same area using a step size of 0.3μm in IPF colouring.

Using Microsoft visual studio it was possible to write a programme which highlighted grains of particular colours within the OIM map once the heat tinted and OIM map had been merged. For example, it could be requested that grains within the OIM map with a high percentage red colour be highlighted on the greyscale image.

Figure 6.7 a) shows the greyscale image produced when grains containing a high percentage of red colours were highlighted. Figures 6.7 b) and c) show grains with green and blue colours respectively.

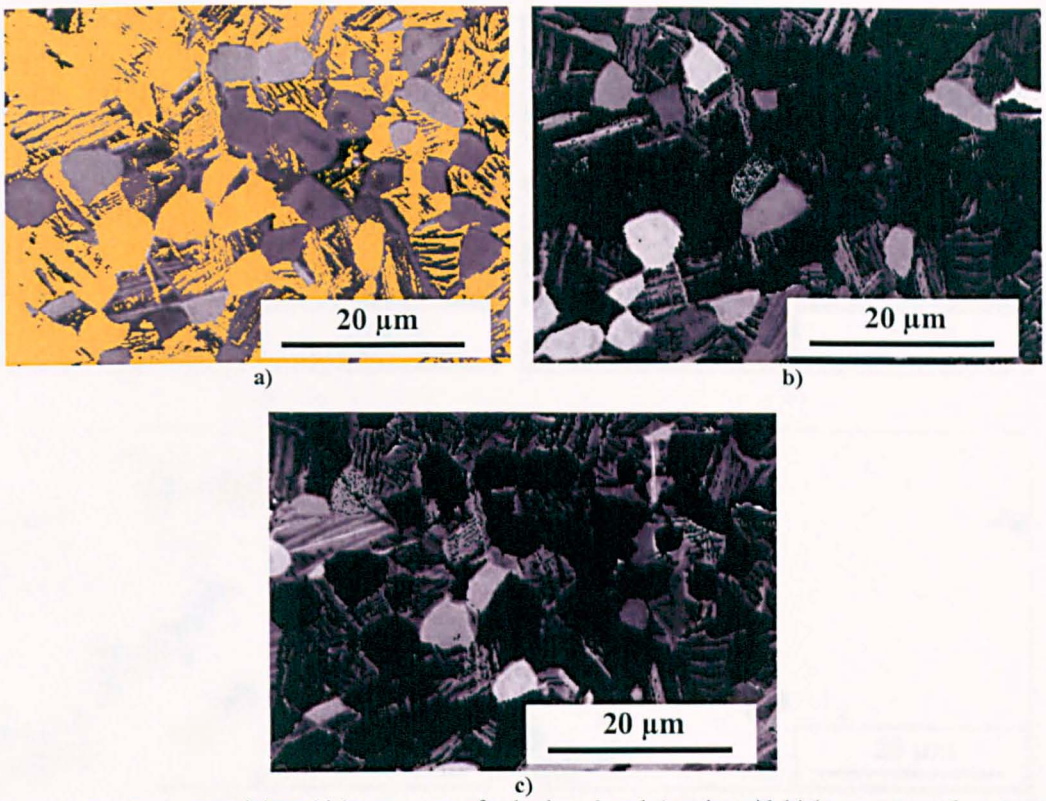

a) b)

c)

Figure 6.7 a) Grains containing a high percentage of red colour, **b** and **c)** grains with high percentage of green and blue colours respectively.

Visual analysis of the result was not conclusive so the program was modified so that the greyscale image was used to highlight grains on the OIM map. There are only 256 shades of grey in the grey scale so it was possible to request that only grains from a certain range of greyscale e.g. 0 to 100 (Figure 6.8 a) be shown in colour on the OIM map. Using this type of analysis it was then possible to determine which colour on the OIM map corresponded to a particular shade of gray.

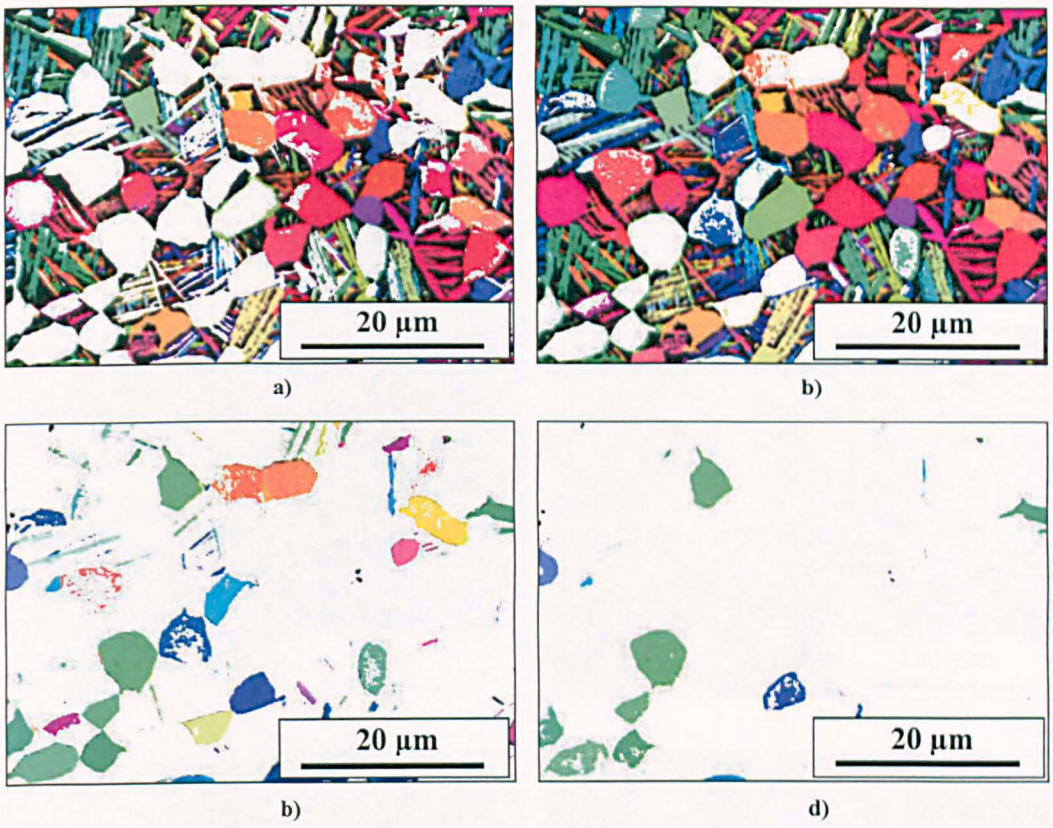

Figure 6.8 a) Greys below 100 **b)** greys below 150 **c)** greys above 150 **d)** greys above 200.

There are three main issues from this experiment that should be evaluated:

- An optimum temperature was not established- the sample was simply heated until contrast between the colours was satisfactory.
- Whether sequent re-oxidations of the sample affected the colours of the oxide? (Sample was heated gradually using a range of temperatures and times and cooled between heatings).
- This experiment was done at high magnification. Would this technique be feasible for use at lower magnification and larger area?

Thus further systematic investigations were required.

6.2.1 Heat tinting Trials

In this study, trial heat tints were conducted using 1.5cm x 1cm x 1cm Ti 6-2-4-6 cubes. Samples were then polished and tinted while monitoring the total time spent in the furnace. The results are shown below.

Figure 6.9 shows a sample that has been heat tinted at 600°C for 20 minutes. It can be seen that some of the α_p grains have a minimal amount of oxidation and so have not developed a pronounced colour, whereas some of the β grains have already burnt and begun to overspill their oxide layer. However, as some of the grains have not oxidised, the next sample was heated at a higher temperature.

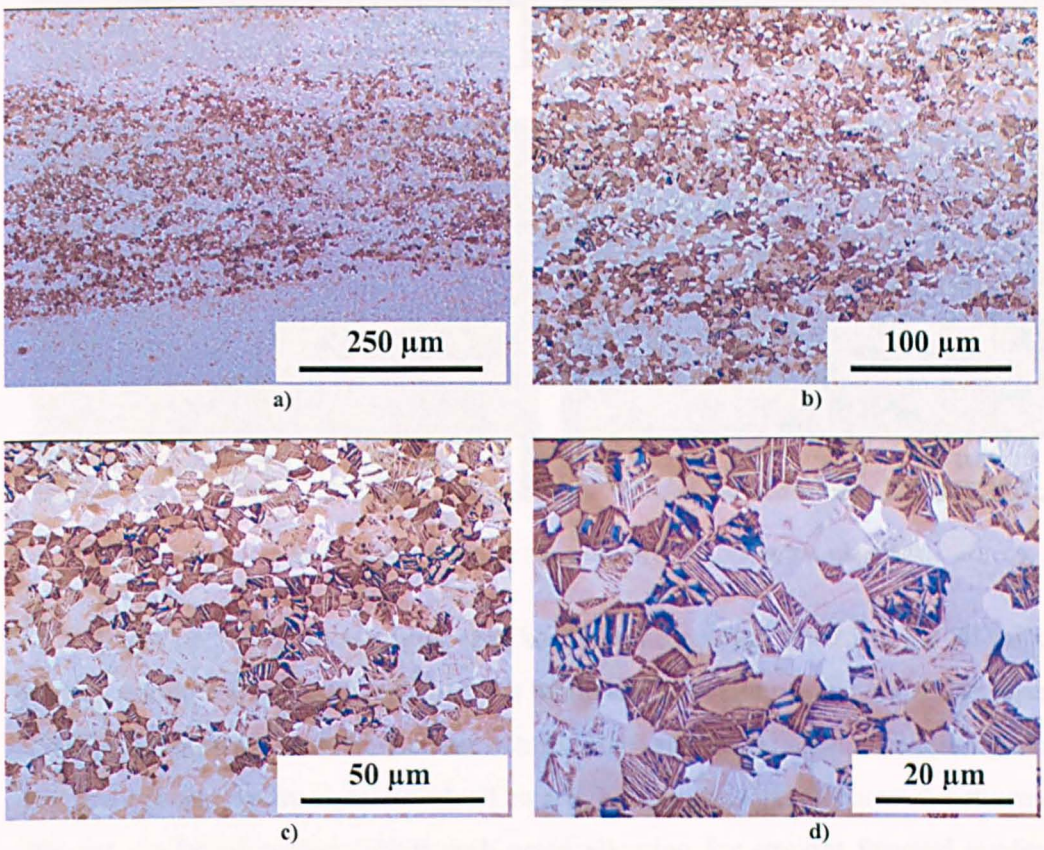

Figure 6.9 Heat tinting at 600°C for 20 minutes **a)** 5x, **b)** 10x, **c)** 20x and **d)** 50x.

Figure 6.10 shows a sample that has been heat tinted at 640°C for 20 minutes. This sample is very distinct with the grain boundaries being clearly visible. Although there is not a broad range of different colours, there is a good range of different shades of the same colour within the individual phases. There are, however, a few grains which are showing the sign that they are beginning to burn by turning to dark shades of a purple-brown colour. To try and eliminate the grains being burnt the temperature was reduced while the time was increased.

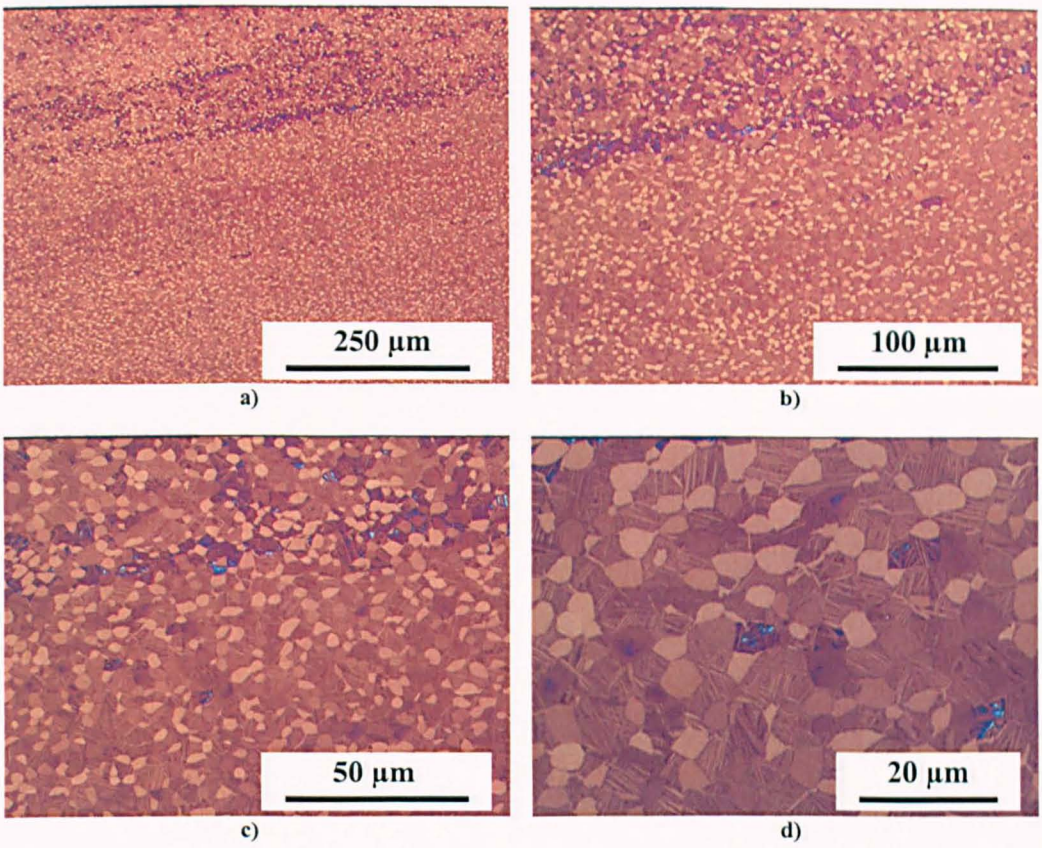

Figure 6.10 Heat tinting at 640°C for 20 minutes **a)** 5x, **b)** 10x, **c)** 20x and **d)** 50x.

Figure 6.11 shows a sample that has been heat tinted at 625°C for 30 minutes. There is minimal burning of the α_p grains while still providing sufficient oxide layers to reveal detailed pictures of the microstructure. Each phase and each individual grain are very distinct and easily determined. There is a large amount of contrast between the different shades of colour within each grain allowing for straight forward qualitative differentiating between the different grain orientations. Although this set-up of time and temperature produces an excellent optical micrograph of the TIMETAL® 6Al-2Sn-4Zr-6Mo microstructure, it is not necessarily the optimum time and temperature. It is possible that if the temperature is increased then the time required to heat tint the titanium can be reduced while still maintaining such high quality results.

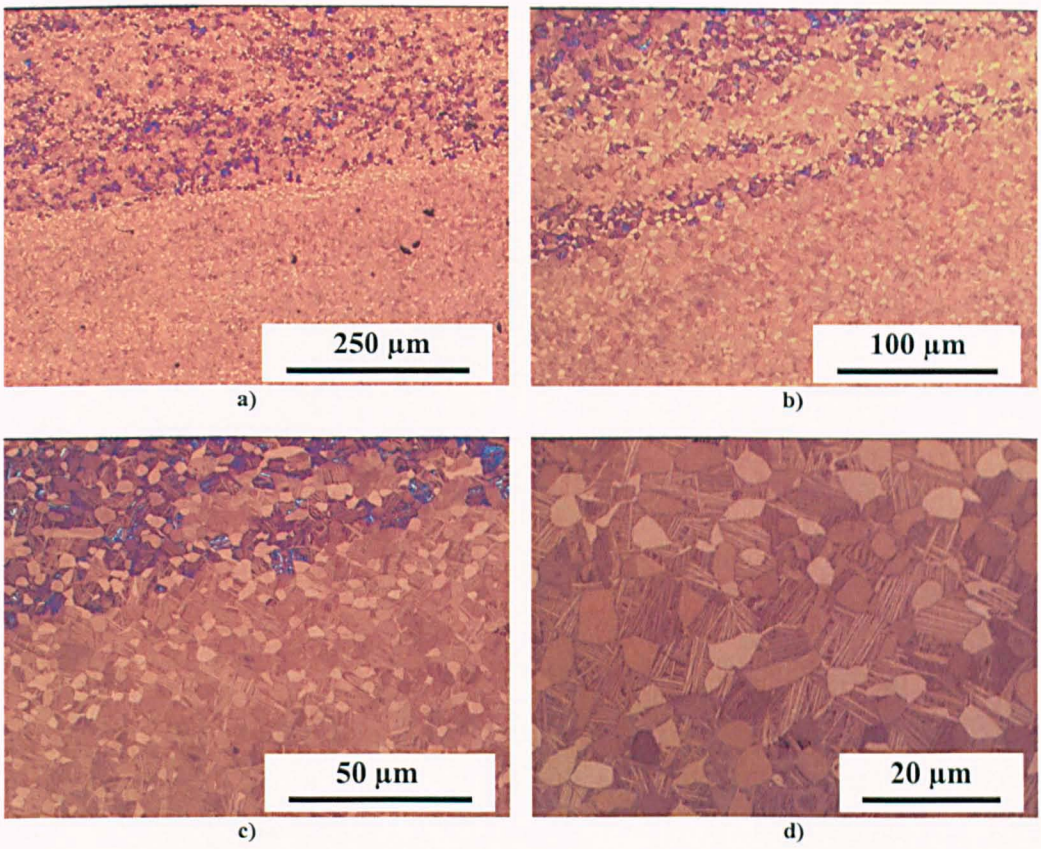

Figure 6.11 Heat tinting at 625°C for 30 minutes **a)** 5x, **b)** 10x, **c)** 20x and **d)** 50x.

Figure 6.12 shows a sample that has been heat tinted at 630°C for 20 minutes. This sample has very little burning of the α_p grains. It is perfectly clear and highly contrasting. This has proved the theory stated previously that it is possible to increase the temperature of the heat tint as long as the time is reduced by a sufficient amount. The next sample tries to take this further, again increasing the temperature while reducing the time. Figure 6.13 shows a sample that has been heat tinted at 640°C for 15 minutes. This sample like that shown in Figure 6.12, has very small burns. It is also perfectly clear allowing every detail of the microstructure to be seen with considerable ease as the different shades of colour are highly contrasting. Some other examples for higher temperature values are presented in Table 6.2.

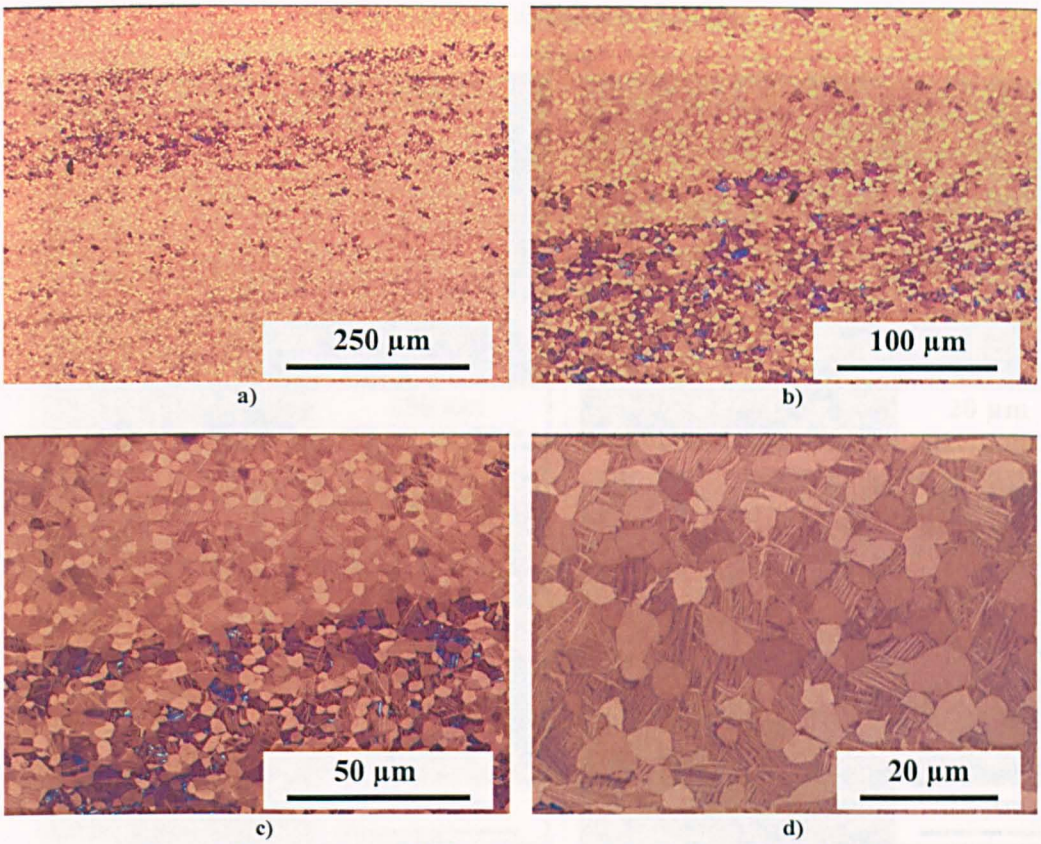

Figure 6.12 Heat tinting at 630°C for 20 minutes **a)** 5x, **b)** 10x, **c)** 20x and **d)** 50x.

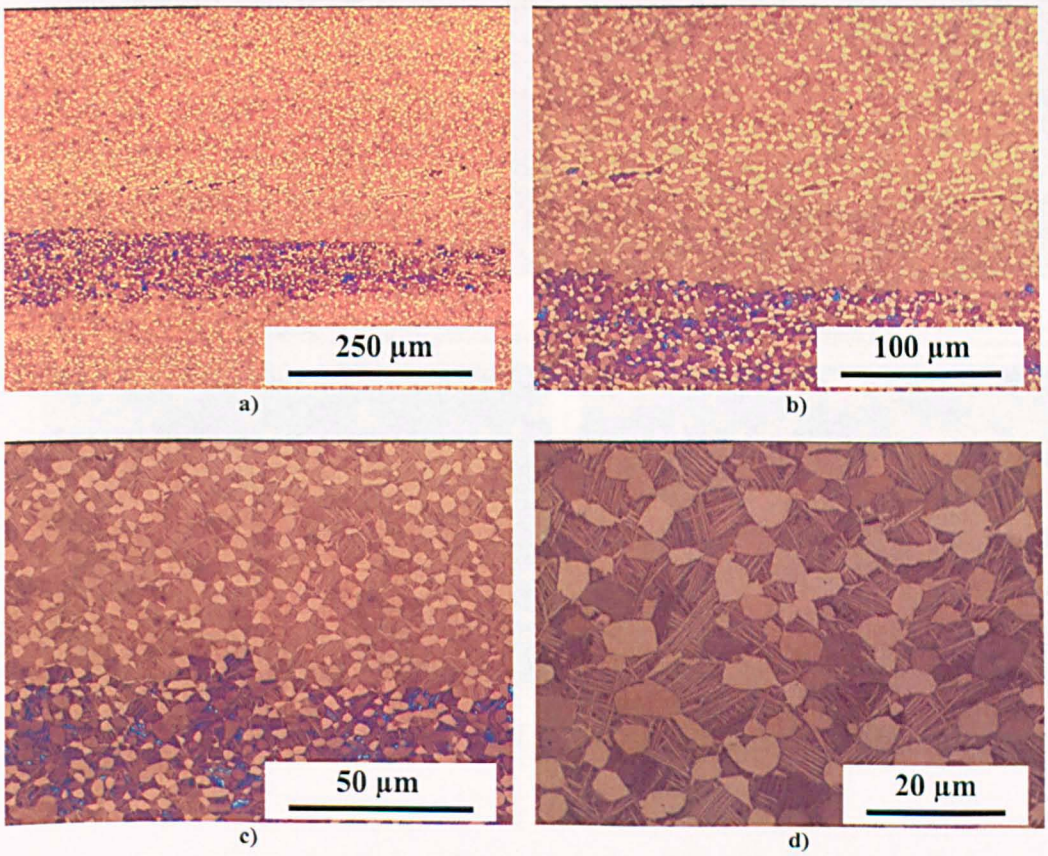

Figure 6.13 Heat tinting at 640°C for 15 minutes **a)** 5x, **b)** 10x, **c)** 20x and **d)** 50x.

Table 6.2 Heat tinting conditions and the results.

660°C, 20 min	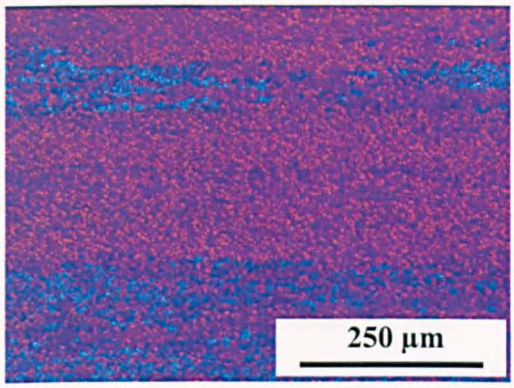	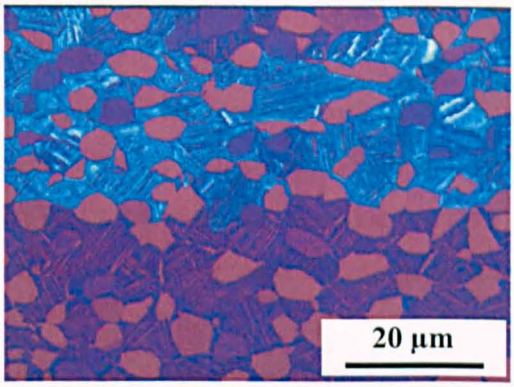
675°C, 10 min	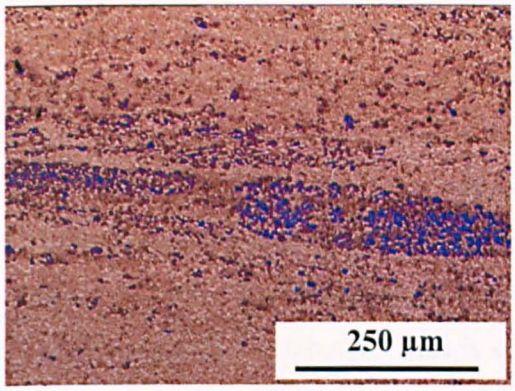	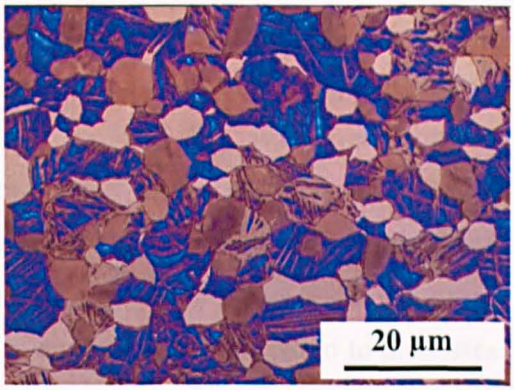
750°C, 5 min	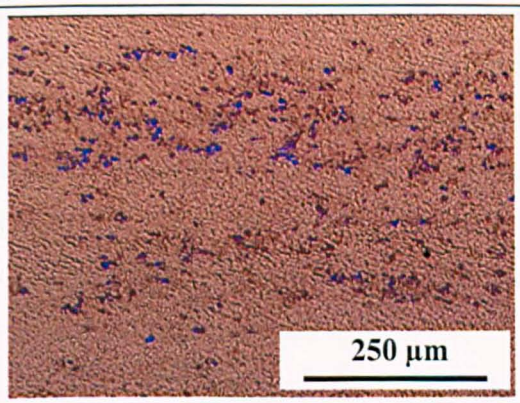	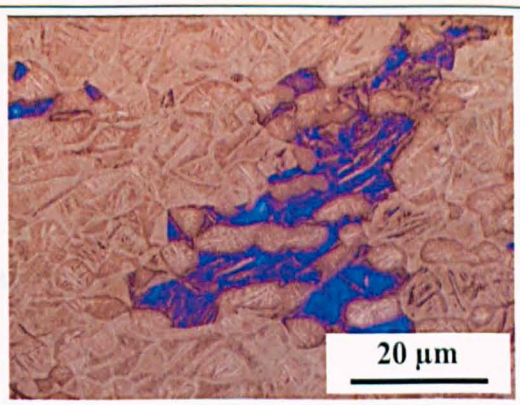
750°C , 20 min	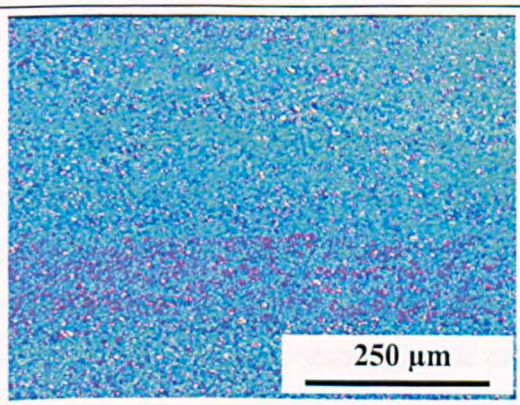	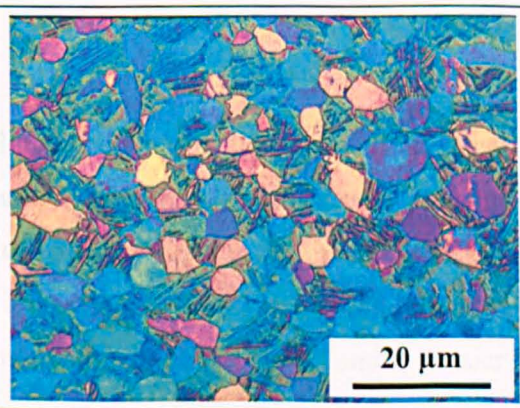

From Table 6.2 it can be noticed that a very high percentage of β and α_s grains have been burnt and that there has been a large amount of oxidation overspill over the α_p grains. Although the grains have been burnt there is still some hint of the texture being recognisable (presence of a macrozone). The sample that was heat tinted at 750°C for 5 minutes (Table 6.2) demonstrates that oxidation of the surface is dependent on both time and temperature as 5 minutes was not sufficient time for an oxide layer to form. It can be observed that it is very difficult to distinguish between the α_p grains as there is almost no contrast between them.

From the optical micrographs of the different heat tinting conditions it can be concluded that heat tinting is a very sensitive process capable of producing widely varying results with very minor changes to the temperature and time. Anything above 650°C and the α_p grains begin to burn while above 675°C the oxide layer forms so rapidly on the β grains that it begins to spill over to the α_p grains and then subsequently burns. In both cases any ability to determine the texture orientation is lost. When tinted at temperatures below approximately 630°C the time required to form a sufficient oxide layer increases to over 30 minutes. This is still very good when compared to processes such as EBSD but with respect to other heat tinting configurations it is quite slow. Also, even though the micrographs produced do allow for texture determination, there is minimal contrast between the grains making it quite difficult. Therefore, the optimum time and temperature for heat tinting is that which can be seen in Figure 6.12 and 6.13. This is because it is the micrograph which produces the greatest degree of contrast between the grains with less burning of the grains or oxidation overspill and so makes for the easiest texture analysis.

6.3 Imaging and analysis

As mentioned before the Polyvar optical microscope was fitted with a Carl Zeiss high resolution digital camera was used to capture the images. In order to produce images with greater contrast a polarizing filter was inserted into the light path within the microscope. As stated previously whilst colour image capture may be desirable, in order to relate the images to the crystallographic orientation maps (EBSD map) and for easier and more accurate interpretation of the images, it was essential to convert the images from colour to greyscale (256 greyscale levels contain sufficient information for most purposes). A variety of images are presented in Figures 6.14, 6.15 and 6.16.

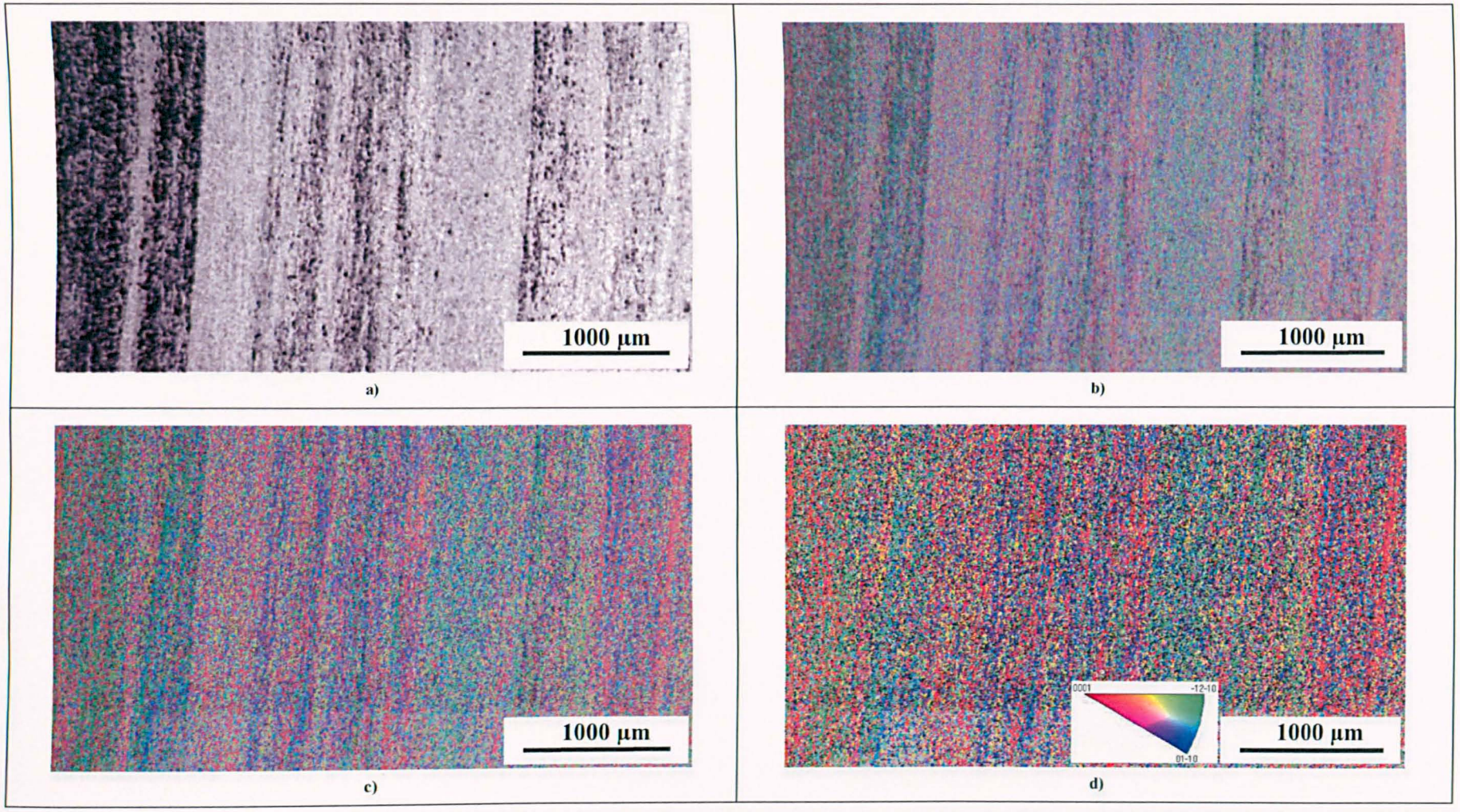

Figure 6.14 TIMETAL® 6-2-4-6 **a)** gray scale image of the heat tinted sample **b, c)** merged images of the greyscale and EBSD map **d)** crystal orientation map of the same area using a step size of 3µm in IPF colouring.

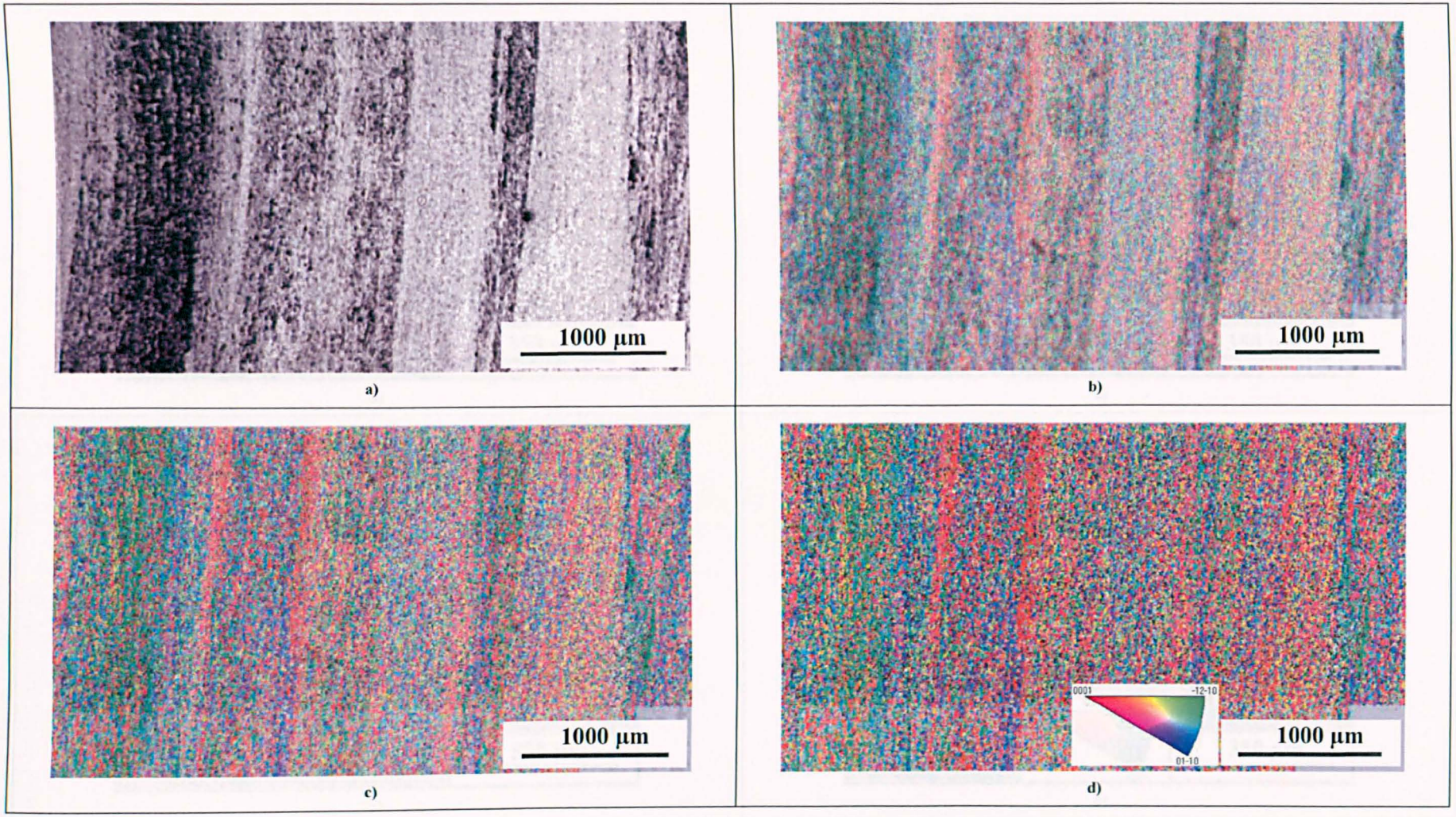

Figure 6.15 TIMETAL® 6-2-4-6 **a)** gray scale image of the heat tinted sample **b, c)** merged images of the greyscale and EBSD map **d)** crystal orientation map of the same area using a step size of 3µm in IPF colouring.

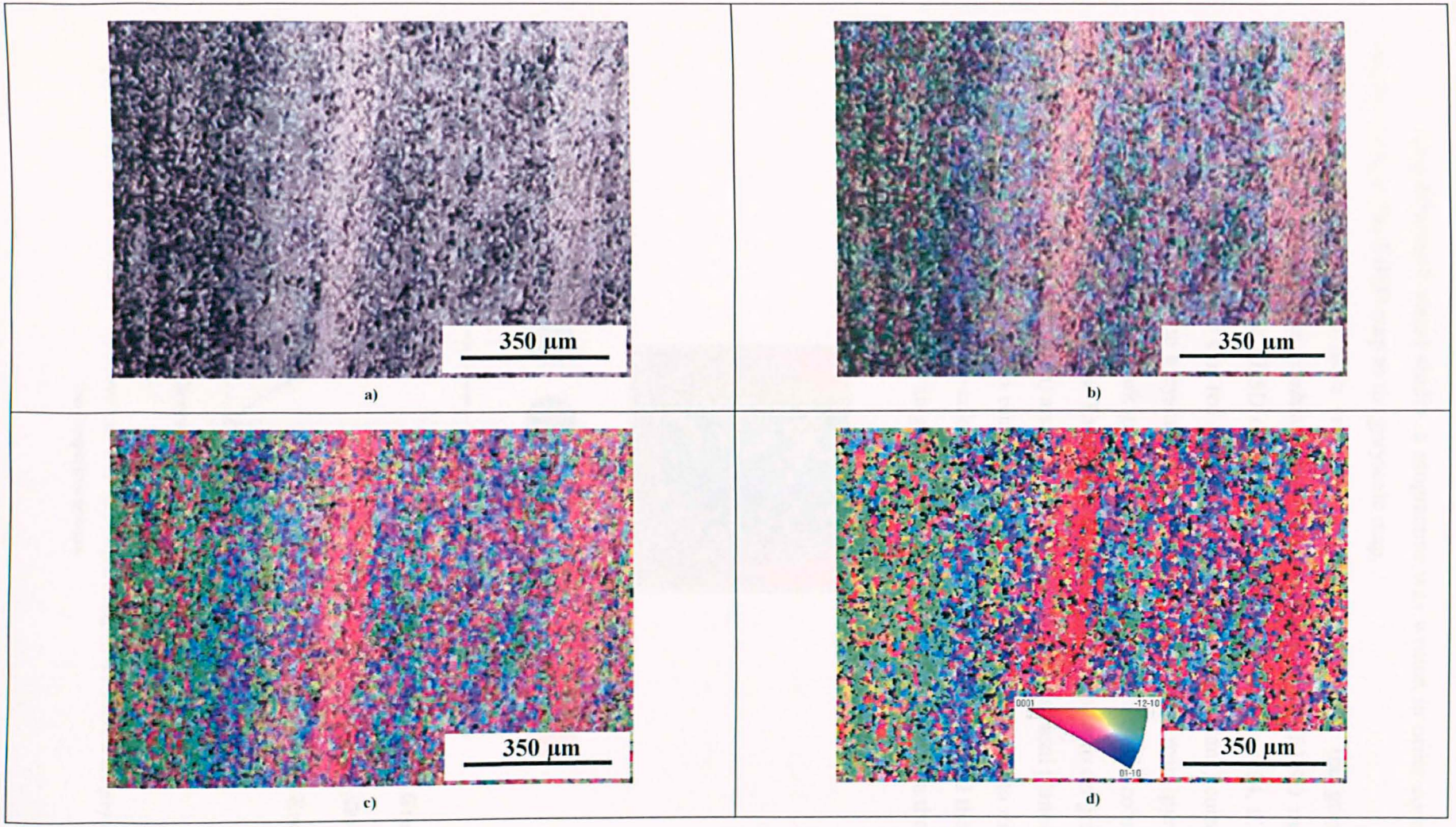

Figure 6.16 TIMETAL® 6-2-4-6 **a)** gray scale image of the heat tinted sample **b, c)** merged images of the greyscale and EBSD map **d)** crystal orientation map of the same area using a step size of 3µm in IPF colouring.

Using Microsoft visual studio, a programme was written in order correspond exact colours of the EBSD map to the greyscale map.

As mentioned before there are only 256 shades of grey in the grey scale compared to the much larger combination of colours found in the EBSD map. By comparing the gray scale and EBSD map in previous figures (Figures 6.14, 6.15 and 6.16) it is possible to assume that red colures in EBSD map (Basal plane) correspond to white and light greys in the greyscale, green colours in the EBSD map (pyramidal planes) correspond to black and dark gray in the greyscale and all the other colours are found between these two extremes. Thus based on this information, zero on greyscale represents pyramidal planes (green) and 255 on greyscale represents basal planes (red).

The next step was to try to relate other colours of the EBSD map to different shades on the greyscale. Using the colour chart shown in Figure 6.17 a) and the above information a graph was created with gray scale on the x and colour scale on the y axis (Figure 6.17 b).

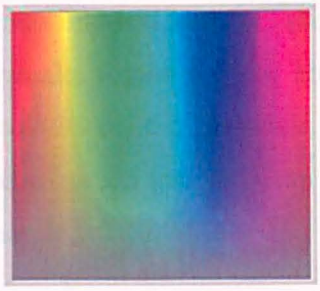

a)

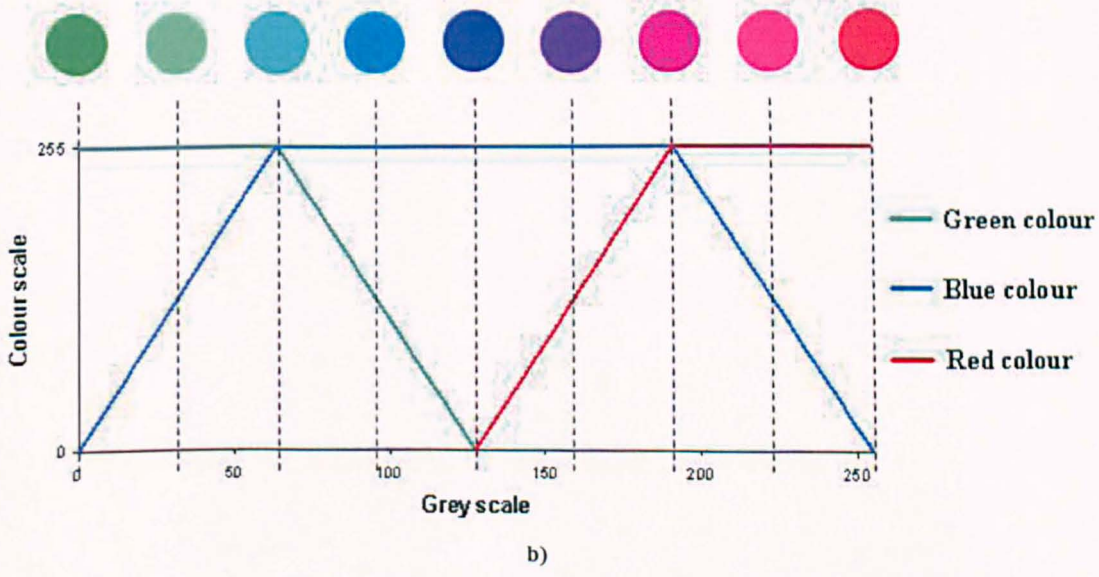

b)

Figure 6.17 a) Colour chart taken from Microsoft paint **b)** graph representing the link between the grey scale and their respective colours.

From the graph shown in Figure 6.17 b) it can be observed that the colours red and green do not meet thus preventing colours such as yellow and orange from being produced. This is due to the greyscale being linear and colour scale being 3D.

To make this more obvious the colour schemes in Euler colouring is shown in Figure 6.18.

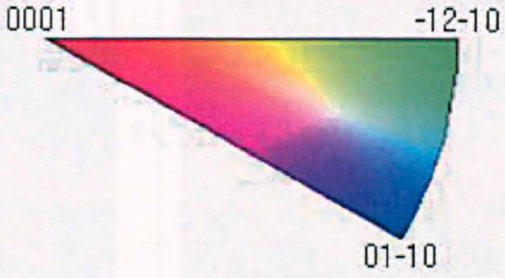

Figure 6.18 Legends illustrating the colour schemes in IPF colouring.

Colour schemes in Euler colouring demonstrates that the colour yellow is produced using both red and green and is therefore it should be found midway between these two colours on the greyscale. Figure 6.17 b) however shows pure blue to be midway between these two colours on the greyscale. As a result of this blue and yellow (or other combinations of green and red) can not appear at the same time. Figure 6.19 is shown as an example.

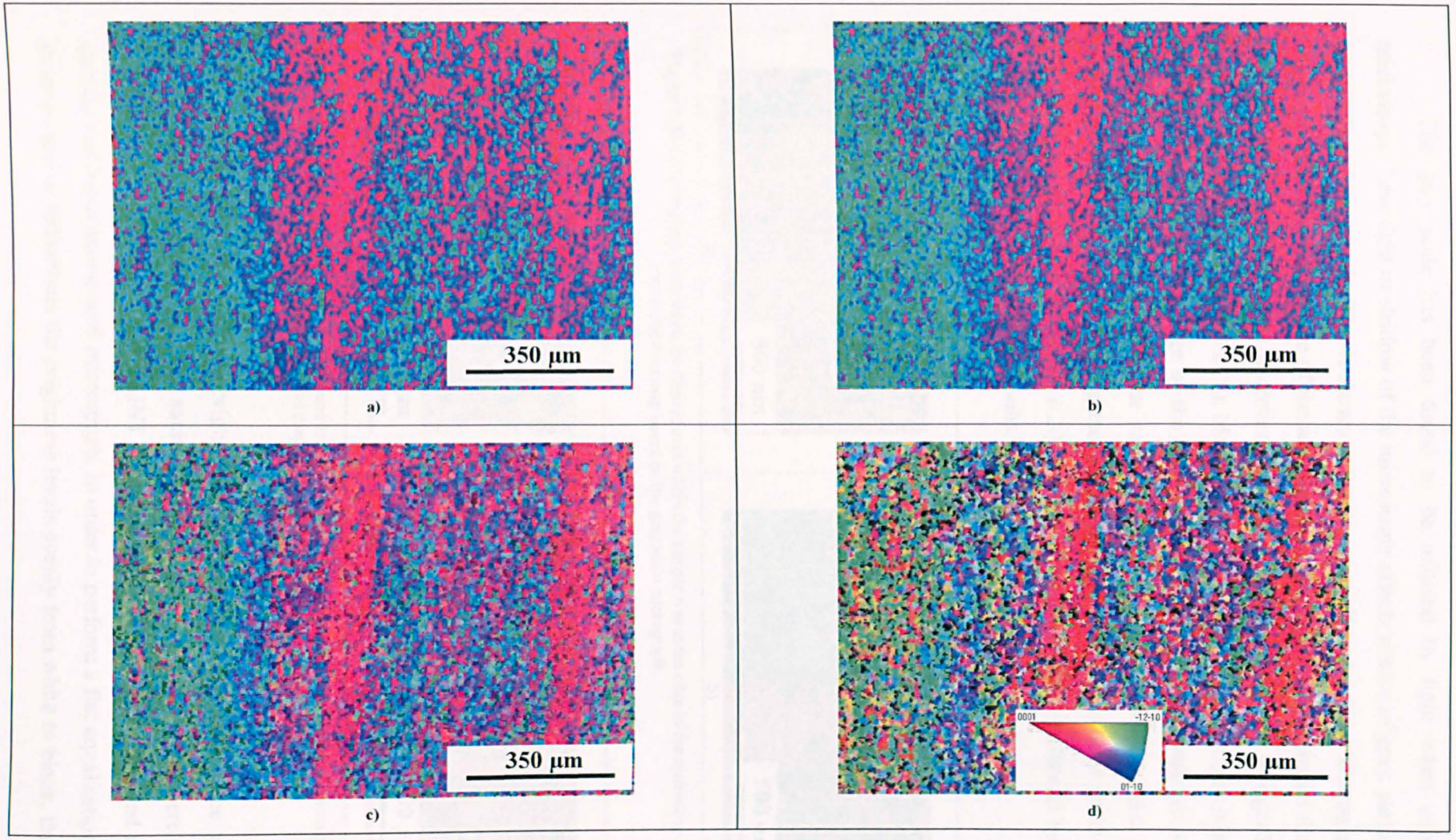

Figure 6.19 TIMETAL® 6Al-2Sn-4Zr-6Mo **a)** Colour map of the gray scale image **b, c)** merged images of the colour map and EBSD map **d)** crystal orientation map using a step size of 3µm in IPF colouring.

The gray scale has been found to be affected by light when using the microscope. Less light or shadow of the microscope affects shades of gray, particularly at the edge of the sample. This is shown in the Figures 6.20 and 6.21. Micrographs in Figures 6.20 a) and 6.21 a) are of the same area within a sample and should therefore have the same shades of gray however micrograph in Figure 6.20 a) is significantly darker than the one in Figure 6.21 a). Micrograph in Figure 6.20 a) was taken when this area of sample was at the edge of the microscope i.e. less light whereas micrograph Figure 6.21 a) was taken when the same area of sample was at the centre of the microscope. The effects of the brightness distribution of the light source on the final coloured map are shown in Figures 6.20 b) and 6.21 b).These findings should be taken into account when evaluating the results.

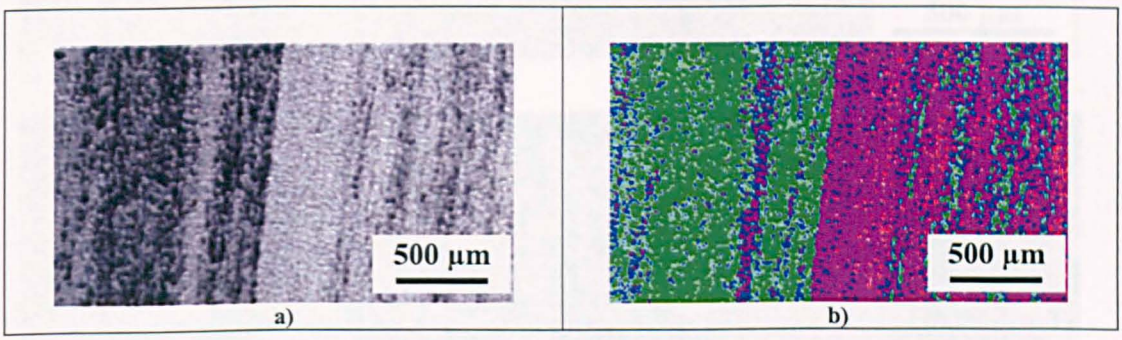

Figure 6.20 a) Micrograph taken when the desired area within the sample was at the edge of the microscope **b)** the corresponding map based on the gray scale micrograph.

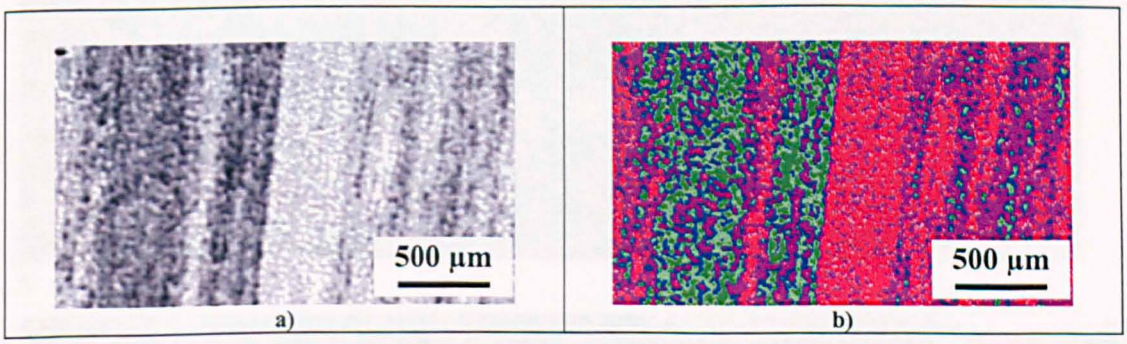

Figure 6.21 a) Micrograph taken when the desired area within the sample was at the centre of the microscope **b)** the corresponding coloured map based on the gray scale micrograph.

Due to the effects of the brightness distribution of the light source and the suspected misalignment of the light source on the sample, the micrographs were subject to adjustment in Corel PHOTO-PAINT to create a more uniform contrast and remove shading variations across each micrograph. In order to perform a flat equalisation of the shadows and to redistribute the brightness levels evenly from white to black, the entire

area of each micrograph was edited using the Corel PHOTO-PAINT Equalize command.

Greyscale images shown in Figures 6.22 a) and 6.23 a) were digitally altered using Corel PHOTO-PAINT auto equalize command for easier and more accurate interpretation. Figures 6.22 d) and 6.23 d) is the corresponding EBSD maps of the same area. Figures 6.22 b, c) and 6.23 b, c) were produced by merging the greyscale and EBSD maps in order to highlight similarities in microstructure of the sample.

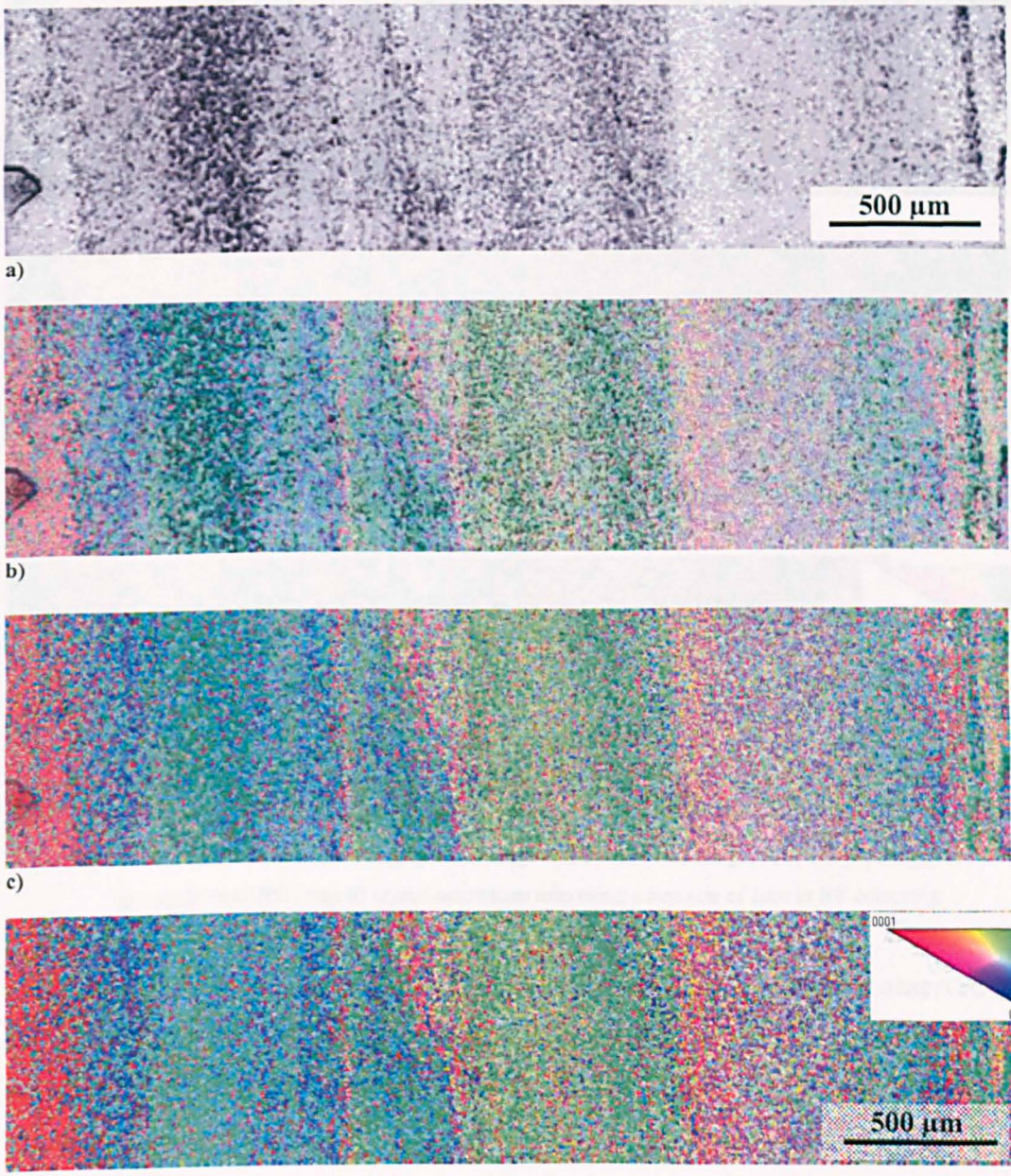

Figure 6.22 TIMETAL® 6-2-4-6 **a)** gray scale image of the heat tinted sample **b, c)** merged images of the greyscale and EBSD map **d)** crystal orientation map using a step size of 3µm in IPF colouring.

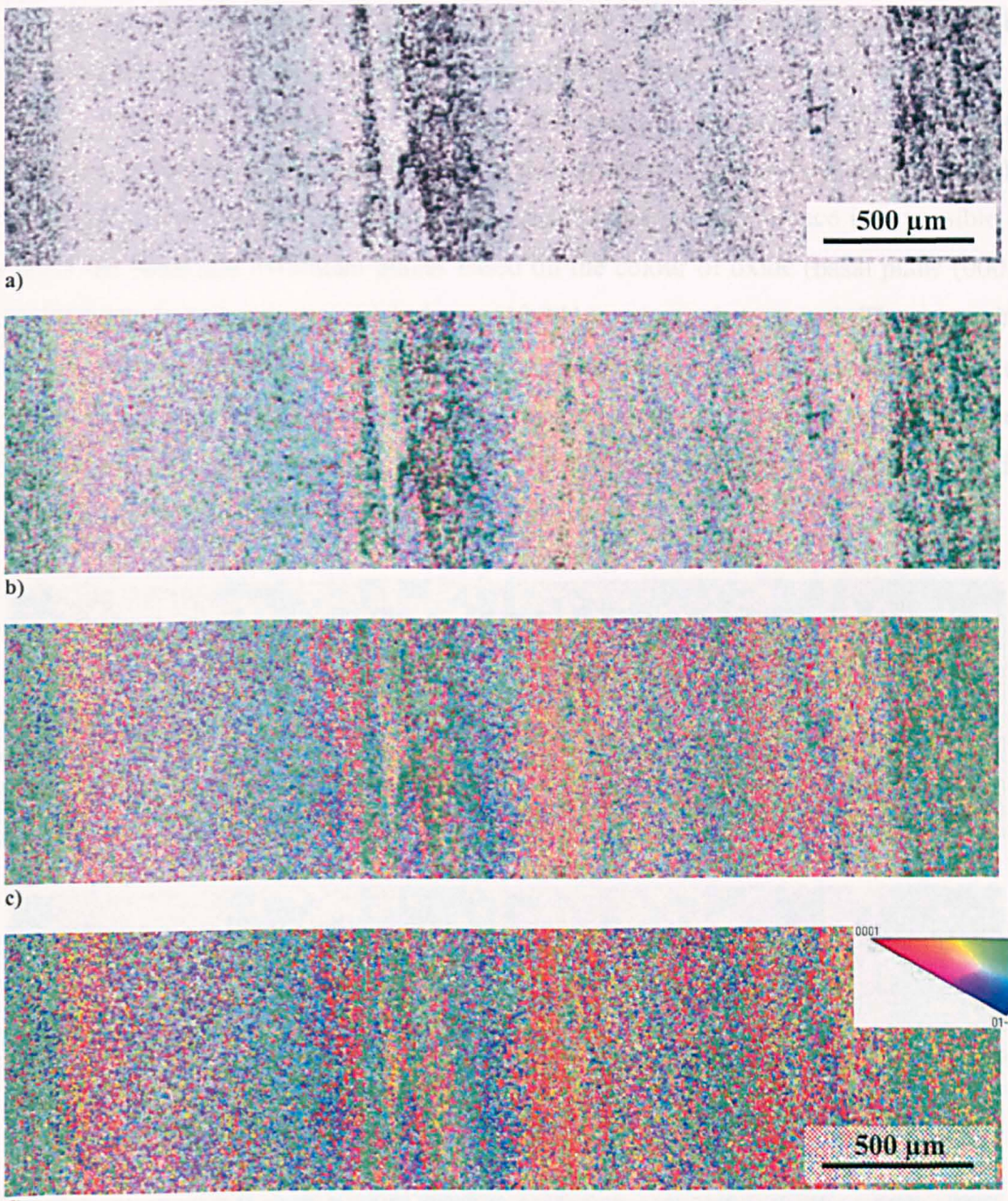

Figure 6.23 TIMETAL® 6-2-4-6 **a)** gray scale image of the heat tinted sample **b, c)** merged images of the greyscale and EBSD map **d)** crystal orientation map using a step size of 3µm in IPF colouring.

From the greyscale maps in Figures 6.22 a) and 6.23 a) it can be observed that the redistribution of black and white colours has improved significantly and the images are more uniform in comparison to the gray scale images in previous figures (e.g. Figures 6.14 a and 6.15 a).

Due to the reasons explained previously, it was not possible to create the exact colours of EBSD map on the greyscale map. In order to generalise the program (due to the difference in quality and type of microscopes used) and to simplify the problem

(because when converted from greyscale to colour map some of the colours might be meaningless in comparison to the EBSD map colours) fewer colours were introduced.

By establishing that the colour red and shades of red correspond to white and lighter greys and different shades of green correspond to black and darker greys on the greyscale, these two colours were defined as the two extremes. Hence it is possible to select the basal and pyramidal planes based on the colour of oxide (basal plane (0001) corresponds to red and pyramidal planes {10-11} corresponds to green). The remaining orientations would therefore be introduced as the colour blue. This method provides an easier way to translate colours and therefore reduce the chances of error when converting from greyscale map to colour map while giving a good knowledge of the texture. Figures 6.24 and 6.25 are shown as an example.

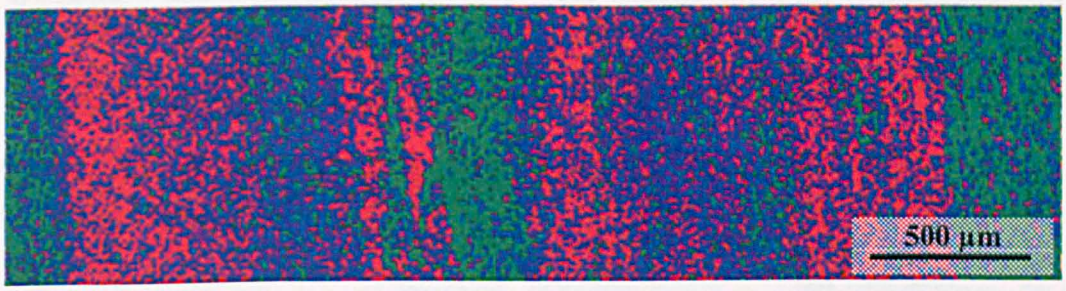

a)

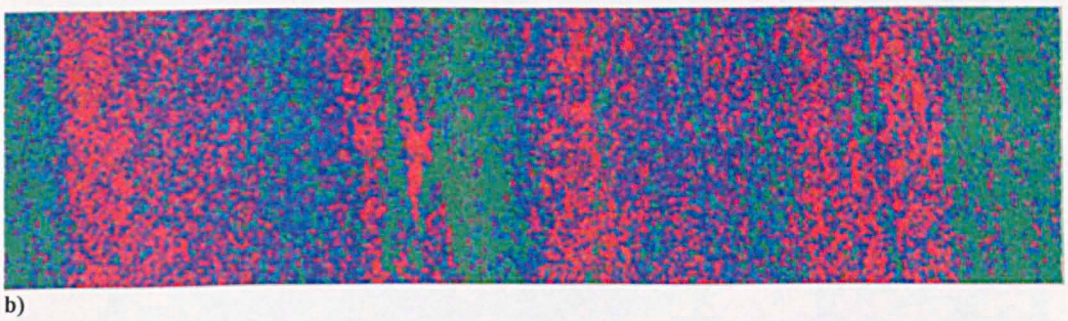

b)

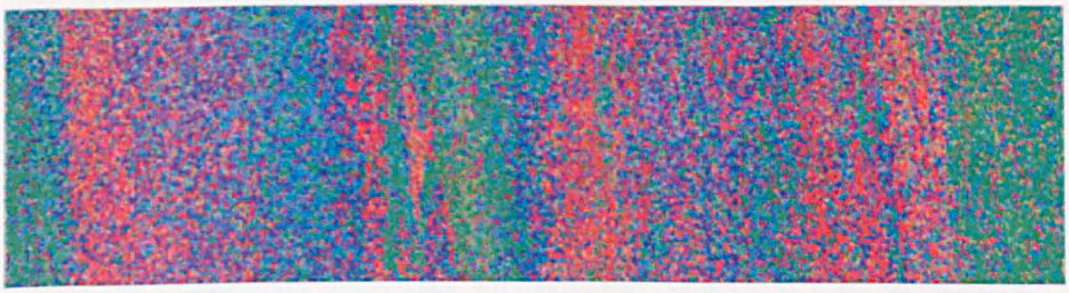

c)

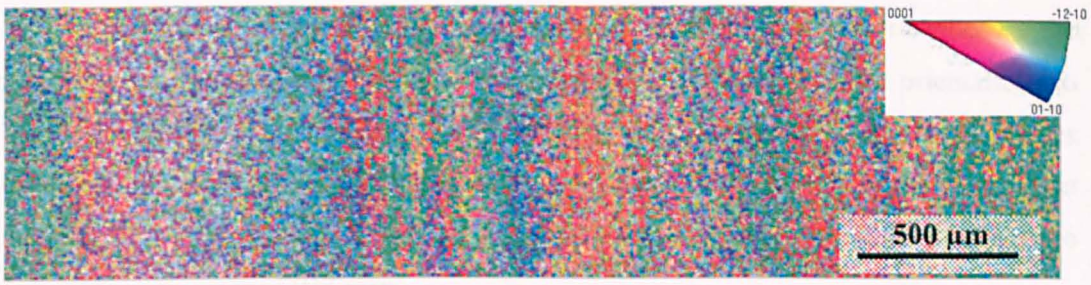

d)

Figure 6.24 TIMETAL® 6-2-4-6 **a)** colour map of the gray scale image **b, c)** merged images of the colour map and EBSD map **d)** crystal orientation map using a step size of 3µm in IPF colouring.

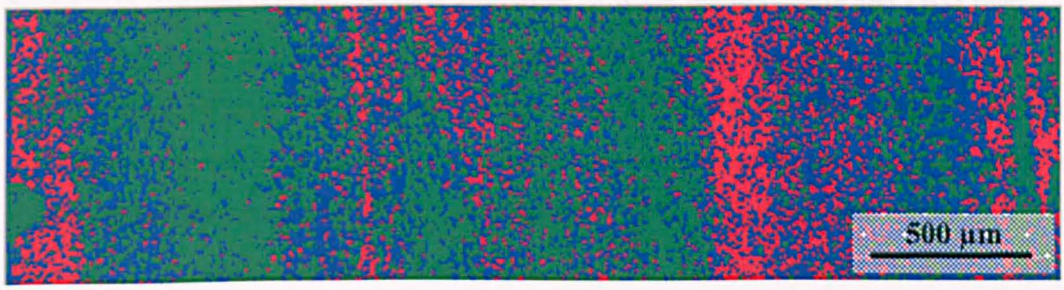

a)

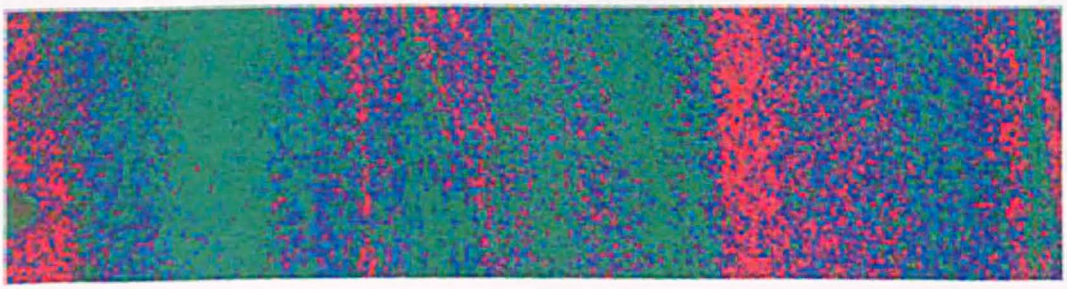

b)

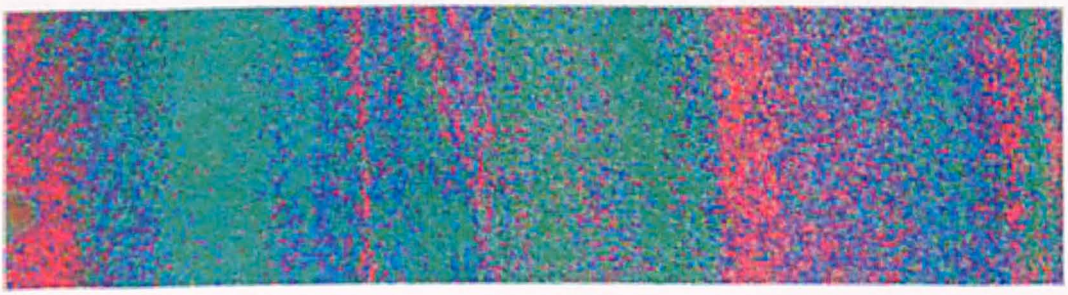

c)

d)

Figure 6.25 TIMETAL® 6-2-4-6 **a)** colour map of the gray scale image **b, c)** merged images of the colour map and EBSD map **d)** crystal orientation map using a step size of 3µm in IPF colouring.

Using these findings it was concluded that the black and darker shades on the grey scale represent pyramidal planes including other planes with close orientations to these planes while white and lighter colours represent basal planes and the other planes with close orientation. On this basis, it was possible to write a program similar to that on page 214 using Microsoft visual studio so that the greyscale image was used to highlight grains on the OIM map.

Figures 6.26 a) and 6.27 a) show grains from 200 to 255 and 0 to 60 on the grey scale respectively highlighted on the OIM map. Using this type of analysis it was then possible to confirm whether there is a relation between the greyscale and OIM map.

This program relies on the fact that both the greyscale and OIM maps are superimposed exactly. Should the images not be perfectly superimposed, the pixel highlighted on one map (within the criteria that we define in the program) may not correspond to the correct pixel on the other map. Due to the step size of the OIM map and the maps being different dimensions (due to the different techniques used in producing the maps) it was very hard to superimpose the two maps perfectly. As a consequence, there may then be some errors in the results.

In order to make this more obvious the data has been plotted in terms of number of pixels and colour purity (Figures 6.26 b) and 6.27 b)).For example, the closer the number to 255, the purer the colour red (Figure 6.17).

From the graph shown in Figure 6.26 b) it can be clearly observed that there is a high percentage of pure red present in the combination of colours within each pixel. In addition, there is a high percentage of green and blue approximately within the range of 80-170 which may explain the reason behind the yellow, orange and purple colours, e.g. high ratio of green and red needed to produce yellow.

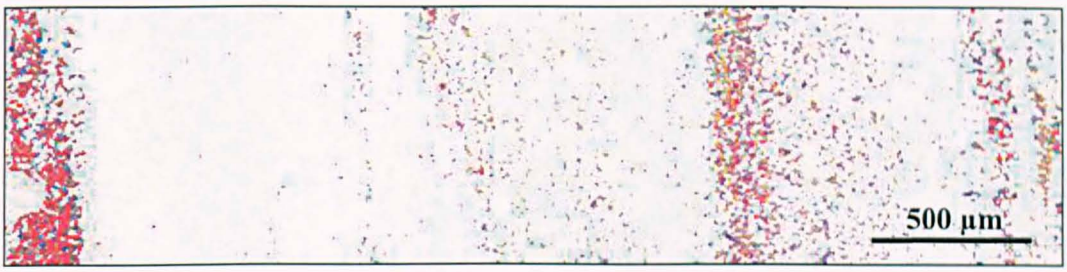

a)

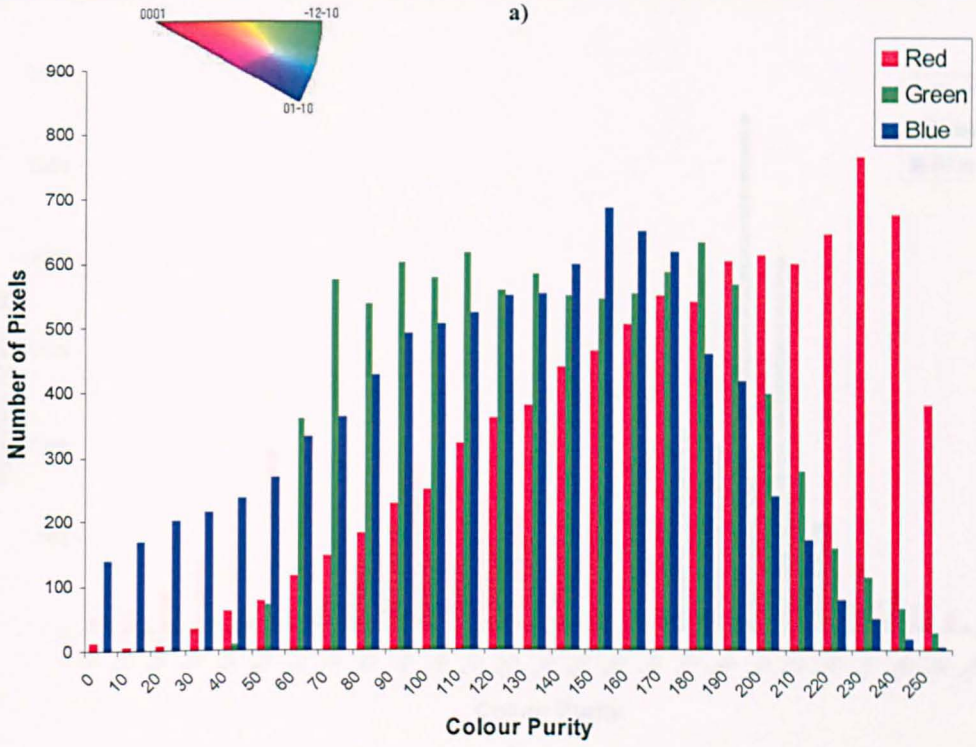

b)

Figure 6.26 a) greys between 200 to 255 being highlighted on the OIM map **b)** data has been plotted in terms of number of pixels and colour purity.

From the graph in Figure 6.27 it can be observed that there is high percentage of green within the range of 170-200. The principles explained above also apply to this graph in that although there is a high percentage of green within the range of 170-200, there is insufficient pure green to counteract the effect of the blue colour resulting in a bluish tinge to the green therefore making it teal coloured. Note that the red on the left hand side of the OIM is an error due to a scratch on the sample.

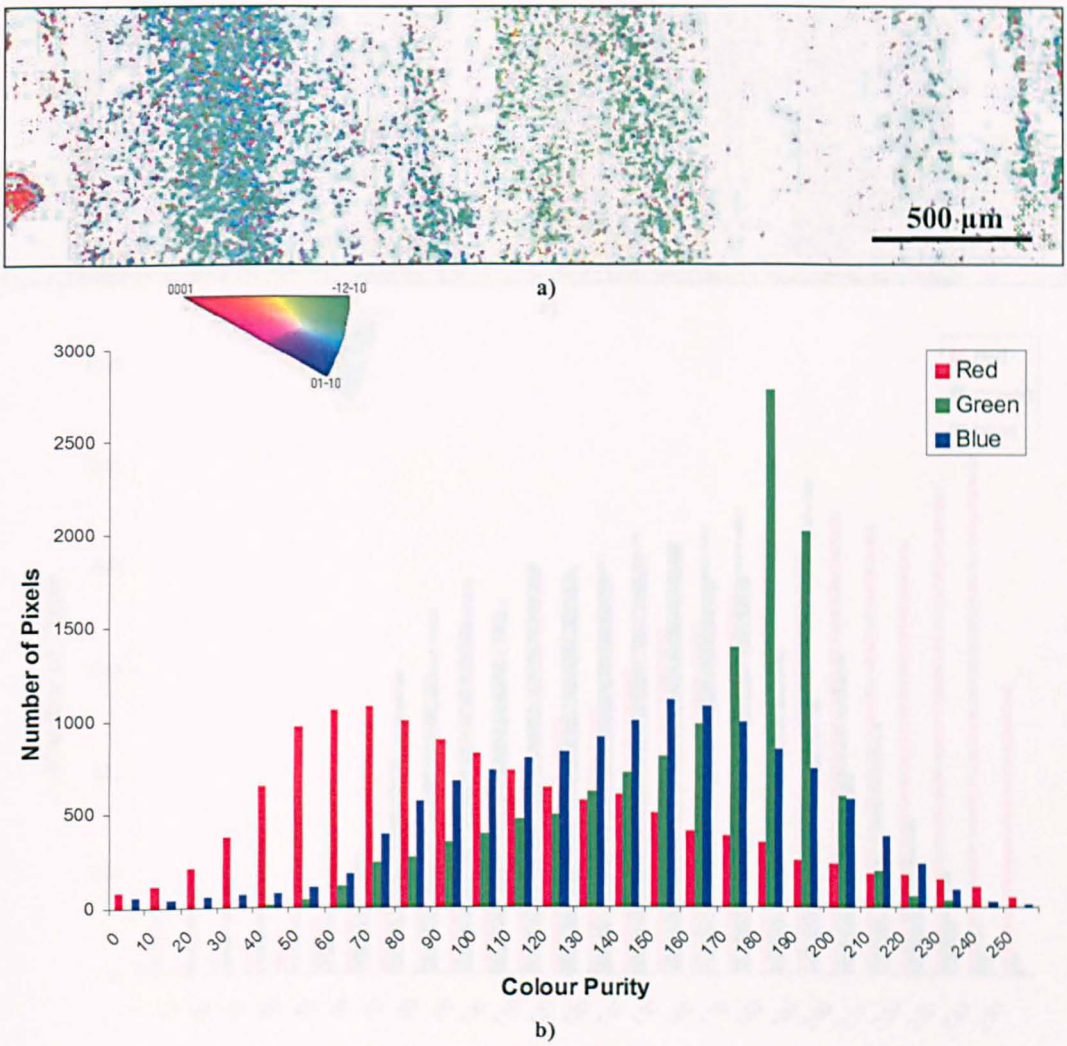

Figure 6.27 a) greys between 0 to 60 being highlighted on the OIM map **b)** data has been plotted in terms of number of pixels and colour purity.

Figure 6.28 shows the result for an additional section within the sample. As was shown in previous OIMs, this figure also has other colours in addition to red. This can be due to the high percentage green and blue colours creating colours like yellow and orange etc.

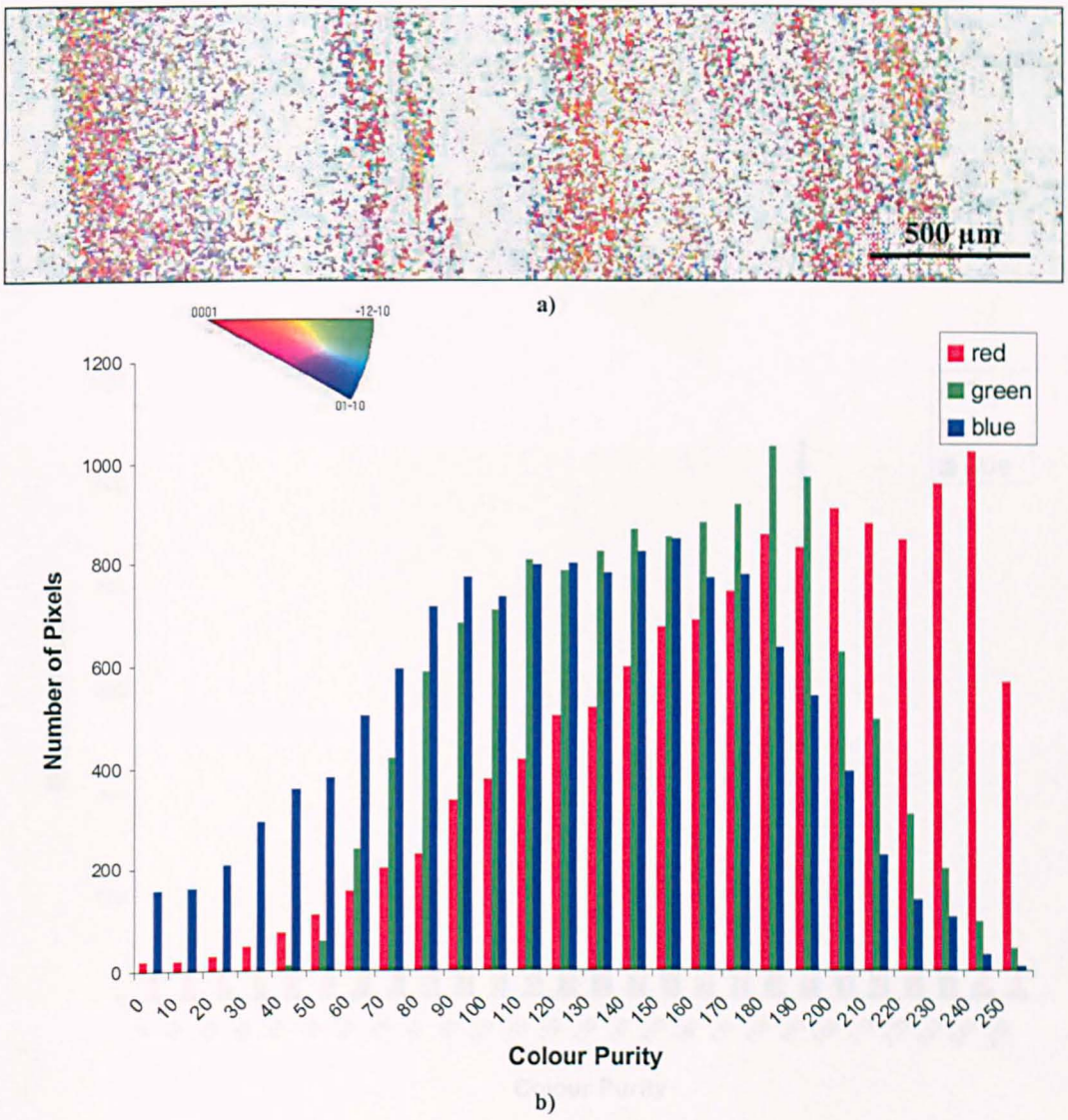

Figure 6.28 a) greys between 200 to 255 being highlighted on the OIM map **b)** data has been plotted in terms of number of pixels and colour purity.

Figure 6.29 a) has a much purer selection of predominantly green colour. This may be explained by the high percentage of green between the ranges of 180 and 210 resulting in the green colours being present. Small ratio of blue and red is available resulting in yellow and purple colours.

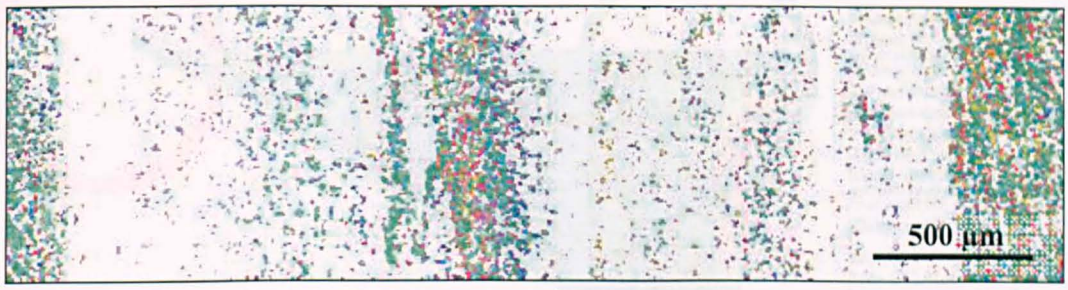

a)

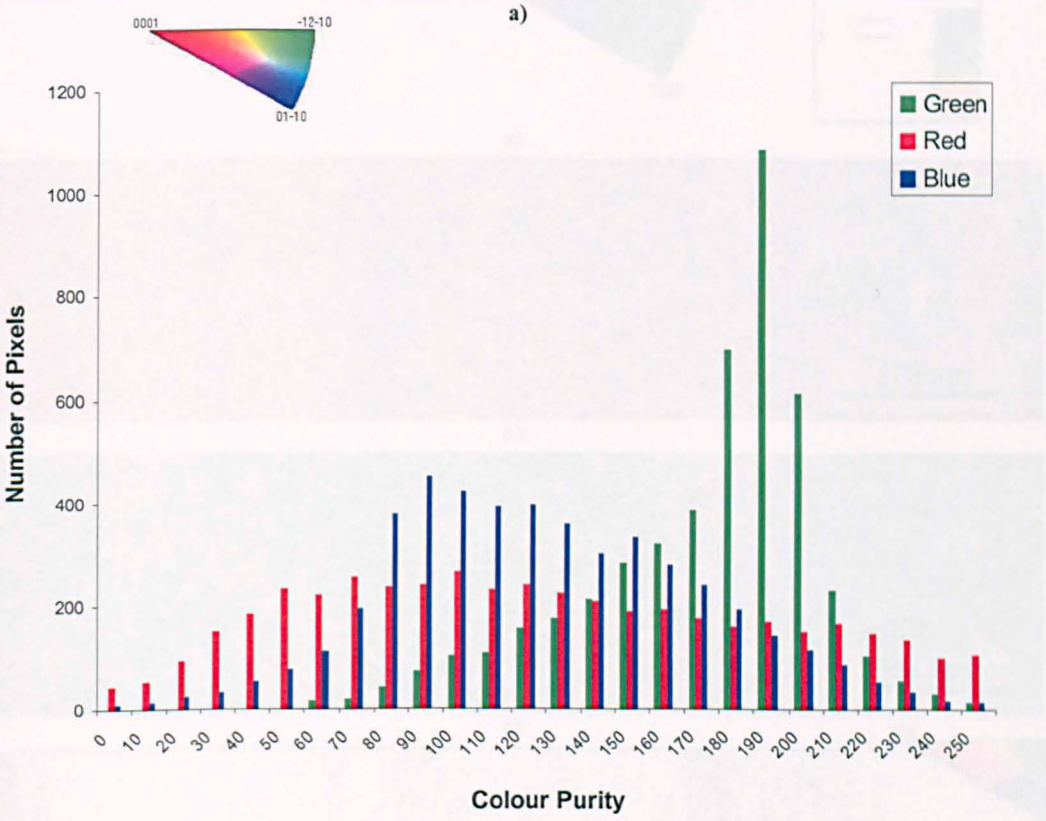

b)

Figure 6.29 a) greys between 0 to 60 being highlighted on the OIM map **b)** data has been plotted in terms of number of pixels and colour purity.

IPF for samples shown in Figures 6.24 d) and 6.25 d) were obtained using Channel 5 software. This allows the crystallographic orientations to be quickly interpreted in terms of the sample coordinate system. The data set of interest were then selected (using subset in channel 5) from the IPF which in this case is the orientations close to basal and pyramidal planes (Figures 6.30 a) and 6.31 a)). The selected areas (subsets) are shown in a separate OIM and compared to those of Figure 6.26 a), 6.27 a), 6.28 a), 6.29 a). This is shown in Figures 6.30 and 6.31.

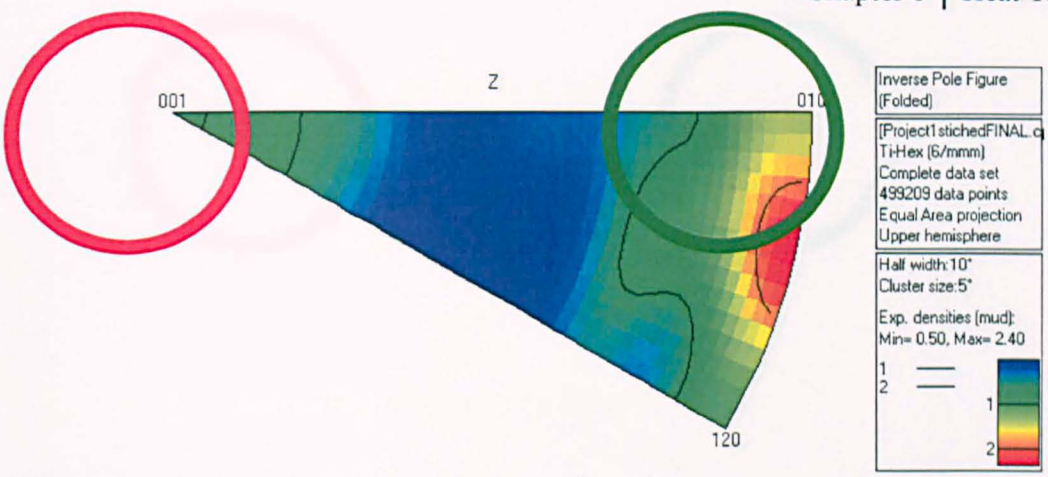

a)

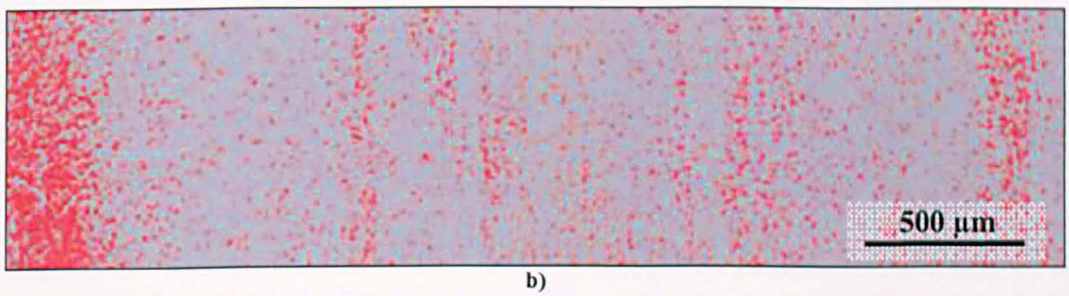

b)

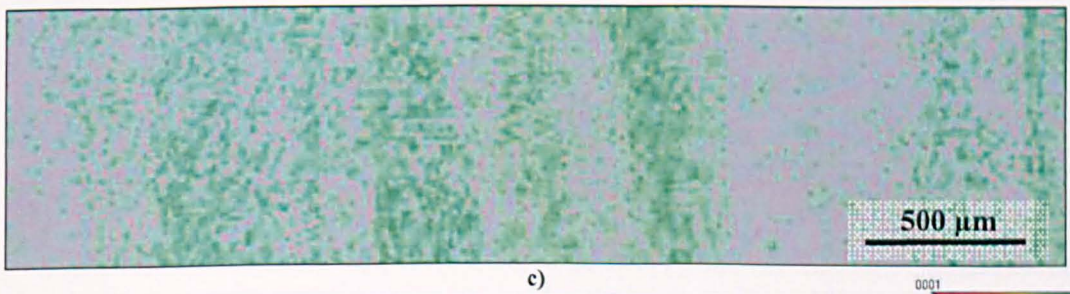

c)

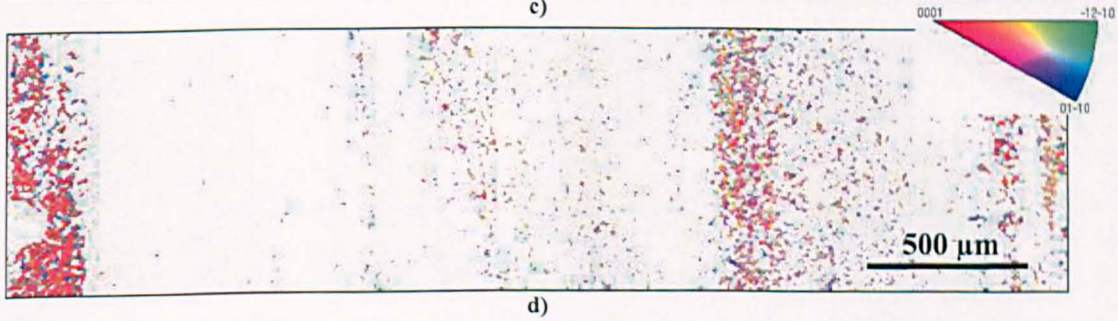

d)

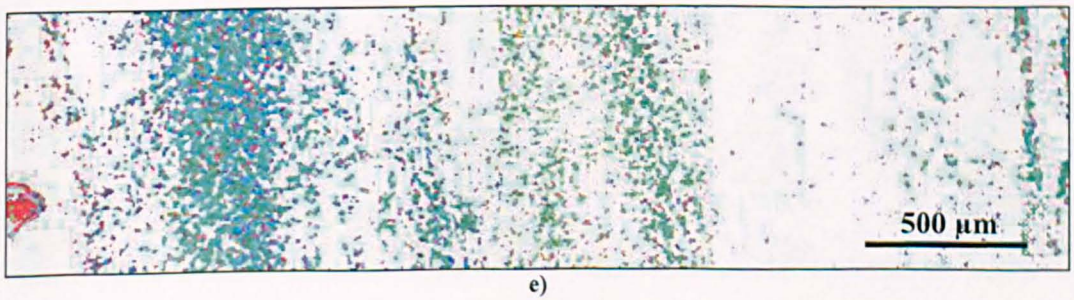

e)

Figure 6.30 a) IPF representation **b, c)** basal plane and pyramidal planes respectively **d, e)** grains from 200 to 255 and 0 to 60 on the grey scale respectively highlighted on the OIM.

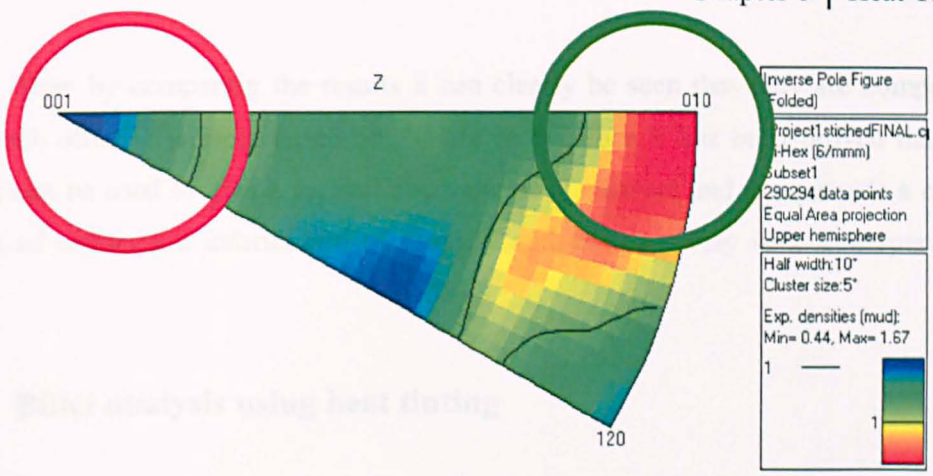

a)

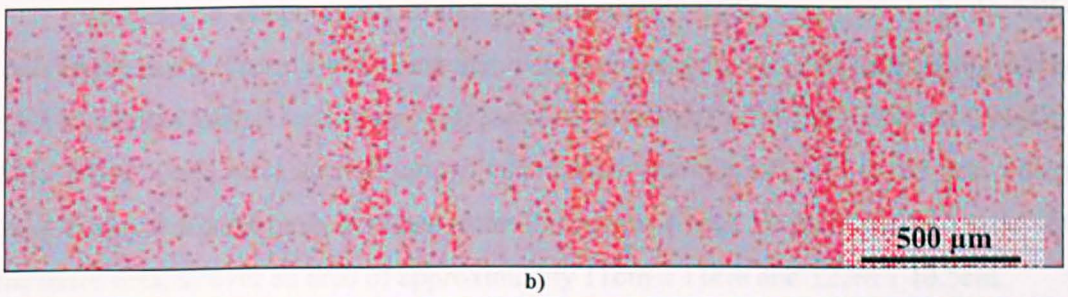

b)

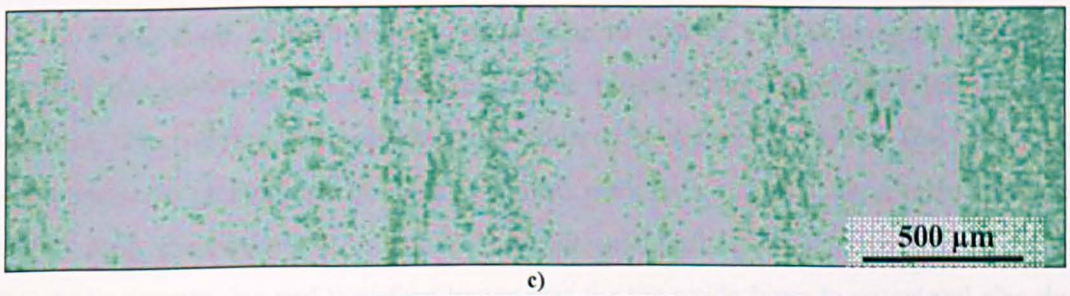

c)

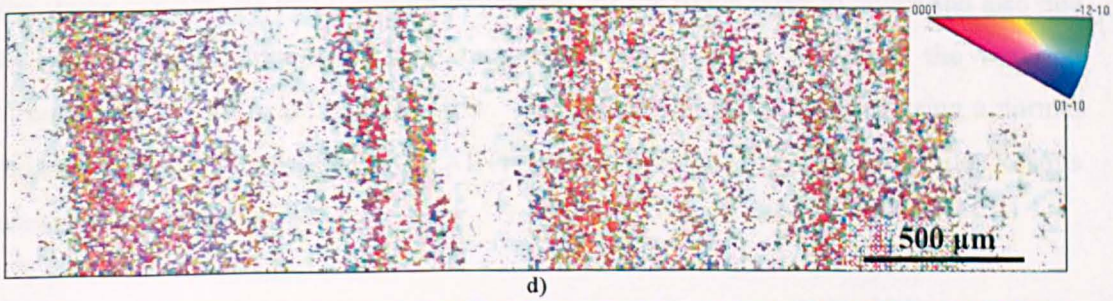

d)

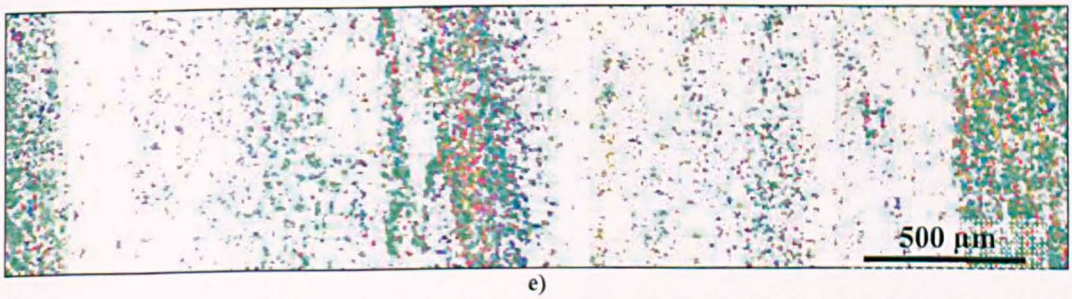

e)

Figure 6.31 a) IPF representation **b, c)** basal plane and pyramidal planes respectively **d, e)** grains from 200 to 255 and 0 to 60 on the grey scale respectively highlighted on the OIM.

Now by comparing the results it can clearly be seen that they are comparable with each other. Therefore based on the above evidence it has been proven that heat tinting can be used to give a general overview of the texture and can provide a certain degree of orientation information both easily and inexpensively in a short period of time.

6.4 Billet analysis using heat tinting

In order to obtain a represented global texture it is important to study the billet on a larger scale. Therefore the next step was to investigate whether heat tinting can be used to analyse global texture through the cross section of a TIMETAL® 6Al-2Sn-4Zr-6Mo billet. Tests were carried out on two quarter sections of a billet (25 mm thick), each having different process routes (refer to Chapter 3 page 50 and Chapter 5 page 160 for more details) over an area of approximately 11cm x 11cm and 12cm x 10.5cm.

Preparation of both billets was similar to that of EBSD samples (shown in Chapter 4), however, due to the size of the billets being larger than the previous samples, the grinding and polishing was undertaken manually and the final polishing step required a greater amount of time. Billets were then heated using a temperature of 630°C for approximately 40 minutes. This increased heating time was necessary due to the larger sample size and therefore larger area for the oxide layer to cover and also due to the increased amount of time required for the sample to reach the required temperature for the oxide layer to grow. The billets were then scanned using a normal scanner and using Corel PHOTO-PAINT images were converted to greyscale. Results are shown in Figures 6.32.

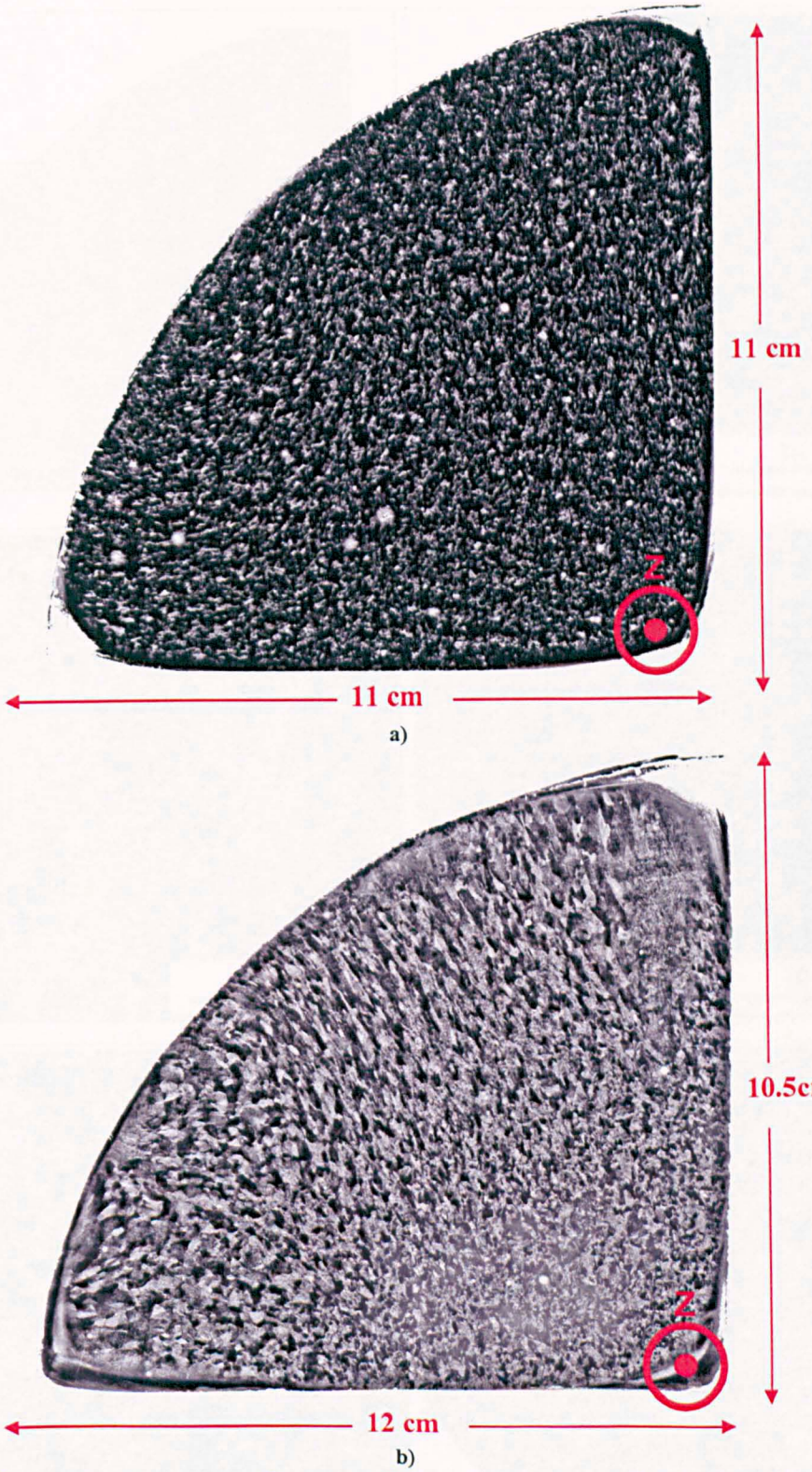

Figure 6.33 Cross section of two quarters of the as-forged billets, with reference axes Z **a)** small billet (chapter 3) **b)** alternatively forging route (chapter 5).

In order to analyse the billets in detail, each billet was sampled as shown in Figures 6.34 and 6.35.

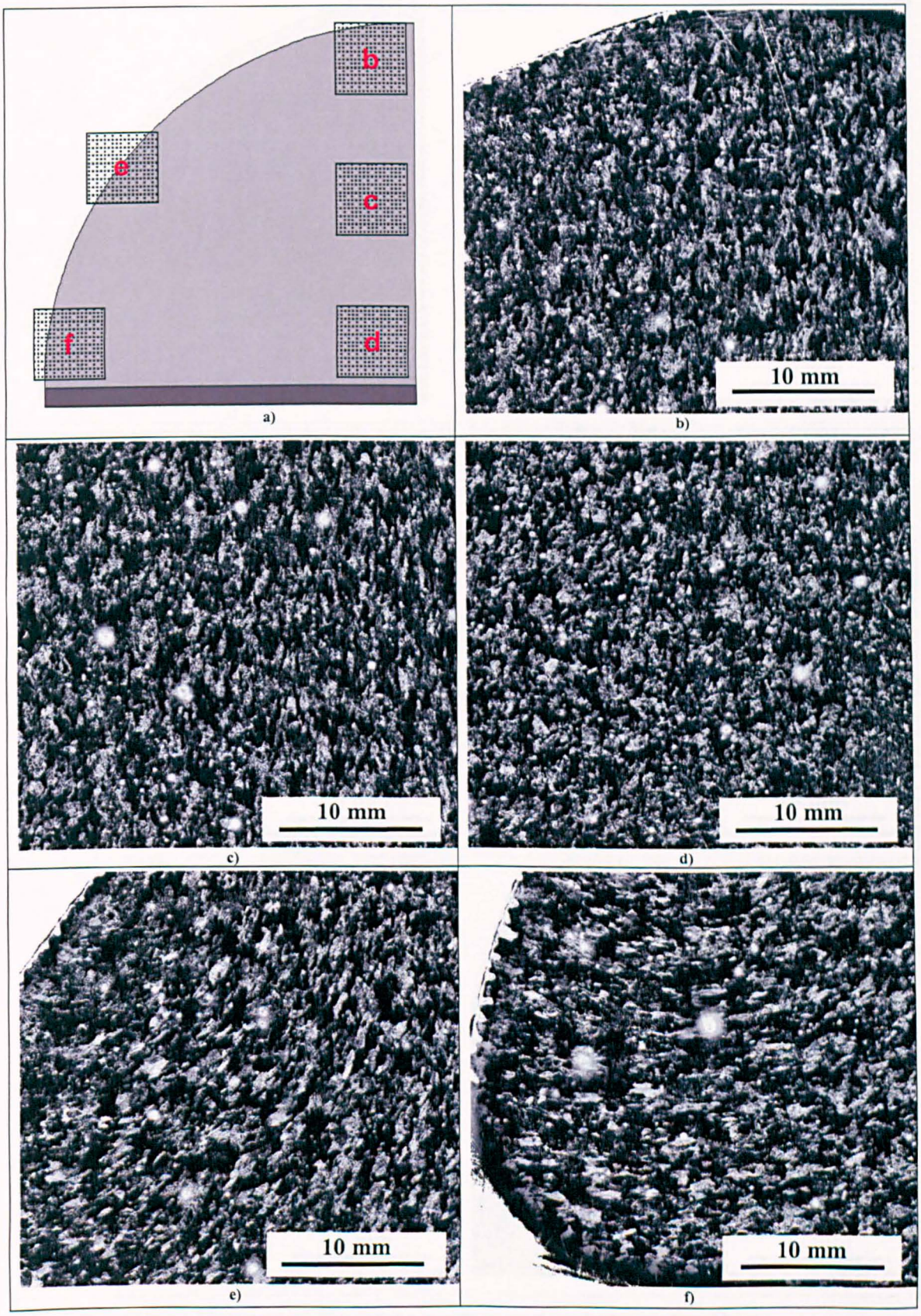

Figure 6.34 Different locations within a quarter section of the small billet.

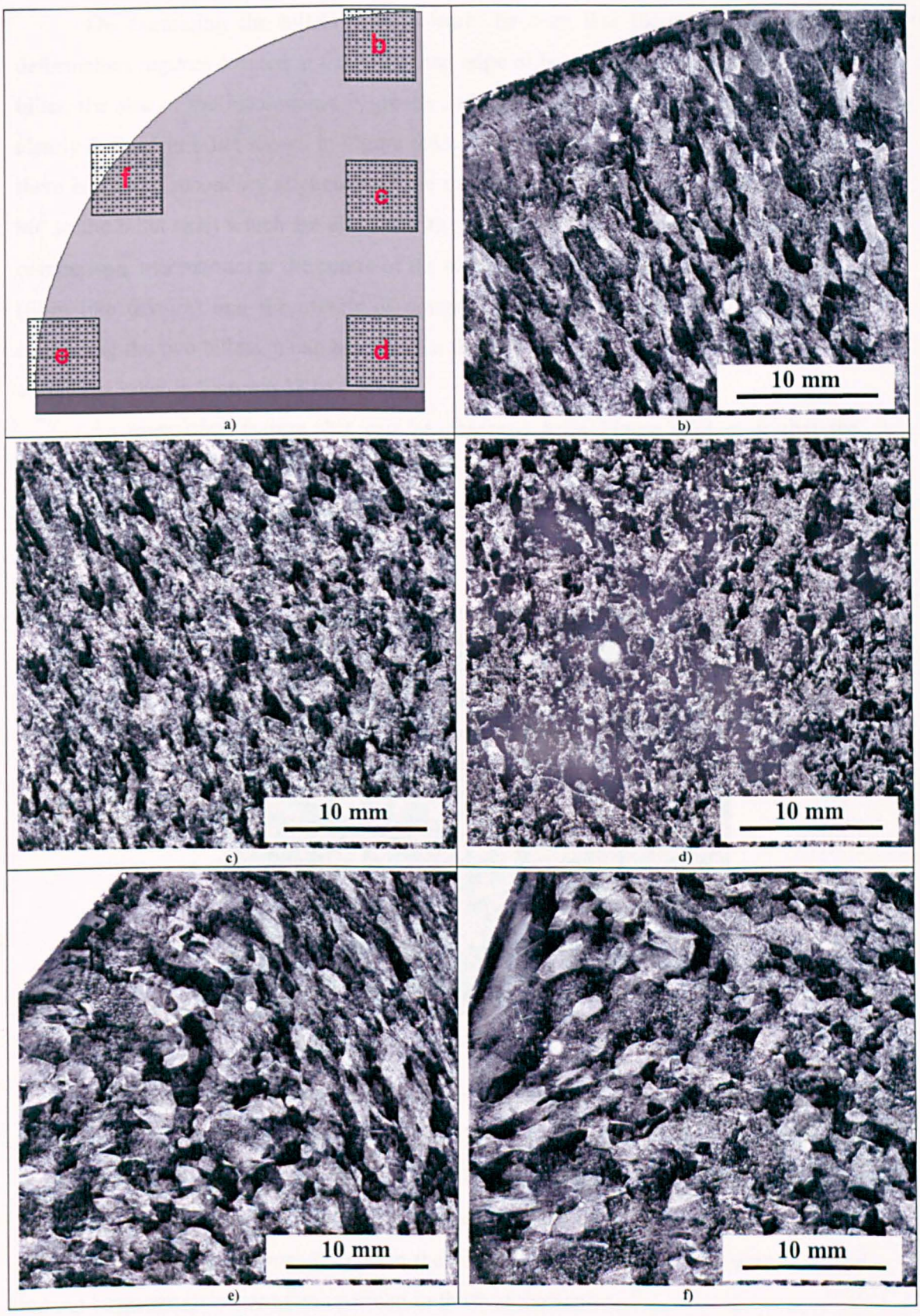

Figure 6.35 Different locations within a quarter section of the alternatively forged billet.

On examining the billets it can clearly be seen that there are two separate deformation regimes located at the centre and edge of both billets. At the edge of each billet, the size of the macrozones is greater in comparison to the centre. This is more clearly defined in billet shown in Figure 6.33 b). In addition, at the edge of each billet there is a clear secondary alignment of the macrozones in the transverse plane (i.e. at 90° to the billet axis) which are aligned with the flow of the compression direction. In comparison, macrozones at the centre of the billet are mainly parallel to the billet axis Z (fibre like texture) and the effects of compression direction are not visual. When comparing the two billets, it can be seen that the size of the macrozones is much greater within the billet in Figure 6.33 b).

An interesting feature that can be observed from Figure 6.34 e) is that the microstructure is not always aligned with the flow of compression direction (shown more clearly in Figure 6.36). This may be due to the formation of dead zones (as explained in chapter 4).

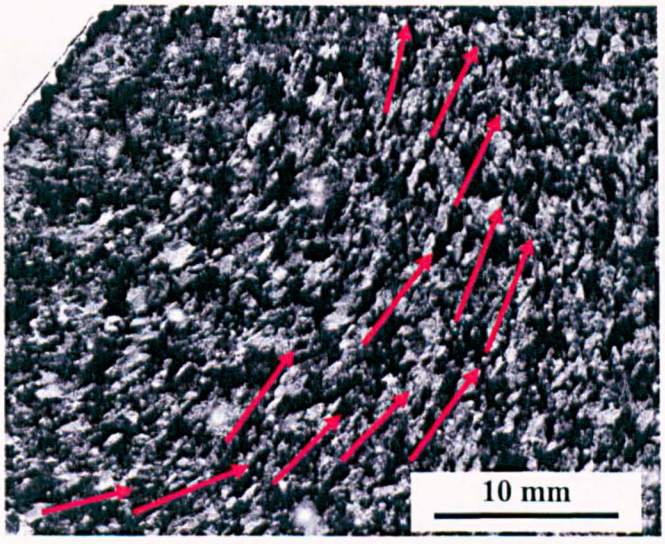

Figure 6.36 Area within the small billet.

Additional analysis was performed for the billet shown in Figure 6.33 b) in a plane containing the longitudinal axis of the billet, Z (i.e. parallel to the billet axis). This is shown in Figure 6.37. Figure 6.37 clearly demonstrates that the billet contains macrozones throughout the whole area. It also confirms the finding that there are two separate deformation regimes located at the centre and edge of the billet with the edge having larger macrozones in comparison to those at the centre.

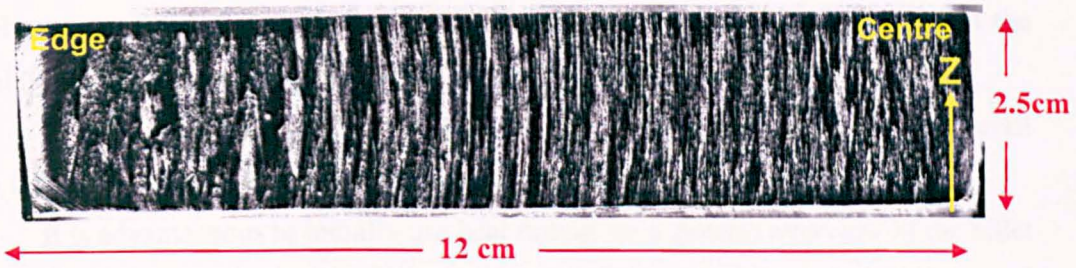

Figure 6.37 Cross section of the alternatively forged billet.

As previously discussed in Chapter 4 It was not possible to draw any strong conclusions regarding the distribution of the texture across the edge of the larger billet because the size of the EBSD maps were smaller in comparison to the size of the macrozones. Heat tinting was therefore carried out in an attempt to confirm these findings on the plane parallel to the billet axis of the larger billet (Figure 6.38) and compared to those shown in Figure 3.10 in chapter 3. This confirmed the EBSD results which demonstrated that the width of the macrozones at the edge of the large billet were wider in comparison to those of the smaller billet.

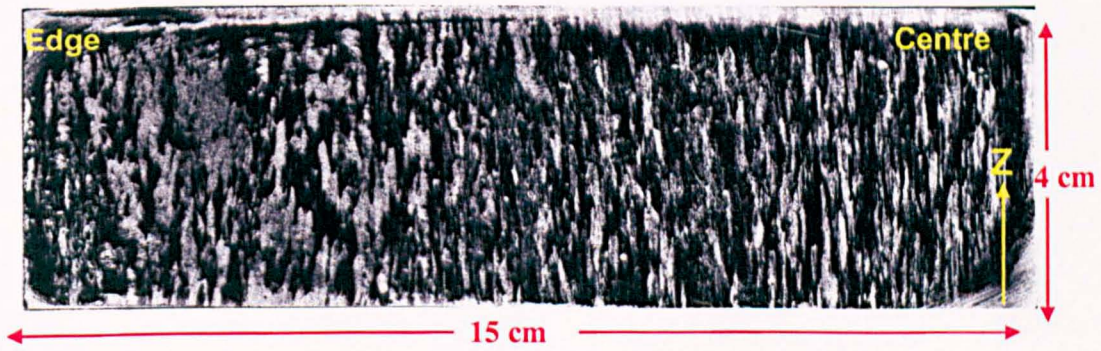

Figure 6.38 Cross section of the large billet (chapter 3).

6.5 Summary

Heat tinting is a metallographic technique which is based on developing an oxide film on a polished surface. This technique is a very sensitive process capable of producing widely varying colours with just small changes to the temperature and time. Laboratory furnaces can be used as a simple heat source in order to obtain a qualitative version of texture. This technique cannot be used for detailed analysis (identifying the texture at a very specific location) however it provides a quick and easy method to identify overall microstructure. Features such as macrozones can be seen without

employing costly texture analysis. By using this technique it is possible to select the basal (0001) and pyramidal planes {10-11} based on the colour of their oxide.

In a laboratory where EBSD is not available or the cross section of the material is to large, this technique can surely save time and money over other methods.

It is advantageous to initially use heat tinting for a general overview of the billet and subsequently utilise EBSD for a more detailed analysis. This can be demonstrated using the example of transformation regions where areas of large to smaller macrozones can first be identified using heat tinting and then analysed in more detail using EBSD.

Chapter 7

CONCLUSIONS AND FURTHER WORK

7.1 Microstructure

- This work has shown the effects of the thermomechanical processing stages via open die forging on the microstructure and crystallographic texture evolution of three different diameter billets of the $\alpha+\beta$ TIMETAL® 6-2-4-6 alloy were analysed. A quantitative study of α_p within the microstructure of these three billets has been included with an objective of determining if any variation within the cross-section of the billet could be related back to macroscopic deformation history during breakdown from the VAR ingot.

- Three features (α_p volume fraction, the size distribution of the α_p, and the aspect ratio of the α_p) were analysed in longitudinal and/or transverse planes within the billet using scanning electron microscopy and quantitative digital analysis software on individual areas of 550 x 550 μm^2.

- Within two of the billets (313 mm and 213 mm diameter) large and small respectively, the deformation axes were noted on the billet at an intermediate stage of processing and remained on the final billet. Hence, all analysis of the microstructure was investigated with respect to these critical axes. The metallographic observation of these billets (as received materials) revealed a bimodal microstructure consisting of relatively equiaxed α_p within an acicular transformed β matrix throughout the whole cross-section of the $\alpha+\beta$ TIMETAL® 6-2-4-6 billets. The results showed, with the exception of the extreme edge to a depth of 10 mm, that the microstructure (at least at the scale at which it was quantified) is homogeneous regardless of its location with respect to the deformation axes.

- Despite the microstructure being homogeneous in these 313 mm and 213 mm diameter billets there were a few differences noted between the two billets. At the centre of the larger billet continuous α grains were observed (grain boundary α) - a feature the smaller billet did not contain. This was explained by two factors: slower cooling rates at the centre of the larger diameter billet in comparison to its edge and penetration of strain at the centre of the larger billet not being enough to break up the grain boundary α. Also at the centre of the large billet there was a slight increase in the total percentage of α_p volume which was again thought to be a result of the slower cooling rate at the centre of the billet in comparison to its edge.

- A variation in the percentage of α_p volume within the 313 mm and 213 mm diameter billets was noted. Although the total percentage of α_p volume in the larger billet was generally uniform, there was a higher percentage of α_p volume in the smaller sized billet when compared to the larger billet. This was thought to be due to a number of reasons such as the recrystallization or solution heat treatment after the forging procedure, a slight difference in the chemical composition of both billets (this can alter the shape of the β transus approach curve) or segregation.

- The third billet (alternatively forged billet) was analysed. This billet underwent a major difference in its forging route when compared to the previous two billets in that it was $\alpha+\beta$ forged following the ingot breakdown above β transus temperature therefore resulting in termination of the prestrain and β recrystallisation stage. Unfortunately unlike the previously discussed billets, deformation axes had not been noted at an intermediate stage therefore samples were picked randomly and they were not linked to any specific forging directions.

- Results from the alternatively forged billet showed a significant difference in the α_p size distribution meaning a higher percentage of primary alphas having a smaller grain areas. In fact the actual scale of the alternatively forged billet microstructure was smaller however there were some larger grains

demonstrating the inhomogeneity of the microstructure. In addition, the grains were longer and thinner in shape. This suggested that the level of globularisation within this billet was lower than the other two billets. Temperature and amount of deformation are therefore the most directly related parameters to α phase refinement since strain provides the driving force for the globularisation. Based on the definition of globularisation by Njall Stefansson [93] only 59% of the alternatively forged billet had been globularised.

7.2 Texture

- It was shown that the textures of both large (313 mm diameter) and small (213 mm diameter) billets were strongly dependent on the strain imposed by the deformation process. Macrozones were observed throughout the whole billet stretching along the billet axis. α_p, α_s and β grains all contributed to this sharp local texture. At the edge of the larger billet however, the widths of the macrozones were wider in comparison to those of the smaller billet. This was found to be due to the lack of strain being applied to the larger diameter billet during its final stage of production. It is not possible at this stage however to draw any strong conclusions regarding the distribution of texture within this area (edge of the larger billet) due to the size of the map being small in comparison to the size of the macrozones.

- In general, the large and small diameter billets' textures were quite weak however there were some noticeable differences in the textures from the edge towards the centre of each billet where the crystallographic texture was very similar for all samples. This was due to the β texture already existing in this location at the recrystallization stage and the strain applied at final $\alpha+\beta$ stage not being sufficient to remove it. For these reasons therefore, this texture may have remained in the final billet. At the edge of the billet however the crystallographic texture was aligned with the compression direction and unlike the centre of the billet strong influence of the variant selection mechanism was observed. Symmetry was particularly noticeable at the centre of the billet which could be explained by the non equal strains imposed about the billet axis during

the forging process when the billet was forged from a rectangular to a circular cross section.

- Analysis of the alternatively forged billet, demonstrated that the strong texture seen at the centre of both previously analysed large and small billets had been replaced by a less intense fibre like texture. There is therefore potential regarding the future development of this process route but it is necessary to determine a method to increase the level of globularization within α_p. It was clear there was insufficient strain in the α+β region to achieve globularization. It was not clear however whether increasing the strain would produce the strong texture dominant in the previous two billets or whether this strong texture was due to the recrystalisation stage that regenerated the strong β texture which was transferred to α texture and could not later be removed.

7.3 Heat tinting

- In order to analyse the global texture of the billet using EBSD, it was necessary to examine a number of samples from a variety of locations within the billet. There were however a number of disadvantages to this procedure as there was a size limitation per sample. In addition, the procedure was very time consuming and the equipment required is very expensive (sirion FEGSEM) therefore institutions may not be able to afford both the initial cost of the equipment and its upkeep. Furthermore, although many samples were analysed, the results were not complete.

- Heat tinting is a very sensitive process capable of producing widely varying colours with very small changes to the heating time and temperature of the samples. During this research, the obvious disadvantage of heat tinting in comparison to EBSD was that it could not identify texture at a very specific location or give a very detailed analysis. However, features such as macrozones could be seen without employing costly texture analysis. On the other hand in comparison to etching, heat tinting did not require the use of dangerous chemicals such as Kroll's reagent (containing hydrofluoric acid) and the colours

generated by heat tinting gave some degree of texture information as the basal (0001) and pyramidal {10-11} planes could be detected based on the colour of their oxide.

- Additional advantages of heat tinting were that there was no size limit to the sample (providing that it was possible to grind and polish the sample and a laboratory furnace was available) and the procedure was less time consuming as a quarter section of a billet was heated and after approximately 40 minutes was ready for analysis. Conclusions could be reached regarding the distribution of texture at the edges of the larger billet which was not possible using EBSD because the size of the map was too small in comparison to the size of the macrozones.

- Heat tinting was also used to confirm that there were two separate deformation regimes located at the centre and edge of both billets. The macrozone arrangement was very similar for all locations at the centre of the billet however at the edge the size of the macrozones was much greater and they were distributed radially across the circumference of the billet. Heat tinting could therefore be used to confirm EBSD findings.

- After using heat tinting to analyse the smaller billet, it was determined that the microstructure alignments were sometimes different in comparison to rest of the billet due to dead zones. Using EBSD to determine this type of feature would be very time consuming as the whole surface area of the sample must be analysed. Another example to highlight the benefits of heat tinting is in determining the transition point from the large macrozones to small macrozones (separate deformation regimes located at the centre and edge of the billet) which would not be feasible using EBSD.

- Heat tinting therefore has advantages as it gives a general overview of the billet with some degree of texture information and large areas of the sample can be analysed quickly. By having the general overview of the billet, interesting

features can then be selected and EBSD subsequently utilised for a more detailed analysis.

7.4 Further work

- In order to be able to analyse the global texture and microstructure of the titanium billets, knowing the process history of the billets is crucial. Although noting the deformation axis provided extra information regarding texture arrangement throughout the billet, it was not sufficient to analyse the data completely. For example, the similarity in texture arrangement at the centre of the small billet (Chapter 4) was assumed to be due to the β texture already existing in this location at the recrystallization stage. Therefore, in order to investigate and confirm this assumption, analysis of samples from all stages (in particular from the recrystallisation stage) of the forging process route is required.

- Due to the size of the map being small in comparison to the size of the macrozones, it was not possible to draw any strong conclusions regarding the distribution of texture across the whole sample. Therefore in order to attain the true statistical texture of each samples, in any future studies, it would be useful to analyse a larger areas of samples with a smaller step size or to use alternative methods such as neutron diffraction which allows analysis of larger areas within each sample.

- As texture is very strain path dependent, final element modelling is useful in obtaining an appreciation of the strain path history for each billet. The modelling that has been completed so far has only given an indication of the total strain applied to each billet and demonstrated there is a variation of strain within the billet with the centre of the billet experiencing more strain than the edge. Therefore in order to undertake final element modelling, the flow behaviour (strain-stress flow curve) in addition to the plain compression test of the material is required.

- In order to confirm the obtained heat tinting results, the relationship between the oxide film and the composition, structure and properties of titanium of different compositions must be analysed in further work.

Chapter 8

REFERENCES

1) S.P. Fox, D.F. Neal. *The role of computer modelling in the development of large scale primary forging of titanium alloys.* Titanium '95: Science and technology ed. by P.A. Blenkinsop, W.J. Evans and H.M. Flower, (The Institute of Materials, London, 1996) pp. 628-635.

2) G. Dumas, Y.M. Saunier, F. Poirier, E. Wey. *Control of large diameter Ti-6-4 billet microstructures through modelling of the forging process.* Titanium '95: Science and technology ed. by P.A. Blenkinsop, W.J. Evans and H.M. Flower, (The Institute of Materials, London, 1996) pp. 651-658.

3) A.F. Wilson, V. Venkatesh, R. Pather, J.W. Brooks, S.P. Fox. *The prediction of microstructural development during TIMETAL ® 6-4 billet manufacture.* Titanium-2003: Science and technology ed. by G. Lütjering and J. Albrecht, (WILEY-VCH Verlag GmbH & Co. KGaA, Weinheim, 2004) pp. 321-328.

4) C. Bescond, D. Lévesque, J.-B. Guénette and J.-P. Monchalin: *Proc. 16th WCNDT 2004 - World Conference on NDT*, Montreal, Canada (2004).

5) L. Germain, N. Gey, M. Humbert, P. Bocher, M. Jahazi. *Analysis of sharp microtexture heterogeneities in a bimodal IMI 834 billet.* Acta Materialia, Vol.53 (2005), pp.3535-3543.

6) M.J. Thomas, B.P. Wynne and W.M. Rainforth. *Texture evaluation of titanium aerospace alloy Ti-834 using hot axisymmetric compression tests.* Materials Science Forum, Vol.495-497 (2005), pp. 693-698.

7) P.S. Davies, B.P. Wynne, W.M. Rainforth, Private communication.

8) RMI titanium (*http://rmititanium.com/tag/index.htm*). Retrieved on 2007-06-26.

9) C. Leyens, M. Peters. *Titanium and titanium alloys: fundamentals and applications*, (wiley-Vch, Weinheim, 2003).

10) W.F. Smith. *Structure and properties of engineering alloys*, (New York; London: McGraw-Hill, 1993).

11) *http://www.republicspecialmetals.com/remelt.html.* Retrieved on 2009-06-29.

12) M.J. Donachie. *Titanium: a technical guide*, (Materials Park, OH : ASM International, 2000).

13) M.A. Daeubler, D. Helm and D.F. Neal. *Applications of IMI 834 in aeroengines-a collaborative IMI/MTU programme*. Titanium 1990: Products and Applications, Florida; USA, pp. 78-87.

14) I.J. Polmear. *Light Alloys: from traditional alloys to nanocrystals, 4th Ed.* (Oxford: Elsevier Butterworth-Heinemann, 2006).

15) D.F. Neal. *Development of Timetal-834*, Materials Design Approaches and Experiences, Indianapolis, USA, ed. by Minerals and Materials Society/AIME, 2001, pp.78-87.

16) J. D. Destefani. ASM Handbook: Properties and Selection Nonferrous Alloys and Special-Purpose Materials. *Introduction to Titanium and Titanium Alloys*, Vol. 2 (1990), p.1770.

17) R.R. Boyer. *An overview on the use of titanium in the aerospace industry.* Materials science and engineering, Vol.A213 (1996), pp 103-114.

18) D.R. Askeland. *The science and engineering of materials, 3rd Ed.* (London: Chapman & Hall, 1996).

19) J.A. Hooker and P.J. Dorbar. *Metal matrix composites for aeroengines.* Materials Science and Technology, Vol.16 (2000), pp 725-731.

20) Military handbook, titanium and titanium alloys, Department of defence, united state of America (1974). *(http://www.combatindex.com/mil_docs/pdf/hdbk/0600/MIL-HDBK-697A.pdf).* Retrieved on 2009-06-29.

21) S. Kalpakjian. *Manufacturing processes of engineering materials, 2nd Ed.* (Wokingham: Addison-Wesley 1991).

22) J.D. Destefani. ASM Handbook: Properties and Selection Nonferrous Alloys and Special-Purpose Materials 10th Ed. Diagram courtesy of Wyman-Gordon Company, Vol. 2 (1990), p.1777.

23) *http://www.msm.cam.ac.uk/phase-trans/mphil/Trent1/sld028.htm.* Retrieved on 2009-06-29.

24) J. Eblinger, D. Helm. *Titanium in Aero-Engines*. Titanium-2003: Science and technology ed. by G. Lütjering and J. Albrecht, (WILEY-VCH Verlag GmbH & Co. KGaA, Weinheim, 2004) pp. 2846-2852.

25) W.D. Callister. *Materials science and engineering: an introduction, 5th Ed.* (New York: Wiley, 2000).

26) G. Lütjering, J.C. Williams. *Titanium.* (Berlin; London: Springer, 2003).

27) F. Warchomicka, M. Stockinger, H.P. Degischer. *Quantitative analysis of the microstructure of near β titanium alloy during compression tests.* Materials Processing Technology, Vol.177 (2006), pp. 473-477.

28) Courtesy Pete Davies, University of Sheffield.

29) http://www.msm.cam.ac.uk/phase-trans/2004/titanium/titanium.html. Retrieved on 2009-06-29.

30) G. Lütjering. *Influence of processing on microstructure and mechanical properties of (α+β) titanium alloys.* Materials Science and Engineering, Vol.A243 (1998), pp. 32-45.

31) C.R. Brooks. *Heat Treatment, Structure and Properties of Nonferrous Alloys.* (Metals Park: American Society for Metals, 1982).

32) H. M. Flower. *Microstructural development in relation to hot working of titanium alloys.* Materials Science and Technology, Vol.6 (1990), pp. 1082-1092.

33) J.C. Williams, E.A. Starke. *The role of thermomechanical processing in tailoring the properties of aluminium and titanium alloys.* (Metals Park: American Society for Metals, 1982).

34) C. Sauer, G. Lütjering. *Processing, microstructure and properties of Ti-6246.* Titanium '99: Science and Technology ed. by I.V. Gorynin, S.S. Ushkov, (CRISM, St. Peterburg, 2000) pp. 390-397.

35) O. M. Ivasishin, P. E. Markovsky. *Enhancing the mechanical properties of titanium alloys with rapid heat treatment.* JOM, Vol.48 (1996), pp. 48-52.

36) G. Lütjering, J. Albrecht, and O.M. Ivasishin. *Microstructure and mechanical properties of conventional titanium alloys.* The Minerals, Metals & Materials Society (1994), pp. 65-74.

37) G. Lütjering, *Property optimization through microstructural control in titanium and aluminum alloys.* Materials Science and Engineering, Vol. A263 (1999), pp. 117-126.

38) D. Helm. *Application of Ti-alloys as compressor discs and blades.* The Minerals, Metals & Materials Society (1999), pp. 291-298.

39) M. Brun, N. Anoshkin, G. Shakhanova. *Physical processes and regimes of thermomechanical processing controlling development of regulated structure in the α+β titanium alloys.* Materials Science and Engineering, Vol. A243 (1998), pp. 77-81.

40) A. Bhattacharjee, Vydehi A. Joshi, A.K. Gogia. *Effect of heat treatment on tensile behavior of a Ti-10V-2Fe-3Al alloy.* Titanium '99: Science and Technology ed. by I.V. Gorynin, S.S. Ushkov, (CRISM, St. Peterburg, 2000) pp. 529-535.

41) I. Weiss, F.H. Froes, D. Eylon, G.E. Welsch. *Modification of alpha morphology in Ti 6-4 by thermomechanical processing.* Metallurgical Transactions A, Volume17A (1986), pp. 1935-1947.

42) S.L. Semiatin, V. Seetharaman, I. Weiss. *Flow behavior and globularization kinetics during hot working of Ti–6Al–4V with a colony alpha microstructure.* Materials Science and Engineering, Vol. A263 (1999), pp. 257-271.

43) N. Stefansson, S.L. Semiatin. *Mechanisms of globularization of Ti 6-4 during static heat treatment.* Metallurgical and materials Transactions A, Volume 34A (2003), pp. 691-698.

44) I. Weiss, S. L. Semiatin. *Thermomechanical processing of alpha titanium alloys-an overview.* Materials Science and Engineering A, Vol.263 (1999), pp. 243-256.

45) E.P. DeGarmo, J.T. Black, R.A. Kohser. *Materials and processes in manufacturing 8th Ed* (New York; Chichester: Wiley, 1999).

46) G.W. Kuhlman, ASM Handbook Forming and forging. *Forging of Titanium Alloys*, Vol. 14 (1998), p. 600.

47) T. Ahmed, H. J. Rack. *Phase transformations during cooling in α+β titanium alloys.* Materials Science and Engineering A, Vol.243 (1998), pp. 206-211.

48) X.D. Zhang, P. Bonniwell, H.L. Fraser, W.A. Baeslack, D.J. Evans, T. Ginter, T. Bayha, and B. Cornell. *Effect of heat treatment and silicon addition on the microstructure development of Ti-6Al-2Cr-2Mo-2Sn-2Zr alloy.* Materials Science and Engineering A, Vol.343 (2003), pp. 210-226.

49) F.J. Gil, J.M. Manero, M.P. Ginebra, and J.A. Planell. *The effect of cooling rate on the cyclic deformation of β-annealed Ti-6Al-4V.* Materials Science and Engineering A, Vol.349 (2003), pp. 150-155.

50) O.N. Senkov, J.J. Valencia, S.V. Senkova, M. Cavusoglu, F.H. Froes. *Effect of cooling rate on microstructure of Ti-6Al-4V forging*. Materials Science and Technology, Vol.18 (2002), pp. 1471-1478.

51) R. Filip, K. Kubiak, W. Ziaja, J. Sieniawski. *The effect of microstructure on the mechanical properties of two-phase titanium alloys*. Journal of Materials Processing Technology, Vol.133 (2003), pp. 84-89.

52) G. Shen, D. Furrer. *Manufacturing of aerospace forgings*. Journal of Materials Processing Technology , Vol. 98 (2000), pp. 189-195.

53) B.D. Cullity, S.R. Stock. *Elements of x-ray diffraction* (Upper Saddle River, N.J: Prentice_Hall, 2001).

54) V. Randle, O. Englar. *Introduction to texture analysis. Macrotexture, Microtexture and orientation mapping* (Amsterdam: Gordon & Breach, 2000).

55) D. Hull, D.j. Bacon. *Introduction to Dislocations* 3rd Ed (Oxford: Pergamon, 1984).

56) S. Balasubramanian, L. Anand. *Plasticity of initially textured hexagonal polycrystals at high homologous temperatures: application to titanium*, Acta Materials, Vol.50 (2002), pp.133-148.

57) R.E. Smallman and R.J. Bishop. *Modern physical metallurgy & materials engineering, 6th Ed* (Oxford: Butterworth Heinemann, 1999).

58) D.R. Askeland. *The science and engineering of materials, 3rd Ed* (Boston, Mass. PWS Publishing Company, 1994).

59) G. E. Dieter. *Mechanical metallurgy, 3rd Ed*, (New York: McGraw-Hill, 1986).

60) H. Yoshimura, J. Nakahigashi. *Tensile and impact properties of mesoscopic-grained $\alpha+\beta$ type titanium alloys obtained through hydrogen treatments*. Journal of Alloys and Compounds, Vols.293-295 (1999), pp. 858-861.

61) J.L. Liu, Y.Q. Zhao, L. Zhou.*Microscopic segregation of Ti-6AL-4V ingot by VAR.*. Titanium-2003: Science and technology ed. by G. Lütjering and J. Albrecht, (WILEY-VCH Verlag GmbH & Co. KGaA, Weinheim, 2004) pp. 165-171.

62) H. Yokoyama, N. Mitsui, H. Ishida, K. Nakayama, T. Kusamichi. *Simulation of macroscopic segregation in titanium alloy VAR ingot*. Titanium' 2007: Science and technology ed. by M. Niinomi, S. Akiyama, M. Hagiwara, M. Ikeda, K. Maruyama (The Japan Institute of Metals, 2007), pp. 163-166.

63) M. Hatherby, W.B. Hutchinson. *An introduction to textures in metals* (London, Institution of Metallurgists, 1979).

64) U.F. Kocks, C.N. Tomé, H.-R. Wenk. *Texture and Anisotropy* (Cambridge: Cambridge University Press, 1998).

65) *http://www.ebsd.com/ebsdexplained.htm*. Retrieved on 2009-06-29.

66) HKL Technology Channel 5 User Manual.

67) T. Maitland, S. Sitzman. Electron Backscatter Diffraction (EBSD) technique and materials characterization examples. (*http://www.springer.com/cda/content/document/cda_downloaddocument/9780387333250-c2.pdf?SGWID=0-0-45-329891-p153034738*), Retrieved on 2009-06-29.

68) W.G. Burgers. The process of transition of the cubic body centered modification into the hexagonal close packed modification of zirconium. Physica, Vol.1 (1934), pp. 561-586.

69) D. Bhattacharyya, G.B. Viswanathan, S.C. Vogel, D.J. Williams, V. Venkatesh, H.L. Fraser. *A study of the mechanism of α to β phase transformation by tracking texture evolution with temperature in Ti–6Al–4V using neutron diffraction*. Vol.54 (2006), pp. 231-236.

70) A.D. McQuillan, M.K. McQuillan. *Titanium* (London: Butterworths Scientific Publications, 1956).

71) Z. S. Zhu, J. L. Gu, R. Y. Liu, N. P. Chen and M. G. Yan. *Variant selection and its effect on phase transformation textures* in *cold rolled titanium sheet.* Vol. 280 (2000), pp. 199-203.

72) M. Preuss, L. Pocock, P. Bate. *Variant selection and texture studies in Ti-6246.* Titanium' 2007: Science and technology ed. by M. Niinomi, S. Akiyama, M. Hagiwara, M. Ikeda, K. Maruyama, (The Japan Institute of Metals, 2007) pp. 527- 530.

73) T. Furuhara, T. Maki.*Variant selection in heterogeneous nucleation on defects in diffusional phase transformation and precipitation.* Vol. 312 (2001) pp. 145-154.

74) N. Stanford and P.S. Bate. Crystallographic variant selection in Ti-6Al-4V. Acta Materialia, Vol 52 (2004), pp. 5215-5224.

75) A. Kostrivas, L. S. Smith, M. F. Gittos. *Sustained load cracking in titanium alloys*. Titanium-2003: Science and technology ed. by G. Lütjering and J.

Albrecht, (WILEY-VCH Verlag GmbH & Co. KGaA, Weinheim, 2004) pp. 2091-2098.

76) M.R. Bache. A review of dwell sensitive fatigue in titanium alloys: the role of microstructure, texture and operating conditions. International journal of fatigue, Vol. 25(2003), pp. 1079-1087.

77) C.A. Stubbington, S. Pearson. *Effect of dwell on the growth of fatigue cracks in Ti-6Al-4V alloy bar.* Engineering Fracture Mechanics, Vol.10 (1978), pp. 723-756.

78) M. E. Kassner, Y. Kosaka, J. Hall. *Low-cycle dwell-time fatigue in Ti-6242.* Metallurgical and Materials Transactions A, Vol. 30 (1999), pp. 2383-2389.

79) W. J. Evans, M. R. Bache. *Hydrogen and fatigue behaviour in a near alpha titanium alloy.* Scripta Metallurgica et Materialia, Vol. 32 (1995), pp. 1019-1024.

80) P. Lefrance, V. Doquet, C. Ssarrazin-Baudoux, M. Gerland. *Creep fatigue interaction mechanisms in a near alpha titanium alloy at room temperature.* Titanium' 2007: Science and technology ed. by M. Niinomi, S. Akiyama, M. Hagiwara, M. Ikeda, K. Maruyama, (The Japan Institute of Metals, 2007) pp. 1357-1360.

81) M.R. Bache. *Processing titanium alloys for optimum fatigue performance.* International Journal of Fatigue, Vol. 21 (1999), pp. 105-111.

82) L. Germain, N. Gey, M.Humbert, A. Hazotte, P. Bocher and M. Jahazi. An automated method to analyze separately the microtextures of primary alpha grains and the secondary alpha inherited colonies in bimodal titanium alloys. Materials Characterisation, Vol. 54 (2005), pp. 216-222.

83) M.J. Thomas, B.P. Wynne and W.M. Rainforth. An alternative method to separate and analyse the microtextures and microstructures of primary alpha grains and transformed beta grains in near alpha titanium alloy Timetal 834. Materials Characterisation, Vol. 55 (2005), pp. 388-394.

84) M.J. Thomas, B.P. Wynne and W.M. Rainforth. *Texture evaluation of titanium aerospace alloy Ti 834 using hot axisymmetric compression tests.* Materials Science Forum, Vols. 495-497 (2005), pp. 693-698.

85) M.R. Bache, W.J. Evans, H.M. Davies. Electron back scattered diffraction (EBSD) analysis of quasi-cleavage and hydrogen induced fracture under cyclic

and dwell loading in titanium alloys. Journal of Materials Science, Vol.32 (1997), pp. 3435-3442.

86) N. Gey, M. Humbert, M.J. Philippe, Y. Combres. *Modeling the transformation texture of Ti-64 sheets after rolling in the β-field.* Materials Science and Engineering A, Volume 230 (1997) pp. 68-74.

87) K. Le biavant, S. Pommier, C. Prioul. *Local texture and fatigue crack initiation in ti-6Al-4V titanium alloy.* Fatigue and fracture of engineering materials and structure, Vol. 25 (2001), pp. 527-545.

88) L. Germain, P. Vo, N. Gey, M. Jahazi, M. Humbert, P. Bocher. *Development of sharp local α microstructures during α/β thermomechanical processing of TIMETAL 834.* Titanium' 2007: Science and technology ed. by M. Niinomi, S. Akiyama, M. Hagiwara, M. Ikeda, K. Maruyama (The Japan Institute of Metals, 2007), pp. 925-928.

89) P. Davies, B.P Wynne, W. M. Rainforth. *Characterisation of Texture and Microtexture Heterogeneities in a Timetal® 834 Billet.* Titanium' 2007: Science and technology ed. by M. Niinomi, S. Akiyama, M. Hagiwara, M. Ikeda, K. Maruyama (The Japan Institute of Metals, 2007), pp. 945-948

90) Private conversation with Pete Davies, University of Sheffield.

91) Private communications with TIMET, UK.

92) R.M. Poths, B.P. Wynne, W.M. Rainforth, S.L. Semiatin, J.H. Beynon. *Strain-path effects on microstructure evolution during the hot deformation of Ti-6Al-4V.* Titanium-2003: Science and technology ed. by G. Lütjering and J. Albrecht (WILEY-VCH Verlag GmbH & Co. KGaA, Weinheim, 2004), pp. 1243-1250.

93) N. Stefansson. Kinetics of static globularization of Ti 6Al-4V. PhD thesis (2000), The school of engineering the university of Dayton, *Ohio,US.*

94) J.G. Malcore, F. Montheillet. *Mechanical and microstructural behaviour of Ti 6-4 alloy in hot working range.* Titanium'84 Science and Technology ed. by G. Lütjering , U. Zwicker, W. Bunk (Deutshe gesellschaft fur metallkunde E. V., Oberursel 1985), p 1495.

95) M. L. Harper, Y. Kosaka, S.P. Fox. *Titanium metallography using heat tinting.* Titanium' 2007: Science and technology ed. by M. Niinomi, S. Akiyama, M. Hagiwara, M. Ikeda, K. Maruyama (The Japan Institute of Metals, 2007), pp. 785-788.

96) L. Bartlett. *An unusual phenomenon observed when anodising CP titanium to produce coloured surfaces for jewellery and other decorative uses.* Optics & Laser Technology, Vol. 38 (2006), pp. 440-444.

97) G. F. Vander Voort. *Metallography principles and practice,* (ASM International, Materials Park, 1999) pp. 182-185.

98) G. F. Vander Voort. *Applied metallography.* (New York; Wokingham: Van Nostrand Reinhold, 1986).

99) G. F. Vander Voort. ASM handbook volume 9: Metallography and microstructures. *Colour Metallography.* Vol. 9 (2004), pp. 135-162.

100) A. Aladjem. *Anodic oxidation of titanium and its alloys.* Journal of Material science, Vol.8 (1973) pp. 688-704.

101) O. Kubaschewski, B.E. Hopkins. *Oxidation of metals and alloys, 2nd Ed.* (London: Butterworths 1962).

102) N.F. Garza-Montes-De-Oca. *Oxidation and wear behaviour of a work roll grade high speed steel.* PhD thesis department of material engineering, University of Sheffield (2008).

103) Birks, N. Meier, G.H. *Introduction to high temperature oxidation of metals* (London: Edward Arnold, 1983).

104) J.P. Gueneau de Mussy, G. Langelaan, J. Decerf, J.L. Delplancke. *TEM and X-ray diffraction investigation of the structural characteristics of the microporous oxide film formed on polycrystalline Ti.* Scripta Materialia Vol. 48 (2003), pp. 23–29.

105) G. Hass. *Preparation, properties and optical applications of thin films of titanium dioxide.* Vacuum, Vol. 11 (1952), pp 331-345.

106) H.F. Flower, P.R. Swann. *An in situ study of titanium oxidation by high voltage electron microscopy.* Acta Materialia Vol. 22 (1974), pp 1339-1347

107) Nassau, K. *The causes of colour.* Scientific American, Vol. 243(1980), pp. 124–154.

108) *http://asm.confex.com/asm/aero07/techprogram/paper_16297.htm.* Retrieved on 2009-06-29.

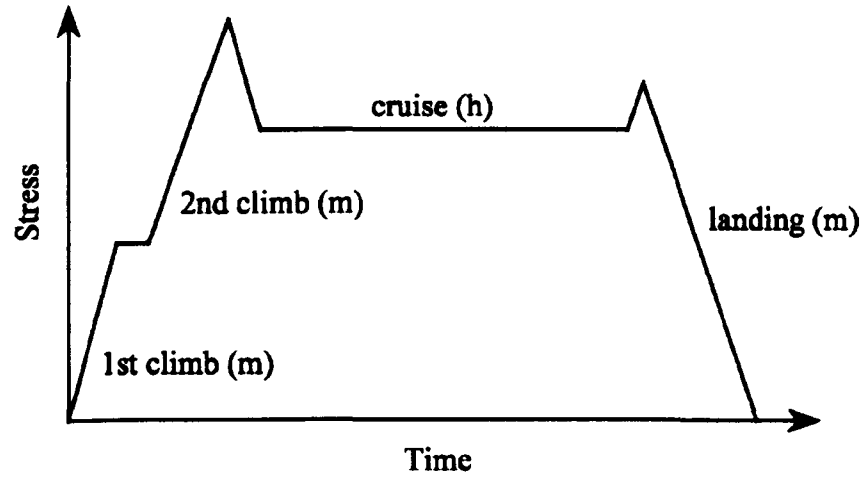

Figure 4.24 Schematic representation of a single duty cycle for a civil gas turbine engine. Operational timescales represented as minutes (m) or hours (h) [76].

The effects of a variety of parameters such as temperature [77], microstructure [76, 78], maximum applied stress [76], dwell periods length and hydrogen content on dwell sensitivity have been investigated in many studies [76, 79]. In addition, several studies specifically analysed the influence of the dwell periods on the crack growth rate of different titanium alloys with contrasted results. Some authors noticed an increase in crack growth rate under dwell loading while others observed no adverse effect of hold periods on crack propagation kinetics [80].

Detailed failure inspections have shown that the dwell failures characterised by the presence of "quasi-cleavage facets" had started subsurface. These features, produced during the early stages of fatigue fracture in all the near α and α+β titanium alloys are shaped on the basal plane of the hexagonal α crystallographic unit. The facets form by the gradual separation of slip damage concentrated within a persistent planar slip band. This observation has been described by the Stroh model (Figure 4.25) which proposes that slip within a favourably orientated (i.e. weak) grain with its basal plane inclined to the applied tensile axis causes a pile up at the border with an adjacent grain. A shear stress in the strong grain is then induced which initiates the formation of a slip band and under the combination of the applied cyclic tensile loading σ_l and the supplementary tensile stress σ, gradually opens up to form the centre of a fatigue crack. In easier terms stress is off loaded from the weakly orientated grains onto the stronger orientated grains [76].